frontiers | Research Topics

Isolation, modification, and characterization of the constituents in biomass and their bio-based applications, volume II

Edited by
Caoxing Huang, Xin Zhou, Chunlin Xu, Xianzhi Meng and Lei Wang

Published in
Frontiers in Bioengineering and Biotechnology

ISSN 1664-8714
ISBN 978-2-8325-2682-8
DOI 10.3389/978-2-8325-2682-8

About Frontiers

Frontiers is more than just an open access publisher of scholarly articles: it is a pioneering approach to the world of academia, radically improving the way scholarly research is managed. The grand vision of Frontiers is a world where all people have an equal opportunity to seek, share and generate knowledge. Frontiers provides immediate and permanent online open access to all its publications, but this alone is not enough to realize our grand goals.

Frontiers journal series

The Frontiers journal series is a multi-tier and interdisciplinary set of open-access, online journals, promising a paradigm shift from the current review, selection and dissemination processes in academic publishing. All Frontiers journals are driven by researchers for researchers; therefore, they constitute a service to the scholarly community. At the same time, the *Frontiers journal series* operates on a revolutionary invention, the tiered publishing system, initially addressing specific communities of scholars, and gradually climbing up to broader public understanding, thus serving the interests of the lay society, too.

Dedication to quality

Each Frontiers article is a landmark of the highest quality, thanks to genuinely collaborative interactions between authors and review editors, who include some of the world's best academicians. Research must be certified by peers before entering a stream of knowledge that may eventually reach the public - and shape society; therefore, Frontiers only applies the most rigorous and unbiased reviews. Frontiers revolutionizes research publishing by freely delivering the most outstanding research, evaluated with no bias from both the academic and social point of view. By applying the most advanced information technologies, Frontiers is catapulting scholarly publishing into a new generation.

What are Frontiers Research Topics?

Frontiers Research Topics are very popular trademarks of the *Frontiers journals series*: they are collections of at least ten articles, all centered on a particular subject. With their unique mix of varied contributions from Original Research to Review Articles, Frontiers Research Topics unify the most influential researchers, the latest key findings and historical advances in a hot research area.

Find out more on how to host your own Frontiers Research Topic or contribute to one as an author by contacting the Frontiers editorial office: frontiersin.org/about/contact

Isolation, modification, and characterization of the constituents in biomass and their bio-based applications, volume II

Topic editors

Caoxing Huang — Nanjing Forestry University, China
Xin Zhou — Nanjing Forestry University, China
Chunlin Xu — Åbo Akademi University, Finland
Xianzhi Meng — The University of Tennessee, Knoxville, United States
Lei Wang — Ocean University of China, China

Citation

Huang, C., Zhou, X., Xu, C., Meng, X., Wang, L., eds. (2023). *Isolation, modification, and characterization of the constituents in biomass and their bio-based applications, volume II*. Lausanne: Frontiers Media SA.
doi: 10.3389/978-2-8325-2682-8

Table of contents

frontiers | Frontiers in Bioengineering and Biotechnology

MINI REVIEW
published: 20 June 2022
doi: 10.3389/fbioe.2022.937266

Fabrication, Properties, and Biomedical Applications of Calcium-Containing Cellulose-Based Composites

Ru-Jie Shi[1]*, *Jia-Qi Lang*[1], *Tian Wang*[1], *Nong Zhou*[1] and *Ming-Guo Ma*[1,2]*

[1]Chongqing Engineering Laboratory of Green Planting and Deep Processing of Famous-region Drug in the Three Gorges Reservoir Region, College of Biology and Food Engineering, Chongqing Three Gorges University, Chongqing, China, [2]Research Center of Biomass Clean Utilization, Engineering Research Center of Forestry Biomass Materials and Bioenergy, Beijing Key Laboratory of Lignocellulosic Chemistry, College of Materials Science and Technology, Beijing Forestry University, Beijing, China

Calcium-containing cellulose-based composites possess the advantages of high mechanical strength, excellent osteoconductivity, biocompatibility, biodegradation, and bioactivity, which represent a promising application system in the biomedical field. Calcium-containing cellulose-based composites have become the hotspot of study of various biomedical fields. In this mini-review article, the synthesis of calcium-containing cellulose-based composites is summarized via a variety of methods such as the biomimetic mineralization method, microwave method, co-precipitation method, hydrothermal method, freeze-drying method, mechanochemical reaction method, and ultrasound method. The development on the fabrication, properties, and applications of calcium-containing cellulose-based composites is highlighted. The as-existed problems and future developments of cellulose-based composites are provided. It is expected that calcium-containing cellulose-based composites are the ideal candidate for biomedical application.

Keywords: cellulose, composites, hydroxyapatite, calcium carbonate, biomedical application

OPEN ACCESS

Edited by:
Caoxing Huang,
Nanjing Forestry University, China

Reviewed by:
Xiaoju Wang,
Åbo Akademi University, Finland
Chao Qi,
Chongqing University, China

***Correspondence:**
Ru-Jie Shi
20050020@sanxiau.edu.cn
Ming-Guo Ma
mg_ma@bjfu.edu.cn

Specialty section:
This article was submitted to Bioprocess Engineering, a section of the journal Frontiers in Bioengineering and Biotechnology

Received: *06 May 2022*
Accepted: *16 May 2022*
Published: *20 June 2022*

Citation:
Shi R-J, Lang J-Q, Wang T, Zhou N and Ma M-G (2022) Fabrication, Properties, and Biomedical Applications of Calcium-Containing Cellulose-Based Composites. Front. Bioeng. Biotechnol. 10:937266. doi: 10.3389/fbioe.2022.937266

1 INTRODUCTION

Cellulose received considerable attention due to its properties of mechanical strength, biocompatibility, and biodegradation and its wide applications in clothing, paper, biofuel, and biomedical fields (Eichhorn *et al.*, 2010; Moon et al., 2011; Huang et al., 2020,2022; Wang et al., 2021; Kang et al., 2022). There are more than 30,000 studies that used "***cellulose***" as the "***title***" on the Web of Science over the last 10 years, indicating that cellulose has become a hot research topic. Calcium-containing inorganic functional materials mainly included hydroxyapatite ($Ca_{10}(PO_4)_6(OH)_2$, HA), $CaCO_3$, calcium silicate, and $CaSO_4$ (Tran and Webster, 2009). HA is used in the fields including drug delivery, toothpaste additive, and dental implants because of its biocompatibility, bioactivity, and biological properties (Suchanek and Yoshimura, 1998; Chu et al., 2002; Ma et al., 2006; Ma and Zhu, 2009; Ma, 2012). Moreover, carbonated hydroxyapatite (CHA), containing carbonate ions of 6~8 mass%, shows high bioactivity in comparison to that of HA (Gibson and Bonfield, 2002; Landi et al., 2003; Morales-Nieto *et al.*, 2013). $CaCO_3$ is abundant in organisms (Politi et al., 2004). The calcium-containing cellulose-based composites combined the characteristics of cellulose and calcium-containing inorganic materials, producing new properties by synergistic effect

(Hokkanen et al., 2016). Therefore, it is expected that calcium-containing cellulose-based composites meet the requirements of applications. As early as 2010, the progress in the fabrication of calcium-based inorganic biodegradable nanomaterials was reviewed by Ma and Zhu (2010). Qi *et al.* (2018) reviewed the synthesis and properties of calcium-based biomaterials for diagnosis, treatment, and theranostics. In the previous review study, we summarized the recent development of multifunctional cellulose and cellulose-based nanocomposites adsorbents (Shi et al., 2022).

In recent years, there are rapid demands for biomedical materials (Habraken et al., 2016; Hu et al., 2018; Fu et al., 2019c; Yi et al., 2020; Yuan et al., 2021). For example, the disabled and bone injury patients need a lot of bone repair materials, the patients with cardiovascular disease need artificial heart valves, and the patients with renal failure need kidney dialyzers. It was reported that the composites, consisting of inorganic materials such as HA, $CaCO_3$, calcium silicate, SiO_2, and polymer including collagen, chitosan, chitin, hyaluronic acid, cellulose, poly lactic acid (PLA), poly glutamic acid (PGA), and poly caprolactone (PCL), were the new generation biomedical materials in the 1990s, which had the features of bioactivity and biodegradability to meet the clinical needs (Kaur et al., 2015; Liu et al., 2020). Chan *et al.* (2002) reported the synthesis of polypropylene/calcium carbonate nanocomposites. In fact, it is believed that cellulose is an organic biomedical material, meanwhile, calcium-containing inorganic functional composites are inorganic biomedical materials. The calcium-containing cellulose-based composites are promising biomedical materials to meet the requirements of applications (Oprea and Voicu, 2020).

This current mini-review study gives an overview of the synthesis, properties, and applications of calcium-containing cellulose-based composites. In section two, various methods including the biomimetic method, the microwave method, the co-precipitation method, the hydrothermal method, the freeze-drying method, the mechanochemical reaction method, and the ultrasound method were summarized for the synthesis of calcium-containing cellulose-based composites. In section three, the properties of calcium-containing cellulose-based composites such as mechanical properties, degradation, bioactivity, biocompatibility, feasibility, viability, cytocompatibility, cell-guiding property, antibacterial properties, and ion-exchangeability were also reviewed. In addition, the applications of these composites were described in the tissue engineering scaffolds, histological, drug delivery, and wastewater treatment. Finally, the future developments of calcium-containing cellulose-based composites were suggested.

1.1 Synthesis of Calcium-Containing Cellulose-Based Composites

1.1.1 Biomimetic Mineralization Method

Biomineralization refers to the generation process of inorganic minerals by the biological macromolecules of the organism (Addadi, Raz, and Weiner, 2003). In comparison to general mineralization, the process of biomineralization involved the biological macromolecules, cells, and organic matrix (Gower, 2008). Based on the biomineralization mechanism, the biomimetic synthesis method is an important route for creating biomedical materials by imitating the synthetic process of natural reaction and structure (Dorozhkin, 2011). The biomimetic synthesis method was developed to fabricate biomedical materials (Tas, 2000). Addadi, Raz, and Weiner (2003) reviewed the amorphous calcium carbonate by the biomineralization method.

Fang *et al.* (2009) prepared bacterial cellulose (BC)/HA nanocomposite scaffolds *in vitro* biocompatibility by the biomimetic technique. As for the fabrication of cellulose/HA composites via the biomimetic method, Wan and coworkers had done system work. In 2006, they developed the biomimetic precipitation of CHA with low crystallite size and crystallinity on BC from simulated body fluid (SBF) (Hong et al., 2006). Then, the biomimetic method was reported to synthesize CHA/BC composites by soaking phosphorylated and $CaCl_2$-treated BC fibers in the SBF (Wan et al., 2006). After that, they applied the biomimetic method to fabricate CHA/BC nanocomposites with a three-dimensional (3D) network and crystallinities below 1% (Wan et al., 2007). It found the formation of HA on BC in the existence of phosphorylation. Furthermore, HA/BC nanocomposites were also carried out via the biomimetic route (Zhang et al., 2009). It carried out the growth of calcium phosphate via phosphorylation reaction.

Generally, HA has a ratio of 1.67 for Ca/P. However, calcium-deficient HA is always obtained with a ratio of Ca/P below 1.67 in nature. Hutchens *et al.* (2006) first synthesized calcium-deficient HA in the BC hydrogel. BC was used as a template for the biomimetic fabrication of apatite. Shi *et al.* (2009) synthesized calcium-deficient HA/BC nanocomposites with improved mineralization efficiency by combining the alkaline treatment and biomimetic mineralization process. Zimmermann and coworkers (Zimmermann et al., 2011) designed calcium-deficient HA/BC nanocomposites using the biomimetic approach in dynamic SBF for bone healing applications. Hammonds *et al.* (2012) prepared calcium-deficient HA/BC composites.

It reports that SBF is a very important media for the formation of HA during the process of biomimetic mineralization. The synthesis of cellulose fabrics with hydroxy carbonated apatite using the biomimetic method in SBF was reported by Hofmann *et al* (2006). Cromme et al. (2007). In Cromme's study (2007), regenerated cellulose (RC) films were obtained with hydrochloric acid vapors, in which the calcium phosphate was formed in SBF. Yin *et al.* (2011) prepared HA/BC nanocomposites by the biomimetic mineralization method. It found that CHA nanorods were grown *in vitro* along with the network of BC via the dynamic SBF treatment. Rodriguez, Renneckar, and Gatenholm (2011) used the electrospinning method to produce cellulose acetate (CA) scaffolds. Li *et al.* (2012) synthesized electrospun cellulose nanofiber (CNF)/HA composites with micro-, meso-, and macro-pores in SBF. It achieved the growth of HA along the fibers in the composites. Petrauskaite *et al.* (2013) developed biomimetic mineralization using the cellulose porous matrix in the SBF solution. It achieved

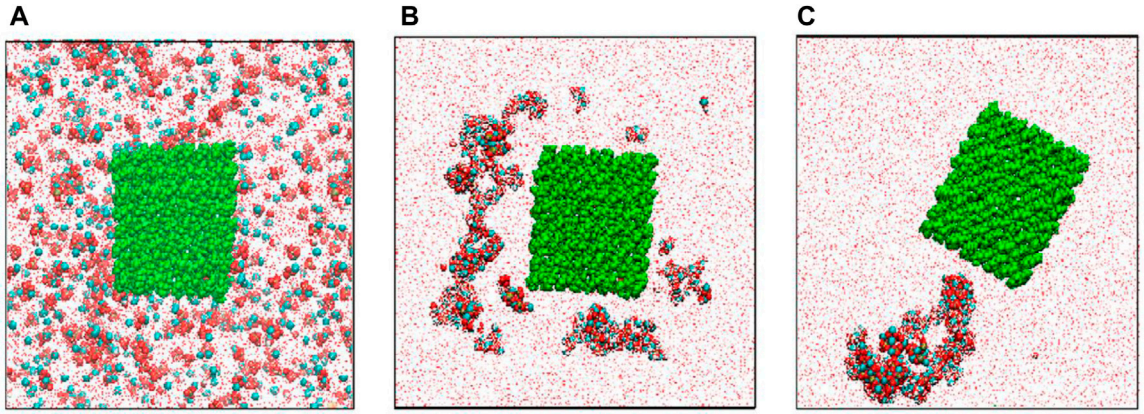

FIGURE 1 | Distributions of ions in the modeling cell: **(A)** in the initial state, **(B)** in 12 ns, and **(C)** at the end (100 ns) of simulation. Red balls-O atoms, cyan balls-Ca^{2+} ions, yellow balls-P atoms, white balls-H atoms, green balls-cellulose atoms (Lukasheva and Tolmachev, 2016).

the improved cell adhesion and growth rate on the porous cellulose matrix. Garai and Sinha (2014) reported the biomimetic synthesis of 3D micro/macro CMC/HA nanocomposites. 3D nanocomposite structures were due to the ionic/polar or electrostatic interactions of HA impregnated CMC matrix. It obtained compressive strength of 1.74–12 MPa and a compressive modulus of 157–330 MPa.

Lukasheva and Tolmachev (2016) presented biomimetic synthesis and molecular dynamics simulation of HA/BC nanocomposites. The CP crystals nucleate initially in solution, and then adsorbed on the surfaces of BC nanofibrils (**Figure 1**). Yang *et al.* (2016) applied the biomimetic process to prepare oxidized BC/HA/gelatin nanocomposites with the 3D network for a potential bone scaffold material. The nanocomposites have a tensile strength of 0.3 MPa and a complete degradation time of approximately 90 days in SBF. Kim *et al.* (2018) fabricated 3D pore-structure biomimetic cellulose/calcium-deficient HA composite scaffolds for bone tissue engineering. It found bone mineralization in the composite scaffold via cellular responses using preosteoblasts (MC3T3-E1). Liu *et al.* (2019) used BC hydrogel to synthesize biomimetic multilevel HA. It observed the weak coordination between the hydroxyl groups of BC molecule with Ca^{2+}. Okuda *et al.* (2022) applied the biomimetic approach to preparing the CMC/HA composites with a stable interface. It achieved the flexural strength of 113 ± 2 MPa and the elastic modulus of 7.7 ± 0.3 GPa. It found an ionic interaction between Ca^{2+} and COO-.

Li and Wu (2009) reported the monodisperse rosette-like calcite mesocrystals in CMC by the biomimetic gas-diffusion method. Xiao *et al.* (2011) prepare calcium carbonate on RC fibers in ethanol-water mixed solvents by the mineralization method. It found that twin-sphere-based vaterite, zonary, and rod-like calcite were embedded in fibers. Liu *et al.* (2011) used electrospun CA fibers modified by poly acrylic acid (PAA) as scaffolds for the mineralization of $CaCO_3$. It showed the calcite film coatings with needle-like shapes on the surfaces of CA fibers. The carboxylic groups of acidic PAA molecules interacted with the OH moieties of CA, then bent with Ca^{2+} ions on the surfaces of CA fibers. Rauch *et al.* (2012) synthesized calcite with minor fractions of aragonite on and in RC gel membranes by a diffusion-driven mineralization approach. The experimental result indicated that the calcium carbonates were assembled from building blocks. Liu *et al.* (2013) fabricated BC/lamellar $CaCO_3$ hybrid induced by egg white *in situ* by the biomimetic mineralization method. The hybrid had a rough surface and an elaborate 3D structure with controllable porosity. Vyroubal *et al.* (2013) fabricated $CaCO_3$ in BC by the biomimetic method. Paulraj *et al.* (2017) used $CaCO_3$ as a template to fabricate microcapsules with controllable permeability properties by the layer-by-layer method in plant polysaccharides of pectin, cellulose nanofibers, and xyloglucan. It obtained the spherical $CaCO_3$ with 16 ± 4 μm (**Figure 2A**), the $CaCO_3$ $(AP/CNF)_5AP/XyG$ microparticles with a thickness of ~60 nm (**Figures 2B, C**), and hollow microcapsule structures after complete core removal (**Figure 2D**).

The biomimetic mineralization method was widely used to synthesize biomaterials, induce bioactive materials, and investigate the synthetic mechanism. However, it needs long reaction times, complex reaction procedures, and precise control conditions. Recently, Qi *et al.* (2019) used the biomolecule-assisted green method for the synthesis of nanostructured calcium phosphates and investigated their biomedical applications.

1.1.2 Microwave-Assisted Method

The microwave-assisted method is a greener technology due to its characteristics of reduced energy consumption, short reaction time, and high yield (Zhu and Chen, 2014). Over the past years, the microwave-assisted method was used to fabricate metals, metal oxides, and metal sulfides (Ma et al., 2014; Meng et al., 2016). In the several review articles, one can find the applications of the microwave-assisted method (Tsuji et al., 2005; Polshettiwar et al., 2009; Baghbanzadeh et al., 2011). For example, Tsuji *et al.* (2005) reviewed the development of the microwave-assisted synthesis of metallic nanostructures in solution. Polshettiwar *et al.* (2009) described the applications of the rapid and sustainable microwave-assisted route to synthesize organics and nanomaterials.

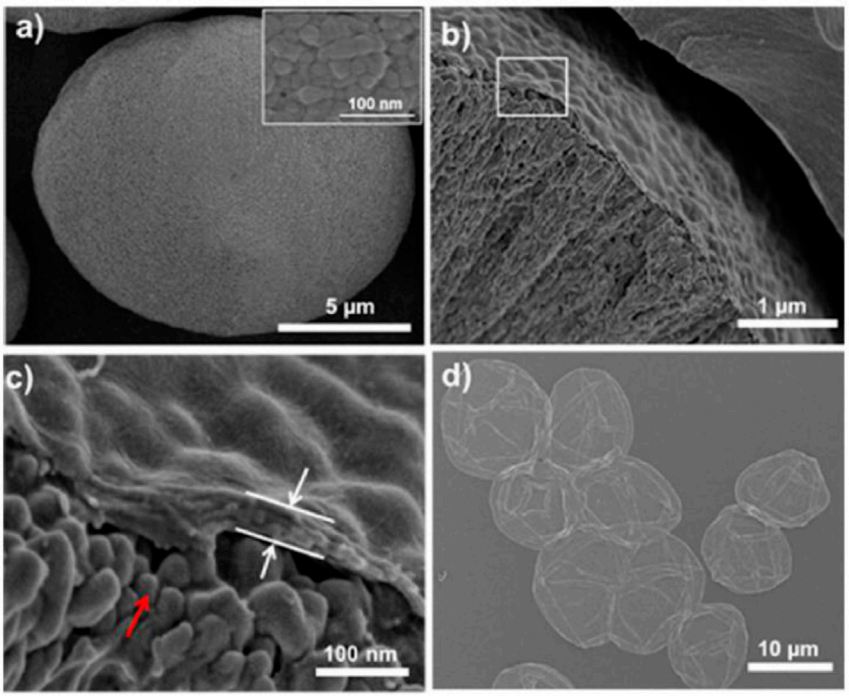

FIGURE 2 | The SEM images of **(A)** spherical $CaCO_3$ microparticles. The inset: details of the $CaCO_3$ surface. **(B)** Cross-section of $CaCO_3$ $(AP/CNF)_5AP/XyG$ microparticles, and **(C)** is a higher magnification of **(B)**. The red arrow points to the surface morphology of $CaCO_3$ microparticles. The white arrows point to the AP/CNF multilayer. **(D)** The SEM image of $(AP/CNF)_5AP/XyG$ microcapsules after core removal (Paulraj et al., 2017).

In the earlier studies, the cellulose/HA nanocomposites were fabricated by the microwave-assisted method (Ma et al., 2010). It found the homogeneous dispersion of HA nanoparticles with a narrow size distribution in the cellulose matrix. The cellulose/CHA nanocomposites were also obtained via the microwave-assisted method in the NaOH/urea solution (Jia et al., 2010b). The cellulose/CHA nanocomposites with a rough surface and aggregated CHA nanorods were also carried out in ionic liquid (IL) by the microwave-assisted method (Ma et al., 2011). It noted that F-substituted HA could enhance the acid resistance and stability of HA. The cellulose/F-substituted HA nanocomposites were also obtained in ILs via the microwave-assisted method (Jia et al., 2012a). It found the increased number of F-substituted HA with increasing heating time. The lignocellulose/HA nanocomposites were also carried out via the microwave-assisted rapid synthesis method (Fu et al., 2015). Both the morphologies and sizes of HA in the nanocomposites were adjusted via heating time. Fu *et al.* (2016) developed the microwave-assisted hydrothermal method for the synthesis of cellulose/HA nanocomposites using sodium dihydrogen phosphate dihydrate or adenosine 5-triphosphate disodium salt, creatine phosphate disodium salt tetrahydrate, or D-fructose 1,6-bisphosphate trisodium salt octahydrate. All the phases, sizes, and morphologies of the nanocomposites were affected by phosphate sources. It obtained various HA morphologies of nanorods, pseudo-cubic, pseudo-spherical, and nano-spherical particles.

The preparation of calcium sulfate nanowires was reported by thermal transformation of calcium dodecyl sulfate in the ethylene glycol and *N,N*-dimethylformamide mixed solvents (Li et al., 2008). The synthesis of cellulose/calcite composites was group explored using alkali extraction cellulose and MCC using the microwave-assisted method (Ma et al., 2012a). It achieved composites with better crystallinity using MCC than that of alkali extraction cellulose. Moreover, it found cellulose fibers and $CaCO_3$ particles using alkali extraction cellulose, and irregular cellulose and $CaCO_3$ microspheres using MCC. The cellulose/$CaCO_3$ nanocomposites were formed in the alkali extraction of cellulose by the microwave-assisted IL method (Ma et al., 2013). IL acted as the solvent for absorbing microwave, dissolving cellulose, and synthesizing cellulose/$CaCO_3$ nanocomposites, and it was found that the change morphologies of $CaCO_3$ from polyhedral to cube to particle occurred with increasing cellulose concentration. Cytotoxicity experiments demonstrated the cellulose/$CaCO_3$ nanocomposites with good biocompatibility. Cheng *et al.* (2016) used the microwave method to fabricate cellulose/$CaCO_3$ composites in an IL/ethylene glycol mixed solution within 10 min. It was found that ILs favored the synthesis of composites. The microwave IL method was reported for the fabrication of cellulose/calcium silicate nanocomposites in ethylene glycol (Jia et al., 2011a). ILs had an effect on the composite of cellulose and calcium silicate. After that, the cellulose/calcium silicate nanocomposites were obtained by the microwave method in ILs and recycled ILs (Jia et al., 2011b). Both the size and microstructure of cellulose/

calcium silicate nanocomposites were influenced by starting ILs and recycled ILs.

In general, the microwave method is green, rapid, and environmentally friendly for the synthesis of cellulose-based nanocomposites. In particular, considerable study should be carried out on the fabrication, structure, and property of cellulose/HA nanocomposites by the microwave-assisted method. This rapid microwave-assisted method is completely different from the aforementioned biomimetic synthesis method, but it could significantly shorten the reaction time and improve the reaction selectively and the yield, and be suitable for the large-scale synthesis in modern industrial production.

1.2 Co-Precipitation Method

As a traditional synthesis method, the co-precipitation method is an important strategy to obtain homogeneous composites with small size and narrow size distribution (Doerner and Hoskins, 1925; Park et al., 2003). The co-precipitation method is similar to the precipitation method, which is cumbersome and time-consuming. As early as 1925, the co-precipitation method was applied for the preparation of radium and barium sulfates by Doerner and Hoskins (1925).

Zakharov *et al.* (2005) obtained HA/CMC composites with a pore structure via the co-precipitation method for biomedical applications. Grande *et al.* (2009) synthesized the CHA/BC nanocomposite via a wet chemical precipitation method. In Kumar's study (Kumar et al., 2010), the co-precipitation method was developed for the preparation of biomimetic CMC/HA nanocomposites. Nunez *et al.* (2020) used *in situ* wet chemical precipitation technique to synthesize BC/HA nanocomposite adsorbent. It carried out a removal capacity of 192 mg g^{-1} in batch experiments and 188 mg g^{-1} in packed-bed column systems for Pb(II). Tabaght *et al.* (2021) developed a dissolving and precipitation technique for the synthesis of biocompatible HA/cellulose composite for bone substitute. Sivasankari *et al.* (2021) reported a chemical precipitation technique to prepare HA incorporated CA/polyetherimide membrane with biocompatibility for adsorption and biomedical applications. The co-precipitation method is an important route for the preparation of HA/cellulose nanocomposites. It is known that the synthesis of HA is a double decomposition reaction with rapid nucleation and growth rate. So it is not easy to obtain homogeneous cellulose/HA composites by the co-precipitation method.

Ciobanu *et al.* (2010) reported the cellulose fibers with $CaCO_3$ by the *in situ* precipitation method. $CaCO_3$ was precipitated into the lumen and wall pores of fibers by the *in situ* precipitation method. The cellulose/calcium silicate nanocomposites were carried out by the precipitation method (Li et al., 2010). Stroescu *et al.* (2012) deposed $CaCO_3$ on BC membranes using sodium dodecyl sulfate (SDS) and cetyl trimethylammonium bromide (CTAB) by a precipitation reaction. It obtained the calcium carbonate with rhombohedral and flower-like by adjusting the surfactant type and concentration. Zhu *et al.* (2020) prepared RC/calcium carbonate biocomposite films with flexibility, optical properties, mechanical strength, and thermal stability by *in situ* precipitation. It found a tensile strength of 84.7 ± 1.5 MPa for biocomposite.

1.3 Hydrothermal Method

The hydrothermal method refers to the synthesis of functional materials with water as the solvent in the vessel sealing at high temperature and high-pressure conditions. In the mid-19th century, geologists simulated the mineralization in nature and found the hydrothermal method. After 1900, the theory of hydrothermal synthesis was constructed. Then, the hydrothermal method was developed to synthesize the functional materials (Byrappa and Adschiri, 2007). It reported the hydrothermal synthesis of 0D, 1D, and 2D materials and composites (Feng and Xu, 2001).

The hydrothermal method of lignocelluloses had an effect on cellulose, hemicellulose, and lignin (Garrote et al., 1999). Jiang and Zhang (2009) prepared HA nanorods with well-controlled particle size and porosity through the hydrothermal method using phosphate ester as the structure-directing agent and sodium salt CMC as the template. The hydrothermal method was applied to prepare cellulose/CHA nanocomposites with CHA nanostructures dispersed in the cellulose matrix in a NaOH-urea aqueous solution (Jia et al., 2010a). In comparison with the biomineralization method, the hydrothermal method needs high temperature and high-pressure conditions, which restrain the wide application in the synthesis of biomedical composites. Moreover, Palaveniene *et al.* (2019) reported the hydrothermal synthesis of an osteoconductive 3D porous RC/HA composite scaffold with a porosity of 85% for bone tissue regeneration. The MG-63 cells proliferated well on scaffolds via *in vitro* cell culture. Pieper *et al.* (2020) prepared cellulose/HA biofilm with good thermal stability using a microwave-assisted hydrothermal synthesis at 140°C for 5 min.

The hydrothermal method was developed to obtain cellulose/$CaCO_3$ bio-nanocomposites with good biocompatibility in the NaOH/urea solution (Jia et al., 2012b). The urea was also used as the CO_3^{2-} source for the preparation of $CaCO_3$. Furthermore, the fabrication of wood powder/$CaCO_3$ composites was investigated by the hydrothermal method (Ma et al., 2012b). This work utilized all the main components of lignocelluloses, compared with cellulose-based composites.

1.3.1 Other Synthesis Methods

The freeze-drying method might be more suitable for the synthesis of biomedical composites, which spray the solution to the organic liquid, then freeze instantaneous, sublimate, dehydrate, and decomposed to produce the comparatively loose products. The freeze-drying method was applied to synthesize cellulose/HA composites by Jiang group (Jiang L. et al., 2008). They incorporated CMC into HA/chitosan to obtain HA/chitosan/CMC composite as 3D scaffold by the freeze-drying method. Then, they applied the freeze-drying method for the preparation of the HA/chitosan/CMC porous composite scaffolds with different weight ratios (Jiang L.-Y. et al., 2008). After that, HA/chitosan and CMC composite scaffolds with good cell biocompatibility and tissue biocompatibility were also carried out by the freeze-drying method (Jiang et al., 2009a).

Generally, the freeze-drying method has characteristics of eliminating 95–99% water, obtaining the loose and porous materials, maintaining the original structure and volume, and restraining microbial growth and enzyme function, which is widely used in the pharmaceutical industry, food industry, and biomedical fields. It noted that these are still some problems requiring improvement for this method. Moreover the requirement of expensive equipment, this method is just a means of posttreatment measure. Of course, this method always needs to combine with other synthetic methods. Chong *et al.* (2015) reported the preparation of calcite $CaCO_3$-loaded cellulose aerogel for removal of Congo Red (CR) from aqueous solution by freeze-drying. The aerogel had significantly enhanced adsorption capacity toward CR. It obtained the maximum adsorption capacity of 75.81 mg g^{-1} for the $CaCO_3$-cellulose aerogel. Narwade *et al.* (2019) used the one-directional freeze-drying technique to obtain flexible and lightweight HA/CNFs nanocomposite films. It observed the detection limit of ammonia at a concentration as low as 5 ppm, sensitivity up to 575%, and response/recovery (210/30s) for nanocomposite films.

The mechanochemical reaction method was also called the high-energy ball milling method. As an energy-saving and efficient technology for the preparation of materials, it significantly reduces the reaction activation energy, refines the grain, and enhances the bonding interface. Yoshida and coworkers (Yoshida et al., 2005) prepared the cellulose/B-type CHA composites through mechanochemical reaction. Then, they applied this method to synthesize cellulose/CHA composites with a bending streng of 10–13 thMPa and Young's modulus of 1.5–2.2 GPa (Yoshida et al., 2006). In general, the mechanochemical reaction method has the disadvantages of low efficiency and energy consumption, as a supplementary method.

The sonochemical method is a green methodology, which has characteristics of intense local heating, high pressures, and extremely rapid cooling rates (Gedanken, 2004; Bang and Suslick, 2010; Cravotto and Cintas, 2010; Chemat et al., 2011). The ultrasound had wide applications in organic and inorganic synthesis. Stoica-Guzun *et al.* (2012) investigated the $CaCO_3$ deposition on BC membranes by ultrasonic irradiation. It obtained the calcite in the presence of ultrasonic irradiation and vaterite in the absence of ultrasonic irradiation. Moreover, it found cubes of calcite to spherical and flower-like vaterite particles in the presence of ultrasonic irradiation. Fu *et al.* did a system study about calcium-containing cellulose-based composites by the ultrasound method. For example, the influences of synthesis strategies of the microwave method and ultrasound method were investigated on the $CaCO_3$ in the cellulose matrix (Fu et al., 2013a). It obtained the vaterite spheres with a diameter of about 320–600 nm by the ultrasound method. The $CaCO_3$ crystals with good biocompatibility on the cellulose substrate had biomedical applications. The growth mechanism of vaterite was explored on the cellulose matrix via the sonochemistry process (Fu et al., 2013b). It achieved the vaterite polymorph using Na_2CO_3 as a reactant in ethylene glycol in the cellulose by the sonochemistry method. Moreover, cellulose/HA nanocomposites with good cytocompatibility were obtained via the sonochemical synthetic method for application in protein adsorption (Fu LH. et al., 2019). It achieved a relatively high protein adsorption ability. Fu *et al.* (2019a) used the sonochemical method to obtain cellulose/vaterite nanospheres with a diameter of 206–246 nm. It found cytocompatibility and a relatively high protein adsorption ability for cellulose/vaterite nanocomposites. Nicoara *et al.* (2020) used the co-precipitation method and ultrasound exposure to *in situ* and *ex situ* design HA/BC/Ag composite with excellent biocompatibility, bioactivity, and antibacterial properties for tissue engineering. It carried out a homogenous porous structure and high water absorption capacity for the composites.

1.4 Properties and Applications of Calcium-Containing Cellulose-Based Composites

1.4.1 Properties and Applications of Cellulose/Hydroxyapatite Composites

It has been accepted that cellulose/HA composites are promising bone substitutes. Therefore, it is very important for cellulose/HA composites to have mechanical properties analogous to natural bone. Yoshida *et al.* (2006) synthesized cellulose/CHA composites with good mechanical properties and bioactivity through mechanochemical reactions. Pure CHA had a density of 1.26 g cm^{-3}, bending strengths of 5.4 MPa, and Young's modulus of 1.58 GPa. However, the cellulose/CHA composites displayed a density of 1.59 g cm^{-3}, bending strengths of 13.0 MPa, and Young's modulus of 2.18 GPa. By immersing in SBF for some time, HA with low crystallinity was carried out at the surface of cellulose/CHA composites, displaying good bioactivity. Undoubtedly, all the mechanical properties, bioactivity, and high chemical durability are very important for cellulose/CHA composites to use as bioactive bone substitutes.

As for HA/chitosan/CMC composites, Jiang and coworkers did system research on the mechanical property, swelling behavior, degradation, and bioactivity. Jiang L. Y. et al. (2008) prepared HA/chitosan/CMC composites by the freeze-drying method. It was found that the HA/chitosan/CMC composites with 30 wt% CMC had a pore size of 100–500 μm and porosity of 77.8%, the compressive strength of 3.54 MPa, and bioactivity *in vitro* in the SBF soaking. Then, the HA/chitosan/CMC composites with high bioactivity and adjustable biodegradation rate were carried out by the cosolution method (Jiang et al., 2009b). It achieved the value compressive strength of 85.03 74.91 MPa in the HA/chitosan/CMC composites for weight ratios of 70/15/15, compared with that of HA/chitosan (61.26 MPa). After that, they also prepared HA/chitosan/CMC composite membrane with the highest tensile strength of 40 MPa by self-assembly of static electricity. By soaking in 1.5 SBF, it observed the increased number of apatite particles on the surface of the HA/chitosan/CMC composite membrane. Generally, it is agreed that the HA/chitosan/CMC composites with mechanical properties, swelling behavior, adjustable degradation, and high bioactivity had applications in bone tissue regeneration.

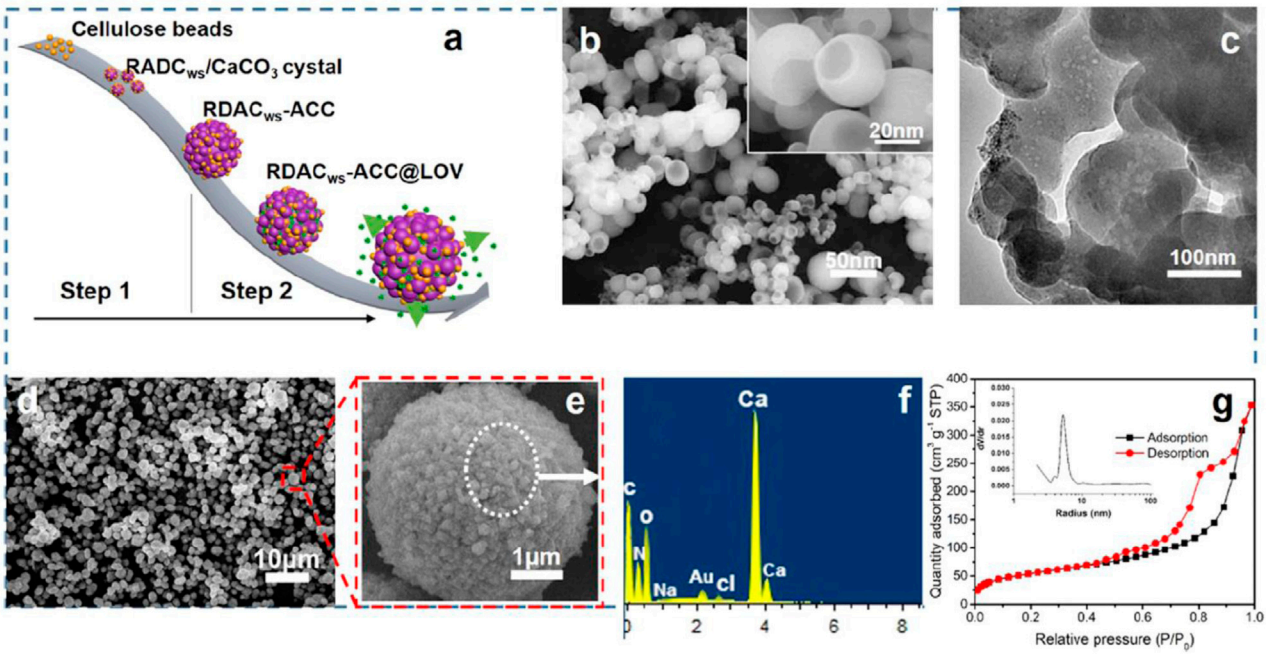

FIGURE 3 | (A) Schematic illustration for the preparation of $CaCO_3$ microspheres and drug loading and release procedures, **(B)** The scanning electron microscopy (SEM) image of the hollow cellulose-based NPs (DACws after aging for 10 days at 60 °C) and the corresponding magnification diagram (inset), **(C)** the transmission electron microscopy (TEM) image of the hollow cellulose-based NPs, **(D)** the SEM image of $CaCO_3$ microspheres with hollow cellulose-based NPs as the template, **(E)** the corresponding enlarged image of the $CaCO_3$ microspheres, **(F)** the corresponding energy-dispersive X-ray spectroscopy (EDS) pattern of the particles, and **(G)** the corresponding N_2 adsorption-desorption isotherm and pore size distribution (inset) of $CaCO_3$ microspheres (Yan et al., 2019).

1.4.2 Biological Properties as Tissue Engineering Scaffolds

Grande *et al.* (2009) prepared BC/calcium-deficient HA nanocomposites with biocompatibility and cell viability by a precipitation method. It found the cell viability of 97.2% for HEK cells in the BC/calcium-deficient HA nanocomposites, more than that of BC (86.8%). They suggested that all pore sizes, fiber diameter, and chemical bond of HA in nanocomposites influenced the cell viability of HEK cells. Saska *et al.* (2011) prepared biocompatible BC/HA nanocomposite membranes with biological properties for bone regeneration by *in vivo* tests. At 4 weeks, BC/HA composites displayed newly formed bone with several osteocytes, blood vessels, and bone matrix filled in bone defects. It found HA of low crystallinity with a Ca/P molar rate (1.5) similar to that of physiological bone.

Tazi *et al.* (2012) used BC scaffold to support osteoblast growth and bone formation and used BC/HA membranes to evaluate osteoblast growth. It observed the significantly increased cell growth and spreading on the surface of BC/HA membranes, compared with that of BC. They demonstrated that BC could sustain osteoblast adhesion and the HA enhanced osteoblast adhesion and spreading. Hammonds *et al.* (2012) investigated the feasibility of generating calcium-deficient HA from BC/calcium-deficient HA composites by thermal and enzymatic methods. The degradation method produced calcium-deficient HA, providing an example for the composites as a bone filler.

Tommila *et al.* (2009) found that cellulose sponges coated with HA attracted circulating hemopoietic and mesenchymal progenitor cells efficiently and contained calcium-sensing receptors-positive cells. It probably suggested that the stem cells were responsible for the richly vascularized granulation tissue formed in HA-coated sponges. Liu *et al.* (2010) used HA/polyurethane composite scaffold to generate an antibiotic drug delivery system with good cytocompatibility and antibacterial properties. It found a sustained release of the model drug for up to 60 days Wang *et al.* (2013) prepared a porous BC membrane with gelatin and CHA with low crystallite size and crystallinity via the laser patterning technique. It showed that the C5.18 cells survived after being cultured in the 3D BC scaffolds for 7 days. The chondrogenic rat cell could keep viability on scaffolds, which indicated the scaffolds with good cytocompatibility. It is known that chitosan possessed innate antimicrobial properties toward both Gram-positive and Gram-negative organisms, which could be used in the wound dressings without antimicrobial infections during the implants produce. Mututuvari *et al.* (2013) synthesized cellulose/chitosan/HA composite with good antimicrobial activity.

Yan *et al.* (2019) prepared biocompatible dialdehyde cellulose/$CaCO_3$ microspheres about 2–3.5 μm and a high specific surface area of similar to 363 $m^2\ g^{-1}$ for tunable pH-responsive drug delivery (**Figure 3A**). It observed a small and uniform template (**Figure 3B**) and a porous structure (**Figure 3C**). It obtained uniform microspheres by hollow cellulose (**Figure 3D**) formed by the aggregation nanoparticles (**Figure 3E**). A strong Ca signal was

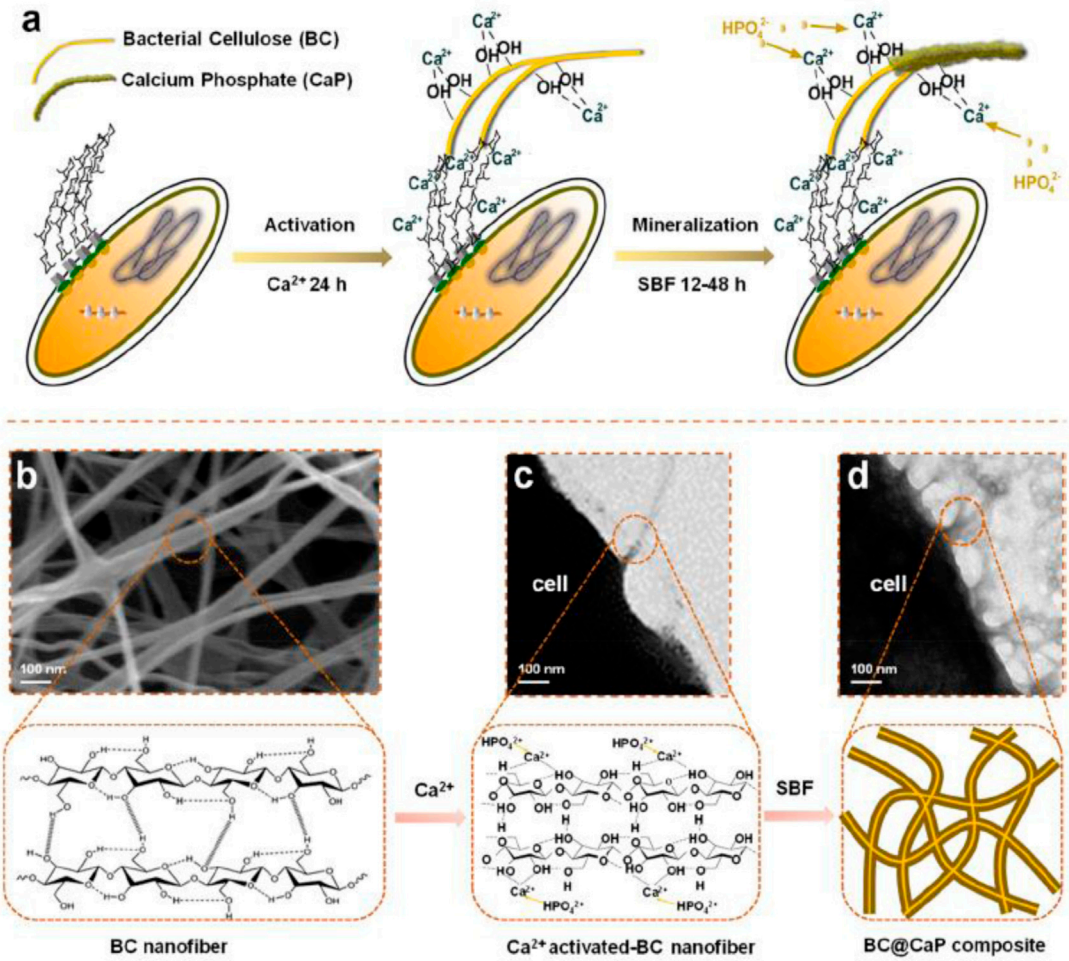

FIGURE 4 | In the experimental design of this study, hydroxyl-rich cellulose molecule chains capture free Ca^{2+} to initiate the nucleation of HAp. **(A)** Schematic diagram of the formation of HAp accompanying the production of cellulose by **(A)** x. **(B)** The representative SEM image of cellulose nanofibers secreted by bacterial cells. **(C)** The representative TEM image of cellulose nanofibers secreted by bacterial cells. **(D)** The representative TEM image of the BC@HAp composite was obtained under biological metabolism conditions. (Chen et al., 2021).

observed (**Figure 3F**). It carried out a surface area of ~363.1 m^2/g and a diameter of 10 nm for $CaCO_3$ microspheres (**Figure 3G**). It found encapsulation efficiency, pH responsiveness, and biocompatibility for the porous microspheres. Chen *et al.* (2021) reported the mineralization of biomimetic HA/nanocellulose nanocomposites with a higher Young modulus. It found the easier capture of Ca^{2+} by the abundant hydroxyl groups on the glucan chain before the formation of hydrogen bonding for the subsequent growth of HA crystals (**Figure 4**). Gao J. et al. (2022) developed flexible and superhydrophilic ultralong HA nanowire-based biopaper with tensile strength (2.57 MPa), porosity (77%), and specific surface area (36.84 m^2 g^{-1}) for a wound dressing. It found the proliferation, migration, and *in vitro* angiogenesis of HUVECs for the biopaper.

Nasrallah and Ibrahim (2022) reported physico-chemical, dielectric, and antimicrobial properties of the PVA/CMC blend films by silver doped HA nanoparticles using the casting technique. The films had antimicrobial properties for antibacterial activity against Bacillus subtilis, Escherichia coli, and Candida albicans. Nanocomposites had improved electrical conductivity and antimicrobial efficiency by doping silver/HA nanoparticles. Gao F. et al. (2022) prepared deacetylate 3D porous CA/HA/polydopamine microspheres coating with excellent attachment, adhesion, and proliferation as the scaffold for bone tissue regeneration. The microspheres coating was capable of differentiating osteogenically via *in vitro* mineralization.

2 FUTURE PERSPECTIVES

It is widely known that there are increasing demands in the biomedical fields. The calcium-containing cellulose-based composites included cellulose/HA, cellulose/calcium carbonate, and cellulose/calcium silicate composites in this review study. Obviously, the calcium-containing cellulose-based composites

had the characteristics of cellulose and HA/$CaCO_3$/$CaSiO_3$ and induced some new properties. As aforementioned, the cellulose/HA composites possessed high mechanical properties, good swelling behavior, adjustable biodegradation, high bioactivity, high chemical durability, good cytocompatibility, and excellent ion-exchangeability. Therefore, it is believed that these materials are promising candidates for the applications in the biomedical fields such as bone regeneration, bone tissue engineering, drug delivery, etc. In order to realize the realistic applications, based on the as-reported works in the literature, the following issues need to be explored in the near future.

First, the interaction mechanism between cellulose and inorganic calcium is still unknown and needs to be explored. There are a few reports on the interaction mechanism between cellulose and $CaCO_3$. As aforementioned, obviously, there exists a strong interaction between these two apartments. Halab-Kessira and Ricard (1996a), and Halab-Kessira and Ricard (1996b) investigated the interaction of $CaCO_3$ particles with cellulose grafted poly acrylate of trimethylaminoethyl chloride (PCMA) copolymers. Experimental results indicated that the retention of calcium carbonate particles was strongly dependent on the cationic content of the copolymer and electro-interactions make the adsorption easier. It obtained the maximum cover of about 750 mg g^{-1} for grafted fiber, and 280 mg g^{-1} for ungrafted fiber. As we all know, it is very important for the composites to display the applications by understanding the surface and interface properties. More importantly, as aforementioned, it showed that apatite particles grow on the surface of the cellulose/HA composites. The surface and interface properties are directly related to biomedical applications. Although some groups suggested the combination between cellulose and HA through hydrogen bonding, obviously, there is still a lack of experimental evidence and theoretical explanation. It assumed that the interaction is the hydrogen bond. The intramolecular hydrogen bonding or intermolecular hydrogen bonding, the strength of the hydrogen bonding, the hydrogen bonding be quantitative or semi-quantitative analysis should be investigated. We would like to know how the hydrogen bonding formed between cellulose and HA and whether the stability of cellulose is enhanced or weakened by hydrogen bonding. In addition to the hydrogen bonding, there exist other interactions such as electrostatic force, van der Waals, etc. Moreover, it is easy to observe the HA crystals dispersed on the surface of cellulose. The formation mechanism should be solved. Therefore, the intrinsic and detailed interaction mechanism between cellulose and HA needs to be further investigated. In fact, the research of mechanism is of great importance for the applications of both the cellulose/HA composites and other composites.

Second, the calcium-containing cellulose-based composites, especially cellulose/HA composites, should be explored for the industrialization application. Although calcium-containing cellulose-based composites are promising biomedical materials, there is a long road ahead for the industrialization application. Undoubtedly, it is a long process for the industrialization process of biomaterials. Obviously, the research on calcium-containing cellulose-based composites is at the initial stage. There are many problems that need to be solved. In comparison with other biomedical materials, the advantages of calcium-containing cellulose-based composites should be highlighted. For example, at present, there is a lack of comparative study of cellulose/HA composites and other biomedical materials. We should pay attention to the comparative study in the next stage. In addition, more biomedical properties including protein adsorption, gene carrier, adsorption/release, the performance of bone repair, and vascular properties should be explored.

Third, cellulose itself is certainly worthy of more attention. It reports that cellulose is extracted from sources including wood, plant, tunicate, algae, bacterial, etc. There are four polymorphs of crystalline cellulose (I, II, III, IV), which consist of crystalline and amorphous regions. Each polymorph has a different crystalline structure. The cellulose was extracted from cellulose sources via the mechanical treatment, acid hydrolysis, and enzymatic hydrolysis method by the complete or partial removal of matrixes (hemicellulose, lignin, etc.). In addition, it reports that there are nine particle types of cellulose. Each particle type has a characteristic size, morphology, crystallinity, and properties. Therefore, choosing an appropriate type of cellulose is important for the formation and applications of calcium-containing cellulose-based composites. For example, the existence of hemicellulose and lignin on the properties of composites should be researched.

As aforementioned, there are many methods for the synthesis of calcium-containing cellulose-based composites. Much attention has been paid to the biomineralization method. Indeed, HA is close to the natural bone in the cellulose/HA composites by the biomineralization method. This is a good method to investigate the mechanism of biomineralization. However, this method has the disadvantages of being time-consuming, low-productivity, and poor reproducibility. Obviously, it is not the best choice for the industrialization process of biomaterials. Moreover, the synthesis method should meet the principles of environment friendliness, economic friendliness, low cost, and high yield.

Finally, the calcium-containing cellulose-based composites itself is certainly worthy of more attention. As described in the literature, it is believed that the composites with specific porous structures could produce bone activity and osteoblast cells could have good adhesion and proliferation at the surface of composites (Yuan et al., 2010). It is reported that the histological evidence on the special micro or nanostructure induces bone regeneration (Zhu et al., 2009). It is well known that both cellulose and inorganic calcium have various morphologies and structures. Therefore, more attention should be paid to the pore and microstructure of calcium-containing cellulose-based composites. For example, cellulose/HA composites with 3D patterning should be fabricated by the electrospinning method and could be processed into film or bio-ceramic. Moreover, it is found that ions could promote cell proliferation and activate the gene expression (Lin et al., 2011). Nature HA also includes the chemical compositions of Na, Mg, Sr, Si, K, F, Cl, and CO_3^{2-},

which favored the improved biological properties of HA. The cellulose/HA composites with other chemical compositions should also be prepared.

3 CONCLUSION

In this mini-review article, we described the recent advances in the synthesis, properties, and biomedical applications of calcium-containing cellulose-based composites including cellulose/HA, cellulose/calcium carbonate, and cellulose/calcium silicate composites. The future developments and applications of calcium-containing cellulose-based composites were given. It expects that more attention is paid to the research of calcium-containing cellulose-based composites.

AUTHOR CONTRIBUTIONS

R-JS, TW, J-QL, NZ, and M-GM: investigation. R-JS, NZ, and M-GM: supervision. R-JS, TW, J-QL, NZ, and M-GM: writing the original draft. R-JS, NZ, and M-GM: writing—review and editing. All authors contributed to the article and approved the submitted version.

FUNDING

The financial support from the National Key R and D Program of China (2019YFC1905901) and the Key Production Innovative Development Plan of the Southern Bingtuan (2019DB007) is gratefully acknowledged.

REFERENCES

Addadi, L., Raz, S., and Weiner, S. (2003). Taking Advantage of Disorder: Amorphous Calcium Carbonate and its Roles in Biomineralization. *Adv. Mat.* 15 (12), 959–970. doi:10.1002/adma.200300381

Baghbanzadeh, M., Carbone, L., Cozzoli, P. D., and Kappe, C. O. (2011). Microwave-assisted Synthesis of Colloidal Inorganic Nanocrystals. *Angew. Chem. Int. Ed.* 50, 11312–11359. doi:10.1002/anie.201101274

Bang, J. H., and Suslick, K. S. (2010). Applications of Ultrasound to the Synthesis of Nanostructured Materials. *Adv. Mat.* 22, 1039–1059. doi:10.1002/adma.200904093

Byrappa, K., and Adschiri, T. (2007). Hydrothermal Technology for Nanotechnology. *Prog. Cryst. Growth Charact. Mater.* 53, 117–166. doi:10.1016/j.pcrysgrow.2007.04.001

Chan, C.-M., Wu, J., Li, J.-X., and Cheung, Y.-K. (2002). Polypropylene/calcium Carbonate Nanocomposites. *Polymer* 43, 2981–2992. doi:10.1016/s0032-3861(02)00120-9

Chemat, F., Zill-E-Humaand Khan, M. K. (2011). Applications of Ultrasound in Food Technology: Processing, Preservation and Extraction. *Ultrason. Sonochemistry* 18, 813–835. doi:10.1016/j.ultsonch.2010.11.023

Chen, C., Qian, J., Chen, H., Zhang, H., Yang, L., Jiang, X., et al. (2021). Molecular Origin of the Biologically Accelerated Mineralization of Hydroxyapatite on Bacterial Cellulose for More Robust Nanocomposites. *Nano Lett.* 21, 10292–10300. doi:10.1021/acs.nanolett.1c03411

Cheng, X. F., Qian, H., Zhang, S. W., Zhang, Z. S., He, Y., and Ma, M. G. (2016). Preparation and Characterization of Cellulose-$CaCO_3$ Composites by an Eco-Friendly Microwave-Assisted Route in a Mixed Solution of Ionic Liquid and Ethylene Glycol. *Bioresources* 11, 4392–4401. doi:10.15376/biores.11.2.4392-4401

Chong, K. Y., Chia, C. H., Zakaria, S., Sajab, M. S., Chook, S. W., and Khiew, P. S. (2015). CaCO3-decorated Cellulose Aerogel for Removal of Congo Red from Aqueous Solution. *Cellulose* 22, 2683–2691. doi:10.1007/s10570-015-0675-2

Chu, T.-M. G., Orton, D. G., Hollister, S. J., Feinberg, S. E., and Halloran, J. W. (2002). Mechanical and *In Vivo* Performance of Hydroxyapatite Implants with Controlled Architectures. *Biomaterials* 23, 1283–1293. doi:10.1016/s0142-9612(01)00243-5

Ciobanu, M., Bobu, E., and Ciolacu, F. (2010). *In-situ* Cellulose Fibres Loading with Calcium Carbonate Precipitated by Different Methods. *Cellul. Chem. Technol.* 44, 379–387.

Cravotto, G., and Cintas, P. (2010). Power Ultrasound in Organic Synthesis: Moving Cavitational Chemistry from Academia to Innovative and Large-Scale Applications. *Chem. Soc. Rev.* 35, 180–196. doi:10.1039/b503848k

Cromme, P., Zollfrank, C., Müller, L., Müller, F. A., and Greil, P. (2007). Biomimetic Mineralisation of Apatites on Ca2+ Activated Cellulose Templates. *Mater. Sci. Eng. C* 27, 1–7. doi:10.1016/j.msec.2005.11.001

Cüneyt Tas, A. (2000). Synthesis of Biomimetic Ca-Hydroxyapatite Powders at 37°C in Synthetic Body Fluids. *Biomaterials* 21, 1429–1438. doi:10.1016/s0142-9612(00)00019-3

Doerner, H. A., and Hoskins, W. M. (1925). Co-Precipitation of Radium and Barium Sulfates1. *J. Am. Chem. Soc.* 47, 662–675. doi:10.1021/ja01680a010

Dorozhkin, S. V. (2011). Calcium Orthophosphates. *Biomatter* 1, 121–164. doi:10.4161/biom.18790

Eichhorn, S. J., Dufresne, A., Aranguren, M., Marcovich, N. E., Capadona, J. R., Rowan, S. J., et al. (2010). Review: Current International Research into Cellulose Nanofibres and Nanocomposites. *J. Mat. Sci.* 45, 1–33. doi:10.1007/s10853-009-3874-0

Fang, B., Wan, Y.-Z., Tang, T.-T., Gao, C., and Dai, K.-R. (2009). Proliferation and Osteoblastic Differentiation of Human Bone Marrow Stromal Cells on Hydroxyapatite/bacterial Cellulose Nanocomposite Scaffolds. *Tissue Eng. Part A* 15, 1091–1098. doi:10.1089/ten.tea.2008.0110

Feng, S., and Xu, R. (2001). New Materials in Hydrothermal Synthesis. *Acc. Chem. Res.* 34, 239–247. doi:10.1021/ar0000105

Fu, L.-H., Dong, Y.-Y., Ma, M.-G., Li, S.-M., and Sun, R.-C. (2013a). Compare Study CaCO3 Crystals on the Cellulose Substrate by Microwave-Assisted Method and Ultrasound Agitation Method. *Ultrason. Sonochemistry* 20, 839–845. doi:10.1016/j.ultsonch.2012.11.001

Fu, L.-H., Dong, Y.-Y., Ma, M.-G., Yue, W., Sun, S.-L., and Sun, R.-C. (2013b). Why to Synthesize Vaterite Polymorph of Calcium Carbonate on the Cellulose Matrix via Sonochemistry Process? *Ultrason. Sonochemistry* 20, 1188–1193. doi:10.1016/j.ultsonch.2013.03.008

Fu, L.-H., Liu, Y.-J., Ma, M.-G., Zhang, X.-M., Xue, Z.-M., and Zhu, J.-F. (2016). Microwave-assisted Hydrothermal Synthesis of Cellulose/hydroxyapatite Nanocomposites. *Polymers* 8, 316. doi:10.3390/polym8090316

Fu, L.-H., Qi, C., Hu, Y.-R., Mei, C.-G., and Ma, M.-G. (2019a). Cellulose/vaterite Nanocomposites: Sonochemical Synthesis, Characterization, and Their Application in Protein Adsorption. *Mater. Sci. Eng. C* 96, 426–435. doi:10.1016/j.msec.2018.11.061

Fu, L.-H., Qi, C., Ma, M.-G., and Wan, P. (2019c). Multifunctional Cellulose-Based Hydrogels for Biomedical Applications. *J. Mat. Chem. B* 7, 1541–1562. doi:10.1039/c8tb02331j

Fu, L.-H., Xie, Y.-M., Bian, J., Ma, M.-G., Tian, C.-H., and Jin, X.-J. (2015). Microwave-assisted Rapid Synthesis of Lignocellulose/hydroxyapatite Nanocomposites. *Mater. Lett.* 159, 51–53. doi:10.1016/j.matlet.2015.06.082

Fu, L. H., Qi, C., Liu, Y. J., Cao, W. T., and Ma, M. G. (2019b). Sonochemical Synthesis of Cellulose/hydroxyapatite Nanocomposites and Their Application in Protein Adsorption. *Sci. Rep.* 8, 8292. doi:10.1038/s41598-018-25566-7

Gao, F., Zeng, D., Liu, H., Qin, R., Zhang, J., Chen, Y., et al. (2022a). Porous Cellulose Microspheres Coated in One Step with a Polydopamine Suspension of Hydroxyapatite for Bone Tissue Engineering. *Cellulose* 29, 1955–1967. doi:10.1007/s10570-021-04395-4

Gao, J., Hao, L.-S., Ning, B.-B., Zhu, Y.-K., Guan, J.-B., Ren, H.-W., et al. (2022b). Biopaper Based on Ultralong Hydroxyapatite Nanowires and Cellulose Fibers

Promotes Skin Wound Healing by Inducing Angiogenesis. *Coatings* 12, 479. doi:10.3390/coatings12040479

Garai, S., and Sinha, A. (2014). Biomimetic Nanocomposites of Carboxymethyl Cellulose-Hydroxyapatite: Novel Three Dimensional Load Bearing Bone Grafts. *Colloids Surfaces B Biointerfaces* 115, 182–190. doi:10.1016/j.colsurfb.2013.11.042

Garrote, G., Domínguez, H., and Parajó, J. C. (1999). Hydrothermal Processing of Lignocellulosic Materials. *Holz als Roh- Werkst.* 57, 191–202. doi:10.1007/s001070050039

Gedanken, A. (2004). Using Sonochemistry for the Fabrication of Nanomaterials. *Ultrason. Sonochemistry* 11, 47–55. doi:10.1016/j.ultsonch.2004.01.037

Gibson, I. R., and Bonfield, W. (2002). Novel Synthesis and Characterization of an AB-type Carbonate-Substituted Hydroxyapatite. *J. Biomed. Mat. Res.* 59, 697–708. doi:10.1002/jbm.10044

Gower, L. B. (2008). Biomimetic Model Systems for Investigating the Amorphous Precursor Pathway and its Role in Biomineralization. *Chem. Rev.* 108, 4551–4627. doi:10.1021/cr800443h

Grande, C. J., Torres, F. G., Gomez, C. M., and Carmen Bañó, M. (2009). Nanocomposites of Bacterial Cellulose/hydroxyapatite for Biomedical Applications. *Acta Biomater.* 5, 1605–1615. doi:10.1016/j.actbio.2009.01.022

Habraken, W., Habibovic, P., Epple, M., and Bohner, M. (2016). Calcium Phosphates in Biomedical Applications: Materials for the Future? *Mater. Today* 19, 69–87. doi:10.1016/j.mattod.2015.10.008

Halab-Kessira, L., and Ricard, A. (1996b). Adsorption of CaCO3Particles on Cationic Cellulose Graft Copolymers. *J. Colloid Interface Sci.* 184, 437–442. doi:10.1006/jcis.1996.0638

Halab-Kessira, L., and Ricard, A. (1996a). Adsorption of CaCO3Particles on Cationic Cellulose Graft Copolymers I Effect of Chemical Parameters. *J. Colloid Interface Sci.* 179, 269–275. doi:10.1006/jcis.1996.0213

Hammonds, R. L., Harrison, M. S., Cravanas, T. C., Gazzola, W. H., Stephens, C. P., and Benson, R. S. (2012). Biomimetic Hydroxyapatite Powder from a Bacterial Cellulose Scaffold. *Cellulose* 19, 1923–1932. doi:10.1007/s10570-012-9767-4

Hofmann, I., Müller, L., Greil, P., and Müller, F. A. (2006). Calcium Phosphate Nucleation on Cellulose Fabrics. *Surf. Coatings Technol.* 201, 2392–2398. doi:10.1016/j.surfcoat.2006.04.007

Hokkanen, S., Bhatnagar, A., Repo, E., Lou, S., and Sillanpää, M. (2016). Calcium Hydroxyapatite Microfibrillated Cellulose Composite as a Potential Adsorbent for the Removal of Cr(VI) from Aqueous Solution. *Chem. Eng. J.* 283, 445–452. doi:10.1016/j.cej.2015.07.035

Hong, L., Wang, Y. L., Jia, S. R., Huang, Y., Gao, C., and Wan, Y. Z. (2006). Hydroxyapatite/bacterial Cellulose Composites Synthesized via a Biomimetic Route. *Mater. Lett.* 60, 1710–1713. doi:10.1016/j.matlet.2005.12.004

Hu, F., Xu, S., and Liu, B. (2018). Photosensitizers with Aggregation-Induced Emission: Materials and Biomedical Applications. *Adv. Mat.* 30, 1801350. doi:10.1002/adma.201801350

Huang, C., Dong, H., Zhang, Z., Bian, H., and Yong, Q. (2020). Procuring the Nano-Scale Lignin in Prehydrolyzate as Ingredient to Prepare Cellulose Nanofibril Composite Film with Multiple Functions. *Cellulose* 27, 9355–9370. doi:10.1007/s10570-020-03427-9

Huang, C., Xu, C., Meng, X., Wang, L., and Zhou, X. (2022). Editorial: isolation, modification, and characterization of the constituents (cellulose, hemicellulose, lignin, et al.) in biomass and their bio-based applications. *Front. Bioeng. Biotechnol.* 10, 866531. doi:10.3389/fbioe.2022.866531

Hutchens, S. A., Benson, R. S., Evans, B. R., O'Neill, H. M., and Rawn, C. J. (2006). Biomimetic Synthesis of Calcium-Deficient Hydroxyapatite in a Natural Hydrogel. *Biomaterials* 27, 4661–4670. doi:10.1016/j.biomaterials.2006.04.032

Jia, N., Li, S.-M., Ma, M.-G., and Sun, R.-C. (2011a). Microwave-assisted Ionic Liquid Preparation and Characterization of Cellulose/calcium Silicate Nanocomposites in Ethylene Glycol. *Mater. Lett.* 65, 918–921. doi:10.1016/j.matlet.2010.12.033

Jia, N., Li, S.-M., Ma, M.-G., and Sun, R.-C. (2012a). Rapid Microwave-Assisted Fabrication of cellulose/F-Substituted Hydroxyapatite Nanocomposites Using Green Ionic Liquids as Additive. *Mater. Lett.* 68, 44–46. doi:10.1016/j.matlet.2011.10.027

Jia, N., Li, S.-M., Ma, M.-G., Sun, R.-C., and Zhu, J.-F. (2012b). Hydrothermal Fabrication, Characterization, and Biological Activity of cellulose/CaCO3 Bionanocomposites. *Carbohydr. Polym.* 88, 179–184. doi:10.1016/j.carbpol.2011.11.086

Jia, N., Li, S.-M., Ma, M.-G., Sun, R.-C., and Zhu, J.-F. (2010a). Hydrothermal Synthesis and Characterization of Cellulose-Carbonated Hydroxyapatite Nanocomposites in NaOH-Urea Aqueous Solution. *Sci. Adv. Mat.* 2, 210–214. doi:10.1166/sam.2010.1086

Jia, N., Li, S.-M., Ma, M.-G., Sun, R.-C., and Zhu, L. (2011b). Green Microwave-Assisted Synthesis of Cellulose/calcium Silicate Nanocomposites in Ionic Liquids and Recycled Ionic Liquids. *Carbohydr. Res.* 346, 2970–2974. doi:10.1016/j.carres.2011.10.006

Jia, N., Li, S.-M., Zhu, J.-F., Ma, M.-G., Xu, F., Wang, B., et al. (2010b). Microwave-assisted Synthesis and Characterization of Cellulose-Carbonated Hydroxyapatite Nanocomposites in NaOH-Urea Aqueous Solution. *Mater. Lett.* 64, 2223–2225. doi:10.1016/j.matlet.2010.07.029

Jiang, D., and Zhang, J. (2009). Calcium Phosphate with Well Controlled Nanostructure for Tissue Engineering. *Curr. Appl. Phys.* 9, S252–S256. doi:10.1016/j.cap.2009.01.029

Jiang, L.-Y., Li, Y. B., Zhang, L., and Wang, X. J. (2008c). Study on Nano-hydroxyapatite/Chitosan-Carboxymethyl Cellulose Composite Scaffold. *J. Inure. Mater.* 23, 135–140. doi:10.3724/sp.j.1077.2008.00135

Jiang, L., Li, Y., Wang, X., Zhang, L., Wen, J., and Gong, M. (2008a). Preparation and Properties of Nano-Hydroxyapatite/chitosan/carboxymethyl Cellulose Composite Scaffold. *Carbohydr. Polym.* 74, 680–684. doi:10.1016/j.carbpol.2008.04.035

Jiang, L. Y., Li, Y. B., and Xiong, C. D. (2009a). A Novel Composite Membrane of Chitosan-Carboxymethyl Cellulose Polyelectrolyte Complex Membrane Filled with Nano-Hydroxyapatite . Preparation and Properties. *J. Mat. Sci. Mat. Medic.* 20, 1645–1652.

Jiang, L. Y., Li, Y. B., and Xiong, C. D. (2009b). Preparation and Biological Properties of a Novel Composite Scaffold of Nano-Hydroxyapatite/chitosan/carboxymethyl Cellulose for Bone Tissue Engineering. *J. Biomed. Sci.* 16, 65.

Jiang, L. Y., Li, Y. B., Zhang, L., and Liao, J. G. (2008b). Preparation and Properties of a Novel Bone Repair Composite: Nano-Hydroxyapatite/chitosan/carboxymethyl Cellulose. *J. Mat. Sci. Mat. Medic.* 19, 981–987.

Kang, S., Zhao, K., Yu, D. G., Zheng, X., and Huang, C. (2022). Advances in Biosensing and Environmental Monitoring Based on Electrospun Nanofibers. *Adv. Fiber Mat.* 4, 404–435. doi:10.1007/s42765-021-00129-0

Kaur, G., Adhikari, R., Cass, P., Bown, M., and Gunatillake, P. (2015). Electrically Conductive Polymers and Composites for Biomedical Applications. *RSC Adv.* 5, 37553–37567. doi:10.1039/c5ra01851j

Kim, M., Yeo, M., Kim, M., and Kim, G. (2018). Biomimetic Cellulose/calcium-Deficient-Hydroxyapatite Composite Scaffolds Fabricated Using an Electric Field for Bone Tissue Engineering. *RSC Adv.* 8, 20637–20647. doi:10.1039/c8ra03657h

Kumar, A. P., Mohaideen, K. K., Alariqi, S. A. S., and Singh, R. P. (2010). Preparation and Characterization of Bioceramic Nanocomposites Based on Hydroxyapatite (HA) and Carboxymethyl Cellulose (CMC). *Macromol. Res.* 18, 1160–1167. doi:10.1007/s13233-010-1208-3

Landi, E., Celotti, G., Logroscino, G., and Tampieri, A. (2003). Carbonated Hydroxyapatite as Bone Substitute. *J. Eur. Ceram. Soc.* 23, 2931–2937. doi:10.1016/s0955-2219(03)00304-2

Li, K., Wang, J., Liu, X., Xiong, X., and Liu, H. (2012). Biomimetic Growth of Hydroxyapatite on Phosphorylated Electrospun Cellulose Nanofibers. *Carbohydr. Polym.* 90, 1573–1581. doi:10.1016/j.carbpol.2012.07.033

Li, L., Zhu, Y.-J., and Ma, M.-G. (2008). Microwave-assisted Preparation of Calcium Sulfate Nanowires. *Mater. Lett.* 62, 4552–4554. doi:10.1016/j.matlet.2008.08.040

Li, S.-M., Jia, N., Zhu, J.-F., Ma, M.-G., and Sun, R.-C. (2010). Synthesis of Cellulose-Calcium Silicate Nanocomposites in Ethanol/water Mixed Solvents and Their Characterization. *Carbohydr. Polym.* 80, 270–275. doi:10.1016/j.carbpol.2009.11.024

Li, W., and Wu, P. (2009). Biomimetic Synthesis of Monodisperse Rosette-like Calcite Mesocrystals Regulated by Carboxymethyl Cellulose and the Proposed Mechanism : An Unconventional Rhombohedra-Stacking Route. *CrystEngComm* 11, 2466–2474. doi:10.1039/b901580a

Lin, K., Chang, J., Liu, X., Chen, L., and Zhou, Y. (2011). Synthesis of Element-Substituted Hydroxyapatite with Controllable Morphology and Chemical Composition Using Calcium Silicate as Precursor. *CrystEngComm* 13, 4850–4855. doi:10.1039/c0ce00835d

Liu, H., Zhang, L., Shi, P., Zou, Q., Zuo, Y., and Li, Y. (2010). Hydroxyapatite/polyurethane Scaffold Incorporated with Drug-Loaded Ethyl Cellulose Microspheres for Bone Regeneration. *J. Biomed. Mat. Res.* 95B, 36–46. doi:10.1002/jbm.b.31680

Liu, L., He, D., Wang, G.-S., and Yu, S.-H. (2011). Bioinspired Crystallization of CaCO3 Coatings on Electrospun Cellulose Acetate Fiber Scaffolds and Corresponding CaCO3 Microtube Networks. *Langmuir* 27, 7199–7206. doi:10.1021/la200738n

Liu, W., Du, H., Zhang, M., Liu, K., Liu, H., Xie, H., et al. (2020). Bacterial Cellulose-Based Composite Scaffolds for Biomedical Applications: A Review. *ACS Sustain. Chem. Eng.* 8, 7536–7562. doi:10.1021/acssuschemeng.0c00125

Liu, X., Li, K., Wu, C., Li, Z., Wu, B., Duan, X., et al. (2019). Biomimetic Assembly of Multilevel Hydroxyapatite Using Bacterial Cellulose Hydrogel as a Reactor. *CrystEngComm* 21, 4859–4863. doi:10.1039/c9ce01086f

Liu, X., Ma, Y., Zhou, Y., Pei, C., and Yin, G. (2013). A Promising Hybrid Scaffold Material: Bacterial Cellulose *In-Situ* Assembling Biomimetic Lamellar CaCO3. *Mater. Lett.* 102-103, 91–93. doi:10.1016/j.matlet.2013.03.121

Lukasheva, N. V., and Tolmachev, D. A. (2016). Cellulose Nanofibrils and Mechanism of Their Mineralization in Biomimetic Synthesis of Hydroxyapatite/native Bacterial Cellulose Nanocomposites: Molecular Dynamics Simulations. *Langmuir* 32, 125–134. doi:10.1021/acs.langmuir.5b03953

Ma, M.-G., Dong, Y.-Y., Fu, L.-H., Li, S.-M., and Sun, R.-C. (2013). Cellulose/CaCO3 Nanocomposites: Microwave Ionic Liquid Synthesis, Characterization, and Biological Activity. *Carbohydr. Polym.* 92, 1669–1676. doi:10.1016/j.carbpol.2012.11.034

Ma, M.-G., Fu, L.-H., Li, S.-M., Zhang, X.-M., Sun, R.-C., and Dai, Y.-D. (2012b). Hydrothermal Synthesis and Characterization of Wood powder/CaCO3 Composites. *Carbohydr. Polym.* 88, 1470–1475. doi:10.1016/j.carbpol.2012.02.043

Ma, M.-G., Fu, L.-H., Sun, R.-C., and Jia, N. (2012a). Compared Study on the cellulose/CaCO3 Composites via Microwave-Assisted Method Using Different Cellulose Types. *Carbohydr. Polym.* 90, 309–315. doi:10.1016/j.carbpol.2012.05.043

Ma, M.-G. (2012). Hierarchically Nanostructured Hydroxyapatite: Hydrothermal Synthesis, Morphology Control, Growth Mechanism, and Biological Activity. *Ijn* 7, 1781–1791. doi:10.2147/ijn.s29884

Ma, M.-G., Zhu, J.-F., Jia, N., Li, S.-M., Sun, R.-C., Cao, S.-W., et al. (2010). Rapid Microwave-Assisted Synthesis and Characterization of Cellulose-Hydroxyapatite Nanocomposites in N,N-dimethylacetamide Solvent. *Carbohydr. Res.* 345, 1046–1050. doi:10.1016/j.carres.2010.03.004

Ma, M.-G., and Zhu, J.-F. (2010). Recent Progress on Fabrication of Calcium-Based Inorganic Biodegradable Nanomaterials. *Nanotec* 4, 164–170. doi:10.2174/187221010792483690

Ma, M.-G., Zhu, J.-F., Zhu, Y.-J., and Sun, R.-C. (2014). The Microwave-Assisted Ionic-Liquid Method: A Promising Methodology in Nanomaterials. *Chem. Asian J.* 9, 2378–2391. doi:10.1002/asia.201402288

Ma, M.-G., Zhu, Y.-J., and Chang, J. (2006). Monetite Formed in Mixed Solvents of Water and Ethylene Glycol and its Transformation to Hydroxyapatite. *J. Phys. Chem. B* 110, 14226–14230. doi:10.1021/jp061738r

Ma, M. G., Jia, N., Li, S. M., and Sun, R. C. (2011). Nanocomposites of Cellulose/carbonated Hydroxyapatite by Microwave-Assisted Fabrication in Ionic Liquid: Characterization and Thermal Stability. *Iran. Polym. J.* 20, 413–421.

Ma, M. G., and Zhu, J. F. (2009). Solvothermal Synthesis and Characterization of Hierarchically Nanostructured Hydroxyapatite Hollow Spheres. *Eur. J. Inorg. Chem.* 2009, 5522–5526. doi:10.1002/ejic.200900839

Meng, L.-Y., Wang, B., Ma, M.-G., and Lin, K.-L. (2016). The Progress of Microwave-Assisted Hydrothermal Method in the Synthesis of Functional Nanomaterials. *Mater. Today Chem.* 1-2, 63–83. doi:10.1016/j.mtchem.2016.11.003

Moon, R. J., Martini, A., Nairn, J., Simonsen, J., and Youngblood, J. (2011). Cellulose Nanomaterials Review: Structure, Properties and Nanocomposites. *Chem. Soc. Rev.* 40, 3941–3994. doi:10.1039/c0cs00108b

Morales-Nieto, V., Navarro, C. H., Moreno, K. J., Arizmendi-Morquecho, A., Chávez-Valdez, A., García-Miranda, S., et al. (2013). Poly(methyl Methacrylate)/carbonated Hydroxyapatite Composite Applied as Coating on Ultra High Molecular Weight Polyethylene. *Prog. Org. Coatings* 76, 204–208. doi:10.1016/j.porgcoat.2012.09.007

Mututuvari, T. M., Harkins, A. L., and Tran, C. D. (2013). Facile Synthesis, Characterization, and Antimicrobial Activity of Cellulose-Chitosan-Hydroxyapatite Composite Material: a Potential Material for Bone Tissue Engineering. *J. Biomed. Mater Res. A* 101, 3266–3277. doi:10.1002/jbm.a.34636

Narwade, V. N., Anjum, S. R., Kokol, V., and Khairnar, R. S. (2019). Ammonia-sensing Ability of Differently Structured Hydroxyapatite Blended Cellulose Nanofibril Composite Films. *Cellulose* 26, 3325–3337. doi:10.1007/s10570-019-02299-y

Nasrallah, D. A., and Ibrahim, M. A. (2022). Enhancement of Physico-Chemical, Optical, Dielectric and Antimicrobial Properties of Polyvinyl Alcohol/carboxymethyl Cellulose Blend Films by Addition of Silver Doped Hydroxyapatite Nanoparticles. *J. Polym. Res.* 29, 86. doi:10.1007/s10965-022-02943-5

Nicoara, A. I., Stoica, A. E., Ene, D.-I., Vasile, B. S., Holban, A. M., and Neacsu, I. A. (2020). *In Situ* and *Ex Situ* Designed Hydroxyapatite: Bacterial Cellulose Materials with Biomedical Applications. *Materials* 13, 4793. doi:10.3390/ma13214793

Núñez, D., Cáceres, R., Ide, W., Varaprasad, K., and Oyarzún, P. (2020). An Ecofriendly Nanocomposite of Bacterial Cellulose and Hydroxyapatite Efficiently Removes Lead from Water. *Int. J. Biol. Macromol.* 165, 2711–2720. doi:10.1016/j.ijbiomac.2020.10.055

Okuda, K., Shigemasa, R., Hirota, K., and Mizutani, T. (2022). *In Situ* crystallization of Hydroxyapatite on Carboxymethyl Cellulose as a Biomimetic Approach to Biomass-Derived Composite Materials. *ACS Omega* 7, 12127–12137. doi:10.1021/acsomega.2c00423

Oprea, M., and Voicu, S. I. (2020). Recent Advances in Composites Based on Cellulose Derivatives for Biomedical Applications. *Carbohydr. Polym.* 247, 116683. doi:10.1016/j.carbpol.2020.116683

Palaveniene, A., Tamburaci, S., Kimna, C., Glambaite, K., Baniukaitiene, O., Tihminlioğlu, F., et al. (2019). Osteoconductive 3D Porous Composite Scaffold from Regenerated Cellulose and Cuttlebone-Derived Hydroxyapatite. *J. Biomater. Appl.* 33, 876–890. doi:10.1177/0885328218811040

Park, K. S., Son, J. T., Chung, H. T., Kim, S. J., Lee, C. H., and Kim, H. G. (2003). Synthesis of LiFePO4 by Co-precipitation and Microwave Heating. *Electrochem. Commun.* 5, 839–842. doi:10.1016/j.elecom.2003.08.005

Paulraj, T., Riazanova, A. V., Yao, K., Andersson, R. L., Müllertz, A., and Svagan, A. J. (2017). Bioinspired Layer-By-Layer Microcapsules Based on Cellulose Nanofibers with Switchable Permeability. *Biomacromolecules* 18, 1401–1410. doi:10.1021/acs.biomac.7b00126

Petrauskaite, O., Gomes, P. d. S., Fernandes, M. H., Juodzbalys, G., Stumbras, A., Maminskas, J., et al. (2013). Biomimetic Mineralization on a Macroporous Cellulose-Based Matrix for Bone Regeneration. *BioMed Res. Int.* 2013, 1–9. doi:10.1155/2013/452750

Pieper, C. M., da Rosa, W. L., Lund, R. G., da Silva, A. F., Piva, E., Salas, M. M., et al. (2020). Biofilms of Cellulose and Hydroxyapatite Composites: Alternative Synthesis Process. *J. Bioact. Compatible Polym.* 35, 469–478. doi:10.1177/0883911520951838

Politi, Y., Arad, T., Klein, E., Weiner, S., and Addadi, L. (2004). Sea Urchin Spine Calcite Forms via a Transient Amorphous Calcium Carbonate Phase. *Science* 306, 1161–1164. doi:10.1126/science.1102289

Polshettiwar, V., Nadagouda, M. N., and Varma, R. S. (2009). Microwave-assisted Chemistry: A Rapid and Sustainable Route to Synthesis of Organics and Nanomaterials. *Aust. J. Chem.* 62, 16–26. doi:10.1071/ch08404

Qi, C., Lin, J., Fu, L.-H., and Huang, P. (2018). Calcium-based Biomaterials for Diagnosis, Treatment, and Theranostics. *Chem. Soc. Rev.* 47, 357–403. doi:10.1039/c6cs00746e

Qi, C., Musetti, S., Fu, L.-H., Zhu, Y.-J., and Huang, L. (2019). Biomolecule-assisted Green Synthesis of Nanostructured Calcium Phosphates and Their Biomedical Applications. *Chem. Soc. Rev.* 48, 2698–2737. doi:10.1039/c8cs00489g

Rauch, M. W., Dressler, M., Scheel, H., Van Opdenbosch, D., and Zollfrank, C. (2012). Mineralization of Calcium Carbonates in Cellulose Gel Membranes. *Eur. J. Inorg. Chem.* 2012, 5192–5198. doi:10.1002/ejic.201200575

Rodríguez, K., Renneckar, S., and Gatenholm, P. (2011). Biomimetic Calcium Phosphate Crystal Mineralization on Electrospun Cellulose-Based Scaffolds. *ACS Appl. Mat. Interfaces* 3, 681–689. doi:10.1021/am100972r

Saska, S., Barud, H. S., Gaspar, A. M. M., Marchetto, R., Ribeiro, S. J. L., and Messaddeq, Y. (2011). *Bacterial Cellulose-Hydroxyapatite Nanocomposites for Bone Regeneration*. New York, NY: Int. J. Biomater. Article ID 175362.

Shi, R.-J., Wang, T., Lang, J.-Q., Zhou, N., and Ma, M.-G. (2022). Multifunctional Cellulose and Cellulose-Based (Nano) Composite Adsorbents. *Front. Bioeng. Biotechnol.* 10, 891034. doi:10.3389/fbioe.2022.891034

Shi, S., Chen, S., Zhang, X., Shen, W., Li, X., Hu, W., et al. (2009). Biomimetic Mineralization Synthesis of Calcium-Deficient Carbonate-Containing Hydroxyapatite in a Three-Dimensional Network of Bacterial Cellulose. *J. Chem. Technol. Biotechnol.* 84, 285–290. doi:10.1002/jctb.2037

Sivasankari, S., Kalaivizhi, R., Gowriboy, N., Ganesh, M. R., and Shazia Anjum, M. (2021). Hydroxyapatite Integrated with Cellulose Acetate/polyetherimide Composite Membrane for Biomedical Applications. *Polym. Compos.* 42, 5512–5526. doi:10.1002/pc.26242

Stoica-Guzun, A., Stroescu, M., Jinga, S., Jipa, I., Dobre, T., and Dobre, L. (2012). Ultrasound Influence upon Calcium Carbonate Precipitation on Bacterial Cellulose Membranes. *Ultrason. Sonochemistry* 19, 909–915. doi:10.1016/j.ultsonch.2011.12.002

Stroescu, M., Stoica-Guzun, A., Jinga, S. I., Dobre, T., Jipa, I. M., and Dobre, L. M. (2012). Influence of Sodium Dodecyl Sulfate and Cetyl Trimethylammonium Bromide upon Calcium Carbonate Precipitation on Bacterial Cellulose. *Korean J. Chem. Eng.* 29, 1216–1223. doi:10.1007/s11814-011-0290-3

Suchanek, W., and Yoshimura, M. (1998). Processing and Properties of Hydroxyapatite-Based Biomaterials for Use as Hard Tissue Replacement Implants. *J. Mat. Res.* 13, 94–117. doi:10.1557/jmr.1998.0015

Tabaght, F. E., Azzaoui, K., Elidrissi, A., Hamed, O., Mejdoubi, E., Jodeh, S., et al. (2021). New Nanostructure Based on Hydroxyapatite Modified Cellulose for Bone Substitute, Synthesis, and Characterization. *Int. J. Polym. Mater. Polym. Biomaterials* 70, 437–448. doi:10.1080/00914037.2020.1725758

Tazi, N., Zhang, Z., Messaddeq, Y., Almeida-Lopes, L., Zanardi, L. M., Levinson, D., et al. (2012). Hydroxyapatite Bioactivated Bacterial Cellulose Promotes Osteoblast Growth and the Formation of Bone Nodules. *Amb. Expr.* 2, 61. doi:10.1186/2191-0855-2-61

Tommila, M., Jokilammi, A., Terho, P., Wilson, T., Penttinen, R., and Ekholm, E. (2009). Hydroxyapatite Coating of Cellulose Sponges Attracts Bone-Marrow-Derived Stem Cells in Rat Subcutaneous Tissue. *J. R. Soc. Interface.* 6, 873–880. doi:10.1098/rsif.2009.0020

Tran, N., and Webster, T. J. (2009). Nanotechnology for Bone Materials. *WIREs Nanomed Nanobiotechnol* 1, 336–351. doi:10.1002/wnan.23

Tsuji, M., Hashimoto, M., Nishizawa, Y., Kubokawa, M., and Tsuji, T. (2005). Microwave-assisted Synthesis of Metallic Nanostructures in Solution. *Chem. Eur. J.* 11, 440–452. doi:10.1002/chem.200400417

Vyroubal, R., Saha, N., Vesela, D., Shah, R., and Saha, P. (2013). Biomimetic Nucleation and Growth of CaCO3 in Bacterial Cellulose Produced by Gluconacetobacter Xylinus (Acetobacter Xylinus). *Curr. Opin. Biotechnol.* 24, S109. doi:10.1016/j.copbio.2013.05.336

Wan, Y., Hong, L., Jia, S., Huang, Y., Zhu, Y., Wang, Y., et al. (2006). Synthesis and Characterization of Hydroxyapatite-Bacterial Cellulose Nanocomposites. *Compos. Sci. Technol.* 66, 1825–1832. doi:10.1016/j.compscitech.2005.11.027

Wan, Y. Z., Huang, Y., Yuan, C. D., Raman, S., Zhu, Y., Jiang, H. J., et al. (2007). Biomimetic Synthesis of Hydroxyapatite/bacterial Cellulose Nanocomposites for Biomedical Applications. *Mater. Sci. Eng. C* 27, 855–864. doi:10.1016/j.msec.2006.10.002

Wang, J., Yang, C. X., Wan, Y. Z., Luo, H. L., He, F., Dai, K. R., et al. (2013). Laser Patterning of Bacterial Cellulose Hydrogel and its Modification with Gelatin and Hydroxyapatite for Bone Tissue Engineering. *Soft Mater* 11, 173–180.

Wang, X., Tang, S., Chai, S., Wang, P., Qin, J., Pei, W., et al. (2021). Preparing Printable Bacterial Cellulose Based Gelatin Gel to Promote *In Vivo* Bone Regeneration. *Carbohydr. Polym.* 270, 118342. doi:10.1016/j.carbpol.2021.118342

Xiao, W., Liu, J., Chen, Q., Wu, Y., Dai, L., and Wu, T. (2011). Controllable Mineralization of Calcium Carbonate on Regenerated Cellulose Fibers. *Cryst. Res. Technol.* 46, 1071–1078. doi:10.1002/crat.201100261

Yan, G., Feng, Y., Gao, Z., Zeng, X., Hong, W., Liu, W., et al. (2019). Stable and Biocompatible Cellulose-Based CaCO3 Microspheres for Tunable pH-Responsive Drug Delivery. *ACS Sustain. Chem. Eng.* 7, 19824–19831. doi:10.1021/acssuschemeng.9b05144

Yang, M., Zhen, W., Chen, H., and Shan, Z. (2016). Biomimetic Design of Oxidized Bacterial Cellulose-Gelatin-Hydroxyapatite Nanocomposites. *J. Bionic Eng.* 13, 631–640. doi:10.1016/S1672-6529(16)60334-7

Yi, L.-J., Li, J.-F., Ma, M.-G., and Zhu, Y.-J. (2020). Nanostructured Calcium-Based Biomaterials and Their Application in Drug Delivery. *Cmc* 27, 5189–5212. doi:10.2174/0929867326666190222193357

Yin, N., Chen, S.-y., Ouyang, Y., Tang, L., Yang, J.-x., and Wang, H.-p. (2011). Biomimetic Mineralization Synthesis of Hydroxyapatite Bacterial Cellulose Nanocomposites. *Prog. Nat. Sci. Mater. Int.* 21, 472–477. doi:10.1016/s1002-0071(12)60085-9

Yoshida, A., Miyazaki, T., Ashizuka, M., and Ishida, E. (2006). Bioactivity and Mechanical Properties of Cellulose/carbonate Hydroxyapatite Composites Prepared *In Situ* through Mechanochemical Reaction. *J. Biomater. Appl.* 21, 179–194. doi:10.1177/0885328206059796

Yoshida, A., Miyazaki, T., Ishida, E., Ashizuka, M., Li, P., Zhang, K., et al. (2005). Preparation of Cellulose-Carbonate Apatite Composites through Mechanochemical Reaction. *Mater* 284-286, 855–858. doi:10.4028/0-87849-961-x.855

Yuan, H., Fernandes, H., Habibovic, P., de Boer, J., Barradas, A. M. C., de Ruiter, A., et al. (2010). Osteoinductive Ceramics as a Synthetic Alternative to Autologous Bone Grafting. *Proc. Natl. Acad. Sci. U.S.A.* 107, 13614–13619. doi:10.1073/pnas.1003600107

Yuan, Q., Bian, J., and Ma, M.-G. (2021). Advances in Biomedical Application of Nanocellulose-Based Materials: a Review. *Cmc* 28 (40), 8275–8295. doi:10.2174/0929867328666201130124501

Zakharov, N. A., Ezhova, Z. A., Koval', E. M., Kalinnikov, V. T., and Chalykh, A. E. (2005). Hydroxyapatite-Carboxymethyl Cellulose Nanocomposite Biomaterial. *Inorg. Mat.* 41, 509–515. doi:10.1007/s10789-005-0159-0

Zhang, S., Xiong, G., He, F., Huang, Y., Wang, Y., and Wan, Y. (2009). Characterisation of Hydroxyapatite/Bacterial Cellulose Nanocomposites. *Polym. Polym. Compos.* 17, 353–358. doi:10.1177/096739110901700602

Zhu, Q., Wang, J., Sun, J., and Wang, Q. (2020). Preparation and Characterization of Regenerated Cellulose Biocomposite Film Filled with Calcium Carbonate by *In Situ* Precipitation. *BioRes* 15, 7893–7905. doi:10.15376/biores.15.4.7893-7905

Zhu, X. D., Fan, H. S., Xiao, Y. M., Li, D. X., Zhang, H. J., Luxbacher, T., et al. (2009). Effect of Surface Structure on Protein Adsorption to Biphasic Calcium-Phosphate Ceramics *In Vitro* and *In Vivo*. *Acta Biomater.* 5, 1311–1318. doi:10.1016/j.actbio.2008.11.024

Zhu, Y.-J., and Chen, F. (2014). Microwave-assisted Preparation of Inorganic Nanostructures in Liquid Phase. *Chem. Rev.* 114, 6462–6555. doi:10.1021/cr400366s

Zimmermann, K. A., LeBlanc, J. M., Sheets, K. T., Fox, R. W., and Gatenholm, P. (2011). Biomimetic Design of a Bacterial Cellulose/hydroxyapatite Nanocomposite for Bone Healing Applications. *Mater. Sci. Eng. C* 31, 43–49. doi:10.1016/j.msec.2009.10.007

Conflict of Interest: The authors declare that the research was conducted in the absence of any commercial or financial relationships that could be construed as a potential conflict of interest.

Publisher's Note: All claims expressed in this article are solely those of the authors and do not necessarily represent those of their affiliated organizations, or those of the publisher, the editors, and the reviewers. Any product that may be evaluated in this article, or claim that may be made by its manufacturer, is not guaranteed or endorsed by the publisher.

frontiers | Frontiers in Bioengineering and Biotechnology

ORIGINAL RESEARCH
published: 19 July 2022
doi: 10.3389/fbioe.2022.943692

Biodegradation of Gramineous Lignocellulose by *Locusta migratoria manilensis* (Orthoptera: Acridoidea)

Hongsen Zhang[1,2], *Zhenya Li*[3], *Hongfei Zhang*[1], *Yan Li*[1], *Fengqin Wang*[1,2], *Hui Xie*[1,2], *Lijuan Su*[1]* *and Andong Song*[1,2]*

[1]College of Life Science, Henan Agricultural University, Zhengzhou, China, [2]Key Laboratory of Enzyme Engineering of Agricultural Microbiology, Ministry of Agriculture, Zhengzhou, China, [3]College of Plant Protection, Henan Agricultural University, Zhengzhou, China

Exploring an efficient and green pretreatment method is an important prerequisite for the development of biorefinery. It is well known that locusts can degrade gramineous lignocellulose efficiently. Locusts can be used as a potential resource for studying plant cell wall degradation, but there are few relative studies about locusts so far. Herein, some new discoveries were revealed about elucidating the process of biodegradation of gramineous lignocellulose in *Locusta migratoria manilensis*. The enzyme activity related to lignocellulose degradation and the content of cellulose, hemicellulose, and lignin in the different gut segments of locusts fed corn leaves were measured in this study. A series of characterization analyses were conducted on corn leaves and locust feces, which included field emission scanning electron microscopy (FE-SEM), Fourier transform infrared (FTIR) spectroscopy, X-ray diffraction pattern (XRD), and thermogravimetric (TG) analysis. These results showed that the highest activities of carboxymethyl cellulase (CMCase), filter paper cellulase (FPA), and xylanase were obtained in the foregut of locusts, which strongly indicated that the foregut was the main lignocellulose degradation segment in locusts; furthermore, the majority of nutritional components were absorbed in the midgut of locusts. The activity of CMCase was significantly higher than that of xylanase, and manganese peroxidase (MnPase) activity was lowest, which might be due to the basic nutrition of locusts being cellulose and hemicellulose and not lignin based on the results of FE-SEM, FTIR, XRD, and TG analysis. Overall, these results provided a valuable insight into lignocellulosic degradation mechanisms for understanding gramineous plant cell wall deconstruction and recalcitrance in locusts, which could be useful in the development of new enzymatic pretreatment processes mimicking the locust digestive system for the biochemical conversion of lignocellulosic biomass to fuels and chemicals.

Keywords: locust (*Locusta migratoria manilensis*), gramineous lignocellulose, biodegradation, lignocellulolytic enzyme activity, digestive system, characterization analysis

OPEN ACCESS

Edited by:
Caoxing Huang,
Nanjing Forestry University, China

Reviewed by:
Xiaoyan Liu,
Huaiyin Normal University, China
Ikram Haq,
Government College University, Pakistan

***Correspondence:**
Lijuan Su
sulijuan816@126.com
Andong Song
songandong@henau.edu.cn

Specialty section:
This article was submitted to Bioprocess Engineering, a section of the journal Frontiers in Bioengineering and Biotechnology

Received: *14 May 2022*
Accepted: *01 June 2022*
Published: *19 July 2022*

Citation:
Zhang H, Li Z, Zhang H, Li Y, Wang F, Xie H, Su L and Song A (2022) Biodegradation of Gramineous Lignocellulose by Locusta migratoria manilensis (Orthoptera: Acridoidea). Front. Bioeng. Biotechnol. 10:943692. doi: 10.3389/fbioe.2022.943692

INTRODUCTION

The most abundant biopolymer on Earth is lignocellulose, which is recognized as a major sustainable resource for biofuels and biomaterial production (Bhatia et al., 2021). The heterogeneous and irregular arrangement of cellulose, hemicellulose, and lignin construction in the cell walls of gramineous plants and woody plants results in resistance to saccharification, which provides protection against enzymatic attack in lignocellulosic materials (Chandel et al., 2018). The

degradation of cellulose to fermentable sugars (saccharification) is the most important limiting step in the biorefinery process, which relies on low-activity cellulases from bacteria and/or fungi under biorefinery conditions and are easily inhibited at present (Jiang et al., 2019). Nonetheless, several species of insects in the orders Orthoptera, Coleoptera, and Dictyoptera have now been shown to produce endogenous cellulases in the midgut or salivary glands for extracting sugars from plant cell walls and for recycling the lignocellulosic biomass in nature (Su et al., 2013; Scharf, 2020). With adequate understanding of the biological systems, especially the catalytic properties of insect enzymes, biological systems will bring more hopes for improved utilization of renewable lignocellulosic biomass.

It is well known that locusts (Orthoptera: Acridoidea) have mouthparts for chewing and always feed on gramineous grasses with cellulose contents as much as 30–50%. Studies indicated that the cellulose degradation efficiency of the locust is similar to that of the termite and beetle by comparing the cellulase activity of different insects (Oppert et al., 2010; Su et al., 2013; Su et al., 2014). A 45-kDa homolog cellulase in *Dissosteira carolina* was isolated and purified from the salivary glands and the anterior foregut (Willis et al., 2010). Endoglucanase belonging to GHF9 was cloned from a whole-body cDNA library of *Teleogryllus emma*, providing the first endoglucanase clone from an orthopteran species (Kim et al., 2008). The gene fusion of endoglucanase from *T. emma* and xylanase from *Thermomyces lanuginosus* were constructed into a fusion enzyme (EG-M-Xyn), which showed great potential in improving the enzymatic hydrolysis of lignocellulose to produce fermentable sugars (Chen et al., 2018). Some species in the Acrididae family were notorious plant feeders; therefore, research on locusts had rarely focused on specific cellulolytic systems in these species but mainly on prevention and control, biological characteristics, and species classification (Zhang et al., 2019). Elucidation of the mode of lignocellulosic digestion by the locust might provide essential information toward efficient lignocellulose degradation that would be potentially useful for the production of high-value lignocellulosic-derived products and cellulosic biofuel. Therefore, the mechanism of the gramineous plant digestion process and the related enzyme systems for lignocellulose degradation in locusts are worth studying. In addition, the degradation of gramineous plants by the locust, which has not yet been documented, could be important for establishing alternate systems to degrade the gramineous plants.

In our preliminary work, the lignocellulolytic activities in the gut fluids of about 54 insect species that belong to seven different taxonomic orders were determined, and the highest carboxymethyl cellulase (CMCase) activity in the gut fluids were found in Coleoptera and Orthoptera (Su et al., 2013; Su et al., 2014). Therefore, the purposes of this study are as follows: 1) to estimate enzyme activity assays related to lignocellulosic degradation in the gut fluids of *Locusta migratoria manilensis*; 2) to measure the content of cellulose, hemicelluloses, and lignin in corn leaves in the different gut segments of the locust; and 3) to analyze the physical–chemical properties of locust feces using field emission scanning electron microscopy (FE-SEM), Fourier transform infrared (FTIR) spectroscopy, X-ray diffraction (XRD) pattern, and thermogravimetric (TG) analysis/differential thermogravimetry (DTG). Overall, the results provide insight into lignocellulose degradation mechanisms for understanding plant cell wall deconstruction, which could be useful in the development of new biological pretreatment processes.

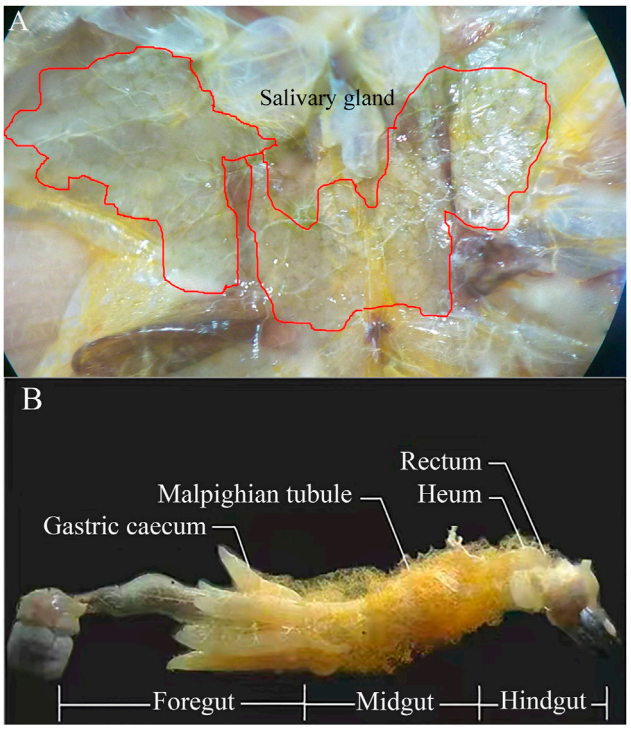

FIGURE 1 | Salivary gland **(A)** and dissection of adult locust digestive tract with labeled regions **(B)**.

MATERIALS AND METHODS

Sample Collection and Preparation of Crude Enzyme Liquid

Locust (*L. migratoria manilensis*) samples were provided by Insect Cultivation Co., Ltd., of Xingyang City in China. Locusts were supplied with *ad libitum* fresh corn leaf blades in the covering with voile (0.5 × 0.5 × 0.5 m) at room temperature after 1 week. Once they reached adulthood, they were divided into three groups (about 100 locusts per group) for three biological replicate samples. The feces and orts of adult locusts were collected every day and stored at −20°C until being freeze-dried to a constant weight. The feces and orts were separated and weighed.

The salivary glands, foregut, midgut, and hindgut of the locusts (**Figure 1**) were dissected on ice using a dissecting needle and ophthalmic forceps. The salivary glands and intestinal contents (foregut, midgut, and hindgut) from 20 adult individuals were taken out, and one part of intestinal contents was soaked in phosphate-buffered saline (PBS) solution (8-g NaCl, 0.2-g KCl, 1.44-g Na_2HPO_4, and 0.24-g

KH_2PO_4, with 1-L deionized water, pH 7.4) and was used to determine the enzymatic activity. The other parts of intestinal contents, feces, orts, and the fresh corn leaves control were ball-milled individually under nitrogen to a fine powder with a Fritsch Planetary Mill (Pulverisette, Germany) using agate bowls and balls for the preservation of the lignin primary structure. Afterward, the fine powders were subjected to further analysis (lignocellulosic content, FE-SEM, FTIR spectroscopy, XRD, and TG analysis/DTG).

Activity Assays of Carboxymethyl Cellulase, Filter Paper Cellulose, Xylanase, and Manganese Peroxidase

Intestinal contents and salivary glands were fully minced using Micro-Tip Scissors in PBS buffer solution, underwent ultrasonic treatment (ultrasonic intensity 300 W, every ultrasonic time 3 s and interval 4 s, 90 times), and centrifuged at 250 g for 30 min. The supernatant was stored at −80°C as coarse enzyme liquid. CMCase, filter paper cellulase (FPA), and xylanase activities were evaluated by measuring the amount of reducing sugars released from the substrate with a modified 3,5-dinitrosalicylic acid assay (Su et al., 2013). The different substrates were carboxymethyl cellulose (CMC) sodium salt, FP (2 × 3 cm), and xylose separately. One unit of enzymatic activity was defined as the amount of enzyme released from 1 μmol of reducing sugar (glucose or xylose equivalents) per minute (U/mg). Manganese peroxidase (MnPase) activity was determined spectrophotometrically at 470 nm using a Pharma-Spec UV-1700 spectrophotometer (Shimadzu, Japan) from samples taken from the enzyme solution. For the determination of MnPase activity, 2,6-DMP was used as a substrate together with $MnSO_4$ and H_2O_2 according to a previous report (Wariishi et al., 1992). The amount of enzyme that catalyzes 1-μmol substrate in 1 min was referred to as an enzyme activity unit (U/mg). In this study, all the experiments were conducted in triplicate, and the statistical analysis of the results was performed using Origin 2018 software.

Cellulose, Hemicellulose, and Lignin Content Analysis

To determine the cellulose, hemicellulose, and lignin content of the dry matter of intestinal contents and feces in locusts, a concentrated sulfuric acid hydrolysis method was used according to a previous report (Sluiter et al., 2012) with minor modifications as described below. The samples were successively extracted in a Soxhlet apparatus using ethanol (200 ml/g) to remove resin and pigment; afterward, a two-step hydrolysis with 72% concentrated sulfuric acid and 4% dilute sulfuric acid to hydrolyze cellulose and hemicellulose into glucose and xylose, respectively, was carried out. Then, the concentrations of glucose and xylose were measured using high-performance liquid chromatography (LC-20 AD, refractive index detector RID-10A, Shimadzu, Kyoto, Japan) with the Aminex HPX-87H column (Bio-rad, Hercules, United States) at 65°C using the mobile phase of 5 mM H_2SO_4 at a flow rate of 0.6 ml/min. The lignin content of extractive-free samples was estimated following the method described previously.

Analysis of Physical and Chemical Structure in Locust Feces

FE-SEM analysis: The surface ultrastructure of samples was observed by using a JSM-7001F field emission scanning electron microscope (JEOL, Japan) after conductive treatment. The corn leaves and locust feces were cut into fragments of approximately 4 mm^2. The fragments were immersed in a fixative solution (5% formaldehyde, 90% ethanol, and 5% acetic acid) for 24 h at room temperature and then were dehydrated with an increasing series of ethanol (70%, 80%, 90%, and 100%). The samples were glued on "stubs" with the adaxial and abaxial surfaces facing up and covered with carbon. The locust feces and fresh corn leaves were analyzed by FE-SEM to correlate directly with the modification resulting from the digestion process of the locusts.

FTIR spectroscopy assays: FTIR provided information on the lignocellulosic structural changes of corn leaves involving the functional groups after going through the gut of the locust. After the samples were ground into powder in a mortar and with KBr tablet treatment, the transmissivity was determined using a Nicolet 5700 FTIR spectroscope (TMAG, United States) using 2 mg of each sample and scanning ranges from 400 to 4,000 cm^{-1}. Baseline and attenuated total reflection corrections for penetration depth and frequency variations were applied using the Shimadzu IR solution 1.30 software supplied with the equipment.

XRD: The crystallinity of corn leaves and locust feces was compared using the XRD profiles. The D8-ADVANCE X-ray diffractometer (Bruker, Germany) was used with the following settings: the X-ray source was copper target, 1.5406 Å wavelength, 40 Kv pipe pressure, DS slit 1, RS 0.2 mm slit, SS 0.2 mm slit with a scanning rate of 4°, and sampling over 0.04 interval time. The relative crystallinity of treatment materials was obtained using the Segal formula (Inoue et al., 2008).

TG analysis: TG analysis is based on the precise study of weight loss during programmed exposure to temperature, to determine digesting-induced changes in the general characteristics of lignocellulose decomposition and activation energies for bond cleavage under pyrolysis and combustion. The determination conditions of a DSC-60 differential scanning calorimeter (TA, United States) were that approximately 5-mg samples were loaded individually in an aluminum pan and vaporized under a nitrogen atmosphere with a flow rate of 20 ml/min and the heating rate was 10°C/min. The TG curve of samples could be measured accurately.

RESULTS AND DISCUSSIONS

Lignocellulolytic Enzyme Activity of Locust

In order to understand the spatial expression of lignocellulolytic enzyme in the different segments of the digestive tract in locusts, the lignocellulolytic enzyme of the locust gut contents within salivary glands and the foregut, midgut, and hindgut segments (**Figure 1**) was evaluated using FP, CMC, xylose, and 2,6-DMP as substrates.

The activities of FPA, CMCase, xylanase, and MnPase showed similar tendency: foregut > salivary glands > midgut

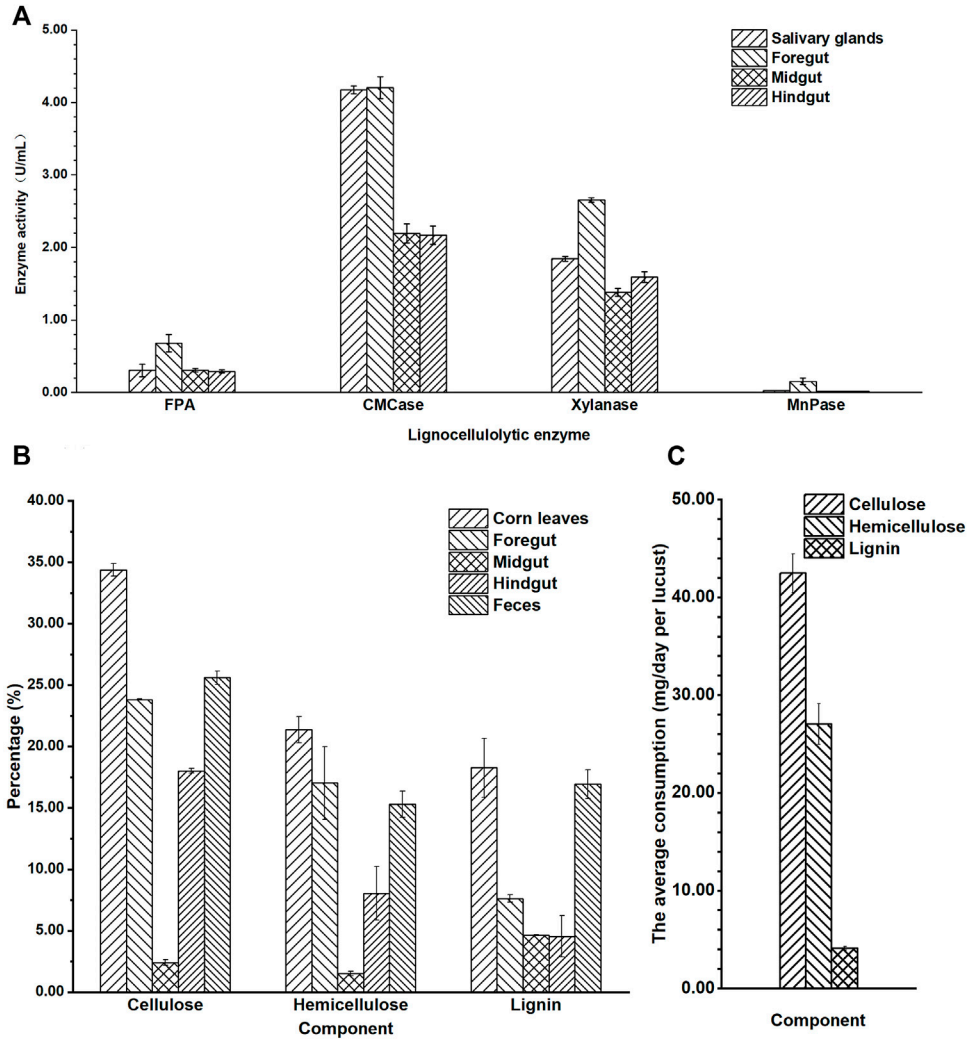

FIGURE 2 | The lignocellulosic degradation of locust. **(A)** Quantitative determination of filter paper cellulase (FPA), carboxymethyl cellulase (CMCase), xylanase, and Mn peroxidase (MnPase) activities in the gut regions of the adult locust. **(B)** The content of cellulose, hemicellulose, and lignin in the different parts of the digestive system in the locust. **(C)** The average consumption of lignocellulose per locust in 1 day.

> hindgut (**Figure 2A**). The highest lignocellulolytic enzyme activities were localized in the foregut segment (FPA 0.68 U/mg, CMCase 4.21 U/mg, xylanase 2.66 U/mg, and MnPase 0.15 U/mg, separately), while they were significantly reduced in the midgut and hindgut regions ($p \leq 0.01$). The activities of FPA, CMCase, xylanase, and MnPase in the foregut were 2.3, 1.9, 1.7, and 7.7 times the relative activities in the hindgut separately. The activities of FPA, xylanase, and MnPase were revealed to be higher in the foregut than in salivary glands, while the CMCase activity was similar in the foregut and salivary glands, which verified that both of them have a stronger secretory ability of CMCase. No significant differences were detected when comparing the activities of FPA, CMCase, and MnPase in the midgut and hindgut, expect for xylanase. It could be speculated from these results that the major segment of lignocellulose degradation in locusts was the foregut, followed by the midgut and hindgut.

The average activity of CMCase (3.18 U/mg) in the gut was significantly higher than that of xylanase (1.86 U/mg), and MnPase activity (0.05 U/mg) was lowest ($p \leq 0.01$). These results showed that the basic nutritional components of locusts from corn leaves were cellulose and hemicellulose, not lignin.

Lignocellulosic Degradation of Locust

To further explain the special characteristic of degradation in the digestive tract, the content of cellulose, hemicellulose, and lignin in the different segments of the gut and feces after the locusts were fed corn leaves for 1 week was analyzed (**Figure 2B**). The content of the three lignocellulosic components (cellulose, hemicellulose, and lignin) was mostly in corn leaves, and then in the feces, foregut, hindgut, and midgut. The lignocellulosic content descended gradually from corn leaves to the foregut, with the lowest

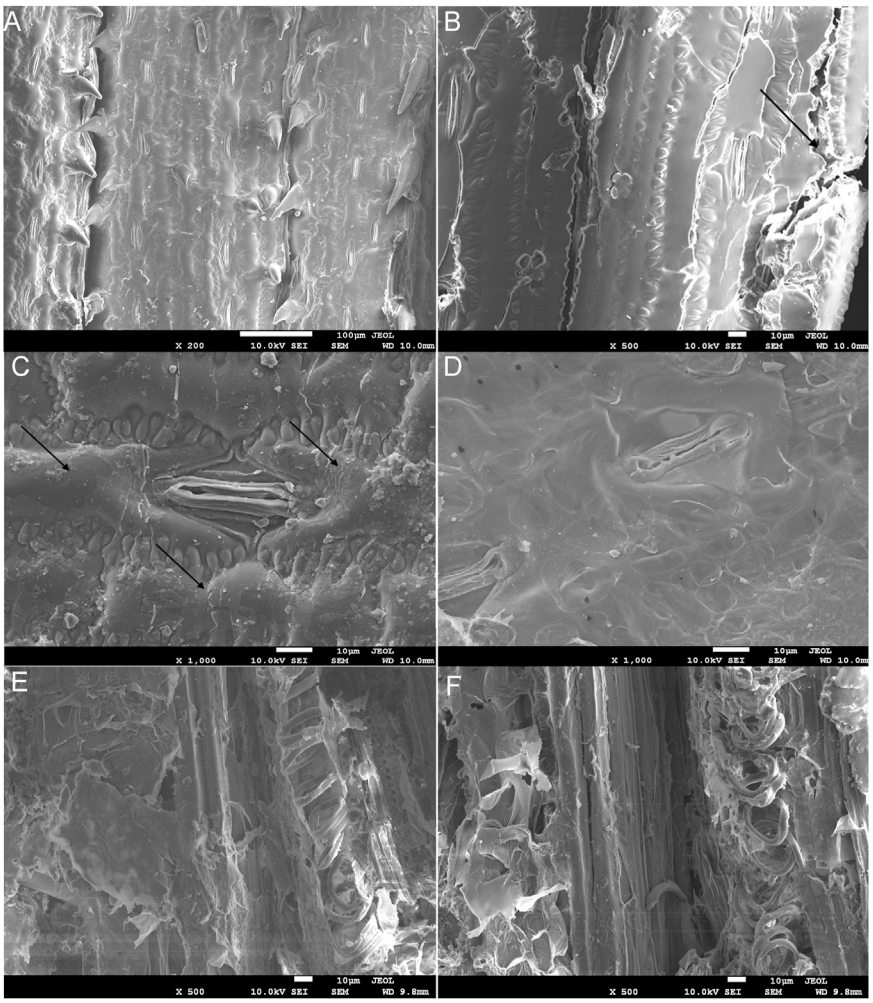

FIGURE 3 | The field emission scanning electron microscopy (FE-SEM) charts of corn leaves **(A)** and undigested corn leaves residue in locust feces **(B–F)**. Note: icon size 10 μm; accelerating voltage 10.0 kV; A–D working distance 10.0 mm, E and F 9.8 mm; amplification of A × 200, B × 500, C and D × 1,000, and E and F × 500. The arrows indicate the edge of the corn leaf being laniated in **(B)**. The arrows indicate silicrete in the cell surface had fallen out using enzymatic hydrolysis in the digestive tract in **(C)**.

content in the midgut, and then a gradual increasing trend was seen from the midgut to the hindgut and feces. The content of cellulose, hemicellulose, and lignin in the midgut was the lowest, being 2.41%, 1.50%, and 8.64%, respectively, and they reduced to 31.97%, 19.87%, and 9.62%, respectively, lower than those of corn leaves (cellulose 34.38%, hemicellulose 21.37%, and lignin 18.26%). In the hindgut, the content of cellulose and hemicellulose suddenly increased accumulation compared with that in the midgut (being 7.47 and 5.36 times, respectively), while there was no significant difference in lignin. The content of lignin decreased gradually from the foregut, to the midgut, and to the hindgut compared with that of corn leaves, and then suddenly it increased accumulation in feces (approximately 2.6 times).

From the consumption of each locust in a day (**Figure 2C**), cellulose was the major component digested and absorbed in locusts (42.4 mg), followed by hemicellulose (27.0 mg) and lignin (4.1 mg), with a significant difference ($p \leq 0.01$).

The Analysis of the Field Emission Scanning Electron Microscopy of Corn Leaves and Locust Feces

The surface structure of corn leaves (**Figure 3A**) and undigested residue of corn leaves in feces (**Figures 3B–F**) were analyzed by FE-SEM. After chewing and digesting by the locusts, the surface structure of corn leaves was subjected to different degrees of destruction, and this decomposition got more and more thorough, as shown in **Figures 3B–F**. Compare with control (**Figure 3A**), the edge of the corn leaves was laniated, as shown in **Figure 3B** (indicated by the black arrows), and epidermal hair near the leaf vein had fallen out by mixing or grinding in the digestive tract. Silicrete in the cell surface had fallen out by enzymatic hydrolysis in

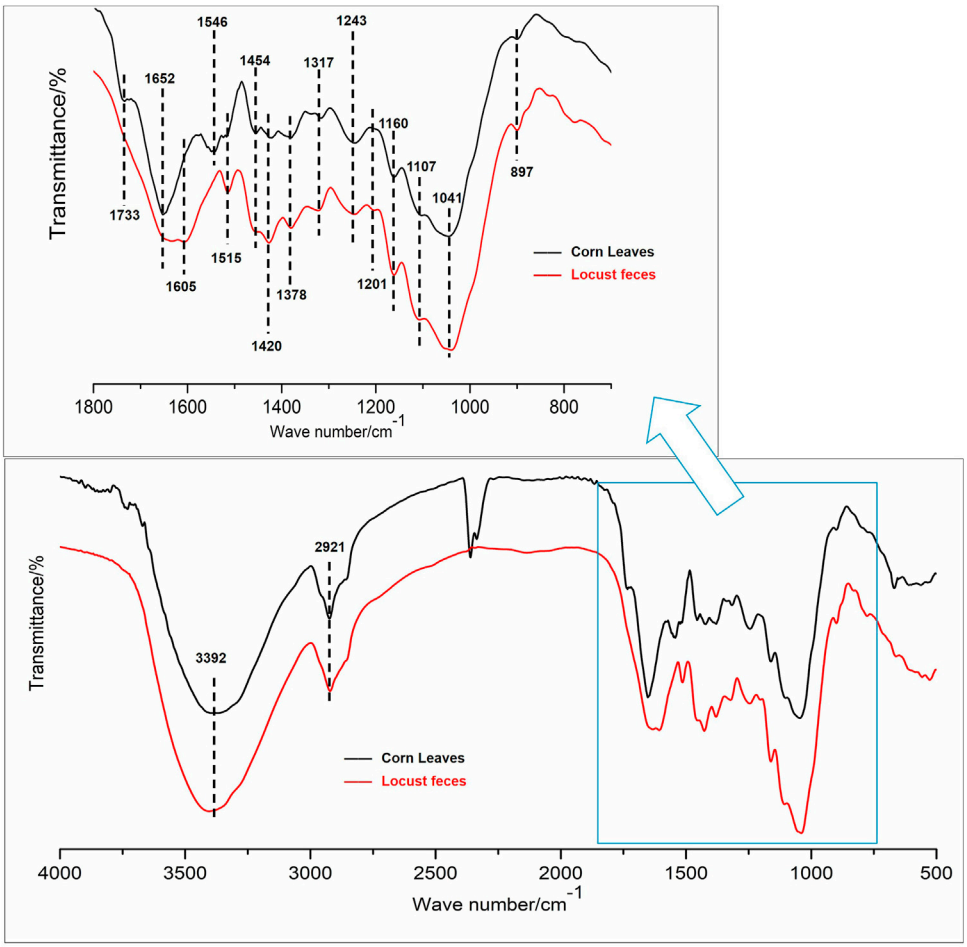

FIGURE 4 | Selected Fourier transform infrared (FTIR) spectroscopy spectra, 400–4,000 cm^{-1} region, for functional group changes by the digestion.

the digestive tract (indicated by the black arrows in **Figure 3C**), but the stomatal apparatus and cell wall were kept perfectly (**Figure 3C**). The stratum corneum of the cell surface had decomposed completely and the cell boundary was out of sight, as shown in **Figure 3D**. The corn leaves had been decomposed more completely in **Figures 3E,F**. Mesophyll tissue had been digested and assimilated, and the phloem and thickened part of the xylem in the tube wall of the vascular bundle with high lignin content could be observed clearly. Moreover, the unthickened part of cellulose and hemicellulose had been broken down.

Fourier Transform Infrared Spectroscopy Analysis of Corn Leaves and Locust Feces

FTIR spectra comparison of corn leaves and locust feces are shown in **Figure 4**, and the assignments of the functional groups in the two samples are shown in **Table 1**. From the functional groups related to cellulose and hemicellulose (Song et al., 2005; Ke et al., 2011), the FTIR transmittance of feces significantly increased intensity in peaks 1, 2, 3, 10, 21, 22, and 25. This could be attributed to the metabolism of N–H and –OH on associating with hydroxybenzene and alcohol, the absorption band of methyl, of C–O–C on esters in peaks 1, 2, and 3. Greater intensities of both symmetric bending of aliphatic C–H and C–O stretching in alcohols in peaks 12 and 19 suggested the existence of polysaccharides in the locust feces.

From the functional groups related to lignin, the FTIR transmittance of feces significantly increased intensity in peaks 4–8, 11, 13–18, and 20, which was absorption, deforming, or stretching vibrations of aromatic rings, phenolic hydroxyl, guaiacyl rings, or benzene rings, and so on (Song et al., 2005; Ke et al., 2011). The increasing intensity of peaks 8 and 13 of the feces sample can be attributed to the metabolism of the $-CH_3$ and $-CH_2$ groups. The most obvious change was observed in the range of 1,655 cm^{-1}, indicating the greater exposure of the stretching of C=O conjugated to aromatic rings (peak 12).

X-Ray Diffraction Analysis and Kinetic Thermogravimetric Analysis of Corn Leaves and Locust Feces

XRD was applied to analyze the changes in the crystalline and amorphous regions of cellulose, which showed that the

TABLE 1 | Main assignments of cellulose, hemicellulose, lignin, polysaccharide, and protein in FTIR spectrum band.

No.	Wave numbers (cm^{-1})	Assignments
Cellulose/hemicellulose		
1	3,409	Symmetric vibrations of N–H
2	3,000–3,400	Vibrations of –OH on associated with hydroxybenzene and alcohol
3	2,842–2,940	Absorption band of methyl, methylene, and methine
10	1,448–1,461	Deforming vibrations of C–H on methyl and methylene
21	1,040	Stretching vibrations of C–O–C on esters
22	917–921	Deforming vibrations of $–CH_2$ at the end of methylene
25	615–637	Deforming vibrations of C–O–H
Lignin		
4	1714–1725	Stretching of C=O unconjugated to aromatic rings (oxidized sidechains)
5	1,655	Stretching of C=O conjugated to aromatic rings
6	1,594–1,609	Aromatic ring vibrations and C=O stretching
7	1,502–1,536	Aromatic ring absorption band
8	1,462–1,464	Asymmetric C–H bending (in CH_3 and $–CH_2–$)
11	1,421–1,424	Aromatic ring vibrations
13	1,365	Symmetric deformation of C–H in methyl groups
14	1,360	Phenolic hydroxyl vibrations
15	1,270	Vibrations of guaiacyl rings and stretching vibrations of C–O bonds
16	1,221–1,240	Aromatic ring absorption band
17	1,216–1,225	C–C, C–O, and C=O stretching (G condensed > G etherified)
18	1,160	Deformation vibrations of C–H bonds on benzene rings
20	1,075–1,090	Deformation vibrations of C–O bonds in secondary alcohols and aliphatic ethers
24	830	Deformation vibrations of C–H bonds on aromatic rings
Polysaccharide		
12	1,370	Symmetric bending of aliphatic C–H
19	1,030–1,170	C–O stretching in alcohols
23	890	β-Glycosidic linkages in pyranose units
Protein		
9	1,516	C=O stretching in amides

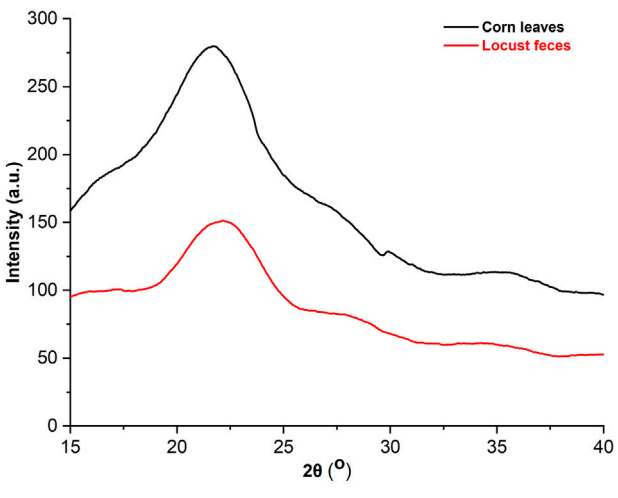

FIGURE 5 | The analysis of the X-ray diffraction (XRD) pattern of corn leaves and locust feces. XRD diffraction conditions: copper target, 1.5406 Å wavelength, 40 Kv pipe pressure, DS slit 1°, RS 0.2-mm slit, SS 0.2-mm slit with a scanning rate of 4°, and sampling over 0.04 interval time.

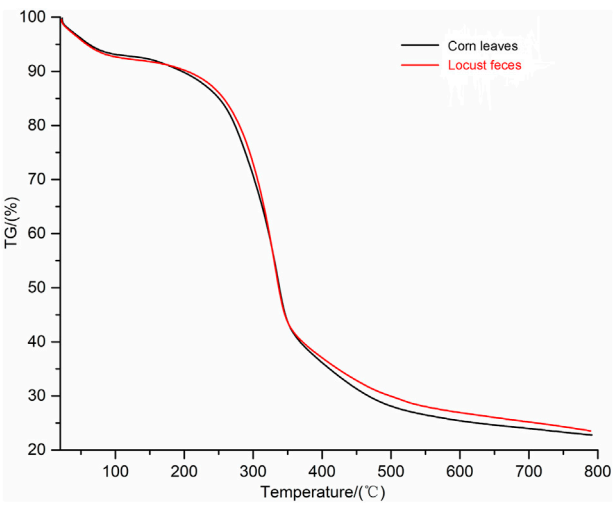

FIGURE 6 | Thermogravimetric (TG) analysis spectra of corn leaves and locust feces. TG analysis kinetics parameters: the heating rate was 10°C/min, and the flow rate of N_2 was 20 ml/min.

characteristic peak of cellulose I at $2\theta = 22.3^{o}$ was observed in both corn leaves and locust feces, and the spectra are presented in **Figure 5**. The relative crystallinity of corn leaves and locust feces were 30.95% and 37.99%, respectively, which was obtained using the Segal formula. Relative crystallinity in locust feces was increased by 23.4% compared with that in corn leaves, indicating that the corn leaves were damaged after digestion.

TG analysis was put into effect to investigate the thermal degradation kinetics of both digested (locust feces) and undigested corn leaves samples. In this work, the major chemical components of corn leaves (cellulose, hemicelluloses, and lignin) were degraded at different temperatures. The TG curves of corn leaves and locust feces are shown in **Figure 6**. TG analysis measured the weight loss as a function of temperature. According to TG analysis, there were two obvious differences in pyrolysis characteristics of corn leaves and locust feces: 1) the volatile content in feces was higher than that of corn leaves, and 2) the temperature interval of locust feces was volatile and tended to be on the high-temperature side compared with that of corn leaves. The volatile content of locust feces reached 76.5%, which was 8.97% higher than that of corn leaves. These results showed that the content of fixed carbon was decreased after digestion and absorption of the locust gut. Because the biggest contributor to fixed carbon content was lignin in lignocellulose fractions, it could be inferred that the lignin content of locust feces was lower than that of corn leaves. The temperature of begin and end to separate out in volatile of locust feces were 289°C and 363°C, which were 22°C and 15°C higher than that of corn leaves respectively. The above results clearly indicate that corn leaves were decomposed or used after the intestinal digestion of locusts.

DISCUSSIONS

In nature, different lignocellulose degradation processes exist that rely on the combined action of many lignocellulolytic enzymes present in the digestive tract of phytophagous and xylophagous organisms (Godon et al., 2013; Gales et al., 2018). To date, most studies focused on phytophagous and xylophagous insects, which have been well known as the most effective lignocellulose digesters (Rizzi et al., 2013; Jang and Kikuchi, 2020). However, only few studies have focused on the mechanism of lignocellulose deconstruction in the gut system of herbivorous locusts in recent years. In this study, we examined the enzyme activity related to the degradation of lignocellulose and the content of cellulose, hemicelluloses, and lignin in the different gut segments of *L. migratoria manilensis* after being fed with corn leaves. Meanwhile, a series of characterization analyses were conducted on corn leaves and locust feces. These results provided evidence of lignocellulose structural alterations during such digestion process of gramineous lignocellulose.

As previously observed for alternative insect samples, the lignocellulolytic enzymes were localized mainly in the foregut or midgut regions, while greatly reduced activity was detected in the hindgut region. For example, the lignocellulolytic enzymes were localized to the midgut regions of the *D. carolina* digestive tract, and then database searches indicated high similarity with the endo-β-1,4-glucanases from invertebrates, bacteria, and plants (Willis et al., 2010). The relative expression levels of 12 digestive enzyme genes in the midgut were significantly higher than those in the other tissues for *Eucryptorrhynchus scrobiculatus* (Gao et al., 2020). High endo-β-1,4-glucanase activity was detected in the midgut of the *Eurycantha calcarata* (Shelomi et al., 2014). In this study, locusts were fed corn leaves for 1 week, and the majority of lignocellulolytic enzyme activities were localized to the salivary glands and foregut regions, while they significantly reduced in the midgut and hindgut regions, which indicated that the main spatial part of lignocellulose degradation was in the foregut of locusts. This conclusion indicated that the location of lignocellulolytic enzyme enrichment in locusts was a little different from the above-mentioned insects. The activities of FPA, CMCase, and xylanase in the foregut were higher than those in the midgut and hindgut (**Figure 2A**), which is probably due to the salivary glands of locusts including many released digestive enzymes that would flow into the foregut and catalyze the hydrolysis of the cellulose and hemicellulose in the foregut region. In this study, the highest activity of CMCase was in the salivary glands and foregut but not in the midgut, which was somewhat different from previous studies.

From the content of cellulose, hemicellulose, and lignin in the different parts of the gut and feces, it was speculated that the locusts had strong lignocellulosic degradation ability in this study. The lower content of cellulose, hemicellulose, and lignin in the midgut than in the foregut indicated that the main region of absorption should be the midgut, while the rest of the unabsorbed ingredients in the midgut would be concentrated in the hindgut, leading to the content of corn leaves in the hindgut and feces being increased significantly. Quantitative and qualitative assays of cellulase identified the foregut as the region with the highest levels of cellulase activity in both *Thermobia domestica* and *Ctenolepisma longicaudata* (Pothula et al., 2019). The midgut had also been identified as the main biological treatment region; alkaline conditions of the midgut could enhance the dissolution of lignin and deesterification of intermolecular ester bonds (Gales et al., 2018), which could further increase the surface area and porosity and decrease the crystallinity of the biomass (Kim et al., 2016; Ozbayram et al., 2020). Hence, combining the data on the enzyme activity and content of lignocellulose, it could be reasonable to infer that the major decomposition of lignocellulose was accomplished in the foregut and midgut and the majority of nutritional components were absorbed in the midgut of locusts. According to the nutrient consumption of each locust in a day, the major component digested and absorbed by the locusts was cellulose, followed by hemicellulose. Meanwhile, only 4.1-mg lignin (1/10th of cellulose) was consumed. If lignin was degraded largely by locusts, many inhibitors would accumulate, which would not be conducive to the degradation of cellulose (Huang et al., 2022). However, there are some interesting results that need to be explored further. One is that even if the hemicellulose component were degraded into sugar monomers, the locusts could not utilize pentoses, such as xylose and arabinose (Dadd, 1960), which constituted the majority of hemicellulose polysaccharides in gramineous plants (Wilkie, 1979). These pentoses might be utilized by microorganisms in the locust guts.

According to the results of FE-SEM, the surface structure of corn leaves was subjected to different degrees of destruction after mastication and digestion. It showed that the lignocellulose of corn leaves could be digested, assimilated, and utilized by the locusts, especially cellulose and hemicellulose. The cell wall degrading enzymes (such as CMCase) could increase the pore size of the pit membrane, and separate adjacent xylem vessels (Pérez-Donoso et al., 2010). Nevertheless, the xylem in the tube wall of the vascular bundle resists lignocellulose degradation in

locusts; as shown by some experimental evidence, the bundle sheath cells appear to pass through the digestive system intact (Caswell and Reed, 1976). Therefore, for orthopteran herbivores, the lignin contents might be considered a barrier that locusts must mechanically rupture to assimilate nutrients and may be more important than was previously thought. It would be contributing as a diluent of the more easily digested cell contents (Clissold et al., 2004). In **Figure 3**, the surface structure of locust feces became rough. A similar phenomenon occurred with bamboo after conventional acid pretreatment (Lin et al., 2021), which suggested that the biodegradation of the locust gut could also achieve the effect of traditional acid pretreatment.

FTIR spectra comparison of corn leaves and locust feces could analyze the changes in the functional groups during the degradation of corn leaves. In this study, the FTIR transmittance of feces increased significantly, and intensity in the functional groups represented cellulose and hemicellulose, which was because the content of cellulose and hemicellulose in feces decreased significantly. It indicated that the cellulose and hemicellulose had been degraded to glucose and xylose, absorbed, and utilized by the locust gut. In addition, according to the functional groups related to lignin, the most obvious change was observed in the range of 1,655 cm^{-1}. It indicated that a greater exposure emerged by the stretching of C=O conjugated to aromatic rings (peak 12). It could be speculated that the removal of C=O conjugated to the aromatic ring group will help alleviate the steric hindrance effect of lignin to enzymes and may help the downstream hydrolysis of cellulose and hemicellulose (Ke et al., 2012). These results indicated that the lignin side-chain structure of corn leaves was modified after digestion and absorption of locusts. In short, the FTIR results of locust feces showed that the intestinal tract of locusts could degrade the corn leaves in two ways: 1) the functional groups of cellulose and hemicellulose (such as N–H, –OH, C–H, C–O–C, and $–CH_2$) had been degraded, absorbed, and utilized by the locust gut and 2) the functional groups of lignin (such as C=O and C–H aromatic rings, phenolic hydroxyl, guaiacyl rings, C–C, and C–O) had been dissociated and performed a side-chain modification of lignin as well as rearrangement of the modified lignin fragments by the locust gut. Furthermore, the majority of the lignin modifications occurred on G lignin sites; meanwhile, G lignin sites had scarcely any modifications in the lignin polymeric framework during the digestion by the locust gut.

After XRD, the relative crystallinity of cellulose in locust feces was significantly increased compared with that in corn leaves. The reason may be that the surface areas of amorphous and crystalline regions overflowed in corn leaves and the crystalline region was exposed outside after digestion and absorption of locusts. Some researchers found that the relative crystallinity of cellulose in sorghum straw increased from 48.7% to 65.5% after weak acid pretreatment (Dai et al., 2022). These results indicated that the biodegradation of locusts also had a similar effect compared with the conventional pretreatment.

The TG method was a technique to measure the relationship between mass and temperature under programmed temperature control. In this study, the major chemical components of corn leaves (cellulose, hemicelluloses, and lignin) degraded at different temperatures. The highly crystalline cellulose was thermally stable (Sharypov et al., 2002), and the amorphous hemicelluloses and lignin started decomposition before cellulose did (Hill, 2006), with hemicelluloses being the least thermally stable components on account of the acetyl groups (Ke et al., 2011), at approximately 300°C. Furthermore, lignin starts to degrade at relatively low temperatures, over a wide temperature range, at approximately 230°C. In this study, the data of TG analysis were consistent with the results of other previous characterization analyses, which ensured the accuracy of the results.

CONCLUSION

In this study, the locust was chosen as the research object and was fed fresh corn leaves for 1 week. In this process, the lignocellulolytic enzyme activities and the lignocellulosic contents in the different parts of the digestive tract were analyzed first. Then, the characterizations of lignocellulosic degradation after digestion in the digestive tract of the locusts were represented comprehensively using FE-SEM, XRD, FTIR, and TG analysis. The data proved conclusively the presence of lignocellulolytic enzyme activity and the efficient lignocellulose degradation ability in the digestive system of the locusts. The major decomposition of lignocellulose was accomplished in the foregut and the minor decomposition in the midgut. Nevertheless, the majority of nutritional components were absorbed in the midgut. According to the nutrient consumption of each locust in a day, the major component digested and absorbed by the locusts was cellulose, followed by hemicellulose, while the lignin component was barely digested by the locusts. The unique gramineous lignocellulose biodegradation system of insects could contribute to the development of new biorefinery pathways.

DATA AVAILABILITY STATEMENT

The raw data supporting the conclusions of this article will be made available by the authors, without undue reservation.

AUTHOR CONTRIBUTIONS

HZ: data curation and writing—review and editing. ZL: experimental guidance. HZ: experimental operation and data analysis. YL: resources. FW: investigation. HX: methodology. LS: supervision and validation. AS: project administration and funding acquisition.

FUNDING

This work was supported by the National Science Foundation of China Grant (31170350), the National Natural Science Foundation of China (21908044), and the Key Scientific Research Project of Universities of Henan Province (20A180012).

REFERENCES

Bhatia, R., Lad, J. B., Bosch, M., Bryant, D. N., Leak, D., Hallett, J. P., et al. (2021). Production of Oligosaccharides and Biofuels from Miscanthus Using Combinatorial Steam Explosion and Ionic Liquid Pretreatment. *Bioresour. Technol.* 323, 124625. doi:10.1016/j.biortech.2020.124625

Caswell, H., and Reed, F. C. (1976). Plant-Herbivore Interactions. The Indigestibility of C4 Bundle Sheath Cells by Grasshoppers. *Oecologia* 26, 151–156. doi:10.1007/BF00582893

Chandel, A. K., Garlapati, V. K., Singh, A. K., Antunes, F. A. F., and da Silva, S. S. (2018). The Path Forward for Lignocellulose Biorefineries: Bottlenecks, Solutions, and Perspective on Commercialization. *Bioresour. Technol.* 264, 370–381. doi:10.1016/j.biortech.2018.06.004

Chen, C.-C., Gao, G.-J., Kao, A.-L., and Tsai, Z.-C. (2018). Bi-Functional Fusion Enzyme EG-M-Xyn Displaying Endoglucanase and Xylanase Activities and its Utility in Improving Lignocellulose Degradation. *Int. J. Biol. Macromol.* 111, 722–729. doi:10.1016/j.ijbiomac.2018.01.080

Clissold, F. J., Sanson, G. D., and Read, J. (2004). Indigestibility of Plant Cell Wall by the Australian Plague Locust, *Chortoicetes Terminifera*. *Entomol. Exp. Appl.* 112, 159–168. doi:10.1111/j.0013-8703.2004.00192.x

Dadd, R. H. (1960). The Nutritional Requirements of Locusts-III Carbohydrate Requirements and Utilization. *J. Insect Physiol.* 5, 301–316. doi:10.1016/0022-1910(60)90012-3

Dai, L., Gu, Y., Xu, J., Guo, J., Jiang, K., Zhou, X., et al. (2022). Toward Green Production of Xylooligosaccharides and Glucose from Sorghum Straw Biowaste by Sequential Acidic and Enzymatic Hydrolysis. *Ind. Crops Prod.* 179, 114662. doi:10.1016/j.indcrop.2022.114662

Gales, A., Chatellard, L., Abadie, M., Bonnafous, A., Auer, L., Carrère, H., et al. (2018). Screening of Phytophagous and Xylophagous Insects Guts Microbiota Abilities to Degrade Lignocellulose in Bioreactor. *Front. Microbiol.* 9, 2222. doi:10.3389/fmicb.2018.02222

Gao, P., Liu, Z., and Wen, J. (2020). Expression Profiling of Plant Cell Wall-Degrading Enzyme Genes in *Eucryptorrhynchus Scrobiculatus* Midgut. *Front. Physiol.* 11, 1111. doi:10.3389/fphys.2020.01111

Godon, J.-J., Arcemisbéhère, L., Escudié, R., Harmand, J., Miambi, E., and Steyer, J.-P. (2013). Overview of the Oldest Existing Set of Substrate-Optimized Anaerobic Processes: Digestive Tracts. *Bioenerg. Res.* 6, 1063–1081. doi:10.1007/s12155-013-9339-y

Hill, A. S. (2006). *Wood Modification: Chemical, Thermal and Other Processes*. Chichester UK: Wiley and Sons. doi:10.1002/0470021748.ch3

Huang, C., Jiang, X., Shen, X., Hu, J., Tang, W., Wu, X., et al. (2022). Lignin-Enzyme Interaction: A Roadblock for Efficient Enzymatic Hydrolysis of Lignocellulosics. *Renew. Sustain. Energy Rev.* 154, 111822. doi:10.1016/j.rser.2021.111822

Inoue, H., Yano, S., Endo, T., Sakaki, T., and Sawayama, S. (2008). Combining Hot-Compressed Water and Ball Milling Pretreatments to Improve the Efficiency of the Enzymatic Hydrolysis of eucalyptus. *Biotechnol. Biofuels.* 1 (1), 2. doi:10.1186/1754-6834-1-2

Jang, S., and Kikuchi, Y. (2020). Impact of the Insect Gut Microbiota on Ecology, Evolution, and Industry. *Curr. Opin. Insect Sci.* 41, 33–39. doi:10.1016/j.cois.2020.06.004

Jiang, L.-Q., Zheng, A.-Q., Meng, J.-G., Wang, X.-B., Zhao, Z.-L., and Li, H.-B. (2019). A Comparative Investigation of Fast Pyrolysis with Enzymatic Hydrolysis for Fermentable Sugars Production from Cellulose. *Bioresour. Technol.* 274, 281–286. doi:10.1016/j.biortech.2018.11.098

Ke, J., Laskar, D. D., and Chen, S. (2011). Biodegradation of Hardwood Lignocellulosics by the Western Poplar Clearwing Borer, *Paranthrene Robiniae* (Hy. Edwards). *Biomacromolecules* 12 (5), 1610–1620. doi:10.1021/bm2000132

Ke, J., Laskar, D. D., Gao, D., and Chen, S. (2012). Advanced Biorefinery in Lower Termite-Effect of Combined Pretreatment during the Chewing Process. *Biotechnol. Biofuels.* 5 (1), 11. doi:10.1186/1754-6834-5-11

Kim, J. S., Lee, Y. Y., and Kim, T. H. (2016). A Review on Alkaline Pretreatment Technology for Bioconversion of Lignocellulosic Biomass. *Bioresour. Technol.* 199, 42–48. doi:10.1016/j.biortech.2015.08.085

Kim, N., Choo, Y. M., Lee, K. S., Hong, S. J., Seol, K. Y., Je, Y. H., et al. (2008). Molecular Cloning and Characterization of a Glycosyl Hydrolase Family 9 Cellulase Distributed throughout the Digestive Tract of the Cricket *Teleogryllus Emma*. *Comp. Biochem. Physiol. B Biochem. Mol. Biol.* 150 (4), 368–376. doi:10.1016/j.cbpb.2008.04.005

Lin, W., Yang, J., Zheng, Y., Huang, C., and Yong, Q. (2021). Understanding the Effects of Different Residual Lignin Fractions in Acid-Pretreated Bamboo Residues on its Enzymatic Digestibility. *Biotechnol. Biofuels.* 14, 143. doi:10.1186/s13068-021-01994-y

Oppert, C., Klingeman, W. E., Willis, J. D., Oppert, B., and Jurat-Fuentes, J. L. (2010). Prospecting for Cellulolytic Activity in Insect Digestive Fluids. *Comp. Biochem. Physiol. Biochem. Mol. Biol.* 155, 145–154. doi:10.1016/j.cbpb.2009.10.014

Ozbayram, E. G., Kleinsteuber, S., and Nikolausz, M. (2020). Biotechnological Utilization of Animal Gut Microbiota for Valorization of Lignocellulosic Biomass. *Appl. Microbiol. Biotechnol.* 104 (2), 489–508. doi:10.1007/s00253-019-10239-w

Pérez-Donoso, A. G., Sun, Q., Roper, M. C., Greve, L. C., Kirkpatrick, B., and Labavitch, J. M. (2010). Cell Wall-Degrading Enzymes Enlarge the Pore Size of Intervessel Pit Membranes in Healthy and Xylella Fastidiosa-Infected Grapevines. *Plant Physiol.* 152 (3), 1748–1759. doi:10.1104/pp.109.148791

Pothula, R., Shirley, D., Perera, O. P., Klingeman, W. E., Oppert, C., Abdelgaffar, H. M. Y., et al. (2019). The Digestive System in Zygentoma as an Insect Model for High Cellulase Activity. *PLoS One* 14 (2), e0212505. doi:10.1371/journal.pone.0212505

Rizzi, A., Crotti, E., Borruso, L., Jucker, C., Lupi, D., Colombo, M., et al. (2013). Characterization of the Bacterial Community Associated with Larvae and Adults of *Anoplophora Chinensis* Collected in italy by Culture and Culture in Dependent Methods. *Biomed. Res. Int.* 2013, 420287. doi:10.1155/2013/420287

Scharf, M. E. (2020). Challenges and Physiological Implications of Wood Feeding in Termites. *Curr. Opin. Insect Sci.* 41, 79–85. doi:10.1016/j.cois.2020.07.007

Sharypov, V. I., Marin, N., Beregovtsova, N. G., Baryshnikov, S. V., Kuznetsov, B. N., Cebolla, V. L., et al. (2002). Co-Pyrolysis of Wood Biomass and Synthetic Polymer Mixtures Part I, Influence of Experimental Conditions on the Evolution of Solids, Liquids and Gases. *J. Anal. Appl. Pyrolysis.* 64, 15–28. doi:10.1016/S0165-2370(01)00167-X

Shelomi, M., Jasper, W., Atallah, J., Kimsey, L. S., and Johnson, B. R. (2014). Differential Expression of Endogenous Plant Cell Wall Degrading Enzyme Genes in the Stick Insect (Phasmatodea) Midgut. *B.M.C Genomics.* 15, 917. doi:10.1186/1471-2164-15-917

Sluiter, A., Hames, B., Ruiz, R., Scarlata, C., Sluiter, J., Templeton, D., et al. (2012). "Determination of Structural Carbohydrates and Lignin in Biomass," in *Laboratory Analytical Procedure (LAP)* (Golden, CO: NREL National Renewable Energy Laboratory). Issue Date: April 2008, Revision Date: August 2012.

Song, A., Zhang, B., Wu, K., and Huang, B. (2005). Production of Lignocellulolytic Enzymes and Rice Straw Biodegradation by *Coriolus Versicolor*. *Chin. J. Process Eng.* 5 (4), 414–419. (In Chinese). doi:10.3321/j.issn:1009-606X.2005.04.01

Su, L.-J., Liu, H., Li, Y., Zhang, H.-F., Chen, M., Gao, X.-H., et al. (2014). Cellulolytic Activity and Structure of Symbiotic Bacteria in Locust Guts. *Genet. Mol. Res.* 13 (3), 7926–7936. doi:10.4238/2014.September.29.6

Su, L.-J., Zhang, H.-F., Yin, X.-M., Chen, M., Wang, F.-Q., Xie, H., et al. (2013). Evaluation of Cellulolytic Activity in Insect Digestive Fluids. *Genet. Mol. Res.* 12 (3), 2432–2441. doi:10.4238/2013.January.4.11

Wariishi, H., Valli, K., and Gold, M. H. (1992). Manganese(II) Oxidation by Manganese Peroxidase from the Basidiomycete *Phanerochaete Chrysosporium*. Kinetic Mechanism and Role of Chelators. *J. Biol. Chem.* 267 (33), 23688–23695. doi:10.0000/PMID1429709

Wilkie, K. C. B. (1979). The Hemicelluloses of Grasses and Cereals. *Adv. Carbohydr. Chem. Biochem.* 36, 215–264. doi:10.1016/S0065-2318(08)60237-1

Willis, J. D., Klingeman, W. E., Oppert, C., Oppert, B., and Jurat-Fuentes, J. L. (2010). Characterization of Cellulolytic Activity from Digestive Fluids of *Dissosteira Carolina* (Orthoptera: Acrididae). *Comp. Biochem. Physiol. B Biochem. Mol. Biol.* 157 (3), 267–272. doi:10.1016/j.cbpb.2010.06.012

Zhang, L., Lecoq, M., Latchininsky, A., and Hunter, D. (2019). Locust and Grasshopper Management. *Annu. Rev. Entomol.* 64, 15–34. doi:10.1146/annurev-ento-011118-112500

Conflict of Interest: The authors declare that the research was conducted in the absence of any commercial or financial relationships that could be construed as a potential conflict of interest.

Publisher's Note: All claims expressed in this article are solely those of the authors and do not necessarily represent those of their affiliated organizations or those of the publisher, the editors, and the reviewers. Any product that may be evaluated in this article, or claim that may be made by its manufacturer, is not guaranteed or endorsed by the publisher.

frontiers | Frontiers in Bioengineering and Biotechnology

TYPE Original Research
PUBLISHED 11 August 2022
DOI 10.3389/fbioe.2022.963128

OPEN ACCESS

EDITED BY
Lei Wang,
Ocean University of China, China

REVIEWED BY
Qi Lian,
Hebei Normal University of Science and Technology, China
Xiao Jiang,
North Carolina State University, United States
Thilina U. Jayawardena,
University of Calgary, Canada

*CORRESPONDENCE
Liangru Wu,
bamshoots@163.com

SPECIALTY SECTION
This article was submitted to Bioprocess Engineering, a section of the journal Frontiers in Bioengineering and Biotechnology

RECEIVED 07 June 2022
ACCEPTED 11 July 2022
PUBLISHED 11 August 2022

CITATION
Yang J, Guo R, Yang H and Wu L (2022), Synthesis, determination, and bio-application in cellular and biomass-bamboo imaging of natural cinnamaldehyde derivatives. *Front. Bioeng. Biotechnol.* 10:963128. doi: 10.3389/fbioe.2022.963128

Synthesis, determination, and bio-application in cellular and biomass-bamboo imaging of natural cinnamaldehyde derivatives

Jinlai Yang[1,2,3,4,5], Rencong Guo[1,2,3,4], Huimin Yang[1,2,3,4] and Liangru Wu[1,2,3,4,5]*

[1]China National Bamboo Research Center, Hangzhou, China, [2]Key Laboratory of Bamboo Forest Ecology and Resource Utilization of National Forestry and Grassland Administration, Hangzhou, China, [3]Key Laboratory of High Efficient Processing of Bamboo of Zhejiang Province, Hangzhou, China, [4]National Longterm Observation and Research Station for Forest Ecosystem in Hangzhou-Jiaxing-Huzhou Plain, Hangzhou, China, [5]Bamboo Industry (Jian'ou) Branch, Fujian Provincial Collaborative Innovation Institute, Jian'ou, China

Cinnamon essential oil (CEO) is the main ingredient in the renewable biomass of cinnamon, which contains natural cinnamaldehyde. To valorize the value of cinnamaldehyde, two simple and useful compounds (**1** and **2**) from CEO were synthesized using a Schiff-base reaction and characterized by infrared spectra (IR), nuclear magnetic resonance (NMR), and high-resolution mass spectrometry (HRMS). Compound **1** was used to confirm the presence of Fe^{3+} and ClO^- in solution, as well as compound **2**. Using fluorescence enhancement phenomena, it offered practicable linear relationship of **1**'s fluorescence intensity and Fe^{3+} concentrations: (0–8.0 × 10^{-5} mol/L), y = 36.232x + 45.054, R^2 = 0.9947, with a limit of detection (LOD) of 0.323 μM, as well as compound **2**. With increasing fluorescence, F_{404}/F_{426} of **1** and the ClO^- concentration (0–1.0 × 10^{-4} mol/L) also had a linear relationship: y = 0.0392x + 0.5545, R^2 = 0.9931, LOD = 0.165 μM. However, the fluorescence intensity of **2** (596 nm) was quenched by a reduced concentration of ClO^-, resulting in a linear. In addition, compounds **1** and **2** were used to image human astrocytoma MG (U-251), brain neuroblastoma (LN-229) cells, and bamboo tissue by adding Fe^{3+} or ClO^-, with clear intracellular fluorescence. Thus, the two compounds based on CEO could be used to dye cells and bamboo tissues by fluorescence technology.

KEYWORDS

natural cinnamaldehyde, cinnamaldehyde derivatives, synthesis, determination, bio-application

Introduction

The main aromatic compound in cinnamon essential oil (CEO) is cinnamaldehyde, with a content of 80%–94.8%, and which can be directly extracted from cinnamon (Liu et al., 2021). This renewable biomass of cinnamaldehyde has many useful functions, such as anti-*Leishmania* activity (Brustolin et al., 2022), antifungal activity (Niu et al., 2022), antibacterial activity (Wang et al., 2021), antimicrobial activity (Thirapanmethee et al., 2021), and improvement of wood decay resistance (Fang et al., 2021). Furthermore, it is easy to synthesize derivatives with biological activity using cinnamaldehyde, such as cinnamaldehyde-based aspirin derivatives (Lu et al., 2018) and chitosan-cinnamaldehyde cross-linked nanoparticles (Gadkari et al., 2019). The Schiff-base fluorescence compounds derived from natural cinnamaldehyde have already been used to sense ClO^- and Cu^{2+}, and to image U-251 and Hu-7 cells (Yang et al., 2021a). In order to further add the value of natural cinnamaldehyde in the field of fluorescence, the continued synthesis of useful fluorescent compounds from cinnamaldehyde is highly desirable.

As an important microelement in the human body, ferric ion (Fe^{3+}) is a vital part of ferrithionein and heme, playing a crucial role in the physiological activities of oxygen delivery, transcription regulation, enzyme catalysis, and metabolism (Huang et al., 2019a; Li S. et al., 2020; Lin et al., 2022). In the human body, levels of endogenous Fe^{3+} that are too high or low can result in heart failure, anemia, and Parkinson's disease (Wang et al., 2019; Li Y. et al., 2020). In recent years, many novel organic fluorescents used to detect Fe^{3+} have been reported (Song et al., 2019; Rani and John, 2020; Perumal et al., 2021). A fluorescence sensor (**AH2**) was developed to sense Fe^{3+} in aqueous media (Petdum et al., 2021), and a fluorescence chemosensor with a microscale multi-functional metal-organic framework was also used to sense Fe^{3+}, as well as Al^{3+} and 2-hydroxy-1-naphthaldehyde (Kang et al., 2016). Interestingly, porous tetraphenylethylene-based organic polymer (**PTOP**) could response Fe^{3+} (turn-off) with high selectivity and sensitivity (Zheng et al., 2020), and a "turn-on" fluorescence sensor (polymer) based on imidazole-functionalized polydiacetylene has also been used to sense Fe^{3+} (Shin et al., 2022). Thus, the synthesis of new, simple, and efficient fluorescence compounds for the determination of Fe^{3+} is of great significance.

As a reactive oxygen species (ROS), hypochlorite anion (ClO^-) can be obtained by the oxidative reaction of H_2O_2 and Cl^- (Dong et al., 2020; Pei et al., 2020; Elmas, 2022; Pei et al., 2022), which is widely used in the field of sterilization agents, bleaching agents, and deodorants (Wang et al., 2015; Huang et al., 2016; Dong et al., 2017; Sitanurak et al., 2018; Mahdizadeh et al., 2020). Nevertheless, there is much evidence that excessive generation of ClO^- can cause diseases, such as cancer, atherosclerosis, neuron degeneration, cardiovascular disease, lung injuries, and kidney disease (Huang et al., 2016; Zhang et al., 2017; Feng et al., 2018; Song et al., 2018; Ma et al., 2020; Zhang et al., 2020). To date, many good organic fluorescence probes for ClO^- have been synthesized, including benzothiazole-based fluorescence and colorimetric chemosensors (Suh et al., 2022), phenanthroimidazole-based fluorescence (Yang et al., 2022), and thiophene-cyanostilbene Schiff-base sensor (Guo et al., 2021). Therefore, it is imperative to design simple sensors for monitoring ClO^-.

We report two simple Schiff-base derivatives (**1** and **2**) based on cinnamaldehyde, with both compounds **1** and **2** sensitive to the presence of Fe^{3+} and ClO^-. The optical properties and application potential in bio-imaging of **1** and **2** are systematically investigated for a further study.

Materials and methods

Materials and instruments

All reagents (without further purification) were purchased from commercial suppliers. All experiments involving all compounds (**1** and **2**) were conducted in a PBS buffer solution (pH = 7.4, 10 mM, 50% (v/v) C_2H_5OH). Fluorescence spectra were obtained using a PerkinElmer LS 55 fluorescence spectrophotometer. UV-vis absorption spectra were measured on a UV-2550 spectrophotometer (SHIMADZU). ^1H and ^{13}C-NMR spectra were determined using a Bruker FT-NMR spectrometer (600 MHz). Infrared spectra were recorded on an FT-IR infrared spectrometer (Nicolet 380). Fluorescence bio-imaging were finished using confocal laser scanning microscopy.

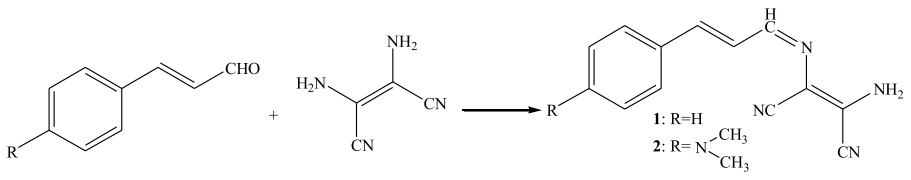

SCHEME 1
Synthesis of cinnamaldehyde Schiff-base derivatives.

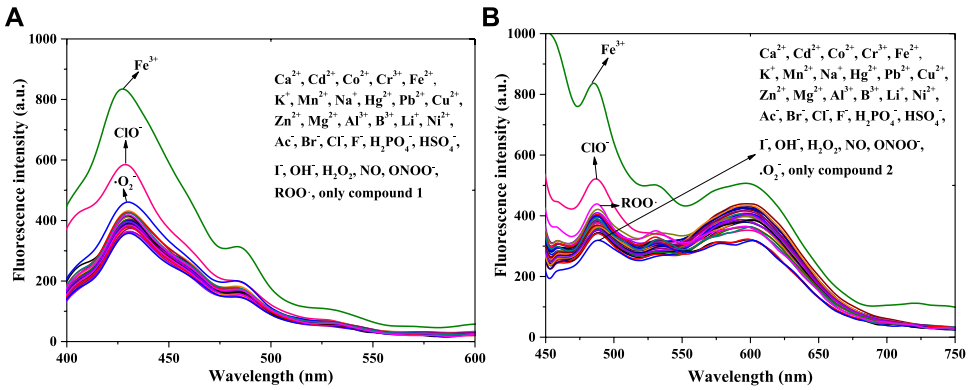

FIGURE 1
Fluorescence spectra of compound **1 (A)** and compound **2 (B)** with equal positive ions or anions or ROS in a PBS buffer solution: **1**: λ_{ex} = 375 nm, Em. Slit = 5.0 nm, Ex. Slit = 7.0 nm; **2**: λ_{ex} = 430 nm, Em. Slit = 5.0 nm, Ex. Slit = 11.0 nm.

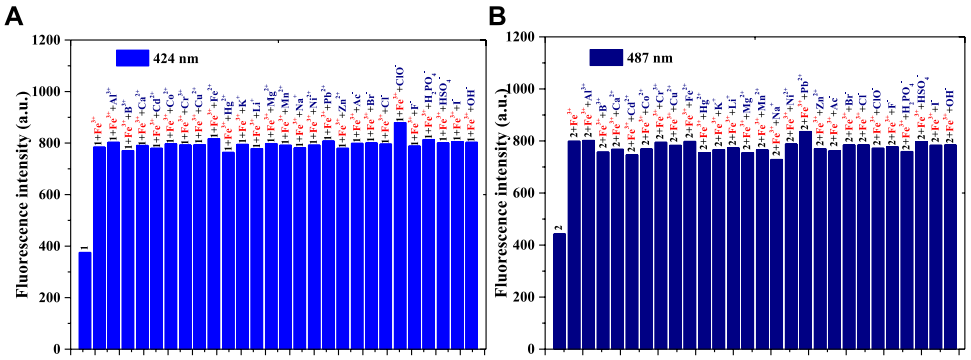

FIGURE 2
(A) Fluorescence intensity (424 nm) of compound **1**, **1** + Fe^{3+}, and **1** + Fe^{3+} when adding another ion to the PBS buffer solution: λ_{ex} = 375 nm, Em. Slit = 5.0 nm, Ex. Slit = 6.0 nm; **(B)** Fluorescence intensity (487 nm) of compound **2**, **2** + Fe^{3+}, and **2** + Fe^{3+} when adding another ion to the PBS buffer solution: λ_{ex} = 430 nm, Em. Slit = 5.0 nm, Ex. Slit = 9.0 nm.

Synthesis

*Synthesis of 2-amino-3-(3-phenyl-allylideneamino)-but-2-enedinitrile (**1**).* Cinnamaldehyde (10 mmol), diaminomaleonitrile (10 mmol), and ethanol (50 ml) were added to a 250 ml dried flask with three necks. The contents were then stirred with refluxing for 3.5 h to offer reactant. Using ethanol to recrystallize, a deep-yellow flaked material was produced (57.5%, yield). FT-IR (KBr) ν (cm^{-1}): 3,447, 3,287, 3,133, 2,231, 2,205, 1,615, 1,602, 1,584, 1,450, 1,372, 1,308, 1,146, 992, 951, 751; ^{1}H NMR (DMSO-d_6, 600 MHz): 7.00-7.04 (m, 1H), 7.35-7.38 (t, 4H), 7.40-7.59 (m, 2H), 7.75 (s, 2H), 8.08-8.09 (d, 1H); ^{13}C NMR (DMSO-d_6, 150 MHz), δ (ppm): 104.15, 114.18, 114.95, 126.72, 127.66, 128.07, 129.47, 130.21, 135.94, 144.46, 157.54; HRMS (m/z): $[M + Na]^+$ calcd for $C_{13}H_{10}N_4$+Na^+, 245.0798; found, 245.0717.

*Synthesis of 2-amino-3-[3-(4-dimethylamino-phenyl)-allylideneamino]-but-2-enedinitrile (**2**).* 4-(Dimethylamino) cinnamaldehyde (10 mmol), diaminomaleonitrile (10 mmol), and ethanol (80 ml) were separately added to a 250 ml dried flask (three necks). Then, the contents were stirred with refluxing for 6.5 h to gain reactant. The solution was recrystallized using ethanol, producing a crimson crystal (61.3%, yield). FT-IR (KBr) ν (cm^{-1}): 3,450, 3,296, 3,175, 2,909, 2,224, 2,205, 1,661, 1,650, 1,604, 1,583, 1,550, 1,440, 1,367, 1,226, 1,186, 1,145, 992, 812; ^{1}H NMR (DMSO-d_6, 600 MHz): 2.98 (s, 6H), 6.73-6.75 (t, 2H), 7.28-7.31 (d, 1H), 7.43-7.49 (m, 4H), 7.55-7.57 (m, 1H), 8.02-8.04 (d, 1H); ^{13}C NMR (DMSO-d_6, 150 MHz), δ (ppm): 104.91, 112.19, 112.44, 122.43, 123.50, 123.74, 125.05, 129.81, 131.11, 145.98, 158.56; HRMS (m/z): $[M + H]^+$ calcd for $C_{15}H_{15}N_5$+H^+, 266.1400; found, 266.1392.

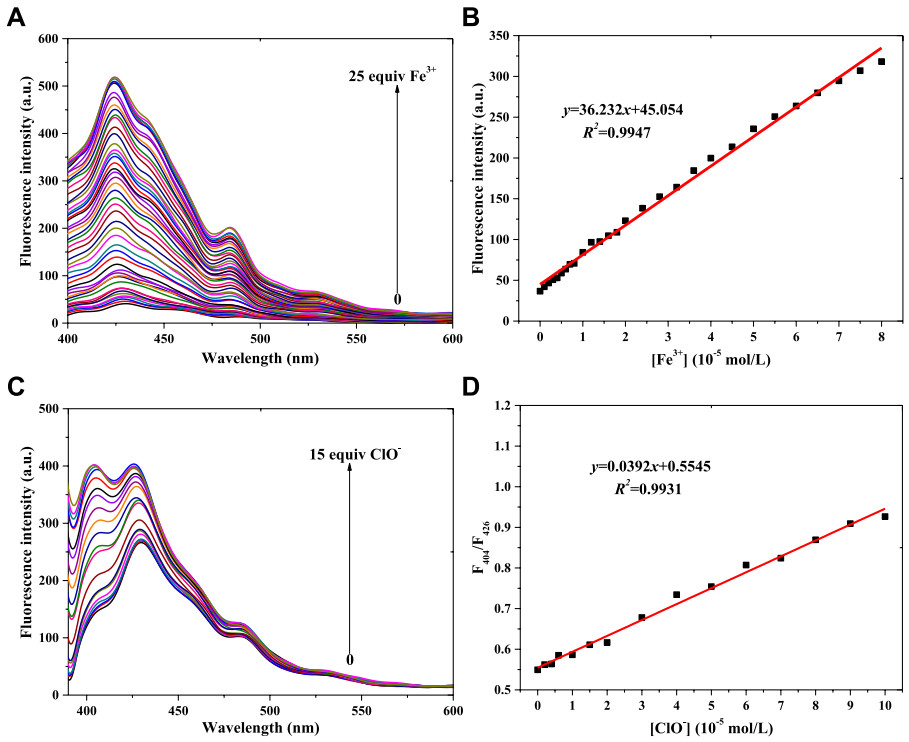

FIGURE 3
Fluorescence spectra of probe **1** in a PBS buffer solution with various concentrations of Fe^{3+} **(A)** and ClO^- **(C)**. **(B)** Linear relationship between the fluorescence intensity of probe **1** and Fe^{3+} concentration. **(D)** Linear relationship between the F_{404}/F_{426} of probe **1** and ClO^- concentration (λ_{ex} = 375 nm): Fe^{3+}: Em. Slit = 5.0 nm, Ex. Slit = 2.5 nm; ClO^-: Em. Slit = 5.0 nm, Ex. Slit = 5.0 nm.

Cellular imaging

Compounds **1** and **2** were used to image human astrocytoma MG cells (U-251 cells) and human brain neuroblastoma cells (LN-229 cells) using the method of Yang J. et al., 2020.

Bamboo imaging

The leafless part of fresh bamboo poles with leaves was immersed in a solution (**1** or **2**: 1×10^{-3} mol/L) for 1.5 h. After that, it was cut into slices to observe their microstructure with or without adding a drop of Fe^{3+} (or ClO^-) solution (1×10^{-3} mol/L) using an LSM710 confocal fluorescent microscope.

Results and discussion

Synthesis

The two derivatives, **1** and **2**, were synthesized using cinnamaldehyde (Scheme 1) (Robertson and Vaughan, 1958) and characterized using IR, NMR, and HRMS. Compounds **1** and **2** were confirmed to be 2-amino-3-(3-phenyl-allylideneamino)-but-2-enedinitrile and 2-amino-3-[3-(4-dimethylamino-phenyl)-allylideneamino]-but-2-enedinitrile.

Fluorescence spectral response

To examine the response of **1** and **2** to the cations Fe^{3+}, Ca^{2+}, Cd^{2+}, Co^{2+}, Cr^{3+}, Fe^{2+}, K^+, Mn^{2+}, Na^+, Hg^{2+}, Pb^{2+}, Cu^{2+}, Zn^{2+}, Mg^{2+}, Al^{3+}, B^{3+}, Li^+, and Ni^{2+}, and to the anions Ac^-, Br^-, Cl^-, F^-, $H_2PO_4^-$, HSO_4^-, OH^-, I^-, ROS of ClO^-, H_2O_2, NO, $ONOO^-$, $\bullet O_2^-$, and ROO•, the fluorescence selectivity of compounds **1** and **2** in PBS buffer solution (pH = 7.4, 10 mM, 50% (v/v) C_2H_5OH) was studied using fluorescence spectra (concentrations: 1×10^{-5} mol/L) (Figure 1).

Figure 1A shows peak fluorescence intensities (400–450 nm**,** compound **1**) with adding equal Fe^{3+} or ClO^- had a significant enhance, after adding other substance in compound **1**'s system, the intensity changed little except $\bullet O_2^-$ (weak fluorescence enhancement). Therefore Fe^{3+} and ClO^- could response with compound **1,** with a fluorescence enhancement in solution. In contrast with compound **1**'s chemical structure, that of

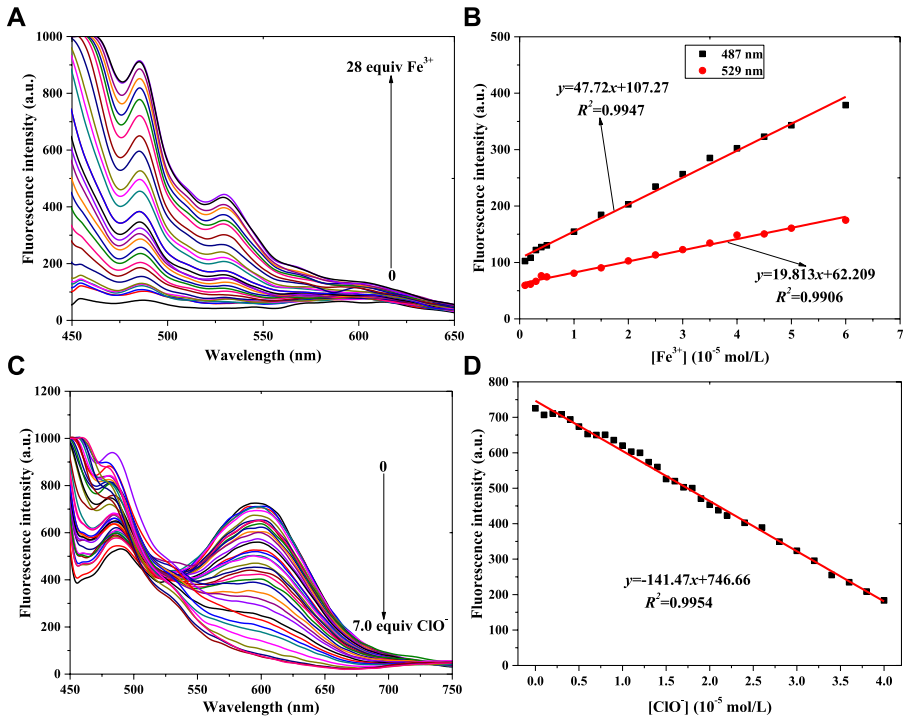

FIGURE 4
Fluorescence spectra of probe **2** in a PBS buffer solution with various concentrations of Fe^{3+} **(A)** and ClO^- **(C)**. Linear relationship between fluorescence intensity of probe **2** and concentration of Fe^{3+} **(B)** and ClO^- **(D)** (λ_{ex} = 430 nm): Fe^{3+}: Em. Slit = 5.0 nm, Ex. Slit = 5.0 nm; ClO^-: Em. Slit = 5.0 nm, Ex. Slit = 18.0 nm.

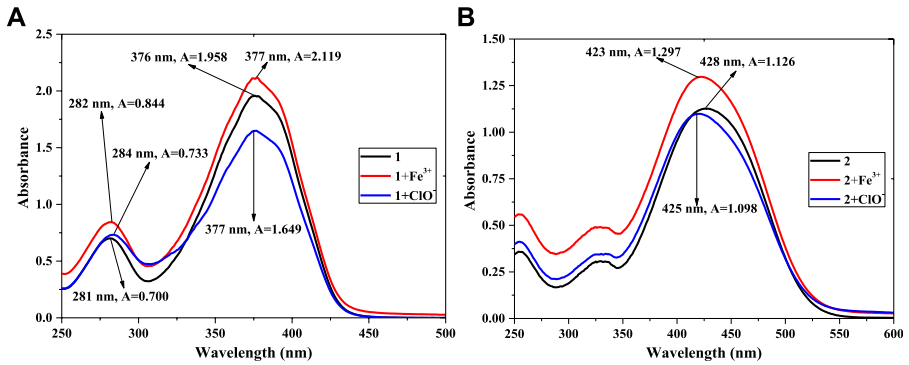

FIGURE 5
UV-vis absorption spectra of **1**, **1** + Fe^{3+}, **1**+ClO^- **(A)** and **2**, **2** + Fe^{3+}, **2**+ClO^- **(B)** in PBS buffer solution.

compound **2** has a *p*-$N(CH_3)_2$ in benzene ring; the remainder of the structure is exactly the same as that of compound **1**. Thus, the 32 positive ions, anions, and ROS were separately used in response with compound **2** [Figure 1B]. The addition of Fe^{3+} or ClO^- (450–550 nm) also enhanced the fluorescence of compound **2** in the PBS buffer solution. That is, compound **2** also responded to Fe^{3+} and ClO^-, which is consistent with the results for compound **1**. However, the intensity (550–650 nm) was quenched after adding ClO^- in **2**'s solution. The reason for this might be connected with the functional group of *p*-$N(CH_3)_2$. Finally, both compounds **1** and **2** had the potential to detect Fe^{3+} and ClO^- in solution.

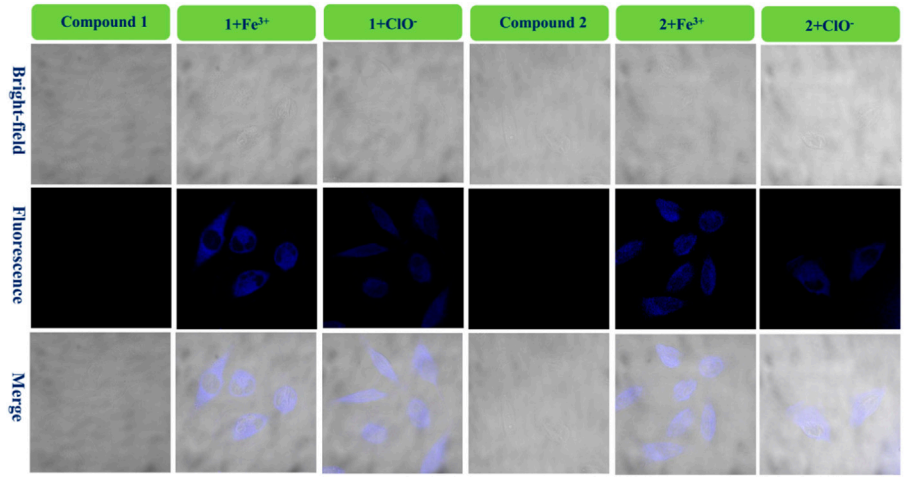

FIGURE 6
Fluorescence bio-images of the U-251 cells of probe **1**, **1** + Fe^{3+}, and **1**+ClO^- and probe **2**, **2** + Fe^{3+}, and **2**+ClO^-.

The anti-interference performance of compounds **1** and **2** (1×10^{-5} mol/L) to Fe^{3+} (1×10^{-5} mol/L) in the same PBS buffer solution was also investigated [Figure 2A (compound **1**) and Figure 2B (compound **2**)]. Figure 2A shows that, compared with those of compound **1**, the other fluorescence intensities increase significantly. Compared with the intensity of **1**+Fe^{3+}, after adding another substance to the **1**+Fe^{3+} system, only the solution of **1**+Fe^{3+}+ClO^- enhanced fluorescence weakly; this might be related to the fluorescence enhancement of ClO^- for compound **1**. The **1** + Fe^{3+} combination resulted in good interference capacities with other substances. As shown in Figure 2B, compared with the results of Figure 2A, the **2** + Fe^{3+} also had an anti-interference performance for other ions. In contrast, the addition of ClO^- in **2**+Fe^{3+} did not enhance the fluorescence, possibly because of the *p*-$N(CH_3)_2$ group in compound **2**. Both compounds **1** and **2**, therefore, have the potential to be used as fluorescence probes for Fe^{3+}.

The anti-interference tests of **1**+ClO^- (or **2**+ClO^-) with the oxidizing agents H_2O_2, NO, $\bullet O_2^-$, $ONOO^-$, and ROO• are detailed in Supplementary Figures S1A–C. The light-emitting systems of **1**+ClO^- and **2**+ClO^- differed in terms of the anti-interference performance of other ROS. The addition of another ROS in the solution of **1**+ClO^- could not significantly change the fluorescence intensity (424 nm), as well as the **2**+ClO^- at 487 nm. However, to add other ROS in the **2**+ClO^- system could quench fluorescence at 596 nm.

Linearity

Linearity is very important for fluorescence probes, so the linear relationships between probe **1** or probe **2** and Fe^{3+} and ClO^- concentration were investigated in a PBS buffer solution [pH = 7.4, 10 mM, 50% (v/v) C_2H_5OH]; the concentration of probe **1** and probe **2** was 1×10^{-5} mol/L, and the results are shown in Figure 3 (compound **1**) and Figure 4 (compound **2**).

Figure 3 shows compound **1**'s fluorescence spectra for different concentrations of Fe^{3+} and ClO^-. Figure 3A shows that the fluorescence intensity (400–450 nm) gradually increases with increasing Fe^{3+} concentration. The peak fluorescence intensity of probe **1** vs. Fe^{3+} concentration is shown in Supplementary Figure S2A. The linear relationship between **1**'s peak intensity and the Fe^{3+} concentration is shown in Figure 3B: $y = 36.232x+45.054$, $R^2 = 0.9947$ (Fe^{3+}: 0–8.0 × 10^{-5} mol/L). Using the IUPAC definition of the limit of detection (LOD), an LOD of 0.323 μM was calculated using Eq. 3 σ_{bi}/m, which was lower than the 9 μM of a **PDA-Im** sensor (Shin et al., 2022). Fluorescence enhancement might be ascribed to a complexation of **1**'s N atom with Fe^{3+} (Zhou et al., 2017). With the same trend of fluorescence enhancement (**1** + Fe^{3+}), the fluorescence intensity was enhanced with increasing ClO^- concentration (Figure 3C; Supplementary Figure S2B), with a linear relationship between F_{404}/F_{426} and ClO^- concentration (Figure 3D). It also showed a good result: $y = 0.0392x+0.5545$, $R^2 = 0.9931$ (ClO^-: 0–1.0 × 10^{-4} mol/L), with an LOD of 0.165 μM. This LOD value is lower than the 0.238 μM of a coumarin-based fluorescence chemosensor (Elmas, 2022). The reason for **1** monitoring ClO^- might be connected with the C=N unit, which reacts with ClO^- (Yang Q. et al., 2020).

With a fluorescence enhancement result, compound **2** can be used to sense Fe^{3+}. The fluorescence spectra of the **2** + Fe^{3+} solutions are shown in Figure 4A. With the addition of Fe^{3+} from 0 mol/L to 2.8×10^{-4} mol/L, the peak fluorescence intensity continuously added (Supplementary Figure S3A). That is,

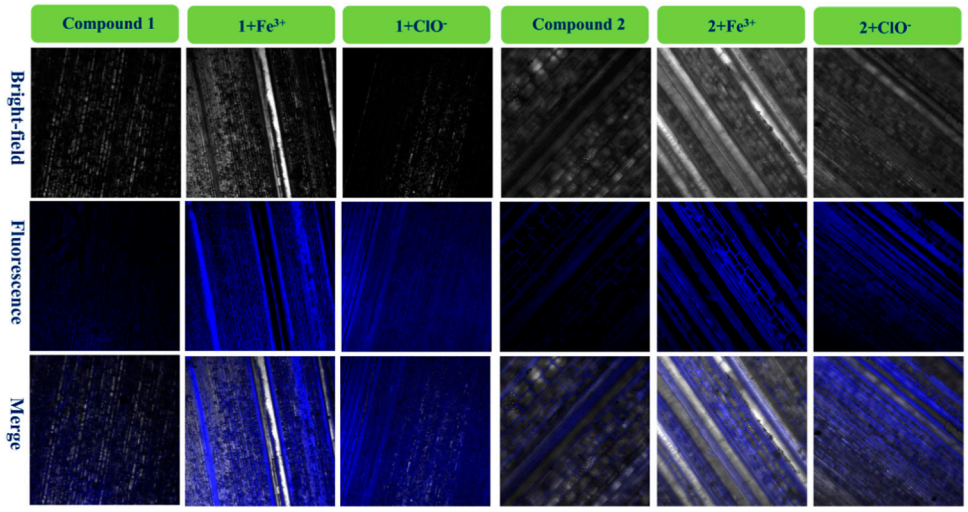

FIGURE 7
Fluorescence images of bamboo structure using compound **1**, **1** + Fe^{3+}, and **1**+ClO^- and compound **2**, **2** + Fe^{3+}, and **2**+ClO^-.

probe **2** might have the same function as probe **1** when helping to determine Fe^{3+} concentration. At the same time, two good linear relationships were obtained, as shown in Figure 4B: 487 nm: y = 47.72x+107.27, R^2 = 0.9947, LOD = 0.373μM; 529 nm: y = 19.813x+62.209, R^2 = 0.9906, LOD = 0.451 μM.

Figure 4C shows that the peak intensity at 550–650 nm decreases gradually when ClO^- concentration increases from 0 to 6.0 × 10^{-5} mol/L. At higher ClO^- concentration, the intensity almost remains constant (Supplementary Figure S3B). The results of adding ClO^- to probe **2**'s solution were different from those of adding it to probe **1**'s solution. It might be affected by the p-$N(CH_3)_2$ group in probe **2**. Finally, the linear relationship was determined, as shown in Figure 4D. With the concentration range of 0–4.0 × 10^{-5} mol/L (ClO^-), the peak intensity of **2**'s light-emitting system had a good linear relationship with ClO^- concentration: y = -141.47x+746.66, R^2 = 0.9954, LOD = 0.434 μM.

UV-vis absorption spectra

To further verify the reaction of **1** (or **2**) and Fe^{3+} or ClO^- in PBS buffer solution (pH = 7.4, 10 mM, 50% (v/v) C_2H_5OH), UV-vis absorption spectra were recorded. The concentration was 5.0 × 10^{-5} mol/L, as shown in Figure 5. Figure 5A shows a maximum absorption peak (compound **1**) at 376 nm, with A = 1.958. After adding equal amounts of Fe^{3+} ions, the value of A increased to 2.119. Meanwhile, the A value of **1**+ClO^- decreased to A = 1.649. This reveals that a chemical reaction had taken place among compound **1** and Fe^{3+} or ClO^- in the solution, agreeing with the results shown Figure 1A. In compared with compound **1**, as shown in Figure 5B, the maximum absorption peak of compound **2** red-shifts from 376 to 428 nm, with a decrease in A of 1.126. It might be affected by the p-$N(CH_3)_2$ group of **2**. The addition of Fe^{3+} (or ClO^-) also changed the peak of probe **2**, which had the same trend as probe **1.** The peak of **2** + Fe^{3+} had a weak blue-shift (428–425 nm), and A decreased slightly (1.126–1.098). The reason might also be related to the p-$N(CH_3)_2$ group. The results showed that Fe^{3+} and ClO^- could response with compounds **1** and **2**, which led to a change in fluorescence intensity in the solution.

Bio-imaging in live cells

To achieve the value of bio-imaging in live cells (Huang et al., 2019b), probes **1** and **2** (1.0 × 10^{-4} mol/L) were used to dye live U-251 and LN-229 cells (Fe^{3+} or ClO^-: 1.0 × 10^{-3} mol/L). After dying, confocal fluorescent microscopic images of the cells were taken (ZEISS LSM510) (Figure 6; Supplementary Figure S4).

Figure 6 shows that there is almost no fluorescence for cells dyed only with probe **1** (U-251 cells). However, the U-251 cells produced clear blue fluorescence after adding a drop of Fe^{3+} solution to response with compound **1**. In addition, the **1**+ClO^- system had the same function as the **1** + Fe^{3+} system in dying U-251 cells. Therefore, the fluorescence enhancement probe **1** for Fe^{3+} or ClO^- could be used in bio-imaging of live U-251 cells. Figure 6 also shows the results for the fluorescence imaging of U-251 cells using compound **2** with the same condition as compound **1**. Probe **2** could sense Fe^{3+} or ClO^- in U-251 cells. In order to find the results of imaging in other cells,

LN-229 cells were chosen to conduct an experiment—the results are provided in Supplementary Figure S4. Probe **2** led to exactly the same result as probe **1**, in keeping with what is shown in Figure 6. The **1** + Fe^{3+} and **2** + Fe^{3+} permeated the LN-229 cells well and provided bright intracellular fluorescence, as well as the **1**+ClO^- and **2**+ClO^-. The addition of ClO^- quenched the intensity of **2**'s fluorescence (550–650 nm) (Figure 4C); however, the **2**+ClO^- could also be used to image cells, which might have been connected with the fluorescence at 450–550 nm. Consequently, probes **1** and **2** for Fe^{3+} and ClO^- could be used in the bio-imaging of U-251 and LN-229 cells.

Bio-imaging in bamboo

Various fluorescence probes can be used to dye plants when required, and bamboo is an important renewable and abundant biomass which can provide wood and shoots (Yang et al., 2021b; Lin et al., 2021; Zheng et al., 2021). In order to investigate the microstructure of bamboo, probes **1** and **2** were used in conjunction with fresh bamboo poles with leaves, the imaging results for **1**, **1** + Fe^{3+}, and **1**+ClO^- and **2**, **2** + Fe^{3+}, and **2**+ClO^- are in Figure 7.

It had very weak fluorescence when the bamboo was dyed with **1** or **2**. After adding a drop of the same concentration of Fe^{3+} solution in the bamboo with **1** or **2**, significant blue fluorescence occurred, and the microstructure of the biological tissues was clearly observed. It also told that these fluorescence tissues transferred **1** or **2**. Furthermore, the images of **1**+ClO^- and **2**+ClO^- were worse than those of **1** + Fe^{3+} and **2** + Fe^{3+}, in keeping with Figure 1. Finally, the **1** + Fe^{3+} and **1**+ClO^- and **2** + Fe^{3+} and **2**+ClO^- could not only dye cells, but could also image the bamboo microstructure.

Conclusion

Two simple and practical derivatives (**1** and **2**) were synthesized using a chemical reaction of Schiff-base originating from natural cinnamaldehyde and developed for monitoring Fe^{3+} or ClO^-. Compound **1** could sense Fe^{3+} or ClO^- selectively, leading to fluorescence enhancement in a PBS solution, and providing the linear relationship between the fluorescence intensity and the ion concentration. Meanwhile, in compared with compound **1**, probe **2** could also detect Fe^{3+} with increased fluorescence intensity in solution. Nevertheless, the addition of ClO^- quenched the fluorescence of **2** at 596 nm. As a result, probe **2** for Fe^{3+} or ClO^- also had a favorable linear relation. Finally, compounds **1** and **2** were used in a fluorescence imaging experiment with U-251 cells, LN-229 cells, and bamboo tissues, offering clear intracellular fluorescence with good results. Thus, these two Schiff-base derivatives based on cinnamaldehyde could be used in future fluorescence detection and bio-imaging, adding to the scientific value of the natural biomass of cinnamaldehyde.

Data availability statement

The original contributions presented in the study are included in the article/Supplementary Material, further inquiries can be directed to the corresponding author.

Author contributions

JY, RG, and HY did the experiments and analyzed experimental data. JY and LW designed the research. JY wrote the manuscript. All authors contributed to the article and approved the submitted version.

Funding

The authors gratefully acknowledge the projects supported by the Talent Development Program of China National Bamboo Research Center (ZXYC202204), the Public Welfare Technology Application Research Project of Zhejiang Province (LGN22C160009), the Key Research and Development Program of Zhejiang Province (2020C02036), the Science and Technology Planned Project of Wenzhou (N20180005), and Guizhou Speciality Forestry Industry Research and Development Project (2020-28).

Conflict of interest

The authors declare that the research was conducted in the absence of any commercial or financial relationships that could be construed as a potential conflict of interest.

Publisher's note

Supplementary material

The Supplementary Material for this article can be found online at: https://www.frontiersin.org/articles/10.3389/fbioe.2022.963128/full#supplementary-material

References

Brustolin, A. Á., Ramos-Milaré Á, C. F. H., de Mello, T. F. P., Aristides, S. M. A., Lonardoni, M. V. C., Silveira, T. G. V., et al. (2022). *In vitro* activity of cinnamaldehyde on *Leishmania* (*Leishmania) amazonensis*. *Exp. Parasitol.* 236, 108244. doi:10.1016/j.exppara.2022.108244

Dong, X., Zhang, G., Shi, J., Wang, Y., Wang, M., Peng, Q., et al. (2017). A highly selective fluorescence turn-on detection of ClO^- with 1-methyl-1, 2-dihydropyridine-2-thione unit modified tetraphenylethylene. *Chem. Commun.* 53, 11654–11657. doi:10.1039/C7CC07092F

Dong, H., Zheng, L., Yu, P., Jiang, Q., Wu, Y., Huang, C., et al. (2020). Characterization and application of lignin-carbohydrate complexes from lignocellulosic materials as antioxidants for scavenging *in vitro* and *in vivo* reactive oxygen species. *ACS Sustain. Chem. Eng.* 8, 256–266. doi:10.1021/acssuschemeng.9b05290

Elmas, S. N. K. (2022). A coumarin-based fluorescence chemosensor for the determination of Al^{3+} and ClO^- with different fluorescence emission channels. *Inorg. Chim. Acta* 537, 120953. doi:10.1016/j.ica.2022.120953

Fang, S., Feng, X., Lei, Y., Chen, Z., and Yan, L. (2021). Improvement of wood decay resistance with cinnamaldehyde chitosan emulsion. *Ind. Crops Prod.* 160, 113118. doi:10.1016/j.indcrop.2020.113118

Feng, Y., Li, S., Li, D., Wang, Q., Ning, P., Chen, M., et al. (2018). Rational design of a diaminomaleonitrile-based mitochondria-targeted two-photon fluorescent probe for hypochlorite *in vivo*: solvent-independent and high selectivity over Cu^{2+}. *Sens. Actuators B Chem.* 254, 282–290. doi:10.1016/j.snb.2017.07.019

Gadkari, R. R., Suwalka, S., Yogi, M. R., Ali, W., Das, A., Alagirusamy, R., et al. (2019). Green synthesis of chitosan-cinnamaldehyde cross-linked nanoparticles: Characterization and antibacterial activity. *Carbohydr. Polym.* 226, 115298. doi:10.1016/j.carbpol.2019.115298

Guo, H., Lin, J., Zheng, L., and Yang, F. (2021). An effective fluorescent sensor for ClO^- in aqueous media based on thiophene-cyanostilbene Schiff-base. *Spectrochim. Acta Part A Mol. Biomol. Spectrosc.* 256, 119744. doi:10.1016/j.saa.2021.119744

Huang, Y., Zhang, P., Gao, M., Zeng, F., Qin, A., Wu, S., et al. (2016). Ratiometric detection and imaging of endogenous hypochlorite in live cells and *in vivo* achieved by using an aggregation induced emission (AIE)-based nanoprobe. *Chem. Commun.* 52, 7288–7291. doi:10.1039/C6CC03415B

Huang, C., Tao, Y., Li, M., Zhang, W., Fan, Y., Yong, Q., et al. (2019a). Synthesis and characterization of an antioxidative galactomannan-iron(III) complex from Sesbania seed. *Polymers* 11, 28. doi:10.3390/polym11010028

Huang, C., Dong, H., Su, Y., Wu, Y., Narron, R., Yong, Q., et al. (2019b). Synthesis of carbon quantum dot nanoparticles derived from byproducts in bio-refinery process for cell imaging and *in vivo* bioimaging. *Nanomaterials* 9, 387. doi:10.3390/nano9030387

Kang, Y., Zheng, X. J., and Jin, L. P. (2016). A microscale multi-functional metal-organic framework as a fluorescence chemosensor for Fe(III), Al(III) and 2-hydroxy-1-naphthaldehyde. *J. Colloid Interface Sci.* 471, 1–6. doi:10.1016/j.jcis.2016.03.008

Li, S., Yang, Y., and Li, W. (2020). Human ferroportin mediates proton-coupled active transport of iron. *Blood Adv.* 4, 4758–4768. doi:10.1182/bloodadvances.2020001864

Li, Y., Yang, C., Wang, S., Yang, D., Zhang, Y., Xu, L., et al. (2020). Copper and iron ions accelerate the prion-like propagation of alpha-synuclein: A vicious cycle in Parkinson's disease. *Int. J. Biol. Macromol.* 163, 562–573. doi:10.1016/j.ijbiomac.2020.06.274

Lin, W., Yang, J., Zheng, Y., Huang, C., and Yong, Q. (2021). Understanding the effects of different residual lignin fractions in acid-pretreated bamboo residues on its enzymatic digestibility. *Biotechnol. Biofuels* 14, 143. doi:10.1186/s13068-021-01994-y

Lin, L., Chen, D., Lu, C., and Wang, X. (2022). Fluorescence and colorimetric dual-signal determination of Fe^{3+} and glutathione with $MoSe_2$@Fe nanozyme. *Microchem. J.* 177, 107283. doi:10.1016/j.microc.2022.107283

Liu, X., Chen, L., Kang, Y., He, D., Yang, B., Wu, K., et al. (2021). Cinnamon essential oil nanoemulsions by high-pressure homogenization: Formulation, stability, and antimicrobial activity. *LWT- Food Sci. Technol.* 147, 111660. doi:10.1016/j.lwt.2021.111660

Lu, S., Obianom, O. N., and Ai, Y. (2018). Novel cinnamaldehyde-based aspirin derivatives for the treatment of colorectal cancer. *Bioorg. Med. Chem. Lett.* 28, 2869–2874. doi:10.1016/j.bmcl.2018.07.032

Ma, Z., Chen, X., Wang, C., and Lv, Q. (2020). A novel ratiometric fluorescence probe for hypochlorite detection and its application in cell imaging. *J. Mol. Struct.* 1221, 128812. doi:10.1016/j.molstruc.2020.128812

Mahdizadeh, S., Sawford, K., van Andel, M., and Browning, G. F. (2020). Efficacy of citric acid and sodium hypochlorite as disinfectants against Mycoplasma bovis. *Vet. Microbiol.* 243, 108630. doi:10.1016/j.vetmic.2020.108630

Niu, A., Wu, H., Ma, F., Tan, S., Wang, G., Qiu, W., et al. (2022). The antifungal activity of cinnamaldehyde in vapor phase against Aspergillus niger isolated from spoiled paddy. *LWT- Food Sci. Technol.* 159, 113181. doi:10.1016/j.lwt.2022.113181

Pei, W., Chen, Z. S., Chan, H. Y. E., Zheng, L., Liang, C., Huang, C., et al. (2020). Isolation and identification of a novel anti-protein aggregation activity of lignin-carbohydrate complex from chionanthus retusus leaves. *Front. Bioeng. Biotechnol.* 8, 573991. doi:10.3389/fbioe.2020.573991

Pei, W., Deng, J., Wang, P., Wang, X., Zheng, L., Zhang, Y., et al. (2022). Sustainable lignin and lignin-derived compounds as potential therapeutic agents for degenerative orthopaedic diseases: a systemic review. *Int. J. Biol. Macromol.* 212, 547–560. doi:10.1016/j.ijbiomac.2022.05.152

Perumal, M. V., Sathish, V., and Mathivathanan, L. (2021). Photophysical and theoretical investigations of diarylimidazole derivative with application as a fluorescence sensor for Fe(III). *J. Mol. Struct.* 1224, 129185. doi:10.1016/j.molstruc.2020.129185

Petdum, A., Kaewnok, N., Panchan, W., Sahasithiwat, S., Sooksimuang, T., Sirirak, J., et al. (2021). New aza[5]helicene derivative for selective Fe(III) fluorescence sensing in aqueous media and its application in water samples. *J. Mol. Struct.* 1245, 131250. doi:10.1016/j.molstruc.2021.131250

Rani, B. K., and John, S. A. (2020). Selective receptor for Fe(III) ion with a fluorescence-ON pyrene motif in semi-aqueous solution. *J. Photochem. Photobiol. A Chem.* 392, 112426. doi:10.1016/j.jphotochem.2020.112426

Robertson, P. S., and Vaughan, J. (1958). Derivatives of the hydrogen Cyanide tetramer: Structure and Chemistry[1]. *J. Am. Chem. Soc.* 80, 2691–2693. doi:10.1021/ja01544a026

Shin, H., Jannah, F., Yoo, E. J., and Kim, J. M. (2022). A colorimetric and fluorescence "turn-on" sensor for Fe(III) ion based on imidazole-functionalized polydiacetylenefluorescence "turn-on" sensor for Fe(III) ion based on imidazole-functionalized polydiacetylene. *Sens. Actuators B Chem.* 350, 130885. doi:10.1016/j.snb.2021.130885

Sitanurak, J., Wangdi, N., Sonsa-Ard, T., Teerasong, S., Amornsakchai, T., Nacapricha, D., et al. (2018). Simple and green method for direct quantification of hypochlorite in household bleach with membraneless gas-separation microfluidic paper-based analytical device. *Talanta* 187, 91–98. doi:10.1016/j.talanta.2018.04.077

Song, X., Dong, B., Kong, X., Wang, C., Zhang, N., Lin, W., et al. (2018). Construction of a ratiometric fluorescent probe with an extremely large emission shift for imaging hypochlorite in living cells. *Spectrochim. Acta Part A Mol. Biomol. Spectrosc.* 188, 394–399. doi:10.1016/j.saa.2017.07.011

Song, F., Shao, X., Zhu, J., Bao, X., Du, L., Kan, C., et al. (2019). Reversible "turn-off-on" fluorescence response of Fe(III) towards Rhodamine B based probe *in vivo* and plant tissues. *Tetrahedron Lett.* 60, 1363–1369. doi:10.1016/j.tetlet.2019.04.025

Suh, B., Kim, H., Jang, S., Kim, K. T., and Kim, C. (2022). A benzothiazole-based fluorescent and colorimetric probe for the detection of ClO^- and its application to zebrafish and water sample. *Spectrochim. Acta Part A Mol. Biomol. Spectrosc.* 270, 120827. doi:10.1016/j.saa.2021.120827

Thirapanmethee, K., Kanathum, P., Khuntayaporn, P., Huayhongthong, S., Surassmo, S., Chomnawang, M. T., et al. (2021). Cinnamaldehyde: A plant-derived antimicrobial for overcoming multidrug-resistant acinetobacter baumannii infection. *Eur. J. Integr. Med.* 48, 101376. doi:10.1016/j.eujim.2021.101376

Wang, B., Chen, D., Kambam, S., Wang, F., Wang, Y., Zhang, W., et al. (2015). A highly specific fluorescent probe for hypochlorite based on fluorescein derivative and its endogenous imaging in living cells. *Dyes Pigm.* 120, 22–29. doi:10.1016/j.dyepig.2015.03.022

Wang, Y., Lao, S., Ding, W., Zhang, Z., and Liu, S. (2019). A novel ratiometric fluorescent probe for detection of iron ions and zinc ions based on dual-emission carbon dotsfluorescent probe for detection of iron ions and zinc ions based on dual-emission carbon dots. *Sensors Actuators B Chem.* 284, 186–192. doi:10.1016/j.snb.2018.12.139

Wang, X., Cheng, F., Wang, X., Feng, T., Xia, S., Zhang, X., et al. (2021). Chitosan decoration improves the rapid and long-term antibacterial activities of cinnamaldehyde-loaded liposomes. *Int. J. Biol. Macromol.* 168, 59–66. doi:10.1016/j.ijbiomac.2020.12.003

Yang, J., Huang, C., Xu, X., Pan, Y., Yang, H., Wu, L., et al. (2021a). Synthesis, optical properties, determination and imaging in living cells and bamboo of cinnamaldehyde derivatives. *Spectrochim. Acta Part A Mol. Biomol. Spectrosc.* 255, 119730. doi:10.1016/j.saa.2021.119730

Yang, J., Wu, L., Yang, H., and Pan, Y. (2021b). Using the major components (cellulose, hemicellulose, and lignin) of phyllostachys praecox bamboo shoot as dietary fiber. *Front. Bioeng. Biotechnol.* 9, 669136. doi:10.3389/fbioe.2021.669136

Yang, X., Zheng, Y., and Zheng, L. (2022). A phenanthroimidazole-based fluorescent probe for ratiometric detection of ClO^-. *J. Photochem. Photobiol. A Chem.* 424, 113575. doi:10.1016/j.jphotochem.2021.113575

Yang, J., Xu, X., Yang, S., Ji, X., and Wu, L. (2020). Synthesis and determination of Zn^{2+}, S^{2-} and live cellular imaging of a benzhydrazide derivative. *J. Photochem. Photobiol. A Chem.* 396, 112544. doi:10.1016/j.jphotochem.2020.112544

Yang, Q., Zhong, X. L., Chen, Y. S., Yang, J., Jin, C., Jiang, Y. L., et al. (2020). A mitochondria-targeted fluorescent probe for hypochlorite sensing and its application in bioimaging. *Analyst* 145 (8), 3100–3105. doi:10.1039/D0AN00245C

Zhang, Y. R., Liu, Y., Feng, X., and Zhao, B. X. (2017). Recent progress in the development of fluorescent probes for the detection of hypochlorous acid. *Sensors Actuators B Chem.* 240, 18–36. doi:10.1016/j.snb.2016.08.066

Zhang, Y. M., Fang, H., Zhu, W., He, J. X., Yao, H., Wei, T. B., et al. (2020). Ratiometric fluorescent sensor based oxazolo-phenazine derivatives for detect hypochlorite *via* oxidation reaction and its application in environmental samples. *Dyes Pigm.* 172, 107765. doi:10.1016/j.dyepig.2019.107765

Zheng, Y., Wang, H., and Jiang, J. (2020). A porous tetraphenylethylene-based polymer for fast-response fluorescence sensing of Fe(III) ion and nitrobenzene. *Dyes Pigm.* 173, 107929. doi:10.1016/j.dyepig.2019.107929

Zheng, Y., Yu, Y., Lin, W., Jin, Y., Yong, Q., Huang, C., et al. (2021). Enhancing the enzymatic digestibility of bamboo residues by biphasic phenoxyethanol-acid pretreatment. *Bioresour. Technol.* 325, 124691. doi:10.1016/j.biortech.2021.124691

Zhou, F., Leng, T. H., Liu, Y. J., Wang, C. Y., Shi, P., Zhu, W. H., et al. (2017). Water-soluble rhodamine-based chemosensor for Fe^{3+} with high sensitivity, selectivity and anti-interference capacity and its imaging application in living cells. *Dyes Pigm.* 142, 429–436. doi:10.1016/j.dyepig.2017.03.057

frontiers | Frontiers in Bioengineering and Biotechnology

TYPE Original Research
PUBLISHED 30 August 2022
DOI 10.3389/fbioe.2022.957268

OPEN ACCESS

EDITED BY
Xin Zhou,
Nanjing Forestry University, China

REVIEWED BY
Abhiram Arunkumar,
Sanofi Genzyme Framingham, United States
Kankan Jiang,
Hangzhou Medical College, China

*CORRESPONDENCE
Laura Soto-Sierra,
laura.sotosierra@mtem.com
Zivko L. Nikolov,
znikolov@tamu.edu

SPECIALTY SECTION
This article was submitted to Bioprocess Engineering, a section of the journal Frontiers in Bioengineering and Biotechnology

RECEIVED 30 May 2022
ACCEPTED 01 August 2022
PUBLISHED 30 August 2022

CITATION
Soto-Sierra L and Nikolov ZL (2022), Feasibility of membrane ultrafiltration as a single-step clarification and fractionation of microalgal protein hydrolysates.
Front. Bioeng. Biotechnol. 10:957268.
doi: 10.3389/fbioe.2022.957268

Feasibility of membrane ultrafiltration as a single-step clarification and fractionation of microalgal protein hydrolysates

Laura Soto-Sierra[1,2]* and Zivko L. Nikolov[2]*

[1]Molecular Templates, Inc. (MTEM), Austin, TX, United States, [2]Texas A&M University, College Station, TX, United States

Protein hydrolysates are one of the most valuable products that can be obtained from lipid-extracted microalgae (LEA). The advantages of protein hydrolysates over other protein products encompass enhanced solubility, digestibility, and potential bioactivity. The development of an economically feasible process to produce protein hydrolysates depends on maximizing the recovery of hydrolyzed native protein from the lipid-extracted algal biomass and subsequent fractionation of hydrolyzed protein slurry. Previously, we reported a method for fractionation of enzymatically generated protein hydrolysates by acidic precipitation of algal cell debris and unhydrolyzed protein, precipitate wash, centrifugation, and depth filtration. The present study evaluates tangential flow ultrafiltration as a single-step alternative to centrifugation, precipitate wash, and depth filtration. The results demonstrate that the tangential flow ultrafiltration process has a potential that deserves further investigation. First, the membrane diafiltration process uses a single and easily scalable unit operation (tangential flow filtration) to separate and "wash out" hydrolyzed protein from the algal residue. Second, the protein recovery yield achieved with the tangential flow process was >70% compared to 64% previously achieved by centrifugation and depth filtration methods. Finally, protein hydrolysates obtained by membrane ultrafiltration exhibited slightly better heat and pH stability.

KEYWORDS

microalgae, biorefinery, protein, membrane ultrafiltration, depth filtration

Introduction

Enzymatic hydrolysis of protein-rich feedstocks has emerged as a versatile method for enhancing protein extractability of complex proteins and increasing the value of protein products. The available data from aqueous extraction of protein-rich meals (soy, rapeseed, and microalgae) indicate that enzyme-assisted protein extraction could significantly improve protein extractability and generate a variety of partially hydrolyzed products (Morris et al., 2008; Safi et al., 2017; Soto-Sierra et al., 2018; López-Pedrouso et al., 2020). Among potential protein products that could be generated from protein-rich feedstocks,

including microalgae, protein hydrolysates are of a particular interest as their thermal and acidic pH stability makes them better suited as protein supplements in sports and nutritional drinks than protein isolates (Olsen and Adler-Nissen, 1979; Adler-Nissen, 1986). Lipid-extracted microalgae (LEA) is a particularly attractive feedstock for protein products because the solvent extraction of high-value lipids such as omega fatty acids (FA) and lutein (Kulkarni and Nikolov, 2017; Soto-Sierra et al., 2020) increases the protein content in extracted biomass residue (% dw) and reduces protein-rich biomass cost ($/kg) as much as an order of magnitude (Soto-Sierra et al., 2020).

Recent studies revealed that *1*) the microalgal cell wall was a barrier to protein (enzyme) hydrolysis and *2*) cell wall disruption/lysis improves enzyme-assisted protein extraction yields by as much as 50% (Safi et al., 2017; Akaberi et al., 2019; Soto-Sierra et al., 2021). Maximizing protein hydrolysis and release of the hydrolyzed protein in the aqueous extract slurry is the first step in the production of hydrolysates followed by recovery and purification of the hydrolyzed protein slurry. To ensure required product purity and stability for specialty food and drink applications, lysed algal residue and nonprotein impurities (chlorophyll pigments and starch) must be efficiently removed from the protein hydrolysates (Soto-Sierra et al., 2021). The removal of undesirable algal residue and soluble impurities can be achieved by a combination of downstream processing methods such as precipitation (Morris et al., 2008; Safi et al., 2017), centrifugation (Schwenzfeier et al., 2011), dead-end filtration (depth filtration), and tangential flow filtration (TFF) (Safi et al., 2014; Kulkarni and Nikolov, 2017; Safi et al., 2017). The selection and sequence of process unit operations depend on target protein molecular weight (MW) and solubility, particle size of lysed lipid-extracted biomass, and product yield and purity.

We recently compared several bench-scale options for preparation of protein hydrolysates from intact (unbroken) LEA, lysed LEA, and algal protein concentrates (Soto-Sierra et al., 2021). Based on the rate for enzymatic hydrolysis, protein yield, and production cost, direct proteolysis of lysed LEA emerged as the best starting material for the preparation of protein hydrolysates. The direct hydrolysis process of lysed LEA consisted of acidic precipitation of insoluble impurities (cell debris and unhydrolyzed protein complex including pigments) followed by centrifugation and depth filtration (Soto-Sierra et al., 2021). To maximize the yield of hydrolyzed proteins, the precipitated material was centrifuged, washed with water to release trapped peptides, and then again centrifuged. Combined supernatants were clarified by depth filtration to yield a hydrolysate that was free of chlorophyll pigments. The hydrolysate contained 63% protein, and protein recovery was about 64%. We determined that the protein content of hydrolysates could be increased to 73% by including an ion-exchange demineralization step. Although the latter step slightly reduced the protein hydrolysate yield, we believe that ion-exchange demineralization would add a significant toll to the product cost. The aforementioned process uses off-the-shelf equipment and reduces the presence of chlorophyll pigments in the final product but delivers an underperforming process yield of 64%. The need for a precipitate wash and extra centrifugation step to release trapped protein hydrolysate molecules led us to consider TFF as a process alternative in place of centrifugation, washing, and depth filtration steps.

In this study, we compare the yield and quality of protein hydrolysates produced on a bench scale by TFF ultrafiltration and the process described previously (centrifugation, wash, and depth-filtration) without the ion-exchange demineralization step. The criteria for evaluating the quality of hydrolysates obtained by each process consisted of heat and pH stability of aqueous hydrolysate samples and discoloration of freeze-dried hydrolysates upon heating.

Methods

Preparation of protein hydrolysate

Lipid extraction

Lipid-extracted algae (LEA) was generated by a previously developed protocol (Soto-Sierra et al., 2021). Frozen *Nannochloropsis sp* biomass (donated by Qualitas Inc.) was first thawed at room temperature and then extracted in 50 ml EtOH/g-DW biomass in two steps at 60°C. Biomass extraction and re-extraction were performed under the same conditions with an incubation time of 45 min/step. An extraction temperature of 60°C was selected to maximize solubility and extractability of carotenoids, chlorophyll, and lipids in EtOH. At the end of the process, the dry base composition of LEA was approximately 40% protein, 19% ash, 10% lipids, and 16% carbohydrates.

LEA disruption and proteolysis

LEA slurry (10% solids) was milled at pH 11 using a 0.4 L High Energy Planetary Ball Mill System from MSE Supplies (Tucson, AZ, United States). The ball mill chamber was filled with 0.5 mm diameter zirconia beads (50% by volume) as per the manufacturer's recommendation. To maximize cell disruption, ball milling time was set to 120 min.

The pH of the lysed LEA slurry was brought to pH 9.5 with 1 M HCl and heated to 50°C under continuous mixing to maximize enzyme activity. The protein hydrolysis reaction was started by adding Alcalase liquid preparation with a specific activity of <0.75 Anson units/ml (Calbiochem®) three doses at preselected concentrations of 0.9, 1.8, and 3.5% v/

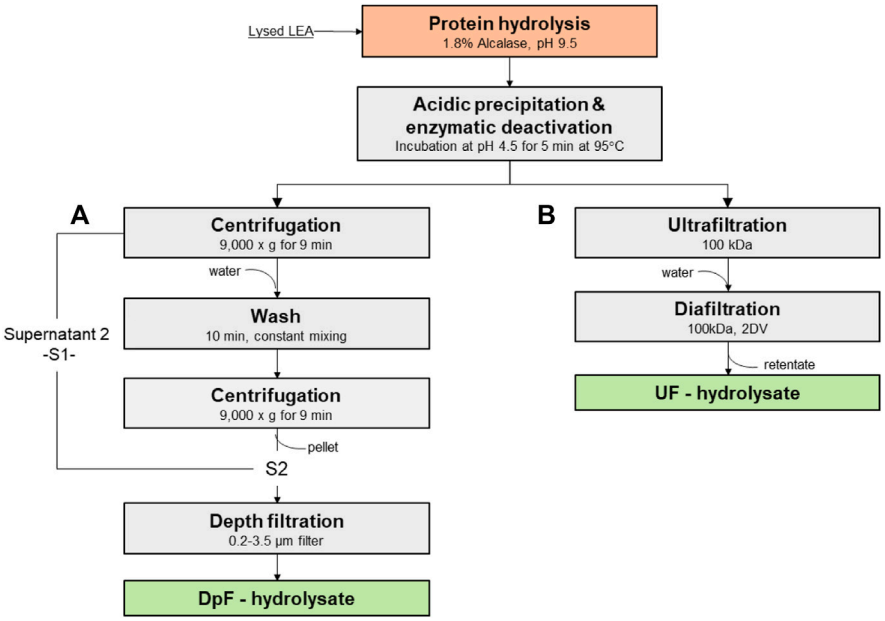

FIGURE 1
Processing routes to protein hydrolysates: **(A)** protein hydrolysates by centrifugation and depth filtration (DpF-hydrolysate) vs. **(B)** protein hydrolysates by ultrafiltration and diafiltration (UF-hydrolysate).

w-protein. During the hydrolysis reaction (3 h), the pH was maintained at 9.5 by the addition of 1 M NaOH. At the end of the reaction, the LEA hydrolysate slurry was acidified with 1 M HCl to pH 4.5 and then incubated at 95°C for 5 min to inactivate the enzyme. The hydrolyzed and acidified LEA slurry was cooled down to room temperature and then clarified by the two methods described in the following sections to obtain clarified (solid-free) protein hydrolysates.

Process for the production of protein hydrolysates by centrifugation and depth filtration (DpF-hydrolysate)

A modified protocol for clarification of protein hydrolysates developed by Soto-Sierra et al. (2021) was used (Figure 1A). After hydrolysis and deactivation, the slurry was centrifuged at 9,000 × *g* for 9 min, and the supernatant (S1) was collected. The pellet solids were resuspended in water at pH 4.3 and mixed thoroughly to release hydrolyzed protein trapped in the pellet. The resuspended pellet was centrifuged again under same conditions, and the supernatant S2 was collected. Supernatants S1 and S2 were combined and clarified using a Supracap 50 Pall® Depth filtration capsule (SC050PDD1). The Supracap 50 Pall depth filter with a retention rating of 0.2–3.5 µm allowed the removal of residual debris and insoluble protein aggregates.

Protein hydrolysates by ultrafiltration and diafiltration (UF-hydrolysate)

TFF and DF were performed using the Spectrum KrosFlo KR2i system with 1 mm inner diameter (ID) hollow fibers (Repligen) (Figure 1B). For all the experiments conducted, the shear rate was maintained at $2{,}000^{-1}$ or a cross-flow flow-rate of 19 L/min/m^2. The membrane filtration process was operated at constant TMP (7 psi) until the system pressure was dictated by the viscosity of the fluid, which organically increased the feed pressure. At that point, the concentration (ultrafiltration) was stopped when a TMP of 10 was reached. The flux, TMP, and weight of permeate were tracked over time using KrosFlo real-time data collection software by Repligen.

Based on previous results (Morris et al., 2008; Soto-Sierra et al., 2021) and the anticipated MW distribution of the hydrolysates, 50 kDa (D02-E050-10-N) and 100 kDa (D02-E100-10-N) Spectrum® hollow fiber filters were selected to clarify and purify protein hydrolysates from hydrolyzed and acidified LEA slurry. After hydrolysis and enzyme deactivation steps, the LEA hydrolysate slurry was concentrated by ultrafiltration until the solids' concentration in the retentate reached ~200 g-DW/L, or the feed pressure exceeded 10 psi. Following the concentration of the slurry, the Spectrum® hollow fiber system was operated under the continuous diafiltration mode for two diafiltration

volumes (DVs). To determine protein recovery in the permeate, samples were taken before and after each diafiltration step (DV1 and DV2), and the protein yield was calculated at each point.

Characterization of protein hydrolysates

The protein hydrolysate yield was estimated using a protocol for quantification of soluble peptides previously developed and modified by Olsen and Adler-Nissen, (1979) and Soto-Sierra et al. (2021). Each sample was digested in 6N HCl for 24 h until hydrolysis. Total amino nitrogen was determined using the nitrogen O-phthaldialdehyde (NOPA) procedure (Cuchiaro and Laurens, 2019), and the protein content in the samples by applying an amino-nitrogen-to-protein conversion factor of 6.25 (Soto-Sierra et al., 2021).

Size exclusion chromatography

MW distribution of the hydrolyzed protein in hydrolysates was performed on an AKTA-purifier system using a TOSOH TSK gel G2000SWxl (30 cm × 7.8 mm) size exclusion analytical column with a TOSOH SWXL guard precolumn. All samples were filtered through a 0.2-μm filter before injection. Protein samples (100 μl) were run at a 0.7 ml/min flow rate using 0.1 M NaCl in RO water as the mobile phase. The protein in the effluent was detected using a UV detector at 280 nm. The retention volumes of a standard protein mixture (Bio-Rad) were used to assign MW to protein hydrolysate peaks.

Analysis of pH stability of hydrolysates at an elevated temperature

Hydrolysate samples (10 mg/ml) prepared by either fractionation methods were adjusted to pH 4, 6, and 8. Only a half of the pH-adjusted samples were subjected to thermal treatment at 95°C for 10 min. A volume of 1 mL of each sample (heated and non-heated) was analyzed by dynamic light scattering (DLS) for particle size measurements in the Zetasizer Nano ZS at 25°C and 173° scattering angle. The DLS data were automatically converted to intensity and volume distribution by particle size.

Data analysis

Statistical analysis of process variables was performed using JMP software. Significant differences between treatments, where applicable, were found using $\alpha_{FAM} = 0.05$.

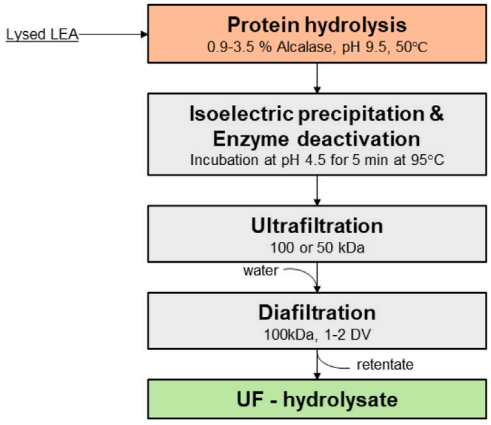

FIGURE 2
Flow diagram of the process for the production of UF-hydrolysates.

Results and discussion

Protein hydrolysate yield using the UF/DF process

To determine conditions for the separation of protein hydrolysate from the rest of the components in the lysate slurry, four key process variables were evaluated: enzyme dosage (0.9, 1.8, and 3.5% w/v), pH (4.5, 5.5, and 7.0), enzyme deactivation temperature (45 and 60°C), and membrane pore size (50 and 100 kDa). The objective of the screening was to determine the optimal extent of hydrolysis and ultrafiltration conditions that allowed maximal passage of hydrolyzed protein while retaining insoluble protein aggregates, chloroplast remnants, and cell debris. From the statistical analysis, we found that enzyme dosage, membrane pore size (MWCO), and their interaction were the only significant factors affecting protein recovery and flux. The effect of these factors was evaluated by testing protein recovery and flux at the conditions shown in Figure 2.

Hydrolysates produced with 0.9% and 1.8% (v/w) enzyme dosages and processed *via* a 50 kDa hollow fiber membrane delivered lower fluxes and cumulative protein yield than those produced by the other three tested combinations (Table 1). The combination of 0.9% dosage and 50-kDa membrane had the lowest flux (16 LMH) and protein yields during UF concentration (33%) and subsequent two diafiltration steps (48% and 56%, respectively).

The increase of Alcalase dosage from 0.9 to 1.8 or 3.5% (v/w) resulted in higher permeate fluxes of 20 and 32 LMH, respectively, when processing the hydrolyzed slurry using a 50-kDa membrane. Similarly, the same dosage increase from 0.9 to 1.8% and 3.5% positively affected the UF permeate protein

TABLE 1 Impact of the MWCO membrane and enzyme dosage on flux and protein recovery in the permeate and after one and two diafiltration volume (DV).

Cumulative permeate protein yield

Alcalase dosage (%v/w)	MWCO membrane (kDa)	Average flux (LMH)	UF (%w/w)	DV1 (%w/w)	DV2 (%w/w)
3.5	100	25 ± 2	50 ± 5	63 ± 4	73 ± 2
1.8	100	25 ± 1	53 ± 5	65 ± 4	73 ± 3
3.5	50	32 ± 6	46 ± 4	61 ± 4	70 ± 3
1.8	50	20 ± 0	41 ± 5	57 ± 2	66 ± 2
0.9	50	16 ± 3	33 ± 7	48 ± 6	56 ± 6

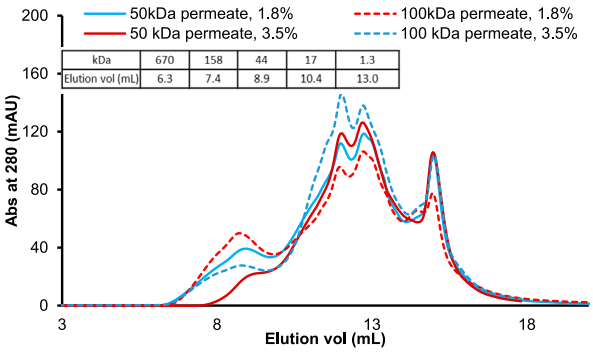

FIGURE 3
MW distribution of UF permeates obtained using 50-kDa (solid line) and 100-kDa (dotted line) hollow fiber membranes and 1.8% v/w and 3.5% v/w enzyme dosages. The chromatograms of UF permeate samples were generated on a TSK gel G2000swxl column (30 × 0.7 cm) at a flow rate of 0.7 ml/min. Bio-Rad protein standard mix ranging from 1.3 to 670 kDa was used to assign the estimated MW of hydrolysate peaks (*see* table inset).

yield (41 and 46%, respectively) and the cumulative yield after the second diafiltration (second DV) step (66% and 70%, respectively) (Table 1).

Interestingly, 100 kDa ultrafiltration and diafiltration (UFDF) of protein hydrolysates that were generated with either 1.8% or 3.5% enzyme dosage did not result in significantly different fluxes or protein yields. The UFDF process of the hydrolyzed slurry at 3.5% Alcalase had a higher permeate flux when processed by 50-kDa rather than 100-kDa hollow fiber membrane, but the protein yield was not substantially different.

To examine further flux and protein yield data, we then investigated the size-exclusion chromatography (SEC) profiles of protein hydrolysates produced with two different enzyme dosages and membrane pore sizes (Figure 3). The hydrolysate MW profiles in Figure 3 were obtained using UF permeates rather than diafiltrates to obtain a stronger UV (280 nm) detector response and detect low concentration protein species. The comparison of the protein elution profiles of hydrolysates produced with 1.8% and 3.5% Alcalase dosages shows that higher enzyme dosage reduces the amount of higher MW protein fragments that elute between 7 and 10 ml elution volumes. The decrease of larger MW fragments is reflected by an increase in lower MW peaks that elute between 11 and 13 ml. Based on the protein standard curve, protein elution volumes of 7–10 ml translate to approximately 158–17 kDa MW range and 11–13 ml to 5–2 kDa. Therefore, one would expect the higher enzyme dosage (3.5%) to impact the performance more of the tighter 50-kDa membrane than the 100-kDa one (Table 1). The data in Table 1 show that the UF permeate flux with the 50-kDa MWCO hollow-fiber membrane increased from 20 to 32 LMH, but the flux through the 100-kDa membrane did not change with the enzyme dosage (25 LMH). Similarly, UF permeate yields were notably affected by the enzyme dosage when processing hydrolysates through the 50-kDa membrane (an increase from 41 to 46%) than 100-kDa membrane (similar ~50% yield).

To increase hydrolysate product yield in the permeate fraction, we implemented a diafiltration step for the recovery of additional hydrolyzed protein that had remained in the retentate at the end of the UF concentration step.

Diafiltration was performed in two stages each with one diafiltration volume exchange. Each diafiltration volume exchange protein yield was calculated, added to the previous step (UF or first DV), and reported as the cumulative protein yield (Table 1). The diafiltration results summarized in Table 1 show cumulative protein yields as a function of membrane pore size and enzyme dosage. The data indicate that diafiltration of UF or first DV retentate increases protein yield by about 10% and that after two DV exchanges one could achieve a cumulative protein yield greater than 70% with a 100-kDa MWCO hollow fiber membrane. The largest jump in protein recovery was observed with the 50-kDa membrane. After the first DV step (first DV), the protein yield was 15% higher followed by additional 10% after the second diafiltration step (second DV), irrespective of the enzyme dosage. As pointed out previously, the separation efficiency of the 50-kDa membrane

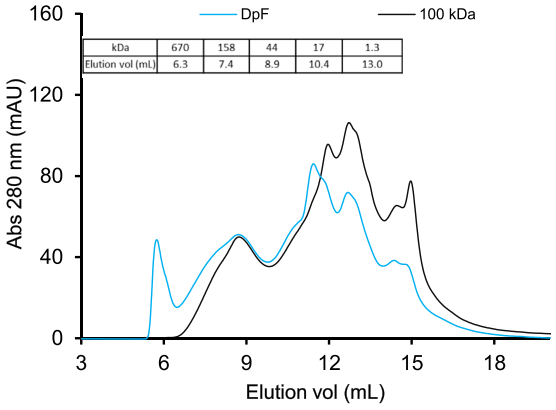

FIGURE 4
Size-exclusion chromatograms of DpF-hydrolysates (blue line) and UF-hydrolysates (black line) using 1.8% enzyme dosage. The chromatograms were generated on a TSK gel G2000swxl column (30 × 0.7 cm) at a flow rate of 0.7 ml/min. Bio-Rad protein standard mix was used to assign the estimated MW of hydrolysate peaks (table inset).

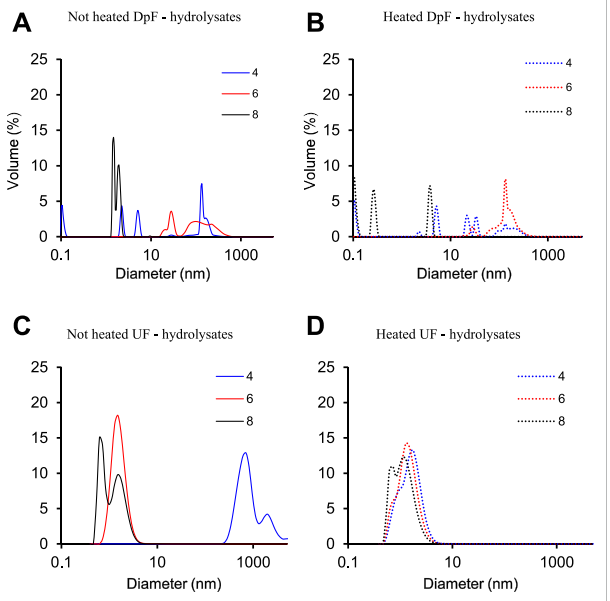

FIGURE 5
Molecular size distribution of **(A)** non-heated DpF-hydrolysates; **(B)** heated DpF-hydrolysates; **(C)** non-heated UF-hydrolysates; **(D)** heated UF-hydrolysates at pH 4, 6, and 8.

was affected by the enzyme dosage and the cumulative protein yield after the second DV could reach 70% only for hydrolysates produced using 3.5% (v/w) Alcalase.

In summary, hydrolysates produced with 3.5% provide greater processing flexibility and, if the enzyme cost does not contribute significantly to the final product cost, one should consider using 3.5% (v/w) irrespective of the MWCO membrane (i.e., 50 or 100 kDa). Otherwise, the use of 1.8% (v/w) dosage would limit LEA hydrolysate processing (UFDF) to a 100-kDa hollow-fiber membrane. Because the lower enzyme dosage of 1.8% (v/w) and 100-kDa MWCO were an effective combination for enhancing the ultrafiltration flux and cumulative protein recovery yield, we selected the latter combination to produce membrane-processed hydrolysates (UF-hydrolysates). From this point forward, we aim to characterize and compare UF-hydrolysates alongside hydrolysates processed by centrifugation and depth filtration (DpF-hydrolyzates), following a process developed in one of our previous studies (Soto-Sierra et al., 2021). The main objective was to understand the advantages and disadvantages of single-step UFDF vs. centrifugation followed by depth filtration in terms of quality of the final hydrolysates. The exact process steps and key process parameters for production UF- and DpF-hydrolyses are depicted in Figure 1.

Temperature (T) and pH stability of depth-filtered (DpF) and ultrafiltered (UF) hydrolysates

The temperature (T) and pH stability of hydrolysates are important quality attributes as these two parameters can contribute to product discoloration and reduced solubility due to protein aggregation (Lan et al., 2018; Edwards and Jameson, 2020; He et al., 2022). Because the stability of protein hydrolysates is known to be affected by the protein MW and composition (Adler-Nissen et al., 1978; Olsen and Adler-Nissen, 1979), we first determined SEC elution profiles of UF-hydrolysates and DpF-hydrolysates (Figure 4)

The MW distribution and peak intensities of the two hydrolysates were similar except for the eluting protein in 5–7 ml and absorption intensity of protein peaks at 12 and 15 ml.

The molecular weight profiles in Figure 4 show that the DpF-hydrolysate (blue elution profile in Figure 4) contained a fraction of high-MW protein (>670 kDa) that eluted in ~6 ml. The latter protein fraction was not present in the UF-processed samples because 100-kDa MWCO membranes are intended to reject most protein molecules greater than 300 kDa size. The data indicate that centrifugation followed by a depth filtration process produces DpF-hydrolysates with a broader MW range than the UF process. This observation is consistent with limited fractionation power of acidic precipitation, which is governed by protein physicochemical properties such as solubility, hydrophobicity, and net charge at the precipitation pH (Bramaud et al., 1997) rather than their MW size as it is the case with membrane separations.

The 100-kDa membrane-processed hydrolysates (black line) shown in Figure 4 consist mostly of protein fractions ranging from 44 to 1.3 kDa that have eluted between 9 and 15 ml elution volumes. Protein peaks at about 15 ml in both samples correspond to an estimated MW of less than 1 kDa and consist of dipeptides,

tripeptides, and free amino acids. The question that remains is whether the slight difference in protein composition would result in detectable stability differences. Specifically, would the absence of the largest MW protein fraction (5–7 ml elution volume) in the UF-processed LEA hydrolysates increase pH and heat stability of the UF-hydrolysates compared to DpF-hydrolysates?

To address this question, the molecular (particle) size distribution of heated and non-heated DpF- and UF-hydrolysate samples was compared at three different pHs (4, 6, and 8) using dynamic light scattering (DLS). The molecular weight size distribution of heated and non-heated DpF- and UF-hydrolysate samples as a function of pH at 95°C is summarized in Figure 5.

The results in Figure 5 show that the size distribution of UF and DpF protein hydrolysates was different for both heated and non-heated samples. A significant size distribution shift in DpF-hydrolysates was observed upon pH adjustment and heating (Figures 5A,B). The DLS graphs of heated and non-heated samples at pH 4.0 (blue line) and 6.0 (red line) show peaks between 100 and 1000 nm, which are an indication of aggregation (Filipe et al., 2010). At pH 8.0 (black solid line), the size distribution changed slightly upon heating but remained between 0.1 and 10 nm.

The UF-hydrolysates (Figures 5C,D), on the other hand, were more stable at the three pHs before and after heating as evidenced by the comparable size distribution profiles. The volumetric fraction diameter of UF-processed LEA-hydrolysates ranged from 0.2 to 10 nm in all the treatments but in the non-heated samples at pH 4.0. The non-heated samples at pH 4.0 (blue solid line) resulted in two peaks with volumetric fraction diameters around 1000 nm. We hypothesize that pH 4.0, which is very close to the average pI of algae proteins (pH 4.0–5.5) (Ursu et al., 2014), induced the association of protein fragments in the hydrolysate that led to the observed shift of the volumetric faction diameter (Goudarzi et al., 2015). The absence of later peaks upon heating of the same samples suggests that thermal energy (95°C) might have reduced/disrupted molecular interactions causing the presumed protein association (Goudarzi et al., 2015). Based on DLS data and SEC profiles, physicochemical properties of UF-hydrolysates would be more predictable and probably a better choice for the development of food and drink formulations.

To further evaluate the impact of heating on the hydrolyzed samples, we compared the browning reaction of freeze-dried DpF-hydrolysates and UF-hydrolysates to a soy protein concentrate control (Figure 6). When the soy protein concentrate did not show any signs of browning, we observed some darkening of the UF-hydrolysate sample, and a significantly greater browning of the DpF sample due to Maillard reactions and potential degradation (Yu et al., 2018; Fu et al., 2020). The results of the browning reaction of the freeze-dried hydrolysates support the aforementioned conclusion that UF-hydrolysates are of superior quality. The higher quality of UF-hydrolysates compared to that of DpF-hydrolysates could be explained by the latter containing larger MW peptides (>10 kDa peptides), which are known to be more propense to degradation (Lan et al., 2010; Yu et al., 2018). The results suggest that the UF-hydrolysates would be a better candidate than DpF-hydrolysates in applications where pH and temperature stability matter.

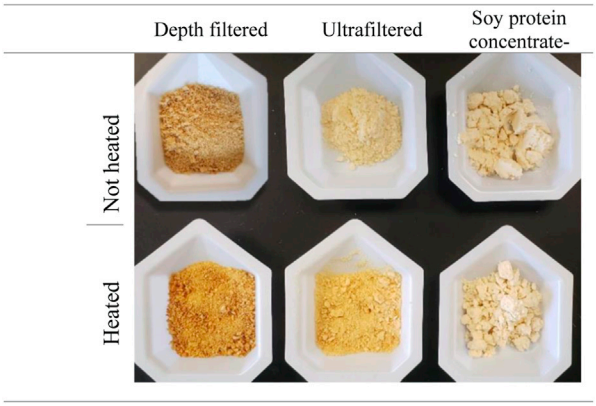

FIGURE 6
Effect of heating (95°C for 10 min) on depth-filtered (DpF-hydrolysates) and ultra-filtered (UF-hydrolysates) hydrolysates. –Non-heated samples are shown in the top row and heated ones on the bottom.

Conclusion

In this study, we evaluated a clarification process option for the production of algal protein hydrolysates using single-step ultrafiltration and diafiltration production of UF-hydrolysates. The results showed that the yields and MW distribution profile of protein hydrolysates were a function of the enzyme dosage during hydrolysis and the membrane (pore size) MWCO. The combination of higher dosage (3.5%) and 50-kDa MWCO membrane produced hydrolyzates with an overall lower molecular weight range, while lower enzyme dosage (0.9 and 1.8%) and 100-kDa MWCO resulted in hydrolysates with a higher number of proteins over 100 kDa. Protein hydrolysates that were generated with either 1.8% or 3.5% enzyme dosage and processed through a 100-kDa MWCO hollow fiber membrane had higher protein yields.

DpF-hydrolysates had a broader MW range and overall higher MW than the UF-hydrolysates. The presented data indicate that UF-hydrolysates would be more stable in pH and temperature and less susceptible to Maillard reactions, thereby probably being a better choice for the development of food and drink formulations.

In summary, this study suggests that the tangential flow ultrafiltration process is a viable process option to the traditional protein fraction method. Potential advantages of TFF include single-step clarification of algal hydrolysates, greater protein recovery yield (70 % vs. 64%), and apparently better pH and heat stability.

Data availability statement

The raw data supporting the conclusion of this article will be made available by the authors, without undue reservation.

Author contributions

LS-S: conceptualization, investigation, and writing—review and editing. ZN: conceptualization, investigation, and writing—review and editing.

Funding

This work was supported by Texas A&M Agrilife Research and Qualitas Health Inc under research agreement no. M1802950. The authors would also like to thank Rebecca White and Nalley from Qualitas Health for kindly providing the biomass and contributing to valuable technical discussions regarding process scalability and yields.

Acknowledgments

We would also like to acknowledge Daniela Oliveira from the department of Biological and Agricultural Engineering at Texas A&M University for her editorial contributions.

Conflict of interest

LS-S is currently employed by MTEM. Most of this work was conducted while she was at Texas A&M.

The author declares that the research was conducted in the absence of any commercial or financial relationships that could be construed as a potential conflict of interest.

Publisher's note

All claims expressed in this article are solely those of the authors and do not necessarily represent those of their affiliated organizations, or those of the publisher, the editors, and the reviewers. Any product that may be evaluated in this article, or claim that may be made by its manufacturer, is not guaranteed or endorsed by the publisher.

References

Adler-Nissen, J. (1986). *Enzymatic hydrolysis of food proteins*. London: Elsevier Applied Science.

Adler-Nissen, J., Poulsen, G., and Andersen, P. (1978). *Enzymatic hydrolysis of soy protein for nutritional fortification of low pH food*. JSTOR: Annales de la Nutrition et de l'Alimentation.

Akaberi, S., Gusbeth, C., Silve, A., Senthilnathan, D. S., Navarro-Lopez, E., Molina-Grima, E., et al. (2019). Effect of pulsed electric field treatment on enzymatic hydrolysis of proteins of Scenedesmus almeriensis. *Algal Res.* 43, 101656. doi:10.1016/j.algal.2019.101656

Bramaud, C., Aimar, P., and Daufin, G. (1997). Whey protein fractionation: Isoelectric precipitation of α-lactalbumin under gentle heat treatment. *Biotechnol. Bioeng.* 56 (4), 391–397. doi:10.1002/(sici)1097-0290(19971120)56:4<391::aid-bit5>3.0.co;2-j

Cuchiaro, H., and Laurens, L. M. (2019). Total protein analysis in algae via bulk amino acid detection: Optimization of amino acid derivatization after hydrolysis with O-phthalaldehyde 3-mercaptopropionic acid (OPA-3MPA). *J. Agric. Food Chem.* 67, 5672–5679. doi:10.1021/acs.jafc.9b00884

Edwards, P. J., and Jameson, G. B. (2020). "Structure and stability of whey proteins," in *Milk proteins* (Elsevier), 251–291.

Filipe, V., Hawe, A., and Jiskoot, W. (2010). Critical evaluation of Nanoparticle Tracking Analysis (NTA) by NanoSight for the measurement of nanoparticles and protein aggregates. *Pharm. Res.* 27 (5), 796–810. doi:10.1007/s11095-010-0073-2

Fu, Y., Zhang, Y., Soladoye, O. P., and Aluko, R. E. (2020). Maillard reaction products derived from food protein-derived peptides: Insights into flavor and bioactivity. *Crit. Rev. food Sci. Nutr.* 60 (20), 3429–3442. doi:10.1080/10408398.2019.1691500

Goudarzi, M., Madadlou, A., Mousavi, M. E., and Emam-Djomeh, Z. (2015). Formulation of apple juice beverages containing whey protein isolate or whey protein hydrolysate based on sensory and physicochemical analysis. *Int. J. Dairy Technol.* 68 (1), 70–78. doi:10.1111/1471-0307.12155

He, W., Guo, F., Jiang, Y., Liu, X., Chen, J., Zeng, M., et al. (2022). Enzymatic hydrolysates of soy protein promote the physicochemical stability of mulberry anthocyanin extracts in food processing. *Food Chem.* 386, 132811. doi:10.1016/j.foodchem.2022.132811

Kulkarni, S. V., and Nikolov, Z. L. (2017). "Selective extraction of carotenoids and proteins from Chlorella vulgaris," in *2017 ASABE annual international meeting* (Michigan, United States: American Society of Agricultural and Biological Engineers).

Lan, X., Liu, P., Xia, S., Jia, C., Mukunzi, D., Zhang, X., et al. (2010). Temperature effect on the non-volatile compounds of Maillard reaction products derived from xylose–soybean peptide system: Further insights into thermal degradation and cross-linking. *Food Chem.* 120 (4), 967–972. doi:10.1016/j.foodchem.2009.11.033

Lan, Y., Chen, B., and Rao, J. (2018). Pea protein isolate–high methoxyl pectin soluble complexes for improving pea protein functionality: Effect of pH, biopolymer ratio and concentrations. *Food Hydrocoll.* 80, 245–253. doi:10.1016/j.foodhyd.2018.02.021

López-Pedrouso, M., Borrajo, P., Pateiro, M., Lorenzo, J. M., and Franco, D. (2020). Antioxidant activity and peptidomic analysis of porcine liver hydrolysates using alcalase, bromelain, flavourzyme and papain enzymes. *Food Res. Int.* 137, 109389. doi:10.1016/j.foodres.2020.109389

Morris, H. J., Almarales, A., Carrillo, O., and Bermudez, R. C. (2008). Utilisation of Chlorellavulgaris cell biomass for the production of enzymatic protein hydrolysates. *Bioresour. Technol.* 99 (16), 7723–7729. doi:10.1016/j.biortech.2008.01.080

Olsen, H. S., and Adler-Nissen, J. (1979). Industrial-production and applications of a soluble enzymatic hydrolyzate of soya protein. *Process Biochem.* 14 (7), 6–11.

Safi, C., Liu, D. Z., Yap, B. H. J., Martin, G. J. O., Vaca-Garcia, C., and Pontalier, P. Y. (2014). A two-stage ultrafiltration process for separating multiple components of Tetraselmis suecica after cell disruption. *J. Appl. Phycol.* 26 (6), 2379–2387. doi:10.1007/s10811-014-0271-0

Safi, C., Olivieri, G., Campos, R., Engelen-Smit, N., Mulder, W., van den Broek, L., et al. (2017). Biorefinery of microalgal soluble proteins by sequential processing and membrane filtration. *Bioresour. Technol.* 225, 151–158. doi:10.1016/j.biortech.2016.11.068

Schwenzfeier, A., Wierenga, P. A., and Gruppen, H. (2011). Isolation and characterization of soluble protein from the green microalgae Tetraselmis sp. *Bioresour. Technol.* 102 (19), 9121–9127. doi:10.1016/j.biortech.2011.07.046

Soto-Sierra, L., Kulkarni, S., Woodard, S. L., and Nikolov, Z. L. (2020). Processing of permeabilized Chlorella vulgaris biomass into lutein and protein rich products. *J. Appl. Phycol.* 32, 1697–1707. **(in review)**. doi:10.1007/s10811-020-02055-x

Soto-Sierra, L., Stoykova, P., and Nikolov, Z. L. (2018). Extraction and fractionation of microalgae-based protein products. *Algal Res.* 36, 175–192. doi:10.1016/j.algal.2018.10.023

Soto-Sierra, L., Wilken, L. R., Mallawarachchi, S., and Nikolov, Z. L. (2021). Process development of enzymatically-generated algal protein hydrolysates for specialty food applications. *Algal Res.* 55, 102248. doi:10.1016/j.algal.2021.102248

Ursu, A.-V., Marcati, A., Sayd, T., Sante-Lhoutellier, V., Djelveh, G., and Michaud, P. (2014). Extraction, fractionation and functional properties of proteins from the microalgae Chlorella vulgaris. *Bioresour. Technol.* 157, 134–139. doi:10.1016/j.biortech.2014.01.071

Yu, M., He, S., Tang, M., Zhang, Z., Zhu, Y., and Sun, H. (2018). Antioxidant activity and sensory characteristics of Maillard reaction products derived from different peptide fractions of soybean meal hydrolysate. *Food Chem.* 243, 249–257. doi:10.1016/j.foodchem.2017.09.139

frontiers | Frontiers in Bioengineering and Biotechnology

TYPE Original Research
PUBLISHED 07 September 2022
DOI 10.3389/fbioe.2022.1002145

OPEN ACCESS

EDITED BY
Caoxing Huang,
Nanjing Forestry University, China

REVIEWED BY
Wu Lan,
South China University of Technology, China
Jia-Long Wen,
Beijing Forestry University, China
Zhiwen Wang,
University of Graz, Austria

*CORRESPONDENCE
Xiaolin Luo,
xluo53@fafu.edu.cn
Li Shuai,
lishuai@fafu.edu.cn

†These authors have contributed equally to this work

SPECIALTY SECTION
This article was submitted to Bioprocess Engineering, a section of the journal Frontiers in Bioengineering and Biotechnology

RECEIVED 24 July 2022
ACCEPTED 11 August 2022
PUBLISHED 07 September 2022

CITATION
Yang G, Gong Z, Luo X and Shuai L (2022), Revisiting alkaline cupric oxide oxidation method for lignin structural analysis.
Front. Bioeng. Biotechnol. 10:1002145.
doi: 10.3389/fbioe.2022.1002145

Revisiting alkaline cupric oxide oxidation method for lignin structural analysis

Guangxu Yang†, Zhenggang Gong†, Xiaolin Luo* and Li Shuai*

College of Materials Engineering, Fujian Agriculture and Forestry University, Fuzhou, China

Lignin structural analysis is important for the comprehensive utilization of lignin as well as delignification and bleaching during pulping while it is difficult to completely elucidate lignin structure due to its structural complexity and heterogeneity. Depolymerization of lignin into simple monomers via alkaline cupric oxide oxidation (Ox^{CuO}) followed by chromatographic analysis of the monomers is an effective method for lignin structural analysis. Here we revisited the Ox^{CuO} of lignin model compounds (monomers and dimers) and three representative lignocelluloses (i.e., Eucalyptus, Masson pine, and corn stover) to understand the effects of reaction conditions and lignin sub-structures on oxidation product yields and distributions. The improved Ox^{CuO} was found to be effective in oxidatively breaking the robust interunit C-C bonds in the β-β′ and β-5′ moieties of lignin other than β-O-4′ linkages at an elevated temperature (210°C). Further degradation of the monomeric oxidation products could also occur to reduce the monomer yields under a severe condition (i.e., high temperature and long reaction time). In addition, O_2 inputs could reduce the monomer yields via nonselective overoxidation, thus having negative effects on accurate structural analysis of lignin. The O_2 removal via ultrasonication combined with N_2 flushing prior to the oxidation reaction could improve the monomer yield about 1.2 times (compared to that without O_2 removal) at a low biomass loading of 5 wt%. By using the improved method of Ox^{CuO}, a monomer yield of 71.9% could be achieved from Eucalyptus (hardwood) lignin, which was much higher than conventional nitrobenzene oxidation (59.8%) and reductive depolymerization (51.9%). Considering the low cost, high availability, and low toxicity of CuO, the improved Ox^{CuO} could be a convenient and economic method for more accurate lignin structural analysis.

KEYWORDS

lignin, depolymerization, oxidation, cupric oxide, model compounds

Introduction

Lignin is synthesized by oxidative radical polymerization of syringyl (S), guaiacyl (G), and p-hydroxyphenyl (H) subunits, and the monomeric units are connected by several types of C-O and C-C linkages (Figure 1) (Deussa and Barta., 2016; Zhang and Wang., 2020). As one of the main component of lignocellulosic biomass (Schutyser et al., 2018), structural analysis of lignin is of great importance for its comprehensive utilization as well

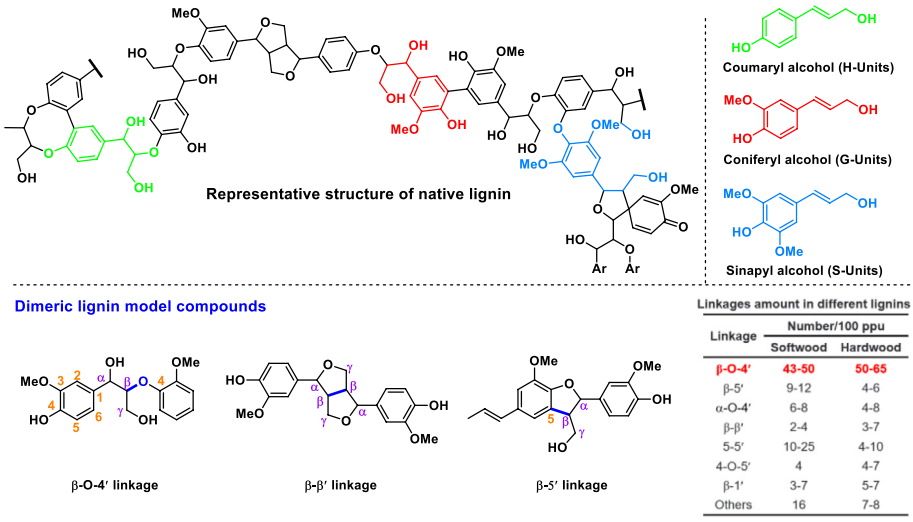

Linkages amount in different lignins

Linkage	Number/100 ppu	
	Softwood	Hardwood
β-O-4′	43-50	50-65
β-5′	9-12	4-6
α-O-4′	6-8	4-8
β-β′	2-4	3-7
5-5′	10-25	4-10
4-O-5′	4	4-7
β-1′	3-7	5-7
Others	16	7-8

FIGURE 1
The representative structure of native lignin and the dimeric lignin model compounds used in this study.

as delignification and bleaching during pulping. However, comprehensive analysis of lignin structure is challenging due to its complex and heterogeneous structure. To obtain lignin structural information, depolymerization (or degradation) of lignin into simple lignin monomers followed by chromatographic analysis is the most convenient and effective method. Many methods such as acidolysis (Voitl and Rohr., 2008; Partenheimer, 2009; Werhan et al., 2011), thioacetolysis (Nimz, 1974), and reductive depolymerization (Lu and Ralph., 1997; Bosch et al., 2015; Shuai et al., 2016; Liao et al., 2020) have been developed to evaluate the content and structure of lignin in lignocellulosic materials. However, these methods have certain drawbacks such as inability to break the C-C bonds, long analysis time, and/or costly catalysts or reagents. For example, oxidative depolymerization of lignin using an oxidant (e.g., nitrobenzene) in an alkaline solution (Ox^{NB}) is effective in cleavage of both C-O and C-C bonds to give a higher lignin monomers yield (Chan et al., 1995; Hirayam et al., 2019), while nitrobenzene is a toxic compound and produces many by-products that can interfere with the analysis of lignin monomers (Lapierre, 2010). In contrast, cupric oxide (CuO) as a common oxidant is more competitive than nitrobenzene due to its low cost, high availability, and low toxicity. Furthermore, CuO and its reduction products (Cu or Cu_2O) have very little interference with the analysis of lignin monomers. CuO as a heterogeneous catalyst has poor solubility in NaOH aqueous solution, thus facilitating the isolation of the catalyst and liquid products via simple centrifugation (Chen, 1992; Lapierre, 2010).

Previously, a reported method of alkaline cupric oxide oxidation (Ox^{CuO}) for lignin structural analysis could achieve a phenolic monomer yield of around 50.7 mol% from native hardwood lignin and the monomers were believed to be resultant from the selective cleavage of C-O interunit linkages such as β-O-4 linkage (Chen, 1992). Since the structure of the aromatic nuclei (i.e., guaiacyl, syringyl, and 4-hydroxyphenyl structures) on lignin are preserved after Ox^{CuO}, Ox^{CuO} can give an indication of the composition of lignin units under investigation, and the yields of the oxidation products can provide information on the composition of lignin interunit linkages (Hedges and Ertel., 1982; Goi et al., 1993). For example, hardwoods such as *Eucalyptus* or birch gave both guaiacyl and syringyl products while softwood only gave guaiacyl products. 4-hydroxyphenyl products are generally observed in the oxidation of grass together with guaiacyl and syringyl products (Schutyser et al., 2018). As for lignin with highly condensed structures, little monomeric oxidation products can be produced (Billa et al., 1996; Villar et al., 1997). Based on the differences of the monomeric oxidation products, Ox^{CuO} can be used to identify biomass species (hardwood, softwood, or grass) and analyze unknown biomass samples.

Recently, we revisited the method of Ox^{CuO} and found that three improved aspects would facilitate more accurate and efficient analysis of lignin structures. First, an elevated temperature and a prolonged reaction time facilitated the cleavage of C-C bonds (e.g., β-β′ and β-5′) in lignin during Ox^{CuO} of lignin while it could also lead to increased degradation of the oxidation products. To obtain high-yield lignin monomers, an optimized reaction condition should be explored to enable the cleavage of C-C bonds meanwhile minimizing the degradation of the desired products. Second, the operation of O_2 removal before oxidative depolymerization was necessary to avoid the overoxidation of the monomeric oxidation products, which

could improve the monomer yields especially at a low biomass loading. Choosing a simpler method (such as ultrasonication combined with N_2 flushing) to effectively remove O_2 could shorten the analysis time compared to the thermal or chemical oxygen removal. Third, for analysis of the lignin monomers in alkaline aqueous solution after oxidative depolymerization, the classical procedures involved acidification of the hydrolysate, followed by the extraction of phenolic products for HPLC or GC analysis (Chen, 1992; Lapierre, 2010; Tamai et al., 2015; Schutyser et al., 2018). The possibility of the incomplete extraction could result in an underrated yield of lignin monomers and poor reproducibility. Therefore, an improved product analysis method should be developed to determine all lignin monomers in the hydrolysate. These thoughts motivate us to develop an improved method of alkaline cupric oxide oxidation for more accurate and readily lignin structural analysis.

Materials and methods

Materials

Chemicals including methylguaiacol (2-methoxy-4-Methylphenol, >98%), ethylguaiacol (2-methoxy-4-ethylphenol, 99%), propylguaiacol (2-methoxy-4-propylphenol, 98%), *p*-methylphenol (99%), methylsyringol (2,6-dimethoxy-4-methylphenol, >97%), vanillin (4-hydroxy-3-methoxybenzaldehyde, 99%), acetovanillone (4′-hydroxy-3′-methoxyacetophenone, 98%), vanillic acid (4-hydroxy-3-methoxybenzoic acid, 98%), syringaldehyde (4-hydroxy-3,5-dimethoxybenzaldehyde, 98%), acetosyringone (4′-hydroxy-3′,5′-dimethoxyacetophenone, 98%), syringic acid (4-hydroxy-3,5-dimethoxybenzoic acid, 98%), nitrobenzene (≥99%), CuO (40 nm particle size, 99.5%), benzoic acid (≥99.9%), anhydrous pyridine (≥99%), Ru/C catalysts (5% metal loadings), and NaOH (≥98%) were purchased from Aladdin® Biochemical Technology Co., Ltd. (Shanghai, China). BSTFA (N, O-bis(trimethylsilyl)trifluoroacetamide, >99%) and hydrochloric acid (37%) were purchased from Sigma Aldrich (Shanghai, China). Guaiacylglycerol-β-guaiacyl ether [1-(4-hydroxy-3-methoxyphenyl)-2-(2-methoxyphenoxy)propane-1,3-diol, 97%] and pinoresinol [4-[(3S,3aR,6S,6aR)-6-(4-hydroxy-3-methoxyphenyl)-1,3,3a,4,6,6a-hexahydrofuro [3,4-c]furan-3-yl]-2-methoxyphenol, 98%] were purchased from TCI Chemicals (Shanghai, China). Dehydrodiisoeugenol (4-(2,3-dihydro-7-methoxy-3-methyl-5-propenyl-2-benzofuranyl)-2-methoxyphenol, 98%) were purchased from Yuanye Bio-Technology Co., Ltd. (Shanghai, China). All commercial chemicals were analytical reagents and were used as received. Water was purified using a Millipore Milli-Q I water purification system to a resistivity higher than 18 MΩ cm.

Corn stover was provided by the State Key Laboratory of Biobased Materials and Green Papermaking at Qilu University of Technology, China. Masson pine and Eucalyptus wood chips were provided by Fujian Qingshan Paper Co., Ltd. (Sanming, China). Wood chips and corn stover were air-dried, carefully milled to pass through a screen of 40 mesh for experiments.

Reductive depolymerization

In the typical reductive depolymerization experiments, 500 mg of air-dried wood particles (>40 mesh) (or 50 mg of dimeric lignin model compounds), 100 mg of Ru/C (5 wt% Ru on Carbon) and 10 ml of methanol were loaded into a 25-ml pressure-resistant reactor. The reactor was closed, purged three times with H_2 and pressurized with 4 MPa H_2. The mixture was stirred with a magnetic bar at 800 rpm, heated with a heating jacket controlled by a PID temperature controller to 220°C and then held at the temperature for 10 h. After the reaction, the reactor was cooled with tap water. One milliliter of internal standard solution (30 mg/ml benzoic acid in dioxane) was directly added into the reactor and mixed with the slurry. One milliliter of the clear solution was sampled and centrifuged. The resultant supernatant was used for GC or GC-MS analysis.

Alkaline nitrobenzene oxidation

Nitrobenzene oxidation of lignins and dimeric lignin model compounds were performed in a 25-ml pressure-resistant reactor. Specifically, 7 ml of 2 mol/L NaOH aqueous solution, 200 mg of air-dried wood particles (>40 mesh) (or 50 mg of dimeric lignin model compounds) and 0.4 ml of nitrobenzene were added to the reactor. The reactor was pressurized with N_2 to 0.2 MPa. Then the reactor was heated to 170°C and held at the temperature for 2.5 h. After cooling, the reaction mixture in the reactor was transferred to a 100-ml separating funnel and extracted by 25 ml of chloroform three times to remove the residual nitrobenzene and its derivatives. The aqueous phase was acidified by concentrated hydrochloric acid to pH < 3. The acidified liquid was extracted with fresh chloroform (3 × 25 ml) and the chloroform phases were combined. One milliliter of internal standard solution (30 mg/ml benzoic acid in dioxane) was mixed with the chloroform phases. The resultant liquid was used for GC and GC-MS analyses.

Alkaline copper oxide oxidation

For the alkaline copper oxide oxidation experiments, 1 g of air-dried wood particles (>40 mesh) (or 50 mg of dimeric lignin model compounds) and 1.5 g of CuO (40 nm) were mixed with 10 ml of NaOH aqueous solution (2.5 mol/L) in a 25-ml pressure-resistant reactor. The mixture was ultrasonically treated for 10 min and the reactor was sealed, flushed with N_2

three times, and then pressurized with N_2 to 0.2 MPa. The reactor was heated in a heating jacket to 210°C and maintained at the temperature for 40 min. The reaction was stirred with a magnetic bar at 800 rpm. After the reaction, the reactor was quickly cooled to room temperature with tap water. Due to its good solubility in both alkaline solution and organic solvent, 1 ml of benzoic acid standard solution (benzoic acid dissolved in dioxane with a concentration of 30 mg/ml) was directly added into the reactor and mixed with the slurry. One milliliter of the clear solution was sampled and centrifuged. The resultant supernatant was neutralized and used for GC or GC-MS analysis.

In order to investigate the effect of O_2 on lignin monomer yields, the operation of O_2 removal was not required for the original mixtures. Alternatively, these reactors were either just pressurized with N_2 to 0.2 MPa or directly pressurized with O_2 to the specified pressure. The other experimental procedures were the same as that mentioned above.

Gas chromatography and gas chromatography-mass spectrometry analyses

Lignin monomers resulted from the alkaline copper oxide oxidation were initially identified by GC-MS and then quantified by GC. Prior to the GC and GC-MS analysis, the sample was derived with BSTFA. Specifically, 10 µl of the sample solution and 5 µl of concentrated HCl (37 wt%) were mixed with 200 µl of pyridine in a 2-ml GC vial. After ultrasonic treatment for 30 s, 700 µl of BSTFA was added to the GC vial which was then kept at 80°C for 1 h. The silylated products were identified by GC-MS using an Agilent 7890B series GC equipped with a HP5-MS capillary column (30 m × 0.45 mm) and an Agilent 5977A series mass spectroscopy detector. The inlet and detector temperature were 300°C, and the injection volume was 1 µl. Helium was used as a carrier gas at a flow rate of 1.5 ml/min. The column was initially kept at 50°C for 5 min, then was heated at a rate of 10°C/min to 300°C and held for 5 min. Most of the products were directly identified with authentic standard compounds. Some of products were directly identified according to the mass spectra. As for the lignin monomers from reductive depolymerization and alkaline nitrobenzene oxidation (chloroform phases), the samples were completely processed with the method used for alkaline copper oxide oxidation, except that the concentrated HCl was not required to add.

The identified products were further quantified by a GC (Agilent 7890B series, United States) equipped with an HP5 capillary column and a flame ionization detector (FID). The yields of the products in the sample solution were calculated based on the effective carbon number rule for convenience. The detailed calculation was as follows:

In the equations,

$$n_{product} = n_{benzoic\ acid} \times \frac{A_{product}}{A_{benzoic\ acid}} \times \frac{ECN_{benzoic\ acid}}{ECN_{product}} \quad (1)$$

$$Y_{product} = \frac{n_{product}}{n_{theoretical}} \quad (2)$$

$n_{benzoic\ acid}$ (mmol): the molar amount of the internal standard (benzoic acid); $n_{product}$ (mmol): the molar amount of the lignin monomers; $A_{product}$: the peak area of monomers in the GC-FID chromatogram; $A_{benzoic\ acid}$: the peak area of benzoic acid in the GC-FID chromatogram; $ECN_{benzoic\ acid}$: the effective carbon number of silylated benzoic acid (Shuai et al., 2016); $ECN_{product}$: the effective carbon number of the lignin monomers; $Y_{product}$: 1) For the depolymerization of lignin model compounds (monomers and dimers), the molar yield of monomers was calculated on the basis of the molar amount of aromatic rings in the model compounds ($n_{theoretical}$); 2) for the depolymerization of lignin, the molar yield of monomers was calculated on the basis of the molar amount of Klason lignin ($n_{theoretical}$); an average molecular weight of 210 g/mol (Chen, 1992) for lignin monomeric units was used for the calculations.

Results and discussion

Alkaline copper oxide oxidation of lignin model compounds

Monomeric lignin model compounds

Several monomeric lignin model compounds with different alkyl side chains (i.e., methylguaiacol, MG; ethylguaiacol, EG; propylguaiacol, PG) that are typically produced from reductive depolymerization (RD) were oxidized with CuO in an alkaline condition. After the reaction, the products were analyzed by gas chromatography with flame ionization detection or mass spectrometry (GC-FID and GC-MS) *via* an improved method as described in the METHODS. The results in Figure 2 suggested that alkaline copper oxide oxidation (Ox^{CuO}) could even break the alkyl side chains (or C-C bonds) of lignin monomers to give oxidation products (e.g., vanillin, vanillic acid, and acetovanillone) at 200°C for 10 min. In contrast, almost no monomeric oxidation products were observed after the Ox^{CuO} of MG (<5%) under a conventional condition (170°C, 30 min) (Chen, 1992), while the yields of the monomeric oxidation products for MG, EG and PG were all significantly increased about two times under a severe condition (210°C, 30 min). Prolongation of the reaction time further improved the yields of the monomeric oxidation products for MG from 47.8% (30 min) to 55.6% (40 min) and 63.1% (60 min), respectively. These results indicated that an elevated temperature and a long reaction time facilitated the C-C cleavage during Ox^{CuO}. Similar monomeric oxidation products were also observed after the

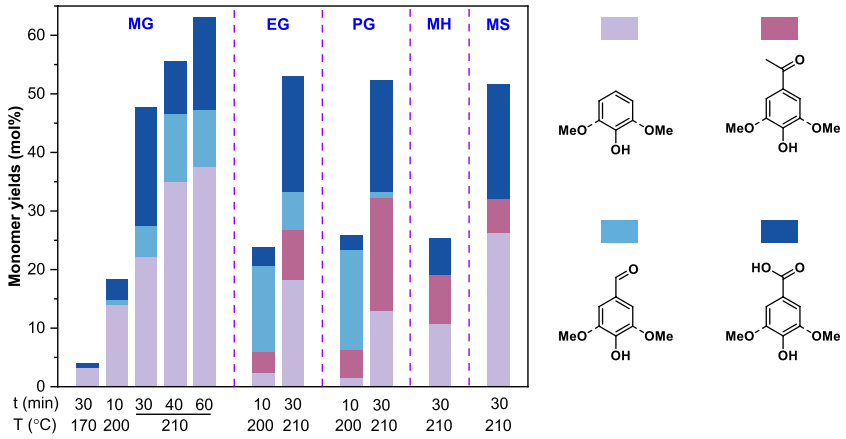

FIGURE 2
Alkaline copper oxide oxidation of monomeric lignin model compounds. MG, EG, PG, MH, and MS represented methylguaiacol, ethylguaiacol, propylguaiacol, *p*-methylphenol, and methylsyringol a respectively. The model compound loadings were 50 mg. All reactions were conducted in 10 ml of 2.5 mol/L NaOH with 2 g CuO addition.

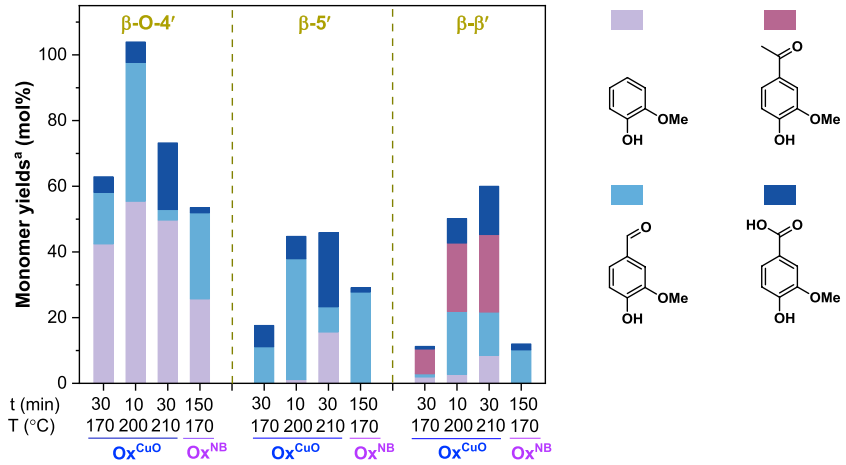

FIGURE 3
Alkaline oxidative depolymerization of dimeric lignin model compounds with CuO or nitrobenzene as the oxidant. [a]The monomer yields were based on the molar amount of aromatic rings in the model compounds. The model compound loadings were 50 mg. All CuO oxidation experiments were conducted in 10 ml of 2.5 mol/L NaOH with 0.5 g CuO addition. All nitrobenzene oxidation experiments were conducted in 7 ml of 2.0 mol/L NaOH with 0.4 ml nitrobenzene addition.

Ox^{CuO} of *p*-methylphenol (MH) and methylsyringol (MS) that had different aromatic nuclei. In addition, an H-type (MH, 25.3%) model gave oxidation products in much lower yield than G-type (MG, 47.8%) and S-type (MS, 51.7%) models (Figure 2). It was in line with the result of nitrobenzene oxidation (Chan et al., 1995), where electron donating groups (i.e., methoxyl groups) on the aromatic nuclei of lignin monomers enhanced the rate of oxidation. Therefore, the structure of the aromatic nucleus could also affect the reactivity of these lignin monomers to give oxidation products apart from the reaction temperature and time, which could be explained by the different ability of the aromatic nuclei to supply electrons to the benzylic carbon atoms (i.e., syringyl > guaiacyl > 4-hydroxyphenyl) (Shuai and Saha., 2017).

Dimeric lignin model compounds

Considering the good performance of Ox^{CuO} on breaking C-C bonds in lignin monomers, we further examined its ability to oxidatively break the robust interunit C-C bonds in the β-β′ and β-5′ moieties of lignin other than β-O-4′ linkages. Three representative

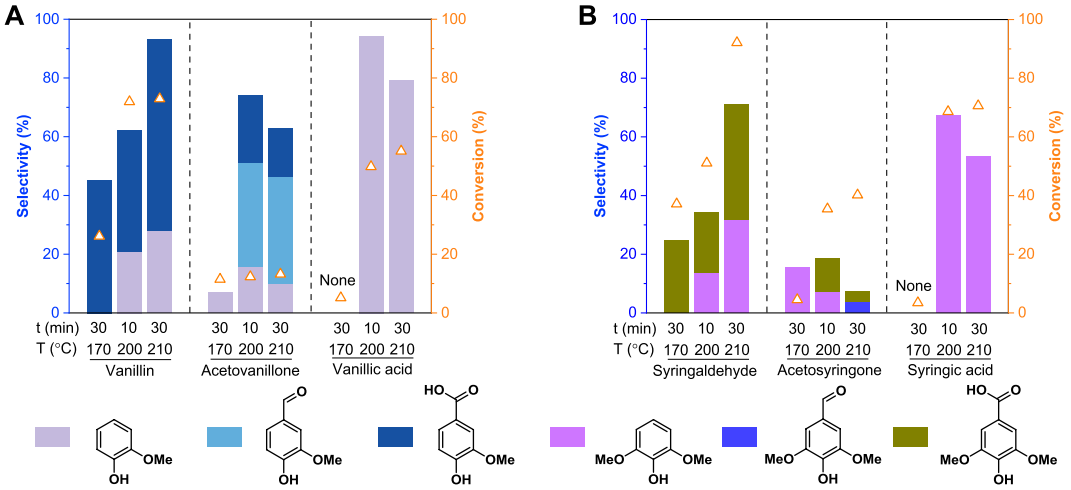

FIGURE 4
Stability tests of **(A)** G-type and **(B)** S-type monomeric oxidation products in the alkaline copper oxide oxidation system. The monomeric oxidation products loadings were 50 mg. All oxidation experiments were conducted in 10 ml of 2.5 mol/L NaOH with 0.5 g CuO addition.

dimeric lignin model compounds present in Figure 1 were selected as substrates for oxidative depolymerization (Ox^{CuO} and Ox^{NB}).

As showed in Figure 3, the β-O-4′ dimeric compound gave a higher monomer yield (62.9%) for Ox^{CuO} at 170°C for 30 min than Ox^{NB} at 170°C for 2.5 h (53.5%). As the reaction condition was intensified, the monomer yield for Ox^{CuO} of the β-O-4′ dimeric compound increased first and then decreased, and a theoretical monomer yield was achieved at 200°C for 10 min. The high monomer yield suggested that no condensation reaction of the monomeric products occurred in such Ox^{CuO} system. The decreased monomers under a severe condition (210°C for 30 min) could be due to the further degradation of the monomer products. Nevertheless, such severe condition facilitated the cleavage of C-C bonds in β-5′ and β-β′ dimeric compounds. The highest monomer yields of 44.8% and 50.2% were achieve at 210°C for 30 min via oxidatively breaking β-5′ and β-β′ bonds, respectively. These results suggested that an elevated temperature (210°C) was necessary for β-5′ and β-β′ cleavage, which was in line with the results of oxidation of alkyl side chains in lignin monomers discussed above.

Stability tests of monomeric oxidation products

As discussed above, the Ox^{CuO} system could not only enable the oxidative depolymerization of lignin, but also could reduce the monomer yields via further oxidative degradation of the oxidation products. To investigate the stability of the oxidation products, we performed the Ox^{CuO} of both G-type and S-type oxidation products under different conditions. The conversion of the substrates and the selectivity of the oxidation products were presented in Figure 4. For example, vanillin could readily be converted to vanillic acid at a relatively low temperature (170°C), guaiacol was only produced from vanillin at an elevated temperature (>200°C). Although the formed vanillic acid showed good stability at 170°C, substantial conversion of vanillic acid (49.8%) and high guaiacol selectivity (94.4%) could be achieved at 200°C for 10 min (Figure 4A). These results suggested that once vanillin was formed in the Ox^{CuO} system, it could be readily oxidized to vanillic acid, followed by the formation of guaiacol via further decarboxylation at an elevated temperature (>200°C). Whereas only 13.2% of the acetovanillone was further converted to other monomer products (i.e., guaiacol, vanillin, and vanillic acid) with a total selectivity of 62.9% even under a severe condition (210°C for 30 min), confirming that acetovanillone was relatively stable in the Ox^{CuO} system. As for S-type monomeric oxidation products, a transformation path similar to G-type monomeric oxidation products was observed. However, compared to G-type monomers, S-type monomers showed higher reactivity (or conversion rate) and were more easily degraded (Figure 4B), which was consistent with the result that S-type alkylphenols had the highest oxidation reactivity (Figure 2). The above results proved that the poor stability of the monomeric oxidation products under a severe oxidation condition was the main reason for the loss of monomer yields during oxidative degradation of lignin (or lignin model compounds). Therefore, the optimal temperatures for the oxidative cleavage of different interunit linkages should be carefully evaluated for the high-yield monomer production and more accurate structural analysis.

Alkaline copper oxide oxidation of native lignin

The effect of oxygen inputs on monomer yields

To examine the performance of Ox^{CuO} on lignin depolymerization, we conducted the reactions with Eucalyptus wood particles. By following the traditional procedure (Chen,

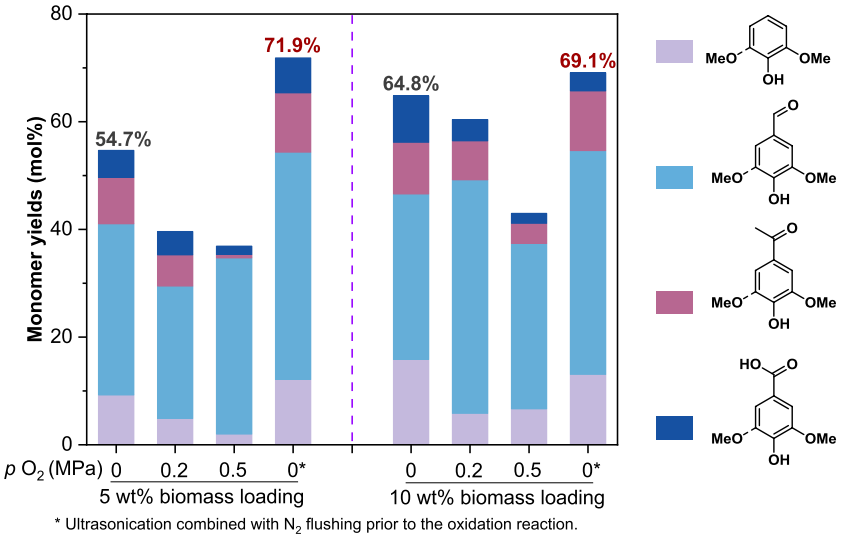

FIGURE 5
The effect of oxygen inputs on lignin monomer yields (on lignin basis). All reactions were conducted at 210°C for 40 min with 1.5 g CuO and 10 ml of 2.5 mol/L NaOH addition.

1992), a monomer yield of only 54.7% was achieved at a 5 wt% biomass loading of 5 wt% (Figure 5). However, the previous model compound studies have shown that the Ox^{CuO} enabled the cleavage of β-O-4′, β-β′, and β-5′, a theoretical monomer yield (based on the total content of β-O-4′, β-β′, and β-5′ moieties of hardwood lignin, Figure 1) could be around 70% if all of these linkages were selectively cleaved. Such difference (54.7% vs. 70%) motived us to explore the possible factors that caused the lowered oxidation product yield and to provide a more accurate method for lignin structural analysis.

Since O_2 was known to facilitate both product formation and degradation during alkaline aerobic lignin oxidation (Mathias and Rodrigues., 1995; Wu and Heitz., 1995; Schutyser et al., 2018), we speculated that the dissolved O_2 in the reaction liquid and residual O_2 in the reactor might be responsible for the low monomer yield especially at a low biomass loading. To validate the speculation, we inspected the lignin monomer yields for Ox^{CuO} of Eucalyptus wood particles with various O_2 inputs. As expected, even a 0.2 MPa O_2 input could significantly reduce the monomer yields from 54.7% to 39.6% at a relatively low biomass loading of 5 wt% (Figure 5), suggesting that the existence of O_2 had negative effect on the Ox^{CuO} process. While further increasing the O_2 input to 0.5 MPa had a slight effect on the monomer yield (36.9%) due to the limited reaction time. Interestingly, an improved monomer yield to 64.8% was observed when the biomass loading was increased to 10 wt%. It was because the high biomass loading mitigated the negative effect of the side reactions (such as overoxidation) on the monomer production in the reactor where a fixed volume of oxygen was present. Under the condition of a limited amount of O_2 input (<0.2 MPa) and a high biomass loading of 10 wt%, a comparable monomer yield (60.4%) to the condition of no extra O_2 input (64.8%) could be obtained. When the reactor was pressurized with up to 0.5 MPa O_2, the monomer yield was dramatically reduced to below 50%. Therefore, the existence of O_2 was an obstacle towards accurate analysis of lignin structure. In order to obtain high yields of monomers, it was preferable to remove O_2 from the reaction liquid and the reactor via ultrasonication combined with N_2 flushing prior to the oxidation reaction (see METHODS); besides, higher biomass loading could mitigate the effect of O_2 on monomer yields. Monomer yields of 71.9% and 69.1% could be achieved via the improved method of Ox^{CuO} at a biomass loading of 5 wt% and 10 wt%, respectively, which were close to the theoretical monomer yield (around 70%).

Comparison of different methods for lignin structural analysis

The types and ratios of subunits as well as the amount of interunit linkages in lignin vary with the types and sources of plants (Vanholme et al., 2010; Maeda, 2016; Tolbert et al., 2016). Therefore, three representative lignocelluloses (i.e., *Eucalyptus*, Masson pine, and corn stover) were selected as feedstocks to study the depolymerization of lignin in hardwood, softwood, and grass, respectively. The oxidative degradation of lignin was conducted in NaOH aqueous solution with CuO or nitrobenzene as an oxidant. Classical reductive depolymerization of lignin was conducted in methanol with Ru/C as a catalyst.

As shown in Figure 6A, reductive depolymerization (Red) of lignin enabled monomer yields of 51.9% for Eucalyptus lignin,

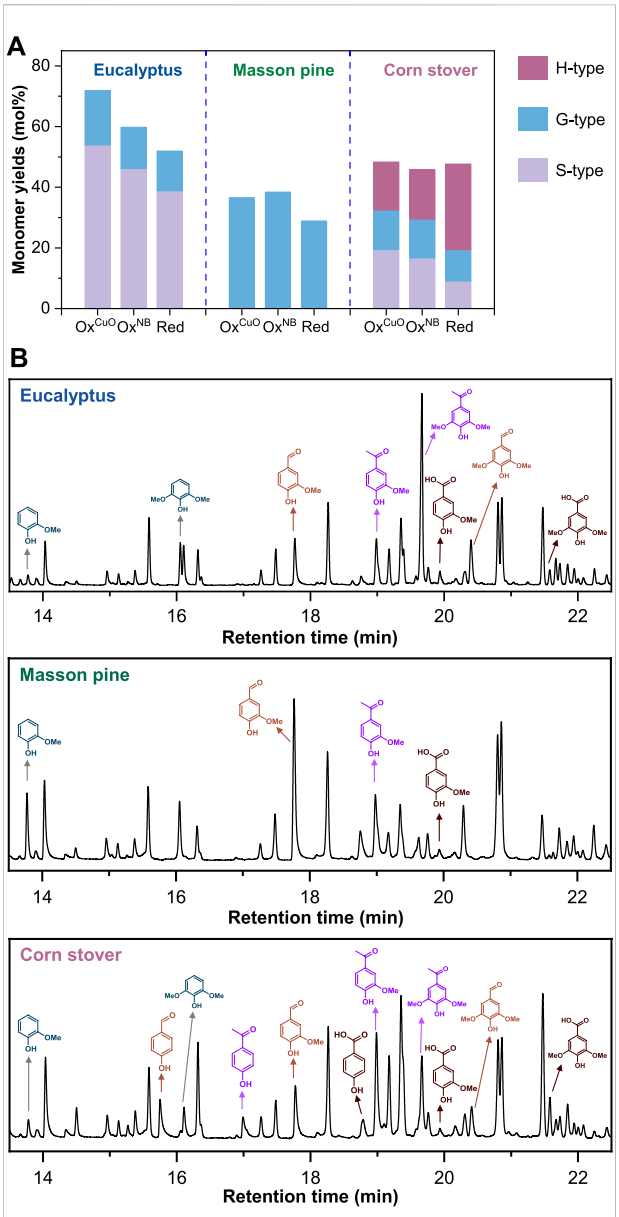

FIGURE 6
(A) Comparison of lignocellulose alkaline copper oxide oxidation with conventional nitrobenzene oxidation and reductive depolymerization. **(B)** Gas chromatograms of the lignin monomers derived from alkaline copper oxide oxidation of lignin. The detailed reaction conditions were described in *Materials and Methods*.

28.9% for Masson pine lignin, 47.6% for corn stover lignin via the cleavage of only labile C-O ether linkages (Bosch et al., 2015; Shuai et al., 2016). In contrast, higher yields of lignin monomers could be obtained *via* oxidative depolymerization due to the additional cleavage of C-C bonds. The total monomer yield of 71.9% for Ox^{CuO} of Eucalyptus was much higher than that of 59.8% for Ox^{NB} and 51.9% for Red, demonstrating that the improved Ox^{CuO} had better performance (shorter reaction time and higher monomer yields) on lignin depolymerization than conventional Red and Ox^{NB}. Although the similar products could be obtained from the three lignocelluloses (Figure 6B), the least monomers yield were provided by Masson pine using the same oxidant (CuO or nitrobenzene) (Figure 6A). Furthermore, the contents of condensed structures such as biphenyl structures (5–5′ linkages) in softwood lignin (10%–25%, Figure 1) were higher than those in hardwood lignin (4%–10%). Such 5-5′ bonds were unable to be broke by such oxidation system (Tamai et al., 2015), limiting the release of monomers. Therefore, the improved method of Ox^{CuO} could increase the lignin monomer yields of Eucalyptus more obviously than Masson pine and corn stover.

Conclusion

The results of the lignin model compound experiments coupled with the chromatographic analysis provide new understanding towards the alkaline copper oxide oxidation of lignin (Ox^{CuO}). First, we found that other than β-O-4′ moieties of lignin, the β-β′ and β-5′ moieties of lignin also contributed to the monomeric oxidation products via the cleavage of C-C interunit linkages even under the classical Ox^{CuO} conditions (170°C, 30 min). Therefore, compared to the classical Ox^{CuO} method which ascribed lignin monomers to the cleavage of C-O ether linkages, the improved Ox^{CuO} method could be more accurate for characterizing the structure of native lignins. Second, the direct addition of benzoic acid as an internal standard in the alkaline solution combined with the direct silylation of the reaction liquor simplified the product analysis procedure, which further improved the accuracy of the improved Ox^{CuO} method for analyzing lignin structure. Third, high temperature and O_2 removal were desirable for the high-yield production of lignin monomers from lignocelluloses via Ox^{CuO}. While the elevated temperature not only increased the degree of lignin depolymerization but also promoted the degradation of the monomeric oxidation products. By optimizing the reaction condition of Ox^{CuO} and the procedure for products analysis, an improved monomer yield of 71.9% could be achieved from Eucalyptus wood particles. This result was better than the classical Ox^{CuO} (54.7%), the conventional nitrobenzene oxidation (59.8%) and reductive depolymerization (51.9%). Since all of the three moieties (β-O-4′, β-β′, and β-5′) of lignin could produce similar monomeric oxidation products *via* Ox^{CuO}, it was difficult to distinguish the source of oxidation products. However, the amount of non-condensed units in lignin could be estimated according to the lignin monomers yield from the reductive depolymerization of lignin while the enhanced lignin monomers yield from the oxidative depolymerization of lignin could be used to estimate the content of breakable C-C interunit linkages (i.e., β-β′ and β-5′) in lignin. Therefore, the improved Ox^{CuO} could be a more applicable method for fast and accurate analysis of lignin non-condensed units and condensed units, estimation of the monomer

yields for lignin depolymerization, and comparison of the condensation degree of lignin polymers.

Data availability statement

The original contributions presented in the study are included in the article/supplementary material, further inquiries can be directed to the corresponding authors.

Author contributions

All authors listed have made a substantial, direct, and intellectual contribution to the work and approved it for publication. XL and LS conceived the idea and edited the manuscript. GY conducted all of the oxidation experiments. ZG conducted the product analysis. Both GY and ZG wrote the manuscript.

Funding

This work was supported by Outstanding Youth Funding (xjq201923) of Fujian Agriculture and Forestry University, National Natural Science Foundation of China (Nos. 32071716, 31870559, and 31901262), Outstanding Youth Funding of National Forestry and Grassland Administration (20201326005).

Acknowledgments

The authors gratefully acknowledge the State Key Laboratory of Biobased Materials and Green Papermaking at Qilu University of Technology as well as Fujian Qingshan Paper Co., Ltd. For providing the lignocellulosic materials.

Conflict of interest

The authors declare that the research was conducted in the absence of any commercial or financial relationships that could be construed as a potential conflict of interest.

Publisher's note

All claims expressed in this article are solely those of the authors and do not necessarily represent those of their affiliated organizations, or those of the publisher, the editors and the reviewers. Any product that may be evaluated in this article, or claim that may be made by its manufacturer, is not guaranteed or endorsed by the publisher.

References

Billa, E., Tollier, M. T., and Monties, B. (1996). Characterisation of the monomeric composition of in situWheat straw lignins by alkaline nitrobenzene oxidation: Effect of temperature and reaction time. *J. Sci. Food Agric.* 72, 250–256.

Bosch, S. V. d., Schutyser, W., Vanholme, R., Driessen, T., Koelewijn, S., Renders, T., et al. (2015). Reductive lignocellulose fractionation into soluble lignin-derived phenolic mono- and dimers and processable carbohydrate pulp. *Energy Environ. Sci.* 8, 1748–1763. doi:10.1002/cssc.201403375

Chan, F. D., Nguyen, K. L., and Wallis, A. F. A. (1995). Contribution of lignin sub-structures to nitrobenzene oxidation products. *J. Wood Chem. Technol.* 15, 329–347. doi:10.1080/02773819508009514

Chen, C.-L. (1992). Nitrobenzene and cupric oxide oxidations. *Methods Lignin Chem.*, 108 301–321. doi:10.1007/978-3-642-74065-7_21

Deussa, P. J., and Barta, K. (2016). From models to lignin: Transition metal catalysis for selective bond cleavage reactions. *Coord. Chem. Rev.* 306, 510–532. doi:10.1016/j.ccr.2015.02.004

Goi, M. A., Nelson, B., Blanchette, R. A., and Hedges, J. I. (1993). Fungal degradation of wood lignins: Geochemical perspectives from CuO-derived phenolic dimers and monomers. *Geochimica Cosmochimica Acta* 57, 3985–4002. doi:10.1016/0016-7037(93)90348-Z

Hedges, J. I., and Ertel, J. R. (1982). Characterization of lignin by gas capillary chromatography of cupric oxide oxidation products. *Anal. Chem.* 54, 174–178. doi:10.1021/ac00239a007

Hirayam, H., Akiyam, T., Kimur, S., Nawaw, D. S., Syafi, W., Yokoyam, T., et al. (2019). Influence of the p-hydroxyphenyl/guaiacyl ratio on the biphenyl and β-5 contents in compression wood lignins. *Holzforschung* 73, 923–935. doi:10.1515/hf-2019-0012

Lapierre, C. (2010). Determining lignin structure by chemical degradations. *Adv. Chem.* 2010, 11–48. doi:10.1201/ebk1574444865-c2

Liao, Y., Koelewijn, S. F., Bossche, G. V. d., Sels, B. F., Van den Bosch, S., Renders, T., et al. (2020). A sustainable wood biorefinery for low–carbon footprint chemicals production. *Science* 367, 1385–1390. doi:10.1126/science.aau1567

Lu, F., and Ralph, J. (1997). Derivatization followed by reductive cleavage (DFRC method), a new method for lignin analysis: Protocol for analysis of DFRC monomers. *J. Agric. Food Chem.* 45, 2590–2592. doi:10.1021/jf970258h

Maeda, H. A. (2016). Lignin biosynthesis: Tyrosine shortcut in grasses. *Nat. Plants* 2, 16080. doi:10.1038/nplants.2016.80

Mathias, A. L., and Rodrigues, A. B. (1995). Production of vanillin by oxidation of pine Kraft lignins with oxygen. *Holzforschung* 49, 273–278. doi:10.1515/hfsg.1995.49.3.273

Nimz, H. (1974). Beech lignin—proposal of a constitutional scheme. *Angew. Chem. Int. Ed. Engl.* 13, 313–321. doi:10.1002/anie.197403131

Partenheimer, W. (2009). The aerobic oxidative cleavage of lignin to produce hydroxyaromatic benzaldehydes and carboxylic acids via metal/bromide catalysts in acetic acid/water mixtures. *Adv. Synth. Catal.* 351, 456–466. doi:10.1002/adsc.200800614

Schutyser, W., Kruger, J. S., Robinson, A. M., Katahira, R., Brandner, D. G., Cleveland, N. S., et al. (2018). Revisiting alkaline aerobic lignin oxidation. *Green Chem.* 20, 3828–3844. doi:10.1039/c8gc00502h

Schutyser, W., Renders, T., Bosch, S. V. d., Koelewijn, S. F., Beckham, G. T., and Sels, B. F. (2018). Chemicals from lignin: An interplay of lignocellulose fractionation, depolymerisation, and upgrading. *Chem. Soc. Rev.* 47, 852–908. doi:10.1039/c7cs00566k

Shuai, L., Amiri, M. T., Santiago, Y. M. Q., Héroguel, F., Li, Y., Kim, H., et al. (2016). Formaldehyde stabilization facilitates lignin monomer production during biomass depolymerization. *Science* 354, 329–333. doi:10.1126/science.aaf7810

Shuai, L., and Saha, B. (2017). Towards high-yield lignin monomer production. *Green Chem.* 19, 3752–3758. doi:10.1039/C7GC01676J

Tamai, A., Goto, H., Akiyama, T., and Matsumoto, Y. (2015). Revisiting alkaline nitrobenzene oxidation: Quantitative evaluation of biphenyl structures in cedar wood lignin (cryptomeria japonica) by a modified nitrobenzene oxidation method. *Holzforschung* 69, 951–958. doi:10.1515/hf-2014-0153

Tolbert, A. K., Ma, T., Kalluri, U. C., and Ragauskas, A. J. (2016). Determining the syringyl/guaiacyl lignin ratio in the vessel and fiber cell walls of transgenic populus plants. *Energy fuels.* 30, 5716–5720. doi:10.1021/acs.energyfuels.6b00560

Vanholme, R., Demedts, B., Morreel, K., Ralph, J., and Boerjan, W. (2010). Lignin biosynthesis and structure. *Plant Physiol.* 153, 895–905. doi:10.1104/pp.110.155119

Villar, J. C., Caperos, A., and Ochoa, F. G. (1997). Oxidation of hardwood Kraft lignin to phenolic derivatives. Nitrobenzene and copper oxide as oxidants. *J. Wood Chem. Tech.* 17, 259–285. doi:10.1080/02773819708003131

Voitl, T., and Rohr, P. R. v. (2008). Oxidation of lignin using aqueous polyoxometalates in the presence of alcohols. *ChemSusChem* 1, 763–769. doi:10.1002/cssc.200800050

Werhan, H., Mir, J. M., Voitl, T., and Rohr, P. R. v. (2011). Acidic oxidation of kraft lignin into aromatic monomers catalyzed by transition metal salts. *Holzforschung* 65, 071. doi:10.1515/hf.2011.071

Wu, G., and Heitz, M. (1995). Catalytic mechanism of Cu^{2+} and Fe^{3+} in alkaline O_2 oxidation of lignin. *J. Wood Chem. Technol.* 15, 189–202. doi:10.1080/02773819508009507

Zhang, C., and Wang, F. (2020). Catalytic lignin depolymerization to aromatic chemicals. *Acc. Chem. Res.* 53, 470–484. doi:10.1021/acs.accounts.9b00573

frontiers | Frontiers in Bioengineering and Biotechnology

TYPE Original Research
PUBLISHED 16 September 2022
DOI 10.3389/fbioe.2022.1006925

OPEN ACCESS

EDITED BY
Lei Wang,
Ocean University of China, China

REVIEWED BY
Jia-Long Wen,
Beijing Forestry University, China
Ali Nawaz,
Government College University,
Pakistan

*CORRESPONDENCE
Qiang Yong,
swhx@njfu.com.cn

SPECIALTY SECTION
This article was submitted to Bioprocess Engineering,
a section of the journal
Frontiers in Bioengineering and Biotechnology

RECEIVED 29 July 2022
ACCEPTED 22 August 2022
PUBLISHED 16 September 2022

CITATION
Wang Q, Su Y, Gu Y, Lai C, Ling Z and Yong Q (2022), Valorization of bamboo shoot shell waste for the coproduction of fermentable sugars and xylooligosaccharides.
Front. Bioeng. Biotechnol. 10:1006925.
doi: 10.3389/fbioe.2022.1006925

Valorization of bamboo shoot shell waste for the coproduction of fermentable sugars and xylooligosaccharides

Qiyao Wang[1], Yan Su[1], Yang Gu[1], Chenhuan Lai[1], Zhe Ling[1] and Qiang Yong[1,2]*

[1]Jiangsu Co-Innovation Center of Efficient Processing and Utilization of Forest Resources, College of Chemical Engineering, Nanjing Forestry University, Nanjing, China, [2]Key Laboratory of Forestry Genetics and Biotechnology (Nanjing Forestry University), Ministry of Education, Nanjing, China

In this work, hydrothermal pretreatment (autohydrolysis) was coupled with endo-xylanase enzymatic hydrolysis for bamboo shoot shell (BSS) to produce glucose and valuable xylooligosaccharides (XOS) rich in xylobiose (X2) and xylotriose (X3). Results showed that the enzymatic hydrolysis efficiency of pretreated BSS residue reached 88.4% with addition of PEG during the hydrolysis process. To enrich the portions of X2–X3 in XOS, endo-xylanase was used to hydrolyze the XOS in the prehydrolysate, which was obtained at the optimum condition (170°C, 50 min). After enzymatic hydrolysis, the yield of XOS reached 25.6%, which contained 76.7% of X2–X3. Moreover, the prehydrolysate contained a low concentration of fermentation inhibitors (formic acid 0.7 g/L, acetic acid 2.6 g/L, furfural 0.7 g/L). Based on mass balance, 32.1 g of glucose and 6.6 g of XOS (containing 5.1 g of X2-X3) could be produced from 100.0 g of BSS by the coupled technology. These results indicate that BSS could be an economical feedstock for the production of glucose and XOS.

KEYWORDS

bamboo shoot shell, enzymatic hydrolysis, hydrothermal pretreatment, glucose, xylooligosaccharides

Introduction

The world needs to focus on sustainable energy development due to the nonrenewable nature of traditional fossil energy. It is urgent to find renewable energy to meet the current energy demand. At the same time, the utilization and development of renewable resources need to become the center of energy policies in many countries. Lignocellulosic resources have the potential to serve as sources of sustainable energy and bio-based materials that can be utilized by biorefineries to alleviate the pressure created by the current energy demand (Huang et al., 2022a; Pei et al., 2022). The main concerns in the biorefinery process are to extract the maximum value from the materials and reduce production costs (Rezania et al., 2020; Huang et al., 2022b). Previous research on biorefineries has mainly focused on agricultural waste (Ma et al., 2021a), while less research has reported the use of food processing waste. For example, bamboo shoot shell (BSS) consists of leaves of

bamboo shoots, and the annual output in China exceeds 30 million tons (Ye et al., 2014). In the past, BSS was incinerated and sent to landfill sites rather than being used effectively, resulting in a considerable waste of resources. BSS has a great cost advantage over other lignocellulosic resources used as energy sources (Ma et al., 2022; Yu et al., 2022). As a type of food processing waste, BSS is inexpensive to acquire. Furthermore, direct purchases from factories reduce the high cost of recycling. In addition, the abundant cellulose and hemicellulose in BBS can greatly enhance the commercial value of the biological refinement of BSS. The partial development and application of hemicellulose will create additional value that helps compensate for the economically inefficient production of ethanol from cellulose (Tang et al., 2019). It should be noted that production costs need to be considered when selecting the pretreatment method for BSS, and the economic value of cellulose and hemicellulose after pretreatment should be maintained as much as possible (Ma et al., 2021b).

The idea of coproducing glucose and XOS builds on previous investigations into high-value fractions developed from lignocellulose (Zhang et al., 2022). The idea is that the extra value of XOS obtained from the coproduction process can increase economic efficiency and reduce the cost during ethanol production (Tang et al., 2019). There are increasing numbers of investigations into the coproduction of XOS and glucose, where the efficiency depends on the selection of pretreatment methods (Ma et al., 2021c). Autohydrolysis stands out among many methods as it is inexpensive, simple, and environmentally friendly. Fang et al. (2022) obtained XOS and glucose from birch via autohydrolysis (170°C, 70 min). The efficiency of enzymatic hydrolysis (enzyme dosage 25 FPU/g) reached 89.4% after adding the surfactant Tween 80, and the yield of XOS with a degree of polymerization (DP) 2-6 also reached 46.1%. Zhang X. et al. (2020) obtained glucose and XOS (DP 2-5) from bagasse *via* autohydrolysis with seawater at 175°C for 30 min. After pretreatment, an enzymatic hydrolysis efficiency of 94.7% could be obtained for the pretreated bagasse, with an enzyme dosage of 30 FPU/g and Tween 80. In addition, the XOS (DP 2-5) yield reached 67.1%. The results showed that autohydrolysis could effectively coproduce glucose and XOS. Inhibitors of fermentation are usually generated during autohydrolysis. Furfural and 5-HMF inhibit the growth of fermenting strains (Zaldivar et al., 2015). Dupont and Suarez (2006) reported that when the concentrations of furfural and hydroxymethyl furfural in the pretreatment liquid exceeded 1 g/L, microbial fermentation could be inhibited. Therefore, the application value of the coproduction of glucose and XOS should be reappraised after taking into consideration the existence of fermentation inhibitors (Dai et al., 2021, 2022).

Autohydrolysis is a suitable method to coproduce glucose and XOS. It is a reaction that occurs in the temperature range of 160°C–240°C with an aqueous medium and does not require additional chemical reagents (Zhuang et al., 2016). Under high-temperature and high-pressure conditions, acetyl groups and some glucuronic acid groups are removed from the hemicellulose units in lignocellulose and then combine with water molecules to form acetic acid and glucuronic acid, respectively. The resultant hydrogen ions from the water molecules can form a weakly acidic reaction environment. After autohydrolysis, a small amount of cellulose and most of the xylan in lignocellulose are degraded to form glucooligosaccharides, XOS, glucose, and xylose. In addition, the degraded components can improve the accessibility of cellulose to cellulase. As the autohydrolysis reaction system is a weakly acidic environment, the number of produced fermentation inhibitors is relatively small (Kim et al., 2009; Kumar et al., 2009). Under high-intensity autohydrolysis conditions, the processing of xylan by acetic acid results in shedding of xylan in fragments of different lengths, including XOS and xylose (Zhang et al., 2018; Yu et al., 2022). XOS is sensitive to the intensity of the reaction conditions, and high-intensity conditions result in a decrease of DP for XOS. Therefore, the optimization of time and temperature should be considered for production of XOS during autohydrolysis.

XOS can be considered single-chain sugars containing 2–20 xyloses, which are linked by the β-1, 4-glycosidic bonds that are formed from loss of water. XOS is a proven prebiotic that can be easily absorbed by intestinal flora. The improvement of intestinal flora activity will have positive effects on human health, for which *Bifidobacterium* makes a great contribution compared to other intestinal flora (Ghosh et al., 2021). As reported, *Bifidobacterium* is one of the important genera among the microbes in the human gut (Ai et al., 2018; Kim et al., 2020). In addition, X2–X3 are preferentially absorbed by *Bifidobacterium*. Hence, the hydrolysis of the prehydrolysate with endo-xylanase to prepare XOS including more X2–X3 has been proven to be a successful method of enhancing the physiological activity of XOS. Su et al. (2021) used endo-xylanase to improve the component ratio of X2–X3 to XOS, and a greater proportion of X2–X3 was observed in the resultant XOS. After enzymatic hydrolysis by endo-xylanase, the yield of XOS in the prehydrolysate decreased from 30.9 to 25.6%, but the X2–X3 proportion increased from 19.7 to 76.7%. Considering the positive effects of X2 and X3 in XOS on human health, the X2–X3 proportion can be used as one of the evaluation indices for XOS. High-value XOS, which contains more X2 and X3, makes the coproduction of glucose and XOS a competitive option.

In this study, a combination of autohydrolysis and enzymatic hydrolysis was used to prepare glucose and XOS (rich in X2–X3) from BSS. Specifically, the effects of autohydrolysis on enzymatic hydrolysis and the XOS yield of BSS were systematically studied. The cellulase accessibility and the removal rate of xylan were correlated with the enzymatic digestibility of BSS. In addition, the effect of surfactants on enzymatic performance in the hydrolysis of the BSS residue was further investigated. Endo-xylanase hydrolysis was used to increase the proportion of X2–X3 in XOS. It is hoped that this work will provide advanced insights into the coproducing of glucose and high-value XOS from BSS.

Materials and methods

Materials

The used BSS was purchased from the Bamboo Processing Factory, which is located in Guilin, Guangxi Province, China. The chemical composition of the BSS was analyzed according to the protocol of the National Renewable Energy Laboratory (Sluiter et al., 2011). The used enzyme of Cellic CTec2 cellulase was supplied by Novozymes NA, Franklinton, United States. The endo-β-1,4-xylanase was supplied by Jiangsu Kangwei Biotechnology Co., Ltd., Yancheng, Jiangsu, China.

Autohydrolysis of BSS

For autohydrolysis of BSS, 10.0 g of dry BSS (20–60 mesh) and 100 ml distilled water were mixed in the reactor (150 ml). The pretreatment was carried out at 150–190°C for 20–80 min in an oil bath. After pretreatment, the reactor was moved immediately from the oil bath and soaked in a cold-water bath for 4 h. Next, the prehydrolysate in the reaction mixture was separated by filtration. The obtained solid (pretreated BSS) was washed with distilled water until neutralized. Finally, the washed BSS solid and prehydrolysate were stored at 4°C for further analysis.

Enzymatic hydrolysis of pretreated BSS

The substrate (2%, w/v) was adjusted to pH 4.8 with a citric acid buffer (0.05 M) during enzymatic hydrolysis with a cellulase dosage of 20 FPU/glucan. The enzymatic hydrolysis was performed for 72 h at 150 rpm and 50°C. After enzymatic hydrolysis, the solid and liquid parts were separated using a centrifuge at 8,000 rpm for 5 min. The sugar content in the enzymatic hydrolysate was analyzed using high-performance liquid chromatography (HPLC).

To further improve the enzymatic digestibility of the pretreated BSS, the surfactants of Tween 80 and PEG were used to reduce the negative effect of lignin (Chen et al., 2016; Lai et al., 2018). Specifically, the surfactant (0.075 g/glucan) was incubated in the mixture at 50°C for 30 min before the addition of cellulase.

Analysis of the accessibility of pretreated BSS

The cellulose accessibility was determined according to work of Inglesby and Zeronia (2002). Specifically, a mixture containing the BSS residue (1%, w/v) and Congo red staining (0, 0.05, 0.1, 0.5, 1.0, 2.0, 3.0, and 4.0 g/L) was shaken at 60°C and 150 rpm for 24 h. Then, cellulase accessibility was calculated by the different absorbance values of the supernate of the mixture at 498 nm. The Langmuir function was used to calculate the accessibility.

Enzymatic hydrolysis of the prehydrolysate by endo-xylanase

The endo-xylanase activity was determined according to the method established by Bailey et al. (1992). The prehydrolysate obtained at optimum pretreatment conditions (170°C, 50 min) was hydrolyzed by endo-xylanase (3 IU/ml) at 50°C and 150 rpm for 48 h. Aliquots were withdrawn at 4, 8, 12, 24, 36, and 48 h to analyze the content of X2–X3. Once an aliquot was removed, the enzyme reaction was stopped by boiling for 5 min, and the aliquot was kept at 4°C.

Analysis methods

The HPLC (1260, USA) system containing an Aminex Bop-Rad HPX-87 column was used to analyze the concentration of monosaccharides and inhibitors. H_2SO_4 (5 mM) was used as the eluent (0.6 ml/min) during analysis. High-performance anion-exchange chromatography (HPAEC, Dionex 3000) containing a CarboPacPA-200 anion-exchange column was used to analyze the concentration of xylobiose (X2), xylotriose (X3), xylotetraose (X4), xylopentaose (X5), and xylohexaose (X6). NaOH (100 mM) and NaAc (500 mM) containing NaOH (100 mM) were used as eluents at 0.3 ml/min.

The content of XOS was determined according to the xylose difference between the hydrolyzed prehydrolysate [using 8% sulfuric acid (121°C, 60 min)] and the unhydrolyzed prehydrolysate. The enzymatic hydrolysis efficiency, XOS yield, and removal yield of xylan/lignin were calculated according to the following equations:

$$\text{Enzymatic hydrolysis efficiency} = \frac{\text{Glucose in enzymatic hydrolysate (g)}}{\text{Glucan in BSS residue (g)} \times 1.11} \times 100\%. \quad (1)$$

$$\text{XOS yield} = \frac{\text{Xylose (sulfuric acid hydrolyzed)} - \text{Xylose (unhydrolyzed)}}{\text{Xylan in raw BSS (g)}} \times 0.88 \times 100\%. \quad (2)$$

$$\text{Removal yield of xylan/lignin} = 1 - \frac{\text{Xylan/lignin in pretreated BSS (g)}}{\text{Xylan/lignin in raw BSS (g)}} \times 100\%. \quad (3)$$

$$\text{Recovery of solid/glucan} = \frac{\text{Solid/glucan in pretreated BSS (g)}}{\text{Solid/glucan in raw BSS (g)}} \times 100\%. \quad (4)$$

TABLE 1 Compositions of the BSS residue after autohydrolysis.

Temperature (°C)	Time (min)	Composition (%)			Removal yield (%)		Recovery yield (%)		Γmax/DR28
		Glucan	Xylan	Lignin	Solid	Glucan	Xylan	Lignin	(mg/g)
BSS	\	38.2 ± 1.0	25.7 ± 0.1	25.6 ± 0.2	\	\	\	\	264.2
150	60	42.1 ± 0.1	21.4 ± 0.2	26.3 ± 0.2	76.3 ± 0.1	87.3 ± 0.1	34.5 ± 0.0	18.4 ± 0.3	401.9
160		44.5 ± 0.2	19.7 ± 0.5	27.8 ± 0.0	74.6 ± 0.1	86.9 ± 0.1	43.2 ± 0.0	18.8 ± 0.2	439.7
170		49.3 ± 0.2	9.6 ± 0.5	30.3 ± 0.0	66.9 ± 0.0	86.1 ± 0.0	75.2 ± 0.1	20.7 ± 0.0	457.8
180		53.5 ± 0.7	5.59 ± 0.6	32.7 ± 0.4	60.8 ± 0.2	85.1 ± 0.0	87.1 ± 0.2	22.1 ± 0.3	405.2
190		55.2 ± 0.9	3.2 ± 0.5	33.2 ± 0.0	58.2 ± 0.0	84.0 ± 0.1	92.9 ± 0.1	23.2 ± 0.5	361.8
170	20	45.3 ± 0.5	17.9 ± 0.8	27.6 ± 1.2	73.8 ± 0.1	87.3 ± 0.4	48.9 ± 0.0	15.8 ± 0.2	425.4
	30	46.1 ± 0.0	16.6 ± 0.7	28.7 ± 0.8	72.4 ± 0.0	87.2 ± 0.2	53.7 ± 0.1	16.2 ± 0.2	403.4
	40	47.8 ± 0.3	14.2 ± 0.4	29.8 ± 0.3	69.5 ± 0.5	87.0 ± 0.0	61.9 ± 0.0	18.3 ± 0.0	450.3
	50	49.0 ± 0.7	12.0 ± 0.4	30.6 ± 0.1	67.2 ± 0.7	86.5 ± 0.1	68.8 ± 0.3	20.4 ± 0.4	509.9
	60	49.3 ± 0.2	9.6 ± 0.5	30.3 ± 0.0	66.9 ± 0.0	86.1 ± 0.2	75.2 ± 1.1	20.7 ± 0.1	457.8
	70	51.2 ± 0.2	6.9 ± 0.2	32.0 ± 0.1	63.8 ± 0.1	85.5 ± 0.1	83.0 ± 0.2	21.3 ± 0.2	442.7
	80	51.5 ± 0.3	6.8 ± 0.1	32.5 ± 0.2	63.3 ± 0.1	85.2 ± 0.1	83.4 ± 0.0	21.7 ± 0.1	441.0

Results and discussion

Composition analysis of the BSS residue

For the hydrothermal pretreatment at high temperature and pressure, a weakly acidic environment can be formed to degrade the xylan in BSS into XOS and xylose (Kim et al., 2009; Kumar et al., 2009). Hence, the compositions of the pretreated BSS were determined and shown in Table 1. It can be seen that the reaction temperature and time significantly affected the composition of the pretreated BSS. For example, the solid yield of recovery decreased from 76.3 to 58.2%, and the removal yield of xylan sharply increased from 34.5 to 92.9% with the temperature increased from 150 to 190°C. In contrast, the recovery yield of glucan slightly decreased from 87.3 to 84.0%, and the removal yield of lignin increased from 18.8 to 23.2% under the same pretreatment conditions. The dramatic decrease of xylan recovery indicates that autohydrolysis has a promising ability to remove xylan. However, autohydrolysis showed a limited contribution in removing lignin. Under the high-energy environment, the electrons of water molecules will be able to escape from the system of water molecules, which will cause the water molecules to be ionized, and this trend of ionization will become stronger with the increase of the pretreatment intensity (Yue et al., 2021). Xylan is selectively ionized by ionization of water during autohydrolysis (Lu et al., 2016). With an increase in temperature, the degree of ionization of water can be increased, which is beneficial for removal of xylan. Meanwhile, the high recovery yield of glucan indicates that autohydrolysis has the potential to produce cellulose from BSS for further bioconversion (Lian et al., 2022).

To further optimize pretreatment conditions for BSS, the pretreatment time was increased from 20 min to 80 min. The changes in the compositions of BSS are shown in Table 1. It can be seen that the recovery yield of the solid residue decreased from 73.8 to 63.3%, and the xylan removal yield increased from 48.9 to 83.4%. It seems, therefore, that glucan degradation is not sensitive to a prolonged reaction time. The recovery yield of glucan decreased only slightly from 87.3 to 85.2%, and the removal of lignin increased from 15.8 to 21.7% when the pretreatment time was increased from 20 to 80 min. These results indicate that the pretreatment duration should also be considered one of the factors affecting the removal of xylan and lignin. Hence, prolonging the pretreatment time also improves the removal of xylan and lignin from BSS during autohydrolysis.

Based on the aforementioned results, it can be seen that autohydrolysis at 170°C for 50 min showed best performance for removing xylan and lignin from BSS. The removal yield of xylan reached 68.8%, which may be of great significance for improving the enzymatic hydrolysis of cellulose into glucose (Huang et al., 2018). The removal of lignin reached 20.4%, which can also be considered a positive factor for improving enzymatic efficiency (Ma et al., 2020; Paz-Cedeno et al., 2021). However, the non-production adsorption interaction between residual lignin and cellulase will reduce the efficiency of enzymatic hydrolysis (Yu et al., 2022). Hence, an approach to intervene in the interaction should be carried out to improve the enzymatic efficiency (Li et al., 2022).

TABLE 2 Sugars and byproducts in prehydrolysates of BSS after autohydrolysis.

Temperature (°C)	Time (min)	Fermentation inhibitor (g/L)				Sugar in prehydrolysate (g/100 g)			
		Formic acid	Acetic acid	5-HMF	Furfural	Glucose	Gluco-oligosaccharide	Xylose	XOS
150	60	0.5 ± 0.0	1.6 ± 0.1	0.0 ± 0.0	0.0 ± 0.0	0.4 ± 0.0	0.8 ± 0.0	0.2 ± 0.0	4.1 ± 0.0
160		0.5 ± 0.1	2.0 ± 0.0	0.0 ± 0.0	0.0 ± 0.0	0.4 ± 0.0	0.9 ± 0.0	0.3 ± 0.0	6.5 ± 0.1
170		0.7 ± 0.0	2.9 ± 0.0	0.0 ± 0.0	1.0 ± 0.1	0.5 ± 0.1	0.9 ± 0.1	1.4 ± 0.3	8.2 ± 0.3
180		0.9 ± 0.0	4.5 ± 0.0	0.0 ± 0.0	3.6 ± 0.2	0.6 ± 0.0	1.1 ± 0.0	3.1 ± 0.4	6.3 ± 0.0
190		0.9 ± 0.0	5.3 ± 0.0	0.2 ± 0.0	5.3 ± 0.1	1.4 ± 0.3	0.6 ± 0.0	3.2 ± 0.2	4.9 ± 0.2
170	20	0.4 ± 0.0	1.5 ± 0.2	0.0 ± 0.0	0.0 ± 0.0	0.4 ± 0.0	0.6 ± 0.1	0.4 ± 0.1	4.6 ± 0.4
	30	0.5 ± 0.0	2.0 ± 0.0	0.0 ± 0.0	0.0 ± 0.0	0.4 ± 0.0	0.7 ± 0.0	0.5 ± 0.0	6.0 ± 0.2
	40	0.6 ± 0.0	2.5 ± 0.0	0.0 ± 0.0	0.3 ± 0.0	0.5 ± 0.0	0.8 ± 0.0	0.7 ± 0.0	7.9 ± 0.0
	50	0.7 ± 0.0	2.6 ± 0.1	0.0 ± 0.0	0.7 ± 0.1	0.5 ± 0.1	0.9 ± 0.0	1.1 ± 0.2	8.0 ± 0.1
	60	0.7 ± 0.0	2.9 ± 0.0	0.0 ± 0.0	1.0 ± 0.0	0.5 ± 0.1	0.9 ± 0.1	1.4 ± 0.0	8.2 ± 0.1
	70	0.9 ± 0.0	3.2 ± 0.0	0.0 ± 0.0	1.2 ± 0.0	0.6 ± 0.0	0.9 ± 0.1	1.8 ± 0.1	8.4 ± 0.1
	80	0.9 ± 0.1	3.5 ± 0.0	0.0 ± 0.0	1.5 ± 0.3	0.6 ± 0.1	1.0 ± 0.0	2.1 ± 0.2	8.8 ± 0.2

Composition analysis of the BSS prehydrolysate

Autohydrolysis results in degradation of the xylan from the lignocellulose into prehydrolysate, including subfractions of glucan and lignin. During the autohydrolysis process, xylan can be broken down into XOS and xylose. In addition, fermentation inhibitors formed from the monomer sugar subsequently undergo a series of reactions (Sipos et al., 2009). Hence, the analysis of the components in the prehydrolysate was performed to understand the amount of dissolved degradation products from BSS during the autohydrolysis process.

Based on the aforementioned results in the "Composition analysis of BSS residue" section, it can be seen that the pretreatment temperature and time affected the removal yield of xylan. The ionization of water results in the degradation of xylan into the liquid phase as XOS. Table 2 shows that the quantity of XOS increased from 4.1 g/100 to 8.2 g/100 g (150–170°C, 60 min), but it decreased from 8.2 g/100 to 4.9 g/100 g when the temperature continued to increase (170–190°C, 60 min). Thhis phenomenon can be explained by the fact that β-1, 4 glycosidic bonds in XOS were broken by the increased acidic environment owing to the increased pretreatment temperature. Wang et al. (2019) also found that the content of XOS began to decline at temperatures over 170°C during autohydrolysis for eucalyptus. To obtain a higher yield of XOS, it was necessary to optimize the reaction time. In Table 2, it can also be seen that the content of XOS increased with the increase in the pretreatment time from 20 to 80 min at 170°C. Fang et al. (2022) also found that prolonging the reaction time of autohydrolysis promoted the production of XOS from birch.

Fermentation inhibitors are also common byproducts during autohydrolysis. As shown in Table 2, both an increase in temperature and prolongation of reaction time resulted in an improvement of the content of formic acid and acetic acid, while it was notable that 5-HMF only appeared at 190°C. The concentration of XOS in the prehydrolysate should be considered when the aim is the coproduction of XOS and glucose. Based on the entire process, it can be seen that autohydrolysis at 170°C for 40 min was the optimum condition to produce XOS with lower furfural and 5-HMF from BSS.

Enzymatic hydrolysis of the BSS residue

Enzymatic hydrolysis efficiency is an extremely important evaluation criterion for the utilization of cellulose in wood (Li et al., 2018). Figures 1A,B display the enzymatic hydrolysis yields of pretreated BSS with cellulase (20 FPU/g glucan) for 72 h. It can be seen that the hydrolysis efficiency of the pretreated BSS was significantly greater than that of raw BSS. The change in the efficiency may be explained by the fact that the hemicellulose was removed to form more pores, which resulted in more active sites for enzyme binding from residual cellulose (Yu et al., 2022). Zhang et al. (2013) also that found increasing the accessibility of cellulose during pretreatment was due to xylan removal. Hence, it can be speculated that autohydrolysis can substantially improve the enzymatic digestibility of BSS.

Figure 1C shows the enzymatic hydrolysis efficiency at 72 h. The optimized hydrolysis results of pretreated BSS can be clearly seen with a small error for parallel samples, indicating the accuracy of enzymatic hydrolysis efficiency. In Figure 1C (Y2),

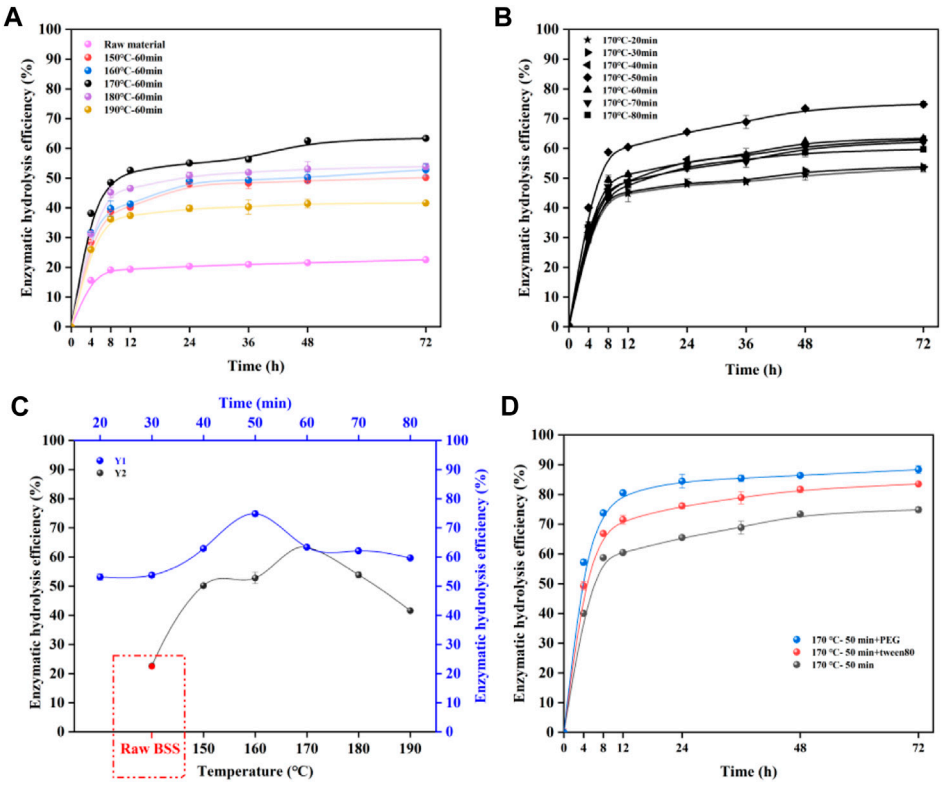

FIGURE 1
Effects of pretreatment temperature **(A)**; duration **(B)**; and surfactant **(D)** on enzymatic hydrolysis; enzymatic hydrolysis efficiency of 72 h **(C)**, (Y1) pretreatment time, (Y2) pretreatment temperature.

the efficiency of enzymatic hydrolysis increased from 50.2 to 63.4% when the pretreatment increased from 150°C to 170°C at 60 min. In addition, the enzymatic hydrolysis efficiency of pretreated BSS (170°C, 60 min) was 63.4%, which was clearly higher than that of raw BSS (22.5%). The increased enzymatic hydrolysis efficiency can be attributed to the increased removal of hemicellulose, while the efficiency decreased rapidly from 63.4 to 41.6% when pretreatment increased from 170°C to 190°C at 60 min. This could be because the increasingly ineffective adsorption of the enzyme by the lignin prevented the enzyme from fully binding to the substrate, thereby decreasing the enzymatic hydrolysis efficiency. Tang et al. (2021) found that the removal of hemicellulose increased the ineffective adsorption capacity of lignin for enzymes. A natural surfactant (humic acid, HA) was successfully used to prevent the ineffective adsorption of enzymes, and this improved the enzymatic hydrolysis efficiency. The trend in enzymatic hydrolysis efficiency reflects the fact that the performance of the enzymatic hydrolysis of pretreated BSS has a strong relationship with temperature. It can be clearly seen that the use of a temperature of 170°C conferred a significant advantage by improving the performance of the enzymatic hydrolysis of BSS after autohydrolysis. As shown in Figure 1C (Y1), the optimum reaction time can be found at 170°C. It was found that the substrate (170°C, 50 min) achieved the best enzymatic hydrolysis efficiency (74.8%). Figure 1C showed that the hydrolysis efficiency of the BSS residue (170°C, 50 min) was significantly higher than that of raw BSS, which was 74.8%.

To make a further improvement to the enzymatic hydrolysis efficiency, nonionic surfactants (PEG, Tween 80) were added to the reaction mixture to reduce the ineffective adsorption of lignin on cellulase (Figure 1D). The results revealed that the enzymatic hydrolysis efficiency increased significantly after the addition of PEG/Tween 80 to the enzymatic system of pretreated BSS (170°C, 50 min), which could achieve a yield of 86.6% (Tween 80) and 88.4% (PEG). It has been reported that the addition of surfactants could reduce the adsorption ability of lignin for enzymes, resulting in freer cellulase in the system for hydrolysis of the cellulose substrate (Huang et al., 2022c). Overall, the enzymatic hydrolysis efficiency of BSS improved substantially after autohydrolysis, and the optimization of temperature and duration further improved it. The addition of surfactants can also improve its enzymatic digestibility efficiency.

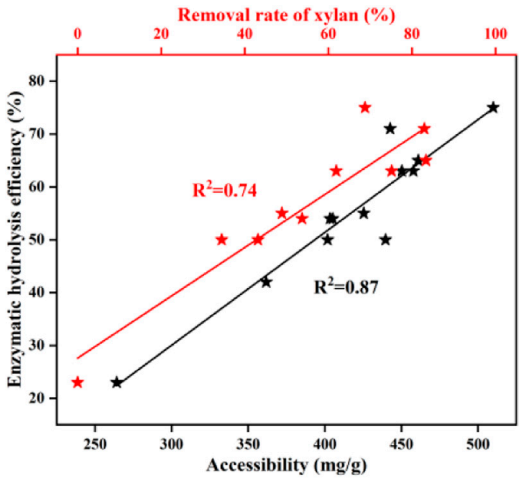

FIGURE 2
Relationships between the structural properties and the efficiency of the enzymatic hydrolysis of pretreated residues.

The relationships between the removal of xylan, cellulose accessibility, and the efficiency of the enzymatic hydrolysis of pretreated BSS

The results of enzymatic hydrolysis had a close connection to the degree of xylan removal (Kruyeniski et al., 2019). As shown in Figure 2, the enzymatic efficiency of pretreated BSS increased with increasing xylan removal. There was a correlation between the performance of the enzymatic hydrolysis and the removal of xylan (R^2 = 0.74). Huang et al. (2018) also found a similar relationship between the amount of xylan removed and the performance of the enzymatic hydrolysis of pretreated bamboo residues. This was due to the fact that the surface area of the residual solid cellulose increased, caused by the removal of xylan, which provided more active sites for cellulase. In addition, both Hu et al. (2012) and Zhang et al. (2013) found that the removal of xylan will contribute to increasing the accessibility of cellulose to cellulases. Autohydrolysis displays beneficial effects on the removal of xylan and thereby improves the performance of enzymatic hydrolysis.

The accessibility of cellulose reflects the degree of cellulase and substrate adsorption (Lai et al., 2018). The cellulase accessibility was determined by Congo red and is shown in Table 1. It was found that untreated BSS yielded 264.2 mg/g of an accessible substrate. As expected, the accessibility was greatly enhanced after autohydrolysis, reaching a maximum of 509.9 mg/g (170°C, 50 min). The accessibility of cellulose increased from 401.9 mg/g to 457.8 mg/g (150–170°C, 60 min) and then declined from 457.8 mg/g to 361.8 mg/g (170–190°C, 60 min). After the optimal pretreatment time (170°C, 20–80 min), the accessibility also initially showed an increase and then it decreased, with the best result of 509.9 mg/g (170°C, 50 min). The pattern of change in accessibility is very similar to that of the change in the efficiency of enzymatic hydrolysis. The relationship (R^2 = 0.87) between accessibility and enzymatic hydrolysis efficiency is linear, which is consistent with the work of Huang et al. (2019). Autohydrolysis breaks the lignocellulosic structural bonds, leading to hemicellulose being removed and lignin redistribution, improving cellulose accessibility resulting from increasing the surface area. As a result, the performance of enzymatic hydrolysis is increased (Kellock et al., 2019; Zhang Q. et al., 2020; Li et al., 2020). Generally, the increased accessibility of cellulase has a positive effect on the efficiency of the enzymatic hydrolysis of BSS with autohydrolysis.

Enzymatic hydrolysis of the prehydrolysate for X2–X3 production

Compared to XOS with a high average DP, it has been suggested that X2–X3 are better at making use of *Bifidobacterium* (Chen et al., 2016). XOS with a higher quantity of X2–X3 will increase the proliferative activity of *Bifidobacterium*. Ai et al. (2018) found that the XOS group with a high X2–X3 proportion was more selective for beneficial bacteria than the higher XOS group (DP > 3). To improve the activity of XOS, it is recommended to increase the X2–X3 proportion of XOS. In this work, the endo-xylanase was used to hydrolyze the prehydrolysate of BSS to increase the proportion of X2–X3 (Su et al., 2021).

The results of endo-xylanase hydrolysis are displayed in Figure 3. Figures 3A–C display the quantity of X2–X6 in the prehydrolysate after enzymatic hydrolysis with the endo-xylanase dosage of 5–15% (v/v). It can be seen that X2–X3 content could be clearly increased after enzymatic hydrolysis for an extended time. In Figure 3A, the amounts of X4–X6 were decreased during the enzymatic hydrolysis time, with a degradation rate of X6 > X5 > X4. It has been confirmed that XOS with high DP has more enzyme binding sites for enzymatic hydrolysis in a higher priority at a similar initial content (Su et al., 2021). Meanwhile, the content of X2–X3 showed a slight increasing trend during 0–12 h. This can be attributed to the degradation of X4–X6 into X2–X3 by endo-xylanase. Based on the results, it can be seen that the accumulation of X2–X3 was originated from the degradation of XOS (DP > 3) and that a higher dosage of the enzyme will enhance the efficiency of degradation (Figure 3C). Therefore, the yield of XOS should be taken into consideration when the maximum ratio of X2–X3 is selected. The change of the X2–X3 ratio to XOS and the XOS yield under different

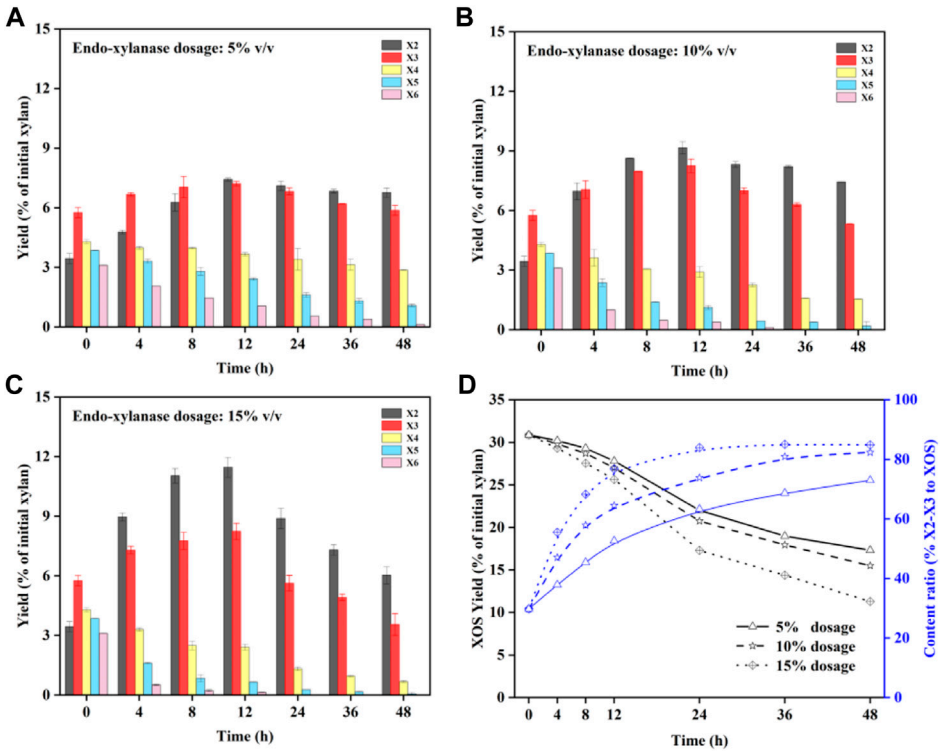

FIGURE 3
Distribution of X2–X6 during enzymatic hydrolysis with different enzyme dosages: 5% **(A)**; 10% **(B)**; 15% **(C)**; concentration of X2–X3 and X2–X3 proportion of XOS **(D)**.

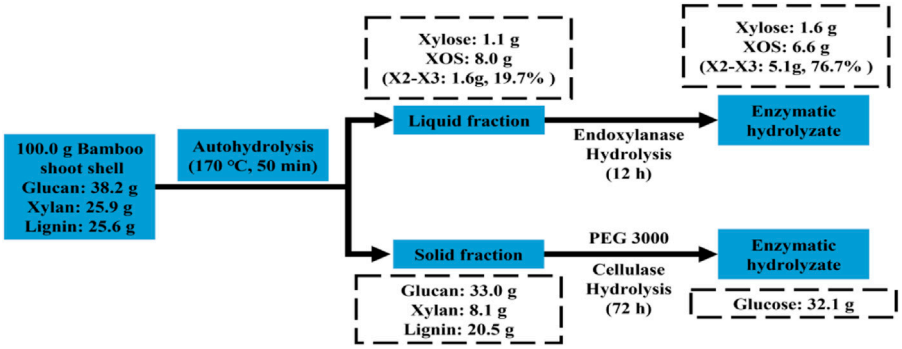

FIGURE 4
Mass balance of BSS during the established process.

enzyme dosages is shown in Figure 3D. It can be seen that XOS with a 15% enzyme dosage decreased faster than enzyme dosages of 5 and 10%, in which high DP will be hydrolyzed preferentially. Although the X2–X3 ratio of XOS is much higher with prolonged time, the total yield of XOS decreases. Hence, it can be speculated that the conditions of 15% enzyme dosage and 12 h reaction time are beneficial for producing the high-value XOS. Compared to the yield of XOS with 30.9% for the prehydrolysate, a yield of XOS with 25.6% was obtained after it was hydrolyzed by the enzyme, while the

X2–X3 proportion in XOS increased to 76.7%, achieving an improvement of 46.9% compared to that in initial XOS. In addition, the XOS satisfies the commercial product standard of 70% purity for autohydrolysis coupled with endo-xylanase hydrolysis (Vázquez et al., 2000).

Mass balance

This work demonstrates an efficient and profitable means of coproducing glucose and valuable XOS using a combination of autohydrolysis and enzymatic hydrolysis. As shown in Figure 4, 67.2 g of the residue could be recovered after the autohydrolysis of 100.0 g of BSS, which contained 33.0 g of glucan, 8.1 g of xylan, and 20.5 g of lignin. A total of 32.1 g of glucose was obtained from 67.2 g of pretreated BSS by cellulase hydrolysis. In addition, 1.1 g of xylose and 8.0 g of XOS dissolved in the prehydrolysate, which were degradation products of xylan. The prehydrolysate hydrolyzed by endo-xylanase could produce 1.6 g of xylose and 6.6 g of XOS, which contains a high proportion (76.7%) of X2–X3.

Analysis of competitive advantages in the coproduction of glucose and XOS from BSS

Autohydrolysis is pretreatment technology that is less corrosive to the equipment, which can improve the service life of the equipment and increase the safety of the production environment (Scapini et al., 2021; Huang et al., 2022d). Compared to other pretreatments, the obtained hydrolyzate possesses fewer fermentation inhibitors by using autohydrolysis. For example, 5 g/L furfural and 3.1 g/L furfural were found in the prehydrolysate from seawater pretreatment (Zhang X. et al., 2020) and synergistic hydrothermal-deep eutectic solvent (DES) pretreatment (Ma et al., 2021b), respectively. It has been reported that 1 g/L furfural can significantly affect the growth of microorganisms and that 5 g/L furfural seriously damages the growth of microorganisms (Zaldivar et al., 2015). In this study, only 0.7 g/L furfural was detected in the XOS. Therefore, the cost of separating the furfural from the XOS was reduced. In addition, the X2–X3 proportion in XOS was 76.7% after enzymatic hydrolysis with endo-xylanase. X2–X3 were the main valuable prebiotics in the XOS (Ai et al., 2018; Kim et al., 2020). Hence, applying this low-intensity method to coproduce glucose and high-value XOS provides a new possibility for the biorefinery of BSS.

Conclusion

A green and efficient method of coproducing glucose and value-added XOS from BSS has been proposed. The enzymatic efficiency reached 88.4% with the addition of PEG (170°C, 50 min). Under these conditions, the yield of XOS reached a maximum of 25.6%, and the X2–X3 proportion reached 76.7% after endo-xylanase hydrolyzed the prehydrolysate. In addition, the concentration of furfural in the prehydrolysate was only 0.7 g/L. Overall, autohydrolysis coupled with enzymatic hydrolysis can be used to coproduce high-value XOS and glucose from BSS as a suitable raw material for biorefinery.

Data availability statement

The raw data supporting the conclusion of this article will be made available by the authors, without undue reservation.

Ethics statement

Written informed consent was obtained from the individual(s) for the publication of any potentially identifiable images or data included in this article.

Author contributions

Investigation, QW, YS, and YG; supervision, QY; writing—original draft, QW; writing—review and editing, CL and ZL.

Funding

This study was funded by the National Key Research and Development Program of China (No. 2019YFB1503803) and the Priority Academic Program Development of Jiangsu Higher Education Institution (PAPD). The authors also thank the National First-class Disciplines (PNFD) for supporting the work.

Conflict of interest

The authors declare that the research was conducted in the absence of any commercial or financial relationships that could be construed as a potential conflict of interest.

Publisher's note

References

Bailey, M., Biely, P., and Poutanen, K. (1992). Interlaboratory testing of methods for assay of xylanase activity. *J. Biotechnol.* 23 (5), 257–270. doi:10.1016/0168-1656(92)90074-j

Chen, M., Bowman, M. J., Cotta, M. A., Dien, B. S., Iten, L. B., Whitehead, T. R., et al. (2016). Miscanthus×giganteus xylooligosaccharides: Purification and fermentation. *Carbohydr. Polym.* 140, 96–103. doi:10.1016/j.carbpol.2015.12.052

Dai, L., Gu, Y., Xu, J., Guo, J., Jiang, K., Zhou, X., et al. (2022). Toward green production of xylooligosaccharides and glucose from sorghum straw biowaste by sequential acidic and enzymatic hydrolysis. *Industrial Crops Prod.* 179, 114662. doi:10.1016/j.indcrop.2022.114662

Dai, L., Huang, T., Jiang, K., Zhou, X., and Xu, Y. (2021). A novel recyclable furoic acid-assisted pretreatment for sugarcane bagasse biorefinery in co-production of xylooligosaccharides and glucose. *Biotechnol. Biofuels* 14, 35. doi:10.1186/s13068-021-01884-3

Dupont, J., and Suarez, P. A. Z. (2006). Physico-chemical processes in imidazolium ionic liquids. *Phys. Chem. Chem. Phys.* 8 (21), 2441–2452. doi:10.1039/b602046a

Fang, L., Su, Y., Wang, P., Lai, C., Huang, C., Ling, Z., et al. (2022). Co-production of xylooligosaccharides and glucose from birch sawdust by hot water pretreatment and enzymatic hydrolysis. *Bioresour. Technol.* 348, 126795. doi:10.1016/j.biortech.2022.126795

Ghosh, A., Chandra, A., Dhar, A., Shukla, P., and Baishya, D. (2021). Multi-efficient thermostable endoxylanase from Bacillus velezensis AG20 and its production of xylooligosaccharides as efficient prebiotics with anticancer activity. *Process Biochem.* 109, 59–71. doi:10.1016/j.procbio.2021.06.011

Ho, L. H., Kosik, O., Lovegrove, A., Charalampopoulos, D., and Rastall, R. A. (2018). *In vitro* fermentability of xylo-oligosaccharide and xylo-polysaccharide fractions with different molecular weights by human faecal bacteria. *Carbohydr. Polym.* 179, 50–58. doi:10.1016/j.carbpol.2017.08.077

Hu, F., Jung, S., and Ragauskas, A. (2012). Pseudo-lignin formation and its impact on enzymatic hydrolysis. *Bioresour. Technol.* 117, 7–12. doi:10.1016/j.biortech.2012.04.037

Huang, C., Jiang, X., Shen, X., Hu, J., Tang, W., Wu, X., et al. (2022a). Lignin-enzyme interaction: A roadblock for efficient enzymatic hydrolysis of lignocellulosics. *Renew. Sustain. Energy Rev.* 154, 111822. doi:10.1016/j.rser.2021.111822

Huang, C., Lin, W., Lai, C., Li, X., Jin, Y., and Yong, Q. (2019). Coupling the post-extraction process to remove residual lignin and alter the recalcitrant structures for improving the enzymatic digestibility of acid-pretreated bamboo residues. *Bioresour. Technol.* 285, 121355. doi:10.1016/j.biortech.2019.121355

Huang, C., Lin, W., Zheng, Y., Zhao, X., Ragauskas, A., and Meng, X. (2022b). Evaluating the mechanism of milk protein as an efficient lignin blocker for boosting the enzymatic hydrolysis of lignocellulosic substrates. *Green Chem.* 24 (13), 5263–5279. doi:10.1039/d2gc01160c

Huang, C., Ma, J., Liang, C., Li, X., and Yong, Q. (2018). Influence of sulfur dioxide-ethanol-water pretreatment on the physicochemical properties and enzymatic digestibility of bamboo residues. *Bioresour. Technol.* 263, 17–24. doi:10.1016/j.biortech.2018.04.104

Huang, C., Yu, Y., Li, Z., Yan, B., Pei, W., and Wu, H. (2022d). The preparation technology and application of xylo-oligosaccharide as prebiotics in different fields: A review. *Front. Nutr.* 9, 996811.

Huang, C., Zhao, X., Zheng, Y., Lin, W., Lai, C., Yong, Q., et al. (2022c). Revealing the mechanism of surfactant-promoted enzymatic hydrolysis of dilute acid pretreated bamboo. *Bioresour. Technol.* 360, 127524. doi:10.1016/j.biortech.2022.127524

Inglesby, M. K., and Zeronian, S. H. (2002). Direct dyes as molecular sensors to characterize cellulose substrates. *Cellulose* 9 (1), 19–29. doi:10.1023/a:1015840111614

Kellock, M., Maaheimo, H., Marjamaa, K., Rahikainen, J., Zhang, H., Holopainen-Mantila, U., et al. (2019). Effect of hydrothermal pretreatment severity on lignin inhibition in enzymatic hydrolysis. *Bioresour. Technol.* 280, 303–312. doi:10.1016/j.biortech.2019.02.051

Kim, H., Kim, J., Jeong, Y., Kim, Y., Paek, J., Kang, N., et al. (2020). Antioxidant and probiotic properties of lactobacilli and bifidobacteria of human origins. *Biotechnol. Bioproc. E* 25 (3), 421–430. doi:10.1007/s12257-020-0147-x

Kim, Y., Hendrickson, R., Mosier, N., and Ladisch, M. (2009). Liquid hot water pretreatment of cellulosic biomass. *Biofuels* 581, 93–102. doi:10.1007/978-1-60761-214-8_7

Kruyeniski, J., Ferreira, P., Videira Sousa Carvalho, M., Vallejos, M., Felissia, E., and Area, M. (2019). Physical and chemical characteristics of pretreated slash pine sawdust influence its enzymatic hydrolysis. *Industrial Crops Prod.* 130, 528–536. doi:10.1016/j.indcrop.2018.12.075

Kumar, P., Barrett, D., Delwiche, M., and Stroeve, P. (2009). Methods for pretreatment of lignocellulosic biomass for efficient hydrolysis and biofuel production. *Ind. Eng. Chem. Res.* 48 (8), 3713–3729. doi:10.1021/ie801542g

Lai, C., Yang, B., He, J., Huang, C. X., Li, X., Song, X. Y., et al. (2018). Enhanced enzymatic digestibility of mixed wood sawdust by lignin modification with naphthol derivatives during dilute acid pretreatment. *Bioresour. Technol.* 269, 18–24. doi:10.1016/j.biortech.2018.08.086

Li, H., Wang, B., Wen, J., Cao, X., Sun, S., and Sun, R. (2018). Availability of four energy crops assessing by the enzymatic hydrolysis and structural features of lignin before and after hydrothermal treatment. *Energy Convers. Manag.* 155, 58–67. doi:10.1016/j.enconman.2017.10.089

Li, M., Jiang, B., Wu, W., Wu, S., Yang, Y., Song, J., et al. (2022). Current understanding and optimization strategies for efficient lignin-enzyme interaction: A review. *Int. J. Biol. Macromol.* 195, 274–286. doi:10.1016/j.ijbiomac.2021.11.188

Li, M., Yi, L., Bin, L., Zhang, Q., Song, J., Jiang, H., et al. (2020). Comparison of nonproductive adsorption of cellulase onto lignin isolated from pretreated lignocellulose. *Cellulose* 27 (14), 7911–7927. doi:10.1007/s10570-020-03357-6

Lian, Z., Zhang, Q., Xu, Y., Zhou, X., and Jiang, K. (2022). Biorefinery cascade processing for converting corncob to xylooligosaccharides and glucose by maleic acid pretreatment. *Biochem. Biotechnol.* 65, 1–13. doi:10.1007/s12010-022-03985-7

Lu, H., Liu, S., Zhang, M., Meng, F., Shi, X., and Yan, L. (2016). Investigation of the strengthening process for liquid hot water pretreatments. *Energy Fuels* 30 (2), 1103–1108. doi:10.1021/acs.energyfuels.5b02658

Ma, C. Y., Gao, X., Peng, X., Gao, Y., Liu, J., Wen, J., et al. (2021b). Microwave-assisted deep eutectic solvents (DES) pretreatment of control and transgenic poplars for boosting the lignin valorization and cellulose bioconversion. *Industrial Crops Prod.* 164, 113415. doi:10.1016/j.indcrop.2021.113415

Ma, C. Y., Peng, X. P., Sun, S., Wen, J. L., and Yuan, T. Q. (2021a). Short-time deep eutectic solvents pretreatment enhanced production of fermentable sugars and tailored lignin nanoparticles from abaca. *Int. J. Biol. Macromol.* 192, 417–425. doi:10.1016/j.ijbiomac.2021.09.140

Ma, C. Y., Wang, H., Wen, J., Shi, Q., Wang, S., Yuan, T., et al. (2020). Structural elucidation of lignin macromolecule from abaca during alkaline hydrogen peroxide delignification. *Int. J. Biol. Macromol.* 144, 596–602. doi:10.1016/j.ijbiomac.2019.12.080

Ma, C. Y., Xu, L., Sun, Q., Sun, S., Cao, X., Wen, T., et al. (2022). Ultrafast alkaline deep eutectic solvent pretreatment for enhancing enzymatic saccharification and lignin fractionation from industrial xylose residue. *Bioresour. Technol.* 352, 127065. doi:10.1016/j.biortech.2022.127065

Ma, C. Y., Xu, L., Zhang, C., Guo, K., Yuan, T., and Wen, J. (2021c). A synergistic hydrothermal-deep eutectic solvent (DES) pretreatment for rapid fractionation and targeted valorization of hemicelluloses and cellulose from poplar wood. *Bioresour. Technol.* 341, 125828. doi:10.1016/j.biortech.2021.125828

Paz-Cedeno, F. R., Henares, L. R., Solorzano-Chavez, E. G., Scontri, M., Picheli, F. P., Miranda Roldán, I. U., et al. (2021). Evaluation of the effects of different chemical pretreatments in sugarcane bagasse on the response of enzymatic hydrolysis in batch systems subject to high mass loads. *Renew. Energy* 165, 1–13. doi:10.1016/j.renene.2020.10.092

Pei, W., Deng, J., Wang, P., Wang, X., Zheng, L., Zhang, Y., et al. (2022). Sustainable lignin and lignin-derived compounds as potential therapeutic agents for

degenerative orthopaedic diseases: A systemic review. *Int. J. Biol. Macromol.* 212, 547–560. doi:10.1016/j.ijbiomac.2022.05.152

Rezania, S., Oryani, B., Cho, J., Talaiekhozani, A., Sabbagh, F., Hashemi, B., et al. (2020). Different pretreatment technologies of lignocellulosic biomass for bioethanol production: An overview. *Energy* 199, 117457. doi:10.1016/j.energy.2020.117457

Scapini, T., dos Santos, M. S. N., Bonatto, C., Wancura, J. H. C., Mulinari, J., Camargo, A. F., et al. (2021). Hydrothermal pretreatment of lignocellulosic biomass for hemicellulose recovery. *Bioresour. Technol.* 342, 126033. doi:10.1016/j.biortech.2021.126033

Sipos, B., Réczey, J., Somorai, Z., Kádár, Z., Dienes, D., and Réczey, K. (2009). Sweet sorghum as feedstock for ethanol production: Enzymatic hydrolysis of steam-pretreated bagasse. *Appl. Biochem. Biotechnol.* 153, 151–162. doi:10.1007/s12010-008-8423-9

Sluiter, A., Hames, B., Ruiz, R., Scarlata, C., Sluiter, J., and Templeton, D. (2011). Determination of structural carbohydrates and lignin in biomass national renewable. *Natl. Renew. Energy Lab.* 10, 1–15.

Su, Y., Fang, L., Wang, P., Lai, C., Huang, C., Ling, Z., et al. (2021). Efficient production of xylooligosaccharides rich in xylobiose and xylotriose from poplar by hydrothermal pretreatment coupled with post-enzymatic hydrolysis. *Bioresour. Technol.* 342, 125955. doi:10.1016/j.biortech.2021.125955

Tang, S., Wang, T., Jiang, M., Huang, C., Lai, C., Fan, Y., et al. (2019). Construction of arabinogalactans/selenium nanoparticles composites for enhancement of the antitumor activity. *Int. J. Biol. Macromol.* 128, 444–451. doi:10.1016/j.ijbiomac.2019.01.152

Tang, W., Wu, X., Huang, C., Ling, Z., Lai, C., and Yong, Q. (2021). Natural surfactant-aided dilute sulfuric acid pretreatment of waste wheat straw to enhance enzymatic hydrolysis efficiency. *Bioresour. Technol.* 324, 124651. doi:10.1016/j.biortech.2020.124651

Vázquez, M. J., Alonso, J. L., Domı´nguez, H., and Parajó, J. C. (2000). Xylooligosaccharides: Manufacture and applications. *Trends Food Sci. Technol.* 11 (11), 387–393.

Wang, C., Yang, J., Wen, J., Bian, J., Li, M., Peng, F., et al. (2019). Structure and distribution changes of Eucalyptus hemicelluloses during hydrothermal and alkaline pretreatments. *Int. J. Biol. Macromol.* 133, 514–521. doi:10.1016/j.ijbiomac.2019.04.127

Ye, L., Zhang, J., Zhao, J., and Tu, S. (2014). Liquefaction of bamboo shoot shell for the production of polyols. *Bioresour. Technol.* 153, 147–153. doi:10.1016/j.biortech.2013.11.070

Yu, Y., Cheng, W., Li, Y., Wang, T., Xia, Q., Liu, Y., et al. (2022). Tailored one-pot lignocellulose fractionation to maximize biorefinery toward versatile xylochemicals and nanomaterials. *Green Chem.* 24 (8), 3257–3268. doi:10.1039/d2gc00264g

Yue, P., Hu, Y., Tian, R., Bian, J., and Peng, F. (2022). Hydrothermal pretreatment for the production of oligosaccharides: A review. *Bioresour. Technol.* 343, 126075. doi:10.1016/j.biortech.2021.126075

Zaldivar, J., Martinez, A., and Ingram, L. O. (2015). Effect of selected aldehydes on the growth and fermentation of ethanologenic *Escherichia coli*. *Biotechnol. Bioeng.* 65 (1), 24–33. doi:10.1002/(sici)1097-0290(19991005)65:1<24::aid-bit4>3.0.co;2-2

Zhang, C., Zhuang, X., Wang, Z. J., Matt, F., John, F. S., and Zhu, J. Y. (2013). Xylanase supplementation on enzymatic saccharification of dilute acid pretreated poplars at different severities. *Cellulose* 20 (4), 1937–1946. doi:10.1007/s10570-013-9934-2

Zhang, F., Lan, W., Zhang, A., and Liu, C. (2022). Green approach to produce xylo-oligosaccharides and glucose by mechanical-hydrothermal pretreatment. *Bioresour. Technol.* 344, 126298. doi:10.1016/j.biortech.2021.126298

Zhang, Q., Wan, G., Li, M., Jiang, H., Wang, S., and Min, D. (2020a). Impact of bagasse lignin-carbohydrate complexes structural changes on cellulase adsorption behavior. *Int. J. Biol. Macromol.* 162, 236–245. doi:10.1016/j.ijbiomac.2020.06.084

Zhang, W., You, Y., Lei, F., Li, P., and Jiang, J. (2018). Acetyl-assisted autohydrolysis of sugarcane bagasse for the production of xylo-oligosaccharides without additional chemicals. *Bioresour. Technol.* 265, 387–393. doi:10.1016/j.biortech.2018.06.039

Zhang, X., Zhang, W., Lei, F., Yang, S., and Jiang, J. (2020b). Coproduction of xylooligosaccharides and fermentable sugars from sugarcane bagasse by seawater hydrothermal pretreatment. *Bioresour. Technol.* 309 (22), 123385. doi:10.1016/j.biortech.2020.123385

Zhuang, X., Wang, W., Yu, Q., Y., Qi, W., Wang, Q., Tan, X., et al. (2016). Liquid hot water pretreatment of lignocellulosic biomass for bioethanol production accompanying with high valuable products. *Bioresour. Technol.* 199, 68–75. doi:10.1016/j.biortech.2015.08.051

frontiers | Frontiers in Bioengineering and Biotechnology

TYPE Review
PUBLISHED 04 October 2022
DOI 10.3389/fbioe.2022.1024453

OPEN ACCESS

EDITED BY
Lei Wang,
Ocean University of China, China

REVIEWED BY
Wenyang Xu,
Åbo Akademi University, Finland
Qiong Wu,
Qingdao University of Science and Technology, China

*CORRESPONDENCE
Ting Xu,
xuting@tust.edu.cn
Xueping Song,
sx_ping@gxu.edu.cn
Sun-Eun Choi,
oregonin@kangwon.ac.kr
Chuanling Si,
sichli@tust.edu.cn

†These authors have contributed equally to this work and share first authorship

SPECIALTY SECTION
This article was submitted to Bioprocess Engineering, a section of the journal Frontiers in Bioengineering and Biotechnology

RECEIVED 21 August 2022
ACCEPTED 09 September 2022
PUBLISHED 04 October 2022

CITATION
Liang Q, Wang Y, Yang Y, Xu T, Xu Y, Zhao Q, Heo S-H, Kim M-S, Jeong Y-H, Yao S, Song X, Choi S-E and Si C (2022), Nanocellulose/two dimensional nanomaterials composites for advanced supercapacitor electrodes. *Front. Bioeng. Biotechnol.* 10:1024453. doi: 10.3389/fbioe.2022.1024453

Nanocellulose/two dimensional nanomaterials composites for advanced supercapacitor electrodes

Qidi Liang[1†], Yaxuan Wang[1†], Yanfan Yang[1], Ting Xu[1,2*], Ying Xu[1], Qingshuang Zhao[1], Su-Hak Heo[3], Min-Seok Kim[4], Young-Hwan Jeong[4], Shuangquan Yao[2], Xueping Song[2*], Sun-Eun Choi[4*] and Chuanling Si[1,2,5*]

[1]Tianjin Key Laboratory of Pulp and Paper, Tianjin University of Science and Technology, Tianjin, China, [2]Guangxi Key Laboratory of Clean Pulp & Papermaking and Pollution Control, College of Light Industry and Food Engineering, Guangxi University, Nanning, China, [3]Department of Medicinal Bioscience, Konkuk University (Glocal Campus), Chungju-si, Chungcheongbuk-do, South Korea, [4]Department of Forest Biomaterials Engineering, College of Forest & Environmental Sciences, Kangwon National University, Chuncheon, South Korea, [5]State Key Laboratory of Tree Genetics and Breeding, Northeast Forestry University, Harbin, China

With the emerging of the problems of environmental pollution and energy crisis, the development of high-efficiency energy storage technology and green renewable energy is imminent. Supercapacitors have drawn great attention in wearable electronics because of their good performance and portability. Electrodes are the key to fabricate high-performance supercapacitors with good electrochemical properties and flexibility. As a biomass based derived material, nanocellulose has potential application prospects in supercapacitor electrode materials due to its biodegradability, high mechanical strength, strong chemical reactivity, and good mechanical flexibility. In this review, the research progress of nanocellulose/two dimensional nanomaterials composites is summarized for supercapacitors in recent years. First, nanocellulose/MXene composites for supercapacitors are reviewed. Then, nanocellulose/graphene composites for supercapacitors are comprehensively elaborated. Finally, we also introduce the current challenges and development potential of nanocellulose/two dimensional nanomaterials composites in supercapacitors.

KEYWORDS

supercapacitor, nanocellulose, MXene, graphene, electrode

1 Introduction

The emission of greenhouse gases and the depletion of fossil fuels have led to an increasing global demand for renewable energy, which has promoted human beings to invest more and more funds in the development, utilization, and storage of new energy (Gross et al., 2003; Lund, 2007; Si et al., 2009a; Si et al., 2013a; Du et al., 2016; Dai et al., 2019; Yang et al., 2019a; Yang et al., 2020; Liu et al., 2021a; Xiong et al., 2021a; Huang et al.,

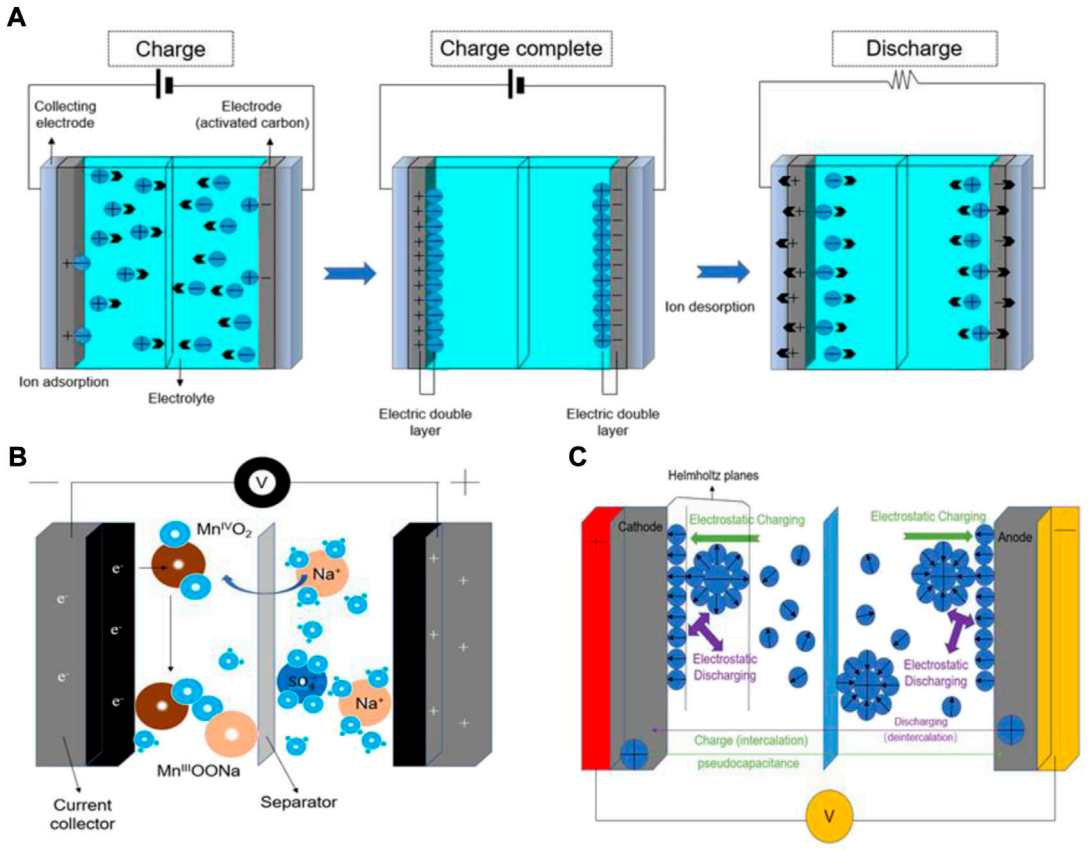

FIGURE 1
The working mechanism of supercapacitors. **(A)** Working principle of EDLC during charging and discharging, **(B)** pseudocapacitor, and **(C)** hybrid capacitor.

2021; Liu et al., 2022a; Xu et al., 2022). As an advanced energy storage technology, supercapacitors have been widely used in portable electronic products, memory backup, electric vehicles, and military equipment, due to their environmental friendliness, high power density, maintenance-free, and long-life properties (Si et al., 2008; Si et al., 2009b; Si et al., 2013b; Dubal et al., 2015; Salunkhe et al., 2016a; Salunkhe et al., 2016b; Salunkhe et al., 2017; Xu et al., 2021a; Liu et al., 2021b; Xiong et al., 2021b; Liu et al., 2021c; Liu et al., 2021d; Ma et al., 2021). Hybrid capacitors, pseudocapacitors, and Electric double-layer capacitors (EDLCs) can be distinguished depending on the storage mechanism or cell configuration. The key characteristic of EDLCs is the double-layer capacitance, for example, it generates at the interface between the liquid electrolyte and the adjacent conductive electrode. At this boundary, two layers of charges of opposite polarity are formed, one in the electrolyte and the other on the electrode surface (Zhang and Zhao, 2009; Zhai et al., 2011; Qiang et al., 2021; Zhang et al., 2021). Figure 1A shows the working mechanism of EDLCs during the charging and discharging process. When charging, the positive and negative electrodes generate a stable electric field. The cathode attracts the anions in the electrolyte, and the anode attracts the cations in the electrolyte to generate an electric double layer; when discharging, the anions and cations in the electrolyte return to the electrolyte to form an electrically neutral solution. As shown in Figure 1B, pseudocapacitors store charges through redox reactions, electrosorption, or intercalation mechanisms (Conway et al., 1997; Zhao et al., 2011; Augustyn et al., 2014). These electrochemical reactions allow pseudocapacitors to achieve higher specific capacitance than EDLCs. Hybrid capacitors have two different electrodes, one electrode mainly exhibits electrostatic capacitance and the other electrode mostly exhibits electrochemical capacitance (Figure 1C) (Ma et al., 2007).

Cellulose, as the most abundant natural polymer on Earth, consists of hundreds of strands β (1 → 4) linked D-glucose units (Updegraff, 1969; Crawford, 1981; Hu, et al., 2019; Liu et al., 2021e; Liu et al., 2022b). Nanocellulose has been extensively studied as the rapid development of nanotechnology. Nanocellulose is a kind of polymer that reduces the size of

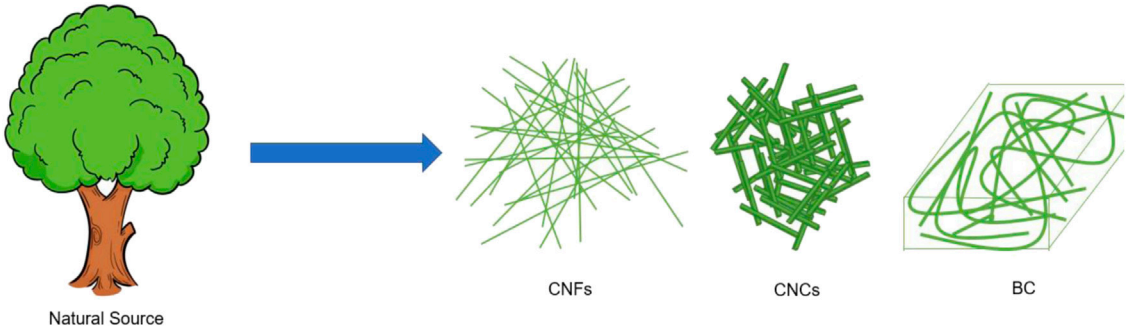

FIGURE 2
Schematic diagram of the classification of nanocellulose.

cellulose in a certain dimension to the nanometer level through chemical, physical and biological methods (Figure 2) (O'sullivan, 1997; Lu et al., 2019; Du et al., 2019; Du et al., 2021a Du et al., 2021b; Du et al., 2022; Liu et al., 2020a; Xu et al., 2020a; Xu et al., 2021b; Xu et al., 2020b; Xu et al., 2020c). In addition to the characteristics of cellulose, nanocellulose also demonstrates large aspect ratio, and specific surface area, excellent mechanical strength, and good chemical reactivity (Dai et al., 2017; An et al., 2019; Li et al., 2019; Li et al., 2020a; An et al., 2020; Wang et al., 2020a; Dai et al., 2020; Si and Xu, 2020; Liu et al., 2021e; Wang et al., 2021; Wang et al., 2022). According to the morphological structure, nanocellulose can be divided into three classes: bacterial cellulose (BC), cellulose nanofibers (CNFs), and cellulose nanocrystals (CNCs) (Ostadhossein et al., 2015; Tayeb et al., 2018; Xie et al., 2018; Xie et al., 2019; Chen et al., 2020a; Chen et al., 2020b; Lu et al., 2020; Li et al., 2022a). Nanocellulose could be mixed with other conductive materials as electrode materials for supercapacitors (Kang et al., 2012; Li et al., 2018; Nie et al., 2018; Zhang et al., 2018; Li et al., 2020b; Liu et al., 2020b; Li et al., 2022b).

Conductive materials are essential in the preparation of energy storage equipments and are considered objects that permit the flow of electrical current. Both MXene and graphene are emerging two-dimensional materials that have been successfully used for supercapacitors as electrode materials. However, the high cost of preparing graphene and easy aggregation affects the surface wettability and dispersibility of graphene in the electrolyte, which reduces the electrical conductivity and thus reduces the effective specific surface area. In the same way, the large van der Waals forces between layers of MXene cause the expansion of inactive pores, limiting the transfer of electrolyte ions, resulting in the decreasing of the electrical conductivity. The introduction of nanocellulose can avoid graphene aggregation and enlarge the active pores between the MXene sheets. At the same time, due to its good properties, including surface wettability, flexibility, high mechanical strength, thermal stability, and hydrophilicity, biomass raw materials can be converted into value-added products, which could promote the economic cycle. Therefore, the composite of nanocellulose with graphene and MXene is the promising electrode materials for supercapacitors (Gao et al., 2013a; Li et al., 2014; Yan et al., 2014). Figures 3, 4 show the recent development of composites (MXene/CNF and graphene/CNF) as electrodes for supercapacitors, respectively.

2 Nanocellulose/two dimensional nanomaterials composites

2.1 Nanocellulose/MXene composites for supercapacitors

2.1.1 MXene and composite strategy

MXene, comprising of transition metal nitrides, carbides, or carbonitrides, is a class of two-dimensional inorganic compounds. It was first reported in 2011 that MXene materials possess metallic conductivity of transition metal carbides due to hydroxyl groups or terminal oxygens on its surface (Naguib et al., 2011; Naguib et al., 2014). Generally, MXene is prepared by selectively etching the A layer from the MAX phases, and the etching solution contains fluoride ions, such as hydrofluoric acid (HF) (Naguib et al., 2014), ammonium bifluoride (NH_4HF_2) (Halim et al., 2014) or hydrochloric acid (HCl), and lithium fluoride (LiF) (Ghidiu et al., 2014). Because of the strong interlayer van der Waals interaction, MXene is easy to stack, which hinders the effective utilization of surfactant sites and the rapid transport of ions (Yang et al., 2019b). To solve the above problems, the "spacer" is needed to increase the space between the MXene sheets, thereby increasing the surfactant sites to achieve effective ion migration.

Nanocellulose is one-dimensional fibrous structure, that can act as a "spacer" and improves ion transport across the electrode/electrolyte interface. For example, Tian et al.

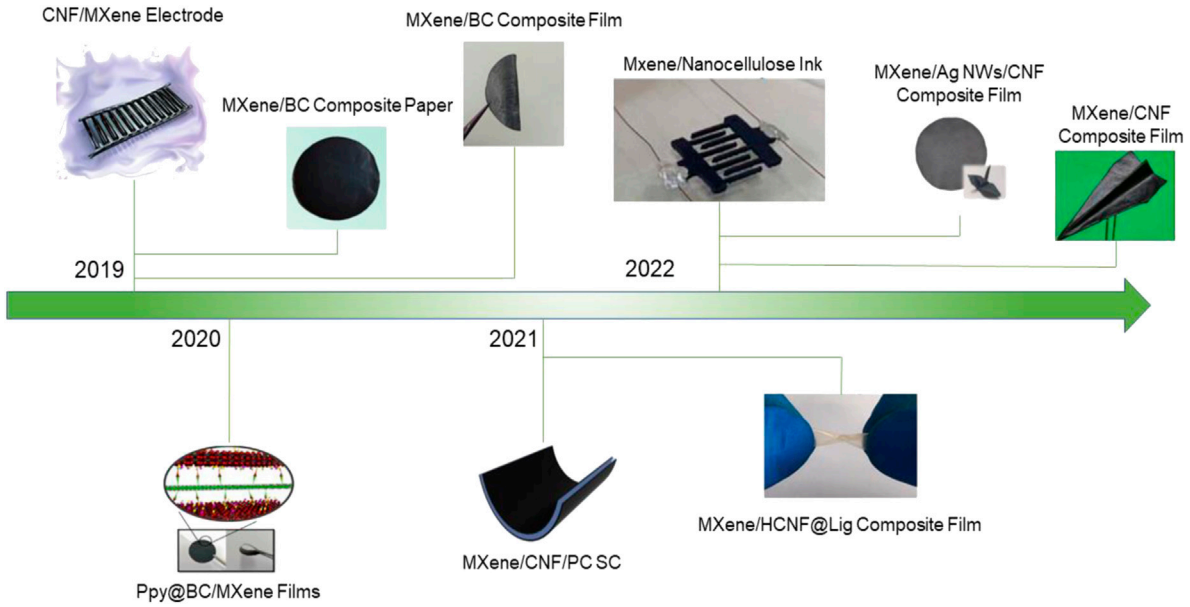

FIGURE 3
Brief timeline of nanocellulose/MXene composites for supercapacitors. Reproduced from: Tian et al. (2019), Wiley-VCH; Jiao et al. (2019), Wiley-VCH; Wang et al. (2019), Wiley-VCH; Song et al. (2020), Springer Nature; Chen et al. (2021a), Elsevier; Chang et al.(2021), Royal Society of Chemistry. Zhou et al. (2022), Wiley-VCH; Tang et al. (2022), Wiley-VCH; Chen et al. (2022), Elsevier.

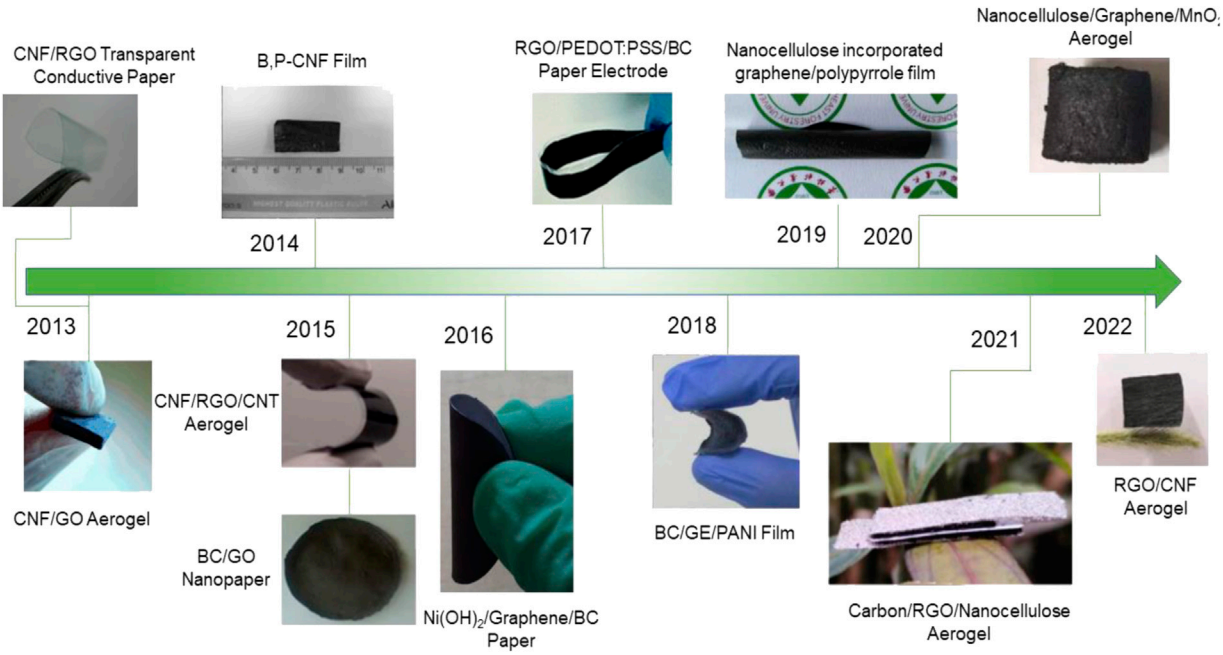

FIGURE 4
Brief timeline of nanocellulose/graphene composites for supercapacitors. Reproduced from: Gao et al. (2013b), Elsevier. Hamedi et al. (2013), Wiley-VCH; Chen et al. (2014), Wiley-VCH; Zheng et al. (2015), American Chemical Society; Liu et al. (2015), Royal Society of Chemistry. Ma et al. (2016a), Elsevier. Zhao et al. (2017), American Chemical Society; Luo et al. (2018), Elsevier. Hou et al. (2019), Elsevier. Wang et al. (2020b), Springer; Chen et al. (2021b), Elsevier; Liu et al. (2022c), Springer.

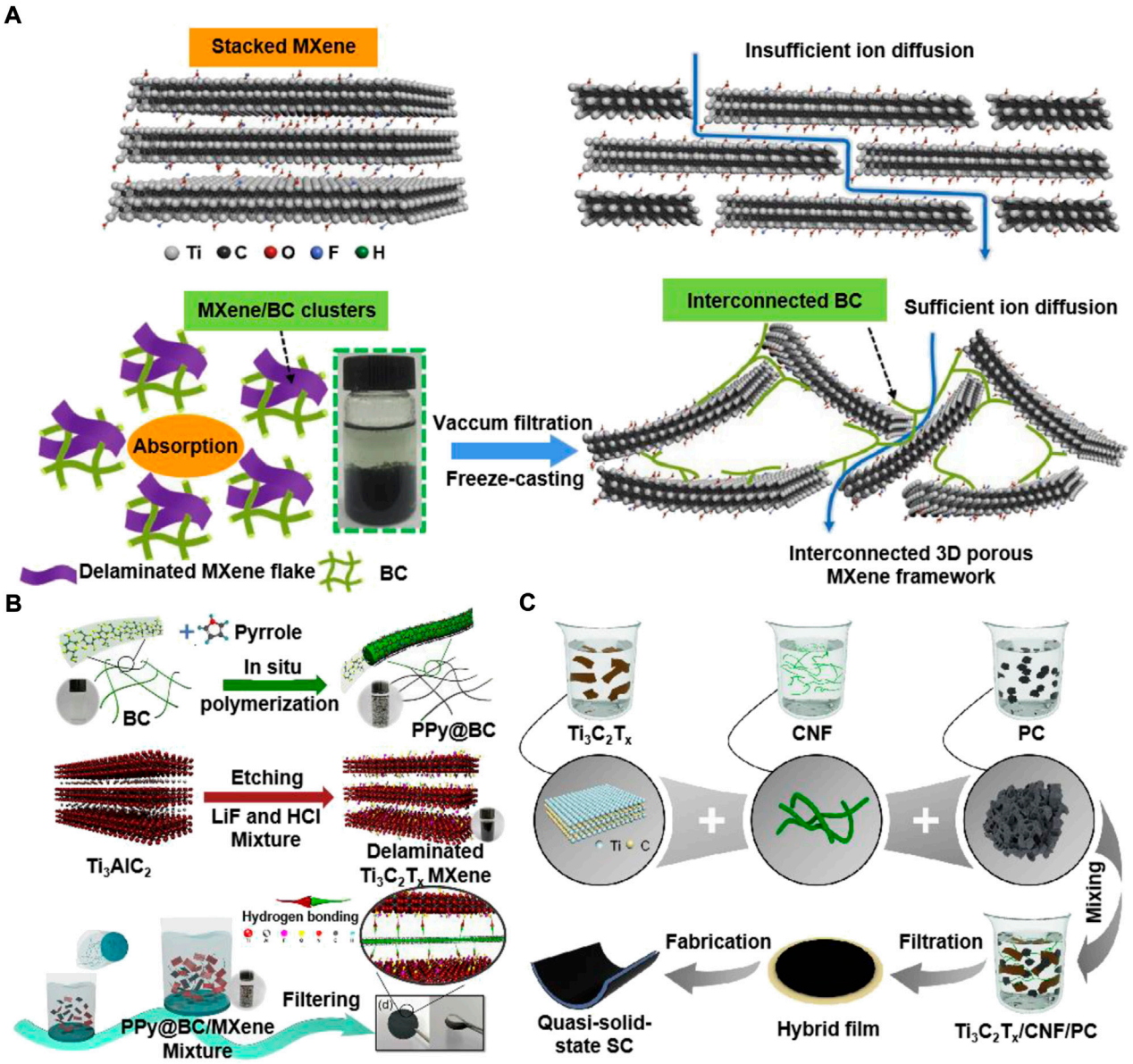

FIGURE 5
The preparation process of the **(A)** porous MXene architecture, **(B)** PPy@BC/MXene composite paper, and **(C)** $Ti_3C_2T_x$/CNF/PC hybrid film. Reproduced from: **(A)** Wang et al. (2019), Wiley. **(B)** Song et al. (2020), Springer. **(C)** Chen et al. (2021a), Elsevier.

(2019) prepared a two-dimensional film composite of nanocellulose and MXene for supercapacitor electrodes with high electronic conductivity (2.95×10^4 S/m). This is because the small width of the CNFs (around 3.5 nm) makes it possible to have better conductivity between two-dimensional sheets. Simultaneously, since the addition of CNFs did not limit the ability of ion transport and pseudocapacitance storage, its gravimetric capacitance was as high as 298 F/g. As shown in Figure 5A, Wang et al. (2019) reported 3D porous BC/MXene self-supporting film using a simple and time-saving method. The prepared BC/MXene film has a good hierarchical porous structure, excellent mechanical properties, and high flexibility and showed ultra-high capacitance of 416 F/g. In addition, the assembled asymmetric supercapacitor with negative electrode of BC/MXene film and positive electrode of BC/polyaniline (PANI) had a high energy density (252 μWh/cm). This work developed a simple method to assemble high

TABLE 1 Electrochemical performance of the nanocellulose/MXene-based supercapacitors.

Materials	Electrolyte	Current density	Specific capacitance	Energy density	Power density	Cycle life-capacitance retention	References
CNFs/MXene	H_2SO_4	0.57 mA/cm^2	25.3 mF/cm^2	0.08 μWh/cm^2	145.00 μWh/cm^2	10000-86.8%	Tian et al. (2019)
BC/MXene	H_2SO_4	3.00 mA/cm^2	87.0 F/g	252.00 μWh/cm^2	2.12 mV/cm^2	10000-96.5%	Wang et al. (2019)
PPy@BC/MXene	H_2SO_4	1.00 mA/cm^2	294.0 F/g	33.10 Wh/kg	243.00 w/kg	10000-83.5%	Song et al. (2020)
CNFs/PC/MXene film	KOH	0.10 mA/cm^2	143.0 mF/cm^2	2.40 μWh/cm^2	17.50 μW/cm^2	10000-90.0%	Chen et al. (2021a)
CNFs@sodium lignosulfonate/MXene	PVA-H_2SO_4	0.5 A/g	248.0 F/g	16.20 Wh/L	633.10 W/L	10000-86.5%	Chang et al. (2021)
CNFs/MXene@SnS_2	PVA-H_2SO_4	1.00 mA/cm^2	205.0 mF/cm^2	6.70 μWh/cm^2	1206.00 μW/cm^2	5000-87.4%	Cai et al. (2021)

performance 3D porous films electrodes of advanced energy storage devices with 2D MXene materials.

2.1.2 Nanocellulose/MXene-based supercapacitors

So far, investigation on nanocellulose-MXene based electrodes for supercapacitors with basic compositions and electrochemical performance have been carried out, as showed in Table 1 in literatures. It can be seen that the future study of nanocellulose and MXene composite materials as electrodes for supercapacitors can be divided into two directions.

One is to pursue higher performance supercapacitors, and the other is to develop multifunctional supercapacitors. Because of the potential synergistic effect, the composite hybrid materials of different compositions are expected to be an effective strategy. For example, Song et al. (2020) prepared an enhanced electrochemical performance freestanding electrode of polypyrrole (PPy)@BC/MXene composite film (Figure 5B). The BC as a template used for depositing PPy nanoparticles uniformly, and PPy@BC nanofibers can also be embedded in the MXene layer to effectively prevent the re-accumulation of MXene and expand its interlayer space, which provided a wide range of accessible electrochemical active sites. The prepared PPy@BC/MXene electrode showed good specific capacitance of 550 F/g and long cycle life (83.5% capacitance retention after 10,000 cycles). The assembled symmetric supercapacitor by PPy@BC/MXene electrodes exhibited a high energy density of 33.1 Wh/kg. As shown in Figure 5C, Chen et al. (2021a) prepared a porous flexible MXene/CNFs/porous carbon (PC) hybrid film through a simple method of vacuum filtration. Abundant micropores were provided by three-dimensional PC for charge storage and amount of meso/macropores were provided by three-dimensional PC for the rapid diffusion of ions. One dimensional CNFs enables the hybrid film to have high mechanical properties by combining adjacent MXene sheets and PC. Supercapacitors assembled with MXene/CNFs/PC films as electrodes showed high capacitance of 143 mF/cm^2 and high energy density of 2.4 μWh/cm^2.

More rational dimensional structure design should be explored. For example, to combine with MXene nanoflakes, Cheng et al. (2021) constructed one-dimensional conductive BC@PPy nanofibers with core-shell structure. The obtained MXene/BC@PPy film electrodes displayed high capacitance of 388 mF/cm^2. Based on a two-dimensional film composite with nanocellulose and MXene, Cai et al. (2021) added SnS_2 to assemble into a nacre-like structure material. The prepared composite material exhibited excellent mechanical strength (78.3 MPa) without sacrificing toughness. The supercapacitor electrodes based on this material maintained 91.5% capacitance, provided 6.7 μWh/cm^2 energy density after 4000 cycles, and exhibited excellent flexibility (over 90% capacitance retention after 500 folding/unfolding cycles). Similarly, Chang et al. (2021) synthesized a nacre-like composite film obtained from MXene, CNFs, and lignosulfonate by a hydrothermal process (Figures 6A–C). The composite film exhibited good mechanical strength (114 MPa) compared with the CNFs film (95 MPa). The supercapacitor assembled by the composite films exhibited an excellent specific capacitance (748.96 F/cm^3).

2.2 Nanocellulose/graphene composites for supercapacitors

2.2.1 Graphene and composite strategy

Graphene has a hexagonal honeycomb lattice structure and is a two-dimensional nanomaterial composed of carbon atoms with sp2 hybrid orbitals. It has high electron mobility, high specific surface area, excellent mechanical properties, and stable chemical properties. It shows great potential for applications in photothermal conversion, electrochemical energy storage,

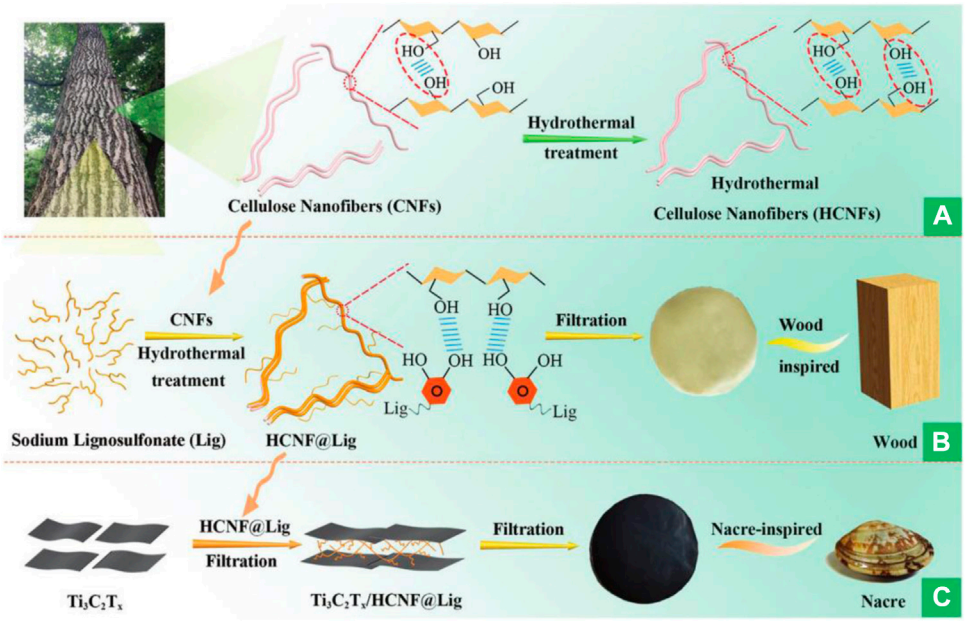

FIGURE 6
The preparation process of the nacre-inspired MXene/HCNF@Lig composite films. Reproduced from: Chang et al. (2021), Royal Society of Chemistry.

TABLE 2 Electrochemical performance of the nanocellulose/graphene-based supercapacitors.

Electrodes (electrolyte)	Voltage (V)	Specific capacitance (F g^{-1})	Energy density (mWh g^{-1})	Power density (mW g^{-1})	Cycle life-capacitance retention	References
BC/GO (1 M H_2SO_4)	1.2	160.0	—	—	2000-90.3%	Liu et al. (2015)
PPy/BC/RGO (1 M H_2SO_4)	1.0	271.0	5.75	587.5	8000-73.5%	Ma et al. (2016b)
PANI/BC/Graphene (1 M H_2SO_4)	0.8	477.0	4.25	930.0	8000-56.3%	Liu et al. (2016)
$Ni(OH)_2$/RGO/BC (2 M KOH)	0.5	877.1	—	—	15000-93.6%	Ma et al. (2016a)
CNFs/CNTs/RGO (PVA/H_2SO_4)	1.0	252	7.10	2375.0	1000-99.5%	Zheng et al. (2015)
HRGO/BC (PVA/H_3PO_4)	0.4	65.9	9.20	112.9	5000-88%	Guan et al. (2019)
TOCN/RGO (1 M H_2SO_4)	0.5	398.5	—	—	10000-99.77%	Yang et al. (2019c)
PPy/Graphene/Cellulose (1 M H_2SO_4)	1.0	630	—	—	—	Aphale et al. (2015)
PPy/TOBC/RGO	0.5	391	4.10	429.3	5000-79%	Sheng et al. (2019)

electronic screens, and industrial catalysis (Novoselov et al., 2012; Ferrari et al., 2015). However, due to the easy accumulation of graphene, the dispersibility and surface wettability of graphene in the electrolyte are affected, and the electrical conductivity is greatly affected. In the composite process of nanocellulose and graphene, nanocellulose acts as a nano-spacer layer, providing a continuous conductive path between different graphene nano-sheet layers and effectively preventing graphene aggregation. This change solves the problem of ion diffusion difficulty in graphene-based materials in electrolytes (Gao et al., 2013a). Table 2 shows the performance of composite materials based on nanocellulose and graphene as electrodes for supercapacitors in recent years. Recent research on supercapacitors mainly focuses on improving electrochemical performance. Nanocellulose-graphene based materials are suitable for selecting electrode materials for high-energy and high-power density supercapacitors. Sheng et al. (2019) constructed a flexible, high-performance fiber-based supercapacitor with synthesized

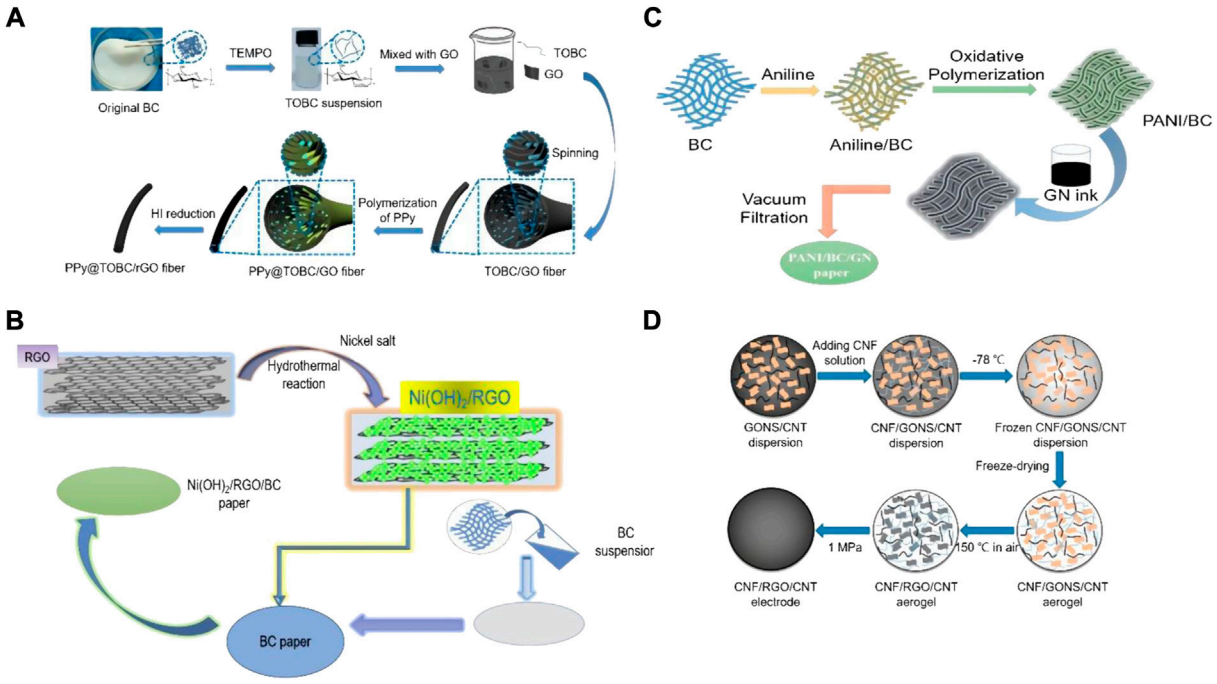

FIGURE 7
The preparation process of the **(A)** PPy@TOBC/rGO macrofibers, **(B)** $Ni(OH)_2$/RGO/BC electrode, **(C)** PANI/BC/GN freestanding paper electrodes, and **(D)** CNF/RGO/CNT electrode. Reproduced from: **(A)** Sheng et al. (2019), Elsevier. **(B)** Ma et al. (2016a), Elsevier. **(C)** Liu et al. (2016), Royal Society of Chemistry. **(D)** Zheng et al. (2015), American Chemical Society.

PPy, 2,2,6,6-Tetramethylpiperidine-1-oxyl (TEMPO)-oxidized BC (TOBC), and graphene oxide (GO) into a fiber by wet spinning (Figure 7A). The assembled supercapacitor showed excellent electrochemical performance because TOBC can prevent the aggregation of graphene nanosheets. Carboxylic acid groups and pyrrole monomers penetrated the fiber's interior, resulting in the generation of PPy inside the fiber, and this unique layered structure provided excellent electrochemical stability. The fiber-based supercapacitor exhibited a high energy density (8.8 mWh/cm^3).

2.2.2 Nanocellulose/graphene-based supercapacitors

Nanocellulose-based two-dimensional paper or film have attracted more and more attention in the field of flexible electrodes for supercapacitors. Vacuum filtration is one of the most common methods to prepare nanopaper or composite film. For instance, Ma et al. (2016a) coated graphene-wrapped $Ni(OH)_2$ on BC to prepare a flexible film using the hydrothermal method and filtration technology (Figure 7B). This method provided an effective pore volume for high-quality loading and provided a fast channel for ion and electron transport. The prepared film electrode achieved a significant area capacitance of 10.44 F/cm^2 under a load of 11.9 mg/cm^2 and had a capacitance retention rate of 93.6% after 15000 cycles. Later, they used simple *in-situ* polymerization and filtration methods to prepare a freestanding conductive film from PPy/BC composite nanofibers combined with graphene (Ma et al., 2016b). The introduction of graphene effectively solves the problem of poor conductivity of PPy/BC to ensure high electron and ion transfer. The prepared flexible electrode showed good flexibility and could be bent to a large extent.

The symmetric supercapacitor made of two PPy/BC/RGO paper electrodes exhibited a large area capacitance (1.67 F/cm^2) and a high energy density of 0.23 mWh/cm at a power density of 23.5 mW/cm^2. The excellent electrochemical performance made it a promising candidate for flexible energy storage devices. Similarly, Liu et al. (2016) prepared a flexible film electrode using PANI, BC and graphene by a simple *in-situ* chemical polymerization and vacuum filtration method, as shown in Figure 7C. The prepared film electrode possessed a regular interconnected pore channel network, which not only contributed to electron transport and ion dispersion in the whole interconnected network, but also overcame the aggregation of graphene and PANI/BC in three-dimensional conductive paper. The symmetric supercapacitor assembled by the film electrodes can provide high area capacitance (1.93 F/cm^2) and energy density (0.17 mWh/cm^2).

Liu et al. (2015) constructed BC/GO nanopaper by covalently intercalating GO and BC fiber through one-step esterification. The tensile strength of the prepared reinforced BC/GO composite increased by 12.2 times and the elongation at break increased by 20.9% compared with the original GO. The prepared composite showed excellent conductivity (171 S/m) and high specific capacitance (160 F/g) and had an outstanding capacitance retention of 90.3% after 2,000 cycles. Compared with the original graphene, porous graphene has a multi-layered pore structure on the graphene base surface, which can not only promote the storage and diffusion of electrolyte ions, but also enhance the electrochemical performance of graphene-based electrode materials. Guan et al. (2019) prepared holey GO (HRGO)/BC composite film materials with porous structure, good wettability, and excellent mechanical flexibility through biological assembly method. HRGO/BC composite film has good foldability and can produce high tensile strength of 204 MPa and elongation of 13.8%. The symmetric supercapacitor assembled by HRGO/BC composite film electrode showed a specific capacity (65.9 F/g) and an energy density (9.2 Wh/kg).

Electrode materials with three-dimensional network structure and high conductivity are the keys to developing high-performance supercapacitors. Therefore, three-dimensional aerogel with porous structure has gradually become a popular candidate for supercapacitor electrode materials. Zheng et al. (2015) used CNFs, RGO, and carbon nanotubes (CNTs) to synthesize aerogels as electrodes (Figure 7D). The assembled supercapacitors exhibited suitable areal capacitance, areal power density, and energy density of 216 mF/cm^2, 9.5 mW/cm^2, and 28.4 μWh/cm^2, respectively. Yang et al. (2019c) used TEMPO-oxidized CNFs (TOCN) and GO as precursors to prepare carbon aerogel (TOCN/RGO) by ion exchange, freeze drying and high-temperature carbonization. The obtained carbon aerogel electrode showed a high specific capacitance (398.5 F/g). At the same time, the carbon aerogel electrode also had excellent capacitance retention of 99.77% after 10,000 charge and discharge cycles. In addition, Gao et al. (2013a) used CNFs/RGO hybrid hydrogel as raw material to prepare hybrid aerogel by supercritical CO_2 drying, and used it as electrode material for all-solid-state flexible supercapacitor. CNFs were used as nano spacers and electrolyte nano reservoirs of hybrid aerogel. The results showed that the supercapacitor had excellent surface capacitance (207 F/g) and energy density (20 mWh/cm^2).

3 Conclusion

Most research on nanocellulose-based supercapacitors mainly concentrated on nanocellulose as a spacer or substrate in composites. As mentioned above, the electrodes of supercapacitors can be a composite of nanocellulose and other conductive materials. Currently, it is still a challenge to produce supercapacitors with high energy density and high capacitance. Therefore, to further improve the electrochemical performance of electrode materials, researchers need to add other materials (such as polypyrrole, sodium lignin thiosulfonate, etc.) to nanocellulose/MXene and nanocellulose/graphene composites. In addition, the composite structure can be changed to obtain different properties. For graphene/MXene and nanocellulose composites, improving the synergy between composites by changing the structure, morphology, distribution, and number of components is the focus of future research (Klemm et al., 2005; Panwar et al., 2011; Liu et al., 2021f; Liu et al., 2022d; Liu et al., 2022e; Liu et al., 2022f; Liu et al., 2022g).

Author contributions

QL, YW, YX, YY, and QZ; investigation and writing—original draft. TX, XS, S-EC, and CS: supervision. QL, TX, S-HH, M-SK, Y-HJ, and SY: writing—review and editing. All authors contributed to the article and approved the submitted version.

Funding

This work was financially supported by the Opening Project of State Key Laboratory of Tree Genetics and Breeding (K2022104), the China Postdoctoral Science Foundation (2021M702456), the Foundation (2021KF32, 2021KF02) of Guangxi Key Laboratory of Clean Pulp & Papermaking and Pollution Control, College of Light Industry and Food Engineering, Guangxi University, and Tianjin Excellent Special Commissioner for Agricultural Science & Technology Project (22ZYCGSN00350, 22YDTPJC00930). This research was also supported by the R&D program for Forest Science Technology (2019151D10-2223-0301) provided by the Korea Forest Service (Korea Forestry Promotion Institute) and partially supported by nurturing open-lab universities connected with regional industries in 2022 to S-EC.

Conflict of interest

The authors declare that the research was conducted in the absence of any commercial or financial relationships that could be construed as a potential conflict of interest.

Publisher's note

References

An, L., Si, C., Wang, G., Sui, W., and Tao, Z. (2019). Enhancing the solubility and antioxidant activity of high-molecular-weight lignin by moderate depolymerization via *in situ* ethanol/acid catalysis. *Ind. Crops Prod.* 128, 177–185. doi:10.1016/j.indcrop.2018.11.009

An, L., Si, C., Bae, J. H., Jeong, H., and Kim, Y. S. (2020). One-step silanization and amination of lignin and its adsorption of Congo red and Cu(II) ions in aqueous solution. *Int. J. Biol. Macromol.* 159, 222–230. doi:10.1016/j.ijbiomac.2020.05.072

Aphale, A., Chattopadhyay, A., Mahakalakar, K., and Patra, P. (2015). Synthesis and electrochemical analysis of algae cellulose-polypyrrole-graphene nanocomposite for supercapacitor electrode. *J. Nanosci. Nanotechnol.* 15 (8), 6225–6229. doi:10.1166/jnn.2015.10280

Augustyn, V., Simon, P., and Dunn, B. (2014). Pseudocapacitive oxide materials for high-rate electrochemical energy storage. *Energy Environ. Sci.* 7 (5), 1597–1614. doi:10.1039/C3EE44164D

Cai, C., Zhou, W., and Fu, Y. (2021). Bioinspired MXene nacre with mechanical robustness for highly flexible all-solid-state photothermo-supercapacitor. *Chem. Eng. J.* 418, 129275. doi:10.1016/j.cej.2021.129275

Chang, L., Peng, Z., Zhang, T., Yu, C., and Zhong, W. (2021). Nacre-inspired composite films with high mechanical strength constructed from MXenes and wood-inspired hydrothermal cellulose-based nanofibers for high performance flexible supercapacitors. *Nanoscale* 13 (5), 3079–3091. doi:10.1039/D0NR08090J

Chen, L. F., Huang, Z. H., Liang, H. W., Gao, H. L., and Yu, S. H. (2014). Three-dimensional heteroatom-doped carbon nanofiber networks derived from bacterial cellulose for supercapacitors. *Adv. Funct. Mat.* 24 (32), 5104–5111. doi:10.1002/adfm.201400590

Chen, S., Wang, G., Sui, W., Parvez, A. M., Dai, L., and Si, C. (2020a). Novel lignin-based phenolic nanosphere supported palladium nanoparticles with highly efficient catalytic performance and good reusability. *Ind. Crops Prod.* 145, 112164. doi:10.1016/j.indcrop.2020.112164

Chen, S., Wang, G., Sui, W., Parvez, A. M., and Si, C. (2020b). Synthesis of lignin-functionalized phenolic nanosphere supported Ag nanoparticles with excellent dispersion stability and catalytic performance. *Green Chem.* 22 (9), 2879–2888. doi:10.1039/C9GC04311J

Chen, R., Li, X., Huang, Q., Ling, H., Yang, Y., and Wang, X. (2021a). Self-assembled porous biomass carbon/RGO/nanocellulose hybrid aerogels for self-supporting supercapacitor electrodes. *Chem. Eng. J.* 412, 128755. doi:10.1016/j.cej.2021.128755

Chen, W., Zhang, D., Yang, K., Luo, M., Yang, P., and Zhou, X. (2021b). Mxene ($Ti_3C_2T_x$)/cellulose nanofiber/porous carbon film as free-standing electrode for ultrathin and flexible supercapacitors. *Chem. Eng. J.* 413, 127524. doi:10.1016/j.cej.2020.127524

Chen, J., Chen, H., Chen, M., Zhou, W., Tian, Q., and Wong, C. P. (2022). Nacre-inspired surface-engineered MXene/nanocellulose composite film for high-performance supercapacitors and zinc-ion capacitors. *Chem. Eng. J.* 428, 131380. doi:10.1016/j.cej.2021.131380

Cheng, W., Fu, J., Hu, H., and Ho, D. (2021). Interlayer structure engineering of MXene-based capacitor-type electrode for hybrid micro-supercapacitor toward battery-level energy density. *Adv. Sci.* 8 (16), 2100775. doi:10.1002/advs.202100775

Conway, B. E., Birss, V., and Wojtowicz, J. (1997). The role and utilization of pseudocapacitance for energy storage by supercapacitors. *J. Power Sources* 66 (1-2), 1–14. doi:10.1016/S0378-7753(96)02474-3

Crawford, R. L. (1981). *Lignin biodegradation and transformation*. John Wiley & Sons.

Dai, L., Liu, R., Hu, L.-Q., Zou, Z.-F., and Si, C.-L. (2017). Lignin nanoparticle as a novel green carrier for the efficient delivery of resveratrol. *ACS Sustain. Chem. Eng.* 5 (9), 8241–8249. doi:10.1021/acssuschemeng.7b01903

Dai, L., Cao, Q., Wang, K., Han, S., Si, C., Liu, D., et al. (2020). High efficient recovery of L-lactide with lignin-based filler by thermal degradation. *Ind. Crops Prod.* 143, 111954. doi:10.1016/j.indcrop.2019.111954

Dai, L., Zhu, W., Lu, J., Kong, F., Si, C., and Ni, Y. (2019). A lignin-containing cellulose hydrogel for lignin fractionation. *Green. Chem.* 21, 5222–5230. doi:10.1039/c9gc01975h

Du, H., Liu, C., Mu, X., Gong, W., Lv, D., Hong, Y., et al. (2016). Preparation and characterization of thermally stable cellulose nanocrystals via a sustainable approach of FeCl3-catalyzed formic acid hydrolysis. *Cellulose.* 23 (4), 2389–2470. doi:10.1007/s10570-016-0963-5

Du, H., Liu, W., Zhang, M., Si, C., Zhang, X., and Li, B. (2019). Cellulose nanocrystals and cellulose nanofibrils based hydrogels for biomedical applications. *Carbohydr. Polym.* 209, 130–144. doi:10.1016/j.carbpol.2019.01.020

Du, H., Parit, M., Liu, K., Zhang, M., Jiang, Z., Huang, T.-S., et al. (2021a). Engineering cellulose nanopaper with water resistant, antibacterial, and improved barrier properties by impregnation of chitosan and the followed halogenation. *Carbohydr. Polym.* 270, 118372. doi:10.1016/j.carbpol.2021.118372

Du, H., Parit, M., Liu, K., Zhang, M., Jiang, Z., Huang, T.-S., et al. (2021b). Multifunctional cellulose nanopaper with superior water-resistant, conductive, and antibacterial properties functionalized with chitosan and polypyrrole. *ACS Appl. Mat. Interfaces* 13 (27), 32115–32125. doi:10.1021/acsami.1c06647

Du, H., Zhang, M., Liu, K., Parit, M., Jiang, Z., Zhang, X., et al. (2022). Conductive PEDOT:PSS/cellulose nanofibril paper electrodes for flexible supercapacitors with superior areal capacitance and cycling stability. *Chem. Eng. J.* 428, 131994. doi:10.1016/j.cej.2021.131994

Dubal, D. P., Ayyad, O., Ruiz, V., and Gomez-Romero, P. (2015). Hybrid energy storage: The merging of battery and supercapacitor chemistries. *Chem. Soc. Rev.* 44 (7), 1777–1790. doi:10.1039/C4CS00266K

Ferrari, A. C., Bonaccorso, F., Fal'Ko, V., Novoselov, K. S., Roche, S., Bøggild, P., et al. (2015). Science and technology roadmap for graphene, related two-dimensional crystals, and hybrid systems. *Nanoscale* 7 (11), 4598–4810. doi:10.1039/C4NR01600A

Gao, K., Shao, Z., Li, J., Wang, X., Peng, X., Wang, W., et al. (2013a). Cellulose nanofiber–graphene all solid-state flexible supercapacitors. *J. Mat. Chem. A* 1 (1), 63–67. doi:10.1039/C2TA00386D

Gao, K., Shao, Z., Wu, X., Wang, X., Li, J., Zhang, Y., et al. (2013b). Cellulose nanofibers/reduced graphene oxide flexible transparent conductive paper. *Carbohydr. Polym.* 97 (1), 243–251. doi:10.1016/j.carbpol.2013.03.067

Ghidiu, M., Lukatskaya, M. R., Zhao, M. Q., Gogotsi, Y., and Barsoum, M. W. (2014). Conductive two-dimensional titanium carbide 'clay'with high volumetric capacitance. *Nature* 516 (7529), 78–81. doi:10.1038/nature13970

Gross, R., Leach, M., and Bauen, A. (2003). Progress in renewable energy. *Environ. Int.* 29 (1), 105–122. doi:10.1016/S0160-4120(02)00130-7

Guan, F., Chen, S., Sheng, N., Chen, Y., Yao, J., Pei, Q., et al. (2019). Mechanically robust reduced graphene oxide/bacterial cellulose film obtained via biosynthesis for flexible supercapacitor. *Chem. Eng. J.* 360, 829–837. doi:10.1016/j.cej.2018.11.202

Halim, J., Lukatskaya, M. R., Cook, K. M., Lu, J., Smith, C. R., Näslund, L. Å., et al. (2014). Transparent conductive two-dimensional titanium carbide epitaxial thin films. *Chem. Mat.* 26 (7), 2374–2381. doi:10.1021/cm500641a

Hamedi, M., Karabulut, E., Marais, A., Herland, A., Nyström, G., and Wågberg, L. (2013). Nanocellulose aerogels functionalized by rapid layer-by-layer assembly for high charge storage and beyond. *Angew. Chem. Int. Ed. Engl.* 125 (46), 12038–12042. doi:10.1002/anie.201305137

Hou, M., Xu, M., Hu, Y., and Li, B. (2019). Nanocellulose incorporated graphene/polypyrrole film with a sandwich-like architecture for preparing flexible supercapacitor electrodes. *Electrochimica Acta* 313, 245–254. doi:10.1016/j.electacta.2019.05.037

Hu, L., Du, H., Liu, C., Zhang, Y., Yu, G., Zhang, X., et al. (2019). Comparative evaluation of the efficient conversion of corn husk filament and corn husk powder to valuable materials via a sustainable and clean biorefinery process. *ACS Sustain. Chem. Eng.* 7, 1327–1336. doi:10.1021/acssuschemeng.8b05017

Huang, L.-Z., Ma, M.-G., Ji, X.-X., Choi, S.-E., and Si, C. (2021). Recent developments and applications of hemicellulose from wheat straw: A review. *Front. Bioeng. Biotechnol.* 9, 690773. doi:10.3389/fbioe.2021.690773

Jiao, S., Zhou, A., Wu, M., and Hu, H. (2019). Kirigami patterning of MXene/bacterial cellulose composite paper for all-solid-state stretchable micro-supercapacitor arrays. *Adv. Sci. (Weinh).* 6 (12), 1900529. doi:10.1002/advs.201900529

Kang, Y. J., Chun, S. J., Lee, S. S., Kim, B. Y., Kim, J. H., Chung, H., et al. (2012). All-solid-state flexible supercapacitors fabricated with bacterial nanocellulose papers, carbon nanotubes, and triblock-copolymer ion gels. *ACS Nano* 6 (7), 6400–6406. doi:10.1021/nn301971r

Klemm, D., Heublein, B., Fink, H. P., and Bohn, A. (2005). Cellulose: Fascinating biopolymer and sustainable raw material. *Angew. Chem. Int. Ed.* 44 (22), 3358–3393. doi:10.1002/anie.200460587

Li, S., Huang, D., Yang, J., Zhang, B., Zhang, X., Yang, G., et al. (2014). Freestanding bacterial cellulose–polypyrrole nanofibres paper electrodes for advanced energy storage devices. *Nano Energy* 9, 309–317. doi:10.1016/j.nanoen.2014.08.004

Li, W., Yang, Y., Sha, J., Zhou, J., Qin, C., and Wang, S. (2018). The influence of mechanical refining treatments on the rheosedimentation properties of bleached

softwood pulp suspensions. *Cellulose* 25 (6), 3609–3618. doi:10.1007/s10570-018-1808-1

Li, X., Xu, R., Yang, J., Nie, S., Liu, D., Liu, Y., et al. (2019). Production of 5-hydroxymethylfurfural and levulinic acid from lignocellulosic biomass and catalytic upgradation. *Ind. Crops Prod.* 130, 184–197. doi:10.1016/j.indcrop.2018.12.082

Li, X., Lu, X., Liang, M., Xu, R., Yu, Z., Duan, B., et al. (2020a). Conversion of waste lignocellulose to furfural using sulfonated carbon microspheres as catalyst. *Waste Manag.* 108, 119–126. doi:10.1016/j.wasman.2020.04.039

Li, X., Lu, X., Nie, S., Liang, M., Yu, Z., Duan, B., et al. (2020b). Efficient catalytic production of biomass-derived levulinic acid over phosphotungstic acid in deep eutectic solvent. *Ind. Crops Prod.* 145, 112154. doi:10.1016/j.indcrop.2020.112154

Li, W., Wang, G., Sui, W., Xu, T., Li, Z., Parvez, A. M., et al. (2022a). Facile and scalable preparation of cage-like mesoporous carbon from lignin-based phenolic resin and its application in supercapacitor electrodes. *Carbon* 196, 819–827. doi:10.1016/j.carbon.2022.05.053

Li, X., Lu, X., Hu, W., Xu, H., Chen, J., Xiong, J., et al. (2022b). Phosphotungstic acid functionalized biochar for furfural production from corncob. *Fuel Process. Technol.* 229, 107178. doi:10.1016/j.fuproc.2022.107178

Liu, Y., Zhou, J., Zhu, E., Tang, J., Liu, X., and Tang, W. (2015). Facile synthesis of bacterial cellulose fibres covalently intercalated with graphene oxide by one-step cross-linking for robust supercapacitors. *J. Mat. Chem. C Mat.* 3 (5), 1011–1017. doi:10.1039/C4TC01822B

Liu, R., Ma, L., Huang, S., Mei, J., Xu, J., and Yuan, G. (2016). Large areal mass, flexible and freestanding polyaniline/bacterial cellulose/graphene film for high-performance supercapacitors. *RSC Adv.* 6 (109), 107426–107432. doi:10.1039/C6RA21920A

Liu, W., Du, H., Liu, H., Xie, H., Xu, T., Zhao, X., et al. (2020a). Highly efficient and sustainable preparation of carboxylic and thermostable cellulose nanocrystals via FeCl3-catalyzed innocuous citric acid hydrolysis. *ACS Sustain. Chem. Eng.* 8 (44), 16691–16700. doi:10.1021/acssuschemeng.0c06561

Liu, W., Du, H., Zhang, M., Liu, K., Liu, H., Xie, H., et al. (2020b). Bacterial cellulose-based composite scaffolds for biomedical applications: A review. *ACS Sustain. Chem. Eng.* 8 (20), 7536–7562. doi:10.1021/acssuschemeng.0c00125

Liu, H., Du, H., Zheng, T., Liu, K., Ji, X., Xu, T., et al. (2021a). Cellulose based composite foams and aerogels for advanced energy storage devices. *Chem. Eng. J.* 426, 130817. doi:10.1016/j.cej.2021.130817

Liu, H., Xu, T., Liu, K., Zhang, M., Liu, W., Li, H., et al. (2021b). Lignin-based electrodes for energy storage application. *Ind. Crops Prod.* 165, 113425. doi:10.1016/j.indcrop.2021.113425

Liu, K., Du, H., Zheng, T., Liu, H., Zhang, M., Zhang, R., et al. (2021c). Recent advances in cellulose and its derivatives for oilfield applications. *Carbohydr. Polym.* 259, 117740. doi:10.1016/j.carbpol.2021.117740

Liu, K., Du, H., Zheng, T., Liu, W., Zhang, M., Liu, H., et al. (2021d). Lignin-containing cellulose nanomaterials: Preparation and applications. *Green Chem.* 23 (24), 9723–9746. doi:10.1039/D1GC02841C

Liu, S., Du, H., Liu, K., Ma, M.-G., Kwon, Y.-E., Si, C., et al. (2021e). Flexible and porous Co3O4-carbon nanofibers as binder-free electrodes for supercapacitors. *Adv. Compos. Hybrid. Mat.* 4 (4), 1367–1383. doi:10.1007/s42114-021-00344-8

Liu, W., Du, H., Liu, K., Liu, H., Xie, H., Si, C., et al. (2021f). Sustainable preparation of cellulose nanofibrils via choline chloride-citric acid deep eutectic solvent pretreatment combined with high-pressure homogenization. *Carbohydr. Polym.* 267, 118220. doi:10.1016/j.carbpol.2021.118220

Liu, H., Xu, T., Liang, Q., Zhao, Q., Zhao, D., and Si, C. (2022a). Compressible cellulose nanofibrils/reduced graphene oxide composite carbon aerogel for solid-state supercapacitor. *Adv. Compos. Hybrid. Mat.* 5, 1168–1179. doi:10.1007/s42114-022-00427-0

Liu, H., Xu, T., Cai, C., Liu, K., Liu, W., Zhang, M., et al. (2022b). Multifunctional superelastic, superhydrophilic, and ultralight nanocellulose-based composite carbon aerogels for compressive supercapacitor and strain sensor. *Adv. Funct. Mat.* 32 (26), 2113082. doi:10.1002/adfm.202113082

Liu, K., Du, H., Liu, W., Liu, H., Zhang, M., Xu, T., et al. (2022c). Cellulose nanomaterials for oil exploration applications. *Polym. Rev.* 62 (3), 585–625. doi:10.1080/15583724.2021.2007121

Liu, K., Du, H., Liu, W., Zhang, M., Wang, Y., Liu, H., et al. (2022d). Strong, flexible, and highly conductive cellulose nanofibril/PEDOT:PSS/MXene nanocomposite films for efficient electromagnetic interference shielding. *Nanoscale*, Advance Article. doi:10.1039/D2NR00468B

Liu, K., Liu, W., Li, W., Duan, Y., Zhou, K., Zhang, S., et al. (2022e). Strong and highly conductive cellulose nanofibril/silver nanowires nanopaper for high performance electromagnetic interference shielding. *Adv. Compos. Hybrid. Mat.* 5, 1078–1089. doi:10.1007/s42114-022-00425-2

Liu, W., Liu, K., Du, H., Zheng, T., Zhang, N., Xu, T., et al. (2022f). Cellulose nanopaper: Fabrication, functionalization, and applications. *Nano-Micro Lett.* 14 (1), 104–127. doi:10.1007/s40820-022-00849-x

Liu, W., Liu, K., Wang, Y., Lin, Q., Liu, J., Du, H., et al. (2022g). Sustainable production of cellulose nanofibrils from Kraft pulp for the stabilization of oil-in-water Pickering emulsions. *Ind. Crops Prod.* 185, 115123. doi:10.1016/j.indcrop.2022.115123

Lu, J., Zhu, W., Dai, L., Si, C., and Ni, Y. (2019). Fabrication of thermo-and pH-sensitive cellulose nanofibrils-reinforced hydrogel with biomass nanoparticles. *Carbohydr. Polym.* 215, 289–295. doi:10.1016/j.carbpol.2019.03.100

Lu, J., Han, X., Dai, L., Li, C., Wang, J., Zhong, Y., et al. (2020). Conductive cellulose nanofibrils-reinforced hydrogels with synergetic strength, toughness, self-adhesion, flexibility and adjustable strain responsiveness. *Carbohydr. Polym.* 250, 117010. doi:10.1016/j.carbpol.2020.117010

Lund, H. (2007). Renewable energy strategies for sustainable development. *Energy* 32 (6), 912–919. doi:10.1016/j.energy.2006.10.017

Luo, H., Dong, J., Zhang, Y., Li, G., Guo, R., Zuo, G., et al. (2018). Constructing 3D bacterial cellulose/graphene/polyaniline nanocomposites by novel layer-by-layer *in situ* culture toward mechanically robust and highly flexible freestanding electrodes for supercapacitors. *Chem. Eng. J.* 334, 1148–1158. doi:10.1016/j.cej.2017.11.065

Ma, S. B., Nam, K. W., Yoon, W. S., Yang, X. Q., Ahn, K. Y., Oh, K. H., et al. (2007). A novel concept of hybrid capacitor based on manganese oxide materials. *Electrochem. Commun.* 9 (12), 2807–2811. doi:10.1016/j.elecom.2007.09.015

Ma, L., Liu, R., Liu, L., Wang, F., Niu, H., and Huang, Y. (2016a). Facile synthesis of Ni(OH) $_2$/graphene/bacterial cellulose paper for large areal mass, mechanically tough and flexible supercapacitor electrodes. *J. Power Sources* 335, 76–83. doi:10.1016/j.jpowsour.2016.10.006

Ma, L., Liu, R., Niu, H., Wang, F., Liu, L., and Huang, Y. (2016b). Freestanding conductive film based on polypyrrole/bacterial cellulose/graphene paper for flexible supercapacitor: Large areal mass exhibits excellent areal capacitance. *Electrochimica Acta* 222, 429–437. doi:10.1016/j.electacta.2016.10.195

Ma, C., Ma, M.-G., Si, C., Ji, X.-X., and Wan, P. (2021). Flexible MXene-based composites for wearable devices. *Adv. Funct. Mat.* 31 (22), 2009524. doi:10.1002/adfm.202009524

Naguib, M., Kurtoglu, M., Presser, V., Lu, J., Niu, J., Heon, M., et al. (2011). Two-dimensional nanocrystals produced by exfoliation of Ti_3AlC_2. *Adv. Mat.* 23 (37), 4248–4253. doi:10.1002/adma.201102306

Naguib, M., Mochalin, V. N., Barsoum, M. W., and Gogotsi, Y. (2014). 25th anniversary article: MXenes: A new family of two-dimensional materials. *Adv. Mat.* 26 (7), 992–1005. doi:10.1002/adma.201304138

Nie, S., Zhang, K., Lin, X., Zhang, C., Yan, D., Liang, H., et al. (2018). Enzymatic pretreatment for the improvement of dispersion and film properties of cellulose nanofibrils. *Carbohydr. Polym.* 181, 1136–1142. doi:10.1016/j.carbpol.2017.11.020

Novoselov, K. S., Colombo, L., Gellert, P. R., Schwab, M. G., and Kim, K. (2012). A roadmap for graphene. *nature* 490 (7419), 192–200. doi:10.1038/nature11458

O'sullivan, A. C. (1997). Cellulose: The structure slowly unravels. *Cellul. (Lond).* 4 (3), 173–207. doi:10.1023/A:1018431705579

Ostadhossein, F., Mahmoudi, N., Morales-Cid, G., Tamjid, E., Navas-Martos, F. J., Soriano-Cuadrado, B., et al. (2015). Development of chitosan/bacterial cellulose composite films containing nanodiamonds as a potential flexible platform for wound dressing. *Materials* 8 (9), 6401–6418. doi:10.3390/ma8095309

Panwar, N. L., Kaushik, S. C., and Kothari, S. (2011). Role of renewable energy sources in environmental protection: A review. *Renew. Sustain. energy Rev.* 15 (3), 1513–1524. doi:10.1016/j.rser.2010.11.037

Qiang, Y., Liao, Y., Liu, J., Tian, C., Xu, H., and Wu, Y. (2021). Research progress of wood-drived energy storage materials. *J. For. Eng.* 6 (5), 1–13. doi:10.13360/j.issn.2096-1359.202012046

Salunkhe, R. R., Tang, J., Kobayashi, N., Kim, J., Ide, Y., Tominaka, S., et al. (2016a). Ultrahigh performance supercapacitors utilizing core–shell nanoarchitectures from a metal–organic framework-derived nanoporous carbon and a conducting polymer. *Chem. Sci.* 7 (9), 5704–5713. doi:10.1039/C6SC01429A

Salunkhe, R. R., Young, C., Tang, J., Takei, T., Ide, Y., Kobayashi, N., et al. (2016b). A high-performance supercapacitor cell based on ZIF-8-derived nanoporous carbon using an organic electrolyte. *Chem. Commun.* 52 (26), 4764–4767. doi:10.1039/C6CC00413J

Salunkhe, R. R., Kaneti, Y. V., and Yamauchi, Y. (2017). Metal–organic framework-derived nanoporous metal oxides toward supercapacitor applications: Progress and prospects. *ACS Nano* 11 (6), 5293–5308. doi:10.1021/acsnano.7b02796

Sheng, N., Chen, S., Yao, J., Guan, F., Zhang, M., Wang, B., et al. (2019). Polypyrrole@TEMPO-oxidized bacterial cellulose/reduced graphene oxide

macrofibers for flexible all-solid-state supercapacitors. *Chem. Eng. J.* 368, 1022–1032. doi:10.1016/j.cej.2019.02.173

Si, C.-L., Liu, Z., Kim, J.-K., and Bae, Y.-S. (2008). Structure elucidation of phenylethanoid glycosides from Paulownia tomentosa Steud. var. tomentosa wood. *Holzforschung* 62, 197–200. doi:10.1515/HF.2008.047

Si, C.-L., Kim, J.-K., Bae, Y.-S., and Li, S.-M. (2009a). Phenolic compounds in the leaves of Populus ussuriensis and their antioxidant activities. *Planta Med.* 75, 1165–1167. doi:10.1055/s-0029-1185476

Si, C.-L., Wu, L., Zhu, Z.-Y., Kim, J.-K., Kwon, D.-J., and Bae, Y.-S. (2009b). Apigenin derivatives from Paulownia tomentosa Steud. var. tomentosa stem barks. *Holzforschung* 63 (4), 440–442. doi:10.1515/HF.2009.063

Si, C.-L., Jiang, J.-Z., Liu, S.-C., Hu, H.-Y., Ren, X.-D., Yu, G.-J., et al. (2013a). A new lignan glycoside and phenolics from the branch wood of Pinus banksiana Lambert. *Holzforschung* 67, 357–363. doi:10.1515/hf-2012-0137

Si, C.-L., Shen, T., Jiang, Y.-Y., Wu, L., Yu, G.-J., Ren, X.-D., et al. (2013b). Antioxidant properties and neuroprotective effects of isocampneoside II on hydrogen peroxide-induced oxidative injury in PC12 cells. *Food Chem. Toxicol.* 59, 145–152. doi:10.1016/j.fct.2013.05.051

Si, C., and Xu, J. (2020). Recent advances in bio-medicinal and pharmaceutical applications of bio-based materials. *Curr. Med. Chem.* 27 (28), 4581–4583. doi:10.2174/0929867327282006212107000

Song, Q., Zhan, Z., Chen, B., Zhou, Z., and Lu, C. (2020). Biotemplate synthesis of polypyrrole@ bacterial cellulose/MXene nanocomposites with synergistically enhanced electrochemical performance. *Cellulose* 27 (13), 7475–7488. doi:10.1007/s10570-020-03310-7

Tang, H., Chen, R., Huang, Q., Ge, W., Zhang, X., Yang, Y., et al. (2022). Scalable manufacturing of leaf-like MXene/Ag NWs/cellulose composite paper electrode for all-solid-state supercapacitor. *EcoMat*, e12247. doi:10.1002/eom2.12247

Tayeb, A. H., Amini, E., Ghasemi, S., and Tajvidi, M. (2018). Cellulose nanomaterials—binding properties and applications: A review. *Molecules* 23 (10), 2684. doi:10.3390/molecules23102684

Tian, W., VahidMohammadi, A., Reid, M. S., Wang, Z., Ouyang, L., Erlandsson, J., et al. (2019). Multifunctional nanocomposites with high strength and capacitance using 2D MXene and 1D nanocellulose. *Adv. Mat.* 31 (41), 1902977. doi:10.1002/adma.201902977

Updegraff, D. M. (1969). Semimicro determination of cellulose inbiological materials. *Anal. Biochem.* 32 (3), 420–424. doi:10.1016/s0003-2697(69)80009-6

Wang, Y., Wang, X., Li, X., Bai, Y., Xiao, H., Liu, Y., et al. (2019). Engineering 3D ion transport channels for flexible MXene films with superior capacitive performance. *Adv. Funct. Mat.* 29 (14), 1900326. doi:10.1002/adfm.201900326

Wang, H., Xie, H., Du, H., Wang, X., Liu, W., Duan, Y., et al. (2020a). Highly efficient preparation of functional and thermostable cellulose nanocrystals via H_2SO_4 intensified acetic acid hydrolysis. *Carbohydr. Polym.* 239, 116233. doi:10.1016/j.carbpol.2020.116233

Wang, Y. Y., Fu, Q. J., Bai, Y. Y., Ning, X., and Yao, C. L. (2020b). Construction and application of nanocellulose/graphene/MnO_2 three-dimensional composites as potential electrode materials for supercapacitors. *J. Mat. Sci. Mat. Electron.* 31 (2), 1236–1246. doi:10.1007/s10854-019-02635-9

Wang, H., Du, H., Liu, K., Liu, H., Xu, T., Zhang, S., et al. (2021). Sustainable preparation of bifunctional cellulose nanocrystals via mixed H_2SO_4/formic acid hydrolysis. *Carbohydr. Polym.* 266, 118107. doi:10.1016/j.carbpol.2021.118107

Wang, H., Zhang, M., Hu, J., Du, H., Xu, T., and Si, C. (2022). Sustainable preparation of surface functionalized cellulose nanocrystals and their application for Pickering emulsions. *Carbohydr. Polym.* 297, 120062. doi:10.1016/j.carbpol.2022.120062

Xie, H., Du, H., Yang, X., and Si, C. (2018). Recent strategies in preparation of cellulose nanocrystals and cellulose nanofibrils derived from raw cellulose materials. *Int. J. Polym. Sci.* 2018, 1–25. doi:10.1155/2018/7923068

Xie, H., Zou, Z., Du, H., Zhang, X., Wang, X., Yang, X., et al. (2019). Preparation of thermally stable and surface-functionalized cellulose nanocrystals via mixed H_2SO_4/Oxalic acid hydrolysis. *Carbohydr. Polym.* 223, 115116. doi:10.1016/j.carbpol.2019.115116

Xiong, R., Hua, D., Hoeck, J. V., Berdecka, D., Léger, M., Munter, S. D., et al. (2021a). Photothermal nanofibres enable safe engineering of therapeutic cells. *Nat. Nanotechnol.* 16, 1281–1291. doi:10.1038/s41565-021-00976-3

Xiong, R., Xu, R. X., Huang, C., De Smedt, S., and Braeckmans, K. (2021b). Stimuli-responsive nanobubbles for biomedical applications. *Chem. Soc. Rev.* 50, 5746–5776. doi:10.1039/C9CS00839J

Xu, J., Li, C., Dai, L., Xu, C., Zhong, Y., Yu, F., et al. (2020a). Biomass fractionation and lignin fractionation towards lignin valorization. *Chemsuschem* 13 (17), 4284–4295. doi:10.1002/cssc.202001491

Xu, R., Liu, K., Du, H., Liu, H., Cao, X., Zhao, X., et al. (2020b). Falling leaves return to their roots: A review on the preparation of gamma-valerolactone from lignocellulose and its application in the conversion of lignocellulose. *Chemsuschem* 13 (24), 6461–6476. doi:10.1002/cssc.202002008

Xu, R., Si, C., Kong, F., and Li, X. (2020c). Synthesis of γ-valerolactone and its application in biomass conversion. *J. For. Eng.* 5 (2), 20–28. doi:10.13360/j.issn.2096-1359.201904004

Xu, R., Du, H., Liu, C., Liu, H., Wu, M., Zhang, X., et al. (2021a). An efficient and magnetic adsorbent prepared in a dry process with enzymatic hydrolysis residues for wastewater treatment. *J. Clean. Prod.* 313, 127834. doi:10.1016/j.jclepro.2021.127834

Xu, T., Du, H., Liu, H., Liu, W., Zhang, X., Si, C., et al. (2021b). Advanced nanocellulose-based composites for flexible functional energy storage devices. *Adv. Mat.* 33 (48), 2101368. doi:10.1002/adma.202101368

Xu, T., Liu, K., Sheng, N., Zhang, M., Liu, W., Liu, H., et al. (2022). Biopolymer-based hydrogel electrolytes for advanced energy storage/conversion devices: Properties, applications, and perspectives. *Energy Storage Mater.* 48, 244–262. doi:10.1016/j.ensm.2022.03.013

Yan, C., Wang, J., Kang, W., Cui, M., Wang, X., Foo, C. Y., et al. (2014). Highly stretchable piezoresistive graphene–nanocellulose nanopaper for strain sensors. *Adv. Mat.* 26 (13), 2022–2027. doi:10.1002/adma.201304742

Yang, J., Bao, W., Jaumaux, P., Zhang, S., Wang, C., and Wang, G. (2019a). MXene-based composites: Synthesis and applications in rechargeable batteries and supercapacitors. *Adv. Mat. Interfaces* 6 (8), 1802004. doi:10.1002/admi.201802004

Yang, Q., Yang, J., Gao, Z., Li, B., and Xiong, C. (2019b). Carbonized cellulose nanofibril/graphene oxide composite aerogels for high-performance supercapacitors. *ACS Appl. Energy Mat.* 3 (1), 1145–1151. doi:10.1021/acsaem.9b02195

Yang, X., Xie, H., Du, H., Zhang, X., Zou, Z., Zou, Y., et al. (2019c). Facile extraction of thermally stable and dispersible cellulose nanocrystals with high yield via a green and recyclable $FeCl_3$-catalyzed deep eutectic solvent system. *ACS Sustain. Chem. Eng.* 7 (7), 7200–7208. doi:10.1021/acssuschemeng.9b00209

Yang, J., Si, C., Liu, K., Liu, H., Li, X., and Liang, M. (2020). Production of levulinic acid from lignocellulosic biomass and application. *J. For. Eng.* 5 (2), 21–27. doi:10.13360/j.issn.2096-1359.201905013

Zhai, Y., Dou, Y., Zhao, D., Fulvio, P. F., Mayes, R. T., and Dai, S. (2011). Carbon materials for chemical capacitive energy storage. *Adv. Mat.* 23 (42), 4828–4850. doi:10.1002/adma.201100984

Zhang, L. L., and Zhao, X. S. (2009). Carbon-based materials as supercapacitor electrodes. *Chem. Soc. Rev.* 38 (9), 2520–2531. doi:10.1039/B813846J

Zhang, K., Zhang, Y., Yan, D., Zhang, C., and Nie, S. (2018). Enzyme-assisted mechanical production of cellulose nanofibrils: Thermal stability. *Cellulose* 25 (9), 5049–5061. doi:10.1007/s10570-018-1928-7

Zhang, M., Du, H., Liu, K., Nie, S., Xu, T., Zhang, X., et al. (2021). Fabrication and applications of cellulose-based nanogenerators. *Adv. Compos. Hybrid. Mat.* 4, 865–884. doi:10.1007/s42114-021-00312-2

Zhao, X., Sánchez, B. M., Dobson, P. J., and Grant, P. S. (2011). The role of nanomaterials in redox-based supercapacitors for next generation energy storage devices. *Nanoscale* 3 (3), 839–855. doi:10.1039/C0NR00594K

Zhao, D., Zhang, Q., Chen, W., Yi, X., Liu, S., Wang, Q., et al. (2017). Highly flexible and conductive cellulose-mediated PEDOT: PSS/MWCNT composite films for supercapacitor electrodes. *ACS Appl. Mat. Interfaces* 9 (15), 13213–13222. doi:10.1021/acsami.7b01852

Zheng, Q., Cai, Z., Ma, Z., and Gong, S. (2015). Cellulose nanofibril/reduced graphene oxide/carbon nanotube hybrid aerogels for highly flexible and all-solid-state supercapacitors. *ACS Appl. Mat. Interfaces* 7 (5), 3263–3271. doi:10.1021/am507999s

Zhou, G., Li, M. C., Liu, C., Wu, Q., and Mei, C. (2022). 3D printed $Ti_3C_2T_x$ MXene/cellulose nanofiber architectures for solid-state supercapacitors: Ink rheology, 3D printability, and electrochemical performance. *Adv. Funct. Mat.* 32 (14), 2109593. doi:10.1002/adfm.202109593

frontiers | Frontiers in Bioengineering and Biotechnology

TYPE Original Research
PUBLISHED 31 October 2022
DOI 10.3389/fbioe.2022.1006386

OPEN ACCESS

EDITED BY
Lei Wang,
Ocean University of China, China

REVIEWED BY
Linlin Yang,
Henan University of Chinese Medicine, China
Lishan Cui,
University of Camerino, Italy
Zhi Chao,
Southern Medical University, China

*CORRESPONDENCE
Tao Zhang,
251073371@qq.com
Changbao Chen,
ccb2021@126.com

SPECIALTY SECTION
This article was submitted to Bioprocess Engineering, a section of the journal Frontiers in Bioengineering and Biotechnology

RECEIVED 29 July 2022
ACCEPTED 17 October 2022
PUBLISHED 31 October 2022

CITATION
Meng X, Zhang T, Chen C, Li Q and Liu J (2022), Regulatory network of ginsenoside biosynthesis under Ro stress in the hairy roots of Panax ginseng revealed by RNA sequencing. *Front. Bioeng. Biotechnol.* 10:1006386. doi: 10.3389/fbioe.2022.1006386

Regulatory network of ginsenoside biosynthesis under Ro stress in the hairy roots of *Panax ginseng* revealed by RNA sequencing

Xiangru Meng, Tao Zhang*, Changbao Chen*, Qiong Li and Jingwan Liu

Key Laboratory of Chinese Medicine Planting and Development, Changchun University of Chinese Medicine, Changchun, Jilin, China

P. ginseng C.A. Meyer is a valuable Chinese herbal medicine that belongs to the Araliaceae family. Major obstacles to the continuous cropping of ginseng have severely restricted the sustainable development of the ginseng industry. The allelopathic effects of triterpenoid saponins play an important role in disorders related to continuous cropping; however, the mechanisms underlying the allelopathic autotoxicity of triterpenoid ginsenosides remain unknown. In this study, we performed mRNA and miRNA sequencing analyses to identify candidate genes and miRNAs that respond differentially to ginsenoside Ro stress in ginseng and their targets. The growth of the ginseng hairy roots was significantly inhibited under Ro stress (0.5 mg/L, Ro-0.5). The inhibition of root growth and injury to root-tip cells promoted the accumulation of the endogenous hormones indole-3-acetic acid and salicylic acid and inhibited the accumulation of abscisic acid and jasmonate acid. The accumulation of ginsenosides, except Rg3, was significantly inhibited under Ro-0.5 stress. An mRNA analysis of the Ro-0.5 and control groups showed that differentially expressed genes were mostly concentrated in the hormone signal transduction pathway. ARF7 and EFM were upregulated, whereas XTH23 and ZOX1 were downregulated. These genes represent important potential candidates for hormone-responsive continuous cropping diseases. In total, 74 differentially expressed miRNAs were identified based on the miRNA sequencing analysis, of which 22 were upregulated and 52 were downregulated. The target genes of ptc-miR156k_L + 1, mtr-miR156b-5p, gma-miR156a_R + 1, and mtr-miR156e all belonged to TRINITY_DN14567_c0_g4, which is a gene in the plant hormone signal transduction pathway. These four miRNAs were all negatively correlated with mRNA, indicating their likely involvement in the response of ginseng to continuous cropping disorders and the regulation of

Abbreviations[1]: ABA, abscisic acid; ANOVA, analysis of variance; IAA, indole-3-acetic acid; JA, jasmonate acid; POD, peroxidase; SA, salicylic acid; SOD, superoxide dismutase; UHPLC-QQQ-MS, ultra-high performance liquid chromatography tandem triple quadrupole mass spectrometry.

1 The abbreviations involved in this manuscript.

ginsenoside synthesis. Our findings provide useful insights for removing the barriers to continuous ginseng cropping and have important implications in the genetic engineering of plant stress responses.

KEYWORDS

P. ginseng, Ro stress, physiological characteristic, ginsenoside, miRNA

Introduction

P. ginseng C.A. Meyer is a perennial herb and valuable traditional Chinese medicinal ingredient with a long history of use. Ginsenosides, which are the major active compounds in ginseng, have numerous medicinal benefits such as immune regulation, anti-stress, anti-fatigue, anti-oxidation, anti-inflammatory, anti-tumor, hypoglycemic, and liver-protective properties (China Pharmacopoeia Commission, 2020; Fan et al., 2019; Riaz M. et al., 2019). Approximately 200 types of ginsenoside monomers have been isolated from ginseng (Lee et al., 2012; Shi et al., 2013). Ginsenosides are critical biomarkers of ginseng quality. The 2020 edition of the Chinese Pharmacopoeia has defined the appropriate amounts of root ginsenosides for therapeutic use. For example, the amount of Rg1 ($C_{42}H_{72}O_{14}$) and Re ($C_{48}H_{82}O_{18}$) should not be lower than 0.30%, and that of Rb1 ($C_{54}H_{92}O_{23}$) should not be lower than 0.20% (China Pharmacopoeia Commission, 2020; Sun et al., 2011). The different aglycones of ginsenosides may be divided into oleanane-type pentacyclic triterpene saponins, protopanaxadiol-type saponins (PPD), and protopanaxatriol-type saponins (PPT), where PPD- and PPT-type saponins are dammarane-type tetracyclic triterpenoids (Zhang et al., 2019).

Ginseng has the highest output value of all Chinese herbal medicines and is an important resource with unique characteristics within the Chinese medicine and general health industries. However, the cultivation period of ginseng is long, and obstacles to the continuous cropping of ginseng have long acted as a major technical bottleneck restricting its sustainable development. Soils in which ginseng has previously been planted cannot be used for ginseng production for the next 30 years because of continuous cropping issues such as burning beard, red skin, and rotten roots, which can lead to a reduced yield or no harvest of the crop. Therefore, to ensure continuous planting, China has cut down forests to plant new ginseng crops. This has resulted in serious problems such as ecological imbalance, soil erosion, and the depletion of rare forest species (Li et al., 2022). Rhizosphere allelopathy is one of the main factors inhibiting the continuous cropping of ginseng medicinal plants as it induces rhizosphere soil acidification, rhizosphere microbial community structure imbalance, and plant diseases. Moreover, the obstacles to continuous cropping have intensified over time (Li et al., 2022). Allelopathy refers to the phenomenon in which plants or microorganisms release chemical substances, or allelochemicals, into the surrounding environment, which then affect the growth and development of surrounding plants. These allelochemicals can exert positive or negative effects on plants, such as autotoxicity, partiality, and self-promotion. Allelopathy mainly occurs in the soil through root exudation, residue decomposition, and rainwater leaching, and directly or indirectly affects the formation of soil structure and plant growth. The secondary metabolites of ginseng biosynthesis are allelopathic substances and are mainly produced by the acetate or shikimate pathways or a combination of both. Allelochemicals mainly originate from root exudation and residue decomposition in the soil during plant growth. Since these components are insoluble in water, they accumulate gradually and may eventually reach a concentration at which they can seriously inhibit plant growth and development. Allelochemicals have significant inhibitory effects on *P. ginseng* and affect seed germination, seedling growth, and root vigor. A study by Chen found that the soil extract of old ginseng could inhibit ginseng seed germination and root elongation (Chen et al., 2006). Moreover, the degree of the inhibition of ginseng seed germination and root elongation increased with increasing extract concentrations. Plant hormones play an important role in the adaptation of ginseng to external environmental stress. The allelochemical ginsenoside Rg1 influences the low promotion and high inhibition of the endogenous hormone levels of ginseng seedlings; that is, low concentrations of Rg1 promote auxin [indole-3-acetic acid (IAA)] and gibberellin contents, whereas high concentrations of Rg1 reduce IAA and gibberellin contents. Furthermore, different concentrations of Rg1 may increase the amount of abscisic acid (Qiong, 2020).

mRNA and miRNA sequencing are key modern biotechnologies and important methods for exploring and mining the key genes in plants that respond to external environmental stimuli. Wu et al. (2012) constructed a miRNA transcriptome database of ginseng roots, stems, leaves, and flowers using high-throughput sequencing technology and obtained a large number of miRNAs related to environmental stress. Gao et al. (2016) used RNA sequencing to study ginseng transcriptome products treated with rust fungus at different timepoints and found that 3,839 of the 73,335 single genes that had been produced were upregulated. Chen et al. (2020) further used methyl jasmonate to stress the adventitious roots of ginseng and reported 136 upregulated PgERF genes and 152 downregulated PgERF genes. Moreover, two POD genes and one SOD gene were upregulated in ginseng root tissue, one

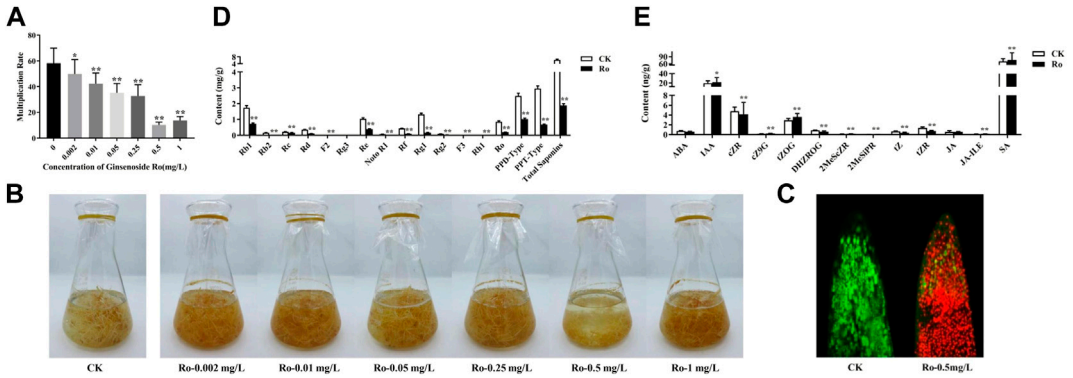

FIGURE 1
Effects of Ro on the appearance, ginsenoside content, and hormone content of the hairy roots of *P. ginseng*. Monthly multiplication rate of *P. ginseng* hairy roots induced by different concentrations of ginsenoside Ro **(A)**. Effects of different Ro concentrations on the appearance of ginseng hairy roots **(B)**. Ro-induced root-tip cell viability differences in ginseng hairy-root injury **(C)**. Changes in the content of ginsenosides in the hairy roots of *P. ginseng* **(D)**. Absolute quantitative results of 13 hormones in the hairy roots of *P. ginseng* **(E)**. * indicates a significant correlation ($p < 0.05$); ** indicates a significant correlation ($p < 0.01$).

SOD gene was upregulated in ginseng leaf tissue, and seven genes related to ginsenoside synthesis were downregulated.

In this study, we simulated the phenomenon of continuous cropping obstacles in ginseng and detected morphological changes in the hairy roots of ginseng by adding ginsenoside Ro exogenously under relatively controllable experimental conditions. We measured the degree of damage to tip cells and the contents of ginsenosides and endogenous hormones in the hairy roots of ginseng. We further explored the effects of ginsenoside Ro stress on ginsenoside biosynthesis and observed ginsenoside-induced allelopathic damage to ginseng endogenous substance accumulation. By combining mRNA and miRNA sequencing technologies, we comprehensively analyzed the toxic mechanisms of ginseng allelopathic interference at the transcriptional and post-transcriptional levels under ginsenoside Ro allelopathic stress. This study provides a theoretical basis for ensuring the continuous and effective supply of land for ginseng production.

Results

Biomass and morphological changes in ginseng hairy roots

The general growth cycle of the ginseng hairy roots lasted 30 days, with a slow growth period from days 1–13 and a logarithmic growth period from days 14–22, during which the metabolic rate was vigorous and growth rate was the highest. The ginseng entered a period of relatively stable growth after 22 days, with no further increases in weight. The final concentrations of saponin Ro in the liquid media of the six treatment groups were 0.002 mg/L (Ro 0.002), 0.01 mg/L (Ro 0.01), 0.05 mg/L (Ro 0.05), 0.25 mg/L (Ro 0.25), 0.50 mg/L (Ro 0.5), and 1.00 mg/L (Ro 1). Distilled water was used for the control group. The hairy roots of ginseng that exhibited good growth were subcultured into conical flasks for the different treatments. The initial weight of each bottle was 3 g, and the samples were weighed after 30 days. The results are shown in Figure 1A. The growth of the ginseng roots was significantly inhibited by treatment with 0.5 mg/L of Ro. The lowest monthly multiplication rate was 10.23 (Ro 0.5), which was lower than that of the CK group (82.41%). The difference was highly significant. The Ro 0.5 treatment had the greatest inhibitory effect on the growth of the ginseng hairy roots.

The growth states of the ginseng hairy roots in liquid media with different Ro concentrations differed as shown in Figure 1B. The hairy roots in the CK group were in good condition overall, with a light-yellow color, multiple hairs, multiple branches, rapid growth, and clumps. Moreover, the hairy roots were longer and thicker than those in the treatment groups with and had many fine branches. Compared to those in the CK group, the hairy roots in the treatment groups were brown in color. The growth of the hairy roots in the Ro 0.5 group showed an apoptotic trend, and their color gradually changed from fresh translucent white to dark yellow before becoming brown and dark brown after 27 days. This indicated that Ro 0.5 had a significant inhibitory effect on the growth of the ginseng hairy roots.

Root-tip cell viability assay results

According to the measured monthly ginseng hairy-root growth rate, the Ro 0.5 treatment group exhibited the greatest inhibitory effect on hairy-root growth; therefore, this group was selected as the treatment group for further study. Confocal laser scanning microscopy was used to measure the viability of apical cells in the hairy roots, observe the ratio of living-to-dead cells,

TABLE 1 Changes in the ratio of ginsenosides in hairy roots after Ro treatment.

Ginsenoside type	CK mean ± SD (%)	Ro 0.5 mg/L mean ± SD (%)
Rb1/Total saponins	27.64% ± 2.23%	38.52% ± 2.39%
Re/Total saponins	16.47% ± 1.10%	20.41% ± 1.16%
Rg1/Total saponins	21.05% ± 1.14%	8.67% ± 0.55%
PPD/Total saponins	39.49% ± 2.89%	54.42% ± 3.32%
PPT/Total saponins	46.98% ± 2.71%	35.39% ± 2.11%
PPD/PPT	84.06% ± 6.16%	153.78% ± 9.39%

and complete the localization of apical cells in the hairy roots. Fluorescein diacetate can rapidly enter living root-tip cells and show strong fluorescence, whereas propidium iodide can rapidly enter dead root-tip cells and display strong fluorescence. The results of the co-staining experiment on the tips of the hairy root in the CK and treatment groups are shown in Figure 1C. The root cells in the CK group exhibited strong vitality and were in good condition. Conversely, the cells at the root tips in the treatment group were severely damaged. It is possible that a large amount of propidium iodide entered the dead cells, combined with DNA, and was repelled by the living cells, thereby resulting in strong red fluorescence. Therefore, red blood cells were more abundant in the treatment group than in the CK group. These results also confirmed the significant inhibitory effect of Ro 0.5 on the growth of ginseng hairy-root cells. The CK and Ro 0.5 groups were further selected for an in-depth omics sequencing analysis.

Ginsenoside contents in ginseng hairy roots

After the exogenous addition of 0.5 mg/L of ginsenoside Ro, the accumulation of ginsenosides (except for Rg3) was significantly inhibited compared to that in the CK group. The results are shown in Figure 1D, which shows that PPD-type saponins decreased by 1.4560 mg/g to 0.59-times less than that in the CK group ($p < 0.01$); PPT-type saponins decreased by 2.2840 mg/g to 0.77-times less than that in the CK group ($p < 0.01$); and OLE-type saponins decreased by 0.6580 mg/g to 0.77-times less than that in the CK group ($p < 0.01$). Moreover, the sum of all 14 saponins decreased by 4.3980 mg/g to 0.71-times less than that in the CK group ($p < 0.01$).

After the Ro 0.5 treatment, the ratio of Rb1, Re, Rg1, PPD-type, and PPT-type ginsenosides-to-total saponins also changed (Table 1). The proportion of Rb1, Re, and PPT-type ginsenosides decreased significantly, whereas the proportion of Rg1 and PPD-type ginsenosides and that of PPD/PPT increased significantly. This indicated that the accumulation of PPD-type ginsenosides was stimulated under the Ro 0.5 treatment, whereas the biosynthesis of PPT-type ginsenosides was inhibited.

Endogenous hormone contents in ginseng hairy roots

Changes in the endogenous hormone contents of the ginseng hairy roots under Ro stress are shown in Figure 1E. Adding ginsenoside Ro exogenously significantly promoted the accumulation of the endogenous hormones IAA and salicylic acid (SA), which increased by 10.0% and 9.6%, respectively, compared with those in the CK group. The accumulation of abscisic acid (ABA) and its synthetic pathway intermediates was inhibited, as was the accumulation of the endogenous hormone jasmonate acid (JA) and its synthetic pathway intermediates. We speculate that the hairy roots of ginseng resist external environmental stimuli by regulating the biosynthesis of endogenous hormones. IAA, SA, JA, and ABA, in particular, are important endogenous signaling molecules in hairy ginseng roots that respond to ginsenoside Ro stress.

Basic information on miRNA sequencing

Statistical and quality controls were performed on the unique sequences of the six detection samples and the copy number corresponding to each sequence. The raw sequencing data were first filtered to remove low-quality bases (<18 nt) at the linker sequence and 3′ ends of the sequences. An overview of the sequencing data and sequence alignments of the six samples (Supplementary Table S1) indicated that the ginseng RNA was of high quality. We then compared and filtered quality-controlled raw data with databases such as RFam and Repbase to obtain valid data. The numbers of valid reads in the six samples were 25,64,382, 35,87,700, 27,58,087, 36,22,380, 36,78,294, and 38,90,141. As shown in Figure 2A, the distribution of the sequence lengths of the six samples was mainly concentrated at 20–24 nt, with 21 and 24 nt being the most common lengths, which was consistent with the typical characteristics of Dicer enzyme cleavage.

miRNAs are highly evolutionarily conserved across many species. Therefore, we speculate that miRNAs identified from the same species may also be evolutionarily conserved. We counted

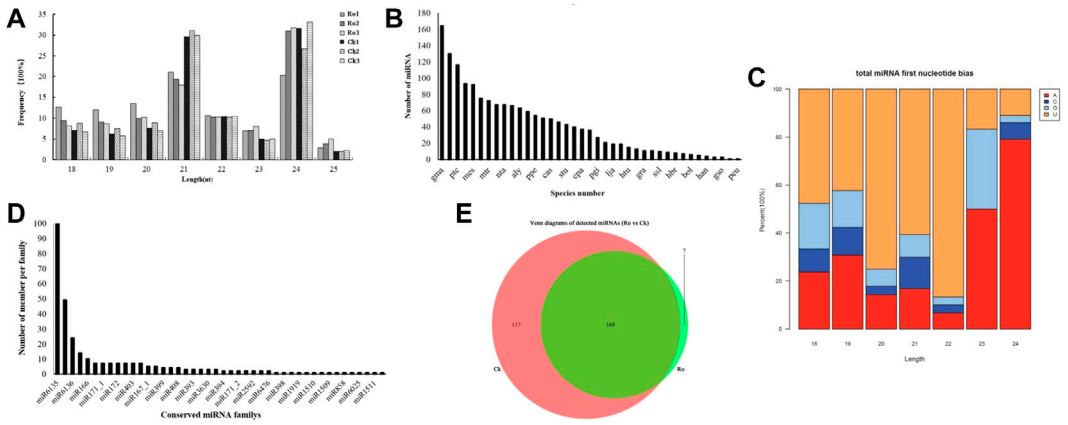

FIGURE 2
Changes in miRNAs in the hairy roots of *P. ginseng* under ginsenoside Ro stress. Length distribution of the total valid reads **(A)**. Statistics on the frequency of miRNA of *P. ginseng* in other species **(B)**. miRNA first nucleotide bias of *P. ginseng* **(C)**. Distribution of the conserved miRNAs of *P. ginseng* **(D)**. Venn diagram of the number of common and unique miRNAs in ginseng under ginsenoside Ro stress **(E)**.

the miRNAs that were detected in ginseng and other species (Figure 2B). Many of the conserved miRNAs in the ginseng were also highly conserved in the evolutionary process and were similar to those in soybean (*glycine*). max (*Linn*. Merr.), apples (*Malus domestica*), poplar (*Populus* L.), *Arabidopsis thaliana* (L. Heynh.), and other species, with high homology.

Regarding the sequence-specificity determinants of plant miRNAs, the first base at the 5′ end has a U bias. Therefore, we analyzed the preference of the 5′ first base of miRNAs in ginseng (Figure 2C). The sequencing results showed that the first bases of the miRNA sequences with lengths of 18–22 nt in ginseng were more inclined to U, whereas the miRNAs with lengths of 23 or 24 nt had a preference for the first base. This was consistent with previous findings on plant miRNA characterization, which enhances our confidence in our identification results (Chen, 2017).

Identification of miRNAs in the hairy roots of ginseng under Ro stress

Next, we identified the types of known miRNAs in ginseng and their families by aligning the obtained miRNA sequences with known miRNA sequences from different species (Figure 2D). We obtained a total of 397 ginseng candidate miRNAs from 44 families. Because the miRNAs detected by the sequencing analysis of the experimental data were predominantly in the form of isoform population expression, the expression of many types of miRNAs in the sequence expression in certain stages and periods was not necessarily the same as that in the miRBase database. The reported miRNA sequences were identical. Among these miRNA families, miR6135 was the largest family and contained 185 miRNAs, followed by the miR6140 family, which contained 40 miRNAs, and the miR166 family, which contained 10 miRNAs. These results were similar to those of previous studies (Jung et al., 2018).

The miRNA Venn diagram is shown in Figure 2E. Based on the principle that the expression level of mature miRNAs in the six samples was not zero, 293 miRNAs were expressed in the samples from the same group. Moreover, 169 miRNAs were expressed in all the samples of the group. Among them, seven miRNAs were specifically expressed in the Ro group and 117 miRNAs were expressed in the CK group.

Differentially expressed miRNAs were analyzed, and the number of reads obtained by sequencing was normalized to obtain the miRNA expression levels. Differentially expressed miRNAs were screened using a threshold of $p \leq 0.05$. A total of 74 differentially expressed miRNAs were detected, of which 22 were upregulated and 52 were downregulated (Figures 3A,B). The expression levels of peu-MIR2916-p5_1ss5AG in the upregulated miRNAs and mdm-miR166a_L+2R-2, mtr-miR166c, and mtr-miR396b-5p_1ss7AG in the downregulated miRNAs were higher, which may have played an important role in the plant response to ginsenoside Ro stress.

Target gene prediction and analysis of differential miRNAs

TargetFinder (Dai et al., 2018) was used to predict the target genes of the miRNAs with significant differences. The functions in which the predicted target genes were enriched in were analyzed using Gene Ontology (GO) and the Kyoto Encyclopedia of Genes and Genomes (KEGG). The results

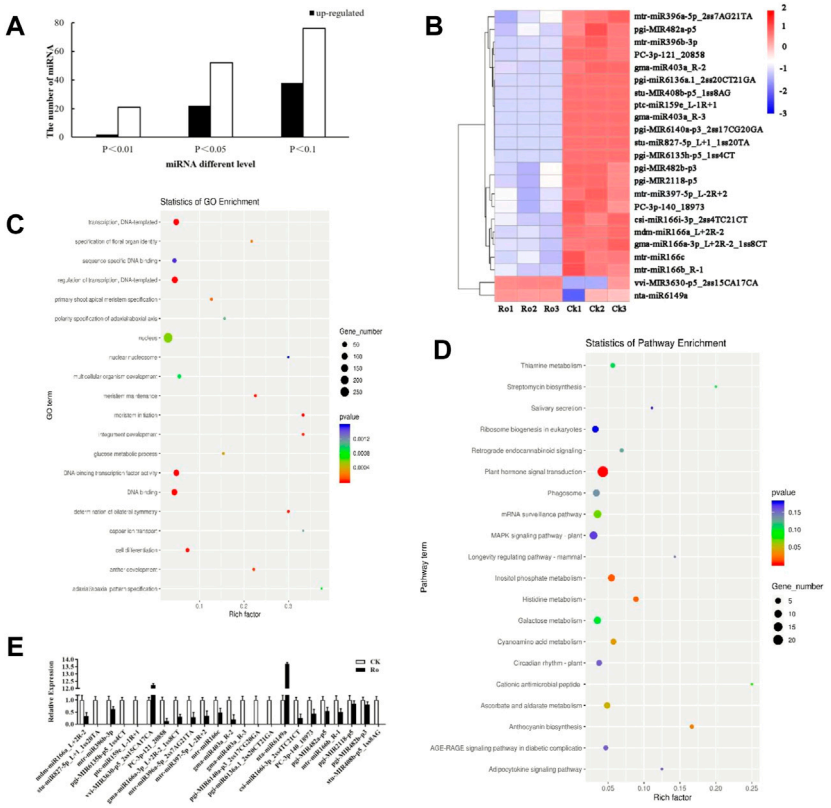

FIGURE 3
Results and validation of the differential miRNA analysis. Number of the differentially expressed miRNAs of *P. ginseng* hairy roots **(A)**. Heatmap of the differentially expressed miRNAs of *P. ginseng* hairy roots **(B)**. GO functional enrichment analysis of miRNA target genes in ginseng under Ro stress **(C)**. KEGG functional enrichment analysis of miRNA target genes in ginseng under Ro stress **(D)**. Verification of the fluorescence and quantitative PCR results of miRNA **(E)**.

of the GO functional annotation analysis of the miRNA target genes are shown in Figure 3C. The target genes were mainly involved in the auxin-activated signaling pathway, multicellular organism development, cell differentiation, meristem initiation, and other processes, which indicated that the miRNAs annotated to the target genes may be involved in or correspond to cell differentiation, hormone levels, and other processes. The results of the KEGG functional annotation analysis of the miRNA target genes are shown in Figure 3D. The target genes were mainly involved in plant hormone signal transduction, terpenoid backbone biosynthesis, and circadian rhythm-plant. In the following sections of this paper, we focus on the hormone synthesis pathway. The miRNA sequencing results were verified by a real-time polymerase chain reaction (RT-PCR) analysis, and the 23 differentially expressed miRNAs were subjected to quantitative fluorescence testing. The miRNA expression patterns were consistent with the sequencing results (Figure 3E), but the sequencing results were more accurate.

Transcriptome sequencing of ginseng hairy roots

The RNA quality results for the ginseng hairy roots are shown in Supplementary Table S1. The total mass of the six samples was greater than 2 μg, and the OD 260/280 was between 1.96 and 2.24. The Agilent Bioanalyzer 2100 was used to analyze the total RNA of the six ginseng hairy root samples. In the quantitative detection, the RNA integrity numbers (RINs) were all >7, which indicated that the integrity of the RNA met the standard and requirements needed for subsequent experiments. The sequencing data has been uploaded to the NCBI database and may be found using the following link (https://www.ncbi.nlm.nih.gov/geo/query/acc.cgi?acc=GSE212097) and accession number GSE212097.

Six cDNA libraries that had been prepared from the ginseng hairy roots were sequenced using an Illumina HiSeq 4000 platform. In total, 83,77,40,362 raw reads were generated (Supplementary Table S2). After removing joint, duplicate, and low-quality reads, the Ro (Ro1, Ro2, and Ro3) and CK (CK1,

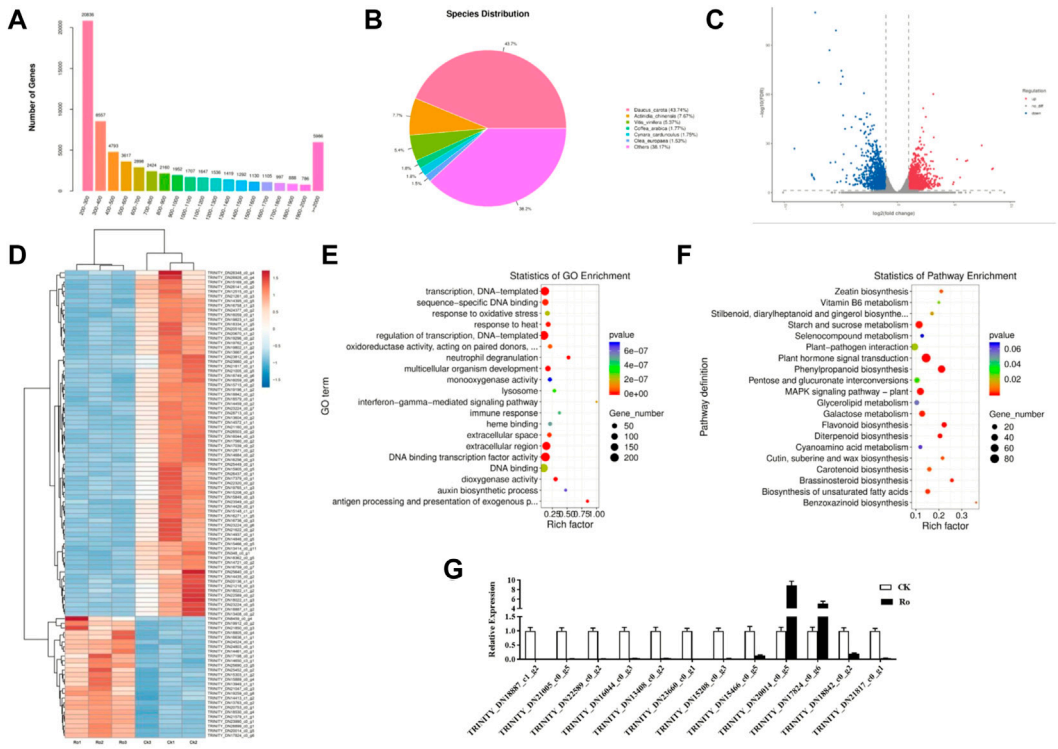

FIGURE 4
Differential mRNA analysis results and validation. Distribution of unigene lengths in the ginseng callus transcriptome; *X*, length of the unigene; *Y*, number of unigenes **(A)**. Non-redundant homologous species distribution **(B)**. Comparison of the differential genes between the Ro and CK treatments **(C)**. Hierarchical analysis of the differentially expressed genes (DEGs) **(D)**. GO enrichment analysis of the DEGs **(E)**. KEGG enrichment analysis of the DEGs **(F)**. Comparison of the RNA-seq and qPCR results **(G)**.

CK2, and CK3) groups comprised a total of 63,72,41,134 reads. The clean reads were determined to be those with Q20 values greater than 98%, Q30 values greater than 93%, and a GC content between 44.19 and 49.33%.

Because the reference genome of ginseng has many repetitive sequences, it is difficult to compare and complete its genome sequence. We therefore used an unparalleled ginseng transcriptome for the comparative analysis. Trinity software was used for the *de novo* assembly of all the clean reads of the six libraries into contigs. The reads were reflected contigs, redundancy was removed, and the longest transcript was defined as the unigene. In total, 65,730 unigenes were obtained with an N50 length of 1,404 nt. The sequencing and assembly results are shown in Supplementary Table S3, and the length distributions of all the unigenes are shown in Figure 4A. Most of the unigenes were 200–300 nt in length. As the length of the unigenes increased, their number decreased, except when they were longer than 2,000 nt.

DIAMOND software was used to obtain functional annotations, and the non-redundant, GO, KEGG, Pfam, Swiss-Prot, and eggNOG databases were compared. The functional annotation results are shown in Table 2. All 65,730 unigenes were annotated to the database, with an annotation ratio of 100%. Among them, 26,381 unigenes could be annotated to the GO database and accounted for 53.04%; 13,518 unigenes could be annotated to the KEGG database and accounted for 27.18%; 22,009 unigenes could be annotated to the Pfam database and accounted for 44.25%; 21,185 unigenes could be annotated to the Swiss-Prot database and accounted for 42.29%; 29,451 unigenes could be annotated to the eggNOG database and accounted for 59.21%; and 30,925 unigenes could be annotated to the non-redundant database and accounted for 62.17%. The quantitative comparison analysis revealed that the highest number of unigenes could be annotated to the non-redundant database, whereas the lowest number could be annotated to the KEGG database.

The non-redundant annotation results showed that 35,431 unigenes were annotated to the non-redundant database (Figure 4B). The most annotated species was carrot (*Daucus carota*) with a total of 15,497 unigenes (approximately 43.74%), which represented a source abundance of 38.17%. As for the other species, the homologous species of kiwifruit (*Actinidia chinensis*), grape (*Vitis vinifera*), coffee seed (*Coffea*

TABLE 2 Functional annotation results.

Annotated database	Number of notes	Note proportion (%)
All	65,730	100.00
GO	29,890	45.47
KEGG	23,835	36.26
Pfam	25,921	39.44
Swiss-Prot	24,274	36.93
eggNOG	33,657	51.20
NR	35,431	53.90

canephora), and olive (*Olea europaea*) accounted for 7.67%, 5.37%, 1.77%, and 1.53% of the source abundance, respectively. Thus, the ginseng hairy-root tissue exhibited the greatest homology with carrots.

Functional analysis and annotation of differentially expressed genes

To explore the molecular mechanisms underlying the response of ginseng hairy roots to ginsenoside Ro stress, a differential comparison analysis of the genes in the six transcriptome libraries was performed to obtain the differentially expressed genes (DEGs). The expression of the unigenes was calculated by transcripts per kilobase of exon model per million mapped reads. The Ro group was compared with the CK group (Ro vs. CK). The resulting differential genes between the treatment and control groups were defined as DEGs ($p \leq 0.05$), which were analyzed using GO and KEGG enrichment analyses. As shown in Figures 4C,D 2,837 differentially expressed unigenes were identified in the Ro vs. CK comparison groups, including 1,380 upregulated and 1,457 downregulated unigenes. This indicated that the Ro treatment affected the expression of related genes in the ginseng hairy-root tissue and may be one of the main factors affecting the growth and development of ginseng hairy roots.

The results of the GO enrichment analysis of the DEGs are shown in Figure 4E. In the Ro vs. CK comparison groups, the DEGs were mainly involved in transcription, DNA-templated, transcriptional regulation, extracellular region, transcription factor activity, sequence-specific DNA binding activity, DNA binding transcription factor activity, DNA binding, response to oxidative stress, response to heat, multicellular organism development, and other processes. The results of the KEGG enrichment analysis of the DEGs are shown in Figure 4F. In the Ro vs. CK comparison groups, the DEGs were mainly involved in starch and sucrose metabolism, plant hormone signal transduction, plant–pathogen interaction, phenylpropanoid biosynthesis, glycerolipid metabolism, flavonoid biosynthesis, and other processes. The results indicated that phytohormone signal transduction played a greater role in the Ro treatment group.

The enrichment analyses of the DEGs revealed that the ginsenoside Ro treatment significantly affected the differential expression of the ginsenosides and genes regulating the hormone synthesis-related signaling pathway. The structures and biosynthesis of triterpenoid saponins are complex and diverse, and their key synthesis enzymes are rich; therefore, these compounds have received much attention in recent studies. Cytochrome P450 (CYP450) is an important enzyme involved in this process. As shown in Table 3, five genes related to CYP450 oxidase synthesis, including CYP82C4 and CYP87A3, were upregulated (TRINITY_DN15708_c0_g5 and TRINITY_DN25396_c0_g), and three genes were downregulated (TRINITY_DN22257_c0_g1, TRINITY_DN26346_c1_g1 and TRINITY_DN26346_c1_CK). The differential expression of the genes of key enzymes was observed in the plant hormone synthesis pathway, including three ARF7 and EFM genes (TRINITY_DN15428_c0_g1, TRINITY_DN15651_c0_g5, and TRINITY_DN22370_c0_g1) that were upregulated and two XTH23 and ZOX1 genes (TRINITY_DN13852_c0_g1 and TRINITY_DN15971_c0_g1) that were downregulated. This indicated that the Ro treatment regulated the expression of ginsenosides and hormone-related pathway genes.

To verify the reliability of the transcriptome data, 12 DEGs were randomly selected for a qPCR analysis to compare the expression levels between the samples. The results are shown in Figure 4G. The qPCR results were similar to the RNA-seq data, and the expression trends were consistent, which verified the reliability of the RNA-seq results.

Combined mRNA and miRNA analysis

Using the ginseng transcriptome sequencing results as a reference, the differential miRNAs and predicted target genes were jointly analyzed, and a network diagram was constructed (Figure 5). miRNA plays a negative regulatory role. In the process of target gene prediction, one miRNA was often targeted to multiple target genes, such as mtr-miR171d and mtr-

TABLE 3 Differentially expressed genes related to ginsenosides and hormones.

Gene name	Gene ID	Swiss-Prot description	Ro TPM	CK TPM	Regulation
CYP82C4	TRINITY_DN22257_c0_g1	Cytochrome P450	37.32	78.79	Down
	TRINITY_DN26346_c1_g1	Cytochrome P450	35.87	88.65	Down
	TRINITY_DN15708_c0_g5	Cytochrome P450	30.80	12.26	Up
	TRINITY_DN26346_c1_g2	Cytochrome P450	16.17	36.10	Down
CYP87A3	TRINITY_DN25396_c0_g1	Cytochrome P450	19.22	9.48	Up
XTH23	TRINITY_DN13852_c0_g1	Plant hormone signal transduction	67.52	193.00	Down
	TRINITY_DN15428_c0_g1	Plant hormone signal transduction	79.97	39.10	Up
ARF7	TRINITY_DN15651_c0_g5	Plant hormone signal transduction	41.51	15.43	Up
EFM	TRINITY_DN22370_c0_g1	Plant hormone signal transduction	60.84	27.92	Up
ZOX1	TRINITY_DN15971_c0_g2	Zeatin biosynthesis	14.05	30.77	Down

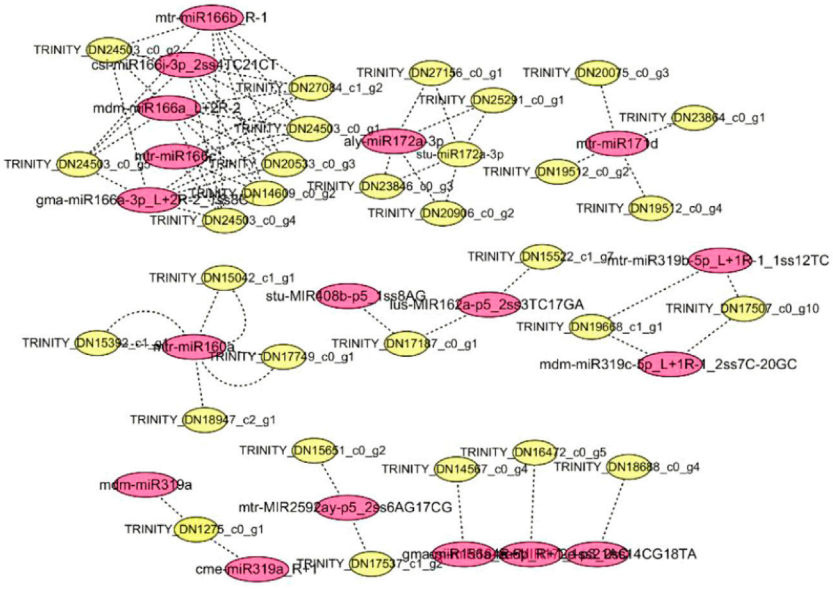

FIGURE 5
Networks of ginsenoside Ro-responsive miRNAs and their targets in ginseng. Red indicates miRNA; yellow indicates mRNA.

miR166b_R-1. Some miRNAs may have common target genes, such as aly-miR172a-3p and stu-miR172a-3p, which not only shows the diversity and specificity of miRNA target genes, but also indicates that miRNAs encoding the same target gene are involved in synergistic effects during plant growth and development. As shown in Figure 5, two known miRNAs (aly-miR172a-3p and mdm-miR166a_L+2R-2) had more predicted target genes, indicating that they play an important role in ginseng growth and the corresponding phytohormone signaling process. Through a combined analysis with mRNA, it was found that the target gene of ptc-miR156k_L+1, mtr-miR156b-5p, gma-miR156a_R+1, and mtr-miR156e was TRINITY_DN14567_c0_g4. TRINITY_DN14567_c0_g4 is a gene in the plant hormone signal transduction pathway. The mRNA sequencing analysis showed that the expression of the ZOX1 gene for zeatin synthesis was downregulated, the accumulation of ABA was inhibited, and the accumulation of ginsenosides decreased. The ZOX1 gene has an important relationship with ABA synthesis. Ginseng targets genes in the plant hormone signal transduction pathway through ptc-miR156k_L+1, mtr-miR156b-5p, gma-miR156a_R+1, and mtr-miR156e, thereby inhibiting their expression and reducing the expression of key enzyme genes in the hormone synthesis pathway. Their expression reduces the accumulation of

phytohormones, which in turn affects the biosynthesis of ginsenosides. All four miRNAs were negatively correlated with mRNA, indicating that ptc-miR156k_L+1, mtr-miR156b-5p, gma-miR156a_R+1, and mtr-miR156e were most likely involved in the response to disorders relating to the continuous cropping of ginseng and the regulation of ginsenoside synthesis.

Discussion

Terpenoids have always been important allelopathic substances and represent the main area of research on allelopathy. Ladhari identified two new dammarane-type triterpenoids and found that they inhibited seed germination and seedling growth in Amphora (Ladhari et al., 2020). The triterpenoid ginsenoside Rg1 has further been found to significantly inhibit the growth of Chinese cabbage seedlings (Hongrui et al., 2019). Furthermore, Yan *et al.* found that *P. notoginseng* releases saponins and other allelopathic substances into the soil through the decomposition of residues and root secretions (Yang et al., 2015). Plant roots secrete allelopathic substances into the soil to create a growth environment for pathogenic microorganisms and induce the growth of corresponding pathogenic microorganisms, thereby resulting in continuous cropping disorders (Adamczyk et al., 2021). *P. notoginseng* can release allelopathic substances such as phenolic acids and saponins into the soil through body decay and root secretion, which result in the death of root tissues (Yang et al., 2015). Ginsenoside Rg1 has further been found to significantly affect ginseng seed germination and seedling growth (Li and Lianxue, 2020). We found that the exogenous addition of different concentrations of ginsenoside Ro produced different degrees of the inhibition of the monthly multiplication rate of ginseng hairy roots. The Ro 0.5 group also exerted a significant inhibitory effect on the visual properties and viability of the ginseng hairy roots. The hairy roots gradually turned from white to dark yellow and brown and exhibited the worst growth state out of the treatment groups. All of the root-tip cells were stained red, which indicated that the cells had been damaged to a greater extent. Ginsenosides and other substances exert self-toxic effects on ginseng plants. Ginsenoside allelochemicals can degrade and shed ginseng fibrous root cells, and when the content of ginsenosides in ginseng plants decreases, the growth of ginseng is inhibited. These findings are consistent with those in this study (Bian et al., 2020; Wu et al., 2016; Zhan and Wang, 2021).

Phytohormones are organic compounds that are produced in plants that are usually transported from the synthesis site to the active site where they can regulate their physiological processes in trace amounts (Cong et al., 2016). Endogenous hormones play an important role in the regulation of physiological levels and gene expression when plants face changes in the external environment during their growth and development (Zhang et al., 2020). In this study, the amounts of the endogenous hormones IAA and SA in the hairy roots of ginseng increased significantly under Ro stress by 10.0% and 9.6%, respectively, compared with those in the CK group. However, the accumulation of ABA and its synthetic pathway intermediates was inhibited, as was the accumulation of the endogenous hormone JA and its synthetic pathway intermediates. IAA is a physiological response involved in identifying signals, inducing the expression of response genes, and regulating the corresponding physiological responses of the body during the early stages of plant growth and development (Qu et al., 2021; Zazimalova and Napier, 2003). SA plays an important role in plant growth and development, fruit ripening, and the stress response; however, environmental stress can promote SA accumulation in *Arabidopsis* and wheat (Cooper et al., 2018; Kosova et al., 2012). ABA regulates the production of secondary metabolites through a variety of factors, such as its synthesis pathway, signal transduction, and the interaction between hormones, whereas drought stress can induce a massive accumulation of ABA, thereby leading to stomatal closure and reduced water loss (Zhang et al., 2010,2013). JA and its methyl ester-based jasmonates comprise a class of plant growth regulators that play important roles in improving plant stress resistance and morphogenesis (Avanci et al., 2010). In this study, we speculated that ginseng hairy roots resist external environmental stimuli by regulating the biosynthesis of endogenous hormones. IAA, SA, JA, and ABA may be important endogenous signaling molecules in hairy ginseng roots that are involved in the response to stress induced by ginsenoside Ro.

In recent years, the application of transcriptomics to study medicinal plants has increased gradually. Medicinal plants that have undergone transcriptome sequencing include *P. ginseng* (Liu et al., 2016), *Panax quiquefolium* L. (Wu et al., 2013), *Salvia miltiorrhiza Bunge* (Gao et al., 2014), *Bupleurum chinense* (Sui et al., 2011), *Glycyrrhiza uralensis Fisch.* (Li et al., 2010), *Gastrodia elata Bl.* (Zeng et al., 2017), and *Dendrobium officinale Kimura et Migo.* (Shen et al., 2017). Through transcriptome sequencing, important progress has been made in the development of new gene mining, functional predictions, and metabolic pathways in medicinal plants. CYP450 is an ancient supergene family in plants. It partakes in a wide range of catalytic activities and is involved in plant biosynthesis and biological detoxification. CYP450 can catalyze the synthesis of compounds affecting plant growth and development, such as terpenoids, flavonoids, steroid alkaloids, alkaloids, and phenylpropanoids (Lee et al., 2010; Morikawa et al., 2006). Loss-of-function mutations in CYP72A69 can convert triterpenoid saponins from unwanted group A saponins to beneficial DDMP saponins (Yano et al., 2017). The CYP82 gene is moderately homologous to plant flavonoid hydroxylase, which is involved in the plant defense response and wound repair (Frank et al., 1996). In this study, we found that

out of five genes (four copies of the CYP82C4 gene and one copy of the CYP87A3 gene) related to CYP450 oxidase synthesis, two genes were upregulated, and three were downregulated. The CYP82C4 and CYP87A3 genes may play an important role in ginsenoside Ro stress. Phytohormones play key regulatory roles in plant stress physiology and signal transduction in plant responses to biotic and abiotic stressors. The XTH23 gene can improve the resistance of plants to drought by increasing the amount of proline and superoxide dismutase and reducing the damage in plant cells under stress (Zhang et al., 2022). ARF and EFM are important transcription factors in plant hormone synthesis and play an important role in the plant response to environmental changes (Wu et al., 2011). In this study, we excavated the differential expression of four key enzyme genes in the plant hormone synthesis pathway. Three genes were upregulated, and one gene was downregulated. The XTH23, ARF, and EFM genes may further play an important role in ginsenoside Ro stress.

As the main means of regulation at the post-transcriptional level, miRNAs have become a popular topic in research on secondary metabolism in medicinal plants. miRNAs can regulate plant development and stress responses and have gradually become the focus of research on plant metabolic processes (Kidner and Martienssen, 2005; Owusu et al., 2021). Currently, 29 ginseng miRNAs have been published in the miRBase database (Wu et al., 2015). miRNA156 is one of the core members of the plant miRNA family and one of the most evolutionarily conserved miRNAs, which have been studied extensively in a variety of plants (Ma et al., 2021). miRNAs also play an important role in regulating the synthesis of plant secondary metabolites. The overexpression of miRNA156A can lead to increased levels of Dihydrofl avonol 4-reductase (DFR), which promotes anthocyanin biosynthesis (Gao et al., 2018). miRNA156 plays a role in *Arabidopsis* sesquiterpene biosynthesis and promotes sesquiterpene biosynthesis in the patchouli plant (Yu et al., 2015). miR156 targets 1-deoxy-D-xylose-5-phosphate synthase (1-deoxy-D-xylulose-5-phosphate synthase; DXS), which is involved in carotenoid synthesis in *Lycium barbarum* (Zeng et al., 2015). The mRNA sequencing analysis showed that the expression of the ZOX1 gene for zeatin synthesis was downregulated, the accumulation of ABA was inhibited, and the accumulation of ginsenosides decreased. The ZOX1 gene has an important relationship with ABA synthesis. The auxin-responsive factor ARF plays an important role in the response of plants to changes in the external environment, and JA and auxin are involved in the regulation of miRNA156 (Jerome et al., 2020). The upregulation of the ARF gene in ginseng in response to Ro stress affects the biosynthesis of the phytohormone JA, which is involved in the regulation of miRNA156. Using the results of the mRNA sequencing analysis as a reference, a joint analysis with mRNA was performed and revealed that the target gene of ptc-miR156k_L+1, mtr-miR156b-5p, gma-miR156a_R+1, and mtr-miR156e was TRINITY_DN14567_c0_g4, which is a gene in the plant hormone signal transduction pathway. Ginseng targets genes in the plant hormone signal transduction pathway through ptc-miR156k_L+1, mtr-miR156b-5p, gma-miR156a_R+1, and mtr-miR156e, thereby inhibiting their expression and reducing the expression of key enzyme genes in the hormone synthesis pathway. Their expression reduces the accumulation of phytohormones, which in turn affects the biosynthesis of ginsenosides.

Conclusion

The results of this study indicate that the growth of ginseng hairy roots is significantly inhibited by Ro-induced stress (0.5 mg/L). The Ro stress also induced root-tip cell injury, which promoted the accumulation of the endogenous hormones IAA and SA and inhibited the accumulation of ABA and JA. Moreover, the accumulation of ginsenosides (except Rg3) was significantly inhibited under Ro stress. The mRNA analysis of the Ro (0.5 mg/L) and CK groups showed that the DEGs were mostly concentrated in the hormone signal transduction pathway. ARF7 and EFM were upregulated, whereas XTH23 and ZOX1 were downregulated, indicating that these genes are important candidates for hormone-responsive continuous cropping disorders. Furthermore, 74 differentially expressed miRNAs were identified from the miRNA sequencing analysis, of which 22 were upregulated and 52 were downregulated. The target gene of ptc-miR156k_L+1, mtr-miR156b-5p, gma-miR156a_R + 1, and mtr-miR156e was TRINITY_DN14567_c0_g4 in the plant hormone signal transduction pathway. These miRNAs were negatively correlated with mRNA, indicating their likely involvement in the ginseng response to continuous cropping disorders and the regulation of ginsenoside synthesis. Our findings provide a useful platform for overcoming the obstacles to the continuous cropping of ginseng and suggest new insights into the genetic engineering of plant stress responses.

Materials and methods

Plant materials and experimental design

Hairy roots have high genetic stability and fast reproduction rates. The hairy roots of *P. ginseng* were induced from the roots of ginseng plants (variety Erma Ya) that were obtained from the Key Laboratory of Chinese Medicine Planting and Development at the Changchun University of Chinese Medicine, Changchun, China. All the hairy roots were derived from the same ginseng root to ensure the uniformity of the test materials. The hairy roots of the ginseng group were selected as the experimental material.

The hairy roots of ginseng were first inoculated into 1/2 MS solid medium. After they had grown stably, 1 cm of the tips of the roots were transferred to liquid media. Six different concentrations of ginsenoside Ro aqueous solutions were prepared so that the final concentrations of the saponin Ro contained in the media were 0.002, 0.001, 0.05, 0.25, 0.5, and 1 mg/L. Distilled water was used for the control group. The control and treatment groups were set up with three biological replicates for each concentration dose and cultured continuously for 30 days. Hairy root samples were collected on day 30. A few of the samples were immediately frozen in liquid nitrogen and stored at −80°C for miRNA and transcriptome sequencing, and another sample was directly ground in a mortar and used for the extraction and analysis of ginsenosides.

Determination of biomass

The growth of the hairy roots was measured using the weighing method. First, the liquid medium attached to the surface of the hairy roots was sucked dry, fresh weight was measured, and monthly multiplication ratio of the hairy roots was calculated. The calculation formula was as follows: monthly multiplication multiple = (harvest amount − inoculum amount)/inoculum amount × 100%. The morphological characteristics of the hairy roots were observed continuously for 30 days, and the shape, color, water content, and other data were recorded.

Determination of cell viability

The hairy roots that had been cultured for 30 days were used to determine cell viability. The root tips of each treatment group were rinsed three times with deionized water and placed in a culture medium mixed with fluorescein diacetate and propidium iodide staining solution. They were then incubated for 40 min. The cells were stained in the dark and rinsed with normal saline for 5 min each to remove excess dye. Slides were mounted with an anti-fluorescence quenching mounting solution and placed under a laser confocal microscope for imaging. The excitation and detection wavelengths were 485 and 530 nm, respectively.

Determination of ginsenoside content

The ginsenoside content in the ginseng hairy roots was detected using ultra-high-performance liquid chromatography tandem triple quadrupole mass spectrometry. The sample preparation method was as follows: A 1.1-g sample of the ginseng hairy roots was weighed accurately and placed into a conical flask containing 80 ml of 80% methanol, followed by ultrasonic oscillation for 0.5 h. This was repeated three times, and the supernatant was combined after centrifugation. Two supernatants were combined, concentrated under reduced pressure on a rotary evaporator to remove the methanol, and extracted with chloroform three times. The chloroform layer was then discarded, and the supernatants were again extracted three times with saturated n-butanol and water. The n-butanol layer was then collected and combined. Finally, the supernatant was subjected to a nitrogen blow-dry, diluted to 1 ml with 80% chromatographic methanol, filtered through a 0.22-μm filter membrane, and stored at 4°C for later use.

The liquid chromatography separation conditions were as follows: Thermo C18 column (50 mm × 3 mm, 1.7 μm), mobile phase with 0.1% formic acid (A)-acetonitrile (B), gradient elution for 0–5 min, 19% B; 5–29 min, 19%–25% B; 29–72 min, 25%–40% B; 72–77 min, 40%–90% B; 77–80 min, 90% B; 80–83 min, 90%–19% B; 83–88 min, 19% B; flow rate of 0.2 ml/min, column temperature of 35°C, sample chamber temperature of 4°C, and injection volume of 5 μl. The mass spectrometry detection conditions were as follows: electrospray ionization, negative ion mode, and multiple reaction monitoring; mass scanning range m/z 100–1,500; spray voltage: 2,500 V; sheath gas pressure: 35 arb; auxiliary gas pressure: 10 arb; transfer capillary temperature: 350°C; nebulizer temperature: 300°C. Notoginsenoside R1, Rg1, Re, Rf, Rg2, Rh1(S), F3, Rb1, Rc, Ro, Rb2, Rd, F2, and Rg3 standards were used to establish a standard curve as shown in Supplementary Table S4. The extracted ion chromatogram is shown in Supplementary Figure S1.

Determination of the endogenous hormone content

The endogenous hormone content in the hairy roots of the ginseng was determined using liquid chromatography with tandem mass spectrometry. The hairy root samples were pre-frozen in an ultra-low-temperature freezer then ground using a grinder at a speed of 30 Hz for 1 min to form a powder. The powder (50 mg) was weighed, an appropriate amount of the internal standard was added, and 1 ml of methanol/water/formic acid (15:4:1) was used as the extraction solvent. The extract was concentrated, reconstituted with 100 μl of an 80% methanol/water solution, passed through a 0.22-μm filter membrane, and placed in a liquid phase bottle for mass spectrometry. The liquid chromatography conditions were as follows: Waters ACQUITY UPLC HSS T3 C18 column (1.8 μm, 100 mm × 2.1 mm). Mobile phase A: 0.04% acetic acid in water; phase B: acetonitrile (0.04% acetic acid). Gradient elution program: 0–1.0 min A/B 95:5, 1.0–8.0 min A/B 95:5, 8.0–9.0 min A/B 5:95, 9.0–9.1 min 5:95, 9.1–12.0 min 95:5, 12.0 min 95:5. The flow rate was 0.35 ml/min, column temperature was 40°C, and injection volume was 2 μl. The mass spectrometry conditions were as follows: electrospray ionization temperature of 550°C, mass spectrometry voltages of 5,500 and −4,500 V in positive and negative ion modes,

respectively, and a curtain gas pressure of 35 psi. In the Q-Trap 6500+, each ion pair was scanned according to the optimized declustering potential and collision energy. All of the samples were measured three times, and the average values were compared.

mRNA library construction and sequencing

Total RNA was extracted from the ginseng hairy-root tissue samples according to the manufacturer's instructions for the TRIzol reagent (Invitrogen, CA, United States) and purified using DNase. We used a NanoDrop 2000 nucleic acid UV spectrophotometer to measure the RNA sample purity at OD 260/280 between 1.8 and 2.2. An Agilent Bioanalyzer 2100 was used to measure the total RNA amount and purity (25 S:18 S ≥ 1.0; total RNA ≥2 μg; RIN value >7.0). Qualified RNA was used to construct an RNA library. Poly-A-tailed mRNA was enriched from the total RNA using magnetic beads with oligo (dT). By adding a fragmentation reagent fragmentation buffer, the extracted mRNA was randomly fragmented into small fragments of approximately 200 bp. Using the fragmented mRNA as a template, one-strand cDNA was synthesized with six-base random hexamers, followed by the addition of buffer, dNTPs, RNase H, and DNA polymerase I to synthesize two-strand cDNA to form a stable double strand. The double-stranded product was purified using AMPure XP Roads, and the DNA cohesive end was repaired to blunt ends using T4 DNA polymerase and Klenow DNA polymerase, followed by the ligation of base A at the 3′ end to ligate the Y-linker. Fragment selection was performed using AMPureXP Roads, and the sorted products were used for PCR amplification and purification to obtain the final library. After the library had been qualified, the Illumina HiSeq 4000 system at LC-BIO (Hangzhou, China) was used for sequencing. The sequencing read length was 2 bp × 150 bp (double-ended) (PE150).

De novo assembly, unigene annotation, functional classification, and differential expression analysis

Cutadapt and Perl scripts were used in-house to remove the reads that contained adaptor contamination, low-quality bases, and undetermined bases (Martin, 2011). Sequence quality was assessed using FastQC (http://www.bioinformatics.babraham.ac.uk/projects/fastqc/) and the Q20, Q30, and GC content of the clean data. All of the downstream analyses were based on the high-quality clean data. The *de novo* assembly of the transcriptome was performed using Trinity 2.4.0 (Grabherr et al., 2011), which groups transcripts into clusters based on the shared sequence content. Such transcript clusters are loosely referred to as "genes." The longest transcript in the cluster was chosen as the "gene" sequence, or unigene. All of the assembled unigenes were aligned against the non-redundant protein database (http://www.ncbi.nlm.nih.gov/) and the GO (http://www.geneontology.org), Swiss-Prot (http://www.expasy.ch/sprot/), KEGG (http://www.genome.jp/kegg/), and eggnog (http://eggnogdb.embl.de/) databases using DIAMOND (Buchfink et al., 2015) with a threshold of Evalue <0.00001. The gene and unigene expression levels (in transcripts per kilobase of exon model per million mapped reads) were quantitatively analyzed using Salmon software. After obtaining the number of gene sequences, the R package edgeR was used to analyze the differences in gene expression between the samples using log2 (fold change) > 1 or log2 (fold change) < −1 as the screening standard ($p < 0.05$). The gene expression was analyzed, and the functions and pathways in which the DEGs were enriched were assessed using GO and the KEGG (Mortazavi et al., 2008; Patro et al., 2017; Robinson et al., 2010).

miRNA library construction and sequencing

The TruSeq Small RNA Sample Prep Kit (Illumina, San Diego, CA, United States) was used to prepare the miRNA sequencing library. We obtained small RNA fragments (15–50 nt) and mixed the total RNA with an equal volume of 2 × loading buffer mix and incubated the mixture at 65°C for 5 min to eliminate the interference of secondary structures in the RNA. We then used 15% TBE polyacrylamide gel electrophoresis (TBE PAGE) for 15 min to separate the total RNA bands and perform further cutting and purification. This allowed us to obtain small RNA fragments with a length of 15–50 nt. T4 RNA ligase 2 from NEB Company (United States) was used to connect the 3′-end adapter to the small RNA fragments. TBE PAGE (15%) was then used for 15 min to separate the RNA bands, which were further cut and purified to obtain small RNA fragments with a length of 41–76 nt. T4 RNA ligase 2 from NEB Company was further used to connect the 5′-end adapter with the small RNA fragments, after which 15% TBE PAGE was used for 15 min to separate the RNA bands, which were further cut and purified to obtain small RNA fragments with a length of 64–99 nt. For the reverse transcription reaction and PCR amplification, we used the SuperScript II Reverse Transcriptase system according to the manufacturer's instructions with incubation in a preheated thermal cycler at 50°C for 1 h to obtain reverse-transcribed single-stranded cDNA. DNA polymerase and amplification primers were cyclically amplified to obtain a cDNA library. To purify the small RNA library, we performed 6% Novex TBE PAGE for 1 h at 145 V and cut the fragment region to a length of 80–115 bp. After the obtained fragment had been eluted and purified, the cDNA was further quantified using a NanoDrop nucleic acid and protein concentration analyzer. The quality of the

library was checked using Agilent 2100 and qPCR. The Illumina HiSeq 2500 was used to sequence the qualified library. The sequencing read length was 1 bp × 50 bp (single-ended).

Analysis of the differentially expressed miRNAs and target gene prediction

The differential expression of the miRNAs based on normalized deep-sequencing counts was analyzed selectively using Fisher's exact test, the Chi-squared 2 × 2 test, Chi-squared nXn test, Student's *t*-test, or an analysis of variance based on the experimental design. The significance threshold was set to 0.01 and 0.05 in each test. To predict the genes targeted by the miRNAs, computational target prediction algorithms (PsRobot, v1.2) were used to identify the miRNA binding sites. The GO terms and KEGG pathways of the most abundant miRNA targets were also annotated.

Verification by qRT-PCR

To verify the reliability of the obtained transcriptome and miRNA data, RT-PCR was performed on 13 randomly selected DEGs in the transcriptome data and 10 differentially expressed miRNAs with different expression levels. Using the actin gene as an internal reference, primers were designed with Primer 5.0 software and synthesized by Shanghai Sangon Bioengineering Co., Ltd. The primer sequences are shown in Supplementary Tables S5, S6.

Data availability statement

The datasets presented in this study can be found in online repositories. The names of the repository/repositories and accession number(s) can be found in the article/Supplementary Material.

Author contributions

XM and TZ conceived and designed the experiments. TZ performed most of the experiments, analyzed the data, and completed the first draft. CC worked with TZ to perform the experiments. All authors have read and approved the manuscript.

Funding

The work was financially supported by the National Natural Science Foundation of China (82204556, 82073969, 82204558), Jilin Province Science and Technology Development Plan (YDZJ202101ZYTS012), The Fifth Batch of Jilin Province Youth Science and Technology Talents Support Project (QT202117), and the Major Science and Technology Project of Jilin Province, China (20200504003YY).

Acknowledgments

The authors thank CC and TZ from Changchun University of Chinese Medicine for their financial support.

Conflict of interest

The authors declare that the research was conducted in the absence of any commercial or financial relationships that could be construed as a potential conflict of interest.

Publisher's note

Supplementary material

The Supplementary Material for this article can be found online at: https://www.frontiersin.org/articles/10.3389/fbioe.2022.1006386/full#supplementary-material

References

Adamczyk, M., Ruthi, J., and Frey, B. (2021). Root exudates increase soil respiration and alter microbial community structure in alpine permafrost and active layer soils. *Environ. Microbiol.* 23 (4), 2152–2168. doi:10.1111/1462-2920.15383

Avanci, N. C., Luche, D. D., Goldman, G. H., and Goldman, M. H. (2010). Review Jasmonates are phytohormones with multiple functions, including plant defense and reproduction. *Genet. Mol. Res.* 9 (1), 484–505. doi:10.4238/vol9-1gmr754

Bian, X., Xiao, S., Zhao, Y., Xu, Y., Yang, H., and Zhang, L. (2020). Comparative analysis of rhizosphere soil physiochemical characteristics and microbial communities between rusty and healthy ginseng root. *Sci. Rep.* 10 (1), 15756. doi:10.1038/s41598-020-71024-8

Buchfink, B., Xie, C., and Huson, D. H. (2015). Fast and sensitive protein alignment using DIAMOND. *Nat. Methods* 12 (1), 59–60. doi:10.1038/nmeth.3176

Chen, C., Liu, J., Wang, Y., Shi, Y., and Xu, S. (2006). Allelopath of ginseng rhizosphere and its effect on germination of essd. *J. Jilin Agric. Univ.* 28 (05), 534–537. doi:10.13327/j.jjlau.2006.05.015

Chen, J., Zhou, Y., Zhang, Q., Liu, Q., Li, L., Sun, C., et al. (2020). Structural variation, functional differentiation and expression characteristics of the AP2/ERF gene family and its response to cold stress and methyl jasmonate in *Panax ginseng* C.a. Meyer. [Journal Article; Research Support, Non-U.S. Gov't]. *PLoS One* 15 (3), e0226055. doi:10.1371/journal.pone.0226055

Chen, Y. (2017). *Identification of microRNA and analysis of target genes in Changbai Mountain ginseng*. GuangZhou: GuangDong Pharmaceutical University. 硕士. Available at: https://kns.cnki.net/kcms/detail/detail.aspx?FileName=1017734667.nh&DbName=CMFD2018.

China Pharmacopoeia Commission (2020). *Pharmacopoeia of the people's Republic of China*. The medicine science and technology press of China.

Cong, Q., Zhang, Q., Song, L., Chen, Y., Cai, H., and Guo, C., (2016). Roles of phytohormones on cold response in plants. *J. Nucl. Agric. Sci.* 30 (03), 614–619.

Cooper, J. W., Hu, Y., Beyyoudh, L., Yildiz, D. H., Kunert, K., Beveridge, C. A., et al. (2018). Strigolactones positively regulate chilling tolerance in pea and in*Arabidopsis*. *Plant Cell Environ.* 41 (6), 1298–1310. doi:10.1111/pce.13147

Dai, X., Zhuang, Z., and Zhao, P. X. (2018). psRNATarget: a plant small RNA target analysis server (2017 release). *Nucleic Acids Res.* 46 (W1), W49–W54. doi:10.1093/nar/gky316

Fan, J., Wang, Y., You, Y., Ai, Z., Dai, W., Piao, C., et al. (2019). Fermented ginseng improved alcohol liver injury in association with changes in the gut microbiota of mice. *Food Funct.* 10 (9), 5566–5573. doi:10.1039/c9fo01415b

Frank, M. R., Deyneka, J. M., and Schuler, M. A. (1996). Cloning of wound-induced cytochrome P450 monooxygenases expressed in pea. *Plant Physiol.* 110 (3), 1035–1046. doi:10.1104/pp.110.3.1035

Gao, R., Gruber, M. Y., Amyot, L., and Hannoufa, A. (2018). SPL13 regulates shoot branching and flowering time in Medicago sativa. *Plant Mol. Biol.* 96 (1-2), 119–133. doi:10.1007/s11103-017-0683-8

Gao, W., Sun, H. X., Xiao, H., Cui, G., Hillwig, M. L., Jackson, A., et al. (2014). Combining metabolomics and transcriptomics to characterize tanshinone biosynthesis in Salvia miltiorrhiza. *BMC Genomics* 15, 73. doi:10.1186/1471-2164-15-73

Gao, Y., He, X., Wu, B., Long, Q., Shao, T., Wang, Z., et al. (2016). Time-Course transcriptome analysis reveals resistance genes of panax ginseng induced by cylindrocarpon destructans infection using RNA-seq. *PLoS One* 11 (2), e0149408. doi:10.1371/journal.pone.0149408

Grabherr, M. G., Haas, B. J., Yassour, M., Levin, J. Z., Thompson, D. A., Amit, I., et al. (2011). Full-length transcriptome assembly from RNA-Seq data without a reference genome. *Nat. Biotechnol.* 29 (7), 644–652. doi:10.1038/nbt.1883

Hongrui, Z., Yunxia, Z., Jihong, L., Yucong, S., Zhiming, G., and Zilong, Z. (2019). Effects of two kinds of saponins and panax notoginseng saponins (PNS) on growth and physiology of Chinese cabbage seedlings. *J. Henan Agric. Sci.* 48 (01), 94–98.

Jerome, J. J., Ali, A., Wang, W. M., and Thiruvengadam, M. (2020). Characterizing the role of the miR156-SPL network in plant development and stress response. *Plants (Basel).* 9, 1206(9). doi:10.3390/plants9091206

Jung, I., Kang, H., Kim, J. U., Chang, H., Kim, S., and Jung, W. (2018). The mRNA and miRNA transcriptomic landscape of Panax ginseng under the high ambient temperature. *BMC Syst. Biol.* 2, 27. doi:10.1186/s12918-018-0548-z

Kidner, C. A., and Martienssen, R. A. (2005). The developmental role of microRNA in plants. *Curr. Opin. Plant Biol.* 8 (1), 38–44. doi:10.1016/j.pbi.2004.11.008

Kosova, K., Prasil, I. T., Vitamvas, P., Dobrev, P., Motyka, V., Flokova, K., et al. (2012). Complex phytohormone responses during the cold acclimation of two wheat cultivars differing in cold tolerance, winter Samanta and spring Sandra. *J. Plant Physiol.* 169 (6), 567–576. doi:10.1016/j.jplph.2011.12.013

Ladhari, A., Tufano, I., and DellaGreca, M. (2020). Influence of new effective allelochemicals on the distribution of *Cleome arabica* L. community in nature. *Nat. Prod. Res.* 34 (6), 773–781. doi:10.1080/14786419.2018.1501688

Lee, I., Hyam, S. R., Jang, S., Han, M. J., and Kim, D. (2012). Ginsenoside re ameliorates inflammation by inhibiting the binding of lipopolysaccharide to TLR4 on macrophages. *J. Agric. Food Chem.* 60 (38), 9595–9602. doi:10.1021/jf301372g

Lee, S., Badieyan, S., Bevan, D. R., Herde, M., Gatz, C., and Tholl, D. (2010). Herbivore-induced and floral homoterpene volatiles are biosynthesized by a single P450 enzyme (CYP82G1) in *Arabidopsis*. *Proc. Natl. Acad. Sci. U. S. A.* 107 (49), 21205–21210. doi:10.1073/pnas.1009975107

Li, Q., Lianxue, Z., Guan, T., Xu, Y., and Chen, C. (2020). Allelopathic effects of ginsenoside Rg1 on seed germination and seedling growth of *Panax ginseng*. *Allelopathy J.* 49, 229–242. doi:10.26651/allelo.j/2020-49-2-1267

Li, T., Choi, K., Jung, B., Ji, S., Kim, D., Seo, M. W., et al. (2022). Biochar inhibits ginseng root rot pathogens and increases soil microbiome diversity. *Appl. Soil Ecol.* 169, 104229. doi:10.1016/j.apsoil.2021.104229

Li, Y., Luo, H. M., Sun, C., Song, J. Y., Sun, Y. Z., Wu, Q., et al. (2010). EST analysis reveals putative genes involved in glycyrrhizin biosynthesis. *BMC Genomics* 11, 268. doi:10.1186/1471-2164-11-268

Liu, S., Wang, S., Liu, M., Yang, F., Zhang, H., Liu, S., et al. (2016). De novo sequencing and analysis of the transcriptome of Panax ginseng in the leaf-expansion period. *Mol. Med. Rep.* 14 (2), 1404–1412. doi:10.3892/mmr.2016.5376

Ma, Y., Xue, H., Zhang, F., Jiang, Q., Yang, S., Yue, P., et al. (2021). The miR156/SPL module regulates apple salt stress tolerance by activating MdWRKY100 expression. *Plant Biotechnol. J.* 19 (2), 311–323. doi:10.1111/pbi.13464

Martin, M. (2011). Cutadapt removes adapter sequences from high-throughput sequencing reads. *EMBnet. J.* 17.1, 10–12. doi:10.14806/ej.17.1.200

Morikawa, T., Mizutani, M., Aoki, N., Watanabe, B., Saga, H., Saito, S., et al. (2006). Cytochrome P450CYP710A encodes the sterol c-22 desaturase inArabidopsis and tomato. *Plant Cell* 18 (4), 1008–1022. doi:10.1105/tpc.105.036012

Mortazavi, A., Williams, B. A., McCue, K., Schaeffer, L., and Wold, B. (2008). Mapping and quantifying mammalian transcriptomes by RNA-Seq. *Nat. Methods* 5 (7), 621–628. doi:10.1038/nmeth.1226

Owusu, A. M., Zhou, X., Mao, M., Rafique, F., and Ma, J. (2021). MicroRNAs roles in plants secondary metabolism. *Plant Signal. Behav.* 16 (7), 1915590. doi:10.1080/15592324.2021.1915590

Patro, R., Duggal, G., Love, M. I., Irizarry, R. A., and Kingsford, C. (2017). Salmon provides fast and bias-aware quantification of transcript expression. *Nat. Methods* 14 (4), 417–419. doi:10.1038/nmeth.4197

Qiong, L. (2020). *Effect of ginsenoside on chemotaxis aggravation of soil rust rot in continuous cropping soil and its mechanism.* Changchun: Jilin Agriculture University.Retrieved from available from

Qu, G., Peng, D., Yu, Z., Chen, X., Cheng, X., Yang, Y., et al. (2021). Advances in the role of auxin for transcriptional regulation of lignin biosynthesis. *Funct. Plant Biol.* 48 (8), 743–754. doi:10.1071/fp20381

Riaz, M., Rahman, N. U., Zia-Ul-Haq, M., Jaffar, H. Z., and Manea, R. (2019). Ginseng a dietary supplement as immune-modulator in various diseases. *Trends Food Sci. Technol.* 83, 12–30. doi:10.1016/j.tifs.2018.11.008

Robinson, M. D., McCarthy, D. J., and Smyth, G. K. (2010). edgeR: a Bioconductor package for differential expression analysis of digital gene expression data. *Bioinformatics* 26 (1), 139–140. doi:10.1093/bioinformatics/btp616

Shen, C., Guo, H., Chen, H., Shi, Y., Meng, Y., Lu, J., et al. (2017). Identification and analysis of genes associated with the synthesis of bioactive constituents in Dendrobium officinale using RNA-Seq. *Sci. Rep.* 7 (1), 187. doi:10.1038/s41598-017-00292-8

Shi, Y., Sun, C., Zheng, B., Gao, B., and Sun, A. (2013). Simultaneous determination of ten ginsenosides in American ginseng functional foods and ginseng raw plant materials by liquid chromatography tandem mass spectrometry. *Food Anal. Methods* 6 (1), 112–122. doi:10.1007/s12161-012-9406-6

Sui, C., Zhang, J., Wei, J., Chen, S., Li, Y., Xu, J., et al. (2011). Transcriptome analysis of Bupleurum chinense focusing on genes involved in the biosynthesis of saikosaponins. *BMC Genomics* 12, 539. doi:10.1186/1471-2164-12-539

Sun, B., Pan, F., and Sung, C. (2011). Repetitious steaming-induced chemical transformations and global quality of black ginseng derived from Panax ginseng by HPLC-ESI-MS/MSn based chemical profiling approach. *Biotechnol. Bioproc. E.* 16 (5), 956–965. doi:10.1007/s12257-011-0079-6

Wu, B., Long, Q., Gao, Y., Wang, Z., Shao, T., Liu, Y., et al. (2015). Comprehensive characterization of a time-course transcriptional response induced by autotoxins in Panax ginseng using RNA-Seq. *BMC Genomics* 16, 1010. doi:10.1186/s12864-015-2151-7

Wu, B., Wang, M., Ma, Y., Yuan, L., and Lu, S. (2012). High-throughput sequencing and characterization of the small RNA transcriptome reveal features of novel and conserved MicroRNAs in panax ginseng. *PLoS ONE* 7 (9), 1–16. doi:10.1371/journal.pone.0044385

Wu, D., Austin, R. S., Zhou, S., and Brown, D. (2013). The root transcriptome for North American ginseng assembled and profiled across seasonal development. *BMC Genomics* 14, 564. doi:10.1186/1471-2164-14-564

Wu, H., Wu, L., Wang, J., Zhu, Q., Lin, S., Xu, J., et al. (2016). Mixed phenolic acids mediated proliferation of pathogens Talaromyces helicus and kosakonia sacchari in continuously monocultured radix pseudostellariae rhizosphere soil. *Front. Microbiol.* 7, 335. doi:10.3389/fmicb.2016.00335

Wu, J., Wang, F., Cheng, L., Kong, F., Peng, Z., Liu, S., et al. (2011). Identification, isolation and expression analysis of auxin response factor (ARF) genes in Solanum lycopersicum. *Plant Cell Rep.* 30 (11), 2059–2073. doi:10.1007/s00299-011-1113-z

Yang, M., Zhang, X., Xu, Y., Mei, X., Jiang, B., Liao, J., et al. (2015). Autotoxic ginsenosides in the rhizosphere contribute to the replant failure of panax notoginseng. *PLoS One* 10, 1–17. doi:10.1371/journal.pone.0118555

Yano, R., Takagi, K., Takada, Y., Mukaiyama, K., Tsukamoto, C., Sayama, T., et al. (2017). Metabolic switching of astringent and beneficial triterpenoid saponins in soybean is achieved by a loss-of-function mutation in cytochrome P450 72A69. *Plant J.* 89 (3), 527–539. doi:10.1111/tpj.13403

Yu, Z. X., Wang, L. J., Zhao, B., Shan, C. M., Zhang, Y. H., Chen, D. F., et al. (2015). Progressive regulation of sesquiterpene biosynthesis in Arabidopsis and patchouli (pogostemon cablin) by the miR156-targeted SPL transcription factors. *Mol. Plant* 8 (1), 98–110. doi:10.1016/j.molp.2014.11.002

Zazimalova, E., and Napier, R. M. (2003). Points of regulation for auxin action. *Plant Cell Rep.* 21 (7), 625–634. doi:10.1007/s00299-002-0562-9

Zeng, S., Liu, Y., Pan, L., Hayward, A., and Wang, Y. (2015). Identification and characterization of miRNAs in ripening fruit of Lycium barbarum L. using high-throughput sequencing. *Front. Plant Sci.* 6, 778. doi:10.3389/fpls.2015.00778

Zeng, X., Li, Y., Ling, H., Liu, S., Liu, M., Chen, J., et al. (2017). Transcriptomic analyses reveal clathrin-mediated endocytosis involved in symbiotic seed germination of Gastrodia elata. *Bot. Stud.* 58 (1), 31. doi:10.1186/s40529-017-0185-7

Zhan, Y., Wang, E., Wang, H., Chen, X., Meng, X., Li, Q., et al. (2021). Allelopathic effects of ginsenoside on soil sickness, soil enzymes, soil disease index and plant growth of Ginseng. *Allelopathy J.* 52, 251–260. doi:10.26651/allelo.j/2021-52-2-1320

Zhang, H., Han, W., De Smet, I., Talboys, P., Loya, R., Hassan, A., et al. (2010). ABA promotes quiescence of the quiescent centre and suppresses stem cell differentiation in the Arabidopsis primary root meristem. *Plant J.* 64 (5), 764–774. doi:10.1111/j.1365-313x.2010.04367.x

Zhang, R., Wang, X., and Gao, W. (2020). Regulation mechanism of plant hormones on secondary metabolites. *China J. Chin. Materia Med.* 45 (17), 4205–4210. doi:10.19540/j.cnki.cjcmm.20190129.007

Zhang, T., Han, M., Yang, L., Han, Z., Cheng, L., Sun, Z., et al. (2019). The effects of environmental factors on ginsenoside biosynthetic enzyme gene expression and saponin abundance. *Molecules* 24 (1), 14. doi:10.3390/molecules24010014

Zhang, Y. T., Zhou, D. Q., Su, Y., Yu, P., Zhou, X. G., and Yao, C. X. (2013). Proteome analysis of potato drought resistance variety in Ninglang 182 leaves under drough stress. *Hereditas* 35 (5), 666–672. doi:10.3724/sp.j.1005.2013.00666

Zhang, Y., Wang, T., Ou, S., Li, F., Huang, L., Mai, C., et al. (2022). Identification and assessment of the role of soybean low phosphate-responsive *Xyloglucan endotransglycosylases/hydrolases* genes in root growth. *J. Plant Nutr. Fertilizers* 28 (07), 1167–1181.

frontiers | Frontiers in Bioengineering and Biotechnology

TYPE Review
PUBLISHED 07 November 2022
DOI 10.3389/fbioe.2022.1054757

OPEN ACCESS

EDITED BY
Xin Zhou,
Nanjing Forestry University, China

REVIEWED BY
Kunming Qin,
Jiangsu Ocean University, China
Qiang-Sheng Wu,
Yangtze University, China
Daijun Liu,
University of Vienna, Austria

*CORRESPONDENCE
Ming-Guo Ma,
mg_ma@bjfu.edu.cn
Wei-Dong Li,
liweidong0801@163.com

†These authors have contributed equally to this work

SPECIALTY SECTION
This article was submitted to Bioprocess Engineering, a section of the journal Frontiers in Bioengineering and Biotechnology

RECEIVED 27 September 2022
ACCEPTED 25 October 2022
PUBLISHED 07 November 2022

CITATION
Zhou N, Mei C-M, Zhu X-Y, Zhao J-J, Ma M-G and Li W-D (2022), Research progress of rhizosphere microorganisms in Fritillaria L. medicinal plants.
Front. Bioeng. Biotechnol. 10:1054757.
doi: 10.3389/fbioe.2022.1054757

Research progress of rhizosphere microorganisms in *Fritillaria* L. medicinal plants

Nong Zhou[1,2†], Chun-Mei Mei[1†], Xing-Yu Zhu[1], Jing-Jing Zhao[2], Ming-Guo Ma[2,3]* and Wei-Dong Li[1]*

[1]College of Pharmacy, Engineering Center of State Ministry of Education for Standardization of Chinese Medicine Processing, Nanjing University of Chinese Medicine, Nanjing, China, [2]Chongqing Engineering Laboratory of Green Planting and Deep Processing of Famous-region Drug in the Three Gorges Reservoir Region, College of Biology and Food Engineering, Chongqing Three Gorges University, Chongqing, China, [3]Research Center of Biomass Clean Utilization, Beijing Key Laboratory of Lignocellulosic Chemistry, College of Materials Science and Technology, Beijing Forestry University, Beijing, China

The soil's rhizosphere is a highly active place where the exchange of substances and information occurs among plants, soils, and microorganisms. The microorganisms involved are crucial to the activities of plant growth and development, metabolism, and reproduction. *Fritillaria* L. medicinal plants are unique Chinese medicinal ingredients, but the continuous cropping obstacles formed in the artificial planting process is severely harmful to the growth and development of these medicinal plants. In this review, we summarized the current species and distribution of *Fritillaria* L. in China, and analyzed the changes in microbial diversity (mainly among bacteria and fungi) in the rhizosphere of these plants under long-term continuous cropping. The fungi showed an increasing trend in the soil rhizosphere, resulting in the transition of the soil from the high-fertility "bacterial type" to the low-fertility "fungal type" as planting years increased. Furthermore, the interaction between *Fritillaria* L. medicinal plants and the rhizosphere microorganisms was reviewed, and promising applications for the rhizosphere microbiome in the cultivation of *Fritillaria* L. medicinal plants were suggested. It is expected that this review will facilitate the in-depth understanding of rhizosphere microorganisms in the growth, accumulation of active ingredients, and disease control of *Fritillaria* L.

KEYWORDS

***Fritillaria* L., soil, rhizosphere microbes, microbiome, research progress**

Introduction

Fritillaria L., a valued traditional Chinese herbal medicine, contains diterpenoids, steroids, alkaloids, polysaccharides, which have broad applications in health care products, food, Chinese herbal formulas, and everyday chemical industries. This plant has the benefits of reducing phlegm, relieving coughs, reducing heat, moistening the lungs, improving blood stasis, and dispersing knots (Chen et al., 2020). It is also one of the main ingredients in cough- and phlegm-relieving Chinese patented medicines. However, the sources of *Fritillaria* medicinal plants in the wild are becoming increasingly reduced

due to its small output, long resource regeneration cycle, overexploitation, and habitat destruction. In 2021, it was listed as a secondary protected plant among the national key protected wild plants (Cunningham et al., 2018). Moreover, the quantity and quality of *Fritillaria* medicinal materials on the market are inconsistent because of the wide variety of *Fritillaria* medicinal plants, the wide production area, and the lack of standardized processing and operation processes in planting and production. There are problems in concerning the medicinal and edible safety of *Fritillaria* medicinal materials, which are restricting the development of the *Fritillaria* medicinal plant industry (Chen et al., 2021). Therefore, developing artificial and standardized cultivation methods for *Fritillaria* medicinal plants is the most effective way to solve the contradiction between the current market demand for medicinal materials and its resource protection.

The rhizosphere is a unique ring-shaped zone mainly characterized by the interaction between the root system and soil microorganisms. A large number of microorganisms, such as bacteria, Actinomycetes, fungi, and soil animals, gathered around the plant root system, which is a part of the soil microenvironment that presenting special physical, chemical, and biological properties (Garcia and Kao-Kniffin, 2018; Mojicevic et al., 2019; Shao et al., 2021). As the most active component in the soil ecosystem, soil microbes mainly participate in the cycling of nutrients, such as carbon, nitrogen, phosphorus, and sulfur in the soil (Hemkemeyer 2021). Rhizosphere microbes improves the utilization rate of nutrients in the soil, thereby affecting the growth and development of plants and stress resistance, and promoting good plant health and soil quality. Therefore, it is of great significance to perform research on the rhizosphere microorganisms of medicinal plants (Mendes et al., 2013; Tian et al., 2018). However, few reports exists on the rhizosphere microorganisms of *Fritillaria* medicinal plants (Qiu, 2010; Pan et al., 2010a,Pan et al., 2010b; Mu et al., 2019a,Mu et al., 2019b,Mu et al., 2019c; Wu et al., 2021b).

This review article systematically describes the research results on the rhizosphere microorganisms associated with *Fritillaria* medicinal plants in detail. The words "*Fritillaria*," "rhizosphere microorganisms," and "Microbiome" were used as keywords to search the literature in the Chinese National Knowledge Infrastructure (CNKI) and Web of Science. Fifty-seven literature was searched in CNKI, and 57.9% of which was published from 2016 to 2021, six literature was searched in Web of Science. It is expected that this review will contribute to further understand the involvement of rhizosphere microorganisms in the growth of *Fritillaria* medicinal plants and the accumulation of alkaloids, which are the most important active ingredients of *Fritillaria*.

Classification of medicinal *Fritillaria* plants in China

The medicinal quality and market price of *Fritillaria* L. from different places of origin have varied in recent years. To meet the requirements of the market, it is imperative to cultivate *Fritillaria* L. medicinal plants artificially. Five types of *Fritillaria* L. plants present in the Chinese Pharmacopoeia (Volume I, 2020 Edition) are collected; these include *Fritillaria ussuriensis* Maxim, *Fritillaria pallidiflora* Schrenk, *Fritillaria thunbergia* Miq., *Fritillaria hupehensis* Hsiao et K. C. Hsia, and *Fritillaria cirrhosa* D. Don. The specific growth environment and distribution of different *Fritillaria* medicinal plants are shown in Figure 1. The various *Fritillaria* medicinal plants have wide distribution range and high adaptability. It has been proven that it is feasible to breed wild *Fritillaria* medicinal plants (Huang et al., 2018; Luo M. et al., 2021a; Luo S. et al., 2021b). Five types of these *Fritillaria* plants all have the function of reducing heat, relieving coughs, reducing phlegm, and there are moistening lung function of *F. ussuriensis* and *F. pallidiflora,* detoxification, dissipating mass and eliminating carbuncle function of *F. thunbergia*, dissipating mass function of *Fritillaria hupehensis,* moistening lung, dissipating mass and eliminating carbuncle function of *F. cirrhosa* (Chinese Pharmacopoeia Commission, 2020).

Diversity of rhizosphere microorganisms associated with medicinal *Fritillaria* plants

As the most active component of the soil ecosystem, rhizosphere microorganisms play an important role in plant growth, nutrient circulation, and improving yields (Mendes et al., 2013). The diversity and colonization ability of soil microbial communities in different microhabitats affect the growth rate of pathogens and also play an important role in improving plant health (Li et al., 2013). The abundance and diversity of soil microbial community decreased in the field evaluation of root rot disease in *Fritillaria ussuriensis*, while the population of pathogens in the healthy soil sample was quite low, indicating that the microbial community structure affected the health of *F. ussuriensis* (Song et al., 2016). The diversity and structure of the microbial community were closely related to the health level of *F. ussuriensis*, this can lay a foundation for the systematic study on the interaction between microbial genera in the pathological process of *F. ussuriensis* (Jiao et al., 2022).

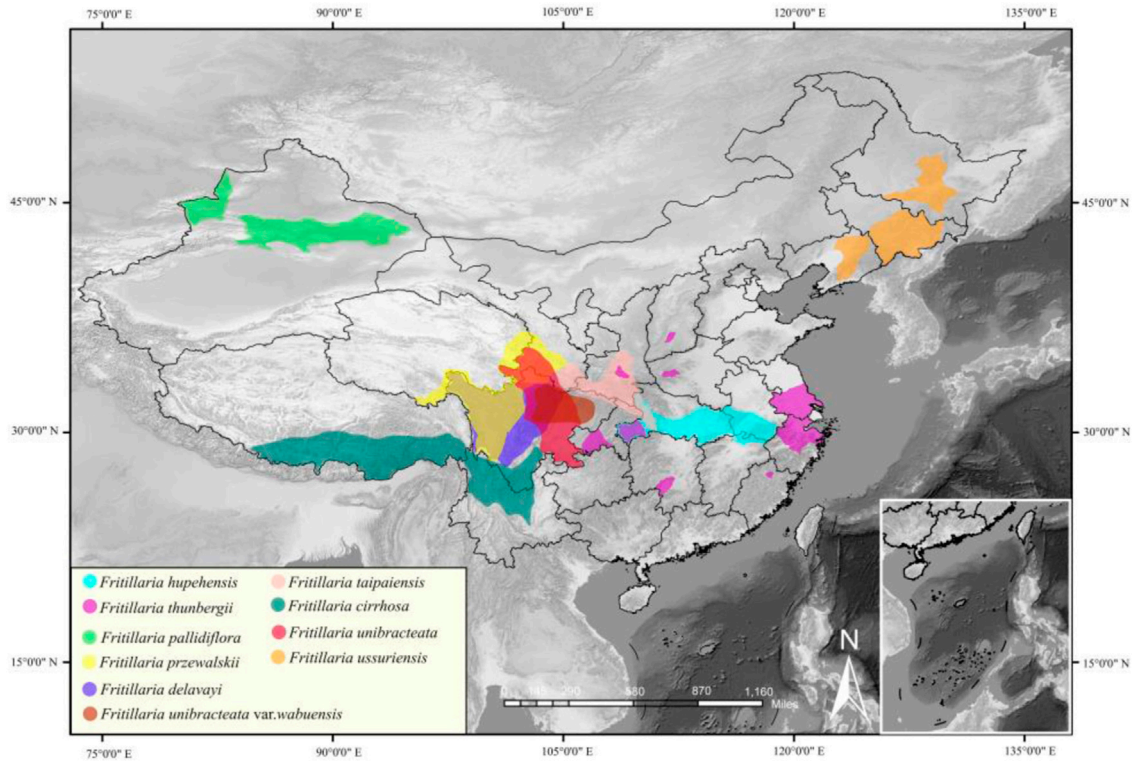

FIGURE 1
Common medicinal plants of the genus *Fritillaria* L. in China.

Diversity of bacteria in rhizosphere soil of *Fritillaria* medicinal plants

As the most abundant and widely distributed group of rhizosphere soil microorganisms, bacteria account for 70–90% of the total number of rhizosphere microorganisms, which are sensitive indicators of nutrient changes in rhizosphere soil (Yu et al., 2019). Researches about the relationship between the number and diversity of bacteria and *Fritillaria* medicinal plants were carried out. Liao (2011) found that the number of culturable bacteria of rhizosphere soil of *F. thunbergii* was decreased with the planting year increaced, which is related with the monocropping obstacle of *F. thunbergii*. In agricultural production, a variety of issues, such as disease accumulation, impaired growth, and quality decline, appeared in the third year after planting *Fritillaria taipaiensis* P. Y. Li seedlings (Mu et al., 2019a). This seriously affected the yield and quality of *F. taipaiensis*. The number of culturable rhizosphere microorganisms associated with wild and cultivated *F. taipaiensis* in different growth years and production areas was measured. It was found that the rhizosphere microorganisms of *F. taipaiensis* were abundant, and the number of bacteria was 2×10^6 cfu·g^{-1}–3×10^7 cfu·g^{-1}, when the total number of microorganisms was 3.8×10^7 cfu·g^{-1}, but which decreaced alongwith the planting years of cultivated *F. taipaiensis* and growth year of wild *F. taipaiensi* (Mu, 2019b).

Using the high-throughput sequencing technology, from the phylum level analysis, it can be seen that the bacterial community within the soil rhizosphere was mainly composed of Proteobacteria Acidobacteria, *Bacteroidetes*, *Verrucomicrobia*, *Firmicutes*, *Gemmatimonadetes*, *Actinobacteria*, *Planctomycetes*, *Nitrospirae*, and Chloroflexi (Mu, 2019). Among them, Proteobacteria belonged to the dominant phylum with the largest relative abundance (54.82%). As planting years increased, the relative abundances of the genera *Lactobacillus*, *Gemmatimonas*, *Bryobacter*, and *Bacteroides* gradually decreased, whereas the relative abundances of the genera *Methylotera*, *Sphingobacterium*, and *Pseudomonas* gradually increased (Mu, 2019). Wu (2021a,Wu 2021b) reported that the composition of phyla and genera within soil bacterial communities changed alongwith the growth years of *F. kansuensis*. Among them, for the relative abundance, Actinomycetes (23.58%–32.08%), Proteobacteria (22.00%–28.80%), Acidobacteria (13.82%–20.86%) and Chloroflexi (8.43%–15.08%) belonging to the dominant phyla, and the continuous planting of *Fritillaria kansuensis* for 5 years would significantly reduce the diversity of bacterial communities in the soil rhizosphere. Tang et al. (2021) discovered that the bacterial

10.3389/fbioe.2022.1054757

TABLE 1 Diversity of potassium solubilizing bacteria and phosphate solubilizing bacteria in the rhizosphere of *Fritillaria* L. medicinal plants.

Microbial strains	Numbering	Latin name	Similarity (%)	Reference strain registration sequence
Organophosphate solubilizing bacteria	YPB1	*Pseudomonas putida*	99	AY823622.1
	YPB2	*Pseudomonas lini*	100	DQ377769.1
	YPB4	*Pseudomonas salomonii*	99	JX840372.1
	YPB5	*Pseudomonas veronii*	99	JQ317807.1
	YPB6	*Pseudomonas mandelii*	100	DQ377771.1
	YPB7	*Pseudomonas fluorescens*	100	KJ420524.1
	YPB8	*Pseudomonas fluorescens*	100	KC018467.1
	YPB9	*Pseudomonas fluorescens*	100	KJ420524.1
	YPB11	*Pseudomonas fluorescens*	100	KJ420524.1
	YPB13	*Pseudomonas fluorescens*	100	KC018467.1
	YPB15	*Pseudomonas koreensis*	100	KF424274.1
	YPB17	*Pseudomonas poae*	100	JX515573.1
	YPB20	*Pseudomonas fluorescens*	100	KC018467.1
	YPB21	*Bacillus thuringiensis*	100	CP004858.1
	YPB22	*Pseudomonas grimontii*	100	KJ420529.1
	YPB24	*Pseudomonas migulae*	100	DQ377742.1
	YPB25	*Pseudomonas azotoformans*	100	KF040474.1
	YPB26	*Pseudomonas fluorescens*	99	KC018467.1
Phosphorus solubilizing bacteria	WP1	*Pseudomonas fluorescens*	99	KJ756336.1
	WP4	*Arthrobacter nicotinovorans*	100	KR922212.1
	WP5	*Arthrobacter nicotinovorans*	100	KR922212.1
	WP10	*Phyllobacterium myrsinacearum*	100	KJ147062.1
	WP11	*Arthrobacter ilicis*	99	KR088423.1
	WP13	*Phyllobacterium myrsinacearum*	100	KJ147062.1
	WP18	*Phyllobacterium myrsinacearum*	100	KJ147062.1
Potassium solubilizer	GB1	*Pseudomonas fluorescens*	100	HQ606463.1
	GB13	*Agrobacterium tumefaciens*	100	CP011247.1
	GB15	*Agrobacterium tumefaciens*	100	CP011247.1
	GB23	*Pseudomonas fluorescens*	100	HQ606463.1
	GB25	*Agrobacterium tumefaciens*	99	CP011247.1
	GB33	*Agrobacterium tumefaciens*	100	CP011247.1

diversity in the rhizosphere gradually decreased as the growth of *Fritillaria thunbergii*.

The bacteria that presented decreased relative abundance in rhizosphere soil included potassium-solubilizing bacteria (PSB), phosphate-solubilizing bacteria, and nitrogen-fixing bacteria, which may because of the increase in the relative abundance of saprophytic fungi. Phosphate solubilizing bacteria can convert insoluble phosphorus into effective phosphorus that can be absorbed and subsequently used by plants. According to the different substrates of phosphate-solubilizing bacteria, they could be divided into organic phosphorus bacteria and inorganic phosphorus bacteria (Chi et al., 2021), which is a type of bacteria isolated from soil that can decompose phosphorus-containing minerals. PSB, also known as potassium bacteria or silicate bacteria, convert mineral potassium into potassium that is available for plant absorption and utilization by adhering to the mineral surface and releasing acidic substances. These are a type of bacteria isolated from the soil that can decompose potassium-containing minerals (Han et al., 2022).

The isolation and screening of organophosphate-solubilizing bacteria, inorganic phosphate-solubilizing bacteria, and PSB from the rhizosphere soil of *F. taipaiensis* in the previous report revealed that these varied with different growth years (Table 1). As the planting years of *F. taipaiensis* increased, there

was an increase and subsequent decrease in the total number of organophosphate-solubilizing bacteria, Actinomycetes, inorganic phosphate-solubilizing bacteria, as well as other bacteria and microorganisms in the rhizosphere. However, there was a decrease in the number of PSB. It was found that fertilization and continuous cropping significantly affected the community composition and function of rhizosphere microorganisms associated with *F. taipaiensis*.

Diversity of fungi in the rhizosphere of *Fritillaria* medicinal plants

It was discovered that the symbiosis between *F. Taipaiensis* and AM fungi was very common; different AM fungi infected the root system of *F. Taipaiensis* to different degrees; and the inoculation of AM fungi significantly increased the mycorrhizal infestation rate, and, in turn, the biomass of *F. taipaiensis* (Zhang, 2020). AM fungi could increase the content of inorganic elements in the rhizome and soil of *Fritillaria taipaiensis* P. Y. Li.; enhance the enrichment ability of inorganic elements, thus improving the growth and development of *F. taipaiensis* P. Y. Li.; and promote the accumulation of nutrients in medicinal material (Wei et al., 2021). *Fritillaria thunbergii* Miq. is a crop that is continually cropped; thus, it is necessary to change the land after 1 year of artificial planting (Yu and Wu, 2017). When the four planting years increased, there was a linear increase in the number of cultivable fungi in the soil from the root zone of *F. thunbergii* Miq., whereas the total amount of cultivable Actinomycetes, bacteria decreased linearly (Liao et al., 2011). In general, fungi prefer acidic environments, Actinomycetes prefer neutral to alkaline environments, while other bacteria mainly live in neutral environments. The continuous cropping of *F. thunbergii* Miq. reduced the pH value of the soil, resulting in the soil being slightly acidic. This, being conducive to the propagation of fungi, results in the transition of the soil from a high fertility "bacterial type" to a low fertility "fungal type" (Liao et al., 2011). As the planting years of *F. taipaiensis* increased, so did the fungi in the rhizosphere. This indicates that long-term continuous cropping would lead to a reduction in the numbers of beneficial microorganisms, and increase the numbers of pathogenic microorganisms in the rhizosphere of *F. taipaiensis* (Mu et al., 2019b; Gu et al., 2020), which is not conducive to the growth of *F. taipaiensis*.

Non-culture methods can more accurately reflect the community structure of rhizosphere microorganisms compared with traditional culture methods. The results of high-throughput sequencing of ITS sequence showed that fungal community in the rhizosphere of *F. taipaiensis* was mainly composed of Ascomycota, Zygomycota, Basidiomycota, Glomeromycota, Neocallistigomycota, and Chytridiomycota. And Ascomycota fungi were the most dominant population. With the increase in planting years, the relative abundance of *Pseudogymnomyces* in the soil rhizosphere gradually decreased, along with the relative abundance of populations such as pathogenic fungi in *Fusarium*, *Gibberella*, *Rhizopus*, *Colletotrichum*, and *Peziza* (Mu, 2019; Zhou et al., 2021).

Interaction between *Fritillaria* plants and rhizosphere microorganisms

Effects of root exudates of *Fritillaria* medicinal plants on rhizosphere microorganisms

The richness and diversity of rhizosphere microorganisms plays a key role in regulating ecological functions, such as organic matter decomposition, nutrient cycling, and soil carbon dynamics (Sasse et al., 2018). In nature, plants release and secrete various compounds into the environment through a variety of ways, such as *via* leaf litter, root residues, and root exudates. This occurrence provides vital carbon sources for the formation of aggregates, and affects the physical and chemical properties of community of rhizosphere microorganisms (Vezzani et al., 2018; Vives-Peris et al., 2020). Conversely, the biological, physical, and chemical characteristics of rhizosphere microorganisms affects host plants and their coexisting plants (Ehrenfeld et al., 2005). Root exudates are important factors in the formation of rhizosphere microorganisms, because the various primary metabolites and secondary metabolites secreted by roots can play the role of shaping, interfering, or transmitting signals to change the rhizosphere microflora, recruit and promote beneficial microorganisms, and resist harmful microorganisms (Venturi and Keel, 2016). Generally, the rhizosphere microorganism of plant are more abundance, active and rich in diversity than the no-rhizosphere microorganism.

Root exudates provided abundant nutrients and energy for the growth of rhizosphere microorganisms, and also affects the distribution, species, and quantity of rhizosphere microorganisms (Wang et al., 2007). The root exudates of *Fritillaria* medicinal plants include organic acids, amino acids, soluble sugars, total phenolic acids, and organic substances (Guo et al., 2013). Various organic substances, such as ethers, olefins, acids, aldehydes and ketones, esters, alkanes, ureas, phenols, and alcohols (Wang et al., 2009) have been found in root exudates. Among them, are high contents of aldehydes and ketones. Phenolic acids secreted by roots promote the growth of black spot fungus and *Botrytis cinerea* (Guo et al., 2013). Phenol and 1,3,5-triallyl-1,3,5-triazine-2,4,6 (1H, 3h, 5H) trione, being the main root exudates of *Fritillaria*, had a significant inhibitory effect on the growth of its seedlings (Wang, 2010; Wang et al., 2010a,b). Generally, the secondary metabolites produced by the roots of medicinal plants? were easily released into the soil,

thereby promoting the colonization and shaping of the rhizosphere microorganism community, and driving the feedback effect of plant soil on defense and growth (Hu et al., 2018). This results in changes in the population structure of plant rhizosphere microorganisms. It should be noted that there are great differences in the species, dominant species and quantity of rhizosphere microorganisms in different growth stages of the same plant or in the same growth stage of different plants. This is due to the variety and quantity of plant root exudates, which vary with growth stage or plant variety (Brimecombe et al., 2001).

Effects of rhizosphere microorganisms on the growth and effective components of *Fritillaria* medicinal plants

The metabolism of rhizosphere microorganisms either directly promotes or inhibits the nutrient absorption and growth of roots, which plays a key role in the secondary metabolism of plants. Therefore, in recent years, much attention has been paid to the interpretation of the quality formation, change, and mechanism of traditional Chinese medicine from the perspective of microecology, to clarify the influence of rhizosphere microorganisms on the growth of medicinal plants and medicinal ingredients. It has been confirmed that rhizosphere microorganisms improve the yield and medicinal components of medicinal plants. Zhang et al. (2020) inoculated four types of arbuscular mycorrhizal fungi (AMF) including *Glomus constrictum* (GC), *Glomus versiforme* (GV), *Glomus mossae* (GM), and *Glomus aggregatum* (GA). AMF alone could significantly increase the fresh weight, dry weight, and drying rate of *F. taipaiensis* bulbs, and increase the contents of Fritillarin A, sibelline glycoside, Fritillarin B, Fritillarin, and alkaloids in the bulb. AM fungi could increase the content of inorganic elements in the rhizome and soil of *F. ussuriensis*, and also enhance the enrichment ability of inorganic elements, thereby improving the growth and development of *F. ussuriensis*, and promoting the accumulation of nutrients in medicinal materials (Wei et al., 2021). Sun et al. (2022a) found that medicinal plants had a great diversity of rhizosphere AM fungi. Fungal colonization improved plant growth performance and root morphology, and significantly increased the content of most disaccharides, but either reduced or did not change the content of most monosaccharides. AM fungi significantly increased the concentration of the medicinal components (chrysophanol, physion, polydatin, and resveratrol) in the root of *P. cuspidatum*, and upregulated the expression of related synthase genes (Sun et al., 2022b). Therefore, AM fungi are beneficial to the growth and nutrient absorption of medicinal plants, thereby accelerating the accumulation of medicinal ingredients.

Pan et al. (2010a) used *Bacillus subtilis* to spray leaves and irrigate roots at different growth stages of *F. pallidiflora*, which increased the yield by 16.8%. The correlation analysis between rhizosphere microorganisms and the content of Siberian in the growth stage of *F. pallidiflora* showed that the fungi in rhizosphere soil had a significant positive correlation with the content of Siberian, while Actinomycetes and bacteria had a positive correlation with the content of Siberian (Pan et al., 2010b). These results are similar with those reported by Qiu (2010), and have the potential to be included in applications to further develop the resources of beneficial fungi in the rhizosphere of *F. pallidiflora* and improve its medicinal quality. Zhao et al. (2021) isolated 20 endophytic bacteria from 3-year-old *F. przewalskii* Maxim. plants, which were distributed in the three phyla of Proteobacteria, Firmicutes, and Actinomycetes. Among them, strains related to *Bacillus, Rhizobium*, and *Pseudomonas* were the dominant growth-promoting bacteria. Foliar spraying of the Firmicutes *Bacillus*, *Rhizobium*, and *Pseudomonas* compound promoted the growth of *F. przewalskii* Maxim. and significantly increased its yield. Tang et al. (2021) found that with the advancement of the growth process of *F. thunbergii* Miq., the content of alkaloids (Fritillarin A and Fritillarin B) in the bulb first increased and then decreased. Correlation analysis showed that the Chao1 index and Shannon index among the bacteria were positively correlated with the content of monomer alkaloids and total alkaloids, indicating that the soil bacterial community was closely related to the content of alkaloids. Furthermore, the secondary metabolites produced by *Fritillaria cirrhosa* D. Don displayed high antioxidant activity. For example, the low polar substances extracted by petroleum ether had weak ABTS free radical scavenging activity, whereas the high polar substances extracted by solvents such as n-butanol and ethyl acetate had high ABTS free radical scavenging activity (Pan et al., 2017). These results indicated that it was feasible to use beneficial rhizosphere microorganisms to improve the yield and quality of *F. taipaiensis* in artificial cultivation. During the long-term artificial cultivation of medicinal plants, agricultural management measures (Tan et al., 2013; Geng et al., 2018), such as the chemical fertilizer, pesticide spraying, and planting method caused a change in the rhizosphere microbial biomass and its community structure, which was mediated by soil physical and chemical properties. This resulted in varying degrees of differences in the medicinal value between wild medicinal materials and cultivated medicinal materials, which further increased the variation in quality of the same type of Chinese medicinal materials from different origins (Schmidt et al., 2019).

Microbial fertilizers are a type of live microbial preparation widely used in agricultural production. These play an irreplaceable role in future advancements in agriculture due to their contributions to environmental protection, soil improvement, fertility improvement, output increase, and quality improvement. For example, the exogenous inoculation

of AMF, phosphorus-dissolving bacteria, potassium-dissolving bacteria, and other microbial fertilizers increased the alkaloid content of 3-year-old *F. taipaiensis* plants (Ma, 2021). Based on the results of the content of secondary metabolites, and relevant physical and chemical properties of rhizosphere soil, the quality of *F. taipaiensis* had a great relationship with rhizosphere microorganisms. However, the growth potential of seedlings co-cultured with a single strain was relatively low, and some even exhibited yellowing. After mixed inoculation of AMF, phosphorus-dissolving bacteria, and potassium-dissolving bacteria, the alkaloid content in bulbs was lower than that in *F. taipaiensis* plants that were co-cultured with single strains. This may be because of the limitation of a single strain, the unstable interaction between rhizosphere promoters and host plants (Rainer and Florian, 2018), or it may be due to the effect of unknown ecological functions (Lebeis et al., 2012). Therefore, the rhizosphere microorganisms of plants may not exist alone, but instead play a role in the active ingredients of *F. taipaiensis* in the form of a specific flora. In addition, the exogenous application of microbial agents increased the number of Actinomycetes and bacteria in the rhizosphere soil of 2-year-old *F. taipaiensis* plants, but had no obvious effect on the number of fungi. It has also significantly improved the activities of soil protease, acid phosphatase, urease, and sucrase, thereby playing an important role in the sustainable utilization and stability of soil nutrients (Dong, 2018). The exogenous application of different doses of microbial fertilizer significantly increased the height of the plant, the fresh weight of the plant and bulb, and the yield of *F. pallidiflora*. Therefore, microbial fertilizer was commonly applied in the cultivation of *F. pallidiflora*. It was more beneficial to increase the production and efficiency of *F. pallidiflora* by opening ditches and applying the microbial fertilizer during the growth period (Chen et al., 2017). Therefore, microbial fertilizer can improve the structure and density of the microbial population in the rhizosphere soil, as well as the quality.

Hazards of rhizosphere microorganisms on *Fritillaria* medicinal plants

Fritillaria Chinese herbal medicines generally take 4–6 years to grown from a germinating seed to flowering and bearing, and take at least 3 years for commercial medicinal materials. However, with the increase in the growth years of *Fritillaria* Chinese herbal medicines, conditions that are favorable for outbreaks of harmful rhizosphere microorganisms have been created in the process of artificial planting. Coupled with poor field management, the quality of medicinal materials gradually decreased. Common soil borne diseases, such as root rot disease, sclerotium disease, ray mold disease, rust disease, and yellow rot rust, occurred frequently and caused serious harm (Wang, 2010). This made it very easy for *Fritillaria* to develop bulb rot and lose its medicinal value (Liu et al., 2020; Wu, 2021a). Using morphological identification method, the pathogen of sclerotium disease and root rot disease of *F. pallidiflora* was identified as *Stromatinia rapulum* (Supi et al., 2012) and *Fusarium solani* var. *coeruleum* (Supi et al., 2015), respectively. But *Sclerotium denigrans* and *Sclerotinia sclerotiorum* caused the sclerotium disease of *F. ussuriensis* with molecular biology methods (Song et al., 2016a). The pathogens of root rot disease in *F. thunbergia* were *Fusarium* oxysporum and *F. incarnatum*, the pathogen of black spot disease was *Alternaria alternata*, and *Phoma* sp. could cause leaf spot disease (Wang, 2017). But the pathogens of root rot disease of *F. przewalskii* were *F. oxysporum*, *F, tricinctum*, *Bionectria ochroleuca* and *Clonostachys rosea* (Wu et al., 2021a). *Botrytis cinerea* was identified as the pathogen of ray mold disease of *F. thunbergia,* and not the *Botrytis elliptica* which was generally considered as the pathogen in the past (Li et al., 2022).

Application of rhizosphere microbiome in the cultivation of *Fritillaria* medicinal plants

The plant microbiome, also known as the pan-genome, refers to the study of the role of the rhizosphere microbial community in the growth of host plants in a holistic manner. It plays an irreplaceable role in the ecological environment and agricultural production (Bulgarelli et al., 2013; Andezej and Philip, 2015), which is recognized as an important determinant of healthy plant growth (Berg et al., 2014). Combining the core strategy of "whole microbiome association analysis," the microbiome accurately decoded the expression spectrum, composition spectrum, and function spectrum of the community/flora, discovered key organisms and their markers, and then clarified the complex causal chain and interaction mechanism between the "microbiome plant soil" (Claire, 2017).

Classification of rhizosphere microbiome

According to the varied distribution of microorganisms on the root system, the rhizosphere microbiome could be divided into the three categories of rhizosphere microbiome, root surface microbiome, and root internal microbiome (Tripathi et al., 2018). Due to the limitations of research technology, these three aspects had been involved in previous studies, but they were not specifically analyzed as a whole to evaluate the importance of these rhizosphere microbiomes to plant growth. In the study of plant rhizosphere microbiome, it is necessary to pay attention to the different sampling methods of different microbiomes. After the plant roots were taken out of the soil, 1 mm-thick soil was

collected from around the roots by shaking and washing. In this way, all the soil on the root surface was placed in a phosphate buffer solution, and the microorganisms close to the root surface were separated for rhizosphere microbiome analysis (Edwards et al., 2015). Because there were few microorganisms on the root surface and it was difficult to collect them, the cleaned roots were put into phosphate buffer solution for ultrasonic treatment for 30 s, and the small amount of plant soil residues in the buffer solution were considered the microbial components on the root surface. After the cleaned roots were chemically treated with sodium hypochlorite and ethanol, or all the microorganisms on the root surface were removed by continuous sonication performed twice, the roots were then crushed by adding glass beads, which was considered the microbial components in the roots (Lundberg et al., 2012; Reinhold-Hurek et al., 2015).

Study on rhizosphere microbiome in the cultivation of *Fritillaria* medicinal plants

A large number of studies have indicated that the rhizosphere microbiome played an important role in promoting the growth and tolerance of host plants. These are mainly divided into two methods of negative interaction such as rhizosphere microorganisms infecting the host to cause diseases or competing with the host for nutrition, and positive interaction such as rhizosphere microorganisms promoting growth, stress resistance, and disease resistance (Bais et al., 2006). This interaction process exerts a strong selection pressure on both the rhizosphere microbiome and host plants, thus forming the mode and rate of rhizosphere microbial evolution and affecting the formation of the rhizosphere microbiome (Cosetta and Wolfe, 2019). An in-depth exploration of the selection mechanism of plants for the rhizosphere microbiome could guide the recombination and improvement of the rhizosphere microbiome in practical applications (Sun et al., 2021). It also improved the understanding of plant microbe interaction in theory, which is of great significance for future agricultural production. For example, using Indica rice and Japonica rice as experimental materials, Zhang et al. (2019) found that Indica rice often showed higher nitrogen utilization efficiency than that of Japonica rice. Furthermore, the diversity of the rhizosphere microbiome of Indica rice was significantly higher than that of Japonica rice, which directly confirmed the relationship between the rhizosphere microbiome and the nitrogen utilization efficiency of plants. Utilizing beneficial members of the rhizosphere microbiome and making microbial fertilizer is a very promising application within fertilizer preparation (Hu et al., 2016). Unfortunately, the current research on the development of the rhizosphere microbiome into microbial fertilizer is still at the experimental stage. Nevertheless, microbial fertilizers have potential use in the natural agricultural environment.

Yuan et al. (2018) found that when plants were infected by pathogenic bacteria, they could recruit and enrich certain beneficial microorganisms by sending specific signals. This phenomenon was the famous "cry for help hypothesis." These beneficial recruited microorganisms in the rhizosphere improved the disease resistance of plants in four ways: competition, parasitism, antibiosis, and the induction of systemic resistance (Mendes et al., 2013). For example, the antibacterial metabolite 2,4-diacetyl-phloroglucinol secreted by *Pseudomonas fluorescens* in rhizosphere microorganisms inhibited *Sclerotium rolfsii* by more than 75% (Asadhi et al., 2013). *P. fluorescens* (WCS417r) that colonized the Arabidopsis rhizosphere could upregulate the expression level of defense-related genes of the host plant pathogen (*Pseudomonas syringae* pv *tomato*) (Wees et al., 1999). In addition, AMF established a good symbiotic system with most terrestrial plants, promoted its external hyphal network to accelerate the absorption of nutrients and water, and enhanced the resistance of host plants (Li et al., 2019). It could be seen that no matter how the rhizosphere microorganisms interact with plants, the successful colonization of microorganisms in the rhizosphere was of great importance to plants. This is because the different secretions secreted by plant roots were signals recognized by rhizosphere microorganisms, and also vectors for mutual communication between rhizosphere microorganisms. Therefore, these signals could, in-turn, be used for the colonization of rhizosphere microorganisms. Consequently, root exudates are considered to be important mediators in the communication between rhizosphere microorganisms and host plants, due to the diversity and complexity of their components. Currently, there is little research on the rhizosphere microbiome of *Fritillaria* plants; thus, the research on the rhizosphere microbiome will facilitate the recruitment of beneficial bacteria, and facilitate the development of *Fritillaria* resources.

Conclusion and future perspectives

In this review article, rhizosphere microorganisms were found to be closely related to the propagation, metabolism, and growth of *Fritillaria* medicinal plants. Therefore, the rhizosphere microorganisms of *Fritillaria* plants have received much attention, which not only helps to solve the practical problems of disease prevention among *Fritillaria* medicinal plants, but also improves the yield and quality of these plants. It also helps to clarify the interaction mechanism between *Fritillaria* medicinal plants and beneficial or harmful microorganisms in the rhizosphere. Based on the authors' knowledge, future research on rhizosphere microorganisms of *Fritillaria* medicinal plants should focus on the following aspects.

Optimizing research methods for rhizosphere microbial diversity among *Fritillaria* medicinal plants

Presently, the traditional method used on rhizosphere microorganisms is the pure culture method. With the development of molecular biology technology, the free culture method is widely used in the research of rhizosphere microorganisms of medicinal plants. However, the free culture method cannot obtain live strains, nor provide strains for the research of growth-promoting bacteria in the rhizosphere. Therefore, in the research of rhizosphere microbial diversity of *Fritillaria*, it is suggested to combine the pure culture method and free culture method. Moreover, there are few reports on the diversity of the rhizosphere microbial population of *Fritillaria* medicinal plants. Because most of the reports are only at the pure culture stage, in the future more attention should be carried out to explore the impact of different *Fritillaria* medicinal plant varieties, growth years, environmental conditions, and climate factors on the rhizosphere microbial diversity of these plants. The relationship between the rhizosphere microorganisms of *Fritillaria* medicinal plants and their growth should be understood in detail.

Improving the understanding of the relationship between medicinal plants of *Fritillaria* and rhizosphere microorganisms

The mechanism of interaction between *Fritillaria* medicinal plants and rhizosphere microorganisms is not clearly understood. In the future, more attention should be paid to the growth-promoting mechanism and the mechanism of the continuous cropping obstacle of *Fritillaria* medicinal plants. Moreover, the development of biocontrol agents should be strengthened. The perennial *Fritillaria* medicinal plants have suffered from widespread and serious underground diseases and insect pests, resulting in a decline in the quality of *Fritillaria* Chinese medicinal materials. Therefore, microbial agents that are safe, efficient, and pollution-free should be developed, which can improve the soil environment, and the output and quality of *Fritillaria* medicinal plants (Dong, 2018).

Revealing the relationship between diseases of *Fritillaria* medicinal plants and rhizosphere microorganisms

At present, pathogens of main diseases of *Fritillary* medicinal plants have been reported (Supi et al., 2012; Supi et al., 2015; Song et al., 2016a; Wang, 2017; Wu et al., 2021; Li et al., 2022), but some pathogens are only identified by morphological identification method, and need to be further identified by molecular biology method. The pathogen of a certain plant of *Fritillaria* may be speculated from the incidence of other *Fritillaria* plants, but the pathogen of the same disease in different *Fritillaria* plants are not exactly the same. Therefore, it is necessary to strengthen the research on the pathogenic microorganisms of diseases and insect pests of *Fritillaria*. Moreover, it is necessary to strengthen the research on rhizosphere microorganisms of diseased plants and healthy plants, explore which changes of rhizosphere microorganisms are *related* to the occurrence of medicinal plant diseases of *Fritillaria*, and screen biocontrol strains from rhizosphere microorganisms. Moreover, it is necessary to strengthen the research on rhizosphere microorganisms of diseased plants and healthy plants, explore which changes of rhizosphere microorganisms are related to the occurrence of medicinal plant diseases of *Fritillaria*, and screen biocontrol strains from rhizosphere microorganisms.

Currently, it would be more meaningful to develop more field applications for rhizospheric microbes rather than potted plants. The research methods on the rhizosphere microorganisms of *Fritillaria* medicinal plants are relatively isolated, thus it is necessary to learn from the research methods between other medicinal plants and rhizosphere microorganisms to understand the interaction mechanism between *Fritillaria* medicinal plants and rhizosphere microorganisms. In summary, it is expected that this review article will facilitate the development of *Fritillaria* medicinal plants.

Author contributions

NZ, C-MM, J-JZ, M-GM, and W-DL: investigation. NZ, W-DL, and M-GM: supervision. NZ, C-MM, J-JZ, and M-GM: writing—original draft. NZ, M-GM, and W-DL: writing—review and editing. All authors contributed to the article and approved the submitted version.

Funding

The financial support from National Natural Science Foundation of Chongqing (cstc2021jcyj-msxmX0115), Natural Science Foundation of Chongqing Municipal Education Commission (KJZD-K202101201) and Science and Technology Innovation of Wanzhou District, Chongqing (wzstc20210216) are gratefully acknowledged.

Conflict of interest

The authors declare that the research was conducted in the absence of any commercial or financial relationships that could be construed as a potential conflict of interest.

Publisher's note

References

Andezej, T., and Philip, P. P. (2015). Role of root microbiota in plant productivity. *J. Exp. Bot.* 66 (8), 2167–2175. doi:10.1093/jxb/erv157

Asadhi, S., Reddy, B. V., Sivaprasad, Y., Prathyusha, M., Murali Krishna, T., Vijay Krishna Kumar, K., et al. (2013). Characterisation, genetic diversity and antagonistic potential of 2, 4-diacetylphloroglucinol producing*Pseudomonas fluorescens*isolates in groundnut-based cropping systems of Andhra Pradesh, India. *Archives Phytopathology Plant Prot.* 46 (16), 1966–1977. doi:10.1080/03235408.2013.782223

Bais, H. P., Weir, T. L., Perry, L. G., Gilroy, S., and Vivanco, J. M. (2006). The role of root exudates in rhizosphere interactions with plants and other organisms. *Annu. Rev. Plant Biol.* 57, 233–266. doi:10.1146/annurev.arplant.57.032905.105159

Berg, G., Grube, M., Schloter, M., and Smalla, K. (2014). The plant microbiome and its importance for plant and human health. *Front. Microbiol.* 5, 491–492. doi:10.3389/fmicb.2014.00491

Brimecomve, M., Lelj, F. D., and Lynch, J. (2001). The effect of root exudates on rhizosphere microbial populations. *Rhizosphere* 361, 717–729. doi:10.1201/9780849384974-10

Bulgarelli, D., Schlaeppi, K., Spaepen, S., Ver, E., Themaat, L. V., and Schulza-Lefert, P. (2013). Structure and functions of the bacterial microbiota of plants. *Annu. Rev. Plant Biol.* 64, 807–838. doi:10.1146/annurev-arplant-050312-120106

Chen, B. Y., Ma, H. H., Yang, T., Cheng, Z. M., Niu, X. X., and Ma, X. W. (2017). Effect of different microbial fertilizer dosage on the elements of Fritillaria pallidiflora Schvek. *Xinjiang Agric. Sci.* 54 (05), 871–877. doi:10.6048/j.issn.1001-4330.2017.05.010

Chen, D. Y., Zhang, Z. Z., Li, R. X., Chen, J. R., Dai, X. F., Kong, Z. Q., et al. (2021). Research progress on quality safety status and analytical methods of Bulbus fritillaria. *J. Food Saf. Qual.* 12 (23), 9242–9250. doi:10.19812/j.cnki.jfsq11-5956/ts.2021.23.036

Chen, T., Zhong, F., Yao, C., Chen, J., Ma, Y., Dong, J., et al. (2020). A systematic review on traditional uses, sources, phytochemistry, pharmacology, pharmacokinetics, and toxicity of Fritillariae cirrhosae bulbus. *Evidence-Based Complementary Altern. Med.* 2020 (5), 1–26. doi:10.1155/2020/1536534

Chi, J. L., Hao, M., Wang, Z. X., and Li, Y. (2021). Advances in research and application of phosphorus-solubilizing microorganism. *J. Microbiol.* 41 (01), 1–7. doi:10.3969/j.issn.1005-7021.2021.01.001

Chinese Pharmacopoeia Commission (2020). *Pharmacopoeia of people's Republic of China: One edition*. Beijing, China: China Medical Science Press, 126–127.

Claire, A. (2017). Microbiome: A bag of surprises. *Nature* 551 (7679), S40–S41. doi:10.1038/551S40a

Cosetta, C. M., and Wolfe, B. E. (2019). Causes and consequences of biotic interactions within microbiomes. *Curr. Opin. Microbiol.* 50, 35–41. doi:10.1016/j.mib.2019.09.004

Cuningham, A. B., Brinckmann, J. A., Pei, S., Luo, P., Schippann, U., Long, X., et al. (2018). High altitude species, high profits: Can the trade in wild harvested Fritillaria cirrhosa (Liliaceae) be sustained? *J. Ethnopharmacol.* 223, 142–151. doi:10.1016/j.jep.2018.05.004

Dong, T. W. (2018). *The effect of combined application of nitrogen phosphorus fertilizer and microbial fertilizer on growth and quality of two-years-old Fritillaria Taipaiensis*. Xianyang, China, Northwestern Agriculture and Forestry University.

Edwards, J., Johnson, C., Santos-Medellin, C., Lurie, E., Sundaresan, V., Bhatnagar, S., et al. (2015). Structure, variation, and assembly of the root-associated microbiomes of rice. *Proc. Natl. Acad. Sci. U. S. A.* 112 (8), 911–920. doi:10.1073/pnas.1414592112

Ehrenfeld, J. G., Ravit, B., and Elgersma, K. (2005). Feedback in the plant-soil system. *Annu. Rev. Environ. Resour.* 30 (1), 75–115. doi:10.1146/annurev.energy.30.050504.144212

Garcia, J., and Kao-Kniffin, J. (2018). Microbial group dynamics in plant rhizospheres and their implications on nutrient cycling. *Front. Microbiol.* 9, 1516. doi:10.3389/fmicb.2018.01516

Geng, Z., Liu, Y. F., Gou, Y., Zhou, Q. M., He, C. J., Guo, L., et al. (2018). Metabolomics study of cultivated bulbus Fritillariae cirrhosae at different growth stages using UHPLC-QTOF-MS coupled with multivariate data analysis. *Phytochem. Anal.* 29 (3), 290–299. doi:10.1002/pca.2742

Gu, W. C., Mu, M. J., Yang, M., Guo, D. Q., and Zhou, N. (2020). Correlation analysis between bulb quality and rhizosphere soil factors of Fritillaria taibaiensis. *Chin. J. Exp. Traditional Med. Formulae* 26 (7), 165–177. doi:10.13422/j.cnki.syfjx.20200713

Guo, X. Y., Yang, Q., Chen, Z. H., Cai, R. X., Fang, F., and Chen, W. R. (2013). Allelopathic effects of Fritillary thunberbg Miqwa root exudate to its seedling. *J. Shanxi Agric. Sci.* 41 (11), 1197–1201. doi:10.3969/j.issn.1002-2481.2013.11.12

Han, M., Zhu, X. Y., Chen, G. W., Wan, X. M., and Wang, G. (2022). Advances on potassium-solubilizing bacteria and their microscopic potassium solubilizing mechanisms. *Acta Pedol. Sin.* 59 (2), 334–348. doi:10.11766/trxb202009190525

Hemkemeyer, M., Schwalb, S. A., Heinze, S., Joergensen, R. G., and Wichern, F. (2021). Functions of elements in soil microorganisms. *Microbiol. Res.* 252 (11), 126832. doi:10.1016/j.micres.2021.126832

Hu, J., Wei, Z., Friman, V. P., Gu, S. h., Wang, X. f., Eisenhauer, N., et al. (2016). Probiotic diversity enhances rhizosphere microbiome function and plant disease suppression. *MBIO* 7 (6), 017900–e1816. doi:10.1128/mBio.01790-16

Hu, L. F., Rbert, C. A. M., Cadot, S., Zhang, X., Ye, M., Li, B. B., et al. (2018). Root exudate metabolites drive plant-soil feedbacks on growth and defense by shaping the rhizosphere microbiota. *Nat. Commun.* 9 (1), 2738. doi:10.1038/s41467-018-05122-7

Huang, Y. S., Liu, H. M., Fang, C. X., Yu, Y., Chen, H. Z., Zhang, S. Y., et al. (2018). Comparative study on the pharmacodynamic differences of the anti-tussive and anti-inflammatory effects of the alkaloids from different varieties of Fritillariae cirrhosae bulbus. *Traditional Chin. Drug Res. Clin. Pharmacol.* 29 (1), 19–22. doi:10.19378/j.issn.1003-9783.2018.01.004

Jiao, N., Song, X., Song, R., Yin, D., and Deng, X. (2022). Diversity and structure of the microbial community in rhizosphere soil of *Fritillaria ussuriensis* at different health levels. *PeerJ* 10, e12778. doi:10.7717/peerj.12778

Lebeis, S. L., Rott, M., Dangl, J. L., and Schulze-Lefert, P. (2012). Culturing a plant microbiome community at the cross-Rhodes. *New Phytol.* 196 (2), 341–344. doi:10.1111/j.1469-8137.2012.04336.x

Li, F., Hao, Z. P., and Chen, B. D. (2019). Molecular mechanism for the adaption of arbuscular mycorrhizal symbiosis to phosphorus deficiency. *J. Plant Nutr. Fertilizers* 25 (11), 1989–1997. doi:10.11674/zwyf.18490

Li, F. L., Liu, M., Li, Z. P., Jiang, C. Y., Han, F. X., and Che, Y. P. (2013). Changes in soil microbial biomass and functional diversity with a nitrogen gradient in soil columns. *Appl. Soil Ecol.* 64, 1–6. doi:10.1016/j.apsoil.2012.10.006

Li, J. E., Wen, S. S., Zhang, Y. J., Jin, L. J., and Zhao, W. C. (2022). Identification of pathogenic fungi species of gray mold disease of *Fritillaria thunbergii*. *Plant protection* 48 (02), 151–156. doi:10.16688/j.zwbh.2021091

Liao, H. B., Li, Y. X., Shao, J. J., Fang, F., Guo, W. D., and Chen, W. R. (2011). Impacts of continuous cropping on Fritillaria thunbergii Miq. growth and rhizosphere soil properties. *Chin. J. Ecol.* 30 (10), 2203–2208. doi:10.13292/j.1000-4890.2011.0292

Liu, L. J., Wei, X. T., Liu, Y. H., and Yu, K. G. (2020). Screening of bio-control strain for rhizosphere soil of Fritillaria ussuriensis maxim. *J. Jilin Teach. Inst. Eng. Technol.* 36 (06), 89–91. doi:10.3969/j.issn.1009-9042.2020.06.028

Lundberg, D. S., Lebeis, S. L., Paredes, S. H., Yourtone, S., Gehring, J., Malfatti, S., et al. (2012). Defining the core arabidopsis thaliana root microbiome. *Nature* 488 (7409), 86–90. doi:10.1038/nature11237

Luo, M., Deng, C. F., Li, P. M., Tan, Q. S., Luo, Y., Xu, G., et al. (2021a). Research progress in medicinal plant *Fritillaria taipaiensis* P. *Y. Li. Chin. Wild Plant Resour.* 40 (2), 4256–4345. doi:10.3969/j.issn.1006-9690

Luo, S., Deng, C. F., Tan, Q. S., Luo, M., and Zhang, W. W. (2021b). Research progress on extraction, purification, structural characterization and biological activity of polysaccharides from *Fritillaria taipaiensis* P. *Y. Li. Agric. Eng. Technol.* 41 (14), 9496. doi:10.16815/j.cnki.11-5436/s.2021.14.059

Ma, M., Mu, M., Yang, M., and Zhou, Y. (2021). The effect of microbial fertilizer on the growth, rhizospheric environment and medicinal quality of *Fritillaria taipaiensis*. *Horticulturae* 7 (11), 500. doi:10.3390/horticulturae7110500

Mendes, R., Gareva, P., and Raaijmakers, J. M. (2013). The rhizosphere microbiome: Significance of plant beneficial, plant pathogenic, and human pathogenic microorganisms. *FEMS Microbiol. Rev.* 37 (5), 634–663. doi:10.1111/1574-6976.12028

Mojicevic, M., D'agostino, P. M., Nikodinovic-Runic, J., Vasiljevic, B., Gulder, T., and Voinovic, S. (2019). Antifungal potential of bacterial rhizosphere isolates associated with three ethno-medicinal plants (poppy, chamomile, and nettle). *Int. Microbiol.* 22 (3), 343–353. doi:10.1007/s10123-019-00054-8

Mu, M. J., and Li, P. Y. (2019c). *Study on effects of continuous cropping obstruction of Fritilliaria taipaiensis and its meitigation measures*. Dali, China, Dali University. doi:10.27811/d.cnki.gdixy.2019.000161

Mu, M. J., Nie, S. Y., Wang, Q., Yang, M., Zhang, G., Guo, D. Q., et al. (2019a). Variation pattern of rhizospheric soil nutrient for *Fritillaria taipaiensis*. *Chin. J. Exp. Traditional Med. Formulae* 25 (7), 189–194. doi:10.13422/j.cnki.syfjx.20190711

Mu, M. J., Zhang, D. G., Zhang, H., Yang, M., Guo, D. Q., and Zhou, N. (2019b). Correlation between rhizospheric microorganisms distribution and alkaloid content of *Fritillaria taipaiensis*. *Chin. J. Chin. Mat. Med.* 44 (11), 2231–2235. doi:10.19540/j.cnki.cjcmm.20190301.013

Pan, F., Su, T. J., Deng, K. L., Wu, W., and Wu, W. (2017). Antioxidant activities and metabolic constituents of endophytic Fusarium tricinctum CBY11 isolated from Fritillaria cirrhosa. *Mycosystema* 36 (6), 752–765. doi:10.13346/j.mycosystema.160190

Pan, H. X., Cheng, Z. M., Mou, S. Y., Qi, X. L., and Bao, Q. (2010a). Distribution of rhizosphere soil microbes of Fritillaria pallidiflora and their correlation with imperialine content. *Microbiol. China* 37 (8), 1253–1257. doi:10.13344/j.microbiol.china.2010.08.024

Pan, H. X., Cheng, Z. M., Qi, X. L., Bao, Q., and Mou, S. Y. (2010b). Influence of rhizosphere useful microbe on the yield of cultivated Fritillaria pallidiflora. *Arid. Land Geogr.* 33 (6), 917–922. doi:10.13826/j.cnki.cn65-1103/x.2010.06.010

Qiu, B. S. (2010). Rhizosphere soil microbes of *Fritillaria pallidiflora*. *Microbiology China* 37 (08), 1252. doi:10.13344/j.microbiol.china.2010.08.023

Rainer, G. J., and Florian, W. (2018). Alive and kicking: Why dormant soil microorganisms matter. *Soil Biol. Biochem.* 116, 419–430. doi:10.1016/j.soilbio.2017.10.022

Reinhold-Hurek, B., Buenger, W., Burbano, C. S., Sabale, M., and Hurek, T. (2015). Roots shaping their microbiome: Global hotspots for microbial activity. *Annu. Rev. Phytopathol.* 53 (1), 403–424. doi:10.1146/annurev-phyto-082712-102342

Sasse, J., Martinoia, E., and Northen, T. (2018). Feed your friends: Do plant exudates shape the root microbiome? *Trends Plant Sci.* 23 (1), 25–41. doi:10.1016/j.tplants.2017.09.003

Schmidt, J. E., Kent, A. D., Brisson, V. L., and Gaudin, A. (2019). Agricultural management and plant selection interactively affect rhizosphere microbial community structure and nitrogen cycling. *Microbiome* 7 (1), 146. doi:10.1186/s40168-019-0756-9

Shao, Q. Y., Dong, C. B., Han, Y. F., and Liang, Z. Q. (2021). Advances in the study of plant rhizosphere microorganisms groups. *J. Plant Nutr. Fertilizer* 27 (01), 144–152. doi:10.11674/zwyf.20203

Song, X. S., Yu, W. J., Yin, D. C., Zhou, Q., and Deng, X. (2016a). Pathogen identification and bionomics of the black rot of Fritillaria ussuriensis. *For. Pest Dis.* 35 (3), 7–11. doi:10.3969/j.issn.1671-0886.2016.03.002

Song, X. S., Yu, W. J., Zhou, Q., and Deng, X. (2016b). Microbial ecological study about the black rot of *Fritillaria ussuriensis* and its biological control bacteria screening. *For. Sci. Technol.* 041 (006), 18. doi:10.3969/j.issn.1001-9499.2016.06.006

Sun, R. T., Feng, X. C., Zhang, Z. Z., Zhou, N., Feng, H. D., Liu, Y. M., et al. (2022a). Root endophytic fungi regulate changes in sugar and medicinal compositions of Polygonum cuspidatum. *Front. Plant Sci.* 13, 818909. doi:10.3389/fpls.2022.818909

Sun, R. T., Zhang, Z. Z., Liu, M. Y., Feng, X. C., Zhou, N., Feng, H. D., et al. (2022b). Arbuscular mycorrhizal fungi and phosphorus supply accelerate main medicinal component production of Polygonum cuspidatum. *Front. Microbiol.* 13, 1006140. doi:10.3389/fmicb.2022.1006140

Sun, Y., Chang, J. J., and Tian, C. J. (2021). Ecological functions of the bacterial chemotaxis systems in rhizosphere microbiome. *Acta Ecol. Sin.* 41 (24), 9963–9969. doi:10.5846/stx202009292520

Supi, R. Z. G. L., Li, K. M., and ShaduhaxiSulaiman, K. S. (2012). Primary study of sclerotiniose on *Fritillaria pallidiflora* schvek in xinjiang. *Tianjin Agric. Sci.* 18 (3), 147–148. doi:10.3969/j.issn.1006-6500.2012.03.036

Supi, R. Z. G. L., Sulaiman, K. S., and Aybiek (2015). Research on identification of pathogeny and biological characteristics of bulbus fritillaria root rot. *Tianjin Agric. Sci.* 21 (3), 118–121. doi:10.3969/j.issn.1006-6500.2015.03.025

Tan, Y., Wang, Q. Q., Gao, T. T., Ma, Y., Shao, H. B., and Shao, C. Y. (2013). Effects of cultivation years on effective constituent content of Fritillaria pallidiflora Schernk. *Plant Biosyst. - Int. J. Deal. all Aspects Plant Biol.* 147 (4), 1184–1190. doi:10.1080/11263504.2013.859181

Tang, Y. J., Huang, X. G., Yan, X. N., and Yuan, X. F. (2021). Accumulation dynamics of alkaloids during the growth of Fritillaria thunbergii Miq. and its correlation with rhizosphere microenvironment. *J. Zhejiang Chin. Med. Univ.* 45 (08), 816–823. doi:10.16466/j.issn1005-5509.2021.08.002

Tian, Q., Qiang, Y., Chen, K. K., and Wang, J. Z. (2018). Research progress on the rare and endangered medicinal plant *Fritillaria taipaiensis* P. Y. Li. . *Shaanxi J. Agric. Sci.* 64 (9), 96–98. doi:10.3969/j.issn.0488-5368.2018.09.028

Tripathi, A., Mcdonald, D., Zhu, Q., Quinn, R. A., Taylor, B. C., Kosciolek, T., et al. (2018). Best practices for analysing microbiomes. *Nat. Rev. Microbiol.* 16 (7), 410–422. doi:10.1038/s41579-018-0029-9

Venturi, V., and Keel, C. (2016). Signaling in the rhizosphere. *Trends Plant Sci.* 21 (3), 187–198. doi:10.1016/j.tplants.2016.01.005

Vezzani, F. M., Andeson, C., Meenken, E., Gillespie, R., Peterson, M., and Bare, M. H. (2018). The importance of plants to development and maintenance of soil structure, microbial communities and ecosystem functions. *Soil Tillage Res.* 175, 139–149. doi:10.1016/j.still.2017.09.002

Vives-Peris, V., Ollas, C., Gomez-Cadenas, A., and Perez-Clemente, R. M. (2020). Root exudates: From plant to rhizosphere and beyond. *Plant Cell Rep.* 39 (1), 3–17. doi:10.1007/s00299-019-02447-5

Wang, D. Y. (2017). *Identification of main pathogenic fungus species isolated from* Fritillaria thunbergu *Miq. and their sensitivity to fungicides*. Hangzhou, China: Zhejiang Chinese Medical University.

Wang, R. H., Zhang, Q. F., Zhou, B. L., Liao, H., and Ma, G. S. (2007). Analysis on the interaction between root exudates and rhizosphere microbes. *Chin. J. Soil Sci.* 38 (1), 167–172. doi:10.19336/j.cnki.trtb.2007.01.037

Wang, Y. (2010). *Autotoxicity of Fritillaria pallidiflora in cropping continuous*. Ürümqi, China, Xinjiang Normal University.

Wang, Y., Kaisar, S., Li, J., Zhang, Y. L., and Zhu, G. Q. (2010b). Autotoxicity of root exudates of Fritillaria pallidiflora Schvek. *Crops* 8 (1), 25–28. doi:10.16035/j.issn.1001-7283.2010.01.009

Wang, Y., Kaisar, S., Li, J., Zhang, Y. L., Zhu, G. Q., and Ayi, B. K. (2010a). Autotoxicity of root exudates of Fritillaria pallidiflora Schvek. *Bull. Botanical Res.* 30 (2), 248–252. doi:10.7525/j.issn.1673-5102.2010.02.021

Wang, Y., Kaisar, S., Li, J., Zhu, G. Q., Song, T. S., and Liu, L. (2009). Analysis of components in root exudates of Fritillaria pallidiflora Schvek seedlings at different ages by gas chromatography-mass spectrometry. *Acta Bot. Boreal. Occident. Sin.* 29 (2), 384–389. doi:10.3321/j.issn:1000-4025.2009.02.028

Wees, M. V., Luijendijk, M., Smoorenburg, I., van Loon, L. C., and Pieterse, C. M. (1999). Rhizobacteria mediated induced systemic resistance (ISR) in Arabidopsis is not associated with a direct effect on expression of known defense-related genes but stimulates the expression of the jasmonate-inducible gene Atvsp upon challenge. *Plant Mol. Biol.* 41 (4), 537–549. doi:10.1023/a:1006319216982

Wei, Z. C., Pan, X. J., Huang, X. L., Li, H. L., Guo, D. Q., and Zhou, N. (2021). Effects of inoculation of *Fritillaria Taipaiensis* P. Y. Li with growth-promoting bacteria on inorganic elements in rhizosphere soil. *Environ. Chem.* 40 (4), 1254–1262. doi:10.7524/j.issn.0254-6108.2020093003

Wu, R., Chen, H., Guo, F. X., Zhou, Y., and Jiao, X. S. (2021b). Effects of growth years on soil bacterial community structure in rhizosphore soil of Fritillaria przewalskii. *Agric. Res. Arid Areas*, 39(06), 153–161. doi:10.7606/j.issn.1000-7601

Wu, R. (2021). *Mechanism of selection for stubbles and their adaptation in domesticated Fritillaria przewalskii maxim*. Lanzhou, China, Gansu Agricultural University. doi:10.27025/d.cnki.ggsnu.2021.000054

Yu, H. P., and Wu, Z. J. (2017). Experimental study on continuous cropping and fallow cultivation of Fritillaria fritillary. *Mod. Agric. Technol.* 12 (04), 45–48. doi:10.3969/j.issn.1007-5739.2017.04.030

Yu, Z. H., Jin, J., Li, Y. S., Yang, Y., Zhao, Y., Liu, C. K., et al. (2019). Distinct effects of short-term reconstructed topsoil on soya bean and corn rhizosphere bacterial abundance and communities in Chinese Mollisol. *R. Soc. open Sci.* 6 (1), 181054. doi:10.1098/rsos.181054

Yuan, J., Zhao, J., Wen, T., Zhao, M., Li, R., Pim, G., et al. (2018). Root exudates drive the soil-borne legacy of aboveground pathogen infection. *Microbiome* 6 (1), 156. doi:10.1186/s40168-018-0537-x

Zhang, J. H., Feng, B. B., and Wu, C. S. (2020). Effects of arbuscular mycorrhizal fungi on the growth and quality markers of *Fritillaria* P. *Y. Li. Chin. J. Inf. Traditional Chin. Med.* 27 (07), 88–93. doi:10.3969/j.issn.1005-5304.201908134

Zhang, J. Y., Liu, Y. X., Zhang, N., Hu, B., Jin, T., Xu, H. R., et al. (2019). NRT1.1B is associated with root microbiota composition and nitrogen use in field-grown rice. *Nat. Biotechnol.* 37 (6), 676–684. doi:10.1038/s41587-019-0104-4

Zhao, J., Liang, S. J., Yang, T., Wu, X. L., Qi, P. N., Wang, S. W., et al. (2021). Isolation of growth-promoting bacteria and effect of compound bacteria on yield of Fritillaria przewalskii. *Chin. J. Exp. Traditional Med. Formulae* 27 (24), 163–170. doi:10.13422/j.cnki.syfjx.20211512

Zhou, N., Mu, M. J., Xie, H., Wu, Y., Zhou, Y., and Li, W. (2021). Rhizospheric fungal diversities and soil biochemical factors of *Fritillaria taipaiensis* over five cultivation years. *Horticulturae* 7 (12), 560. doi:10.3390/horticulturae7120560

frontiers | Frontiers in Bioengineering and Biotechnology

TYPE Original Research
PUBLISHED 17 November 2022
DOI 10.3389/fbioe.2022.1059399

OPEN ACCESS

EDITED BY
Chunlin Xu,
Åbo Akademi University, Finland

REVIEWED BY
Ming-Guo Ma,
Beijing Forestry University, China
Jinhan Jeon,
Bosch, Singapore

*CORRESPONDENCE
Xiaoning Zhang,
xzhang@swu.edu.cn

This paper is dedicated to the memory of Professor Yong Zhu, whose devotion to understanding the biology of *Bombyx mori* was unsurpassed

SPECIALTY SECTION
This article was submitted to Bioprocess Engineering, a section of the journal Frontiers in Bioengineering and Biotechnology

RECEIVED 01 October 2022
ACCEPTED 04 November 2022
PUBLISHED 17 November 2022

CITATION
Ji Y, Zhang X, Zhu Y, Norton ML, Shen L, Tan W, Zheng X and Li S (2022), *In situ* preparation of molybdenum-dioxide-incorporated carbonized silk fiber and its application in supercapacitors. *Front. Bioeng. Biotechnol.* 10:1059399. doi: 10.3389/fbioe.2022.1059399

In situ preparation of molybdenum-dioxide-incorporated carbonized silk fiber and its application in supercapacitors

Yansong Ji[1], Xiaoning Zhang[1]*, Yong Zhu[1], Michael L. Norton[2], Lunfu Shen[3], Wenhui Tan[3], Xi Zheng[1] and Shuo Li[3]

[1]State Key Laboratory of Silkworm Genome Biology, College of Sericulture, Textile and Biomass Sciences, Southwest University, Chongqing, China, [2]Department of Chemistry, Marshall University, Huntington, WV, United States, [3]Chongqing Sericulture Science and Technology Research Institute, Chongqing Sericulture Technology Extension Station, Chongqing, China

A previous study found that the capacitive behavior of nanoparticles fed to the silkworm can be delivered to carbonized silk fibers, which can be used to fabricate electrodes for the construction of flexible supercapacitors. However, the tendency of nanoparticles to aggregate decreases the quantity of nanoparticles that enter the silk and therefore reduces the capacitance performance of the prepared carbonized silk. Here, we sprayed ammonium molybdate tetrahydrate (AMT) on the surface of mulberry leaves used for feeding silkworms and investigated the effect of feeding AMT on the growth of silkworms and the properties of spun silk. The precursor incorporated into the silk was converted into scattered MoO_2 NPs, which were embedded within the carbonized silk fiber (CSF) *via* carbothermal reduction. The specific capacitance of CSF obtained from silkworms fed with an aqueous solution of AMT-treated mulberry leaves reached up to 298 F/g at 0.2 g/A, which is much higher than that of the control group (102 F/g). Since AMT is highly water-soluble, and its concentration can be easily modulated, we believe that the proposed strategy is feasible for the large-scale fabrication of CSF with enhanced capacitive performance.

KEYWORDS

silkworms, modified mulberry leaves, carbonized silk, molybdenum dioxide, supercapacitors

1 Introduction

In recent years, the huge demand for wearable devices has promoted the rapid growth of flexible electronic components such as supercapacitors, which can serve as energy-storage devices in self-powered wearable systems (Wang et al., 2021). It is noteworthy that N doping can effectively enhance the capacitive performance of carbon-electrode supercapacitors (Wei et al., 2022). The carbonization of N-containing biomaterials is

an effective strategy for the production of N-doped carbon (Feng et al., 2021), and much research has focused on the fabrication of N-doped carbon electrodes from the graphitization of natural silk (Yang et al., 2021; Zhou et al., 2022).

Such carbonized silk has been shown to exhibit high electrical conductivity and flexibility (Hou C. et al., 2021); therefore, it is a suitable candidate for use as an electrode material in flexible supercapacitors. Multiple strategies to improve the capacitance of carbonized silk have been reported (Li et al., 2019; Pan et al., 2020). A common strategy involves the incorporation of electrochemically active substances after preparing the carbonized silk (Li et al., 2019; Xia et al., 2021). Such a post functionalization method is likely to suffer from the detachment of the active material from the silk-derived carbon support, resulting in capacity-fading behavior during the charge and discharge cycles.

Feeding silkworms with electrochemically active nanomaterials is an alternative strategy for generating carbonized silk with an enhanced supercapacitive performance. In this process, the nanoparticles are incorporated into silk and retained in the encapsulated form after pyrolysis. Although this approach is sufficient to prevent detachment of these active particles from the carbonized silk, previous studies (Liang et al., 2020) have indicated that the aggregation of nanoparticles during feeding appears to compromise the nanoparticle characteristics crucial for their application in supercapacitors. In addition, aggregation results in a loss of uniformity in the active-substance distribution in the silk product because the nanoparticles cannot pass across the epithelial tissue of the silk gland when they aggregate into large clusters.

Zhuang et al. (2014) reported that molybdenum dioxide (MoO_2) particles can be prepared *in situ* by the carbothermal reduction of ammonium molybdate tetrahydrate (AMT). Owing to its metal-like conductivity and environmental friendliness, MoO_2 is a promising pseudocapacitive candidate and has been used extensively in supercapacitor-related devices (Zhang et al., 2020). We assume that AMT will uniformly disperse in silk because it can be evenly distributed over the mulberry leaf owing to its good solubility. Furthermore, because silkworm silk is constructed from oriented nanofibrils (Wang et al., 2020), the AMT incorporated within the silk can be converted into MoO_2 nanoparticles after pyrolysis owing to its limited diffusion within the void spaces of the nanosized filaments.

In this study, the mechanically enhanced silk were obtained by feeding silkworm AMT-solution-sprayed mulberry leaves. In addition, a strategy for the *in situ* preparation of MoO_2 NPs embedded in silk-derived carbon was explored. The composites exhibited enhanced capacitance. In comparison with feeding nanoparticles to silkworms, the proposed strategy effectively avoids the aggregation of nanoparticles. Therefore, the precursor amount can be modulated, allowing the electrochemically active substance to be more efficiently incorporate into the CSF. Additionally, metallic salts are less expensive than metallic nanoparticles, making them more practical for the large-scale fabrication and application of CSF.

2 Materials and methods

2.1 Materials and reagents

The silkworm strain used in the experiment was *Bombyx mori* (871 × 872), sourced from the Chongqing Sericulture Science and Technology Research Institute (Chongqing, China). Ammonium molybdate tetrahydrate (AMT) was purchased from Shanghai Darui Fine Chemical Co., Ltd. (Shanghai, China); sodium chloride was purchased from Shanghai Aladdin Bio-Chem Technology Co., Ltd. (Shanghai, China); nitric and perchloric acids were purchased from Beijing Institute of Chemical Reagents (Beijing, China); sodium carbonate and ethanol were purchased from Chongqing Chuandong Chemical Co., Ltd. (Chongqing, China); potassium bromide was purchased from Sangon Biotech Co., Ltd. (Shanghai, China); hematoxylin and eosin (H&E) staining kits were purchased from Nanchang Yulu Experimental Equipment Co., Ltd. (Nanchang, China); dimethylbenzene and poly (tetrafluoroethylene) were purchased from Shanghai Macklin Biochemical Co., Ltd. (Shanghai, China); Super P was purchased from Canrd New Energy Technology Co., Ltd. (Guangzhou, China); and foam Ni was purchased from Taiyuan Lizhiyuan Co., Ltd. (Shanxi, China). All chemicals were of analytical grade and used without further purification. The deionized (DI) water used in this work was produced using a Milli-Q Direct-8 purification system (resistivity >18 MΩ cm, Millipore Inc., France) onsite.

2.2 Rearing of silkworms

The AMT was weighed and dissolved in DI water to obtain Mo dosages of 0.05, 0.1, 0.5, 1, 5, and 10 g/L in the prepared solutions. Fresh mulberry leaves were rinsed with DI water and air-dried at room temperature until the surface was free of residual water. Then, 200 g of mulberry leaves were weighed, and 30 ml of AMT solution containing various dosages of Mo was sprayed evenly on each side of the mulberry leaves. Subsequently, the moisture on the mulberry leaves were dried at room temperature, and the leaves were preserved in a refrigerator at 4°C for later use.

Silkworms were reared with mulberry leaves at 25°C from the first to the fourth instar, three times per day. On the first day of the fifth instar, silkworm larvae were divided into seven groups of 50 larvae each, as listed in Supplementary Table S1.

2.3 Effects of AMT on the growth of the silkworm larvae and their cocooning

From the first day of the fifth instar, the weight of ten silkworms selected randomly from each group was measured.

The appearance of the silkworms on the eighth day of the fifth instar was recorded using a camera (D3400, Nikon, Japan). After harvesting the cocoons, the cocooning rate of each group was calculated. In addition, the length and width of each cocoon were measured using calipers. The cocooning rates and cocoon-shell ratios were determined using the following equations:

$$\text{Cocooning rate} = \frac{n_1}{n_2} \times 100\% \quad (1)$$

$$\text{Cocoon shell ratio} = \frac{m_1}{m_2} \times 100\% \quad (2)$$

where n_1 is the number of cocoons harvested; n_2 is 45, the number of silkworms reared from the five silkworms selected for dissection; m_1 is the mass of the cocoon shell (g); and m_2 is the mass of the whole cocoon (g).

2.4 Effects of AMT on the morphology and histology of silk glands

On the eighth day of the fifth instar, five silkworms were randomly selected from each group immediately before cocooning. The silk glands were dissected and rinsed three times with physiological saline before imaging with a camera.

Subsequently, the posterior silk glands were removed and immersed in formaldehyde solution (4%, v/v) for fixation. The posterior silk glands were then embedded in paraffin and sliced (5 μm thick) using a microtome (RM2235; Leica Microsystems Co., Ltd., Germany). For histopathology, the posterior silk glands were stained with H&E and observed under an optical microscope (DM3000, Leica Microsystems Co., Ltd., Germany).

2.5 Preparation and characterization of degummed silk

Silk cocoons were degummed by boiling a solution of Na_2CO_3, according to a previously published method (Liang et al., 2020). The resultant degummed silk fibers were observed using scanning electron microscopy (SEM; TM4000Plus, HITACHI, Japan) and transmission electron microscopy (TEM; Talos F200X, Thermo Scientific, United States). Prior to the SEM observation, the specimens were sputter-coated with gold to achieve high conductivity. For TEM observation, the degummed silk fibers were cut into fine pieces and sonicated in ethanol for 10 min. A drop of the dispersion was subsequently placed on a carbon-coated copper grid and dried in an oven at 60°C.

Samples were prepared for FTIR analysis following the KBr pellet method (Liang et al., 2020). Each sample was scanned 32 times, from 400 cm^{-1} to 4,000 cm^{-1}, with a resolution of 4 cm^{-1}. Quantitative analysis of the protein secondary structure was performed for the amide I band from 1,600 cm^{-1} to 1,720 cm^{-1} using a Fourier-transform infrared (FTIR) spectrometer (Nicolet iN10, Thermo Scientific, United States). The baseline of the amide I band was first corrected, and the peak was fitted with a Gaussian function using Origin 9.1 Pro software (Origin Lab, United States).

2.6 Molybdenum content determination

Both the degummed silk fibers and cocoons were cut into small pieces, rinsed with DI water three times, and then dried in an oven at 60°C. Based on a previously reported method (Liang et al., 2021), the molybdenum (Mo) contents of both the degummed silk fiber and cocoon were analyzed using inductively coupled plasma optical-emission spectrometry (ICP-OES; Agilent 730, Agilent Technologies, United States).

2.7 Silk reeling and mechanical property evaluation

Six cocoons from each group were selected randomly, and each cocoon was placed in boiling water, untangled, and processed using a cocoon-reeling apparatus (YG731, Changzhou First Textile Equipment Co., Ltd., China). For each cocoon, 100 silk strands were reeled and combined to form a single thread. One meter of initially reeled silk thread was cut into three segments. For each segment, the widths of the front, middle, and rear parts were measured at six different positions using optical microscopy. The average width of each thread was calculated from 18 measurements.

Prior to testing, the reeled silk threads were maintained in an artificial climate chamber (HQH-250, Shanghai Yuejin Medical Instrument, China) at 20°C and 65% relative humidity for 24 h. The stress–strain curve of each silk thread was then measured using an electronic tensile-strength measuring machine (YG020, Changzhou First Textile Equipment Co., Ltd., China) according to the China National Standard GB/T 1798-2008 (Standardization Administration of China, 2009). The fracture strength and elongation at break were calculated using Eqs 3, 4. The area under the stress-strain curve was integrated using Origin software to obtain the toughness modulus of each silk thread.

The fracture strength was calculated using the following equation:

$$\sigma = \frac{F}{C} \times 100\% \quad (3)$$

where σ is the fracture strength (MPa), F is the force applied parallel to its length (N), and C is the cross-sectional area of the silk fiber (cm^2).

The elongation at break was calculated using the following equation:

$$\varepsilon = \frac{L - L_0}{L_0} \times 100\% \quad (4)$$

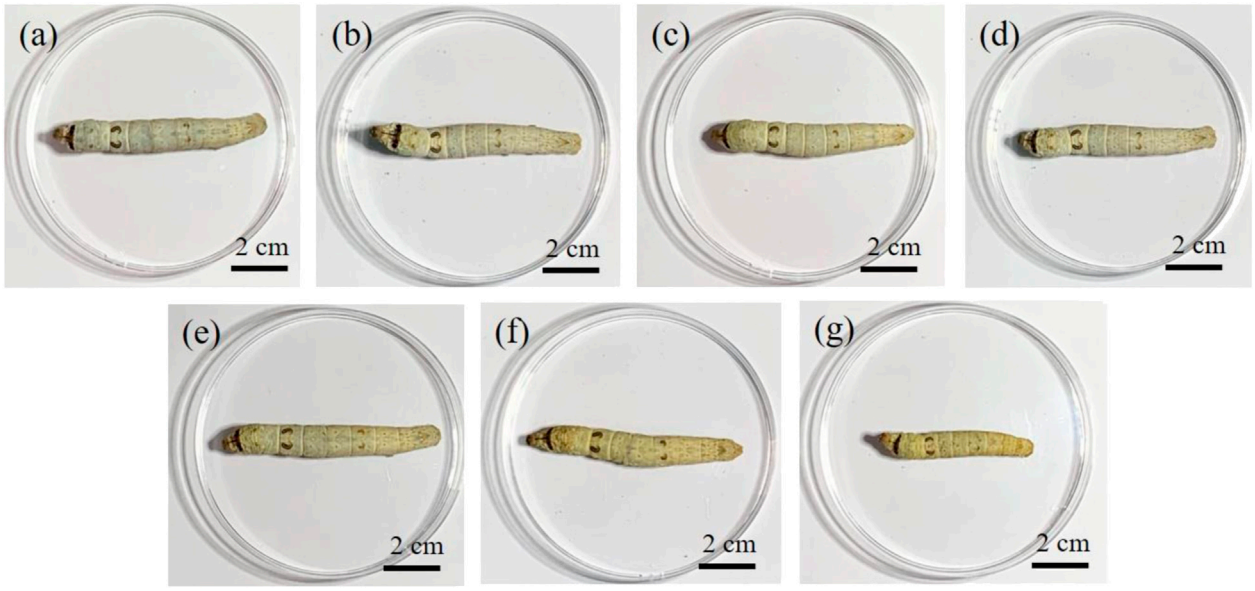

FIGURE 1
Effect of AMT feeding on the appearance of the silkworm larvae: **(A)** control group, **(B)** Mo-0.05 g/L group, **(C)** Mo-0.1 g/L group, **(D)** Mo-0.5 g/L group, **(E)** Mo-1 g/L group, **(F)** Mo-5 g/L group, and **(G)** Mo-10 g/L group.

where ε is the elongation at break (%), L_0 is the original length of the silk fibers (cm), and L is the length of the silk fiber at break (cm).

2.8 Preparation and characterization of carbonized silk fibers

The carbonized silk fibers (CSF) were prepared based on a previously reported heating protocol (Liang et al., 2020). The micromorphology and structure of the CSF were observed using SEM and TEM following the procedure described in Section 2.5. It should be noted that sputtering the CSF is unnecessary owing to their inherent electroconductivity.

Subsequently, the Raman spectra of each group were obtained using a Raman spectrometer (inVia, Renishaw, United Kingdom). The analysis was performed at an excitation wavelength of 532 nm, scanning range of 100–3,500 cm^{-1}, and spectral resolution of 2 cm^{-1}. All data were processed using Origin software. Following a previously reported method (Sadezky et al., 2005; Khatibi et al., 2019), a mixed Gaussian–Lorentzian peak morphology was used to deconvolve the experimental Raman spectrum into a Gaussian-shaped D3 band (1,500 cm^{-1}), Lorentzian-shaped D (1,350 cm^{-1}), D2 (1,620 cm^{-1}), D4 (1,200 cm^{-1}), and G bands. As the G band spans from 1,585 cm^{-1} to 1,600 cm^{-1}, 1,585 cm^{-1} was chosen to best fit the Lorentzian-shaped band. The relative intensity (peak area) ratio of the D and G bands was calculated.

2.9 Electrical conductivity test

The CSF was cut into fine pieces for electrical conductivity measurements following the method reported by Liang et al. (Liang et al., 2020). A Keithley source meter (2,400, Tektronix, United States) and homemade apparatus (Supplementary Figure S1) were used for the test. The electrical conductivity was calculated using the following equation:

$$\rho = \frac{R}{L} \times S \tag{5}$$

$$\sigma = \frac{1}{\rho} \tag{6}$$

where ρ is the resistivity (Ω·m), R is the measured resistance (Ω), S is the cross-sectional area of the container containing the packed sample (m^2), L is the length of the sample packed within the container (m), and σ is the electrical conductivity (S/m).

2.10 Electrochemical measurements

The preparation of a nickel-foam-supported carbonized silk anode is described in the third section of the Supplementary Materials. Cyclic voltammetry (CV), galvanostatic charge–discharge (GCD), and electrochemical impedance spectroscopy (EIS) measurements were performed using an electrochemical workstation (CS350H, Wuhan Corrtest Instruments, China). All these analyses were performed in a

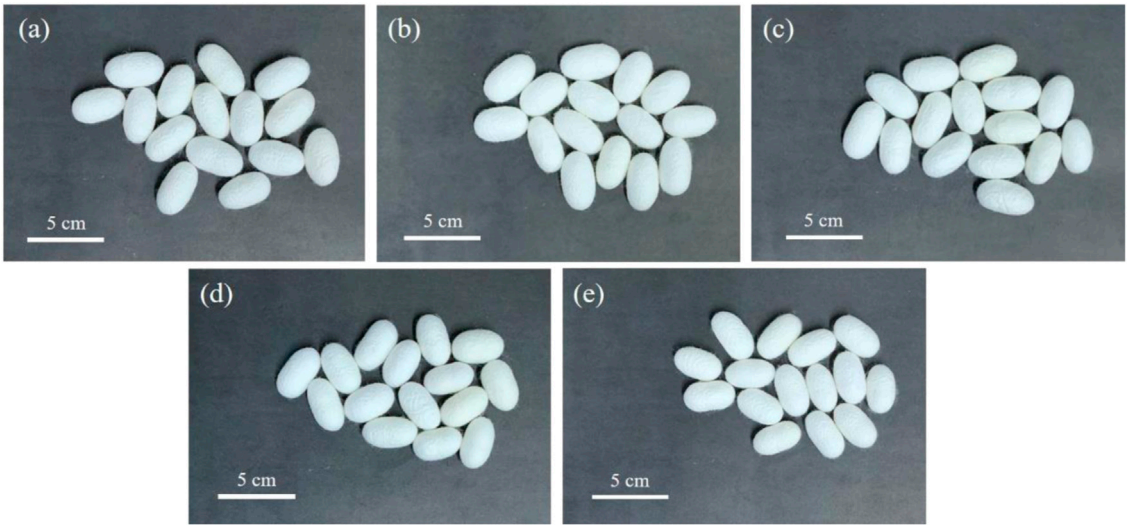

FIGURE 2
Effect of AMT feeding on the appearance of silkworm cocoons: **(A)** control group, **(B)** Mo-0.05 g/L group, **(C)** Mo-0.1 g/L group, **(D)** Mo-0.5 g/L group, and **(E)** Mo-1 g/L group.

6 M KOH aqueous electrolyte using a three-electrode system composed of a nickel-foam composite as the working electrode, Hg/HgO as the reference electrode, and Pt wire as the counter electrode. CV measurements were performed in a potential window from −1 V to −0.2 V at scan rates of 5, 10, 20, 40, 60, and 80 mV/s. The GCD curves were recorded within a potential window from −1 V to −0.2 V at various current densities, including 0.2, 0.4, 0.6, 0.8, 1, and 2 A/g. The specific capacitance of each sample was calculated using the following equation:

$$C_m = \frac{I \times \Delta t}{M \times \Delta V} \quad (7)$$

where C_m (F/g) is the mass specific capacitance, I (A) is the discharge current, Δt (min) is the discharge time, M (g) is the mass of the CSF loaded on the nickel foam, and ΔV (V) is the potential window.

3. Results and discussion

3.1 Investigation of AMT-fed silkworm growth and cocooning

The effect of AMT on the growth of silkworm larvae was investigated. As shown in Figure 1, the body lengths of the silkworms from the Mo-5 g/L and Mo-10 g/L groups were much shorter than those of the other groups. Combining the experimental data for silkworm growth (Supplementary Figure S3), it can be concluded that the AMT-solution-sprayed mulberry leaves fed to both Mo-5 g/L and Mo-10 g/L groups exerted a strong toxic effect on the silkworm.

It was found that only a few silkworms in the Mo-5 g/L and Mo-10 g/L groups could survive through cocooning and began to pupate, resulting in a low cocooning rate (Supplementary Figure S4). In addition, it is noteworthy that the cocoons spun by the surviving silkworm in both the Mo-5 g/L and Mo-10 g/L groups were unreelable owing to their very thin cocoon shells (Supplementary Figure S5), thereby exhibiting a poor economic value. Therefore, the Mo-5 g/L and Mo-10 g/L groups were not included in the subsequent experiments. Fortunately, the silkworm in the control, Mo-0.05 g/L, Mo-0.1 g/L, Mo-0.5 g/L, and Mo-1 g/L groups displayed acceptable cocooning rates (Supplementary Figure S4).

A further investigation of the cocoons of the silkworms from the control, Mo-0.05 g/L, Mo-0.1 g/L, Mo-0.5 g/L, and Mo-1 g/L groups, as shown in Figure 2, revealed that the width and length of the cocoon, as well as the cocoon shell ratio, declined with an increase in AMT dosage fed to the silkworm (Figure 3). This finding suggests that AMT had a negative effect on silkworm cocooning.

3.2 Morphology and histology of the silk gland

The posterior silk gland (PSG) is the only organ that synthesizes and secretes silk fibroin (Hou et al., 2007). Here, H&E-stained PSG histopathological images were used to

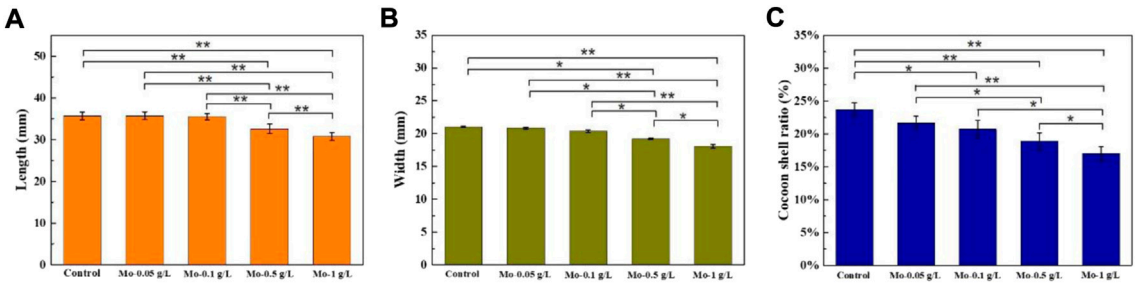

FIGURE 3
Effect of AMT feeding on the cocoon **(A)** length, **(B)** width, and **(C)** shell ratios. (n = 5, *$p < 0.05$, **$p < 0.01$).

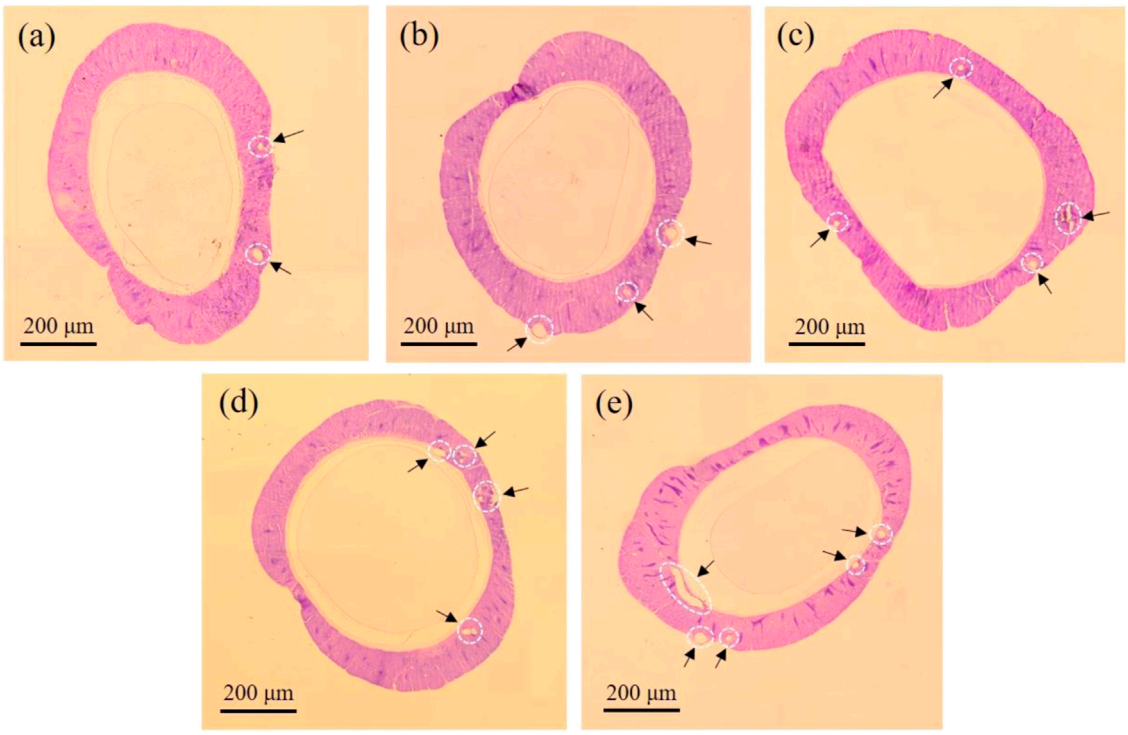

FIGURE 4
Histophysiological image of posterior silk gland from **(A)** control group, **(B)** Mo-0.05 g/L group, **(C)** Mo-0.1 g/L group, **(D)** Mo-0.5 g/L group, and **(E)** Mo-1 g/L group. The dark arrows point to the areas of vacuolation.

understand the impact of AMT on PSG development. Silkworm silk-gland tissue includes the outer epithelial membrane, gland cells, and inner epithelial membrane (Akai, 1983). Among these, gland cells are involved in the secretion of silk proteins. The number of gland cells is positively correlated with the silk production quantity (Wu et al., 1961). Therefore, the sparseness of silk gland cells reflects the degree of silk gland injury (Cheng et al., 2018). As shown in Figure 4, the gland cell population decreased with increasing AMT feeding dosage, and the H&E-stained section of the Mo-1 g/L group demonstrated the most severe vacuolation. Such damage may be responsible for the decreased cocoon shell ratio and cocoon size as the AMT feeding amount increased.

In addition to PSG, adverse effects caused by feeding silkworms high dosages of AMT were apparent in the anterior and middle silk glands, as shown in Supplementary Figure S6. The results indicate that feeding silkworms with a high dosage of AMT suppressed silk gland development.

3.3 Mo content determination

Degummed silk is commonly used in the textiles industry. ICP-OES was employed to determine the elemental Mo content remaining in the degummed silk. As shown in Supplementary Table S2, compared with the Mo content in the control group, the Mo content in the degummed silk continued to increase as the AMT feeding dose increased. The Mo content in the cocoons of each group exhibited a similar trend (Supplementary Table S3), indicating that Mo was distributed in both silk sericin (SS) and silk fibroin (SF). These results show that feeding silkworms AMT can effectively enrich the Mo content of silk.

3.4 Microstructural study of degummed silk

Raw silk consists of two components, SF and SS, where the former endows silk with good mechanical properties and stability (Kim et al., 2005). Figure 5 presents a SEM image showing the micromorphology of degummed silk. It is clear that the morphologies of the degummed silk from each group are similar, but their widths vary. The average width of the degummed silk decreased with increasing AMT dosage (Supplementary Figure S7). We assume this is due to the reduced silk production caused by vacuolation of the silk gland, as discussed in Section 3.2.

3.5 Transmission electron microscopy investigation

Transmission electron microscopy was used to evaluate the interior structure of degummed silk. As shown in Figure 6, neither particles nor crystal structures were observed within the degummed silk of any group. Whereas EDS analysis confirmed the uniform distribution of Mo along the degummed silk fiber (Supplementary Figure S8, S9). Therefore, we believe that AMT fed to the silkworm entered silk as a precursor.

3.6 FTIR spectroscopy characterization of degummed silk

The mechanical behavior of silk fiber is expected to be highly dependent on its secondary structure (Wang et al., 2017). Here, FTIR spectroscopy was used to determine the distribution of the secondary structure in the degummed silk to explore the effect of feeding AMT to each group and to provide detailed information on the mechanical properties of the silk. As shown in Figure 7A, each group shares a similar protein molecular structure profile containing three different amide groups: amide I (1,600–1720 cm^{-1}), amide II (1,500–1,600 cm^{-1}), and amide III (1,200–1,350 cm^{-1}) (Cheng et al., 2018; Chen et al., 2019). Deconvolution of the amide I band of each group (Supplementary Figure S10) revealed variations in the percentages of β-sheets, random coils/α-helixes, and β-turns (Figure 7B). The composition of the secondary structure (Supplementary Table S4) revealed that the percentages of both β-sheets and β-turns increased once AMT was fed to the silkworm and was maximal when the Mo feeding dosage reached 0.1 g/L. This value then decreased when the Mo feeding dosage was greater than 0.1 g/L. By contrast, the percentages of random coils/α-helixes exhibited the opposite trend, declining initially, subsequently increasing, and then reaching its minimum value when the Mo feeding dosage was 0.1 g/L.

Metal ions can coordinate with silk fibroin, promoting its conformational transition (Xu and Zhang, 2008; Liu et al., 2019). We believe that a low concentration of molybdate can induce the formation of β-sheets and β-turns through coordination and chelation with SF, thereby helping to align and orient SF molecular chains. In addition, the formation of intermolecular hydrogen bonds among the SF molecules facilitates the transformation of the SF secondary structure (Viles et al., 1999). Thus, when the Mo feeding dosage ranged from 0.05 g/L to 0.1 g/L, we observed a rise in the percentage distributions of both β-sheets and β-turns, while the percentage of random coils/α-helixes declined. It is reasonable to infer that the repulsive force arising from the excess molybdate coordinated with SF would inhibit the interactions among SF molecular chains, thus inhibiting its conformational transition. Such an inference can explain the decrease in the percentage distributions of both β-sheets and β-turns and increase in the percentage of random coils/α-helixes when the AMT feeding dosage ranged from 0.5 g/L to 1 g/L. A schematic representation of this process is shown in Supplementary Figure S11.

3.7 Determination of silk-thread mechanical properties

Before the mechanical tests were carried out, the silk threads were observed using an optical microscope and their widths were measured, as presented in Supplementary Figure S12. According to the analysis (Supplementary Figure S13), the width of the silk thread from each group decreased continuously as the AMT feeding dosage increased. This trend is consistent with the variation of the degummed silk width with AMT feeding dosage (Supplementary Figure S7).

Subsequently, the mechanical properties of silk threads from each group were evaluated by performing tensile tests, with results from all testing summarized in Supplementary Table S5–S9. The stress–strain curves are shown in Figure 8. It can be observed that both the fracture strength and elongation at break initially increased as the AMT feeding dosage increased,

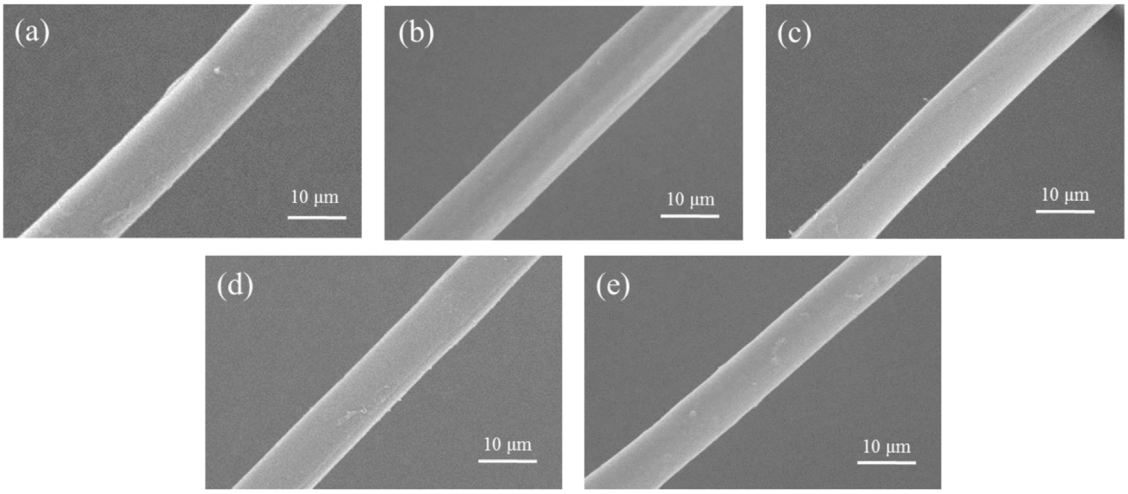

FIGURE 5
Representative SEM images of the degummed silk fiber from the **(A)** control group, **(B)** Mo-0.05 g/L group, **(C)** Mo-0.1 g/L group, **(D)** Mo-0.5 g/L group, and **(E)** Mo-1 g/L group.

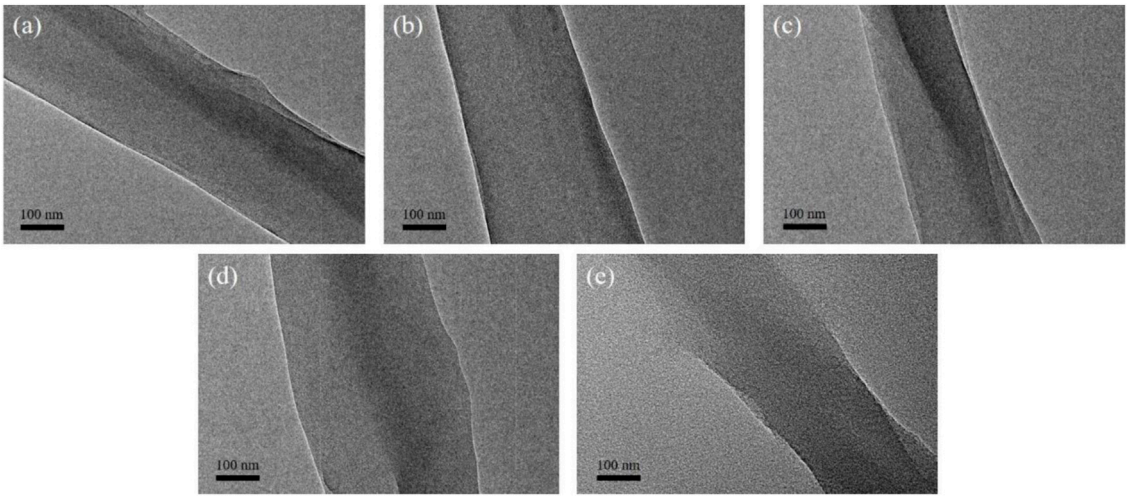

FIGURE 6
Representative TEM images of the degummed silk fiber from the **(A)** control group, **(B)** Mo-0.05 g/L group, **(C)** Mo-0.1 g/L group, **(D)** Mo-0.5 g/L group, and **(E)** Mo-1 g/L group.

and both reached a maximum when the Mo feeding dosage reached 0.1 g/L. Subsequently, both the fracture strength and elongation at break decreased when the Mo feeding dosage was greater than 0.1 g/L.

The effect of AMT on the mechanical properties of silk can be attributed to the secondary structure of silk fibroin. As described in Section 3.6, feeding silkworms ≤0.1 g/L of Mo can promote the formation of β-sheets and β-turns (Xu and Zhang, 2008). It is known that the β-sheet structure imparts stiffness and toughness to silk (Porter and Volrath., 2010; Mandal et al., 2012); therefore, the enhanced percentage distribution of the β-sheet structure would lead to a higher fracture strength of the silk thread. On the other hand, folding the β-sheet structure back onto itself is a function of the β-turn structure, which can facilitate the formation of crystalline β-sheet stacks stabilized by hydrogen bonds and Van der Waals interactions between sheets (Nelson

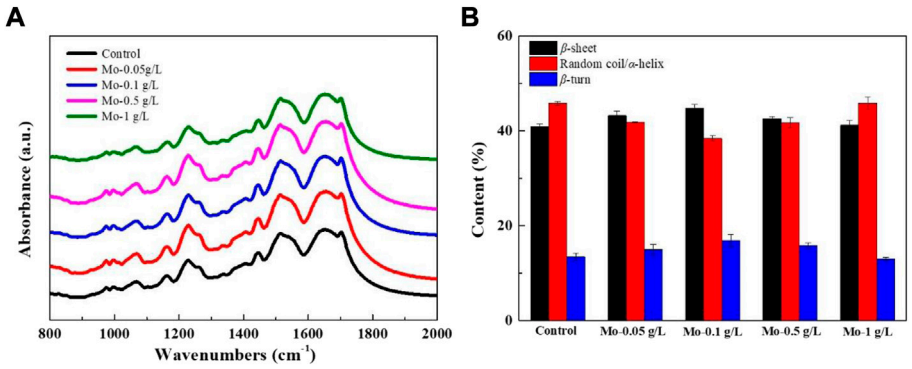

FIGURE 7
Effect of AMT feeding on the secondary structures of silk fibroin. **(A)** FTIR spectra of silk fibroin from each group, and **(B)** the percentage contents of secondary structures in the amide I band of silk fibroin from each group.

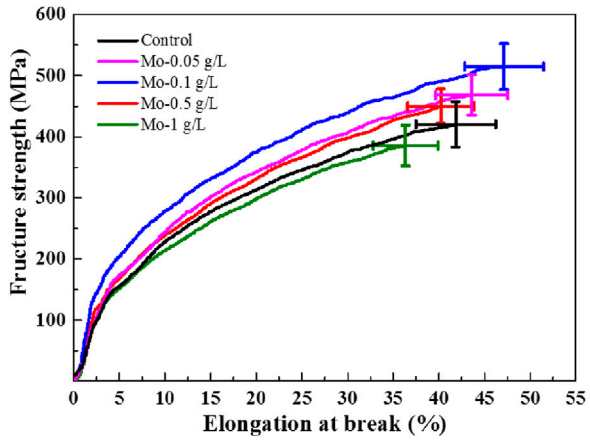

FIGURE 8
Strain–stress curves of the obtained silk threads.

and Cox., 2005). Such weak interactions are responsible for the flexibility and softness of silk, thereby increasing its elongation at break. When the Mo feeding dosage exceeded 0.1 g/L, the repulsion from the protein-bound molybdate inhibited the secondary structural transition of silk from random coil/α-helix to β-sheet and β-turn structures, as well as the interactions among all peptides, resulting in a decline in fracture strength and elongation at break.

With the molybdate concentration is further increased, electrostatic repulsion among molybdate–silk fibroin complexes can be expected, hindering the aggregation of molybdate-bound silk fibroin and ultimately inhibiting the transformations of α-helixes/random coils into β-sheet structures. The decrease in β-sheet content caused the silk fibers to break easily. Moreover, electrostatic repulsion may affect the supramolecular interactions of the α-helix/random coil itself, such as hydrogen bonds and Van der Waals forces, unfolding the amorphous chains and ultimately affecting the flexibility of the silk fibers (Pérez-Rigueiro et al., 2000).

The modulus of toughness can be calculated from the integral area under the stress–strain curve and represents the total energy absorbed by the silk thread before it fractures (Vollrath and Porter 2006). As shown in Table 1, the modulus of toughness for the silk thread from each group followed a similar trend to those of both fracture strength and elongation at break, reaching its maximum value when the Mo feeding dosage was 0.1 g/L.

3.8 SEM and TEM analyses of carbonized silk fibers

SEM was used to observe the morphology of the CSF derived from each group. As shown in Figure 9, the degummed silk remained fibrous after carbonization. In addition, the width of the CSF is smaller than that of the degummed silk, which can be attributed to the pyrolysis process (Fisher et al., 2002). It should be noted that the SEM images were acquired without coating the sample with gold owing to the good conductivity of CSF.

TEM was used to characterize the structure and composition of CSF. As shown in Figure 10, nanoscale opacities or "dark spots" are visible within the CSF of each AMT feeding group. In addition, the number of dark spots associated with each group gradually increased with an increase in AMT feeding dosage. By contrast, no dark spots were observed within the CSF of the control group.

High-resolution TEM (HRTEM) was used to elucidate the crystallographic orientation of the inclusions, which appear as dark spots in the images shown in Figure 10. Figure 11 displays the magnified HRTEM images of the particles delineated by the white dotted boxes in Figure 10. The lattice-resolved HRTEM

TABLE 1 Mechanical properties of the obtained silk threads.

Sample	Properties		
	Fracture strength [MPa]	Elongation at break [%]	Modulus of toughness [GJ/m3]
Control	418.88 ± 37.04	42.06 ± 4.36	11.80 ± 1.54
Mo-0.05 g/L	468.29 ± 33.32	44.03 ± 3.97	14.20 ± 2.44
Mo-0.1 g/L	508.46 ± 37.66	46.22 ± 4.32	16.02 ± 1.83
Mo-0.5 g/L	459.30 ± 28.16	41.26 ± 3.63	12.57 ± 0.94
Mo-1 g/L	399.69 ± 33.48	37.22 ± 3.55	9.95 ± 1.18

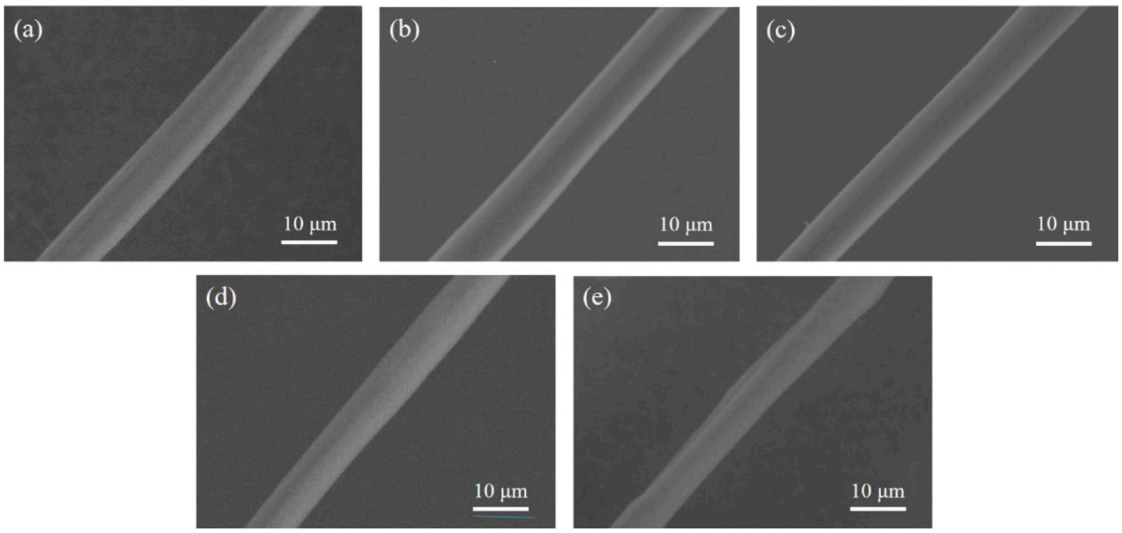

FIGURE 9
Representative SEM images of CSF derived from the **(A)** control group, **(B)** Mo-0.05 g/L group, **(C)** Mo-0.1 g/L group, **(D)** Mo-0.5 g/L group, and **(E)** Mo-1 g/L group.

images of the particles embedded in the CSF display interplanar spacings of 0.152, 0.231, and 0.275 nm, corresponding to the (011), (021), and (102) planes, respectively, of MoO_2 (JCPDS 73-1249). Amorphous carbon derived from SF can also be observed, as indicated by the solid red boxes in each image. Furthermore, the insets show the fast Fourier transforms (FTT) of the areas within the white solid boxes in each image; the (011), (021), and (102) lattice planes of MoO_2 can be identified. Additionally, the EDS analysis confirmed that the dark spots embedded in the CSF contained Mo (Supplementary Figure S14).

Since silk fiber consists of a bundle of nanofibrils with a geometric width ranging from 90 to 170 nm (Putthanarat et al., 2000), we believe that this architecture limits the growth and aggregation of MoO_2 particles, resulting in the uniform dispersion of MoO_2 NPs in the silk, as shown in Figures 10, 11.

3.9 Raman characterization of carbonized silk fibers

To investigate the effect of MoO_2 NPs generated *via* pyrolysis on the graphitization degree of CSFs, the Raman spectra of the CSFs from each group were deconvoluted (Supplementary Figure S15) and analyzed. As shown in Figure 12A, the Raman spectra of each group display two characteristic peaks at 1,350 cm^{-1} (D band) and 1,585 cm^{-1} (G band). The D band represents the defects and disorder in the carbon lattice, while the G band represents the in-plane stretching vibration of sp^2-hybridized carbon atoms in the graphite layers (Yang et al., 2020). The graphitization degree can be determined by the relative intensity ratio of the D and G bands, I_D/I_G, where a lower I_D/I_G value indicates a higher graphitization degree (Dong et al., 2014).

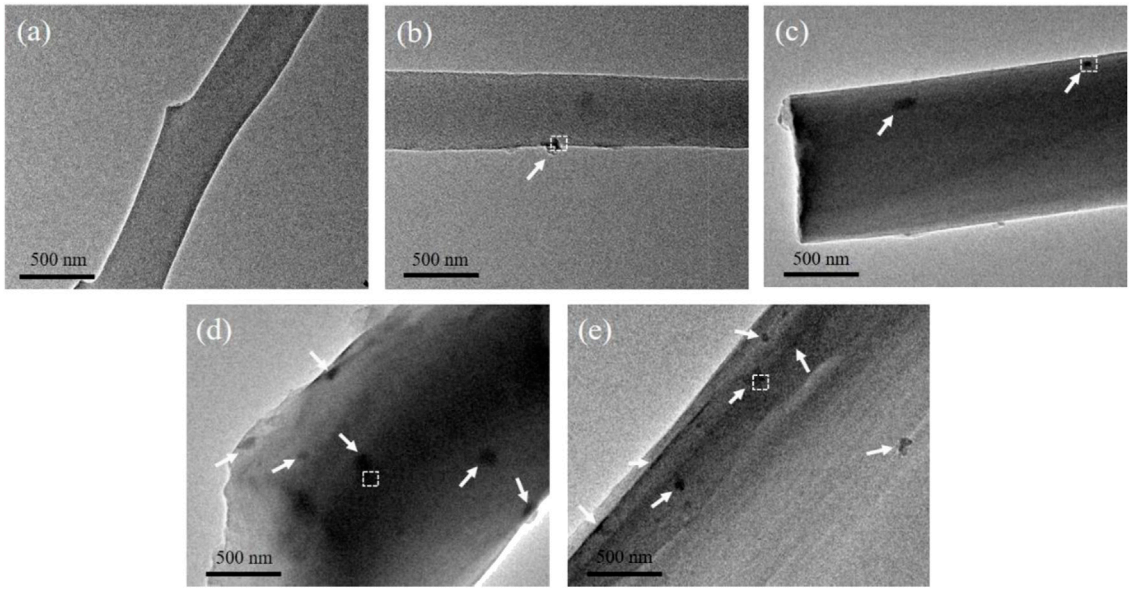

FIGURE 10
Representative TEM images of CSF derived from **(A)** control group, **(B)** Mo-0.05 g/L group, **(C)** Mo-0.1 g/L group, **(D)** Mo-0.5 g/L group, and **(E)** Mo-1 g/L group. The white arrows point to nanoparticles.

As shown in Figure 12B, the I_D/I_G value of the CSFs gradually decreased as the AMT feeding dosage increased, and the CSF derived from the Mo-1 g/L group possessed the highest graphitization degree among all the samples. Based on the fact that MoO_2 NPs can induce the phase transformation of amorphous carbon into graphite (Liu et al., 2014), we believe that the growing number of MoO_2 NPs generated during carbonization progressively improved the graphitization degree of the CSFs.

The conductivity of the CSF derived from each group generally supports the variation in graphitization degree indicated by the Raman spectra, as it has been reported that carbonaceous materials with higher graphitization degrees tend to have higher electrical conductivities (Hou Y. et al., 2021). It can be seen from Supplementary Table S10 that the conductivity of the CSF started to rise when the Mo feeding dosage was 0.1 g/L, reaching its maximum at a dosage of 1 g/L. The difference in conductivities of CSF derived from the control, Mo-0.05 g/L, and Mo-0.1 g/L groups were insignificant, which might be attributed to the relatively small difference in graphitization degree among those samples.

3.10 Electrochemical test

The CSFs derived from the control group (CSF) and Mo-1 g/L group (CSF-MoO_2) were evaluated as electrode materials for supercapacitors. Figures 13A,B show the CV curves of the electrodes prepared from CSF and CSF-MoO_2. The curves exhibit a quasi-rectangular shape, indicating that the mechanism of charge storage can be attributed to the electric double-layer capacitance (EDLC) and pseudo-capacitance. This pseudo-capacitance behavior is due to the doping of CSF with nitrogen sourced from the SF protein (Sahu et al., 2015; Li et al., 2016). In addition, it can be seen from Figures 13A,B that with an increase in the scan rate, the response current for both electrodes increases owing to fast ion- and electron-migration rates (An et al., 2019). Furthermore, the area enclosed by the CV curves of the CSF-MoO_2 electrode is greater than that of the CSF electrode at each scan rate, indicating that the CSF-MoO_2 electrode has a much better specific capacitance than the CSF electrode (Sun et al., 2021).

The galvanostatic charge–discharge (GCD) curves at different current densities from 0.2 A/g to 2.0 A/g were acquired for the CSF and CSF-MoO_2 electrodes, and the results are presented in Figures 13C,D. The GCD curves of the CSF electrode deviate from the ideal triangular shape (Figure 13C), which confirms the existence of both EDLC and pseudocapacitive behavior (Vijeth et al., 2018; Potphode et al., 2020). In addition, the significant voltage drop at a current density of 2.0 A/g indicates that the CSF electrode has a lower charge and discharge efficiency, with a relatively high internal resistance (Mo et al., 2018).

By contrast, the GCD curves of the CSF-MoO_2 electrode generated using different applied current densities all show a nearly symmetrical triangular shape (Figure 13D), indicating

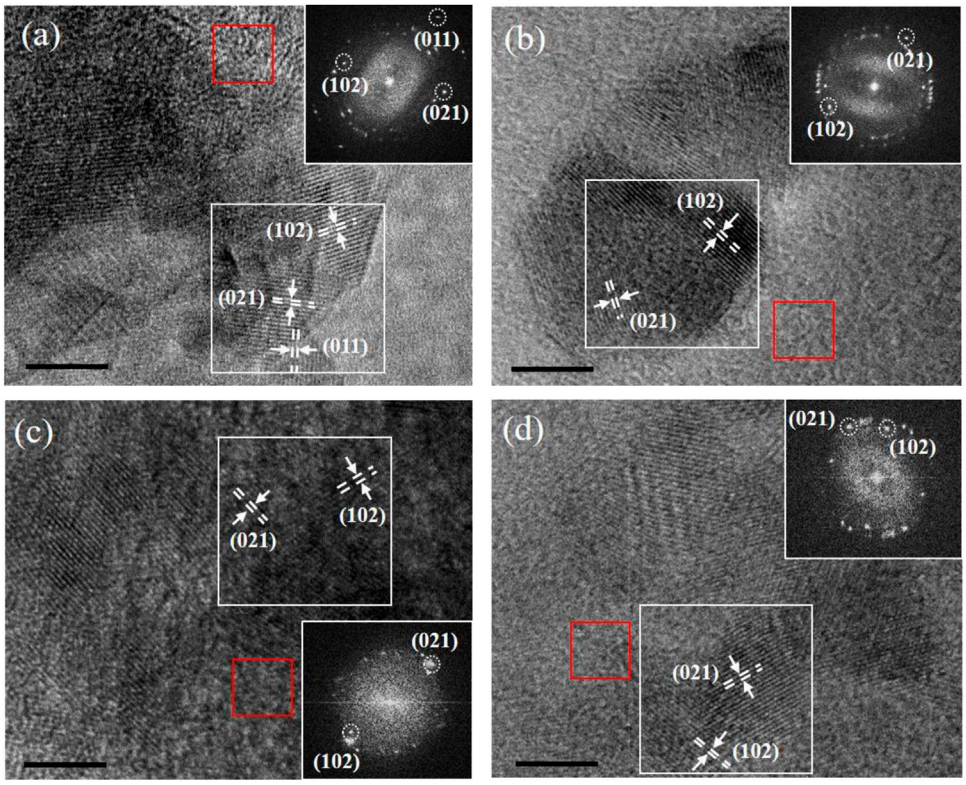

FIGURE 11
Representative HRTEM images of nanoparticles from **(A)** Mo-0.05 g/L group, **(B)** Mo-0.1 g/L group, **(C)** Mo-0.5 g/L group, and **(D)** Mo-1 g/L group. The insets show the corresponding FFT images of the areas framed by the white boxes (scale bar = 5 nm).

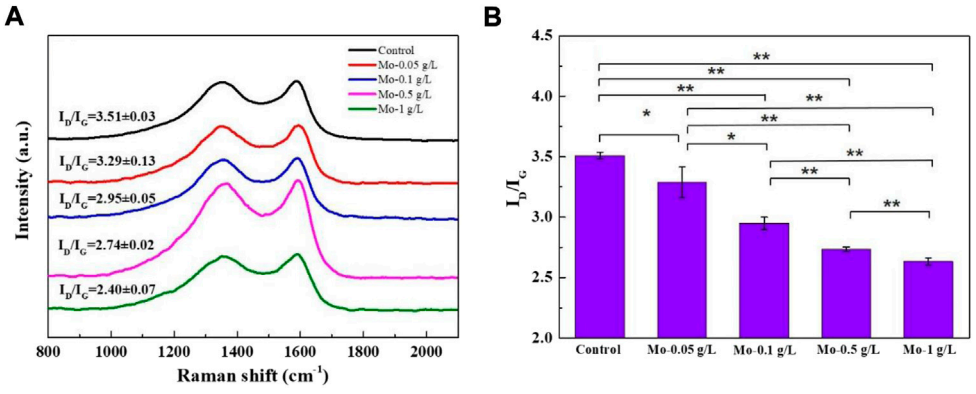

FIGURE 12
Effect of MoO_2 NP incorporation on the graphitization degree of CSFs: **(A)** Raman spectra and **(B)** I_D/I_G value of CSFs from each group (n = 3, *p < 0.05, **p < 0.01).

excellent capacitive performance with a high degree of electrochemical reversibility (Song et al., 2019). Furthermore, the discharge time of the CSF-MoO_2 electrode was much longer than that of the CSF electrode, revealing a significant improvement in the specific capacitance and energy storage of the electrode (Maher et al., 2021). This enhancement was also

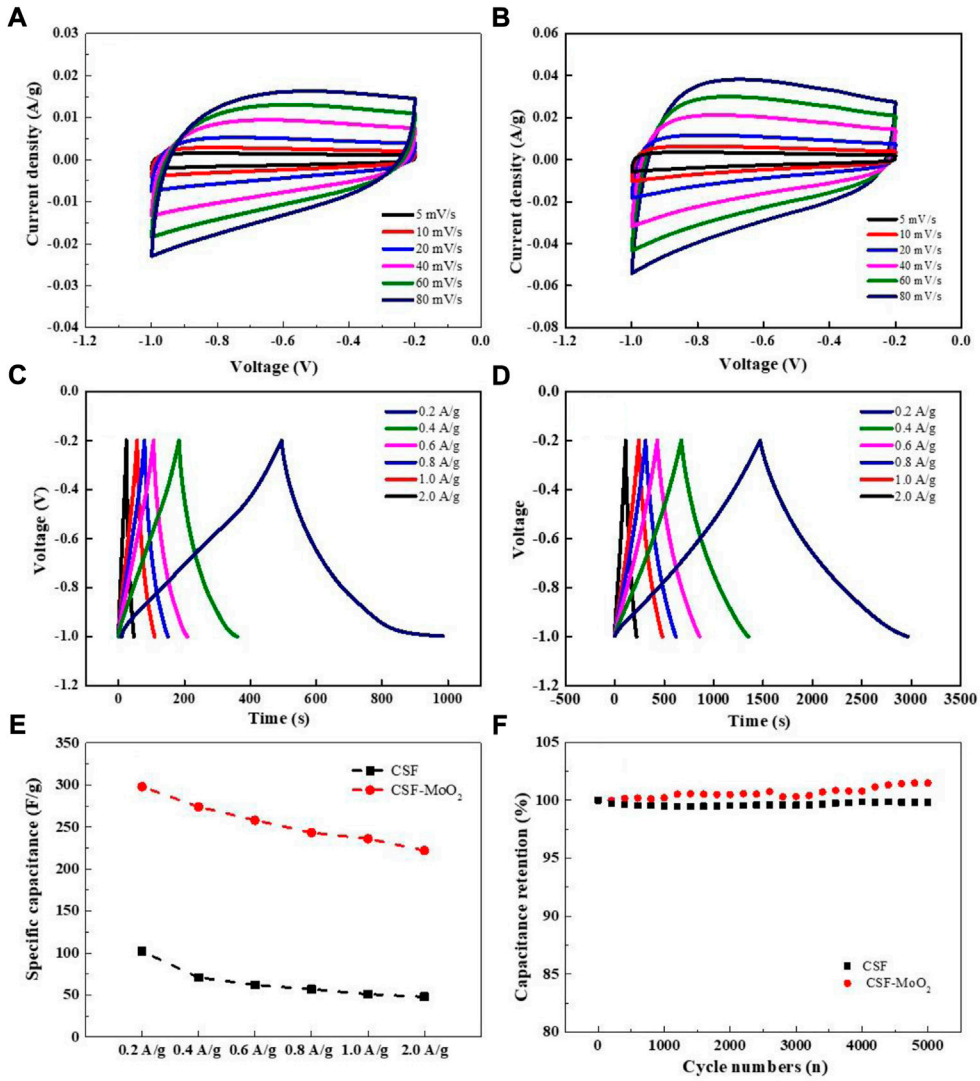

FIGURE 13
Capacitance characterization of electrode prepared from the carbonized silk. CV curves of **(A)** CSF and **(B)** CSF-MoO_2 electrodes at different scan rates. GCD curves generated at current densities of 0.2–2 A/g for **(C)** CSF and **(D)** CSF-MoO_2 electrodes. **(E)** Specific capacitances of CSF and CSF-MoO_2 electrodes at different current densities. **(F)** Cycling stability of CSF and CSF-MoO_2 electrodes at a current density of 2 A/g.

supported by the calculated specific capacitance of both electrodes shown in Figure 13E, indicating that the CSF-MoO_2 electrodes have higher specific capacitances at various current densities compared with those of the CSF electrodes. The CSF-MoO_2 electrode exhibited a maximum capacitance of 298 F/g at a current density of 0.2 g/A. We believe that the CSF-MoO_2 electrodes achieve better energy storage capability than the CSF electrodes owing to the generation of MoO_2 at the nanoscale, which is an essential feature of pseudocapacitive behavior (Hercule et al., 2013; Zhou et al., 2016), as well as the high graphitization degree induced by this nanoscale MoO_2.

The GCD curves and specific capacitance of the CSF electrodes prepared from groups Mo-0.05 g/L, Mo-0.1 g/L, and Mo-0.5 g/L were measured and demonstrated in Supplementary Figure S16 and Supplementary Table S10, respectively. It can be concluded that the capacitance of the CSF electrodes prepared from various groups increased as the AMT feeding dosage increased.

Maintaining good cycling stability is important for the practical application of supercapacitors (Sharma et al., 2021). Therefore, the cycle retention was determined by performing a GCD test at a current density of 2 A/g for 5,000 cycles. The gradual increase in capacitance of the CSF-MoO_2 electrode during charging and discharging can be attributed to the penetration of the electrolyte and its contact with MoO_2 NPs embedded within the CSF. In addition, the high Coulombic

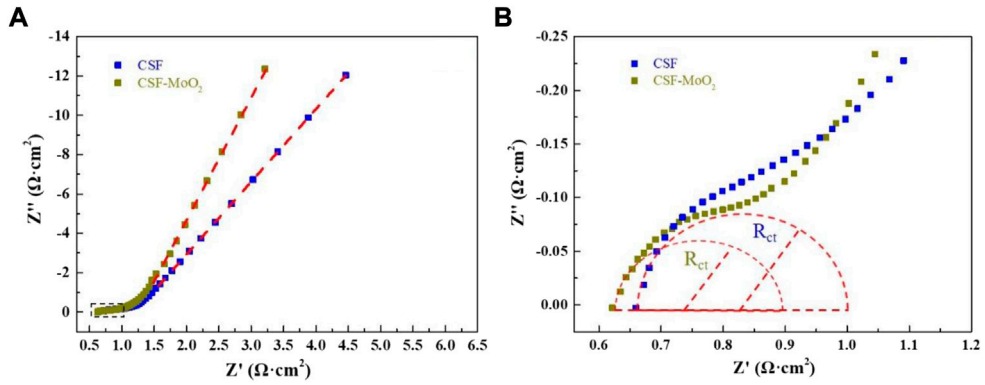

FIGURE 14
EIS spectra: **(A)** Nyquist plots of the CSF and CSF-MoO_2 electrodes, and **(B)** magnified image of the area within the dashed box in **(A)**.

efficiency of the CSF-MoO_2 electrode also demonstrates its long-term cycle-life performance (Supplementary Figure S17).

The Nyquist plot, representing the impedance characteristic as a function of frequency, was applied to evaluate the kinetics and interfacial resistance of both the CSF electrode and CSF-MoO_2 electrode (Mo et al., 2018). As shown in Figure 14, the Nyquist plot contains a semicircle in the high-frequency region, followed by a straight line in the low-frequency region. The initial semicircle intercept in the high-frequency region of the real impedance axis provides the internal resistance (R_s), which includes the resistance of the electrolyte, the intrinsic resistance of the active material, and the electrode/electrolyte interfacial contact resistance. As shown in Figure 14A, the R_s of the CSF-MoO_2 electrode is lower than that of the CSF electrode, indicating that the CSF-MoO_2 electrode tested in the KOH electrolyte possesses a lower internal resistance.

In addition, the diameter of the semicircle represents the charge-transfer resistance (R_{ct}), which can be used to determine the rates of charge and discharge of the supercapacitor and can be considered a very important factor in determining the power densities of the supercapacitor (Mo et al., 2018). Figure 14B reveals that the CSF-MoO_2 electrode has a smaller diameter than that of the CSF electrode, indicating a smaller R_{ct}. Furthermore, the EIS curve of the CSF-MoO_2 electrode was steeper in the low-frequency region, demonstrating a better capacity for ion transmission in the KOH electrolyte (Sun et al., 2021).

4 Conclusion

In summary, AMT-solution-sprayed mulberry leaves were fed to silkworms to introduce the precursor of an electrochemically active substance into silk. It was found that feeding AMT-solution-sprayed mulberry leaves to silkworms had some negative effects on the growth, silk spinning, and cocooning of the silkworms but positively impacted the mechanical strength of the silk fiber when the Mo feeding dosage was less than 0.5 g/L. We confirmed the *in situ* growth of MoO_2 NPs during the pyrolysis process. Electrochemical experiments revealed that the pseudocapacitor electrodes prepared from silk spun by silkworms in the Mo-1 g/L group had a specific capacitance of 298 F/g, which was higher than that of the control group (102 F/g). This specific capacitance was also higher than the value (245 F/g) obtained by feeding silkworms mulberry leaves sprayed with an aqueous solution of 5 g/L of MoO_2 NPs, as reported in our previous work (Liang et al., 2020). Remarkably, the cycling stability of the electrode was exceptional, with the specific capacitance remained unchanged after 5000 GCD cycles.

In comparison with feeding nanoparticles to the silkworms, the presented strategy avoids the aggregation of nanoparticles effectively. Especially, the strategy is able to modulate the amount of precursor of the electrochemically active substance that is incorporated within silk fiber, therefore is beneficial for the design of functionalized CSF programmatically. Furthermore, the metallic salt is generally less expensive than its corresponding metallic nanoparticles, and can make a homogenous solution more conveniently, which is promising for the fabrication of carbonized silk with desired property in large-scale.

Data availability statement

The original contributions presented in the study are included in the article/Supplementary Materials, further inquiries can be directed to the corresponding author.

Author contributions

Experiment design: XnZ and MN. Experiment implementation: YJ, XnZ, XZ, and SL. Data analysis: YJ and

XnZ. Material contribution and equipment coordination: XnZ, YZ, LS, and WT. Paper write: XnZ, YJ, and MN.

Funding

This research was funded by Chongqing Municipal Commission of Commerce (grant number 20220409210947761); the Fundamental Research Funds for the Central Universities (grant number SWU117036); Chongqing Municipal Training Program of Innovation and Entrepreneurship for Undergraduates (grant number S202210635149); Venture and Innovation Support Program for Chongqing Overseas Returnees (grant number cx2019098). And this research was partially supported by the National Science Foundation under Award No. OIA-1458952.

Acknowledgments

We would like to thank Dr. Zhu Li from College of Plant Protection, Southwest University, for her assistance with SEM measurements.

Conflict of interest

The authors declare that the research was conducted in the absence of any commercial or financial relationships that could be construed as a potential conflict of interest.

Publisher's note

All claims expressed in this article are solely those of the authors and do not necessarily represent those of their affiliated organizations, or those of the publisher, the editors and the reviewers. Any product that may be evaluated in this article, or claim that may be made by its manufacturer, is not guaranteed or endorsed by the publisher.

Supplementary material

The Supplementary Material for this article can be found online at: https://www.frontiersin.org/articles/10.3389/fbioe.2022.1059399/full#supplementary-material

References

Akai, H. (1983). The structure and ultrastructure of the silk gland. *Experientia* 39 (5), 443–449. doi:10.1007/BF01965158

An, C., Dong, C., Shao, L. H., and Deng, Q. (2019). Monitoring the length change of Ni@C composite electrodes during charging/discharging processes. *Electrochem. Commun.* 103, 94–99. doi:10.1016/j.elecom.2019.05.012

Chen, S., Liu, M., Huang, H., Cheng, L., and Zhao, H. P. (2019). Mechanical properties of *Bombyx mori* silkworm silk fibre and its corresponding silk fibroin filament: A comparative study. *Mat. Des.* 181, 108077. doi:10.1016/j.matdes.2019.108077

Cheng, L., Huang, H., Zeng, J., Liu, Z., Tong, X., Li, Z., et al. (2018). Effect of different additives in diets on secondary structure, thermal and mechanical properties of silkworm silk. *Materials* 12 (1), 14. doi:10.3390/ma12010014

Cheng, X., Hu, J., Li, J., Chen, J., Wang, H., Mao, T., et al. (2018). The silk gland damage and the transcriptional response to detoxifying enzymes-related genes of *Bombyx mori* under phoxim exposure. *Chemosphere* 209, 964–971. doi:10.1016/j.chemosphere.2018.06.167

Dong, Q., Wang, G., Qian, B., Hu, C., Wang, Y., and Qiu, J. (2014). Electrospun composites made of reduced graphene oxide and activated carbon nanofibers for capacitive deionization. *Electrochim. Acta* 137 (10), 388–394. doi:10.1016/j.electacta.2014.06.067

Fisher, T., Hajaligol, M., Waymack, B., and Kellogg, D. (2002). Pyrolysis behavior and kinetics of biomass derived materials. *J. Anal. Appl. Pyrolysis* 62 (2), 331–349. doi:10.1016/S0165-2370(01)00129-2

Hercule, K. M., Wei, Q., Khan, A. M., Zhao, Y., Tian, X., and Mai, L. (2013). Synergistic effect of hierarchical nanostructured MoO_2/$Co(OH)_2$ with largely enhanced pseudocapacitor cyclability. *Nano Lett.* 13 (11), 5685–5691. doi:10.1021/nl403372n

Hou, C., Yang, W., Xie, X., Sun, X., Wang, J., Naik, N., et al. (2021b). Agaric-like anodes of porous carbon decorated with MoO_2 nanoparticles for stable ultralong cycling lifespan and high-rate lithium/sodium storage. *J. Colloid Interface Sci.* 596 (15), 396–407. doi:10.1016/j.jcis.2021.03.149

Hou, Y., Quan, J., Su, X., Deng, C., Yang, Y., and Khoo, B. C. (2021a). Carbonized silk fiber mat: A flexible and broadband microwave absorber, and the length effect. *ACS Sustain. Chem. Eng.* 9 (38), 12747–12754. doi:10.1021/acssuschemeng.1c02857

Hou, Y., Xia, Q., Zhao, P., Zou, Y., Liu, H., Guan, J., et al. (2007). Studies on middle and posterior silk glands of silkworm (*Bombyx mori*) using two-dimensional electrophoresis and mass spectrometry. *Insect biochem. Mol. Biol.* 37 (5), 486–496. doi:10.1016/j.ibmb.2007.02.011

Khatibi, S., Ostadhassan, M., Hackley, P., Tuschel, D., Abarghani, A., and Bubach, B. (2019). Understanding organic matter heterogeneity and maturation rate by Raman spectroscopy. *Int. J. Coal Geol.* 206, 46–64. doi:10.1016/j.coal.2019.03.009

Kim, U. J., Park, J., Kim, H. J., Wada, M., and Kaplan, D. L. (2005). Three-dimensional aqueous-derived biomaterial scaffolds from silk fibroin. *Biomaterials* 26 (15), 2775–2785. doi:10.1016/j.biomaterials.2004.07.044

Li, X., Sun, C., Cai, Z., and Ge, F. (2019). High-performance all-solid-state supercapacitor derived from PPy coated carbonized silk fabric. *Appl. Surf. Sci.* 473, 967–975. doi:10.1016/j.apsusc.2018.12.244

Li, X., Wang, J., Zhao, Y., Ge, F., Komarneni, S., and Cai, Z. (2016). Wearable solid-state supercapacitors operating at high working voltage with a flexible nanocomposite electrode. *ACS Appl. Mat. Interfaces* 8 (39), 25905–25914. doi:10.1021/acsami.6b06156

Liang, J., Zhang, X., Ji, Y., Chen, Z., Norton, M. L., Wang, Y., et al. (2021). Feeding silkworms with HPMC dispersed MoO_2 NPs: An efficient strategy to enhance the supercapacitance performance of carbonized silk. *Compos. Sci. Technol.* 215, 109025. doi:10.1016/j.compscitech.2021.109025

Liang, J., Zhang, X., Yan, C., Wang, Y., Norton, M. L., Wei, X., et al. (2020). Preparation and enhanced supercapacitance performance of carbonized silk by feeding silkworms MoO_2 nanoparticles. *Mat. Des.* 196, 109137. doi:10.1016/j.matdes.2020.109137

Liu, Q., Wang, X., Tan, X., Xie, X., Xia, Q., Li, X., et al. (2019). Disruption of the metal ion environment by edta for silk formation affects the mechanical properties of silkworm silk. *Int. J. Mol. Sci.* 20 (12), 3026. doi:10.3390/ijms20123026

Liu, S., Yin, H., Wang, H., He, J., and Wang, H. (2014). Synthesis, characterization and electrochemical performances of MoO_2 and carbon co-coated $LiFePO_4$ cathode materials. *Ceram. Int.* 40 (2), 3325–3331. doi:10.1016/j.ceramint.2013.09.102

Maher, M., Hassan, S., Shoueir, K., Yousif, B., and Abo-Elsoud, M. E. A. (2021). Activated carbon electrode with promising specific capacitance based on potassium bromide redox additive electrolyte for supercapacitor application. *J. Mat. Res. Technol.* 11, 1232–1244. doi:10.1016/j.jmrt.2021.01.080

Mandal, B. B., Grinberg, A., Gil, E. S., Panilaitis, B., and Kaplan, D. L. (2012). High-strength silk protein scaffolds for bone repair. *Proc. Natl. Acad. Sci. U. S. A.* 109 (20), 7699–7704. doi:10.1073/pnas.1119474109

Mo, H., Nan, H., Lang, X., Liu, S., Qiao, L., Hu, X., et al. (2018). Influence of calcium doping on performance of $LaMnO_3$ supercapacitors. *Ceram. Int.* 44 (8), 9733–9741. doi:10.1016/j.ceramint.2018.02.205

Nelson, D. L., and Cox, M. M. (2005). *Lehninger principles of biochemistry*. USA: Macmillan Education Press.

Pan, P., Hu, Y., Wu, K., Cheng, Z., Shen, Z., Jiang, L., et al. (2020). Growth of $ZnCo_2O_4$ nanocubes on flexible biochar substrate derived from natural silk waste fabric for lithium-ion battery anode. *J. Alloys Compd.* 814, 152306. doi:10.1016/j.jallcom.2019.152306

Pérez-Rigueiro, J., Viney, C., Llorca, J., and Elicesa, M. (2000). Mechanical properties of silkworm silk in liquid media. *Polymer* 41 (23), 8433–8439. doi:10.1016/S0032-3861(00)00179-8

Porter, D., and Vollrath, F. (2010). Silk as a biomimetic ideal for structural polymers. *Adv. Mat.* 21 (4), 487–492. doi:10.1002/adma.200801332

Potphode, D., and Sharma, C. S. (2020). Pseudocapacitance induced candle soot derived carbon for high energy density electrochemical supercapacitors: Non-aqueous approach. *J. Energy Storage* 27, 101114. doi:10.1016/j.est.2019.101114

Putthanarat, S., Stribeck, N., Fossey, S. A., Eby, R. K., and Adams, W. W. (2000). Investigation of the nanofibrils of silk fibers. *Polymer* 41 (21), 7735–7747. doi:10.1016/S0032-3861(00)00036-7

Sadezky, A., Muckenhuber, H., Grothe, H., Niessner, R., and Pöschl, U. (2005). Raman microspectroscopy of soot and related carbonaceous materials: Spectral analysis and structural information. *Carbon* 43 (8), 1731–1742. doi:10.1016/j.carbon.2005.02.018

Sahu, V., Grover, S., Tulachan, B., Sharma, M., Srivastava, G., Roy, M., et al. (2015). Heavily nitrogen doped, graphene supercapacitor from silk cocoon. *Electrochim. Acta* 160 (1), 244–253. doi:10.1016/j.electacta.2015.02.019

Sharma, M., Adalati, R., Kumar, A., Chawla, V., and Chandra, R. (2021). Single step fabrication of nanostructured Cr_2O_3-MoO_2 composite flexible electrode for top-notch asymmetric supercapacitor. *Appl. Surf. Sci.* 555, 149721. doi:10.1016/j.apsusc.2021.149721

Song, X., Ma, X., Li, Y., Ding, L., and Jiang, R. (2019). Tea waste derived microporous active carbon with enhanced double-layer supercapacitor behaviors. *Appl. Surf. Sci.* 487, 189–197. doi:10.1016/j.apsusc.2019.04.277

Standardization Administration of the People's Republic of China (2009). *Testing method for raw silk (GB/T 1798-2008)*. China: Standardization Administration of the People's Republic of China. Available at: http://www.doc88.com/p-3327762495558.html (accessed June 25, 2022)

Sun, C., Guo, Z., Zhou, M., Li, X., Cai, Z., and Ge, F. (2021). Heteroatoms-doped porous carbon electrodes with three-dimensional self-supporting structure derived from cotton fabric for high-performance wearable supercapacitors. *J. Power Sources* 482 (15), 228934. doi:10.1016/j.jpowsour.2020.228934

Vijeth, H., Ashokkumar, S. P., Yesappa, L., Niranjana, M., Vandana, M., and Devendrappa, H. (2018). Flexible and high energy density solid-state asymmetric supercapacitor based on polythiophene nanocomposites and charcoal. *RSC Adv.* 8 (55), 31414–31426. doi:10.1039/c8ra06102e

Viles, J. H., Cohen, F. E., Prusiner, S. B., Goodin, D. B., Wright, P. E., and Dyson, H. J. (1999). Copper binding to the prion protein: Structural implications of four identical cooperative binding sites. *Proc. Natl. Acad. Sci. U. S. A.* 96 (5), 2042–2047. doi:10.1073/pnas.96.5.2042

Vollrath, F., and Porter, D. (2006). Spider silk as a model biomaterial. *Appl. Phys. A* 82, 205–212. doi:10.1007/s00339-005-3437-4

Wang, Q., Ling, S., Yao, Q., Li, Q., Hu, D., Dai, Q., et al. (2020). Observations of 3 nm silk nanofibrils exfoliated from natural silkworm silk fibers. *ACS Mat. Lett.* 2 (2), 153–160. doi:10.1021/acsmaterialslett.9b00461

Wang, X., Li, Y., Liu, Q., Chen, Q., Xia, Q., and Zhao, P. (2017). *In vivo* effects of metal ions on conformation and mechanical performance of silkworm silks. *Biochimica Biophysica Acta - General Subj.* 1861 (3), 567–576. doi:10.1016/j.bbagen.2016.11.025

Wang, Y., Wu, X., Han, Y., and Li, T. (2021). Flexible supercapacitor: Overview and outlooks. *J. Energy Storage* 42, 103053. doi:10.1016/j.est.2021.103053

Wei, F., Zhang, H., Wang, J., Zhuang, J., and Lv, Y. (2022). N, S co-doped porous carbons with well-developed pores for supercapacitor and zinc ion hybrid capacitor. *J. Alloys Compd.* 907 (25), 164536. doi:10.1016/j.jallcom.2022.164536

Wu, D. (1961). *Silkworm anatomy and physiology*. Beijing: Agricultural Press.

Xia, T., Wang, Q., Wu, W., Ao, C., Zheng, Z., Lu, C., et al. (2021). Fabrication and characterization of MnO_2-coated carbon fabrics from silk for shape-editable supercapacitors. *J. Alloys Compd.* 854 (15), 157289. doi:10.1016/j.jallcom.2020.157289

Xu, X., and Zhang, B. (2008). The mechanism research of metal ions on the conformation transition of silk fibroin. *Chin. Polym. Bull.* 2008 (03), 48–51.

Yang, J., Tan, Z., Chen, X., Liang, Y., Zheng, M., Hu, H., et al. (2021). A mild method to prepare nitrogen-rich interlaced porous carbon nanosheets for high-performance supercapacitors. *J. Colloid Interface Sci.* 599, 381–389. doi:10.1016/j.jcis.2021.04.119

Yang, X., Xiong, Z., Meng, X., Zhu, H., and Xia, Y. (2020). Broad-spectrum adsorption property of chondrus crispus activated carbon for ionic and solvent dyes. *Water Air Soil Pollut.* 231 (2), 64. doi:10.1007/s11270-020-4442-0

Zhang, L., Yang, G., Chen, Z., Liu, D., Wang, J., Qian, Y., et al. (2020). MXene coupled with molybdenum dioxide nanoparticles as 2D-0D pseudocapacitive electrode for high performance flexible asymmetric micro-supercapacitors. *J. Materiomics* 6 (1), 138–144. doi:10.1016/j.jmat.2019.12.013

Zhou, E., Wang, C., Zhao, Q., Li, Z., Shao, M., Deng, X., et al. (2016). Facile synthesis of MoO_2 nanoparticles as high performance supercapacitor electrodes and photocatalysts. *Ceram. Int.* 42 (2), 2198–2203. doi:10.1016/j.ceramint.2015.10.008

Zhou, L., Hou, J., Chen, Y., Li, S., and Zou, B. (2022). Porous carbon composite generated from silk fibroins and graphene for supercapacitors. *ACS Omega* 7 (32), 28284–28292. doi:10.1021/acsomega.2c02735

Zhuang, L., Li, Q., Chen, S., Hou, X., and Lin, J. (2014). *In-situ* preparation of porous carbon-supported molybdenum dioxide and its performance in the oxidative desulfurization of thiophene. *J. Mat. Sci.* 49, 5606–5616. doi:10.1007/s10853-014-8273-5

frontiers | Frontiers in Bioengineering and Biotechnology

TYPE Original Research
PUBLISHED 04 January 2023
DOI 10.3389/fbioe.2022.1104041

OPEN ACCESS

EDITED BY
Xin Zhou,
Nanjing Forestry University, China

REVIEWED BY
Limin Cao,
Capital Normal University, China
Yu-Cai He,
Changzhou University, China

*CORRESPONDENCE
Kequan Chen,
kqchen@njtech.edu.cn

SPECIALTY SECTION
This article was submitted to Bioprocess Engineering,
a section of the journal
Frontiers in Bioengineering and Biotechnology

RECEIVED 21 November 2022
ACCEPTED 19 December 2022
PUBLISHED 04 January 2023

CITATION
Li H, Chen X, Tang Y, Yang Y, He F, Wang X, Li G, Chen K, Ouyang P and Yang Y (2023), Separation, purification, and crystallization of 1,5-pentanediamine hydrochloride from fermentation broth by cation resin. *Front. Bioeng. Biotechnol.* 10:1104041. doi: 10.3389/fbioe.2022.1104041

Separation, purification, and crystallization of 1,5-pentanediamine hydrochloride from fermentation broth by cation resin

Hui Li[1], Xu Chen[1], Yibo Tang[1], Yue Yang[1], Feng He[2], Xin Wang[1], Ganlu Li[1], Kequan Chen[1]*, Pingkai Ouyang[1] and Yuning Yang[3]

[1]College of Biotechnology and Pharmaceutical Engineering, Nanjing Tech University, Nanjing, China, [2]Jiangsu Institute of Industrial Biotechnology, JITRI Co., Ltd., Nanjing, China, [3]Gansu Yinguang Juyin Chemical Co., Ltd., Baiyin, China

1,5-Pentanediamine hydrochloride (PDAH) was an important raw material for the preparation of bio-based pentamethylene diisocyanate (PDI). PDI has shown excellent properties in the application of adhesives and thermosetting polyurethane. In this study, PDAH was recovered from 1,5-pentanediamine (PDA) fermentation broth using a cation exchange resin and purified by crystallization. D152 was selected as the most suitable resin for purifying PDAH. The effects of solution pH, initial temperature, concentration of PDA, and adsorption time were studied by the static adsorption method. The equilibrium adsorption data were well fitted to Langmiur, Freundlich, and Temkin-Pyzhev adsorption isotherms. The adsorption free energy, enthalpy, and entropy were calculated. The experimental data were well described by the pseudo first-order kinetics model. The dynamic experiment in the fixed bed column showed that under optimal conditions, the adsorption capacity reached 96.45 mg g^{-1}, and the recovery proportion of the effective section reached 80.16%. In addition, the crystallization of the PDAH solution obtained by elution proved that the crystal product quality of resin eluting solution was highest. Thus, our research will contribute to the industrial scale-up of the separation of PDAH.

KEYWORDS

1,5-pentanediamine hydrochloride, resin, purification, crystallization, separation

1 Introduction

Bio-based polyurethane (PU) coatings have been widely used in recent decades and are gradually replacing petrochemical coatings because of their advantages of low environmental impact, easy access, low cost, and good biodegradability (Noreen et al., 2016; Paraskar et al., 2021; Ma et al., 2022). Bio-based pentamethylene diisocyanate (PDI) has shown excellent properties in the application of adhesives and thermosetting polyurethane, in which approximately 71% of the carbon content was bio-based. In theory, it is possible to replace petrochemical-based hexamethylene diisocyanate (HDI) (Zeng et al., 2022). At present, the industrial preparation of PDI is mainly liquid-phase phosgenation (Li W et al., 2021). The raw material for PDI is 1,5-pentanediamine (PDA), which needs to be obtained from biomass such as feed corn starch through biological fermentation engineering (Wang et al., 2021). In the two-step reaction, PDA initially reacts with a cold phosgene solution to produce 1,5-pentanediamine

hydrochloride (PDAH) and carbamate. Phosgene is then further introduced and gradually heated to produce PDI. There are inevitably some problems in this process, such as the production of tar compounds and chloride by-products, and it is difficult to control the particle size and rate in the salt forming process, all of which result in many impurities and reduced yield (Liu et al., 2020; Li et al., 2020). Therefore, the high-quality PDAH can reduce the occurrence of side reactions by the phosgenation reaction, and this can improve the yield and purity of the final PDI (Takahashi et al., 2019).

A variety of technologies have been used to separate and purify products from fermentation broth, including precipitation, solvent extraction, adsorption, distillation, and membrane separation (Chen et al., 2007; Jeon et al., 2014; Szczygiełda and Prochaska., 2020; Hu et al., 2022; Lee and Lee., 2022). However, there are still a large number of bacteria, proteins, residual sugars and inorganic salts in the fermentation broth. Therefore, it is very important to choose an efficient, low pollution and low-cost technology to improve the yield. The advantages of using macroporous resin are strong adsorption capacity, high selectivity, low material cost, high regeneration possibility, and less pollutants (Li C et al., 2021). Commonly used resins are adsorption and ion exchange resins, which utilize a non-specific physical adsorption mechanism and an ion-exchange mechanism, respectively (Xiong et al., 2019). Macroporous adsorption resins are often used for the separation and purification of natural products, such as flavonoids (Dong et al., 2015), phenolic compounds (Park and Lee., 2021), alkaloids (Zhang et al., 2012), anthocyanin (Yang et al., 2022), and antioxidants (Zou et al., 2017). Macroporous ion exchange resins are commonly used to separate amino acids (Dong et al., 2015; Chen et al., 2016; Zhang et al., 2018), lactic acid (Ahmad et al., 2021), nutrients (Ke et al., 2021), succinic acid (Alexandri et al., 2019), and decolorization (Shi et al., 2017) from fermentation broth. However, there are few reports on the separation and purification of bio-based PDAH from pretreated fermentation broth by macroporous ion exchange resin.

Crystallization is an ancient separation process that is usually the last step in the purification process, and its control is crucial. Crystallization is a common and necessary unit operation in the chemical industry, and it is widely used in various industries, from the production of basic materials to complex pharmaceuticals (Ms et al., 2020; Weng et al., 2020). Compared with other purification processes, crystallization has the advantages of high recovery rate, good quality of recovered solid-liquid products, high yield, low energy consumption, good operability, and good stability (Sparenberg et al., 2021). At present, there are many products obtained by separation and purification using macroporous resin from fermentation broth and crystallization, such as bio-based carboxylic acids (Karp et al., 2018), antibiotics (Zheng et al., 2013), and hormones (Xu et al., 2018). In this study, higher purity and more uniform particle size of PDAH were obtained through crystallization, which provided a basis for the industrial production of PDI.

In order to master the separation performance of the resin and understand the basic principle of PDAH separation, this paper studied the influence of ion exchange resin on the static adsorption of PDA, the related adsorption thermodynamic kinetics, the optimization of the separation process, and the penetration and desorption curves of the fixed bed chromatographic column. The cooling crystallization products of the resin desorption solution and other two raw materials were compared. The results indicate that we were able to separate and purity high-quality PDAH through separation and purification, which can be used in the production of PDI.

2 Experiment section

2.1 Chemicals and reagents

D113, D150, D152, and D155 resins used in experiment are weakly acidic cation exchange resins, which were purchased from Yuan Ye Biotechnology Co., Ltd. (Shanghai, China). The chemical reagents used in the experiment, ethanol, hydrochloric, acetonitrile and trifluoroacetic acid were purchased from Aladdin (Shanghai, China). The PDA fermentation broth and deionized water were provided by our laboratory.

2.2 HPLC conditions

A YMC Carotenoid column (250 mm × 4.6 mm, s-5 μm, Grace, Columbia, MD, United States) was used for these experiments with the following conditions: the mobile phase consisted of a mixture of 5% acetonitrile and 0.5% trifluoroacetic acid at a flow rate of 0.8 ml min^{-1}. The injection volume was 10 μl. The column temperature was 35°C, and the differential detector (1,290, Agilent Technologies, Santa Clara, CA, United States) temperature was 35°C (Wang et al., 2021).

2.3 Static adsorption and desorption experiments

Before use, four cation exchange resins were soaked in three times the volume of ethanol overnight, then washed with three times the volume of 1.0 M hydrochloric acid, 1.0 M sodium hydroxide, and 1.0 M hydrochloric acid. The resin was then washed with deionized water until the washing solution was neutral. The resin was used after filtration.

Static equilibrium adsorption experiments were carried out in a 20°C constant temperature oscillator. Wet resin (10 ± 0.1 g) was added to 30 ml of 100 g L^{-1} PDA fermentation broth in a 100 ml conical flask. The speed of the thermostatic oscillator was set to 200 r min^{-1} and the reaction time was set to 2.0 h; under these conditions, the PDA fermentation liquid reached adsorption equilibrium. After adsorption, the adsorption solution was filtered and the concentration of filtrate was determined by HPLC. The resin was then washed with deionized water three times, and 20 ml 1.0 M hydrochloric acid solution was added for desorption. The flask was held in a 20°C constant temperature oscillator and shaken for 2.0 h. The desorption solution was analyzed by HPLC (Figueira et al., 2022). The resin was screened according to the equilibrium adsorption capacity, desorption capacity, and desorption rate, and these parameters were calculated according to the following formulas:

$$q_e = \frac{(C_0 - C_e)V_i}{W} \quad (1)$$

$$q_d = \frac{C_d V_d}{W} \quad (2)$$

$$D = \frac{q_d}{q_e} \times 100\% \quad (3)$$

10.3389/fbioe.2022.1104041

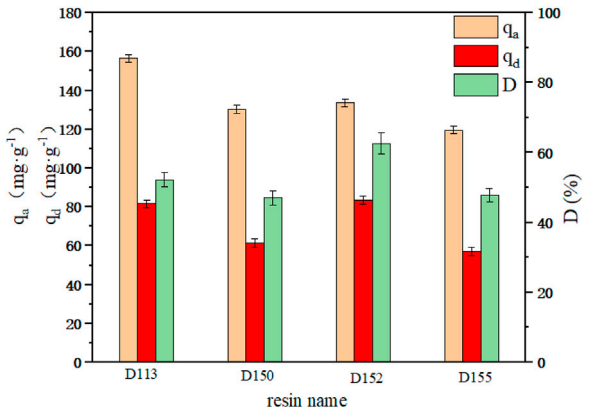

FIGURE 1
Adsorption and desorption capacity of different cation exchange resins.

where q_e was the equilibrium adsorption capacity, mg g^{-1};C_0 was the initial concentration of adsorption solution, mg L^{-1}; C_e was the equilibrium concentration of adsorption solution, mg L^{-1}; V_i was the total volume of adsorbed solution, L; W was the mass of the wet resin, g. q_d was the equilibrium desorption amount, mg g^{-1}; C_d was the desorption solution concentration, mg L^{-1}; V_d was the volume of desorption solution, L; D was desorption rate, %.

2.4 Thermodynamic experiments

The static equilibrium adsorption experiment was carried out at 20°C in a constant temperature oscillator. Wet resin (10 ± 0.1 g) was added to 30 ml PDA fermentation liquid of different concentrations (50–200 g L^{-1}) in a 100 ml conical flask. The speed of the thermostatic oscillator was set to 200 r min^{-1} and the reaction time was set to 2.0 h; under these conditions, the PDA fermentation liquid reached adsorption equilibrium. The adsorption solution was then filtered, and the concentration of filtrate after adsorption was determined by HPLC at different initial concentrations.

2.5 Kinetic experiments

Kinetic adsorption experiments were carried out at different temperatures (20–40°C) with a thermostatic oscillator. Wet resin (10 ± 0.1 g) was added to 30 ml 100 g L^{-1} PDA fermentation broth in a 100 ml conical flask. The speed of the thermostatic oscillator was set at 200 r min^{-1}, and 200 μl was taken from the flask periodically for HPLC. The instantaneous concentration was analyzed until adsorption equilibrium was reached, and was calculated according to:

$$q_t = \frac{(C_0 - C_t)V_i}{W} \tag{4}$$

where q_t was the instantaneous adsorption capacity, mg g^{-1}; C_0 was the initial concentration of adsorption solution, mg L^{-1}; C_t was the concentration of adsorption solution at time t, mg L^{-1}; V_i was the total volume of adsorbed solution, L; W was the mass of the wet resin, g.

2.6 Dynamic adsorption and desorption experiment

A certain amount of wet resin was added to the glass adsorption column by the wet method. The inner diameter of the adsorption column was 2.0 cm and the heights were 10.0, 14.0, 20.0, and 30.0 cm. A peristaltic pump was used to control the flow rate of the liquid at the outlet of the column, and a distributed collector was used to collect the sample outflow quantitatively. When the concentration of PDA at the column outlet was equal to the initial concentration of PDA solution, the adsorption experiment was completed. The effluent concentration of different volume sections was determined by HPLC. The penetration curve of PDA on the resin column was drawn with the effluent volume V (ml) as the abscissa and the effluent concentration of PDA as the ordinate. The effects of PDA concentration, flow rate, and the H/D on the dynamic penetration curve of PDA were investigated. In dynamic adsorption experiments, the adsorption capacity of the resin unit was determined by integrating the area above the penetration curve (Figueira et al., 2022), and was calculated according to:

$$m_a = \int_0^{V_t} (C_1 - C_{ta})dV \tag{5}$$

$$Q_a = \frac{m_a}{m_s} \tag{6}$$

where C_1 was the initial concentration of dynamic adsorption, g L^{-1}; C_{ta} was the concentration of PDA effluent at a certain time, g L^{-1}; V_t was the outflow volume corresponding to C_{ta} time, ml; m_a was the mass of total PDA adsorbed by resin column, mg; m_s was the amount of resin used, g; Q_a was the adsorption capacity of PDA per unit of resin, mg g^{-1}.

Hydrochloric acid was used as the desorbing agent, a collector was used to collect the desorbing effluent at the outlet of the chromatographic column, measure the pigment OD value of the effluent, and draw the pigment curve with the effluent product V (ml) as the abscissa and the effluent pigment OD value as the ordinate and the concentration of PDA in the desorbing effluent was detected

TABLE 1 Different cation exchange resin parameters.

Resins	Matrix	Particle size (mm)	Exchange capacity (mmol g^{-1})	Moisture content (%)	Active functional group
D113	Acrylic	0.30–1.2≧95%	10.8	45–52	carboxyl
D150	Acrylic	0.315–1.25≧90%	10	42–50	carboxyl
D152	Acrylic	0.315–1.25≧95%	11.2	50–60	carboxyl
D155	Acrylic	0.45–1.25≧95%	9.5	42–50	carboxyl

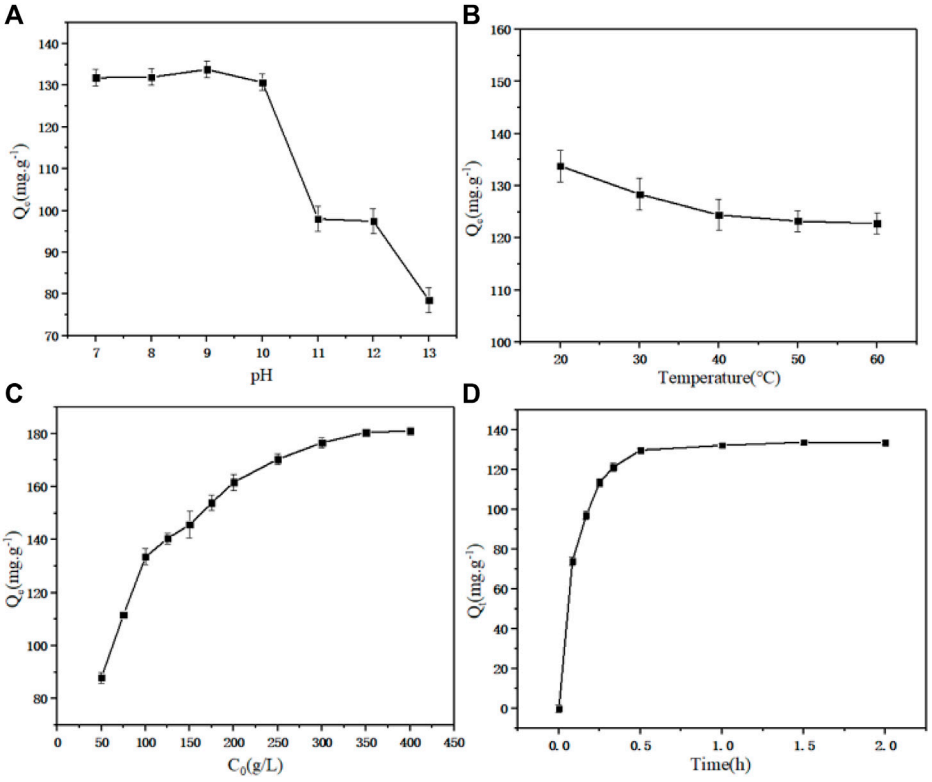

FIGURE 2
(A) Effect of pH on equilibrium adsorption capacity. **(B)** Effect of temperature on equilibrium adsorption capacity. **(C)** Effect of initial concentration of PDA on equilibrium adsorption capacity. **(D)** Effect of adsorption time on equilibrium adsorption capacity.

by HPLC. The desorption curve of PDA on the resin column was drawn with the effluent volume V_m (ml) as the abscissa and the concentration of PDA effluent as the ordinate. The effects of hydrochloric acid concentration, flow rate, and H/D on the pigment curve and the dynamic desorption curve of PDA were investigated. In order to obtain the eluent with high concentration, we selected the material solution of the section that reached more than 80% of the peak value of the eluent, and calculated these concentrations according to the following equations:

$$m_b = \int_0^{V_m} C_{td} dV \tag{7}$$

$$m_c = 0.8C_{max} \int_{V_1}^{V_2} dV \tag{8}$$

$$F = \frac{m_b}{m_c} \times 100\% \tag{9}$$

where V_m was the volume of eluent required for complete desorption of PDA, ml; C_{td} was the concentration of PDA desorption solution at time t, g L^{-1}; m_b was the mass of total PDA eluted by resin column, g; C_{max} was the peak concentration of desorption solution, g L^{-1}; V_1 was the volume of eluent when the absorption reached $0.8C_{max}$ for the first time, ml; V_2 was the volume of eluent when the absorption reached $0.8C_{max}$ for the second time, ml; m_c was the mass of total PDA $0.8C_{max}$ twice by the resin column, g; F was the proportion of the mass of total PDA in the section with the concentration above the peak of 80% in the mass of total PDA eluted by resin column,%.

2.7 Crystallization of PDAH

The PDAH solution after fermentation (PHF), the PDAH solution decolorization by activated carbon after fermentation (PHDF), and the PDAH solution after elution of resin (PHER) were dissolved into the jacket beaker, preheated to 60°C, then cooled to 20°C–10°C; the crystals were observed 1.0 h after the introduction of crystal precipitates. After the crystallization was complete, the product was extracted by filtration, washed, and dried. The experiment was repeated three times under the same operating conditions to determine the average purity and yield of the product (Sparenberg et al., 2021). A small number of samples were placed on a slide, covered with a cover slide, and observed with an optical microscope and photographed. The purity and yield were calculated according to the following equations:

$$Purity = \frac{m_1}{M_1} \times 100\% \tag{10}$$

$$Yield = \frac{m_1}{M_2} \times 100\% \tag{11}$$

where m_1 was the mass of PDAH actually measured in the final product, g; M_1 was the total mass of the final product to be tested, g; M_2 was the mass of PDAH in the initial solution, g.

The product structure was analyzed by Nicolet Summit FTIR (Thermo Fisher Technology Co., Ltd. United States). The sample clip was placed in the sample window for infrared scanning determination.

A D8Advance powder X-ray diffractometer (Brock Technology Co., LTD. Germany) was used to detect CuKα rays (1.54056 A) under

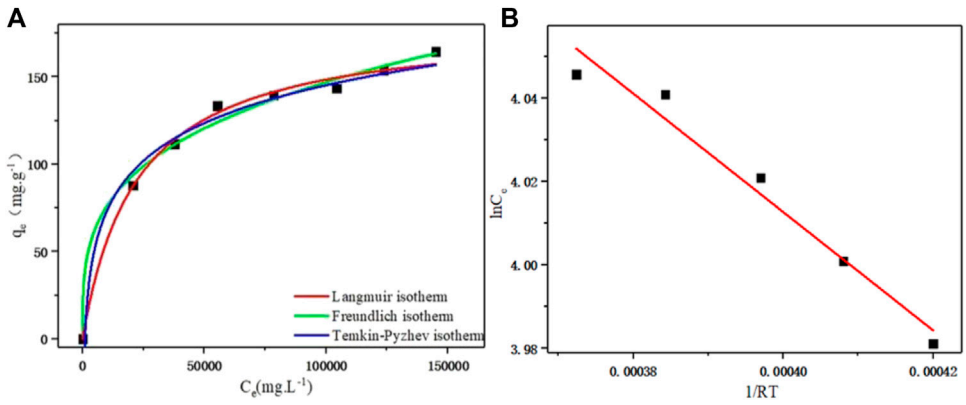

FIGURE 3
(A) Langmuir, Freundlich, and Temkin-Pyzhev adsorption isothermal curves of D152 cation exchange resin for PDA. **(B)** Linear fit of the Clapeyron-Clausius equation.

TABLE 2 Relevant parameters of the Langmuir, Freundlich and Temkin-Pyzhev adsorption isothermal models.

Model	Parameters	D152
Langmuir	K_L ($L\ mg^{-1}$)	4.5×10^{-5}
	q_m	181.49
	R^2	0.993
Freundlich	K_F [$(mg\ g^{-1})\cdot(mg\ L^{-1})^{1/n}$]	4.671
	n	3.335
	R^2	0.989
Temkin-Pyzhev	a_T ($L\ mg^{-1}$)	1.13×10^{-3}
	b_T ($J\ mol^{-1}$)	78.702
	R^2	0.985

the following conditions: emission slit 1o; room temperature measuring; working voltage 40 kV; scanning Angle 5–60o; scanning step size 0.05o; scanning speed 1 step/second.

3 Results and discussions

3.1 Resin selection

The adsorption and desorption capacities of cation exchange resins D113, D150, D152 and D155 are shown in Figure 1. Among the four resins, the unit adsorption capacity of D113 reached the highest of 156.51 mg g^{-1}. However, the highest desorption capacity and desorption rate was observed with D152 (83.48 mg g^{-1} and 62.53%, respectively). As can be seen from Table 1, the particle size of D113 was smaller than the other three resins, which increased the contact area between D113 and PDA fermentation broth, and made the adsorption capacity of D113 higher than the other three resins. However, the exchange capacity of D152 was the best among the four resins, which was also the reason why its desorption capacity and desorption rate were higher than the other three resins (Du et al., 2012). Therefore, D152 was selected to further study the adsorption process of PDA fermentation broth.

3.2 Effects of pH and temperature on the adsorption process

The equilibrium adsorption capacity of static adsorption under different pH values (7.0–13.0) is shown in Figure 2A. With the increase of pH, the adsorption capacity of D152 for PDA reached 133.80 mg g^{-1} when the pH reached 9.0. There were three main forms of PDA in aqueous solution: $C_5H_{14}N_2$, $C_5H_{15}N_2^+$ and $C_5H_{16}N_2^{2+}$, which can be interconverted by adjusting the pH. When the pH was 9, PDA existed in ionic form, with more $C_5H_{15}N_2^+$ and less $C_5H_{16}N_2^{2+}$. Under these conditions, it was more conducive to ion adsorption (Lee et al., 2019). When the pH value reached 11, the unit adsorption capacity of PDA decreased significantly. When the pH value was high, the PDA mostly existed in the solution in molecular form. At this time, the adsorption was mostly through non-ionic interactions, which were difficult to exchange through with the ionic resin. The adsorption capacity of D152 to PDA decreased with increasing pH.

The equilibrium adsorption capacity of static adsorption under different temperatures (20–60°C) is shown in Figure 2B. It can be seen that when the temperature increased, the equilibrium adsorption capacity showed a negative correlation trend. The increase of temperature caused the adsorption reaction to move in the opposite direction, since the adsorption process was an exothermic event (Zhuang et al., 2020).

The equilibrium adsorption capacity of static adsorption under different initial PDA concentrations (50–400 g L^{-1}) is shown in Figure 2C. At low concentration, the total number of adsorption sites was limited for fixed resin dosage, resulting in decreased adsorption efficiency with increasing of concentration. Before reaching the saturation adsorption capacity, the adsorption capacity increased with increaseing initial concentration (Ren et al., 2020). The saturated adsorption capacity of unit resin was 181.06 mg g^{-1}.

The equilibrium adsorption capacity of static adsorption for different adsorption times (0–2.0 h) is shown in Figure 2D. As expected, increasing the contact time between D152 and PDA

TABLE 3 Relevant parameters of pseudo first-order and pseudo second-order models at different temperatures.

T (°C)	$q_{e,exp}$ (mg g^{-1})	Pseudo-1st-order			Pseudo-2nd-order		
		$q_{e,cal}$ (mg g^{-1})	K_1 (min^{-1})	R^2	$q_{e,cal}$ (mg g^{-1})	K_2 [g·(mg min)$^{-1}$]	R^2
20	133.78	131.77	0.1438	0.994	144.27	0.2241	0.994
30	128.37	127.02	0.1277	0.999	141.17	0.1832	0.986
40	124.41	120.70	0.1182	0.987	135.11	0.16	0.968

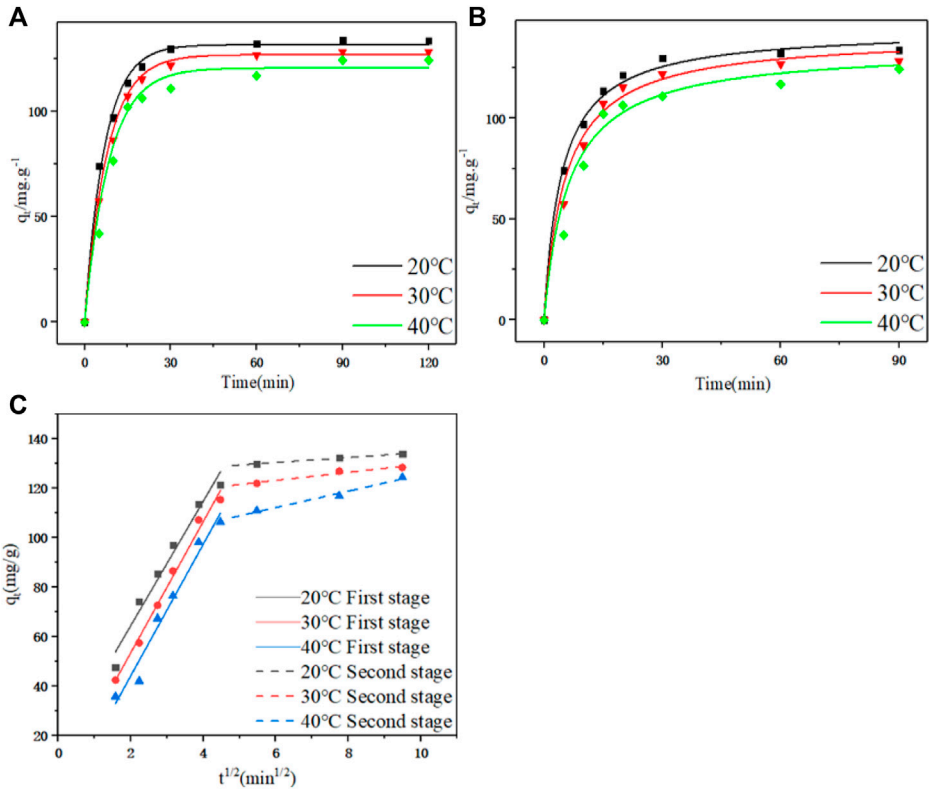

FIGURE 4
(A) Pseudo first-order kinetic curves at different temperatures. **(B)** Pseudo second-order and pseudo first-order dynamic curves at different temperatures. **(C)** Linear fitting diagram of particle diffusion at different temperatures.

fermentation broth increased the adsorption capacity to a constant level. In the experimental device, when the adsorption time reached 1 h, the equilibrium adsorption capacity did not increase further; there were a large number of surface adsorption sites on the resin, which were able to accommodate the ion mass transfer in the fermentation broth, thus promoting rapid adsorption. With the saturation of the surface adsorption sites, the influence of time on the adsorption rate decreased until it reached equilibrium (Moghimi et al., 2020).

3.3 Adsorption isotherm model

The adsorption performance of D152 for PDA was further tested by the adsorption isotherm model. Finding the best correlation for equilibrium curve was for optimizing the adsorption system. The Langmuir model is based on the following assumptions:① the adsorbate is adsorbed on the surface of the adsorbent as a monolayer; ② Adsorption is dynamic, and the adsorbed molecules will return to the original solution under the influence of thermal motion; ③ There is no interaction between the adsorbate molecules adsorbed on the surface of the adsorbent (Vinco et al., 2022). The following formula was used to calculate the equilibrium absorption capcity:

$$q_e = \frac{q_m K_L c_e}{1 + K_L c_e} \tag{12}$$

where q_e was the equilibrium adsorption capacity, mg g^{-1}; q_m was the maximum adsorption capacity, mg g^{-1}; K_L was adsorption equilibrium constant, L mg^{-1}; C_e was the equilibrium adsorption concentration, mg L^{-1}.

TABLE 4 Relevant parameters of particle diffusion model at different temperatures.

T(°C)	First stage			Second stage		
	k_{p1} (mg g^{-1}·$min^{0.5}$)	C	R^2	k_{p2} (mg g^{-1}·$min^{0.5}$)	C	R^2
20	25.18	14.02	0.972	1.01	124.37	0.998
30	26.57	0.25	0.990	1.64	113.31	0.974
40	26.65	−9.25	0.970	3.32	92.25	0.990

The Freundlich model is an empirical adsorption model with non-uniform surface (Ahmad et al., 2021), and can be expressed by the following equation:

$$q_e = K_F C_e^{1/n} \tag{13}$$

where q_e was the equilibrium adsorption capacity, mg g^{-1}; C_e was the equilibrium adsorption concentration, mg L^{-1}; K_F was the adsorption capacity, (mg g^{-1})·(mg L^{-1})$^{1/n}$; n was the characteristic parameter of the equation.

The Temkin-Pyzhev model assumes a linear, rather than logarithmic, decrease in the heat of adsorption for surface molecules of adsorbents (Foo and Hameed., 2010), and can be described as:

$$q_e = \frac{RT}{b_T} ln(a^T C_e) \tag{14}$$

where q_e was the equilibrium adsorption capacity, mg g^{-1}; C_e was the equilibrium adsorption concentration, mg L^{-1}; a_T was the thermodynamic constant, L mg^{-1}; b_T was the thermodynamic constant, J mol^{-1}.

The fitting of different adsorption isotherm models is shown in Figure 3A. With the increase of PDA equilibrium concentration, the distribution coefficient between the solid phase and liquid phase gradually decreased, and the saturation of resin phase gradually increased. With the increase of the equilibrium concentration, the slope of the equilibrium curve gradually decreased, indicating that the affinity between the exchange ion and the resin decreased with the increase of the solution equilibrium concentration (Hou et al., 2022). The second derivative of the adsorption isotherm (second derivative of f" (C_e) < 0) showed that the ion exchange equilibrium of PDA on D152 cation exchange resin was favorable.

The basic characteristics of the Langmuir isotherm can be expressed by a dimensionless constant R_L (Zhou et al., 2019):

$$R_L = \frac{1}{1 + R_L C_0} \tag{15}$$

where $R_L > 1$ indicates that the adsorption was unfavorable, $R_L = 1$ indicates that the adsorption was linear, and $R_L < 1$ indicates that the adsorption was favorable. The R_L values under different PDA concentrations were <1, indicating that D152 cation exchange resin had a good adsorption effect on PDA.

In the Freundlich model, when $1/n$ was in the range of 0.1–0.5, the adsorbent was easily adsorbed by the resin, and when $1/n$ was greater than 2.0, the adsorption was inhibited. The results are shown in Table 2. n value was 3.335 and $1/n$ value was 0.30, which ranged from 0.1 to 0.5, indicating that the adsorption process of PDA on D152 cation exchange resin was easy to carry out.

The Temkin-Pyzhev adsorption isotherm model was used to fit the adsorption isotherm data of PDA on D152 resin. As shown in Figure 3A, it can be seen that the fitting effect was good, and the uniform distribution of molecular binding energy of the adsorption layer was deduced (Foo and Hameed, 2010).

It can be seen from Table 2 that the correlation coefficients obtained by fitting the three isothermal models are all good (R^2 > 0.98), but the correlation coefficient (R^2 = 0.993) fitted by the Langmuir isothermal model is better than the Freundlich (R^2 = 0.989) and Temkin-Pyzhev (R^2 = 0.985) models, and the theoretical maximum adsorption capacity of the Langmuir isothermal model was 181.49 mg g^{-1}, which was closer to the experimental maximum adsorption capacity of 181.06 mg g^{-1}. Therefore, the adsorption data of D152 for PDA was closer to the Langmuir isothermal model. It is concluded that PDA is adsorbed on the surface of D152 resin as a monolayer, and the adsorption process is dynamic. There is no interaction force between PDA molecules adsorbed on the resin surface.

3.4 Adsorption thermodynamic parameters

In order to understand the thermodynamic characteristics of PDA adsorption on D152, the thermodynamic parameters of the adsorption process at 20°C were studied. Due to the good correlation of the Freundlich model, the calculation formulas of Gibbs free energy change (Δ G), enthalpy change (ΔH), and entropy change (ΔS) parameters were defined as (Chen and Zhang, 2014; Wang et al., 2019):

$$ln C_e = \frac{\Delta H}{RT} + C_K \tag{16}$$

$$\Delta G = -nRT \tag{17}$$

$$\Delta S = \frac{\Delta H - \Delta G}{T} \tag{18}$$

where C_K was a constant; R was the general gas constant, 8.314 J·(mol·K)$^{-1}$; T was the thermodynamic temperature, K; n is the coefficient of Freundlich equation.

According to the Clapeyron-Clausius Eq. 16, the linear fitting is shown in Figure 3B, and the fitting correlation coefficient was R^2 = 0.965. Finally, the enthalpy change was calculated as ΔH = −1.412 kJ mol^{-1}, indicating an exothermic reaction; ΔG = −10.474 kJ mol^{-1}, indicating that the adsorption reaction described as spontaneous; ΔS = 29.89 J·(mol·K)$^{-1}$, indicating that the disorder degree of solid-liquid interface increased (Chen and Zhang, 2014; Guo et al., 2014), and the arrangement of PDA adsorbed on the resin surface was more disordered after adsorption.

10.3389/fbioe.2022.1104041

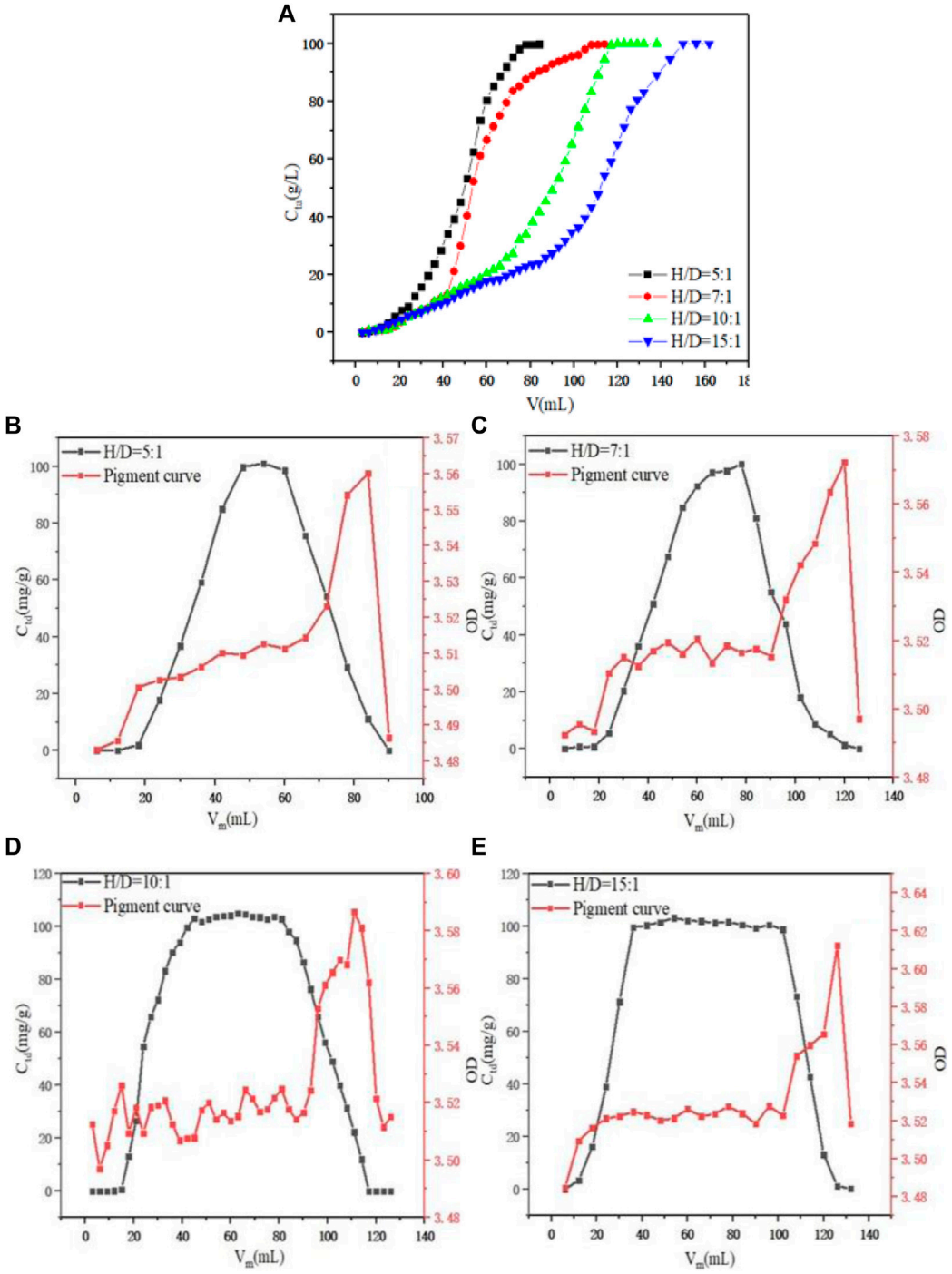

FIGURE 5
(A) Effect of H/D on dynamic adsorption. **(B)** Effect of H/D = 5:1 on dynamic desorption. **(C)** Effect of H/D = 7:1 on dynamic desorption. **(D)** Effect of H/D = 10:1 on dynamic desorption. **(E)** Effect of H/D = 15:1 on dynamic desorption.

3.5 Adsorption kinetic model

The pseudo first-order kinetics and pseudo second-order kinetics models, which are widely used in kinetics research, are used to fit kinetic data. The pseudo first-order equation model can be described as:

$$q_t = q_e\left(1 - e^{-K_1 t}\right) \tag{19}$$

where q_t was the resin adsorption capacity at t time, mg g^{-1}; q_e was the equilibrium resin adsorption capacity, mg g^{-1}; t was the adsorption instantaneous time, min; K_1 was the pseudo first-order rate constant, min^{-1}.

The pseudo-second order equation model can be described as:

$$q_t = \frac{K_2 q_e^2 t}{1 + K_2 q_e t} \tag{20}$$

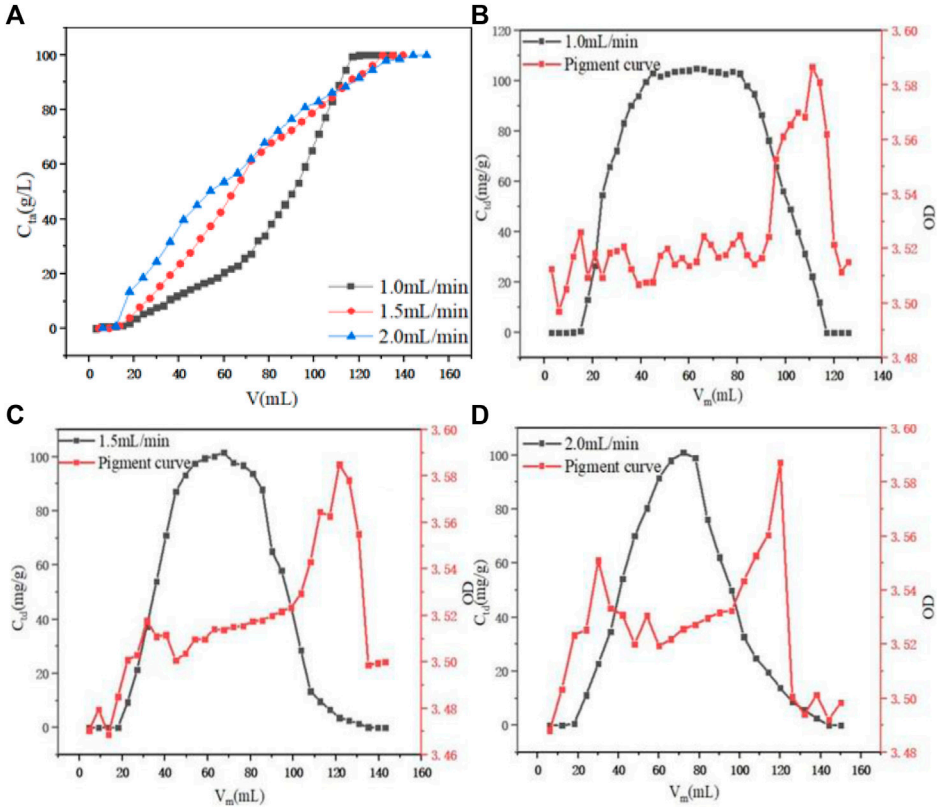

FIGURE 6
(A) Effect of flow rate on dynamic adsorption. **(B)** Effect of 1.0 ml min^{-1} on dynamic desorption. **(C)** Effect of 1.5 ml min^{-1} on dynamic desorption. **(D)** Effect of 2.0 ml min^{-1} on dynamic desorption.

where q_t was the resin adsorption capacity at t time, mg g^{-1}; q_e was the equilibrium resin adsorption capacity, mg g^{-1}; t was the adsorption instantaneous time, min; K_2 was a quasi-second-order rate constant, g·(mg min)$^{-1}$.

According to the fitting parameters in Table 3 and the model fitting diagram in Figures 4A, B, the pseudo first-order kinetics model can better fit the adsorption kinetic data of PDA than the pseudo second-order kinetic model, and the correlation coefficient (R^2) of the pseudo first-order kinetics model was higher than the pseudo second-order kinetics model at different temperatures. The equilibrium adsorption calculated by the pseudo first-order kinetics model was closer to the experimental data, indicating that adsorption may be dominated by ion exchange and other processes and more unit point adsorption. According to the rate constants K_1 and K_2 obtained by model fitting, the adsorption rate decreased with the increase of temperature, which may be because the adsorption process is an exothermic process (Hou et al., 2022). In this case, the increase of temperature led to the reverse reaction direction of adsorption equilibrium, and reduced the adsorption rate.

In order to further analyze the adsorption rate limiting steps on the resin, we also used the particle diffusion model to fit the adsorption kinetic data. The particle diffusion model is as follows:

$$q_t = k_p t^{1/2} + C \tag{21}$$

where q_t was the resin adsorption capacity at t time, mg g^{-1}; t was the adsorption instantaneous time, min; k_p was the particle diffusion constant, (mg·g^{-1}·$min^{1/2}$); C was the parameter related to boundary layer thickness.

The diffusion mechanism of PDA on D152 was characterized by a particle diffusion model. The curves of q_t and $t^{1/2}$ at different temperatures and initial concentrations are shown in Figure 4C. It is clear that these curves show multi-linear graphs, indicating that intra - particle diffusion is not the only rate-limiting step (Zhuang et al., 2020). It can be speculated that the initial stage (0–20 min) was the film diffusion stage, while the later stage (20–90 min) was due to an intra - particle diffusion effect.

The boundary layer thickness related parameter C is directly proportional to the range of boundary layer thickness; the greater the value of C, the greater the boundary layer effect. If the value of C is negative, this indicates that the thickness of the boundary layer delays the diffusion in the particles, while a positive value of C indicates that the adsorption is fast (Deng et al., 2020). It can be seen from Table 4 that no matter whether in the film diffusion stage (0 min–20 min) or in the particle diffusion stage (20 min–90 min), the C value decreased significantly with the increase of temperature, indicating that the increase of temperature was not conducive to adsorption.

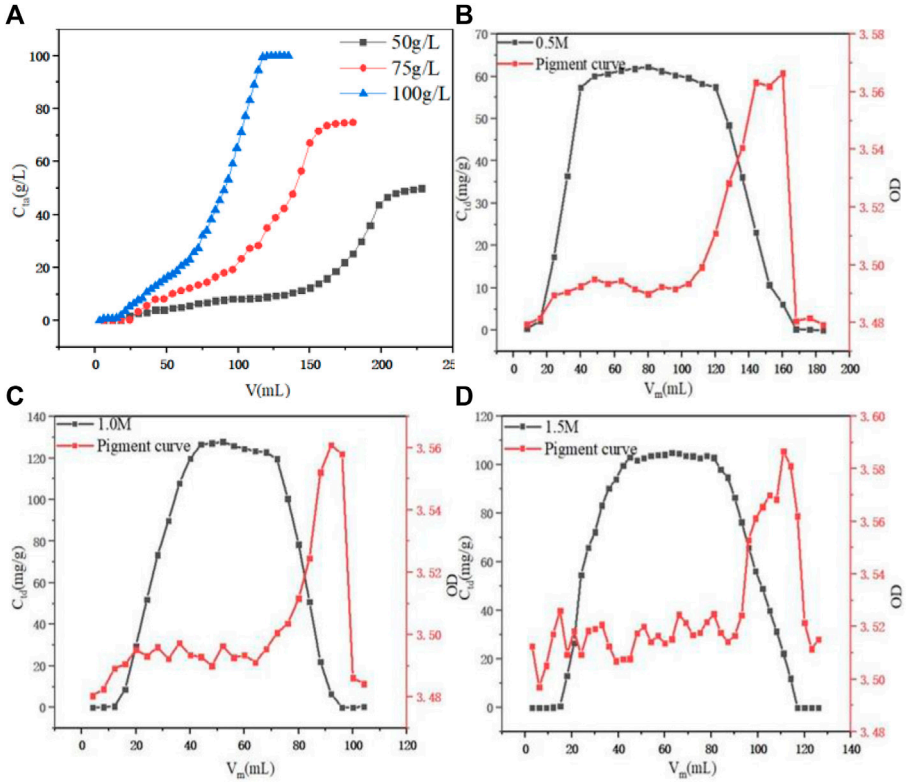

FIGURE 7
(A) Effect of initial PDA concentration on dynamic adsorption. **(B)** Effect of initial 0.5 M HCl on dynamic desorption. **(C)** Effect of initial 1.0 M HCl on dynamic desorption. **(D)** Effect of initial 1.5 M HCl on dynamic desorption.

3.6 Dynamic adsorption and desorption results

The dynamic adsorption process of PDA on D152 was investigated under the conditions of single factor variation, different PDA concentration, different flow rate and different height-diameter ratio (H/D), and the penetration curve was used to describe these parameters. The dynamic desorption process of PDA on D152 was investigated under different hydrochloric acid concentrations, flow rates and height-diameter ratios, and desorption curve and pigment curve were used to describe the changes in these parameters and the impact on desorption.

Under the condition of a constant flow rate of 1.0 ml min^{-1} and initial concentration of PDA fermentation liquid at 100 g L^{-1}, the dynamic adsorption process of PDA on D152 under H/D was investigated, as shown in Figure 5A. When the aspect ratio was 5:1–10:1, the unit adsorption capacity of the resin also increased with the increase of the H/D. The unit adsorption capacity of resin was 87.39, 92.78, 99.68, and 100.26 mg g^{-1}, respectively, because the H/D of the column theoretical plate number was larger, and the separation efficiency was improved (Xiong et al., 2019). However, when the H/D reached 10:1, the unit adsorption capacity did not increase significantly. Under the condition of a constant flow rate of 1.0 ml min^{-1} and an initial concentration of desorption solution of 1.5 M HCl, the desorption situation in the elution process was considered. By comparing the F value of the eluted feed solution under different aspect ratios, as shown in Figures 5B–E, the H/D was 5:1–15:1 and it reached 66.85, 75.48, 81.45, and 81.47%, respectively. It can be seen that the F value increased as the H/D increased, but when it reached 10:1, the F value did not change significantly. At the same time, it can be seen that when the section corresponded to the desorption curve was selected, when the H/D was 5:1, 7:1, and 10:1, the OD value was stable at 3.5–3.52, while when the H/D reached 15:1, the OD value exceeded 3.52, and the ability to remove pigment was weaker than the other H/D. Therefore, considering the situation of adsorption and desorption comprehensively, when the H/D was too large, industrial scale up will lead to high operating pressure and higher equipment cost. Therefore, the H/D of 10:1 was selected as the best ratio.

When the aspect ratio was fixed at 10:1 and the initial concentration of PDA fermentation liquid was 100 g L^{-1}, the dynamic adsorption process of PDA on D152 resin under different flow rates was investigated. As shown in Figure 6A, with the increase of flow velocity, component adsorption was quickly initiated, but when adsorption was complete, the required volume was significantly increased. The adsorption capacity of 1.0 ml min^{-1} at low flow rate was 96.48 mg g^{-1}, while at flow rates of 1.5 ml min^{-1} and 2.0 ml min^{-1}, the adsorption capacity was diminished to 88.71 and 77.64 mg g^{-1}, respectively. It was inferred that when the flow rate increased, the contact residence time between fermentation liquid and resin decreased, resulting in inadequate adsorption and decreased adsorption capacity (Zhuang et al., 2020). When considering desorption in the elution process when the H/D was fixed at 10:1 and the initial

10.3389/fbioe.2022.1104041

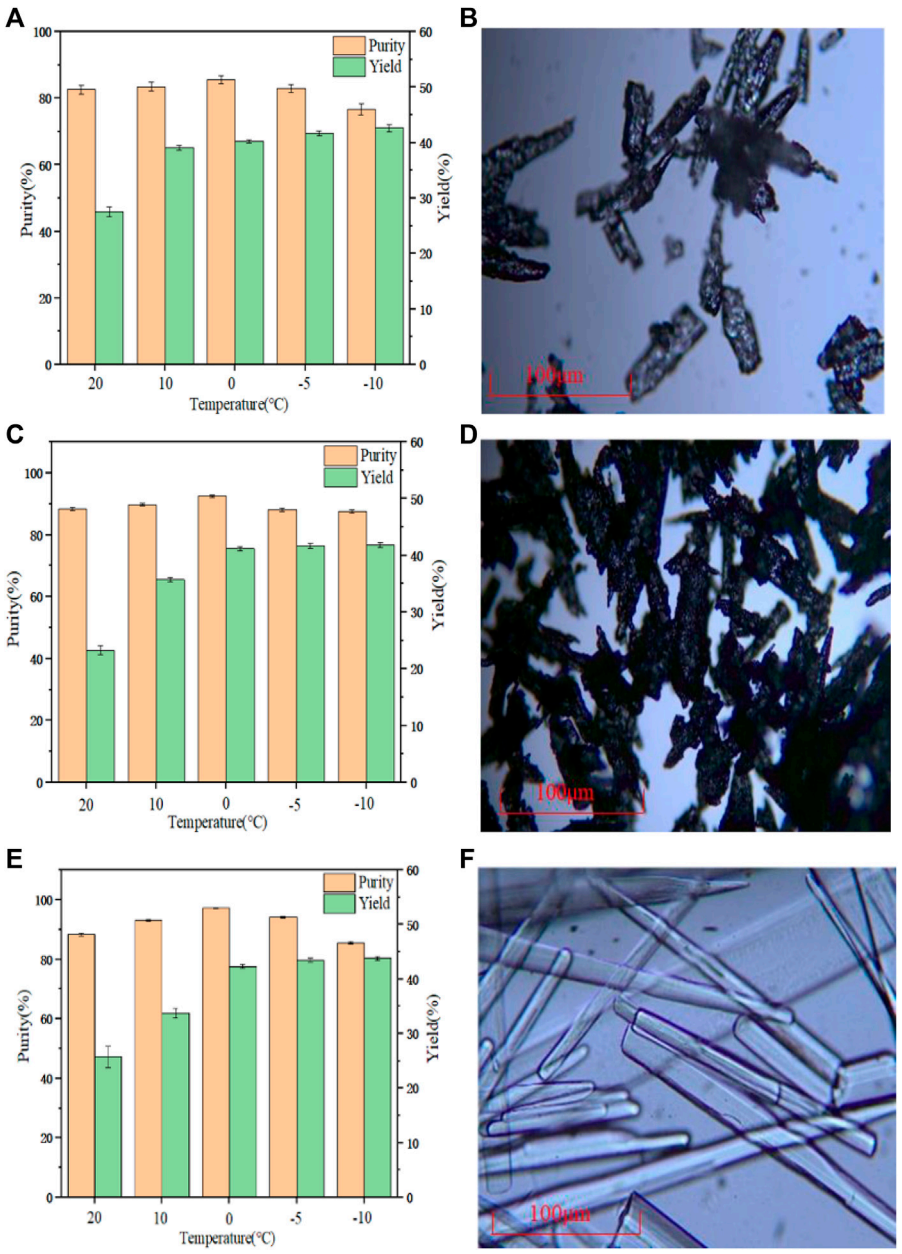

FIGURE 8
(A) Crystallization yield and purity of PHF **(B)** Microscope image of PHF **(C)** Crystallization yield and purity of PHDF **(D)** Microscope image of PHDF **(E)** Crystallization yield, purity of PHER **(F)** Microscope image of PHER.

concentration of desorption solution HCl was 1.0 M, as shown in Figures 6B–D, the desorption flow rate increased and the amount of desorption agent required for complete desorption increased, and the elution peak had a certain trailing phenomenon. When the flow rate was 1.0 and 1.5 ml min^{-1}, the F value did not differ much, reaching 81.49 and 82.01%, respectively. However, when the flow rate rose to 2.0 ml min^{-1}, the F value decreased significantly to 66.43%. This observation may be due to the excessive flow rate, resulting in too fast discharge in the desorption process. After C_{max} was reached, the concentration of feed liquid decreased rapidly. With the increase of the flow rate from 1.0 to 2.0 ml min^{-1}, the overall OD value of the corresponding section of the pigment curve was also increased, indicated that 1.0 ml min^{-1} was the best flow rate to removed pigment. Therefore, 1.0 ml min^{-1} was selected as the best flow rate in combination with adsorption.

When the initial PDA fermentation liquid concentration was optimized with a fixed H/D of 10:1 and a constant flow rate of 1.0 ml min^{-1}, as shown in Figure 7A, it was found that as the initial PDA fermentation liquid concentration increased from 50 g L^{-1} to 100 g L^{-1}, the penetration volume decreased. This may be due to the slow mass transfer process and that the breakthrough time of the low concentration was delayed. This observation was reinforced by the accompanied leftward deviation of the penetration curve, and an increase in the slope of the curve as PDA concentration increased, leading to the reduction of the mass transfer interface (Show et al., 2022). The final adsorption capacity was 76.54, 94.85,

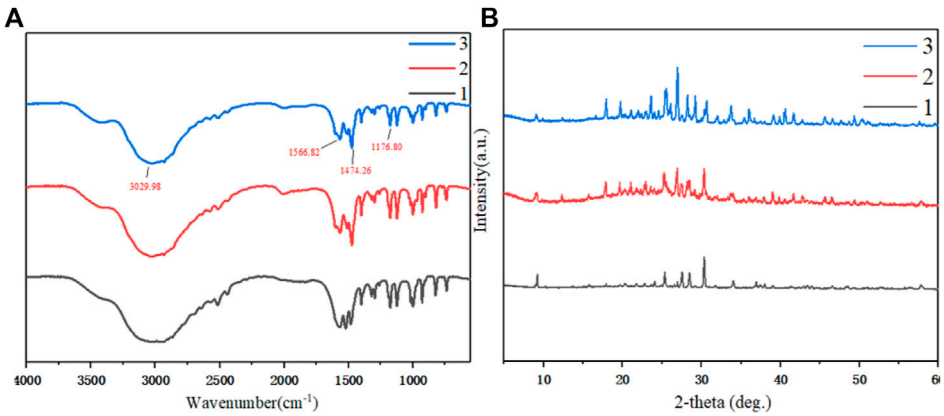

FIGURE 9
(A) Infrared spectrum characterization of cooling crystallization products from three different raw materials **(B)** PXRD characterization of cooled crystalline products from three different raw materials 1. Crystallization of PHF 2. Crystallization of PHDF 3. Crystallization of PHER.

and 96.45 g L^{-1} with the initial PDA fermentation liquid concentration was 50, 75, and 100 g L^{-1}, respectively. There was little difference between the initial concentration of 75 g L^{-1} and the equilibrium adsorption capacity of 100 g L^{-1}, but the required amount of 100 g L^{-1} was lower and the time required for complete penetration was shorter. Therefore, 100 g L^{-1} was selected as the best fermentation liquid concentration.

The concentration of hydrochloric acid was optimized, as shown in Figures 7B–D; it was found that when the concentration of hydrochloric acid was 0.5, 1.0, and 1.5 M, the F value of the eluted liquid was 80.78, 80.16, and 81.49%, respectively, which were relatively close. However, when the concentration of hydrochloric acid was 1.0 M, the maximum concentration value of the eluent reached 127.82 g L^{-1}, the overall peak pattern was good. With the concentration of hydrochloric acid increasing from 0.5 M to 1.0 M, the overall OD value of the corresponded section of the pigment curve was stable at 3.48–3.50, while when the concentration of hydrochloric acid reached 1.5 M, the overall OD value of the section was 3.50–3.52, increased significantly. Therefore, the 1.0 M hydrochloric acid was selected as the best elution concentration.

3.7 PDAH crystallization

The cooling crystallization experiment was carried out under the same conditions of three different raw materials, and the results are shown in Figures 8A, C, E. When the temperature was reduced to 0°C, the purity of the PHF, PHDF and PHER was the highest with 85.55, 92.75, and 97.23% respectively. This result may be because when the temperature was lower than 0°C, although the yield was improved, more impurities precipitated, and it was more difficult to separate in the suction filtration process. It can be seen from Figure 8B that there were many impurities in the PHF. Figure 8D shows that the crystal form of PHDF was more complex, while it can be seen from Figure 8F that the crystal form of PHER was long rod type. Therefore, PHER was used for crystallization. The water content of PDAH obtained by Karl Fischer was 0.8%, and the molar ratio of PDA to HCl was 1:1.81 in the obtained PADH crystals which was determined by element analysis.

The cooling crystallization products of three different raw materials were characterized by infrared spectroscopy. As shown in Figure 9A, when the amine was salted, the stretching vibration absorption peak of the N-H group shifted significantly to a lower frequency, overlapped with the stretching vibration absorption peak of the C-H bond, and formed a wide and strong spectral band in the range of 3,200–2,200 cm^{-1}. Due to the deformation and vibration of the N-H group, the band has a strong absorption peak at 1,600–1,510 cm^{-1}. The C-H group had an absorption peak near 1,475 cm^{-1} due to a deformation vibration. The C-N group had a stretching vibration peak at 1,230–1,050 cm^{-1}. Through infrared spectrum analysis, it can be confirmed that the main groups of the material structure are basically the same as PDAH. In addition, in the three raw materials, the impurity peak of PHER was less, indicating that its purity was higher.

The products obtained by cooling and crystallization of different raw materials were characterized by PXRD, as shown in Figure 9B. The main peaks of X-ray powder diffraction 2θ = 9.06o, 17.96o, and 25.52o appeared in the same position. These peaks belong to the same crystal form, and the main peak of PHER was sharper, the impurity peak was diminished, and the relative crystallinity was higher (Liu et al., 2020).

4 Conclusion

In this study, the adsorption and desorption properties of D152 for PDA in fermentation broth were the best. The Langmiur, Freundlich, and Temkin-Pyzhev equations all fit well with the adsorption equilibrium data of PDA on D152 at 20°C. The adsorption free energy, enthalpy, and entropy were calculated. The results showed that the adsorption of PDA on D152 was a spontaneous exothermic process. The pseudo-first-order model best described the adsorption kinetics of PDA on D152. The dynamic experiment in a fixed bed column showed that the desorption capacity reached 96.45 mg g^{-1}, and the F value reached 80.16%. The cooling crystallization of three kinds of raw materials showed that the resin eluting crystallization product had higher quality, the purity reached 97.23%, and the

yield was 42.32%. This study provides a low-cost and efficient method for the separation and purification of PDAH from PDA fermentation broth, and contributes to the industrial scale-up of the separation of PDAH.

Data availability statement

The original contributions presented in the study are included in the article/Supplementary Material; further inquiries can be directed to the corresponding author.

Author contributions

All authors listed have made a substantial, direct, and intellectual contribution to the work and approved it for publication.

Funding

This work was supported by the National Key Research and Development Program of China (2021YFC2104100, 2020YFE0100100, and 2018YFA0901500), Joint Funds of the National Natural Science Foundation of China (U21B2097) and Basic Science (Natural Science) Research Project of Jiangsu Province Colleges and Universities (21KJB530014).

Conflict of interest

FH was employed by the company of Jiangsu Institute of Industrial Biotechnology, JITRI Co., Ltd. YnY was employed by the company of Gansu Yinguang Juyin Chemical Co., Ltd.

The remaining authors declare that the research was conducted in the absence of any commercial or financial relationships that could be construed as a potential conflict of interest.

Publisher's note

All claims expressed in this article are solely those of the authors and do not necessarily represent those of their affiliated organizations, or those of the publisher, the editors and the reviewers. Any product that may be evaluated in this article, or claim that may be made by its manufacturer, is not guaranteed or endorsed by the publisher.

References

Ahmad, A., Othman, I., Taher, H., and Banat, F. (2021). Lactic acid recovery from date pulp waste fermentation broth by ions exchange resins. *Environ. Technol. Inno.* 22, 101438. doi:10.1016/j.eti.2021.101438

Alexandri, M., Vlysidis, A., Papapostolou, H., Tverezovskaya, O., Tverezovskiy, V., Kookos, I. K., et al. (2019). Downstream separation and purification of succinic acid from fermentation broths using spent sulphite liquor as feedstock. *Sep. Purif. Technol.* 209, 666–675. doi:10.1016/j.seppur.2018.08.061

Chen, H. L., Chen, Y. S., and Juang, R. S. (2007). Separation of surfactin from fermentation broths by acid precipitation and two-stage dead-end ultrafiltration processes. *J. Membr. Sci.* 299 (1-2), 114–121. doi:10.1016/j.memsci.2007.04.031

Chen, X. S., Gao, Y., Zhen, B., Han, D., Zhang, J. H., and Mao, Z. G. (2016). Separation and purification of ε-poly- l -lysine from fermentation broth. *Process Biochem.* 51 (1), 134–141. doi:10.1016/j.procbio.2015.11.010

Chen, Y., and Zhang, D. (2014). Adsorption kinetics, isotherm and thermodynamics studies of flavones from Vaccinium Bracteatum Thunb leaves on NKA-2 resin. *Chem. Eng. J.* 254, 579–585. doi:10.1016/j.cej.2014.05.120

Deng, Z., Oraby, E. A., and Eksteen, J. J. (2020). Cu adsorption behaviours onto chelating resins from glycine-cyanide solutions: Isotherms, kinetics and regeneration studies. *Sep. Purif. Technol.* 236, 116280. doi:10.1016/j.seppur.2019.116280

Dong, Y., Zhao, M., Sun-Waterhouse, D., Zhuang, M., Chen, H., Feng, M., et al. (2015). Absorption and desorption behaviour of the flavonoids from Glycyrrhiza glabra L. leaf on macroporous adsorption resins. *Food Chem.* 168, 538–545. doi:10.1016/j.foodchem.2014.07.109

Du, H., Wang, H., Yu, J., Liang, C., Ye, W., and Li, P. (2012). Enrichment and purification of total flavonoid C-glycosides from Abrus mollis extracts with macroporous resins. *Ind. Eng. Chem. Res.* 51 (21), 7349–7354. doi:10.1021/ie3004094

Figueira, M., Reig, M., Fernandez de Labastida, M., Cortina, J. L., and Valderrama, C. (2022). Boron recovery from desalination seawater brines by selective ion exchange resins. *J. Environ. Manage.* 314, 114984. doi:10.1016/j.jenvman.2022.114984

Foo, K. Y., and Hameed, B. H. (2010). Insights into the modeling of adsorption isotherm systems. *Chem. Eng. J.* 156 (1), 2–10. doi:10.1016/j.cej.2009.09.013

Guo, Y., Hong Nhung, N. T., Dai, X., He, C., Wang, Y., Wei, Y., et al. (2014). Strontium ion removal from artificial seawater using a combination of adsorption with biochar and precipitation by blowing CO_2 nanobubble with neutralization. *Front. Bioeng. Biotechnol.* 10, 819407. doi:10.3389/fbioe.2022.819407

Hou, Y., Liu, L., He, Q., Zhang, D., Jin, J., Jiang, B., et al. (2022). Adsorption behaviors and kinetics studies of chitooligosaccharides with specific degree of polymerization on a novel ion-exchange resin. *Chem. Eng. J.* 430, 132630. doi:10.1016/j.cej.2021.132630

Hu, M., Yu, J., Zhang, H., and Xu, Q. (2022). An efficient method for the recovery and separation of surfactin from fermentation broth by extraction-back extraction. *Process Biochem.* 114, 59–65. doi:10.1016/j.procbio.2022.01.014

Jeon, S., Kim, D. K., Song, H., Lee, H. J., Park, S., Seung, D., et al. (2014). 2, 3-Butanediol recovery from fermentation broth by alcohol precipitation and vacuum distillation. *J. Biosci. Bioeng.* 117 (4), 464–470. doi:10.1016/j.jbiosc.2013.09.007

Karp, E. M., Cywar, R. M., Manker, L. P., Saboe, P. O., Nimlos, C. T., Salvachúa, D., et al. (2018). Post-fermentation recovery of biobased carboxylic acids. *ACS Sustain. Chem. Eng.* 6 (11), 15273–15283. doi:10.1021/acssuschemeng.8b03703

Ke, C., Ren, Y., Gao, P., Han, J., Tao, Y., Huang, J., et al. (2021). Separation and purification of pyrroloquinoline quinone from fermentation broth by pretreatment coupled with macroporous resin adsorption. *Sep. Purif. Technol.* 257, 117962. doi:10.1016/j.seppur.2020.117962

Lee, H. I., and Lee, P. S. (2022). Zeolite adsorbents for the separation of n-butyric acid from fermentation broths via adsorption. *Microporous Mesoporous Mater* 334, 111768. doi:10.1016/j.micromeso.2022.111768

Lee, J. A., Ahn, J. H., Kim, I., Li, S., and Lee, S. Y. (2019). Separation and purification of three, four, and five carbon diamines from fermentation broth. *Chem. Eng. Sci.* 196, 324–332. doi:10.1016/j.ces.2018.11.018

Li, C., Gao, M., Zhu, W., Wang, N., Ma, X., Wu, C., et al. (2021). Recent advances in the separation and purification of lactic acid from fermentation broth. *Process Biochem.* 104, 142–151. doi:10.1016/j.procbio.2021.03.011

Li, W., Li, H., Wu, C., Han, B., Ouyang, P., and Chen, K. (2021). An effective synthesis of bio-based pentamethylene diisocyanate in a jet loop reactor. *Chem. Eng. J.* 425, 131527. doi:10.1016/j.cej.2021.131527

Liu, H., Yang, P., Li, Z., Wen, Q., Li, X., Zhu, C., et al. (2020). Thermodynamics, characterization, and polymorphic transformation of 1, 5-pentanediamine carbonate. *Ind. Eng. Chem. Res.* 59 (21), 10185–10194. doi:10.1021/acs.iecr.0c00365

Ma, Y., Xiao, Y., Zhao, Y., Bei, Y., Hu, L., Zhou, Y., et al. (2022). Biomass based polyols and biomass based polyurethane materials as a route towards sustainability. *React. Funct. Polym.* 175, 105285. doi:10.1016/j.reactfunctpolym.2022.105285

Moghimi, F., Jafari, A. H., Yoozbashizadeh, H., and Askari, M. (2020). Adsorption behavior of Sb(III) in single and binary Sb(III)—Fe(II) systems on cationic ion exchange resin: Adsorption equilibrium, kinetic and thermodynamic aspects. *Trans. Nonferrous Met. Soc. China* 30 (1), 236–248. doi:10.1016/s1003-6326(19)65195-2

Ms, A., Hazra, D., Steele, G., and Pal, S. (2020). Crystallization process modifications to address polymorphic and particle size challenges in early stage development of an API salt. *Chem. Eng. Res. Des.* 164, 400–411. doi:10.1016/j.cherd.2020.09.021

Noreen, A., Zia, K. M., Zuber, M., Tabasum, S., and Zahoor, A. F. (2016). Bio-based polyurethane: An efficient and environment friendly coating systems: A review. *Prog. Org. Coat.* 91, 25–32. doi:10.1016/j.porgcoat.2015.11.018

Paraskar, P. M., Prabhudesai, M. S., Hatkar, V. M., and Kulkarni, R. D. (2021). Vegetable oil based polyurethane coatings – a sustainable approach: A review. *Prog. Org. Coat.* 156, 106267. doi:10.1016/j.porgcoat.2021.106267

Park, J. J., and Lee, W. Y. (2021). Adsorption and desorption characteristics of a phenolic compound from *Ecklonia cava* on macroporous resin. *Food Chem.* 338, 128150. doi:10.1016/j.foodchem.2020.128150

Ren, Y., Han, Y., Lei, X., Lu, C., Liu, J., Zhang, G., et al. (2020). A magnetic ion exchange resin with high efficiency of removing Cr (VI). *Colloid Surf. A- physicoche. Eng. Asp.* 604, 125279. doi:10.1016/j.colsurfa.2020.125279

Shi, Y., Liu, T., Han, Y., Zhu, X., Zhao, X., Ma, X., et al. (2017). An efficient method for decoloration of polysaccharides from the sprouts of Toona sinensis (A. Juss.) Roem by anion exchange macroporous resins. *Food Chem.* 217, 461–468. doi:10.1016/j.foodchem.2016.08.079

Show, S., Sarkhel, R., and Halder, G. (2022). Elucidating sorptive eradication of ibuprofen using calcium chloride caged bentonite clay and acid activated alginate beads in a fixed bed upward flow column reactor. *Sustain. Chem. Pharm.* 27, 100698. doi:10.1016/j.scp.2022.100698

Sparenberg, M. C., Chergaoui, S., Sang Sefidi, V., and Luis, P. (2021). Crystallization control *via* membrane distillation-crystallization: A review. *Desalination* 519, 115315. doi:10.1016/j.desal.2021.115315

Szczygiełda, M., and Prochaska, K. (2020). Downstream separation and purification of bio-based alpha-ketoglutaric acid from post-fermentation broth using a multi-stage membrane process. *Process Biochem.* 96, 38–48. doi:10.1016/j.procbio.2020.05.026

Takahashi, J., Shinagawa, A., Ezaki, A., and Kise, M. (2019). *Method for producing pentane diisocyanate*. JP2019199444A.

Vinco, J. H., Botelho Junior, A. B., Duarte, H. A., Espinosa, D. C. R., and Tenório, J. A. S. (2022). Purification of an iron contaminated vanadium solution through ion exchange resins. *Min. Eng.* 176, 107337. doi:10.1016/j.mineng.2021.107337

Wang, T., Shen, C., Wang, N., Dai, J., Liu, Z., and Fei, Z. (2019). Adsorption of 3-Aminoacetanilide from aqueous solution by chemically modified hyper-crosslinked resins: Adsorption equilibrium, thermodynamics and selectivity. *Colloid Surf. A- physicoche. Eng. Asp.* 575, 346–351. doi:10.1016/j.colsurfa.2019.05.029

Wang, X., Guo, X., Wang, J., Li, H., He, F., Xu, S., et al. (2021). Ameliorating end-product inhibition to improve cadaverine production in engineered *Escherichia coli* and its application in the synthesis of bio-based diisocyanates. *Synth. Syst. Biotechnol.* 6 (4), 243–253. doi:10.1016/j.synbio.2021.09.004

Weng, J., Huang, Y., Hao, D., and Ji, Y. (2020). Recent advances of pharmaceutical crystallization theories. *Chin. J. Chem. Eng.* 28 (4), 935–948. doi:10.1016/j.cjche.2019.11.008

Xiong, N., Yu, R., Chen, T., Xue, Y. P., Liu, Z. Q., and Zheng, Y. G. (2019). Separation and purification of l-methionine from *E. coli* fermentation broth by macroporous resin chromatography. *J. Chromatogr. B* 1110-1111, 108–115. doi:10.1016/j.jchromb.2019.02.016

Xu, S. D., Ning, F. H., Jiang, B. H., Xu, H. X., and Liu, Z. Z. (2018). Refining androstenedione and bisnorcholenaldehyde from mother liquor of phytosterol fermentation using macroporous resin column chromatography followed by crystallization. *J. Chromatogr. B* 1079, 9–14. doi:10.1016/j.jchromb.2017.09.032

Yang, D., Li, M. M., Wang, W. J., Zheng, G. D., Yin, Z. P., Chen, J. G., et al. (2022). Separation and purification of anthocyanins from Roselle by macroporous resins. *Lwt -Food Sci. Technol.* 161, 113371. doi:10.1016/j.lwt.2022.113371

Zeng, J., Yang, Y., Tang, Y., Xu, X., Chen, X., Li, G., et al. (2022). Synthesis, monomer removal, modification, and coating performances of biobased pentamethylene diisocyanate isocyanurate trimers. *Ind. Eng. Chem. Res.* 61 (6), 2403–2416. doi:10.1021/acs.iecr.1c04673

Zhang, H., Liang, H., Kuang, P., Yuan, Q., and Wang, Y. (2012). Simultaneously preparative purification of Huperzine A and Huperzine B from *Huperzia serrata* by macroporous resin and preparative high performance liquid chromatography. *J. Chromatogr. B* 904, 65–72. doi:10.1016/j.jchromb.2012.07.019

Zhang, J., Zhu, C., Zhou, F., and Ma, L. (2018). Adsorption behavior and kinetics for L-valine separation from aqueous solution using ion exchange resin. *React. Funct. Polym.* 130, 51–60. doi:10.1016/j.reactfunctpolym.2018.05.010

Zheng, W., Chen, K., Zhu, J., and Ji, L. (2013). A novel process for erythromycin separation from fermentation broth by resin adsorption–aqueous crystallization. *Sep. Purif. Technol.* 116, 398–404. doi:10.1016/j.seppur.2013.06.019

Zhou, K., Wu, Y., Zhang, X., Peng, C., Cheng, Y., and Chen, W. (2019). Removal of Zn(II) from manganese-zinc chloride waste liquor using ion-exchange with D201 resin. *Hydrometallurgy* 190, 105171. doi:10.1016/j.hydromet.2019.105171

Zhuang, H., Zhong, Y., and Yang, L. (2020). Adsorption equilibrium and kinetics studies of divalent manganese from phosphoric acid solution by using cationic exchange resin. *Chin. J. Chem. Eng.* 28 (11), 2758–2770. doi:10.1016/j.cjche.2020.07.029

Zou, Y., Zhao, M., Yang, K., Lin, L., and Wang, Y. (2017). Enrichment of antioxidants in black garlic juice using macroporous resins and their protective effects on oxidation-damaged human erythrocytes. *J. Chromatogr. B* 1060, 443–450. doi:10.1016/j.jchromb.2017.06.026

frontiers | Frontiers in Bioengineering and Biotechnology

TYPE Review
PUBLISHED 09 January 2023
DOI 10.3389/fbioe.2022.1110004

OPEN ACCESS

EDITED BY
Caoxing Huang,
Nanjing Forestry University, China

REVIEWED BY
Bailiang Xue,
Shaanxi University of Technology, China
Guodong Wu,
Auburn University, United States

*CORRESPONDENCE
Ting Xu,
xuting@tust.edu.cn
Sun-Eun Choi,
oregonin@kangwon.ac.kr
Chuanling Si,
sichli@tust.edu.cn

†These authors have contributed equally to this work and share first authorship

SPECIALTY SECTION
This article was submitted to Bioprocess Engineering, a section of the journal Frontiers in Bioengineering and Biotechnology

RECEIVED 28 November 2022
ACCEPTED 21 December 2022
PUBLISHED 09 January 2023

CITATION
Xu Y, Liu K, Yang Y, Kim M-S, Lee C-H, Zhang R, Xu T, Choi S-E and Si C (2023), Hemicellulose-based hydrogels for advanced applications.
Front. Bioeng. Biotechnol. 10:1110004.
doi: 10.3389/fbioe.2022.1110004

Hemicellulose-based hydrogels for advanced applications

Ying Xu[1†], Kun Liu[1†], Yanfan Yang[1], Min-Seok Kim[2], Chan-Ho Lee[2], Rui Zhang[1,3], Ting Xu[1*], Sun-Eun Choi[2*] and Chuanling Si[1,4*]

[1]Tianjin Key Laboratory of Pulp and Paper, Tianjin University of Science and Technology, Tianjin, China, [2]Department of Forest Biomaterials Engineering, College of Forest and Environmental Sciences, Kangwon National University, Chuncheon, South Korea, [3]Department of Finance, Tianjin University of Science and Technology, Tianjin, China, [4]State Key Laboratory of Tree Genetics and Breeding, Northeast Forestry University, Harbin, China

Hemicellulose-based hydrogels are three-dimensional networked hydrophilic polymer with high water retention, good biocompatibility, and mechanical properties, which have attracted much attention in the field of soft materials. Herein, recent advances and developments in hemicellulose-based hydrogels were reviewed. The preparation method, formation mechanism and properties of hemicellulose-based hydrogels were introduced from the aspects of chemical cross-linking and physical cross-linking. The differences of different initiation systems such as light, enzymes, microwave radiation, and glow discharge electrolytic plasma were summarized. The advanced applications and developments of hemicellulose-based hydrogels in the fields of controlled drug release, wound dressings, high-efficiency adsorption, and sensors were summarized. Finally, the challenges faced in the field of hemicellulose-based hydrogels were summarized and prospected.

KEYWORDS

hemicellulose, hydrogel, biomedical material, adsorption, sensor

1 Introduction

Hydrogels are polymer materials with three-dimensional spatial network structure, which are usually formed by physical or chemical crosslinking of long chain hydrophilic polymers. Physical cross-linking method refers to the formation of cross-linking structure between polymer chains through winding or various weak interactions such as hydrogen bonds or ionic bonds, without the formation of new chemical bonds. The chemical cross-linking method refers to the formation of new covalent bonds, the formation of structural units through copolymerization or condensation reaction of hydrogel, its structure is irreversible, heating will not change its structure (Hoffman, 2012). Compared with the physical cross-linking method, the chemical cross-linking hydrogel has better stability, and the cross-linking density is also controllable, so the physical properties of the hydrogel can be adjusted freely (Mondal et al., 2020). The high cross-linking degree of hydrogels enables them to have good water absorption and retention capacity, and will not dissolve after absorbing a large amount of water (Warren et al., 2017). Due to the differences in raw materials and preparation methods, hydrogels can be endowed with different physical and chemical properties and have been widely used in industrial adsorption (Baghbadorani et al., 2019), medical treatment (Hassan et al., 2018; Liu et al., 2020a; Wang H. et al., 2021; Deng et al., 2022), agriculture (Cheng et al., 2018; Wei et al., 2019), sensor (Lu et al., 2020; Suneetha et al., 2021) and other fields.

Hydrogels can be divided into natural polymer-based hydrogels and synthetic polymer-based hydrogels according to the source of the polymer. Although natural polymer including polysaccharides, gelatin, proteins and nucleic acid hydrogels have good biocompatibility, they

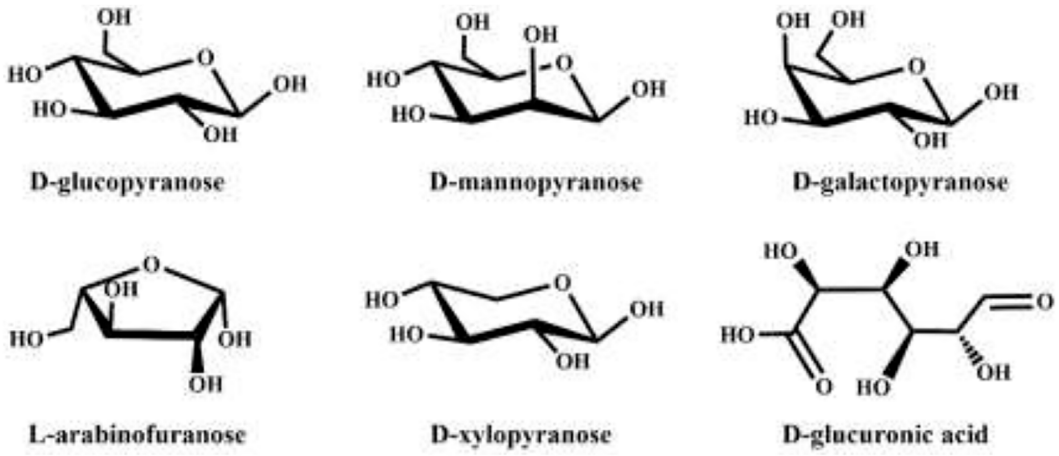

FIGURE 1
The monosaccharide composition of hemicellulose reproduced from: Kong et al. (2018), Springer.

are unstable and easy to be degraded (Shi et al., 2016). The composition, structure, and strength of synthetic polymer hydrogels such as polyacrylic acid, polyacrylamide, acrylic acid, methacrylic acid, N-isopropyl acrylamide, N-vinyl-2-pyrrolidone, *etc.* Are stable and controllable, but their biocompatibility is poor (Martínez-Gómez et al., 2017; Kesharwani et al., 2021). Therefore, the combination of natural polymers and synthetic polymers to prepare hydrogels will be a major development trend (Du et al., 2016; Yang et al., 2021). Hydrogels will have the advantages of both natural polymers and synthetic polymers, showing higher service life, gel strength and water absorption capacity, and more importantly, good biocompatibility.

Lignocellulose is the most abundant natural polymer on the earth, which has the advantages of extensive sources and renewable (Si et al., 2008; Si et al., 2013; An et al., 2019; Liu et al., 2021e; Huang et al., 2021; Qian et al., 2023). It is widely used in energy storage (Liu et al., 2021b; Xu et al., 2021b; Liu et al., 2021c; Liu et al., 2021f; Liu et al., 2022b; Du et al., 2022; Li et al., 2022; Xu et al., 2022), electromagnetic shielding (Liu et al., 2022d; Liu et al., 2022e), biomedicine (Du et al., 2019; Liu et al., 2020c; Xiong et al., 2021a; Xiong et al., 2021b; Ha et al., 2021), sensing (Lu et al., 2019; Ma et al., 2021; Liu et al., 2022a), antibacterial (Du et al., 2021a; Du et al., 2021b) and many other fields (Dai et al., 2017; Xie et al., 2019; Yang et al., 2019; Chen et al., 2020a; An et al., 2020; Wang H. et al., 2020a; Chen et al., 2020b; Liu et al., 2020b; Dai et al., 2020; Xu et al., 2021a; Zhang et al., 2021a; Liu et al., 2021g; Wang H. et al., 2021; Wang et al., 2022a; Liu et al., 2022c; Liu et al., 2022f; Liu et al., 2023). At present, there are many physical and chemical methods to extract lignocellulose from various raw materials, such as ultrasonic, grinding, enzymatic hydrolysis, acid treatment and alkali treatment (Chen et al., 2016; Liu et al., 2017a; Hu et al., 2017; Dai et al., 2018; Xie et al., 2018; Li et al., 2019; Xu et al., 2020a; Xu et al., 2020b; Li X. et al., 2020; Liu et al., 2021d; Zhang et al., 2021d; Liu et al., 2022g). Hemicellulose is a kind of heteroglycan, mainly composed of five-carbon sugars and six-carbon sugars, including xylose, galactose, arabinose, mannose, *etc.* (Figure 1). Hemicellulose, together with cellulose and lignin, constitutes plant cells and is the main component of lignocellulose, which is characterized by high degree of branching and low degree of polymerization (Feng et al., 2012). Hemicellulose has attracted much attention due to its low cost, good biocompatibility, and wide sources. Hemicellulose is rich in oxygen-containing groups, such as hydroxyl, acetyl and carboxyl groups and so on, which can be modified by etherification (Sun et al., 2019), esterification (Wang et al., 2017), graft copolymerization (Farhat et al., 2018) and other means. Thus, it can be used to synthesize hydrogels with excellent properties (Li et al., 2014). With the deepening of the research on hemicellulose structure, the preparation methods and application range of hemicellulose hydrogels are also expanding. In this paper, the preparation methods, and advantages of hemicellulose hydrogels as well as the advanced application fields and prospects are summarized, hoping to provide a reference for the research and development of new hemicellulose hydrogels in the future.

2 Preparation of hemicellulose-based hydrogels

2.1 Chemically cross-linking hydrogel

Chemical cross-linking refers to the method of forming covalent bonds between polymeric monomers, which makes the polymers bond more closely and thus have stronger stability and mechanical properties than physical cross-linking (Table 1).

2.2.1 Radical polymerization

Free radical polymerization refers to the process in which monomers produce free radicals under the action of light, heat, radiation or initiator, and form polymer through a series of copolymerization. Polymers can be cross-linked by adding cross-linking agents, such as N,N′-methylenebisacrylamide (MBA) or glutaraldehyde, and so on (Peng et al., 2012). Chen T. et al. (2020) isolated hemicellulose from eucalyptus alkaline peroxide mechanical pulping (APMP) waste liquor. Hydrogen atoms on the hydroxyl group of xylan were captured in the initiator system of anhydrous sodium sulfite (Na_2SO_3) and ammonium persulfate (APS) to generate free radicals. With the addition of acrylic acid (AA), acrylamide (AM) and the cross-linking agent (MBA), the unsaturated double bond on MBA

molecule is opened, and the hydroxyl group on the polymer is cross-linked, and the hydrogel with excellent water absorption and water retention is prepared by free radical polymerization. Seera et al. (2021) mixed xylan and gelatin in a certain proportion and used ethylene glycol diglycidyl ether (EDGE) as cross-linking agent to prepare hydrogel. The two epoxy rings of EGDE cross-linker were opened in a high alkaline medium of 1.5 M NaOH solution to form covalent bonds with the hydroxyl moieties of xylan and the amine moieties of gelatin. The opening of epoxy rings and the formation of covalent bonds will happen simultaneously so that the hydrogel can be cross-linked successfully.

Konjac glucomannan (KGM) has excellent film-forming ability, good biocompatibility, biodegradability, and gel-forming properties. However, its poor pH sensitivity behavior and strong water absorption limit its application (Chen et al., 2018; Wu et al., 2018; Wang et al., 2019a). The carboxyl modification of KG introduced carboxymethyl group, which reduced the intermolecular hydrogen bond and water absorption and could be used to prepare hydrogels (Xiao et al., 2015). Iron ion can also be used as a crosslinking agent in the preparation of hemicellulose hydrogels. Therefore, Wang et al. (2020b) prepared a novel hydrogel based on Dopamine–carboxymethyl konjac glucomannan (DCKGM) and L-Cysteine–carboxymethyl konjac glucomannan (CCKGM) with Fe^{3+} as cross-linker. The stable construction of the hydrogel is based on covalent coordination bonds between Fe^{3+} and catechol, and hydrogen bonding between DCKGM, CCKGM, and Fe^{3+}. Due to the strong interaction of Fe^{3+} with DCKGM and CCKGM, the resultant is adherent, injectable, formable and pH sensitive. Furthermore, the hydrogel shows great potential in various applications (e.g., active compounds delivery) because of the ability to load EGCG.

The modification of hemicellulose can endow it with new functional groups and improve the polymerization degree, water solubility and thermal stability of hemicellulose. Thus, the properties of hemicellulose hydrogel can be improved or endowed, and its application scope can be expanded. Carboxymethyl hemicelluloses, the derivatives of hemicelluloses, have better solubility in water than hemicelluloses, and have hydroxyl and carboxyl functional groups as well (Ren et al., 2008).

Liu et al. (2022h) prepared carboxymethyl xylan (CMX) by mixing hemicellulose, NaOH and sodium monochloroacetate (SMCA) through etherification reaction. Then dopamine was grafted onto carboxymethyl xylan, and the resulting dopamine-grafted carboxymethyl xylan was denoted as CMX-DA. And AM, initiator APS and cross-linker MBA were added to prepare xylan-based hydrogels through free radical polymerization. APS could not only polymerize AM into PAM, but also capture hydrogen atoms from the hydroxyl group of CMX-DA to generate free radicals as the active site, so that PAM could be grafted onto the CMX chain and finally fabricate hydrogel. In addition, the catechol of dopamine imparted nanocomposite hydrogels with adhesion properties. Li et al. (2021) build a plant catechol-metal ion autocatalytic system composed of sodium lignosulfonate/iron ion (SL/Fe^{3+}), and prepared a transparent hydrogel with elastic, electrical conductivity and UV blocking properties by grafting vinyl monomer onto carboxymethyl xylan (CMX). The introduction of Fe^{3+} could form coordination bonds with CMX to form DN structure during cross-linking, giving rise to improve mechanical performance (extension ratio: 460%, tensile stress: 23 kPa). Furthermore, the SL/Fe^{3+} system can activate KPS to generate a large number of free radicals, and rapidly initiate the graft copolymerization of AM on the carboxymethyl xylan (CMX) backbone at room temperature instead of heating, oxygen removal, or UV treatment for the preparation of multifunctional xylan hydrogels.

IA is a hydrophilic unsaturated organic acid with good biocompatibility. It can copolymerize and introduce carboxylic side groups into polymers that are able to form hydrogen bonds with corresponding groups. Liu et al. (2017b) prepared the hydrogels by free radical copolymerization from NIPAAm/IA mixtures as the monomers in the presence of APS and TEMDA as the initiator and acylated hemicellulose as the macromolecular cross-linker. The acylated hemicellulose chain, acting as framework, was grafted by NIPAAm or IA and was cross-linked with other acylated hemicellulose chains containing unsaturated double bonds, resulting in the formation of the hydrogels. PVA was used as an enhancer to produce the temperature- and pH-sensitive hydrogels and it also had good biocompatibility.

Photoinduced crosslinking has the advantages of no pollution, fast curing and low energy consumption in the gelling process. In the reaction process, photoinitiator is needed to trigger the formation of free radicals, which is an efficient and environmentally friendly cross-linking technology. Firstly, hemicellulose was esterified with maleic anhydride (MA) to prepare hemicellulose derivatives containing vinyl, which were cross-linked with unsaturated functional groups of NIPAAm under UV light to form gels (Yang et al., 2011). Gao et al. (2015) used MBA as cross-linker and 2, 2-dimethoxyphenylacetophenone as photoinitiator to graft and copolymerize xylan and glycidyl methacrylate-modified xylan (GMAX) with N-isopropylacrylamide and acrylamide respectively *via* ultraviolet irradiation. The hydrogels were prepared and the properties of hydrogels of two different materials were compared. This method has been shown to be a mild and efficient method with applications in hemicellulose-based hydrogels.

Radiation cross-linking refers to a method in which polymers can produce free radicals under the induction of high-energy rays such as γ-rays and electron beams, and thus polymerize to form three-dimensional networks. It has the advantages of rapid reaction, good selectivity, safety, non-toxic and mild conditions. It is a common method in the preparation of hydrogels by free radical polymerization (Wiesbrock et al., 2004; Fekete et al., 2016). Meena et al. (2014) mixed kappa-carrageenan (kC) with xylan, added water soluble sodium persulfate (KPS) as initiator, and then added polyvinylpyrrolidone (PVP) to get composite hydrogel with microwave radiation. The introduction of PVP can significantly improve the physicochemical and rheological properties of kC/Xylans, and also lead to the formation of semi-IPN structure, thus improved the gelling properties of the resulting hydrogels. It has been proven that the combination of KPS initiator and microwave irradiation can improve the incorporation rate of PVP.

Enzymatic cross-linking has the advantages of mild reaction conditions, simple operation, and good biocompatibility, which can not only avoid the toxicity of chemical cross-linking agents, but also improve mechanical strength. In recent years, its application in biomedicine has attracted more and more attention (Jafari et al., 2022; Wang et al., 2023). Kuzmenko et al. (2014) conjugated xylan from spruce to tyramine, and the conjugated compound was cross-linked under the initiation system of horseradish peroxidase (HRP) and hydrogen peroxide. The primary amine group in tyramine is coupled to the carboxyl group of glucuronic acid unit in xylan. Under

the HRP/H_2O_2 initiation system, the two carbons in the ortho position of xylan-tyramine conjugate form C-C bond, and the C-O bond is formed between the ortho carbon atom and the oxygen atom of phenolic hydroxyl group, thus crosslinking into hydrogel in 20 ± 5 s at room temperature. This study reduced the amount of H_2O_2 in the initiation system and made the product have excellent biocompatibility. Markstedt et al. (2017) prepared hydrogels based on O-acetyl-galactoglucomannans (GGMs) from spruce functionalized with tyramine induced GGMs polymerization to form gels through HRP/H_2O_2 system. Due to the advantages of low cost, cell friendliness and adjustable mechanical properties, the hydrogel can be applied to biomedical materials.

In order to overcome the problems of chemical by-products, chemical residues and energy consumption, *etc.*, the glow discharge electrolytic plasma (GDEP) trigger system has been applied in the field of hemicellulose hydrogels due to its advantages such as mild and controllable reaction, simple device, low cost and no pollution (Zhang et al., 2015). Zhang et al. (2015) used hemicellulose as backbone, hydroxyl radicals which were produced by GDEP as initiators, acrylic acid (AA) and N-isopropyl acrylamide (NIPAAm) as monomers, N, N-methylene double acrylamide (MBA) as crosslinking agents to prepare temperature/pH dual sensitivity reed hemicellulose-based hydrogel. They prepared reed hemicellulose hydrogel for adsorption of heavy metal ions in aqueous solution. The results showed that discharge voltage and discharge time have important effects on the adsorption of hydrogel (Zhang et al., 2016).

Photoinitiation, radiation crosslinking and enzyme crosslinking are currently environmentally friendly, mild, and safe methods for hydrogel synthesis. However, these methods have not been fully developed due to some limitations. With the progress of science and technology in the future, the development of non-toxic, environmentally friendly crosslinking agents and mild, energy-saving crosslinking methods is an important research direction of hemicellulose-based hydrogels.

2.2.2 Click chemistry

The concept of "click chemistry" was first proposed by Kolb et al. (2001) in the early 21st century, which is a method for synthesizing macromolecules based on carbon-heteroatom bonds. This simple and rapid reaction can avoid the limitations of traditional modification methods such as esterification and etherification. And it can provide a mild and efficient modification way for hemicellulose modification, endowing it with specific structure, properties and functions (Mamidyala and Finn, 2010; Meng and Edgar, 2016). Copper-catalyzed azide-alkyne cycloaddition (CuAAC) and thiol-ene/yne click reaction are representative reactions of click chemistry, which can be used for polymer modification (Hoyle and Bowman, 2010; Enomoto-Rogers and Iwata, 2012; Meng and Edgar, 2016). Compared with thiol-ene/yne click reaction, there are few reports on modification of hemicellulose by CuAAC reaction. There is still a lot of space for the development of future.

The thiol–ene reaction has gained much attention in chemical synthesis. The reaction can usually be performed under mild reaction conditions giving high conversion and selectivity, using water as solvent. In addition, no toxic metal catalysts are needed, making the use of thiol-ene chemistry tempting for the modification of polysaccharides. Thiols and amines are valuable functional groups having high reactivity. Pahimanolis et al. (2015) designed a simple method for functionalizing xylan with thiols, amines and amino acids by combining traditional etherification and thiol-ene reactions. Firstly, the hydroxyl group on xylan reacts with allyl chloride under alkaline conditions at 40°C to introduce the allyl group into the backbone of xylan, and then thiols are introduced into the backbone of xylan by click chemistry. This method provides a broad possibility for the development of new polysaccharide-based materials, and through thiol-thiol oxidative coupling, free thiol groups can be used to form hydrogels, and the shape of the resulting hydrogels can be well controlled, thus the fields of application were expanded. Maleki et al. (2017) designed a fully interpenetrating double network structure hydrogel from O-acetyl-galactoglucomannan (AcGGM), which was formed by the click reaction of thiol-ene and free radical polymerization. Firstly, the single-network hydrogels were prepared by grafting AA oligomeric chains from the unsaturated sites of AcGGM-Ma *via* free radical cross-linking. The cross-linking of the second network was then mediated through two separate pathways: thiol-ene IPN cross-linking (the thiol-ene click reaction between sulfhydryl functionalized AcGGM and polyethylene glycol diacrylate (PEG-DA)) and free-radical IPN cross-linking. While both strategies effectively afford IPNs, the route involving making the second network from thiolated AcGGM and PEG-da clearly affords IPNs with much higher shear moduli. In addition, the fraction of renewable material will be significantly higher in this case where both individual networks are based on AcGGM and from these perspectives the thiol-ene crosslinking strategy may be more viable and the resulting IPNs more suitable as membranes, absorbants and supports serving in more or less pressurized environments.

Wang et al. (2022b) propose an injectable nanocomposite hydrogel that prepared by light-induced thiol-ene addition between methacrylate modified O-acetyl-galactoglucomannan (GGMMA) and thiolated cellulose nanocrystal (CNC-SH). CNC-SH reinforced the GGMMA hydrogel as both a nanofiller and a crosslinker to GGMMA resulting in an interpenetrating network *via* thiol-ene addition. This light-induced thiol-ene cross-linking method is a mild and fast cross-linking method, the addition of thiol-ene makes the internal network of the hydrogel uniform, but also has good mechanical properties.

2.2 Physically cross-linking hydrogel

Physical cross-linking method refers to the formation of hydrogels using freezing, ultrasound, light and other methods. Hydrogen bonds, ionic bonds and intermolecular forces play a role in gelation. The hydrogel is greatly affected by the environment, and the size of holes in it cannot be adjusted easily (González et al., 2018). Although the strength and stability of hydrogels formed by physical cross-linking method are not as good as those formed by chemical cross-linking method, there is no need to add initiator, cross-linking agent or some organic solvents in the preparation process, so as to reduce the chemical toxicity and increase the application scope of hydrogels (Yan et al., 2010).

2.2.1 Non-covalent forces

Gabrielii et al. (2000) separated xylan from poplar by alkali extraction combined with ultrafiltration and mixed it with chitosan. Through the electrostatic interaction between the microcrystalline domain formed by the combination of chitosan chain and xylan chain and the acid group of xylan and the amino group in chitosan, hemicellulose-chitosan hydrogel was prepared for the first time.

Studies have shown that hydrogels can be formed when the content of chitosan is 5%–20%, and the swelling degree of hydrogels is positively correlated with the content of chitosan, and hydrogels dissolve when the content of chitosan exceeds 20%. Qi et al. (2015) grafted methylguanidine hydrochloride onto the backbone of xylose to prepare xylose modified by guanidine ion. Then, ethylene glycol was used as the crosslinking agent, and the modified xylose was entangled with the exfoliated layered anionic montmorillonite (MMT) clay nanosheet under the dispersion of sodium polyacrylate (PAAS) to form xylose-based hydrogel. The xylan-based hydrogel is connected by hydrogen bonds and shows intermolecular adsorption due to its internal sponge like porous structure, which has a rapid self-healing ability and shows good swelling performance. In addition, due to the addition of inorganic MMT, this xylan-based hydrogel has good heat resistance. Gabrielii et al. (2000) added chitosan into the xylan solution. The microcrystalline structure was formed between xylan and chitosan and served as a physical cross-linking point. The microcrystalline was connected to conduct the crystal arrangement of the polymer, forming a eutectic network structure. When the content of chitosan reaches 5%–20%, the co-crystalline structure forms a network structure, and the hemicellulose/chitosan composite hydrogel is prepared.

2.2.2 Freeze-thaw cycle technique

Freeze-thaw technique is a physical cross-linking method that promotes the generation of hydrogen bonds in polymers through repeated freezing and thawing. As a hydrogel formation method, freeze-thaw method can not only cross-link polymers in solution, but also avoid the residue of cross-linker that can cause inflammation in human body (Liu et al., 2009). Zhang et al. (2021b) simply and efficiently prepared hemicellulose/polypyrrole (H/PPY) composite hydrogel by freeze-thaw technique. First, all reactants including H/PPY suspension, PVA, glycerol, and borax were initially mixed, and the solution was frozen at 20°C for 12 h to gelatinize and thawed at room temperature for 4 h. After two freeze–thaw cycles, the resultant hydrogels were soaked into NaCl solution. Borax was decomposed into $B(OH)^{3-}$ and $B(OH)^{4-}$ which could further form a variety of complexation and cross-linking with H/PPY, glycerol, and PVA. The strong hydrogen bonds among PVA, H/PPY complex, and glycerol promoted the formation of hydrogels. The hydrogel has good mechanical strength and can be stretched 250 times at 50% strain and still have good reproducibility.

Guan Y. et al. (2014) prepared hemicellulose, PVA and chitin nanowhiskers with compact structure, high strength and thermal stability hydrogels by freeze-thawing cycle. Because these polymers are rich in hydroxyl groups, hydrogen bonds are easily formed between them, and the hydrogen bond network is very stable at low temperatures. Therefore, during the freeze-thaw cycle, their molecular chains are closely bound by physical cross-linking and shows good mechanical properties. The chitin nanowhiskers embedded homogeneously in PVA/hemicellulose form more hydrogen bonds, which significantly improves the mechanical strength and thermal stability of hydrogel. And the hydrogel structure becomes stronger with the increasing times of freeze/thaw cycle. Multiple cycles make the polymer network more compact and reduce the space for water. After three freeze-thaw cycles, the hydrogel forms a layered structure and the swelling degree is reduced (Guan et al., 2015).

2.3 Composite hydrogel

As hemicellulose macromolecular structure has many branches and complex chemical composition, the relative interaction between molecules in hydrogels prepared from pure hemicellulose is weak, resulting in unsatisfactory mechanical strength (Liu et al., 2022h). However, hemicellulose and other kinds of polymers or nanoparticles can be combined to produce hemicellulose based composite hydrogels with different functions. For example, the combination of hemicellulose and chitosan can improve the swelling and mechanical properties of hydrogels, and can also give hydrogels the adsorption performance of heavy metal ions (Ayoub et al., 2013). The composite of nanocellulose and hemicellulose can enhance the toughness, viscosity and self-recovery properties of hydrogels (Karaaslan et al., 2011). In hemicellulose hydrogels, the introduction of chitin nanocrystalline whiskers with average length of 200 nm and width of 40 nm can improve the mechanical and thermal properties of hydrogels (Guan Z. et al., 2014).

Polypyrrole (PPY) has emerged as a polymer with the advantages of easy synthesis, high conductivity, stability and good biocompatibility, which can be introduced into hydrogels and applied to wearable strain sensors (Kenry, 2018). Zhang et al. (2021b) firstly, mixed hemicellulose white poplar and pyrrole monomer in water to form H/PY composite. $FeCl_3$ was then added to induce the growth of the PPY chain. Afterwards it is then mixed with PVA, glycerol and borax and polymerized into hydrogels by strong hydrogen bonding. Glycerol can form a large number of hydrogen bonds with water molecules, which can greatly improve the water retention of hydrogel (71.8%). The introduction of glycerol and NaCl could inhibit the ice crystals in the hydrogels and reduce the freezing and thawing temperatures of the hydrogels to −43.1°C and −22.1°C. The conductivity of the hydrogel increases from 2.1 S/m to 5.1 S/m when PPY is introduced into the hemicellulose hydrogel. And the introduction of glycerol can improve the conductive path of hydrogel network.

Polyaniline (PANI) is a kind of polymer with attractive properties such as easy synthesis, environmental friendliness, electrical conductivity, and excellent biocompatibility. However, its application is limited because it is not degradable and cannot be dissolved in ordinary non-polar or even weakly polar organic solvents. To overcome this shortcoming, the use of aniline oligomers has been proposed instead of polymers, because they have similar electrical conductivity, in addition to good solubility and clear structure. Moreover, the degradation byproducts of oligomers can be taken up by macrophages and can subsequently undergo renal clearance to exit the body. Wen et al. (2020) prepared conductive hemicellulose hydrogels (CHHs) with tunable swelling behavior, controllable conductivity, and stable network structure by introducing carboxyl terminated aniline pentamer (CTAP) and epichlorohydrin into xylan-rich hemicellulose network through a facile one-pot approach. The equilibrium swelling ratio of the hydrogel can be adjusted by changing the content of CTAP and epichlorohydrin. Due to the hydrophobicity, thermal stability, and electrical conductivity of CTAP, when the content of CTAP increases, the water absorption of hydrogel decreases, the thermal stability increases, and the electrical conductivity increases to 2.11×10^{-3} S/m.

When hemicellulose is added to other polymer networks, it often acts as an enhancer (Prakobna et al., 2015) or cross-linker (Karaaslan et al., 2011). Berglund et al. (2020) investigated the influence of xylans

and glucomannans in cellulose/hemicellulose composite hydrogel on the mechanical properties of hydrogel. The study showed that glucomannans improved the compressive elastic modulus of composite hydrogel, and xylans increased the elongation at break of composite hydrogel. Dax et al. (2016) prepared a green cross-linking agent based on O-acetyl galactoglucomannan. When hemicellulose is used as a cross-linking agent, the hydrogel has excellent swelling performance and can quickly absorb water 154 times its weight, but its mechanical strength is low. Adding NFC to the hydrogel can effectively improve the mechanical strength without affecting its adsorption performance. Gong et al. (2022a) modified hemicellulose nanoparticles (HC) with tannic acid (TA) and the composite hydrogels were formed by mixing acrylic acid with APS (initiator) and MBA (cross-linking agent) evenly and adding TA@HC nanoparticles as nanometer filler. Then the hydrogel was immersed in $AlCl_3$ solution and Al^{3+} was introduced to obtain PAA-TA@HC-Al^{3+} hydrogel. The hydrogels were multi-network structures of covalent bonds and non-common bonds, which can improve the mechanical properties of hydrogels. It was also found that the hydrogel had good electrical conductivity, toughness and antimicrobial properties. The cross-linking mechanisms of Al^{3+} in hydrogel structures are Al^{3+}-TA@HC-carboxylate hybrid coordination and Al^{3+}-TA@HC coordination, and Al^{3+}-carboxylate coordination. In addition, the hydrogel has antioxidant and UV resistance properties.

The introduction of inorganic particles into hydrogels has been shown to improve the strength and toughness of hydrogels (Lei et al., 2019). Nanomaterials such as calcium phosphate nanoparticles (Nie et al., 2019), bentonite (Liu et al., 2021a), metal nanoparticles (Arvizo et al., 2012) or graphene (Mohammadrezaei et al., 2018) can also give gels a variety of properties, enabling them to have a wide range of applications in many fields (Han et al., 2020).

Bentonite is a natural non-metallic mineral with montmorillonite as main component. It has the structure of two-dimensional nanomaterials and has the characteristics of expandability, hydrophilicity, stability, non-toxicity, and adsorption (Feng et al., 2004). Liu et al. (2022h) introduced bentonite into hydrogels prepared by cross-linking dopamine grafted carboxymethyl xylan with PAM. The exfoliation of bentonite would improve the compatibility between inorganic phase and organic phase. The bentonite formed physical interaction with polymer chain. The PAM chains could be integrated with the neighboring bentonite sheets by a mutual combination of polymer chains, and they could be cross-linked through non-covalent bonding such as hydrogen bonding and polymer chain entanglement, resulting in a nanocomposite hydrogel 3D network formation. With the introduction of bentonite, the Young's modulus of the hydrogel increased to 1,449.3 kpa, indicating that the addition of bentonite could enhance the cross-linking density and improve the mechanical strength of the hydrogel.

The combination of iron oxide nanoparticles (Fe_3O_4) and polysaccharide hydrogels can be used as magnetic field response hydrogels due to their large magnetic moment, excellent superparamagnetization and high stability in water medium. Zhang and Sun (2020) added Fe_3O_4 nanoparticles to acrylic acid (AAC), then added hemicellulose and cross-linking agent, and formed semi-interpenetrating magnetic composite hydrogel by using H_2O_2-VC initiated system. The redox initiator system H_2O_2-Vc generated oxygen anion radical (O^{2-}) which initiated the polymerization of acrylic acid, and modified Fe_3O_4 nanoparticles joined into this polymerization by covalent bonds through the vinyl group on the surface. The introduction of Fe_3O_4 can not only increase the crosslinking density of the hydrogel, but also give the hydrogel superparamagnetic property, and the magnetization intensity increased with an increase in the content of Fe_3O_4 nanoparticles. The HC/PAAc semi-IPN magnetic hydrogel showed high adsorption capacity and smart swelling property in lysozyme adsorption experiments, which has potential applications in drug delivery and magnetic separation.

Graphene oxide (GO) and reduced graphene oxide (RGO) have gained wide attention due to their potential role in enhancing cellular response and modulating protein adsorption and cell behavior. Graphene and its derivatives contain reactive oxygen functional groups, making the surface easy to form covalent, electrostatic and hydrogen bonds with biomolecules (polypeptides, nucleic acids and growth factors). Ali et al. (2022) introduced graphene oxide/reduced graphene oxide (GO/RGO) as nano-filler into hemicellulose/chitosan/nano-hydroxyapatite (HAp) composite hydrogel scaffold. The fillers are uniformly distributed in the hydrogel, forming a porous three-dimensional network with good mechanical properties. The addition of GO/RGO can improve the mineralization tendency of apatite and increase the osteogenic capacity of the composite. Further studies showed that the composite hydrogel has cellular activity and protein affinity, which is helpful for bone repair and regeneration, and is a potential material for bone tissue engineering.

Due to the low molecular weight and heterogeneity of hemicellulose, the mechanical strength of the composite hydrogel is limited. The introduction of interpenetrating polymeric network (IPN) or semi-interpenetrating polymeric network (semi-IPN) structure into the composite hydrogel makes there exist some non-covalent forces between the polymers, that is, the method of physical and chemical double cross-linking can effectively improve the mechanical strength of the hydrogel (Zhao et al., 2016; Zhang et al., 2019a). It can also make the hydrogel have certain self-healing property (Ai et al., 2021). Li N. et al. (2020) designed a hemicellulose hydrogel with high toughness by combining the chain expansion reaction of xylan with semi-IPN structure. Xylan was successfully modified to overcome the main limitation of brittleness through reductive amination reaction. Firstly, a cross-linking agent is added to construct a chemical cross-linking network of chain extended xylan (CEX). Then Fe^{3+} are introduced into it, and a physical cross-linking network is constructed by metal-ligand interactions. The hydrogel prepared by this method shows excellent mechanical properties and good water absorbency. And the water absorption and electrical conductivity can be adjusted by changing the mole fraction of metal ions. This method provides a way to prepare xylan hydrogels with high mechanical properties. Han et al. (2022) mixed hemicellulose, polyvinyl alcohol (PVA) and non-toxic sodium trimetaphosphate (STMP) crosslinker, heated and stirred, and formed a semi-interpenetrating structure by physical and chemical cross-linking. PVA contains rich hydroxyl groups that react with ring opened STMP to form a chemical cross-linking network. Xylan macromolecules do not react with PVA or STMP, but form a physical network connected by hydrogen bonds with the PVA-STMP chemical cross-linking system. This is a safe and facile method, and the hydrogel prepared shows high compressive strength (84.2 MPa at fracture strain of 90%), excellent compressive resilience, and thermal stability (showing a degradation temperature between 350 and 370°C). Moreover, due to its good biocompatibility

TABLE 1 Fabrication methods and their advantages.

Methods	Characteristic	References
Physical crosslinking by hydrogen bond, ionic interaction, or hydrophobic interaction	Hypotoxicity, weak strength and stability	Zhang et al. (2021b)
IPN or semi-IPN	High strength, self-healing property	Li N. et al. (2020)
Chemical cross-linking by cross-linkers	Facile and common	Liu et al. (2022h)
Photoinitiated	Simple and efficient	Gao et al. (2015)
Enzymatic	Excellent biocompatibility	Markstedt et al. (2017)
Microwave irradiation	Rapid response, no hysteresis effect and good selectivity	Meena et al. (2014)
Glow discharge plasma	Environmentally friendly, easy to operate, low cost, small environmental pollution	Zhang et al. (2015)

and non-toxicity, it offers a great potential application in the field of biomedicine.

In the future, the mechanism of composite hydrogels should be studied comprehensively and deeply, so as to regulate its performance and expand its application range.

3 The applications of hemicellulose-based hydrogels

Hemicellulose-based hydrogels can respond to temperature (Liu et al., 2017a), PH (Zhao et al., 2014a), electricity (Zhao et al., 2014b), magnetism (Li et al., 2014), light (Cao et al., 2014) and other stimuli, and have a wide range of applications in drug delivery, bone tissue engineering, wound dressing, sewage purification, flexible electronic sensor and other fields (Kong et al., 2018).

3.1 Biomedical material

Hemicellulose has good biological activity, so it has broad application prospects in the field of biomedicine. It has been reported that xylan hemicellulose has the effect of inhibiting cell mutation, and has the function of detoxification and anti-inflammation, which greatly broadens the application of xylan in the field of biomedicine (Oliveira et al., 2010; Chang et al., 2021). Drugs and polymer solutions are mixed and injected into the human body and gelatinized under certain physiological conditions. Drugs can be released at a specific time and location through hydrogel decomposition or other means (Gupta et al., 2002; Yan et al., 2010). Some functional molecules such as PAA, poly (N-isopropylacrylamide) (Gao et al., 2016), Fe_3O_4 (Zhao et al., 2015) *etc.* And hemicellulose are used together to prepare intelligent hydrogels, which can be applied to drug delivery.

Figure 2 shows some effects of hemicellulose based hydrogels on controlled release of drugs and antibacterial activities. Gao et al. (2016) prepared xylan-based temperature/pH sensitive hydrogels by the crosslinking copolymerization of xylan with NIPAm and AA using MBA as a cross-linker and 2,2-dimethoxy-2-phenylacetophenone as a photoinitiator *via* ultraviolet irradiation. Then they tested the hydrogels for drug encapsulation and release and for its biological activity on cells. The drug loaded and controlled release behaviors and the diagram of cell proliferation of the xylan-based P(NIPAm-g-AA) hydrogels networks were illustrated in Figure 2A. The porous structure appeared during drug release. And the porosity of hydrogels permits loading of drugs into the hydrogel matrix and subsequent drug-controlled release at a rate dependent on the diffusion coefficient of the small molecule or macromolecule through the gel network. After the cells were cultivated in hydrogel, the number of cells increased significantly after 72 h compared with 24 h. Photodynamic antimicrobial chemotherapy or PACT has been shown to be a promising antibacterial treatment that could overcome the challenge of multidrug-resistant bacteria; Elkihel et al. (2021) report a simple strategy to synthesize a cross-linked hydrogel from beech xylan as shown in Figure 2B. The 5, 10, 15, 20-tetrakis (1-methylpyridinium-4-yl)-porphyrin tetraiodide (TMPyP) was chosen as a model of hydrophilic photosensitizer (PS) and was encapsulated inside the xylan-based hydrogel. The positively charged ammonium groups of PS will allow the TMPyP to make ionic bonds with the carboxyl groups of the hydrogel, which facilitates its encapsulation. The hydrogel showed good properties of high swelling ratio, interconnected porous structure, and good mechanical integrity. TMPyP-loaded hydrogel prolonged release of PS up to 24 h with a cumulative amount that could reach 100%. TMPyP-loaded hydrogel showed a photocytotoxic effect against *Pseudomonas aeruginosa*, *Escherichia coli*, *Staphylococcus aureus* strains, and *Bacillus cereus*, while no cytotoxicity was observed in the dark and a strong potential for photodynamic antimicrobial chemotherapy. Ge et al. (2021) prepared hemicellulose-based composite hydrogels by adding polydopamine (PDA) microsphere as reinforcing agents (the synthetic route was showed in Figure 2C). Hemicellulose was extracted from bagasse and mixed with dopamine microspheres to form hydrogel under the action of crosslinking agent. The gaps in the network are filled with PDA and increased the density of the hydrogel. The hemicellulose-based hydrogel has an obvious drug release effect, and the release behavior of the composite hydrogel shows more obvious pH responsiveness. The result showed that complex hydrogels, delivered orally to the stomach as drug carriers, can reduce swelling of the gels and inhibit drug release under acidic conditions. As shown in Figure 2D, the xylan/borax/PVA double-network hydrogels were fabricated by Ai et al. (2021). The first physically and chemical network formed *via* numerous hydrogen bonds from PVA associated xylan and borax–PVA complexation between hydroxyl groups and borax. Then the hydrogel was

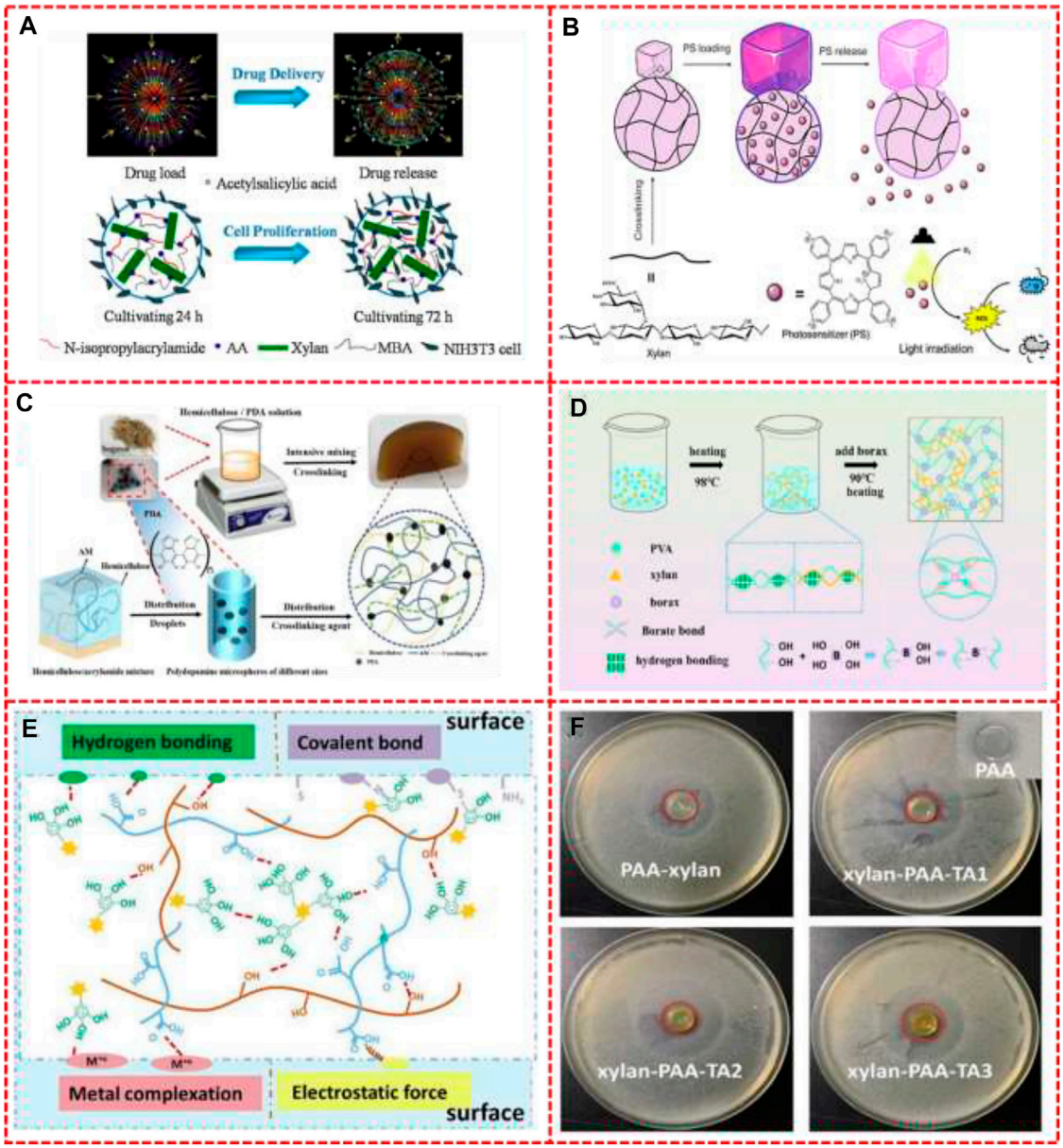

FIGURE 2
(A) The diagram of drug delivery behaviors and cell proliferation of the xylan-based P(NIPAm-g-AA) hydrogels copolymer networks, **(B)** The strategy of formation of hydrogels and photodynamic antimicrobial chemotherapy, **(C)** The synthetic route of hemicellulose/PDA hydrogel, **(D)** Schematic illustration of the preparation process of xylan/PVA/B DN hydrogel and possible reversible diol-borate ester bonds, **(E)** The adhesion mechanism of xylan-PAA-TA hydrogels, **(F)** Photographs of the inhibition zone of the PAA, PAA-xylan hydrogel, xylan-PAA-TA1, xylan-PAA-TA2 and xylan-PAA-TA3 hydrogels, **(F)** Photographs of the inhibition zone of the PAA, PAA-xylan hydrogel, xylan-PAA-TA1, xylan-PAA-TA2 and xylan-PAA-TA3 hydrogels. Reproduced from: **(A)** Gao et al. (2016), Elsevier; **(B)** Elkihel et al. (2021), ACS Publications; **(C)** Ge et al. (2021), MDPI; **(D)** Ai et al. (2021), Elsevier **(E)** Chang et al. (2021), Springer; **(F)** Chang et al. (2021), Springer.

subjected to a freeze-thaw process to form the second physically cross-linked network through the generation of the PVA crystal domain. The complexation between the tetrafunctional borate ion and the hydroxyl group of PVA is reversible resulting in the self-healing properties of hydrogels. The network between xylan and PVA and PVA crystal domain will provide a stable structure to withstand stress. Therefore, the hydrogels show nice strength, toughness, and stability. As shown in Figure 2E, the light blue rectangle meant the surface of different materials. There were several kinds of interaction between the hydrogel and different surfaces including hydrogen bonding, metal complexation, electrostatic force, and some kinds of covalent bond. And as shown in Figure 2F, for PAA hydrogel (control sample), there was no obvious inhibition zone in the disk. For PAA-xylan hydrogel, only a small inhibition zone was observed, which might be due to the antibacterial properties of xylan. In contrast, the xylan-PAA-TA hydrogels has the larger inhibition zone.

Modifications of hemicelluloses can improve their drug release and encapsulation properties of the prepared hydrogels. Gao et al. (2015) compared the acetylsalicylic acid release properties and biological activities of xylan and glycidyl methacrylate-modified

xylan (GMAX) based hydrogels. The introduction of GMAX makes the pore size of hydrogels smaller and the network of hydrogels more uniform and orderly, so GMAX-Gels have a stronger electrostatic effect on acetylsalicylic acid, while xylan hydrogels have a low electrostatic interaction with acetylsalicylic acid due to the irregular internal structure. Compared with xylan hydrogel, GMAX hydrogel has higher cumulative drug release (84.2%) and longer release time in intestinal fluid, and also has higher encapsulation efficiency (95.21%). Because of their low release rate in gastric fluid and good cell compatibility, they can alleviate the side effects of long-term use of acetylsalicylic acid in patients.

Kong et al. (2017) prepared a novel hydrogel with temperature/pH dual sensitivity good swelling–deswelling properties, and honeycomb-like architecture through polymerizing maleic anhydride modified xylan (MAHX) with NIPAm and acrylic acid under UV light. The degree of substitution MAHX could control the pore volume, the mechanical properties, and the drug release rate of the hydrogel. Besides, in the gastrointestinal sustained drug release, the acetylsalicylic acid release rate was extremely slow at initial 3 h in the gastric fluid (24.26%), and then the cumulative release rate reached 90.5% after sustained release for 5 h in the stimulated intestinal fluid. Importantly, MAHX-based hydrogels had satisfactory biocompatibility with NIH3T3 cells. Therefore, MAHX-based hydrogels as drug carriers have potential application in human drug-delivery fields. Liu et al. (2017b) synthesized a temperature- and pH-sensitive hydrogel from NIPAAm, IA, hemicellulose and PVA. IA is rich in hydrophilic groups (-COOH). The lower critical solution temperature (LCST), the network dimension and equilibrium swelling rate of hydrogels can be adjusted by IA content. The LCSTs and equilibrium swelling ratio of the hydrogels increased with the increase of IA dosage in hydrogels. The LCST of the hydrogel could be adjusted to around body temperature by manipulating mass ratio of NIPAAm to IA 96/4. The carboxyl-carboxyl hydrogen bonding, existing between carboxyl in IA and carboxyl in salicylic acid, is in favor of the drug loading capacities of the hydrogels. The controlled release properties make the hydrogels as possible carriers in terms of controlled drug release. Gami et al. (2020) synthesized xylan-β-cyclodextrin hydrogel (XCD) by chemical crosslinking method and studied the absorption and release properties of the hydrogel on curcumin and 5-fluorouracil (FU) *in vitro*. When the hydrogels were in PBS, the drugs on the surface of the gel can be released immediately, so the initial release rate is faster. Curcumin could form inclusion complexes with βCD in the gel to prevent its release. XCD5 gel has a lower βCD content, so it has a better release effect on curcumin. The absorption of XCD1 to 5-FU was better because of the high content of βcd, which can provide more binding sites for 5-FU and promote the release of XCD1. After 24 h, the release of 5-FU and curcumin in PBS was 56% and 37%, which showed a favorable potential in the field of controlled drug release. Wang et al. (2022b) introduced BaGNP into the GGMMA/CNC-SH-based injectable hydrogel prepared through light-induced thiol-ene reaction. BaGNP is a kind of nano-filler with good biocompatibility. When combined with hydrogel, BaGNP is known to be a nano-filler with good biocompatibility. Combined with hydrogel, BAGNP can be used as a delivery system for some therapeutic ions, such as Si, Ca, or/and Cu ions to be released in the human body. It has been shown that the GGMMA/CNC-SH/BaGNP hydrogel can achieve sustained release of Si and Ca ions/species.

In addition, the combination of xylan and chitosan has superior antioxidant, antibacterial and cell proliferation ability than its parent polymer, and the hydrogel formed by the combination of hemicellulose and chitosan has long-term biocompatibility (Ali et al., 2020). Studies have shown that xylose hydrogels can be applied to injectable biological materials and contribute to fracture healing (Bush et al., 2016). Ali et al. (2022) introduced hydroxyapatite (HAP), whose chemical composition is similar to inorganic composition of bone, and oxide/reduced graphene oxide (GO/RGO), which has the advantages of enhancing cell response and regulating protein adsorption and cell behavior, into hemicellulose chitosan hydrogel. The pore size of the hydrogel samples containing GO/RGO came to be between 100 and 200 μm, which is beneficial for nutrient and gas exchange, angiogenesis and osteoinduction in human body. Due to the variety of species on GO, the addition of GO can improve the adsorption efficiency of composite hydrogels for proteins. The addition of GO also improved the mineralization tendency of deposited apatite and showed good osteogenic capability. The synergistic effect of HAP and GO together improves the ALP activity of the composite hydrogel, making it a potential application in bone tissue engineering.

The flexibility and biocompatibility of hemicellulose-based hydrogels make them also useful as nanofibrous scaffolds for the application of cardiac tissue engineering. Venugopal et al. (2013) prepared a nanofiber scaffold formed by crosslinking xylan/polyvinyl alcohol and glutaraldehyde vapor and conducted experiments in rat neonatal cardiomyocytes. The result shows that the nanofiber scaffolds can enhance the proliferation of cardiomyocytes and can be used in cardiac tissue engineering.

Hemicellulose dressings have been shown to be able to treat various skin lesions or skin diseases and are a safe and effective wound dressing (Melandri et al., 2006). Liu et al. (2016) composed polysaccharide composite hydrogels with different types of hemicellulose and nanocellulose. Then the morphology, mechanical strength and cell compatibility of the composite hydrogel were changed by changing the type, amount and way of hemicellulose incorporation. The performance of the hydrogel scaffold can be evaluated by observing the proliferation of 3T3 fibroblasts in the composite hydrogel. Therefore, this polysaccharide composite hydrogel has the potential to support cell growth and proliferation and can be used in wound healing. The Xylan-tyramine composite hydrogel prepared by Kuzmenko et al. (2014) through enzymatic cross-linking showed good mechanical property and high swelling property. The hydrogel showed the ability to differentiate into adipocytes in cell differentiation assays and could be used to encapsulate mesenchymal stem cells. Markstedt et al. (2017) prepared ACGGM-based hydrogels in the initiator system of hydrogen peroxide/horseradish peroxidase. In the cytotoxicity test, the cell survival rate of hydrogel was 95%, indicating that it had no cytotoxicity, which may be used in cell encapsulation, cell delivery and 3D cell culture.

Gelatin is a low-cost, non-toxic, and biodegradable natural collagen polymer, which is able to improve its properties by chemical cross-linking due to its large number of functional side groups, thus preparing a variety of stable materials. Synthetic polymers as crosslinkers inevitably cause a decrease in biocompatibility, but the combination with xylan solves these problems. Fu et al. (2020) directly oxidized xylan to dialdehyde xylan and used it as a cross-linking agent of gelatin to prepare hydrogel. Glycerol (Gly) and nicotinamide

(NCA) were further introduced into the gel, and the *in vitro* release, Antibacterial activity and cytocompatibility test were conducted. NCA diffused rapidly in the resultant hydrogels, releasing them faster than most bio-based hydrogels. The resultant hydrogel had obvious inhibitory effect on the growth of yeast, *Bacillus subtilis* and *Staphylococcus aureus*, and has good viability and cell cytocompatibility. The results show that the hydrogel has a good application prospect in skin care.

In conclusion, Hemicelluloses-based hydrogels have been widely used in the field of medical materials due to their biological activity, controllable swelling, and mechanical properties. In addition, it can be combined with some organic or inorganic particles to further expand its range of applications, including controlled release of drugs, wound dressings, bone tissue engineering, even cardiac tissue engineering and facial care. However, most of the research still exists in the laboratory stage and needs to be scaled up in future studies to really make a difference.

3.2 Industrial adsorption

Nowadays, environmental pollution has attracted global attention. The pollution of water resources caused by heavy metal ions released by industry has become one of the most serious problems. Traditional methods for removing heavy metal ions from aqueous solutions have some disadvantages, such as high cost, low efficiency and other wastes (Ahluwalia and Goyal, 2005). Bioadsorption refers to the adsorption of heavy metals by organisms and their derivatives on water. It is a method with high efficiency, repeatability and other advantages, which is an alternative to traditional adsorption methods (Peng et al., 2012). The swelling of hydrogel increases its surface area, and some solute molecules interact with hydroxyl, carboxyl and amine groups in hydrogels through ionic and covalent bonds, so that hydrogels can be used as adsorbents (Seera et al., 2021). The chemical composition of hemicellulose and the network structure of hydrogel are the fundamental factors affecting the adsorption performance of hemicellulose hydrogel. Hemicellulose is easily hydrolyzed by acid, so it cannot be used in highly acidic environment (Xiang et al., 2022). Studies have shown that hemicellulose-based hydrogels as adsorbents have good adsorption effects on metal ions such as Pb^{2+}, Cd^{2+}, Cu^{2+}, and Zn^{2+}.

The addition of acrylamide, acrylic acid and other synthetic polymers into hemicellulose hydrogels can also improve the adsorption performance of hydrogels (Peng et al., 2012; Zhong et al., 2013). AA, an unsaturated carboxylic acid with pH sensitivity, is a common hydrogel additive that can be used not only to adsorb heavy metal ions but also polymer dyes. Xylan and AA graft copolymerized hydrogels showed good repeatability in plenty of adsorption/desorption cycles (Peng et al., 2012; Xu et al., 2019). In addition, the introduction of some adsorbable materials, such as chitosan (Shu-Ping et al., 2017), montmorillonite (MMT) (Zhang et al., 2014) and Fe_3O_4 (Sun et al., 2015), can also improve the adsorption efficiency of hydrogels. Shan et al. (2021) prepared environment-friendly hydrogels with cellulose, hemicellulose and lignin extracted from straw. Cellulose fibrils had crosslinked with lignin and hemicellulose by PAA chains in the presence of MBA. The resultant hydrogel had higher swelling rate, which was conducive to the diffusion of metal ions in the hydrogel, so the adsorption performance was improved. The adsorption behavior of straw biopolymer-based hydrogel was the result of ion exchange, which was spontaneous and reversible, and the prepared hydrogel adsorbent had good performance. The experimental results show that the hydrogel has good removal rate for heavy metal ions and water retention performance and has potential applications in water treatment and soil remediation. Kundu et al. (2019) prepared a composite hydrogel from xylan and β-cyclodextrin (βCD), capable of adsorption of Cd^{2+} and Ni^{2+}, using ethylene glycol glyceride as cross-linking agent. The hydrogels had better adsorption abilities toward Cd II) than Ni II). This is a strategy to enhance the adsorption performance by enriching hydroxyl groups in hydrogels. Studies have shown that hydroxyl groups have strong affinity for heavy metal ions, so increasing the content of carboxyl groups in hemicellulose hydrogels is another strategy to improve the adsorption performance of hydrogels (Qu et al., 2017).

Figure 3 shows the preparation and adsorption effect of hemicellulose-based hydrogel with wastewater adsorption. Xylan-g-/P (AA-co-AM)/Graphene oxide (GO) hydrogels were prepared by Kong et al. (2019) for the adsorption of metal ions. A large number of hydroxyl groups in the xylan chain react with ammonium persulfate (APS) to produce a large number of free radicals, which triggers the polymerization of acrylic acid (AA), acrylamide (AM) and GO sheets on the xylan branch chains. The active functional groups of hydroxyl and carboxyl in GO are polymerized through indirect branches of the polymer chain to form covalent or hydrogen bonds. Xylan/GO/P (AA-co-AM) hydrogels formed complex networks under the action of the crosslinking agent MBA, as shown in Figure 3A. Figure 3B illustrates the influence of pH on the adsorption property of hydrogels. With the increase of pH, the adsorption capacity of Pb^{2+} Cd^{2+} Zn^{2+} by hydrogel increases. When pH is low, protonation of active functional groups in hydrogel reduces the adsorption binding site of heavy metal ions and hinders adsorption. With the increase of pH, protonation gradually weakened, more active groups and metal ions chelate, improve the adsorption capacity. Sun et al. (2022) prepared composite hydrogel based on acylated xylan and silanized graphene oxide *via* free radical polymerization as a novel adsorbent for the removal of Cu^{2+} ions from aqueous solution. The synthetic scheme is described as Figure 3C, the carbon-carbon double bond was first introduced into xylan and GO, and then the hydrogel was polymerized with AA under the action of crosslinking agent. An ideal reusability of the hydrogel was also obtained and showed good potential in the removal of heavy metal ions in wastewater.

In the wastewater discharged by leather, textile, printing and other industries, there are toxic substances such as refractory dyes that threaten the water quality of the ocean and the living things in it (Ren et al., 2018). Methylene blue is a common dye in these industries. The presence of methylene blue in aqueous solution is usually cationic and electrostatic attraction is the main factor of ionic dye adsorption, so hemicellulose adsorbent containing anions has a good adsorption effect on it. Gelatin is composed of protein (90%–92%), mineral salts and water. Gelatin molecules can be used as adsorbents for toxic substances because of its large number of multifunctional groups (Thakur et al., 2017). Seera et al. (2021) synthesized xylan/gelatin composite hydrogels and studied their adsorption of methylene blue. Firstly, Xylan and gelatin were mixed in aqueous NaOH solution and stirred at 65°C (steps 1 and 2 of Figure 3D). The precursor solution was then transferred to a round-bottled flask and stored in an oil bath of 50°C. The crosslinking agent EGDE was then dropped for 30–40 min until the gel formation was visually confirmed (step 3). Afterward,

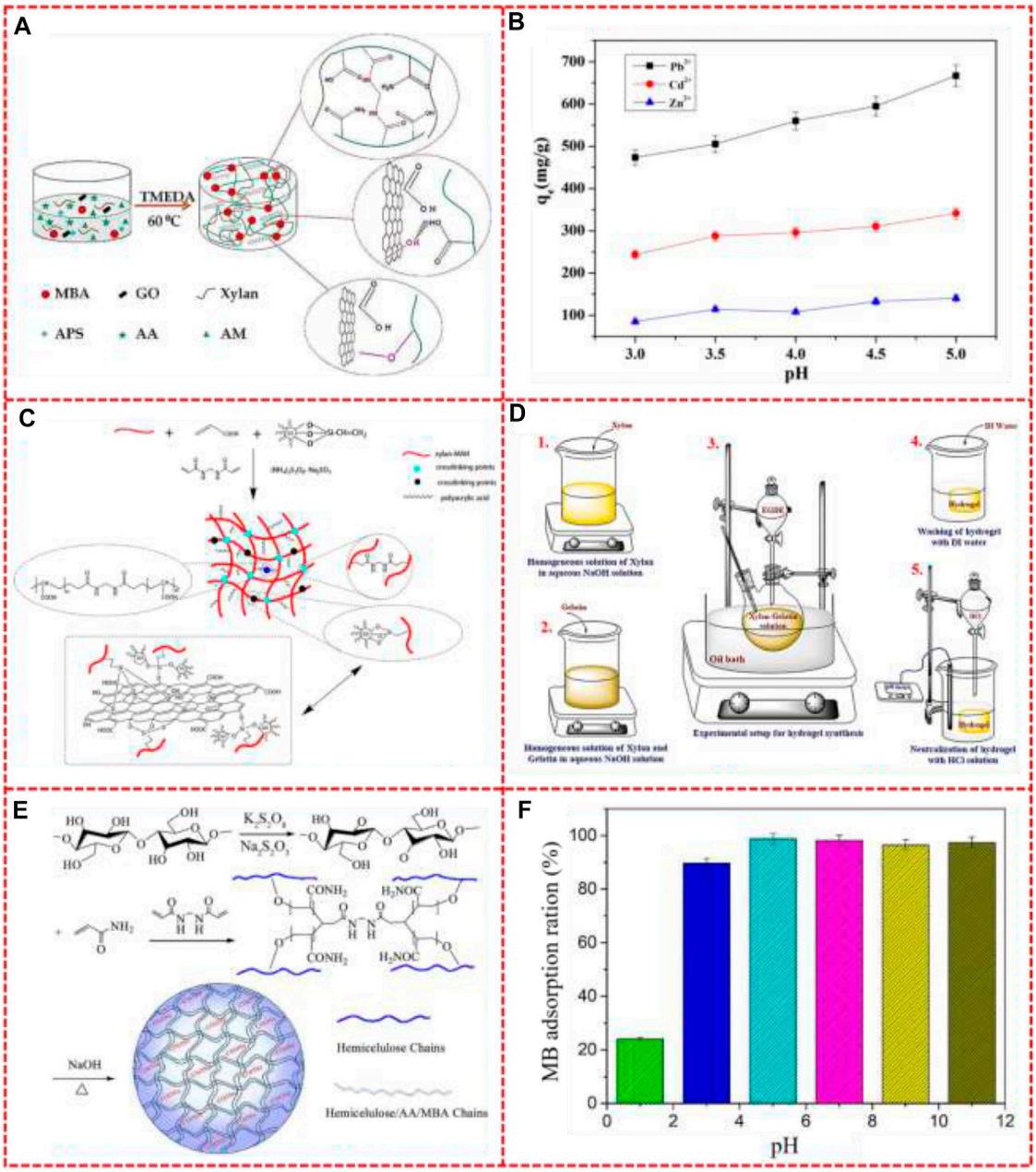

FIGURE 3
(A) The preparation process of xylan-g-/P (AA-co-AM)/GO nanocomposite hydrogels, **(B)** The influence of pH on the adsorption property of xylan-g-/P (AA-co-AM)/GO nanocomposite hydrogel, **(C)** Synthetic scheme of the chemically crosslinked xylan/GO composite hydrogel, **(D)** Synthesis procedure in the preparation of xylan and gelatin-based hydrogel, **(E)** The mechanism for the synthesis of the porous EIHs-g-PAA hydrogels, **(F)** Adsorption ratio for 250 mg/L of MB solution with different pH. Reproduced from: **(A)** Kong et al. (2019), MDPI; **(B)** Kong et al. (2019). MDPI; **(C)** Sun et al. (2022), Springer; **(D)** Seera et al. (2021), Elsevier; **(E)** Hu et al. (2022), Taylor & Francis Online; **(F)** Hu et al. (2022), Taylor & Francis Online.

hydrogels were scrupulously washed with DI water and neutralized with .1 M HCl to remove the excess number of precursors and NaOH (steps 4 and 5). The binding sites formed by the crosslinking of gelatin and xylan have electrostatic interaction with dye molecules. When the ratio of xylan to gelatin in hydrogel is 87:13 mol%, the adsorption efficiency of methylene blue is the highest.

Hu et al. (2022) prepared hydrogels based on hemicellulose from cold caustic extraction wastewater for efficiently adsorbing methylene blue. The mechanism for the synthesis of the EIHs-g-PAA hydrogels was shown in Figure 3E. When enough hydroxyl groups in the hemicellulose chains are activated to form hydroxyl radicals, the carbon-carbon double bond in Am reacts with hydroxyl radicals and MBA to form a massive gel material with a network structure in $Na_2S_2O_3/K_2S_2O_8$ oxidation–reduction catalysis system. And the resultant hydrogel has been evaluated at different pH (the result shows in Figure 3F). It can be seen that for a 250 mg/L MB solution, the removal rate of MB from the hydrogel increases from 24% to 89% as the PH increases from 1.0 to 3.0. When PH is higher than 3.0, -COOH, which has weak binding ability with positive charge MB molecule, starts to transform into -COO-, which has strong binding ability with

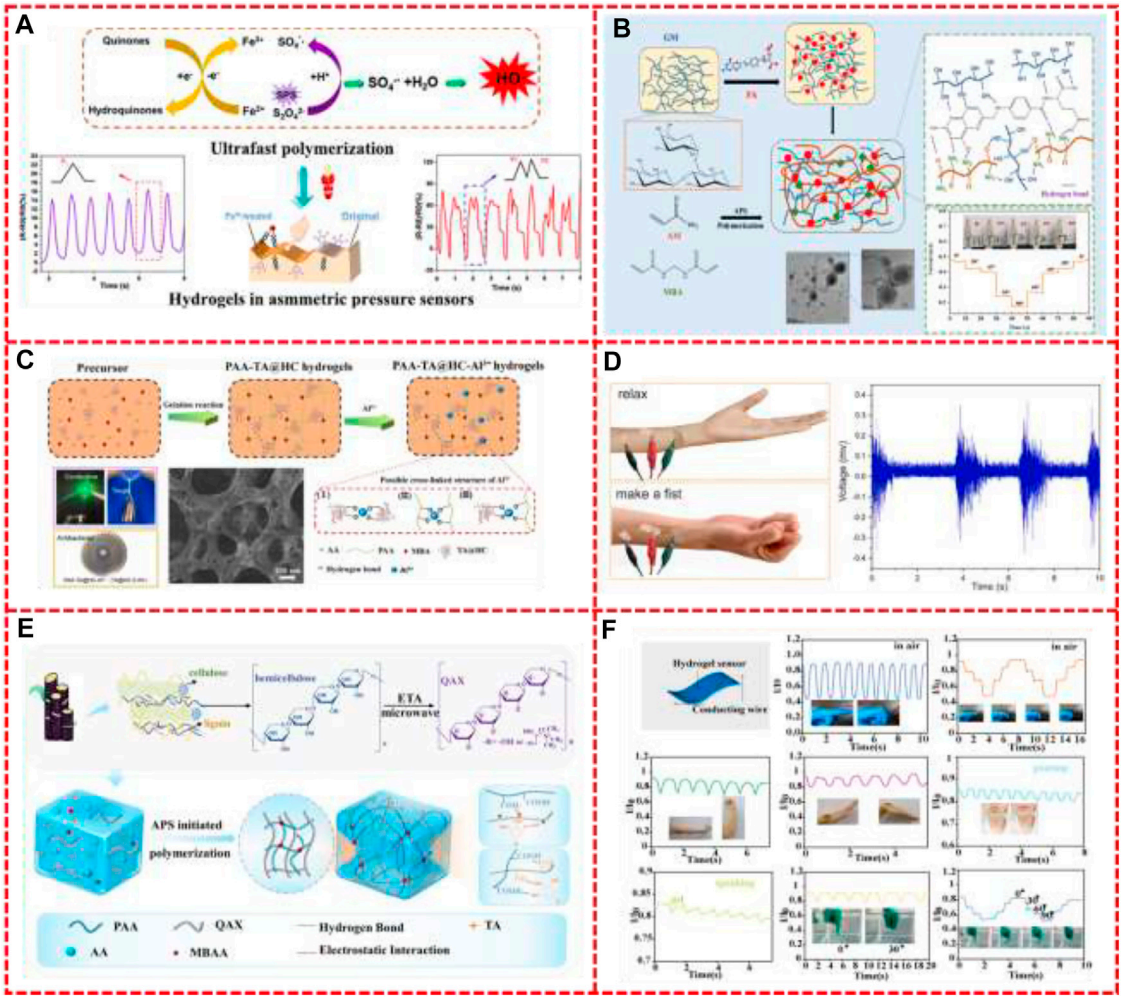

FIGURE 4
(A) Mechanism and pressure sensor signals recorded of PAA/TA@HC/Fe^{3+} hydrogels with or without Fe^{3+} treatment, **(B)** Schematic illustration of the preparation process of GM hydrogels and monitor arm bending as a strain sensor, **(C)** A schematic diagram of the ionic PAA-TA@HC-Al^{3+} hydrogel synthesis process and mechanism, **(D)** PAA-TA@HC-Al^{3+} hydrogel acts as a self-adhesive sensor, which can EMG signals, **(E)** Fabrication of the PAA-QAX-TA hydrogels, **(F)** PAA-QAX-TA hydrogel-based sensor model and sensing performance test, Reproduced from: **(A)** Gong et al. (2022b), ACS; **(B)** Ling et al. (2022), Elsevier; **(C)** Gong et al. (2022a), Elsevier; **(D)** Gong et al. (2022a), Elsevier; **(E)** Chang et al. (2022), Elsevier; **(F)** Chang et al. (2022), Elsevier.

MB molecule. Therefore, when pH value at 4.0, the adsorption capacity of the gel to MB was larger (98%). In addition, the electrostatic repulsion between -coo-groups enlarges the network structure of the hydrogel and promotes the diffusion of MB molecules into the hydrogel for adsorption. Moreover, the negative charge on the surface of inorganic nanoparticles can provide active sites to enhance the interaction between cationic dye molecules and hydrogels, and inorganic particles can also improve their mechanical properties.

Cheng et al. (2016) prepared composite hydrogels from hemicellulose in corn stover under mild alkaline conditions and introduced clay nanosheets. The addition of clay can improve the mechanical strength of hemicellulose hydrogels, and the adsorption rate mainly depends on the number of active sites on the surface of the hydrogel, so the negative charge on the surface of clay nanoparticles provides more active sites, thus improving the adsorption capacity of methylene blue on hydrogels. Zhao et al. (2020) extracted hemicelluloses from corn cob, added acrylic acid and acrylamide, and introduced Fe_3O_4 through *in situ* precipitation method, successfully prepared hemicelluloses based magnetic hydrogel. The Fe_3O_4 can increase the adsorption sites of methylene blue in the composite hydrogel, so that it shows good adsorption performance to methylene blue solution, which has broad application prospects in the field of industrial dye wastewater treatment.

In general, the hemicellulose hydrogels can adsorb metal ions or dyes in wastewater either by copolymerizing with other adsorptive polymers or by introducing other particles. On the one hand, the bioadsorption capacity of hemicellulose-based hydrogels is attractive and has potential in the field of industrial wastewater treatment. On the other hand, compared with other hydrogels, it is still in a relatively backward stage and cannot be applied on a large scale. The hemicellulose-based adsorbent hydrogels will provide potential choice for heavy metal ions and dyes removal.

3.3 Sensor

To realize the preparation of green, environmentally friendly, and non-toxic hydrogel sensor, biomass resources can be used as the skeleton or additive of hydrogel to control the performance of the sensor. Recent studies have shown that adding cellulose (Tong et al., 2019) or lignin (Wang et al., 2019a) as additives to hydrogels can modify their properties and enable them to be used in flexible strain sensors. As one of the biomass resource, hemicellulose is also a good choice in the field of flexible strain sensor.

Figure 4 shows the synthetic mechanism and sensing properties of some hemicellulose based hydrogels. As Figure 4A, the resistivity of the PAA-TA@HC-Al^{3+} hydrogel prepared by Gong et al. (2022a) decreased as the strain increased, because of the weakening of its conductive network (Zhang et al., 2021c). This hydrogel sensor can detect the movement on stretching, finger bending and weak pulse on the wrist. And the hydrogel sensor can detect throat vibration and it can also recognize different frequencies of breathing and phrases. Moreover, the hydrogels can accurately detect the weak ECG and EMG signals when it was used as ionic hydrogel electrodes. Additionally, skin tension-induced electrical signals can also be detected as Figure 4D. They also selectively applied Fe^{3+} on the surface of the hydrogel to obtain hydrogels with different adhesive properties on the upper and lower surfaces (Figure 4A). The strong adhesive side adhered to the skin, while the low adhesive side was resistant to external pollutants and could be used as a pressure sensor, which has great potential in the field of wearable flexible sensors (Gong et al., 2022b).

Ling et al. (2022) combined polygalactomannose (GM) with folic acid (FA), introduced hydrogen bond connection, and then added initiator and crosslinker to polymerize with AM to form a double network structure, as shown in Figure 4B. Compared with ordinary hemicellulose hydrogel, the hydrogel exhibited better mechanical strength and good anti-fatigue properties. The results showed that FA improved the electrical conductivity of the composite hydrogel, and the hydrogel showed antibacterial properties with inhibition against more than 80% of *E. coli*. In addition, they sticked GM4 on the knee of a wooden doll. The knee was bending with increasing angles (0°, 30°, 45°, 60° and 80°), accompanied with stretching of the hydrogel sample. As detected, the current decreased with stepwise increased bending angle and can remain stable in each angle stage. The CMX-PAM hydrogel prepared by Li et al. (2021) has impressive mechanical properties, UV blocking and electrical conductivity, so it shows potential for applications in human motion sensors. The more CMX contents, the hydrogel network structure became tighter *via* the ion coordination (−COO− from CMX and Fe^{3+}). This tight structure may hinder the path of conductive ions and increase the resistance of the sample. This hydrogel-based sensor can respond to the movements and detect the micro-bending angles of the neck, the finger and wrist. These movements can yield distinct response behaviors, and the resistance signals were fully recoverable and repeatable.

An underwater adhesive xylan-based hydrogel was prepared by Chang et al. (2022) through chemical and physical crosslinking. Firstly, xylan and ETA were mixed under microwave to obtain QAX. The hydrogel is then synthesized under the initiation of APS. The mechanism of fabrication is shown in Figure 4E, in which AA is polymerized into PAA and grafted to QAX through covalent bond, and hydrogen bond can be formed between TA and PAA or QAX. Moreover, due to its attractive adhesion ability, the hydrogel can be directly and tightly attached to the surface without additional fixation and can be used as a wearable soft strain sensor for monitoring human movement. The experimental results are shown in Figure 4F, when the hydrogel sensor is attached to the finger, elbow and wrist for periodic bending and stretching motion, it shows significant electrical changes, and also has the ability to distinguish different bending angles, with good repeatability.

Introducing conductive materials such as conductive polymers (Chen et al., 2019) or metal ions (Zhang et al., 2019b) into hydrogels is a common scheme to improve their sensing performance. PPY has excellent biocompatibility and conductivity, and as a conductive polymer, it can be used in wearable strain sensors (Kenry, 2018). Zhang et al. (2021b) prepared a hemicellulose/polypyrrole antifreeze conductive hydrogel, which has good strain sensitivity. By converting deformation into electrical signals, the relative resistance of the hydrogel rapidly increases with the tensile strain from 0% to 500%. The hydrogel can be used for flexible wearable sensors to detect the strain signals of human joints bending and stretching.

In summary, the current research on hemicellulose-based hydrogel sensors mainly focuses on wearable flexible sensors and medical signal sensors, and a lot of achievements have been made. In the future, more types of hemicellulose derivatives or some nanoparticles that can improve their properties should be developed to expand their application range and maintain their biocompatibility.

4 Conclusion and perspectives

Hemicellulose-based hydrogels demonstrate wide application prospects in medical materials, wastewater adsorption and sensors due to their renewable, good processability, environmental friendliness and low cost. Up to now, lots of research have been reported on raw material selection, crosslinking agent screening, physical and chemical crosslinking method, *etc.* However, there are still many problems to be solved.

(1) To improve the mechanical strength of hemicellulose hydrogels, toxic chemicals are inevitably used, which greatly limits their application. In the future, green and low energy consumption hemicellulose hydrogel polymerization methods need to be explored.
(2) The intelligent hemicellulose hydrogels with multiple responses should be widely concerned in order to have different applications in more fields.
(3) Most of the research on hemicellulose-based hydrogels are still in the laboratory stage. How to accelerate the large-scale application of hemicellulose-based hydrogels in sensing, wastewater treatment, biomedicine and other fields is another major problem.

It is believed that with the further research on hemicellulose-based hydrogels, these challenging problems will be solved. In conclusion, hemicellulose hydrogels have a certain position in the future, and we believe that through continuous in-depth research on them, they will become one of the substitutes for fossil-based materials.

Author contributions

YX and KL: investigation and writing original draft. TX, S-EC, and CS: supervision. YY, C-HL, M-SK, and RZ: review and editing. All authors contributed to the article and approved the submitted version.

Funding

This work was sponsored by the by the Opening Project of State Key Laboratory of Tree Genetics and Breeding (K2022104), Tianjin Excellent Special Commissioner for Agricultural Science and Technology Project (22ZYCGSN00350) and Tianjin Enterprise Technology Commissioner Project (22YDTPJC00930). This work was supported by the Commercializations Promotion Agency for R&D Outcomes (COMPA) grant funded by the Korean Government (Miinistery of Science and ICT) (2022). KL acknowledges the Innovation Project of Excellent Doctoral Dissertation of Tianjin University of Science and Technology (YB2022009) and the financial support from the China Scholarship Council (No. 202208120049).

Conflict of interest

The authors declare that the research was conducted in the absence of any commercial or financial relationships that could be construed as a potential conflict of interest.

Publisher's note

References

Ahluwalia, S., and Goyal, D. (2005). Removal of heavy metals by waste tea leaves from aqueous solution. *Eng. life Sci.* 5 (2), 158–162. doi:10.1002/elsc.200420066

Ai, J., Li, K., Li, J., Yu, F., and Ma, J. (2021). Super flexible, fatigue resistant, self-healing PVA/xylan/borax hydrogel with dual-crosslinked network. *Int. J. Biol. Macromol.* 172, 66–73. doi:10.1016/j.ijbiomac.2021.01.038

Ali, A., Hasan, A., and Negi, Y. S. (2022). Effect of carbon based fillers on xylan/chitosan/nano-HAp composite matrix for bone tissue engineering application. *Int. J. Biol. Macromol.* 197, 1–11. doi:10.1016/j.ijbiomac.2021.12.012

Ali, A., Pandey, A., Ram Patra, N., Sharma, P., and Singh Negi, Y. (2020). Effect of bioactive ceramics on Xylan/Chitosan conjugate scaffold for bone tissue engineering. *Mater. Today Proc.* 33, A1–A7. doi:10.1016/j.matpr.2020.12.1173

An, L., Si, C., Bae, J. H., Jeong, H., and Kim, Y. S. (2020). One-step silanization and amination of lignin and its adsorption of Congo red and Cu(II) ions in aqueous solution. *Int. J. Biol. Macromol.* 159, 222–230. doi:10.1016/j.ijbiomac.2020.05.072

An, L., Si, C., Wang, G., Sui, W., and Tao, Z. (2019). Enhancing the solubility and antioxidant activity of high-molecular-weight lignin by moderate depolymerization via *in situ* ethanol/acid catalysis. *Industrial Crops Prod.* 128, 177–185. doi:10.1016/j.indcrop.2018.11.009

Arvizo, R. R., Bhattacharyya, S., Kudgus, R. A., Giri, K., Bhattacharya, R., and Mukherjee, P. (2012). Intrinsic therapeutic applications of noble metal nanoparticles: Past, present and future. *Chem. Soc. Rev.* 41 (7), 2943–2970. doi:10.1039/C2CS15355F

Ayoub, A., Venditti, R. A., Pawlak, J. J., Salam, A., and Hubbe, M. A. (2013). Novel hemicellulose–chitosan biosorbent for water desalination and heavy metal removal. *Acs Sustain. Chem. Eng.* 1 (9), 1102–1109. doi:10.1021/sc300166m

Baghbadorani, N. B., Behzad, T., Etesami, N., and Heidarian, P. (2019). Removal of Cu2+ ions by cellulose nanofibers-assisted starch-g-poly(acrylic acid) superadsorbent hydrogels. *Compos. Part B Eng.* 176, 107084. doi:10.1016/j.compositesb.2019.107084

Berglund, J., Mikkelsen, D., Flanagan, B. M., Dhital, S., Gaunitz, S., Henriksson, G., et al. (2020). Wood hemicelluloses exert distinct biomechanical contributions to cellulose fibrillar networks. *Nat. Commun.* 11 (1), 4692. doi:10.1038/s41467-020-18390-z

Bush, J. R., Liang, H., Dickinson, M., and Botchwey, E. A. (2016). Xylan hemicellulose improves chitosan hydrogel for bone tissue regeneration. *Polym. Adv. Technol.* 27 (8), 1050–1055. doi:10.1002/pat.3767

Cao, X., Peng, X., Zhong, L., and Sun, R. (2014). Multiresponsive hydrogels based on xylan-type hemicelluloses and photoisomerized azobenzene copolymer as drug delivery carrier. *J. Agric. Food Chem.* 62 (41), 10000–10007. doi:10.1021/jf504040s

Chang, M., Liu, X., Lin, Q., Li, W., Wang, X., and Ren, J. (2022). A highly stretchable, UV resistant and underwater adhesive hydrogel based on xylan derivative for sensing. *Int. J. Biol. Macromol.* 220, 1084–1094. doi:10.1016/j.ijbiomac.2022.08.077

Chang, M., Liu, X., Wang, X., Peng, F., and Ren, J. (2021). Mussel-inspired adhesive hydrogels based on biomass-derived xylan and tannic acid cross-linked with acrylic acid with antioxidant and antibacterial properties. *J. Mater. Sci.* 56 (26), 14729–14740. doi:10.1007/s10853-021-06228-y

Chen, H., Lan, G., Ran, L., Xiao, Y., Yu, K., Lu, B., et al. (2018). A novel wound dressing based on a Konjac glucomannan/silver nanoparticle composite sponge effectively kills bacteria and accelerates wound healing. *Carbohydr. Polym.* 183, 70–80. doi:10.1016/j.carbpol.2017.11.029

Chen, J., Yu, Q., Cui, X., Dong, M., Zhang, J., Wang, C., et al. (2019). An overview of stretchable strain sensors from conductive polymer nanocomposites. *J. Mater. Chem. C* 7 (38), 11710–11730. doi:10.1039/C9TC03655E

Chen, S., Wang, G., Sui, W., Parvez, A. M., Dai, L., and Si, C. (2020a). Novel lignin-based phenolic nanosphere supported palladium nanoparticles with highly efficient catalytic performance and good reusability. *Industrial Crops Prod.* 145, 112164. doi:10.1016/j.indcrop.2020.112164

Chen, S., Wang, G., Sui, W., Parvez, A. M., and Si, C. (2020b). Synthesis of lignin-functionalized phenolic nanosphere supported Ag nanoparticles with excellent dispersion stability and catalytic performance. *Green Chem.* 22 (9), 2879–2888. doi:10.1039/C9GC04311J

Chen, T., Liu, H., Dong, C., An, Y., Zhang, M., Li, J., et al. (2020). Synthesis and characterization of temperature/pH dual sensitive hemicellulose-based hydrogels from eucalyptus APMP waste liquor. *Carbohydr. Polym.* 247, 116717. doi:10.1016/j.carbpol.2020.116717

Chen, X., Yang, Q., Si, C-L., Wang, Z., Huo, D., Hong, Y., et al. (2016). Recovery of oligosaccharides from prehydrolysis liquors of poplar by microfiltration/ultrafiltration membranes and anion exchange resin. *Acs Sustain. Chem. Eng.* 4 (3), 937–943. doi:10.1021/acssuschemeng.5b01029

Cheng, D., Yan, L., Yang, G., and Zhang, A. (2018). Water- and fertilizer-integrated hydrogel derived from the polymerization of acrylic acid and urea as a slow-release N fertilizer and water retention in agriculture. *J. Agric. Food Chem.* 66 (23), 5762–5769. doi:10.1021/acs.jafc.8b00872

Cheng, H-L., Feng, Q-H., Liao, C-A., Liu, Y., Wu, D-B., and Wang, Q-G. (2016). Removal of methylene blue with hemicellulose/clay hybrid hydrogels. *Chin. J. Polym. Sci.* 34 (6), 709–719. doi:10.1007/s10118-016-1788-2

Dai, L., Cao, Q., Wang, K., Han, S., Si, C., Liu, D., et al. (2020). High efficient recovery of L-lactide with lignin-based filler by thermal degradation. *Industrial Crops Prod.* 143, 111954. doi:10.1016/j.indcrop.2019.111954

Dai, L., Liu, R., Hu, L-Q., Zou, Z-F., and Si, C-L. (2017). Lignin nanoparticle as a novel green carrier for the efficient delivery of resveratrol. *Acs Sustain. Chem. Eng.* 5 (9), 8241–8249. doi:10.1021/acssuschemeng.7b01903

Dai, L., Liu, R., and Si, C. (2018). A novel functional lignin-based filler for pyrolysis and feedstock recycling of poly(l-lactide). *Green Chem.* 20 (8), 1777–1783. doi:10.1039/C7GC03863A

Dax, D., Chavez Bastidas, M. S., Honorato, C., Liu, J., Spoljaric, S., Seppala, J., et al. (2016). Tailor-made hemicellulose-based hydrogels reinforced with nanofibrillated cellulose. *Nordic Pulp Pap. Res. J.* 30 (3), 373–384. doi:10.3183/npprj-2015-30-03-p373-384

Deng, J., Song, Q., Liu, S., Pei, W., Wang, P., Zheng, L., et al. (2022). Advanced applications of cellulose-based composites in fighting bone diseases. *Compos. Part B* 245, 110221. doi:10.1016/j.compositesb.2022.110221

Du, H., Liu, C., Mu, X., Gong, W., Lv, D., Hong, Y., et al. (2016). Preparation and characterization of thermallystable cellulose nanocrystals via a sustainable approach of

$FeCl_3$-catalyzed formic acid hydrolysis. *Cellulose* 23, 2389–2407. doi:10.1007/s10570-016-0963-5

Du, H., Liu, W., Zhang, M., Si, C., Zhang, X., and Li, B. (2019). Cellulose nanocrystals and cellulose nanofibrils based hydrogels for biomedical applications. *Carbohydr. Polym.* 209, 130–144. doi:10.1016/j.carbpol.2019.01.020

Du, H., Parit, M., Liu, K., Zhang, M., Jiang, Z., Huang, T-S., et al. (2021a). Engineering cellulose nanopaper with water resistant, antibacterial, and improved barrier properties by impregnation of chitosan and the followed halogenation. *Carbohydr. Polym.* 270, 118372. doi:10.1016/j.carbpol.2021.118372

Du, H., Parit, M., Liu, K., Zhang, M., Jiang, Z., Huang, T-S., et al. (2021b). Multifunctional cellulose nanopaper with superior water-resistant, conductive, and antibacterial properties functionalized with chitosan and polypyrrole. *ACS Appl. Mater. Interfaces* 13 (27), 32115–32125. doi:10.1021/acsami.1c06647

Du, H., Zhang, M., Liu, K., Parit, M., Jiang, Z., Zhang, X., et al. (2022). Conductive PEDOT:PSS/cellulose nanofibril paper electrodes for flexible supercapacitors with superior areal capacitance and cycling stability. *Chem. Eng. J.* 428, 131994. doi:10.1016/j.cej.2021.131994

Elkihel, A., Christie, C., Vernisse, C., Ouk, T-S., Lucas, R., Chaleix, V., et al. (2021). Xylan-based cross-linked hydrogel for photodynamic antimicrobial chemotherapy. *ACS Appl. Bio Mater.* 4 (9), 7204–7212. doi:10.1021/acsabm.1c00760

Enomoto-Rogers, Y., and Iwata, T. (2012). Synthesis of xylan-graft-poly(l-lactide) copolymers via click chemistry and their thermal properties. *Carbohydr. Polym.* 87 (3), 1933–1940. doi:10.1016/j.carbpol.2011.09.092

Farhat, W., Venditti, R., Ayoub, A., Prochazka, F., Fernández-De-Alba, C., Mignard, N., et al. (2018). Towards thermoplastic hemicellulose: Chemistry and characteristics of poly-(ε-caprolactone) grafting onto hemicellulose backbones. *Mater. Des.* 153, 298–307. doi:10.1016/j.matdes.2018.05.013

Fekete, T., Borsa, J., Takács, E., and Wojnárovits, L. (2016). Synthesis of cellulose-based superabsorbent hydrogels by high-energy irradiation in the presence of crosslinking agent. *Radiat. Phys. Chem.* 118, 114–119. doi:10.1016/j.radphyschem.2015.02.023

Feng, J., Hu, X., and Yue, P. L. (2004). Novel bentonite clay-based Fe−Nanocomposite as a heterogeneous catalyst for photo-fenton discoloration and mineralization of orange II. *Environ. Sci. Technol.* 38 (1), 269–275. doi:10.1021/es034515c

Feng, P., Peng, P., Feng, X., and Sun, R. C. (2012). Fractional purification and bioconversion of hemicelluloses. *Biotechnol. Adv.* 30 (4), 879–903. doi:10.1016/j.biotechadv.2012.01.018

Fu, G-Q., Zhang, S-C., Chen, G-G., Hao, X., Bian, J., and Peng, F. (2020). Xylan-based hydrogels for potential skin care application. *Int. J. Biol. Macromol.* 158, 244–250. doi:10.1016/j.ijbiomac.2020.04.235

Gabrielii, I., Gatenholm, P., Glasser, W. G., Jain, R. K., and Kenne, L. (2000). Separation, characterization and hydrogel-formation of hemicellulose from aspen wood. *Carbohydr. Polym.* 43 (4), 367–374. doi:10.1016/S0144-8617(00)00181-8

Gami, P., Kundu, D., Seera, S. D. K., and Banerjee, T. (2020). Chemically crosslinked xylan–β-Cyclodextrin hydrogel for the *in vitro* delivery of curcumin and 5-Fluorouracil. *Int. J. Biol. Macromol.* 158, 18–31. doi:10.1016/j.ijbiomac.2020.04.237

Gao, C., Ren, J., Kong, W., Sun, R., and Chen, Q. (2015). Comparative study on temperature/pH sensitive xylan-based hydrogels: Their properties and drug controlled release. *RSC Adv.* 5 (110), 90671–90681. doi:10.1039/C5RA16703E

Gao, C., Ren, J., Zhao, C., Kong, W., Dai, Q., Chen, Q., et al. (2016). Xylan-based temperature/pH sensitive hydrogels for drug controlled release. *Carbohydr. Polym.* 151, 189–197. doi:10.1016/j.carbpol.2016.05.075

Ge, J., Gu, K., Sun, K., Wang, X., Yao, S., Mo, X., et al. (2021). Preparation and swelling behaviors of high-strength hemicellulose-g-polydopamine composite hydrogels. *Materials* 14, 186. doi:10.3390/ma14010186

Gong, X., Fu, C., Alam, N., Ni, Y., Chen, L., Huang, L., et al. (2022b). Preparation of hemicellulose nanoparticle-containing ionic hydrogels with high strength, self-healing, and UV resistance and their applications as strain sensors and asymmetric pressure sensors. *Biomacromolecules* 23, 2272–2279. doi:10.1021/acs.biomac.1c01640

Gong, X., Fu, C., Alam, N., Ni, Y., Chen, L., Huang, L., et al. (2022a). Tannic acid modified hemicellulose nanoparticle reinforced ionic hydrogels with multi-functions for human motion strain sensor applications. *Industrial Crops Prod.* 176, 114412. doi:10.1016/j.indcrop.2021.114412

González, K., García-Astrain, C., Santamaria-Echart, A., Ugarte, L., Avérous, L., Eceiza, A., et al. (2018). Starch/graphene hydrogels via click chemistry with relevant electrical and antibacterial properties. *Carbohydr. Polym.* 202, 372–381. doi:10.1016/j.carbpol.2018.09.007

Guan, Y., Bian, J., Peng, F., Zhang, X-M., and Sun, R-C. (2014). High strength of hemicelluloses based hydrogels by freeze/thaw technique. *Carbohydr. Polym.* 101, 272–280. doi:10.1016/j.carbpol.2013.08.085

Guan, Y., Qi, X-M., Zhang, B., Chen, G-G., Peng, F., Sun, R-C., et al. (2015). Physically crosslinked composite hydrogels of hemicelluloses with poly (vinyl alcohol phosphate) and chitin nanowhiskersHydrogels: From controlled release to pH-responsive drug delivery. *Bioresour. Discov. today* 107 (110), 1378569–1393579. doi:10.1016/S1359-6446(02)02255-9

Guan, Z., Bian, P., Sun, R., and Peng, F. (2014). Nanoreinforced hemicellulose-based hydrogels prepared by freeze-thaw treatment. *Cellulose* 21 (3), 1709–1721. doi:10.1007/s10570-014-0211-9

Ha, E. J., Yun, J-H., Si, C., Bae, Y. S., Jeong, Y-H., Park, K-H., et al. (2021). Application of ethanol extracts from alnus sibirica fisch. Ex turcz in hair growth promotion. *Front. Bioeng. Biotechnol.* 9, 673314. doi:10.3389/fbioe.2021.673314

Han, T., Song, T., Pranovich, A., and Rojas, O. J. (2022). Engineering a semi-interpenetrating constructed xylan-based hydrogel with superior compressive strength, resilience, and creep recovery abilities. *Carbohydr. Polym.* 294, 119772. doi:10.1016/j.carbpol.2022.119772

Han, X., Xu, H., Che, L., Sha, D., Huang, C., Meng, T., et al. (2020). Retracted: Application of inorganic nanocomposite hydrogels in bone tissue engineering. *iScience* 23 (12), 101845. doi:10.1016/j.isci.2020.101845

Hassan, N., Mohsen, H., and Mehdi, Y. (2018). Antibacterial oxidized starch/ZnO nanocomposite hydrogel: Synthesis and evaluation of its swelling behaviours in various pHs and salt solutions. *Int. J. Biol. Macromol.* 126, 578–584. doi:10.1016/j.ijbiomac.2018.12.242

Hoffman, A. S. (2012). Hydrogels for biomedical applications. *Adv. Drug Deliv. Rev.* 64, 18–23. doi:10.1016/j.addr.2012.09.010

Hoyle, C. E., and Bowman, C. N. (2010). Thiol–ene click chemistry. *Angew. Chem. Int. Ed.* 49 (9), 1540–1573. doi:10.1002/anie.200903924

Hu, L., Wang, K., Li, G., Zhang, R., Luo, Y., Si, C-L., et al. (2017). Isolation and structural elucidation of heartwood extractives of Juglans sigillata. *Holzforschung* 71 (10), 785–791. doi:10.1515/hf-2017-0036

Hu, N., Chen, D., Guan, Q., Peng, L., Zhang, J., He, L., et al. (2022). Preparation of hemicellulose-based hydrogels from biomass refining industrial effluent for effective removal of methylene blue dye. *Environ. Technol.* 43 (4), 489–499. doi:10.1080/09593330.2020.1795930

Huang, L-Z., Ma, M-G., Ji, X-X., Choi, S-E., and Si, C. (2021). Recent developments and applications of hemicellulose from wheat straw: A review. *Front. Bioeng. Biotechnol.* 9, 690773. doi:10.3389/fbioe.2021.690773

Jafari, H., Ghaffari-Bohlouli, P., Podstawczyk, D., Nie, L., and Shavandi, A. (2022). Tannic acid post-treatment of enzymatically crosslinked chitosan-alginate hydrogels for biomedical applications. *Carbohydr. Polym.* 295, 119844. doi:10.1016/j.carbpol.2022.119844

Karaaslan, M. A., Tshabalala, M. A., Yelle, D. J., and Buschle-Diller, G. (2011). Nanoreinforced biocompatible hydrogels from wood hemicelluloses and cellulose whiskers. *Carbohydr. Polym.* 86 (1), 192–201. doi:10.1016/j.carbpol.2011.04.030

Kenry, L. B. (2018). Recent advances in biodegradable conducting polymers and their biomedical applications. *Biomacromolecules* 19 (6), 1783–1803. doi:10.1021/acs.biomac.8b00275

Kesharwani, P., Bisht, A., Alexander, A., Dave, V., and Sharma, S. (2021). Biomedical applications of hydrogels in drug delivery system: An update. *J. Drug Deliv. Sci. Technol.* 66, 102914. doi:10.1016/j.jddst.2021.102914

Kolb, H. C., Finn, M., and Sharpless, K. B. (2001). Click chemistry: Diverse chemical function from a few good reactions. *Angew. Chem. Int. Ed.* 40 (11), 2004–2021. doi:10.1002/1521-3773(20010601)40:11<2004:aid-anie2004>3.0.co;2-5

Kong, W., Chang, M., Zhang, C., Liu, X., He, B., and Ren, J. (2019). Preparation of Xylan-G-/P (AA-co-AM)/GO nanocomposite hydrogel and its adsorption for heavy metal ions. *Polymers* 11 (4), 621. doi:10.3390/polym11040621

Kong, W., Dai, Q., Gao, C., Ren, J., Liu, C., and Sun, R. (2018). *Polymer gels*. Springer, 87–127. doi:10.1007/978-981-10-6086-1_3

Kong, W-Q., Gao, C-D., Hu, S-F., Ren, J-L., Zhao, L-H., and Sun, R-C. (2017). Xylan-modified-based hydrogels with temperature/pH dual sensitivity and controllable drug delivery behavior. *Materials* 10 (3), 304. doi:10.3390/ma10030304

Kundu, D., Mondal, S. K., and Banerjee, T. (2019). Development of β-cyclodextrin-cellulose/hemicellulose-based hydrogels for the removal of Cd (II) and Ni (II): Synthesis, kinetics, and adsorption aspects. *J. Chem. Eng. Data* 64 (6), 2601–2617. doi:10.1021/acs.jced.9b00088

Kuzmenko, V., Hägg, D., Toriz, G., and Gatenholm, P. (2014). *In situ* forming spruce xylan-based hydrogel for cell immobilization. *Carbohydr. Polym.* 102, 862–868. doi:10.1016/j.carbpol.2013.10.077

Lei, Y., Zhang, G., Jiang, H., Li, F., Liu, H., Xia, Y., et al. (2019). Synergistic toughening of nanocomposite hydrogel based on ultrasmall aluminum hydroxide nanoparticles and hydroxyapatite nanoparticles. *Polym. Compos.* 40 (3), 942–951. doi:10.1002/pc.24765

Li, N., Hu, Y. J., Bian, J., Li, M. F., Hao, X., Peng, F., et al. (2020). Enhanced mechanical performance of xylan-based composite hydrogel via chain extension and semi-interpenetrating networks. *Cellulose* 27 (8), 4407–4416. doi:10.1007/s10570-020-03080-2

Li, N., Sun, D., Su, Z., Hao, X., Li, M., Ren, J., et al. (2021). Rapid fabrication of xylan-based hydrogel by graft polymerization via a dynamic lignin-Fe3+ plant catechol system. *Carbohydr. Polym.* 269, 118306. doi:10.1016/j.carbpol.2021.118306

Li, W., Wang, G., Sui, W., Xu, T., Li, Z., Parvez, A. M., et al. (2022). Facile and scalable preparation of cage-like mesoporous carbon from lignin-based phenolic resin and its application in supercapacitor electrodes. *Carbon* 196, 819–827. doi:10.1016/j.carbon.2022.05.053

Li, X., Lu, X., Nie, S., Liang, M., Yu, Z., Duan, B., et al. (2020). Efficient catalytic production of biomass-derived levulinic acid over phosphotungstic acid in deep eutectic solvent. *Industrial Crops Prod.* 145, 112154. doi:10.1016/j.indcrop.2020.112154

Li, X., Xu, R., Yang, J., Nie, S., Liu, D., Liu, Y., et al. (2019). Production of 5-hydroxymethylfurfural and levulinic acid from lignocellulosic biomass and catalytic upgradation. *Industrial Crops Prod.* 130, 184–197. doi:10.1016/j.indcrop.2018.12.082

Li, Y. J., Sun, X. F., Ye, Q., Liu, B. C., Wu, Y. G., and Yao-Guo, W. (2014). Preparation and properties of a novel hemicellulose-based magnetic hydrogel. *Acta Phys. Chim. Sin.* 30 (1110), 111–120. doi:10.3866/PKU.WHXB201310313

Ling, Z., Ma, J., Zhang, S., Shao, L., Wang, C., and Ma, J. (2022). Stretchable and fatigue resistant hydrogels constructed by natural galactomannan for flexible sensing application. *Int. J. Biol. Macromol.* 216, 193–202. doi:10.1016/j.ijbiomac.2022.06.185

Liu, C., Fu, L., Jiang, T., Liang, Y., and Wei, Y. (2021a). High-strength and self-healable poly (acrylic acid)/chitosan hydrogel with organic-inorganic hydrogen bonding networks. *Polymer* 230, 124006. doi:10.1016/j.polymer.2021.124006

Liu, C., Wang, G., Sui, W., An, L., and Si, C. (2017a). Preparation and characterization of chitosan by a novel deacetylation approach using glycerol as green reaction solvent. *ACS Sustain. Chem. Eng.* 5 (6), 4690–4698. doi:10.1021/acssuschemeng.7b00050

Liu, H., Du, H., Zheng, T., Liu, K., Ji, X., Xu, T., et al. (2021b). Cellulose based composite foams and aerogels for advanced energy storage devices. *Chem. Eng. J.* 426, 130817. doi:10.1016/j.cej.2021.130817

Liu, H., Xu, T., Cai, C., Liu, K., Liu, W., Zhang, M., et al. (2022a). Multifunctional superelastic, superhydrophilic, and ultralight nanocellulose-based composite carbon aerogels for compressive supercapacitor and strain sensor. *Adv. Funct. Mater.* 32 (26), 2113082. doi:10.1002/adfm.202113082

Liu, H., Xu, T., Liang, Q., Zhao, Q., Zhao, D., and Si, C. (2022b). Compressible cellulose nanofibrils/reduced graphene oxide composite carbon aerogel for solid-state supercapacitor. *Adv. Compos. Hybrid Mater.* 5 (2), 1168–1179. doi:10.1007/s42114-022-00427-0

Liu, H., Xu, T., Liu, K., Zhang, M., Liu, W., Li, H., et al. (2021c). Lignin-based electrodes for energy storage application. *Industrial Crops Prod.* 165, 113425. doi:10.1016/j.indcrop.2021.113425

Liu, J., Chinga-Carrasco, G., Cheng, F., Xu, W., Willför, S., Syverud, K., et al. (2016). Hemicellulose-reinforced nanocellulose hydrogels for wound healing application. *Cellulose* 23 (5), 3129–3143. doi:10.1007/s10570-016-1038-3

Liu, J., Li, J., Yu, F., Zhao, Y. X., and Pan, J. F. (2020a). *In situ* forming hydrogel of natural polysaccharides through Schiff base reaction for soft tissue adhesive and hemostasis. *Int. J. Biol. Macromol.* 147, 653–666. doi:10.1016/j.ijbiomac.2020.01.005

Liu, K., Du, H., Liu, W., Liu, H., Zhang, M., Xu, T., et al. (2022c). Cellulose nanomaterials for oil exploration applications. *Polym. Rev.* 62 (3), 585–625. doi:10.1080/15583724.2021.2007121

Liu, K., Du, H., Liu, W., Zhang, M., Wang, Y., Liu, H., et al. (2022d). Strong, flexible, and highly conductive cellulose nanofibril/PEDOT:PSS/MXene nanocomposite films for efficient electromagnetic interference shielding. *Nanoscale* 14 (40), 14902–14912. doi:10.1039/D2NR00468B

Liu, K., Du, H., Zheng, T., Liu, H., Zhang, M., Zhang, R., et al. (2021d). Recent advances in cellulose and its derivatives for oilfield applications. *Carbohydr. Polym.* 259, 117740. doi:10.1016/j.carbpol.2021.117740

Liu, K., Du, H., Zheng, T., Liu, W., Zhang, M., Liu, H., et al. (2021e). Lignin-containing cellulose nanomaterials: Preparation and applications. *Green Chem.* 23 (24), 9723–9746. doi:10.1039/D1GC02841C

Liu, K., Liu, W., Li, W., Duan, Y., Zhou, K., Zhang, S., et al. (2022e). Strong and highly conductive cellulose nanofibril/silver nanowires nanopaper for high performance electromagnetic interference shielding. *Adv. Compos. Hybrid Mater.* 5 (2), 1078–1089. doi:10.1007/s42114-022-00425-2

Liu, S., Chen, F., Song, X., and Wu, H. (2017b). Preparation and characterization of temperature- and pH-sensitive hemicellulose-containing hydrogels. *Int. J. Polym. Analysis Charact.* 22 (3), 187–201. doi:10.1080/1023666X.2016.1276257

Liu, S., Du, H., Liu, K., Ma, M-G., Kwon, Y-E., Si, C., et al. (2021f). Flexible and porous Co3O4-carbon nanofibers as binder-free electrodes for supercapacitors. *Adv. Compos. Hybrid Mater.* 4 (4), 1367–1383. doi:10.1007/s42114-021-00344-8

Liu, W., Du, H., Liu, H., Xie, H., Xu, T., Zhao, X., et al. (2020b). Highly efficient and sustainable preparation of carboxylic and thermostable cellulose nanocrystals via FeCl3-catalyzed innocuous citric acid hydrolysis. *Acs Sustain. Chem. Eng.* 8 (44), 16691–16700. doi:10.1021/acssuschemeng.0c06561

Liu, W., Du, H., Liu, K., Liu, H., Xie, H., Si, C., et al. (2021g). Sustainable preparation of cellulose nanofibrils via choline chloride-citric acid deep eutectic solvent pretreatment combined with high-pressure homogenization. *Carbohydr. Polym.* 267, 118220. doi:10.1016/j.carbpol.2021.118220

Liu, W., Du, H., Zhang, M., Liu, K., Liu, H., Xie, H., et al. (2020c). Bacterial cellulose-based composite scaffolds for biomedical applications: A review. *Acs Sustain. Chem. Eng.* 8 (20), 7536–7562. doi:10.1021/acssuschemeng.0c00125

Liu, W., Liu, K., Du, H., Zheng, T., Zhang, N., Xu, T., et al. (2022f). Cellulose nanopaper: Fabrication, functionalization, and applications. *Nano-Micro Lett.* 14 (1), 104. doi:10.1007/s40820-022-00849-x

Liu, W., Liu, K., Wang, Y., Lin, Q., Liu, J., Du, H., et al. (2022g). Sustainable production of cellulose nanofibrils from Kraft pulp for the stabilization of oil-in-water Pickering emulsions. *Industrial Crops Prod.* 185, 115123. doi:10.1016/j.indcrop.2022.115123

Liu, W., Zhang, S., Liu, K., Yang, H., Lin, Q., Xu, T., et al. (2023). Sustainable preparation of lignocellulosic nanofibrils and cellulose nanopaper from poplar sawdust. *J. Clean. Prod.* 384, 135582. doi:10.1016/j.jclepro.2022.135582

Liu, X., Chang, M., Zhang, H., and Ren, J. (2022h). Fabrication of bentonite reinforced dopamine grafted carboxymethyl xylan cross-linked with polyacrylamide hydrogels with adhesion properties. *Colloids Surfaces A Physicochem. Eng. Aspects* 647, 129024. doi:10.1016/j.colsurfa.2022.129024

Liu, Y., Vrana, N., Cahill, P., and Mcguinness, G. (2009). Physically crosslinked composite hydrogels of PVA with natural macromolecules: Structure, mechanical properties, and endothelial cell compatibility. *J. Biomed. Mater. Res. Part B Appl. Biomaterials Official J. Soc. Biomaterials Jpn. Soc. Biomaterials, Aust. Soc. Biomaterials Korean Soc. Biomaterials* 90 (2), 492–502. doi:10.1002/jbm.b.31310

Lu, J., Han, X., Dai, L., Li, C., Wang, J., Zhong, Y., et al. (2020). Conductive cellulose nanofibrils-reinforced hydrogels with synergetic strength, toughness, selfadhesion, flexibility and adjustable strain responsiveness. *Carbohydr. Polym.* 250, 117010. doi:10.1016/j.carbpol.2020.117010

Lu, J., Zhu, W., Dai, L., Si, C., and Ni, Y. (2019). Fabrication of thermo- and pH-sensitive cellulose nanofibrils-reinforced hydrogel with biomass nanoparticles. *Carbohydr. Polym.* 215, 289–295. doi:10.1016/j.carbpol.2019.03.100

Ma, C., Ma, M-G., Si, C., Ji, X-X., and Wan, P. (2021). Flexible MXene-based composites for wearable devices. *Adv. Funct. Mater.* 31 (22), 2009524. doi:10.1002/adfm.202009524

Maleki, L., Edlund, U., and Albertsson, A-C. (2017). Synthesis of full interpenetrating hemicellulose hydrogel networks. *Carbohydr. Polym.* 170, 254–263. doi:10.1016/j.carbpol.2017.04.091

Mamidyala, S. K., and Finn, M. G. (2010). *In situ* click chemistry: Probing the binding landscapes of biological molecules. *Chem. Soc. Rev.* 39 (4), 1252–1261. doi:10.1039/B901969N

Markstedt, K., Xu, W., Liu, J., Xu, C., and Gatenholm, P. (2017). Synthesis of tunable hydrogels based on O-acetyl-galactoglucomannans from spruce. *Carbohydr. Polym.* 157, 1349–1357. doi:10.1016/j.carbpol.2016.11.009

Martínez-Gómez, F., Guerrero, J., Matsuhiro, B., and Pavez, J. (2017). *In vitro* release of metformin hydrochloride from sodium alginate/polyvinyl alcohol hydrogels. *Carbohydr. Polym.* 155, 182–191. doi:10.1016/j.carbpol.2016.08.079

Meena, R., Lehnen, R., and Saake, B. (2014). Microwave-assisted synthesis of kC/xylan/PVP-based blend hydrogel materials: Physicochemical and rheological studies. *Cellulose* 21 (1), 553–568. doi:10.1007/s10570-013-0155-5

Melandri, D., De Angelis, A., Orioli, R., Ponzielli, G., Lualdi, P., Giarratana, N., et al. (2006). Use of a new hemicellulose dressing (Veloderm®) for the treatment of split-thickness skin graft donor sites: A within-patient controlled study. *Burns* 32 (8), 964–972. doi:10.1016/j.burns.2006.03.013

Meng, X., and Edgar, K. J. (2016). Click" reactions in polysaccharide modification. *Prog. Polym. Sci.* 53, 52–85. doi:10.1016/j.progpolymsci.2015.07.006

Mohammadrezaei, D., Golzar, H., Rezai Rad, M., Omidi, M., Rashedi, H., Yazdian, F., et al. (2018). *In vitro* effect of graphene structures as an osteoinductive factor in bone tissue engineering: A systematic review. *J. Biomed. Mater. Res. Part A* 106 (8), 2284–2343. doi:10.1002/jbm.a.36422

Mondal, S., Das, S., and Nandi, A. K. (2020). A review on recent advances in polymer and peptide hydrogels. *Soft Matter* 16 (6), 1404–1454. doi:10.1039/C9SM02127B

Nie, L., Wu, Q., Long, H., Hu, K., Li, P., Wang, C., et al. (2019). Development of chitosan/gelatin hydrogels incorporation of biphasic calcium phosphate nanoparticles for bone tissue engineering. *J. Biomaterials Sci. Polym. Ed.* 30 (17), 1636–1657. doi:10.1080/09205063.2019.1654210

Oliveira, E. E., Silva, A. E., Júnior, T., Gomes, M., Aguiar, L. M., Marcelino, H. R., et al. (2010). Xylan from corn cobs, a promising polymer for drug delivery: Production and characterization. *Bioresour. Technol.* 101 (14), 5402–5406. doi:10.1016/j.biortech.2010.01.137

Pahimanolis, N., Kilpeläinen, P., Master, E., Ilvesniemi, H., and Seppälä, J. (2015). Novel thiol- amine- and amino acid functional xylan derivatives synthesized by thiol–ene reaction. *Carbohydr. Polym.* 131, 392–398. doi:10.1016/j.carbpol.2015.06.007

Peng, X. W., Zhong, L. X., Ren, J. L., and Sun, R. C. (2012). Highly effective adsorption of heavy metal ions from aqueous solutions by macroporous xylan-rich hemicelluloses-based hydrogel. *J. Agric. Food Chem.* 60 (15), 3909–3916. doi:10.1021/jf300387q

Prakobna, K., Kisonen, V., Xu, C., and Berglund, L. A. (2015). Strong reinforcing effects from galactoglucomannan hemicellulose on mechanical behavior of wet cellulose nanofiber gels. *J. MATER Sci.* 50, 7413–7423. doi:10.1007/s10853-015-9299-z

Qi, X., Guan, Y., Chen, G., Zhang, B., Ren, J., Peng, F., et al. (2015). A non-covalent strategy for montmorillonite/xylose self-healing hydrogels. *RSC Adv.* 5 (51), 41006–41012. doi:10.1039/C5RA04115E

Qian, H., Liu, J., Wang, X., Pei, W., Fu, C., Ma, M., et al. (2023). The state-of-the-art application of functional bacterial cellulose-based materials in biomedical fields. *Carbohydr. Polym.* 300, 120252. doi:10.1016/j.carbpol.2022.120252

Qu, J., Meng, X., You, H., Ye, X., and Du, Z. (2017). Utilization of rice husks functionalized with xanthates as cost-effective biosorbents for optimal Cd (II) removal from aqueous solution via response surface methodology. *Bioresour. Technol.* 241, 1036–1042. doi:10.1016/j.biortech.2017.06.055

Ren, J., Dai, Q., Zhong, H., Liu, X., Meng, L., Wang, X., et al. (2018). Quaternized xylan/cellulose nanocrystal reinforced magnetic hydrogels with high strength. *Cellulose* 25 (8), 4537–4549. doi:10.1007/s10570-018-1858-4

Ren, J-L., Sun, R-C., and Peng, F. (2008). Carboxymethylation of hemicelluloses isolated from sugarcane bagasse. *Polym. Degrad. Stab.* 93 (4), 786–793. doi:10.1016/j.polymdegradstab.2008.01.011

Seera, S. D. K., Kundu, D., Gami, P., Naik, P. K., and Banerjee, T. (2021). Synthesis and characterization of xylan-gelatin cross-linked reusable hydrogel for the adsorption of methylene blue. *Carbohydr. Polym.* 256, 117520. doi:10.1016/j.carbpol.2020.117520

Shan, S., Sun, X-F., Xie, Y., Li, W., and Ji, T. (2021). High-performance hydrogel adsorbent based on cellulose, hemicellulose, and lignin for copper (II) ion removal. *Polymers* 13 (18), 3063. doi:10.3390/polym13183063

Shi, Z., Gao, X., Ullah, M. W., Li, S., Wang, Q., and Yang, G. (2016). Electroconductive natural polymer-based hydrogels. *Biomaterials* 111, 40–54. doi:10.1016/j.biomaterials.2016.09.020

Shu-Ping, W., Xiang-Zi, D., Jia-Rui, K., Fang-Di, S., and Mai-Yong, Z. (2017). Fabrication of carboxymethyl chitosan–hemicellulose resin for adsorptive removal of heavy metals from wastewater. *Chin. Chem. Lett.* 28, 625–632. doi:10.1016/j.cclet.2016.11.015

Si, C-L., Jiang, J-Z., Liu, S-C., Hu, H-Y., Ren, X-D., Yu, G-J., et al. (2013). A new lignan glycoside and phenolics from the branch wood of Pinus banksiana Lambert. *Holzforschung* 67 (4), 357–363. doi:10.1515/hf-2012-0137

Si, C-L., Liu, Z., Kim, J-K., and Bae, Y-S. (2008). Structure elucidation of phenylethanoid glycosides from Paulownia tomentosa Steud. var. tomentosa wood. *tomentosa wood* 62 (2), 197–200. doi:10.1515/HF.2008.047

Sun, X. F., Liu, B., Jing, Z., and Wang, H. (2015). Preparation and adsorption property of xylan/poly(acrylic acid) magnetic nanocomposite hydrogel adsorbent. *Carbohydr. Polym.* 118, 16–23. doi:10.1016/j.carbpol.2014.11.013

Sun, X. F., Zeng, Q., Wang, H., and Hao, Y. (2019). Preparation and swelling behavior of pH/temperature responsive semi-IPN hydrogel based on carboxymethyl xylan and poly(N-isopropyl acrylamide). *Cellulose* 26, 1909–1922. doi:10.1007/s10570-018-2180-x

Sun, X-F., Xie, Y., Shan, S., Li, W., and Sun, L. (2022). Chemically-crosslinked xylan/graphene oxide composite hydrogel for copper ions removal. *J. Polym. Environ.* 30 (9), 3999–4013. doi:10.1007/s10924-022-02475-5

Suneetha, M., Moo, O. S., Choi, S. M., Zo, S., Han, S. S., and Soo Han, S. (2021). Tissue-adhesive, stretchable, and self-healable hydrogels based on carboxymethyl cellulose-dopamine/PEDOT:PSS via mussel-inspired chemistry for bioelectronic applications. *Chem. Eng. J.* 426 (3), 130847. doi:10.1016/j.cej.2021.130847

Thakur, S., Govender, P. P., Mamo, M. A., Tamulevicius, S., and Thakur, V. K. (2017). Recent progress in gelatin hydrogel nanocomposites for water purification and beyond. *Vacuum* 146, 396–408. doi:10.1016/j.vacuum.2017.05.032

Tong, R., Chen, G., Pan, D., Qi, H., Li, R. A., Tian, J., et al. (2019). Highly stretchable and compressible cellulose ionic hydrogels for flexible strain sensors. *Biomacromolecules* 20 (5), 2096–2104. doi:10.1021/acs.biomac.9b00322

Venugopal, J., Rajeswari, R., Shayanti, M., Sridhar, R., Sundarrajan, S., Balamurugan, R., et al. (2013). Xylan polysaccharides fabricated into nanofibrous substrate for myocardial infarction. *Mater. Sci. Eng. C* 33 (3), 1325–1331. doi:10.1016/j.msec.2012.12.032

Wang, H., Chen, Y., Yi, W., Zhang, A., and Liu, C. (2017). Homogeneous esterification mechanism of bagasse modified with phthalic anhydride in ionic liquid. Part 2: Reactive behavior of hemicelluloses. *Carbohydr. Polym.* 157 (2), 1365–1373. doi:10.1016/j.carbpol.2016.11.007

Wang, H., Du, H., Liu, K., Liu, H., Xu, T., Zhang, S., et al. (2021). Sustainable preparation of bifunctional cellulose nanocrystals via mixed H2SO4/formic acid hydrolysis. *Carbohydr. Polym.* 266, 118107. doi:10.1016/j.carbpol.2021.118107

Wang, X., Tang, S., Chai, S., Wang, P., Qin, J., Pei, W., et al. (2021). Preparing printable bacterial cellulose based gelatin gel to promote *in vivo* bone regeneration. *Carbohydr. Polym.* 270, 118342. doi:10.1016/j.carbpol.2021.118342

Wang, H., Xie, H., Du, H., Wang, X., Liu, W., Duan, Y., et al. (2020a). Highly efficient preparation of functional and thermostable cellulose nanocrystals via H2SO4 intensified acetic acid hydrolysis. *Carbohydr. Polym.* 239, 116233. doi:10.1016/j.carbpol.2020.116233

Wang, L., Li, Y., Lin, L., Mu, R., and Pang, J. (2020b). Novel synthesis of mussel inspired and Fe3+ induced pH-sensitive hydrogels: Adhesion, injectable, shapeable, temperature properties, release behavior and rheological characterization. *Carbohydr. Polym.* 236, 116045. doi:10.1016/j.carbpol.2020.116045

Wang, L., Mu, R-J., Lin, L., Chen, X., Lin, S., Ye, Q., et al. (2019a). Bioinspired aerogel based on konjac glucomannan and functionalized carbon nanotube for controlled drug release. *Int. J. Biol. Macromol.* 133, 693–701. doi:10.1016/j.ijbiomac.2019.04.148

Wang, Q., Pan, X., Lin, C., Lin, D., Ni, Y., Chen, L., et al. (2019b). Biocompatible, self-wrinkled, antifreezing and stretchable hydrogel-based wearable sensor with PEDOT:sulfonated lignin as conductive materials. *Chem. Eng. J.* 370, 1039–1047. doi:10.1016/j.cej.2019.03.287

Wang, H., Zhang, M., Hu, J., Du, H., Xu, T., and Si, C. (2022a). Sustainable preparation of surface functionalized cellulose nanocrystals and their application for Pickering emulsions. *Carbohydr. Polym.* 297, 120062. doi:10.1016/j.carbpol.2022.120062

Wang, Q., Xu, W., Koppolu, R., Van Bochove, B., Seppälä, J., Hupa, L., et al. (2022b). Injectable thiol-ene hydrogel of galactoglucomannan and cellulose nanocrystals in delivery of therapeutic inorganic ions with embedded bioactive glass nanoparticles. *Carbohydr. Polym.* 276, 118780. doi:10.1016/j.carbpol.2021.118780

Wang, R., Huang, X., Zoetebier, B., Dijkstra, P. J., and Karperien, M. (2023). Enzymatic co-crosslinking of star-shaped poly(ethylene glycol) tyramine and hyaluronic acid tyramine conjugates provides elastic biocompatible and biodegradable hydrogels. *Bioact. Mater.* 20, 53–63. doi:10.1016/j.bioactmat.2022.05.020

Warren, D. S., Sutherland, S. P., Kao, J. Y., Weal, G. R., and Mackay, S. M. (2017). The preparation and simple analysis of a clay nanoparticle composite hydrogel. *J. Chem. Educ.* 94 (11), 1772–1779. doi:10.1021/acs.jchemed.6b00389

Wei, H., Wang, H., Chu, H., and Li, J. (2019). Preparation and characterization of slow-release and water-retention fertilizer based on starch and halloysite. *Int. J. Biol. Macromol.* 133, 1210–1218. doi:10.1016/j.ijbiomac.2019.04.183

Wen, J., Yang, J., Wang, W., Li, M., Peng, F., Bian, J., et al. (2020). Synthesis of hemicellulose hydrogels with tunable conductivity and swelling behavior through facile one-pot reaction. *Int. J. Biol. Macromol.* 154, 1528–1536. doi:10.1016/j.ijbiomac.2019.11.035

Wiesbrock, F., Hoogenboom, R., and Schubert, U. S. (2004). Microwave-assisted polymer synthesis: State-of-the-art and future perspectives. *Macromol. Rapid Commun.* 25 (20), 1739–1764. doi:10.1002/marc.200400313

Wu, K., Zhu, Q., Qian, H., Xiao, M., Corke, H., Nishinari, K., et al. (2018). Controllable hydrophilicity-hydrophobicity and related properties of konjac glucomannan and ethyl cellulose composite films. *Food Hydrocoll.* 79, 301–309. doi:10.1016/j.foodhyd.2017.12.034

Xiang, Z., Tang, N., Jin, X., and Gao, W. (2022). Fabrications and applications of hemicellulose-based bio-adsorbents. *Carbohydr. Polym.* 278, 118945. doi:10.1016/j.carbpol.2021.118945

Xiao, M., Dai, S., Wang, L., Ni, X., Yan, W., Fang, Y., et al. (2015). Carboxymethyl modification of konjac glucomannan affects water binding properties. *Carbohydr. Polym.* 130, 1–8. doi:10.1016/j.carbpol.2015.05.001

Xie, H., Du, H., Yang, X., and Si, C. (2018). Recent strategies in preparation of cellulose nanocrystals and cellulose nanofibrils derived from raw cellulose materials. *Int. J. Polym. Sci.* 2018, 1–25. doi:10.1155/2018/7923068

Xie, H., Zou, Z., Du, H., Zhang, X., Wang, X., Yang, X., et al. (2019). Preparation of thermally stable and surface-functionalized cellulose nanocrystals via mixed H2SO4/Oxalic acid hydrolysis. *Carbohydr. Polym.* 223, 115116. doi:10.1016/j.carbpol.2019.115116

Xiong, R., Hua, D., Van Hoeck, J., Berdecka, D., Léger, L., De Munter, S., et al. (2021a). Photothermal nanofibres enable safe engineering of therapeutic cells. *Nat. Nanotechnol.* 16 (11), 1281–1291. doi:10.1038/s41565-021-00976-3

Xiong, R., Xu, R. X., Huang, C., De Smedt, S., and Braeckmans, K. (2021b). Stimuli-responsive nanobubbles for biomedical applications. *Chem. Soc. Rev.* 50 (9), 5746–5776. doi:10.1039/C9CS00839J

Xu, D., Liu, Z., Zhou, W., Zhao, X., Fu, C., Fatehi, P., et al. (2019). Preparation of xylan–acrylic acid polymer with high molecular weight and its application as a dye removal flocculant. *J. Wood Chem. Technol.* 39 (2), 75–89. doi:10.1080/02773813.2018.1508300

Xu, J., Li, C., Dai, L., Xu, C., Zhong, Y., Yu, F., et al. (2020a). Biomass fractionation and lignin fractionation towards lignin valorization. *ChemSusChem* 13 (17), 4284–4295. doi:10.1002/cssc.202001491

Xu, R., Liu, K., Du, H., Liu, H., Cao, X., Zhao, X., et al. (2020b). Falling leaves return to their roots: A review on the preparation of γ-valerolactone from lignocellulose and its application in the conversion of lignocellulose. *ChemSusChem* 13 (24), 6461–6476. doi:10.1002/cssc.202002008

Xu, R., Du, H., Liu, C., Liu, H., Wu, M., Zhang, X., et al. (2021a). An efficient and magnetic adsorbent prepared in a dry process with enzymatic hydrolysis residues for wastewater treatment. *J. Clean. Prod.* 313, 127834. doi:10.1016/j.jclepro.2021.127834

Xu, T., Du, H., Liu, H., Liu, W., Zhang, X., Si, C., et al. (2021b). Advanced nanocellulose-based composites for flexible functional energy storage devices. *Adv. Mater.* 33 (48), 2101368. doi:10.1002/adma.202101368

Xu, T., Liu, K., Sheng, N., Zhang, M., Liu, W., Liu, H., et al. (2022). Biopolymer-based hydrogel electrolytes for advanced energy storage/conversion devices: Properties, applications, and perspectives. *Energy Storage Mater.* 48, 244–262. doi:10.1016/j.ensm.2022.03.013

Yan, S., Yin, J., Tang, L., and Chen, X. (2010). Novel physically crosslinked hydrogels of carboxymethyl chitosan and cellulose ethers: Structure and controlled drug release behavior. *J. Appl. Polym. Sci.* 119 (4), 2350–2358. doi:10.1002/app.32678

Yang, J. Y., Zhou, X. S., and Fang, J. (2011). Synthesis and characterization of temperature sensitive hemicellulose-based hydrogels. *Carbohydr. Polym.* 86 (3), 1113–1117. doi:10.1016/j.carbpol.2011.05.043

Yang, X., Xie, H., Du, H., Zhang, X., Zou, Z., Zou, Y., et al. (2019). Facile extraction of thermally stable and dispersible cellulose nanocrystals with high yield via a green and recyclable $FeCl_3$-catalyzed deep eutectic solvent system. *ACS Sustain. Chem. Eng.* 7 (7), 7200–7208. doi:10.1021/acssuschemeng.9b00209

Yang, X., Xie, H., Zou, Y., Huang, Y., Jiang, L-W., Wang, X., et al. (2021). Cost-effective and efficient plum-pudding-like $Fe_xNi_{1-x}S_2$/C composite electrocatalysts for oxygen evolution reaction. *Renew. Energy* 168, 416–423. doi:10.1016/j.renene.2020.12.072

Zhang, S., Guan, Y., Fu, G-Q., Chen, B-Y., Peng, F., Yao, C-L., et al. (2014). Organic/inorganic superabsorbent hydrogels based on xylan and montmorillonite. *J. Nanomater.* 2014, 1–11. doi:10.1155/2014/675035

Zhang, T., and Sun, X-F. (2020). Hemicellulose/poly (acrylic acid) semi-IPN magnetic nanocomposite hydrogel for lysozyme adsorption. *Int. J. Nanomater. Nanotechnol. Nanomedicine* 6 (1), 001–005. doi:10.17352/2455-3492.000032

Zhang, W., Liang, Z., Feng, Q., Wei, N., Liu, Z., Fu, N., et al. (2016). Reed hemicellulose-based hydrogel prepared by glow discharge electrolysis plasma and its adsorption properties for heavy metal ions. *Fresenius Environ. Bull.* 25, 1791–1798.

Zhang, W., Zhu, S., Bai, Y., Xi, N., Wang, S., Bian, Y., et al. (2015). Glow discharge electrolysis plasma initiated preparation of temperature/pH dual sensitivity reed hemicellulose-based hydrogels. *Carbohydr. Polym.* 122, 11–17. doi:10.1016/j.carbpol.2015.01.007

Zhang, L., Zhang, Q., Yu, J., Ma, J., Kuga, S., Fan, Y., et al. (2019a). Strengthened cellulosic gels by the chemical gelation of cellulose via crosslinking with TEOS. *Cellulose* 26 (18), 9819–9829. doi:10.1007/s10570-019-02765-7

Zhang, X., Zhang, M., Cui, T., Li, J., Liu, Q., and Wang, H. (2019b). The enhancement of the mechanical properties and the shape memory effect for the Cu-13.0Al-4.0Ni alloy by boron addition. *J. Alloys Compd.* 776, 326–333. doi:10.1016/j.jallcom.2018.10.176

Zhang, M., Du, H., Liu, K., Nie, S., Xu, T., Zhang, X., et al. (2021a). Fabrication and applications of cellulose-based nanogenerators. *Adv. Compos. Hybrid Mater.* 4 (4), 865–884. doi:10.1007/s42114-021-00312-2

Zhang, W., Wen, J. Y., Ma, M. G., Li, M. F., and Bian, J. (2021b). Anti-freezing, water-retaining, conductive, and strain-sensitive hemicellulose/polypyrrole composite hydrogels for flexible sensors. *J. Mater. Res. Technol.* 14, 555–566. doi:10.1016/j.jmrt.2021.06.088

Zhang, Y., Mao, J., Jiang, W., Zhang, S., Tong, L., Mao, J., et al. (2021c). Lignin sulfonate induced ultrafast polymerization of double network hydrogels with anti-freezing, high strength and conductivity and their sensing applications at extremely cold conditions. *Compos. Part B Eng.* 217, 108879. doi:10.1016/j.compositesb.2021.108879

Zhang, Y., Xu, H., Kong, Y., Hua, J., Tang, X., Zhuang, Y., et al. (2021d). Wood forming tissue-specific expression of PdSuSy and HCHL increases holocellulose content and improves saccharification in Populus. *J. For. Res.* 32 (4), 1681–1688. doi:10.1007/s11676-020-01220-9

Zhao, D., Huang, J., Zhong, Y., Li, K., Zhang, L., and Cai, J. (2016). High-strength and high-toughness double-cross-linked cellulose hydrogels: A new strategy using sequential chemical and physical cross-linking. *Adv. Funct. Mater.* 26 (34), 6279–6287. doi:10.1002/adfm.201601645

Zhao, L., Li, W., Plog, A., Xu, Y., Buntkowsky, G., Gutmann, T., et al. (2014a). Multi-responsive cellulose nanocrystal–rhodamine conjugates: An advanced structure study by solid-state dynamic nuclear polarization (DNP) NMR. *Phys. Chem. Chem. Phys.* 16 (47), 26322–26329. doi:10.1039/C4CP04096A

Zhao, W., Glavas, L., Odelius, K., Edlund, U., and Albertsson, A. C. (2014b). Facile and green approach towards electrically conductive hemicellulose hydrogels with tunable conductivity and swelling behavior. *Chem. Mater.* 26 (14), 4265–4273. doi:10.1021/cm501852w

Zhao, L-T., Zhang, J., Li, N., Niu, M-H., and Ping, Q-W. (2020). Preparation of hemicellulose-based magnetic hydrogel and its adsorption properties for dye. *Cailiao Gongcheng/Journal Mater. Eng.* 48 (11), 85–91. doi:10.11868/j.issn.1001-4381.2019.000076

Zhao, W., Odelius, K., Edlund, U., Zhao, C., and Albertsson, A-C. (2015). *In situ* synthesis of magnetic field-responsive hemicellulose hydrogels for drug delivery. *Biomacromolecules* 16 (8), 2522–2528. doi:10.1021/acs.biomac.5b00801

Zhong, L., Peng, X., Song, L., Yang, D., Cao, X., and Sun, R. (2013). Adsorption of Cu 2+ and Ni 2+ from aqueous solution by arabinoxylan hydrogel: Equilibrium, kinetic, competitive adsorption. *Sep. Sci. Technol.* 48 (17), 2659–2669. doi:10.1080/01496395.2013.804085

frontiers | Frontiers in Bioengineering and Biotechnology

TYPE Original Research
PUBLISHED 21 February 2023
DOI 10.3389/fbioe.2023.1135424

OPEN ACCESS

EDITED BY
Caoxing Huang,
Nanjing Forestry University, China

REVIEWED BY
Norazah Mohammad Nawawi,
Universiti Selangor, Malaysia
Azhar Hussain,
Islamia University of Bahawalpur, Pakistan

*CORRESPONDENCE
Kankan Jiang,
jiangkankan@126.com

†These authors have contributed equally to this work

SPECIALTY SECTION
This article was submitted to Bioprocess Engineering,
a section of the journal
Frontiers in Bioengineering and Biotechnology

RECEIVED 31 December 2022
ACCEPTED 07 February 2023
PUBLISHED 21 February 2023

CITATION
Nawaz A, Qadoos K, Haq IU, Feng Y, Mukhtar H, Huang R and Jiang K (2023), Effect of pretreatment strategies on halophyte *Atriplex crassifolia* to improve saccharification using thermostable cellulases.
Front. Bioeng. Biotechnol. 11:1135424.
doi: 10.3389/fbioe.2023.1135424

Effect of pretreatment strategies on halophyte *Atriplex crassifolia* to improve saccharification using thermostable cellulases

Ali Nawaz[1,2†], Khadija Qadoos[2†], Ikram Ul Haq[2], Yiwei Feng[3], Hamid Mukhtar[2], Rong Huang[1] and Kankan Jiang[1*]

[1]School of Basic Medical Sciences and Forensic Medicine, Hangzhou Medical College, Hangzhou, China, [2]Institute of Industrial Biotechnology, Government College University, Lahore, Pakistan, [3]School of Clinical Medicine, Hangzhou Medical College, Hangzhou, China

Bioethanol is believed to be an influential revolutionary gift of biotechnology, owing to its elevating global demand and massive production. Pakistan is home to a rich diversity of halophytic flora, convertible into bounteous volumes of bioethanol. On the other hand, the accessibility to the cellulosic part of biomass is a major bottleneck in the successful application of biorefinery processes. The most common pre-treatment procedures existent include physicochemical and chemical approaches, which are not environmentally benign. To overcome these problems, biological pre-treatment has gained importance but the drawback is the low yield of the extracted monosaccharides. The current research was aimed at exploring the best pre-treatment method for the bioconversion of halophyte *Atriplex crassifolia* into saccharides using three thermostable cellulases. *Atriplex crassifolia* was subjected to acid, alkali and microwave pre-treatments, followed by compositional analysis of the pre-treated substrates. Maximum delignification i.e. 56.6% was observed in the substrate pre-treated using 3% HCl. Enzymatic saccharification using thermostable cellulases also validated the results where the highest saccharification yield i.e. 39.5% was observed for the sample pre-treated using same. Maximum enzymatic hydrolysis of 52.7% was obtained for 0.40 g of the pre-treated halophyte *Atriplex crassifolia* where Endo-1,4-β-glucanase (300U), Exo-1,4-β-glucanase (400U) and β-1,4-glucosidase (1000U) were simultaneously added and incubated for 6 h at 75°C. The reducing sugar slurry obtained after optimization of saccharification was utilized as glucose in submerged fermentation for bioethanol production. The fermentation medium was inoculated with *Saccharomyces cerevisiae,* incubated at 30°C and 180 rpm for 96 h. Ethanol production was estimated using potassium dichromate method. Maximum production of bioethanol i.e. 16.33% was noted at 72 h. It can be concluded from the study that *Atriplex crassifolia* owing to its high cellulosic content after pre-treatment using dilute acid method, yields substantial amount of reducing sugars and high saccharification rates when subjected to enzymatic hydrolysis using thermostable cellulases, under optimized reaction conditions. Hence, the halophyte *Atriplex crassifolia* is a beneficial substrate that can be utilized to extract fermentable saccharides for bioethanol production.

KEYWORDS

biorefinery, bioethanol, halophytes, pre-treatment, delignification, enzymatic hydrolysis, thermostable cellulases

1 Introduction

Fossil-based fuels are not only non-renewable energy resources having detrimental impact on the environment, but their limited availability in depleting reservoirs is not sufficient to fulfill the global energy needs (Li et al., 2020; Vu et al., 2020). Renewable energy comes along sustainable development, energy security and economic growth (Den et al., 2018). Biorefinery is based on the sustainable conversion and efficient valorization of raw material (lignocellulosic biomass, waste, etc.) into wide range of bio-based energy products (Hingsamer and Jungmeier, 2019).

Bioethanol fuel is believed to be an influential revolutionary gift of biotechnology, owing to its elevating global demand and massive production. Biofuels, based on their source of biomass have been categorized into four generations. First-generation biofuels are a product of edible crops, for instance, wheat and corn (Nanda et al., 2018). Second-generation biofuels are a product of non-edible crops; this includes the waste of food crops, agricultural and forest residues, chips of wood, and waste from cooking oil (Nanda et al., 2018). In the modern world of today where overpopulation and poverty are major concerns, employing first generation biofuels is not that favorable, keeping in view the scarcity of available food, fresh water, and arable land resources. Whereas, the second-generation biofuel energy crops can be easily produced on degraded saline lands using scarce water resources to minimize the competition with food production (Moioli et al., 2018).

It is true that 70% of the earth is made of water; on the other hand, a bulk amount of this percentage remains unsuitable for irrigational purposes and does not support human intake, owing to high salinity rates. Moreover, the limited availability of arable land is also subject to increasing salinity, because of continuous irrigation, (that adds to the existing salts); this remains a major challenge to enhance agricultural practices (Flowers and Colmer, 2008). Precise and recent estimates on the global extent of salinity-afflicted land is unavailable, data is variable according to different information sources (Shahid et al., 2018). However, a global figure of 952.2 million ha has been reported (Arora et al., 2016). Evidently, the utilization of this massive chunk of space to grow and harvest biofuel feedstocks, which can be subjected to irrigation using seawater, can help eliminate the major barrier linked to farming for biofuel production (Brown, 2019).

Halophytes, which are capable of growth in salinity-afflicted soils are inexpensive sources of lignocellulosic biomass (Joshi et al., 2020). Halophytes produce oilseeds and lignocellulosic biomass; both the products can be exploited for biofuel production. Among the topmost promising genera exist *Salicornia* (glasswort), *Suaeda* (sea-blite), *Atriplex* (saltbush), *Distichlis* (saltgrass) and *Batis* (saltwort) (Abideen et al., 2011). Cultivation of halophytes in saline-afflicted regions will spare fresh water resources and arable agricultural soils for food, and provide lignocellulosic feedstock of desirable quality for conversion into biofuel (Yuan et al., 2011).

The genus *Atriplex* belongs to the family Amaranthaceae and is home to approximately 300 saltbush species. Saltbush species are resistant towards adaptation; majority of them have their habitats in semi-arid and arid areas globally (Paneque, 2018). Species named *Atriplex crassifolia*, a wild, annual halophyte native to semi-arid and arid areas of Punjab, was the subject of study in this research.

Pre-treatment of lignocellulosic biomass is a basic prerequisite for effective enzymatic hydrolysis of biomass. Pre-treatment ensures disruption of the complicated network of lignocellulose and ensures sustainable production of valuable products by enhancing the surface area of biomass, so that the cellulases can easily act upon the cellulosic content (Meng et al., 2020; Padilla-Rascón et al., 2020). The most common pre-treatment procedures existent include physicochemical and chemical approaches, which are not environmentally benign. To overcome these problems, biological pre-treatment has gained importance but the drawback is the low yield of the extracted monosaccharides (Rezania et al., 2020). Furthermore, different green processes have evolved for the pre-treatment of biomass (Lyu et al., 2019). Although, these techniques offer promising benefits, their wide-scale applicability at industrial level demands high capital cost (Bhatia et al., 2020; Shen et al., 2020). Therefore, extensive research is a requirement to develop the most applicable technique for pre-treatment that ensures ease of applicability along with affordability.

Alkaline solutions have been long used for the pre-treatment of lignocellulosic biomass. The complex structure of lignin composed of alkyl-aryl linkages are subjected to disruption utilizing alkalis such as ammonium hydroxide, sodium hydroxide, calcium hydroxide and lime (Chen et al., 2013). The use of acids for pre-treatment is another chemical pre-treatment technique used to degrade the lignocellulosic biomass, as it cleaves the glycosidic bonds present within the biomass structure (Sahoo et al., 2018). Nitric acid, phosphoric acid, sulfuric acid and hydrochloric acid are various examples of the acids that have been analyzed for their capability to pre-treat lignocellulosic biomass, even at industrial levels (Solarte-Toro et al., 2019).

Pre-treatment using microwave is another technique to disrupt the construction of lignocellulosic biomass. Irradiation of the microwave causes acceleration of chemical reactions within the biomass. The vibrations created by the heat of microwave, generate hot spots within the structure of biomass (Hassan et al., 2018). Microwave irradiation for pre-treatment of biomass is a favorable method in the domain of biomass biorefinery, owing to the heat that not affects the surface of biomass but also elevates the temperature inside the structure of biomass, being more energetic and effective compared to conventional heating techniques (Pellera and Gidarakos, 2017).

Saccharification is the process where complex carbohydrates are broken down into simple sugars. Following the pre-treatment of lignocellulosic biomass, saccharification is the next significant step in the bioconversion of cellulosic content into monosaccharides (Kucharska et al., 2020). Enzymatic saccharification is generally conducted employing cellulases and hemicellulases (Kumar and Sharma, 2017). Cellulase is not a term used to define a single enzyme, infact it is a complex of multiple enzymes (Thapa et al., 2020). Generally, the term cellulases is used to denote three glycoside hydrolases i.e., (endocellulases, exocellulases and β-glucosidases), which play role in the bioconversion of cellulosic content within biomass to reducing sugars (Champreda et al., 2019). Hydrolysis efficiency depends upon different physicochemical parameters which include incubation pH, time, temperature, agitation speed, particle size, enzyme/substrate ratio, etc. (Chavan and Gaikwad, 2021; Faizal et al., 2021).

Fermentation is an important step in bioethanol production, which can be conducted either separately or in combination with saccharification. In this research, separate hydrolysis and fermentation (SHF) has been conducted, as it is the most favorable technique concerning bioethanol production. It facilitates self-regulating optimization of saccharification for maximizing sugar extraction and that of fermentation for ethanol production (Moodley and Kana, 2019).

Pakistan is home to a rich diversity of halophytic flora, convertible into bounteous volumes of bioethanol. The current research, utilizing halophytes, aimed to provide promising results in developing sustainable bioethanol fuel for the citizens, which is also a foremost need of the country, keeping in view the ever-increasing hike in petroleum prices, climatic vulnerability, decreasing arable land, high salinity, scarce fresh water resources, food insecurity, overpopulation, energy demand and poverty.

2 Materials and methods

2.1 Chemicals

All chemicals used in the present study were of analytical grade and purchased from authentic suppliers of Sigma, Daejung, Acros Organics and Merck Ltd.

2.1.1 Thermophilic cellulases

The genetically engineered thermophilic cellulases were obtained from the project entitled "Production of bioenergy from plant biomass" at Institute of Industrial Biotechnology, GC University Lahore, Pakistan.

2.1.2 Substrate

The halophyte *Atriplex crassifolia* was collected in early January 2021 from the fields of KSK campus, GCU Lahore, Punjab Pakistan. The biomass was grinded into fine powder and dried in hot air oven at 105°C for 2 h. The dried biomass was sieved and stored in labelled zip-lock bags at room temperature for further use.

2.2 Reagent preparation and pre-treatment

2.2.1 Alkali pre-treatment

Alkali pre-treatment of *Atriplex crassifolia* was out using different concentrations of NaOH (1%, 2%, 3%, 4% and 5%) as the pre-treatment reagents. Oven dried substrates were taken in an amount of 5 g and mixed in 50 mL of NaOH solution with varying concentrations, using 100 mL air tight reagent bottles. The screw capped reagent bottles were subjected to a temperature of 121°C for a time period of 60 min in an autoclave. Pre-treated substrates were filtered and washed by distilled water twice to eliminate attached alkali and other components produced during the pre-treatment. The substrates were air-dried. The dried substrates were put in sterilized polythene zipper bags for further use (Binod et al., 2011).

2.2.2 Acid pre-treatment

Acid pre-treatment of *Atriplex crassifolia* was carried out using different concentrations of HCl (1%, 2%, 3%, 4% and 5%) as the pre-treatment reagents. Oven dried substrates were taken in an amount of 5 g and mixed in 50 mL of HCl solution with varying concentrations, using 100 mL airtight reagent bottles. The screw capped reagent bottles were subjected to a temperature of 121°C for 60 min in an autoclave. Following pre-treatment, the substrates were filtered and washed twice using distilled water to remove any acidic content or other byproducts formed during pre-treatment. The substrates were allowed to air dry. The dried substrates were stored in sterilized polythene zipper bags for further use (Binod et al., 2011).

2.2.3 Microwave pre-treatment

Microwave pre-treatment of *Atriplex crassifolia* was carried out by varying residence times. Substrates (1 g) were weighed and placed in five different airtight reagent bottles of 50 mL capacity, having 10 mL of distilled water each. The respective airtight bottles were subjected to microwave irradiation for residence time of 1 min, 2 min, 3 min, 4 min and 5 min, respectively. Following pre-treatment, the substrates were filtered. Air dried substrates were stored in sterilized zipper bags for further use (Binod et al., 2011).

2.3 Biomass compositional analysis

The untreated and pretreated biomass was analysed for lignocellulosic content using Technical Association of Pulp and Paper Industry (TAPPI) standards.

2.4 Enzymatic saccharification of pre-treated *Atriplex crassifolia* biomass

The enzymatic saccharification of pre-treated biomass *Atriplex crassifolia* was carried out by adding 0.25 g of pre-treated substrate in a screw-capped reagent bottle. For enzymatic hydrolysis, Endo-1,4-β-glucanase (200 U) was added to both experimental and control (without substrate) reagent bottles. Both the reagent bottles were incubated at 75°C in a shaking water bath with rpm set at 50 for a period of 2 h. Next, Exo-1,4-β-glucanase (400 U) was added to the same reagent bottles and after incubating the mixture for another 2 h, β-1,4-glucosidase (1000 U) was added to both the reagent bottles. The samples (1 mL) were withdrawn after regular intervals of 1 h to note the release of reducing sugars *via* DNS method, using straight line equation obtained from the standard curve. The percentage saccharification was determined by using Vallander and Eriksson (1987) proposed equation;

$$\%\,\textbf{\textit{Saccharification}} = \frac{\textbf{\textit{R.S}} \times \textbf{\textit{V}} \times \textbf{\textit{F1}}}{\textbf{\textit{M}} \times \textbf{\textit{F2}}} \times \textbf{100}$$

2.5 Optimization of physicochemical parameters to enhance enzymatic saccharification

The physicochemical parameters i.e., incubation time, incubation temperature, substrate concentration, concentration of endo-1,4-β-glucanase, exo-1,4-β-glucanase and β-glucosidase

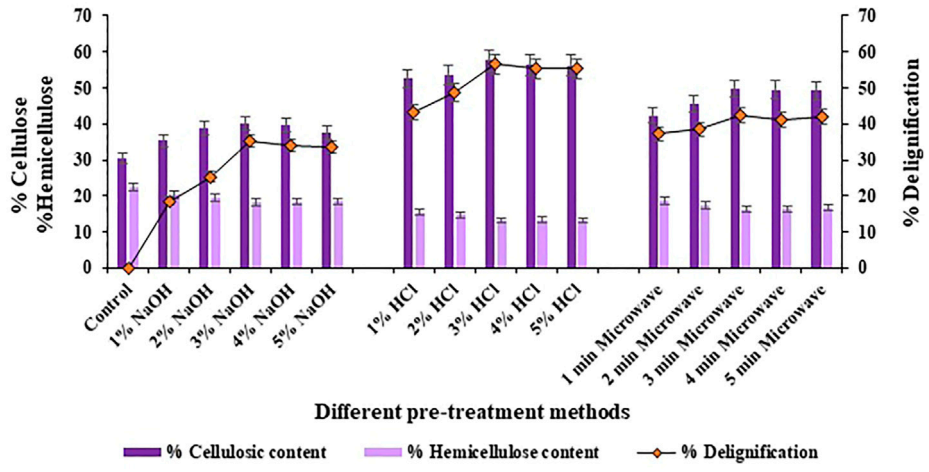

FIGURE 1
Compositional analysis of halophyte *Atriplex crassifolia* before and after pre-treatment with different methods.

affecting the rate of enzymatic hydrolysis were subjected to optimization studies. One variable at a time experimental design was chosen for the optimization of saccharification parameters.

2.5.1 Sequential addition of cellulases

In sequential addition of cellulases, beginning with the addition of Endo-1,4-β-glucanase (200 U) to the screw-capped reagent bottle enclosing the pre-treated substrate i.e., halophyte *Atriplex crassifolia* (0.25 g), the reaction was carried out in a shaking water bath set at 75°C and 50 rpm. After 2 h of incubation time, Exo-1,4-β-glucanase (400 U) was added to the same reagent bottle for another 2 h. Next, the cellulase i.e., β-1,4-glucosidase was added to the same reagent bottle and incubated for a period of 2 h. In this way, in sequential addition of cellulases, each cellulase was added one after the other and each was incubated for a period of 2 h.

2.5.2 Simultaneous addition of cellulases

Whereas, in simultaneous addition of cellulases, all the three cellulases i.e., Endo-1,4-β-glucanase (200 U), Exo-1,4-β-glucanase (400 U) and β-1,4-glucosidase (1000 U) were added altogether to the screw-capped reagent bottle enclosing the pre-treated substrate i.e., halophyte *Atriplex crassifolia* (0.25 g). The saccharification mixture containing cellulases and the substrate was incubated for a period of 6 h, in a shaking water bath set at 75°C and 50 rpm.

2.6 Ethanol fermentation

The saccharified slurry was subjected to ethanol fermentation following the method of Nawaz et al. (2022).

2.7 Statistical analysis

All the experiment were run in triplicates and subjected to statistical analysis using SPSS version 16.00. Error bars in the figures of results section depicted standard deviation (± SD) among the replicates run, varying significantly at $p < 0.05$.

3 Results and Discussions

3.1 Biomass compositional analysis

The results of compositional analysis of halophyte *Atriplex crassifolia* after subjecting it to three different pre-treatment techniques revealed that the maximum rate of delignification (56.6%; $p < 0.05$), the maximum cellulosic content (57.7%; $p < 0.05$) and the maximum degradation of hemicellulose was shown by the halophyte pre-treated using 3% hydrochloric acid as the pre-treatment reagent, as shown in Figure 1. Acids when used as pre-treatment reagents are quite competent. Although, they work excellent for the degradation of hemicellulosic content of the biomass, but also contribute well in the removal of lignin, hence enhancing the ease of availability of cellulose for the enzymes, in turn maximizing the release of fermentable saccharides (Sahoo et al., 2018). Few important considerations regarding the associated parameters ensure the appropriate applicability of this method; this includes residence time, pre-treatment temperature, substrate concentration and acid strength. The use of acids maximize the cleaving of the bonds within recalcitrant lignocellulosic structure and ensure effective conversion of the cellulosic material into reducing sugars (Solarte-Toro et al., 2019).

3.2 Enzymatic saccharification of pre-treated *Atriplex crassifolia* biomass

Comparison of the overall saccharification yields of the halophyte *Atriplex crassifolia* pre-treated using different methods revealed that the maximum saccharification rate (39.5%; $p < 0.05$) as well as the maximum yield of reducing sugars was shown by the halophyte pre-treated using 3%

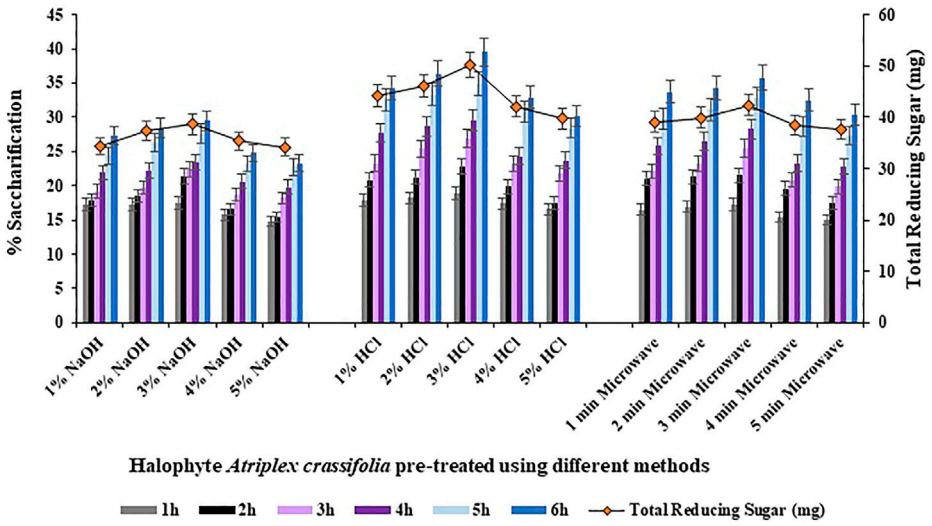

FIGURE 2
Saccharification studies using halophyte *Atriplex crassifolia* pre-treated with different methods.

hydrochloric acid as the pre-treatment reagent, as shown in Figure 2. The results of enzymatic saccharification were parallel to the results of compositional analysis. Therefore, the halophyte *Atriplex crassifolia* pre-treated using 3% hydrochloric acid was chosen for further experiments. The results were in line with those found by Kumar et al. (2020), who worked on varied pre-treatment methods to efficiently convert *Lantana camara* stem into reducing sugars. Of all the pre-treatment methods used, the substrate subjected to pre-treatment using acid in an autoclave, was found to give maximum yield of reducing sugar upon enzymatic hydrolysis. The results were also consistent with Ansari et al. (2021), who screened different halophytes for enzymatic hydrolysis. Results of saccharification revealed that acid pre-treated *P. karka* yielded maximum monosaccharides. Selection of the best pre-treatment method is the key to successful enzymatic hydrolysis, owing to the fact that saccharification of pre-treated substrate is greatly increased when the accessibility and ease of cellulases to the cellulosic fibers is ensured (López-Linares et al., 2015). To carry out pre-treatment of lignocellulosic feedstock, dilute acid method is most frequently studied and is believed to be an economical process for industrial scale production of bioethanol utilizing lignocellulosic biomass (Ruiz et al., 2013).

3.3 Optimization of physicochemical parameters affecting saccharification

3.3.1 Effect of cellulases addition method on saccharification

Saccharification was conducted using both, sequential addition of cellulases and by simultaneous addition of cellulases, in order to evaluate the best method of cellulases addition to achieve maximum rate of enzymatic saccharification. Overall, simultaneously adding the cellulases resulted in improved hydrolysis (42.4%; $p < 0.05$) of the substrate i.e., pre-treated halophyte *Atriplex crassifolia* compared to sequential addition of cellulases (39.1%; $p < 0.05$), as shown in Figures 3, 4, respectively. This might be due to the increased activity of cellulases when they act together synergistically, rather than individually. These results were found consistent with Mcintosh and Vancov (2011), who also simultaneously added three enzymes i.e., cellulase, β-glucosidase and xylanase in combination to conduct saccharification of wheat straw, and found favorable results. The synergistic action of enzymes by simultaneous addition of cellulases was found to increase the total sugar release and it was also found to reduce the enzyme loadings 3-fold, making the process economical. Hence, the next optimization reactions of saccharification were conducted using simultaneous method of cellulases addition.

3.3.2 Effect of incubation time on saccharification

Different incubation times of 1, 2, 3, 4, 5, 6, 7 and 8 h were analyzed for the bioconversion of substrate i.e., halophyte *Atriplex crassifolia* into saccharides. Maximum bioconversion of (42.5%; $p < 0.05$) was detected after 6 h of incubating the reaction mixture that contained the cellulases and the pre-treated substrate i.e., *Atriplex crassifolia*, as depicted in Figure 5. Increasing the time resulted in a decrease in the yield of saccharification, as evident from Figure 5. It might be because of the reason that with additional rise in incubation time, either the process of product inhibition comes into action due to accretion of glucose and cellobiose, or due to less availability of free cellulose with the passage of time. Results of this research are in accordance with those of Aftab et al. (2017) that highest saccharification of sugarcane bagasse was observed after 6 h of incubation using thermophilic cellulases. These alike results can be attributed to the reason that thermophilic cellulases act more energetically and that when an amalgam of enzymes is employed for saccharification, the overall reaction time for hydrolysis is lessened (Shokrkar and Ebrahimi, 2018).

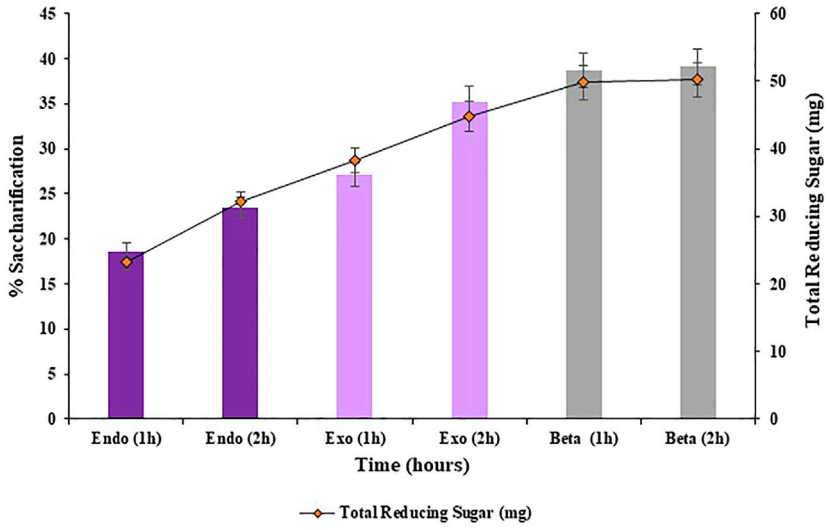

FIGURE 3
Saccharification of pre-treated halophyte *Atriplex crassifolia* using sequential addition of cellulases.

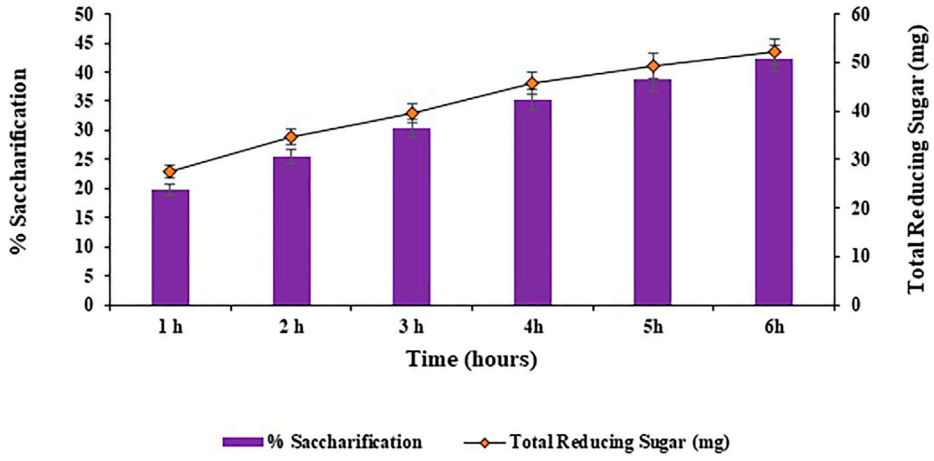

FIGURE 4
Saccharification of pre-treated halophyte *Atriplex crassifolia* using simultaneous addition of cellulases.

3.3.3 Effect of incubation temperature on saccharification

Different incubation temperatures i.e. 70, 75, 80, 85°C and 90°C were analyzed for the bioconversion of substrate i.e., *Atriplex crassifolia* into saccharides. Maximum bioconversion of 42.7% ($p < 0.05$) was observed at 75°C after 6 h of incubating the reaction mixture that contained the cellulases and the pre-treated substrate i.e., *Atriplex crassifolia*, as shown in Figure 6. Increasing the temperature began to decrease the yield of saccharification, as shown in Figure 6. Hence, temperature of 75°C was optimized for the saccharification of pre-treated halophyte *Atriplex crassifolia*. Next saccharification experiments for the optimization of the remaining physicochemical parameters were conducted at temperature 75°C for a period of 6 h. This might be because enzymes work best at their optimum temperature. As the enzymes used in this study were cloned using thermophilic microorganisms, the maximum activity was exhibited at a high temperature. Further increase in temperature resulted in decreased saccharification, which might be due to enzyme denaturation (Saha et al., 2005). A temperature higher or lower compared to the optimum results in reduced transport across cell wall or enzyme denaturation (Dutt and Kumar 2014). Increasing both, the incubation time as well as temperature increases the saccharification rates, but upto a certain optimum point after which, the enzymes tend to lose their stability and activity, and the saccharification yields tend to decrease (Mondal et al., 2021). Majority of the hyperthermophilic microorganisms reported in

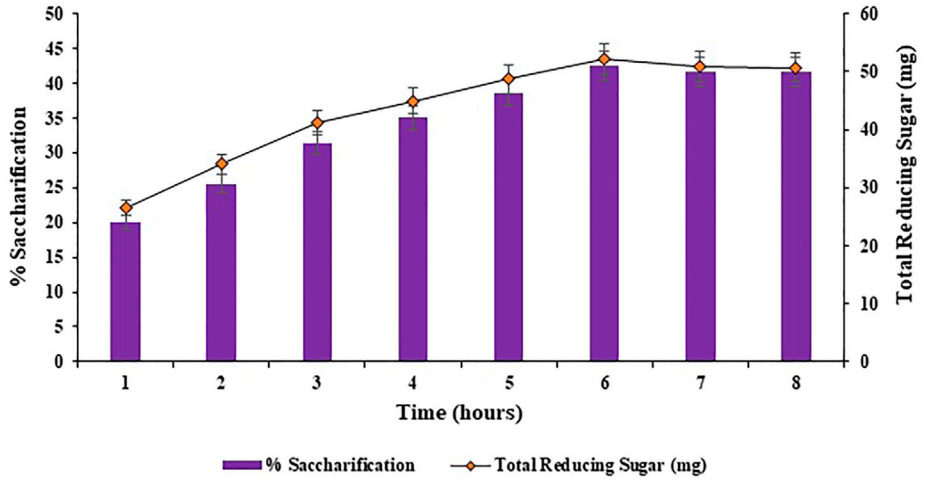

FIGURE 5
Effect of incubation time on saccharification of pre-treated halophyte *Atriplex crassifolia*.

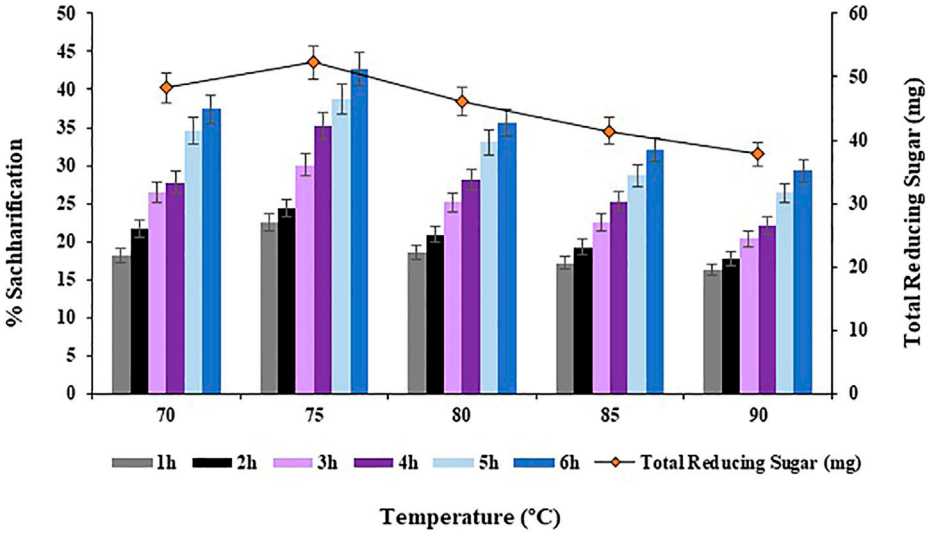

FIGURE 6
Effect of incubation temperature on saccharification of pre-treated halophyte *Atriplex crassifolia*.

literature do not efficiently cleave crystalline cellulose at temperatures <75 °C, because of the lack of carbohydrate-binding modules (Blumer-Schuette et al., 2008; Maki et al., 2009; Graham et al., 2011).

3.3.4 Effect of substrate concentration on saccharification

The concentration of substrate i.e., *Atriplex crassifolia* was varied i.e. 0.20, 0.25, 0.30, 0.35, 0.40, 0.45 and 0.50 g in order to achieve maximum saccharification. On comparing the saccharification yields achieved using the abovementioned concentrations of substrate, the highest saccharification yield of 48.8% ($p < 0.05$) was observed using 0.40 g of substrate at 75°C after 6 h of incubating the reaction mixture containing the cellulases and the pre-treated substrate i.e., *Atriplex crassifolia*, as depicted in Figure 7. Increasing the concentration of substrate while keeping other parameters constant, resulted in no additional increase in the yield of saccharification, as evident from Figure 7. Hence, substrate i.e., pre-treated halophyte *Atriplex crassifolia* concentration of 0.40 g was found optimum for maximum saccharification. Next saccharification experiments for the optimization of the remaining physicochemical parameters were conducted using 0.40 g of substrate i.e., pre-treated halophyte *Atriplex crassifolia* at temperature 75°C for a period of 6 h. One of the possibilities could be that all the pre-available enzymes ended up as enzyme-substrate complexes, and

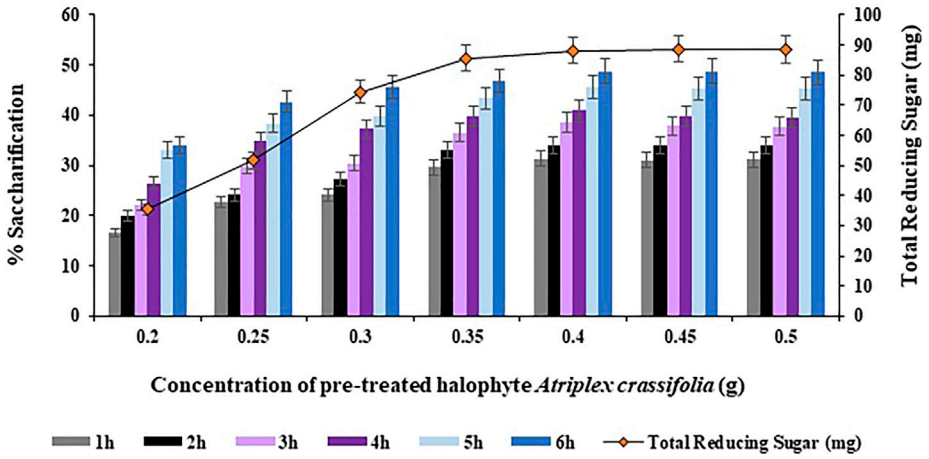

FIGURE 7
Effect of substrate i.e., pre-treated halophyte *Atriplex crassifolia* concentration on saccharification.

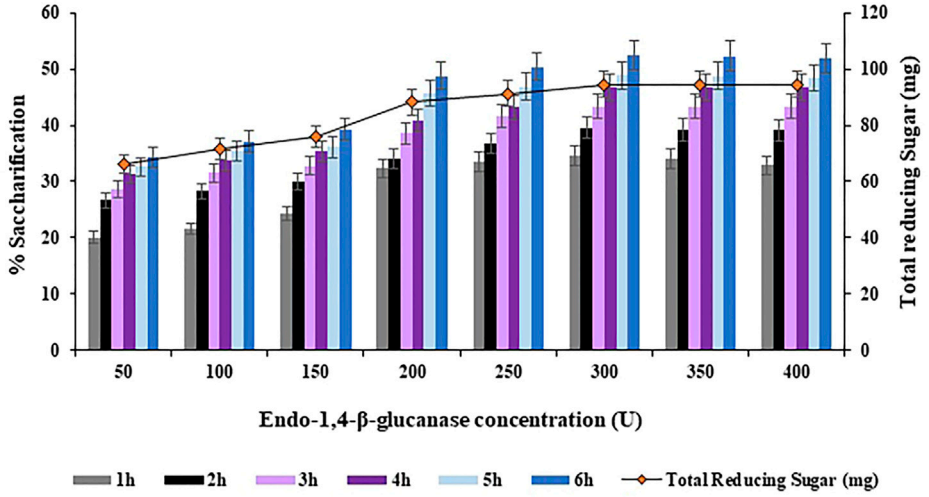

FIGURE 8
Effect of Endo-1,4-β-glucanase concentration on saccharification of pre-treated halophyte *Atriplex crassifolia*.

no additional free enzymes must be available to bind with the rest of the substrate, so as a result, exceeding the substrate concentration brings no change (Levine et al., 2011). Increased substrate concentration might also result in improper mixture ratio leading to lower yields because of improper interaction of enzymes with substrates. Besides that, substrate in a less quantity may become the limiting factor and prevent the bioconversion of substrate. The results were observed to be different compared to Bhagwat et al. (2016), who found 2 g of substrate to give best results for the bioconversion of *Parthenium hysterophorus*, by using a mixture of two enzymes i.e., cellulase and β-glucosidase. This is due to the reason that the optimum concentration of substrate differs depending on the substrate type and the enzymes in use.

3.3.5 Effect of endo-1,4-β-glucanase, exo-1,4-β-glucanase and β-1,4-glucosidase concentration on saccharification

The concentration of Endo-1,4-β-glucanase was varied in a range of 50–400 U with an increment of 50 U in order to achieve maximum saccharification of the halophyte *Atriplex crassifolia*. On comparing the saccharification yields achieved using the abovementioned concentrations of Endo-1,4-β-glucanase, the highest saccharification yield of 52.4% ($p < 0.05$) was obtained with Endo-1,4-β-glucanase concentration of 300 U, using 0.40 g of substrate at 75°C after 6 h of incubation, as depicted in Figure 8. Increasing the concentration of Endo-1,4-β-glucanase while keeping other parameters constant, resulted in no additional increase in the yield of saccharification.

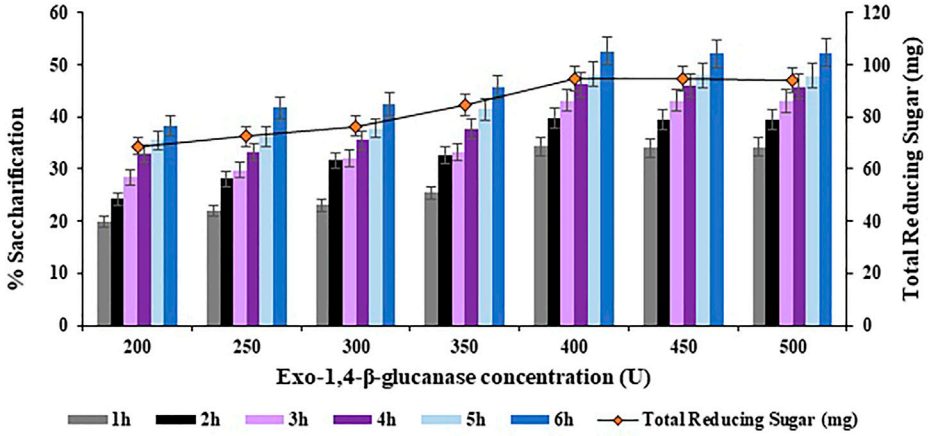

FIGURE 9
Effect of Exo-1,4-β-glucanase concentration on saccharification of pre-treated halophyte *Atriplex crassifolia*.

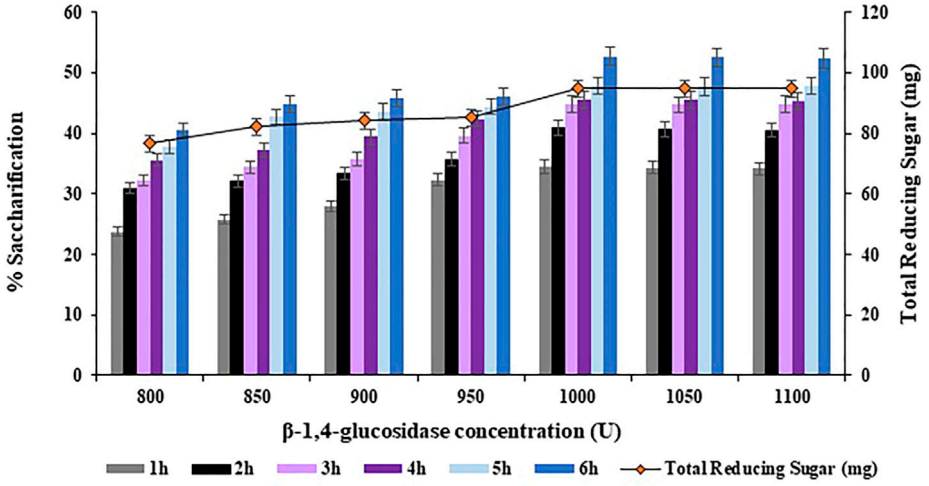

FIGURE 10
Effect of β-1,4-glucosidase concentration on saccharification of pre-treated halophyte *Atriplex crassifolia*.

The concentration of Exo-1,4-β-glucanase was varied in a range of 200–500 U with an increment of 50 U in order to achieve maximum saccharification of the halophyte *Atriplex crassifolia*. On comparing the saccharification yields achieved using the abovementioned concentrations of Exo-1,4-β-glucanase, the highest saccharification yield i.e. 52.6% ($p < 0.05$) was obtained with Exo-1,4-β-glucanase concentration of 400 U, along with Endo-1,4-β-glucanase concentration of 300 U, using 0.40 g of substrate at 75°C after 6 h of incubation, as depicted in Figure 9. Increasing the concentration of Exo-1,4-β-glucanase while keeping other parameters constant, resulted in no additional increase in the yield of saccharification, as evident from Figure 9. Hence, Exo-1,4-β-glucanase concentration of 400 U was found optimum for maximum saccharification of the halophyte *Atriplex crassifolia*.

The concentration of β-1,4-glucosidase was varied in a range of 800–1100 U with an increment of 50 U in order to achieve maximum saccharification of the halophyte *Atriplex crassifolia*. The highest saccharification yield of 52.7% ($p < 0.05$) was obtained with β-1,4-glucosidase concentration of 1000 U, along with Endo-1,4-β-glucanase concentration of 300 U, and Exo-1,4-β-glucanase concentration of 400 U, using 0.40 g of substrate at 75°C after 6 h of incubation, as depicted in Figure 10. Increasing the concentration of β-1,4-glucosidase while keeping other parameters constant, resulted in no additional increase in saccharification yield, as evident from Figure 10. Hence, Exo-1,4-β-glucanase concentration of 1000 U was found optimum for maximum saccharification of the halophyte *Atriplex crassifolia*.

Maximum saccharification of halophyte *Atriplex crassifolia* i.e. 52.7% was obtained with Endo-1,4-β-glucanase concentration of

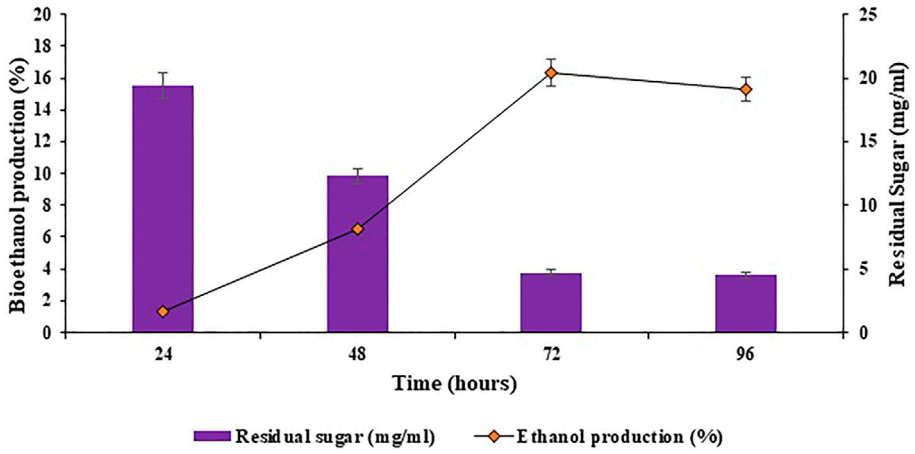

FIGURE 11
Production of bioethanol using the reducing sugar slurry obtained after optimization of physicochemical parameters for saccharification.

300 U (Figure 8), Exo-1,4-β-glucanase concentration of 400 U (Figure 9) and with β-1,4-glucosidase concentration of 1000 U (Figure 10), when added simultaneously to conduct enzymatic hydrolysis, keeping other parameters as optimized above. Increasing the concentration of enzymes further resulted in constant saccharification yield, might be due to the onset of saturation point. As the time passes, the substrate would be converted into product, using up the enzymes' active sites (Yang and Wyman, 2004). Hence, an optimum amount of each of the three enzymes is a pre-requisite to increase percentage saccharification. Enzyme loading is directly linked to the yield of reducing sugars, where higher enzyme loading yields greater quantities of reducing sugars, but upto a certain extent (Mota et al., 2021). Yu and Li (2015) obtained slightly different results, who utilized 200 U of an enzyme mixture sourced from *Gracilibacillus* sp. SK1, exhibiting a collective activity of endoglucanase, exoglucanase and β-glucosidase, for the saccharification of lignocellulosic biomas. The difference in the enzyme concentration might be because the optimum ratio of enzymes required to carry out hydrolysis may vary with each substrate and the source of enzymes being used (Chandel et al., 2010).

3.4 Bioethanol production

The slurry containing reducing sugars obtained after optimization of physicochemical parameters for saccharification was utilized in submerged fermentation, in replacement to glucose, for bioethanol production. The submerged fermentation for ethanol production was done in fermentation medium by making use of the reducing sugar slurry. The fermentation medium was inoculated with 2.5% of seed inoculum of *Saccharomyces cerevisiae,* under aseptic conditions. The inoculated reagent bottles were incubated at 30°C and 180 rpm for 96 h. The samples were harvested after regular intervals to estimate the ethanol content during fermentation. Maximum bioethanol production percentage observed was 16.33% at 72 h, as shown in Figure 11. Exceeding the incubation time further did not exceed the rate of bioethanol production, as evident in Figure 11. This might be because of the unavailability of enough reducing sugar to produce more bioethanol. Cotana et al. (2015) obtained comparable results for bioethanol production using *Phragmites australis* (common reed) as the feedstock, the highest yield of ethanol noted was 16.56 g ethanol/100 g of sample.

4 Conclusion and future recommendations

It can be concluded from the study that the halophyte *Atriplex crassifolia* owing to its high cellulosic content after pre-treatment using dilute acid method, yields substantial amount of reducing sugars and high saccharification rates when subjected to enzymatic hydrolysis using thermophilic cellulases, under optimized reaction conditions. Hence, the halophyte *Atriplex crassifolia* is a beneficial substrate that can be utilized to extract fermentable saccharides for bioethanol production.

As a means to enhance the overall yield and the techno-economic feasibility of the process, certain aspects must be taken into consideration:

1. Every component of the halophyte *Atriplex crassifolia* encompasses the ability to produce industrially important products. It will require additional research to discover its full potential.
2. The plantation of suitable species of halophytes with low lignin contents will enable easy enzymatic action on the main cellulosic structure, and result in improved saccharification yields, hence add to the techno-economic feasibility of the overall bioconversion process.
3. Research on more competent enzyme cocktails is needed with more powerful and compatible enzymes to enhance the efficiency of the bioconversion process.

4. Metabolic engineering can be applied to produce the enzymes required for pre-treatment, saccharification and fermentation from a single microorganism. This could reduce the process time; hence add to the cost-effectiveness of the process and ease of application.
5. Moreover, the most common pre-treatment procedures existent are not environmentally benign. Although different green processes have evolved for the pre-treatment of biomass that offer promising benefits, however, their wide-scale applicability at industrial level demands high capital cost. Therefore, extensive research is a requirement to develop the most applicable techniques for pre-treatment that ensure ease of applicability along with affordability.

Data availability statement

The original contributions presented in the study are included in the article/supplementary material, further inquiries can be directed to the corresponding author.

Author contributions

AN, KQ, and YF conceptualized the study and developed and conducted the research idea. IH and KJ helped in manuscript preparation. AN, KQ, HM, and RH helped in manuscript proofreading and statistical analysis.

Funding

The authors acknowledge the financial support of the Doctoral Scientific Research Foundation of Hangzhou Medical College (0004F1RCYJ 1905).

Conflict of interest

The authors declare that the research was conducted in the absence of any commercial or financial relationships that could be construed as a potential conflict of interest.

Publisher's note

All claims expressed in this article are solely those of the authors and do not necessarily represent those of their affiliated organizations, or those of the publisher, the editors and the reviewers. Any product that may be evaluated in this article, or claim that may be made by its manufacturer, is not guaranteed or endorsed by the publisher.

References

Abideen, Z., Ansari, R., and Khan, M. A. (2011). Halophytes: Potential source of ligno-cellulosic biomass for ethanol production. *Biomass Bioenerg.* 35 (5), 1818–1822. doi:10.1016/j.biombioe.2011.01.023

Aftab, M. N., Zafar, A., and Awan, A. R. (2017). Expression of thermostable β-xylosidase in *Escherichia coli* for use in saccharification of plant biomass. *Bioengineered* 8 (5), 665–669. doi:10.1080/21655979.2016.1267884

Ansari, I., Ejaz, U., Abideen, Z., Gulzar, S., Syed, M. N., Liu, J., et al. (2021). Wild halophytic *Phragmites karka* biomass saccharification by bacterial enzyme cocktail. *Front. Microbiol.* 12, 714940. doi:10.3389/fmicb.2021.714940

Arora, S., Singh, Y. P., Vanza, M., and Sahni, D. (2016). Bio-remediation of saline and sodic soils through halophilic bacteria to enhance agricultural production. *J. Soil Water Conserv.* 15 (4), 302–305. doi:10.5958/2455-7145.2016.00027.8

Bhagwat, S., Girma, A. D., and Kumar, A. (2016). Statistical optimization of enzymatic saccharification of acid pretreated *Parthenium hysterophorus* biomass using response surface methodology. *Biofuels* 7 (5), 501–509. doi:10.1080/17597269.2016.1163214

Bhatia, S. K., Jagtap, S. S., Bedekar, A. A., Bhatia, R. K., Patel, A. K., Pant, D., et al. (2020). Recent developments in pretreatment technologies on lignocellulosic biomass: Effect of key parameters, technological improvements and challenges. *Bioresour. Technol.* 300, 122724. doi:10.1016/j.biortech.2019.122724

Binod, P., Janu, K. U., Sindhu, R., and Pandey, A. (2011). "Hydrolysis of lignocellulosic biomass for bioethanol production," in *Biofuels* (Berlin: Academic Press), 229–250. doi:10.1016/B978-0-12-385099-7.00010-3

Blumer-Schuette, S. E., Kataeva, I., Westpheling, J., Adams, M. W., and Kelly, R. M. (2008). Extremely thermophilic microorganisms for biomass conversion: Status and prospects. *Curr. Opin. Biotechnol.* 19 (3), 210–217. doi:10.1016/j.copbio.2008.04.007

Brown, J. J. (2019). "Considerations for producing bioenergy from halophyte feedstocks," in *Biorefinery* (Cham: Springer), 657–668. doi:10.1007/978-3-030-10961-5_28

Champreda, V., Mhuantong, W., Lekakarn, H., Bunterngsook, B., Kanokratana, P., Zhao, X. Q., et al. (2019). Designing cellulolytic enzyme systems for biorefinery: From nature to application. *J. Biosci. Bioeng.* 128 (6), 637–654. doi:10.1016/j.jbiosc.2019.05.007

Chandel, A. K., Singh, O. V., Chandrasekhar, G., Rao, L. V., and Narasu, M. L. (2010). Key drivers influencing the commercialization of ethanol-based biorefineries. *J. Commer. Biotechnol.* 16 (3), 239–257. doi:10.1057/jcb.2010.5

Chavan, S., and Gaikwad, A. (2021). Optimization of enzymatic hydrolysis of bamboo biomass for enhanced saccharification of cellulose through Taguchi orthogonal design. *J. Environ. Chem. Eng.* 9 (1), 104807. doi:10.1016/j.jece.2020.104807

Chen, Y., Stevens, M. A., Zhu, Y., Holmes, J., and Xu, H. (2013). Understanding of alkaline pretreatment parameters for corn stover enzymatic saccharification. *Biotechnol. Biofuels.* 6 (1), 8–10. doi:10.1186/1754-6834-6-8

Cotana, F., Cavalaglio, G., Pisello, A. L., Gelosia, M., Ingles, D., and Pompili, E. (2015). Sustainable ethanol production from common reed (*Phragmites australis*) through simultaneuos saccharification and fermentation. *Sustainability* 7 (9), 12149–12163. doi:10.3390/su70912149

Den, W., Sharma, V. K., Lee, M., Nadadur, G., and Varma, R. S. (2018). Lignocellulosic biomass transformations via greener oxidative pretreatment processes: Access to energy and value-added chemicals. *Front. Chem.* 6, 141. doi:10.3389/fchem.2018.00141

Dutt, D., and Kumar, A. (2014). Optimization of cellulase production under solid-state fermentation by *Aspergillus flavus* (AT-2) and *Aspergillus niger* (AT-3) and its impact on stickies and ink particle size of sorted office paper. *Cell. Chem. Technol.* 48 (3-4), 285–298.

Faizal, A., Sembada, A. A., and Priharto, N. (2021). Production of bioethanol from four species of duckweeds (*Landoltia punctata, Lemna aequinoctialis, Spirodela polyrrhiza*, and *Wolffia arrhiza*) through optimization of saccharification process and fermentation with *Saccharomyces cerevisiae*. *Saudi J. Biol. Sci.* 28 (1), 294–301. doi:10.1016/j.sjbs.2020.10.002

Flowers, T. J., and Colmer, T. D. (2008). Salinity tolerance in halophytes. *New Phytol.* 179 (4), 945–963. doi:10.1111/j.1469-8137.2008.02531.x

Graham, J. E., Clark, M. E., Nadler, D. C., Huffer, S., Chokhawala, H. A., Rowland, S. E., et al. (2011). Identification and characterization of a multidomain hyperthermophilic cellulase from an archaeal enrichment. *Nat. Commun.* 2 (1), 375–379. doi:10.1038/ncomms1373

Hassan, S. S., Williams, G. A., and Jaiswal, A. K. (2018). Emerging technologies for the pretreatment of lignocellulosic biomass. *Bioresour. Technol.* 262, 310–318. doi:10.1016/j.biortech.2018.04.099

Hingsamer, M., and Jungmeier, G. (2019). "Biorefineries," in *The role of bioenergy in the bioeconomy* (Berlin: Academic Press), 179–222. doi:10.1016/B978-0-12-813056-8.00005-4

Joshi, A., Kanthaliya, B., and Arora, J. (2020). Halophytes: The nonconventional crops as source of biofuel production *Handbook of halophytes: From molecules to ecosystems towards biosaline agriculture*. Berlin, Germany: Springer, 1–28. doi:10.1007/978-3-030-17854-3_126-1

Kucharska, K., Słupek, E., Cieśliński, H., and Kamiński, M. (2020). Advantageous conditions of saccharification of lignocellulosic biomass for biofuels generation via

fermentation processes. *Chem. Pap.* 74 (4), 1199–1209. doi:10.1007/s11696-019-00960-1

Kumar, A. K., and Sharma, S. (2017). Recent updates on different methods of pretreatment of lignocellulosic feedstocks: A review. *Bioresour. Bioprocess.* 4 (1), 7–19. doi:10.1186/s40643-017-0137-9

Kumar, A., Singh, S., Rajulapati, V., and Goyal, A. (2020). Evaluation of pre-treatment methods for *Lantana camara* stem for enhanced enzymatic saccharification. *3 Biotech.* 10 (2), 37–11. doi:10.1007/s13205-019-2029-5

Levine, S. E., Fox, J. M., Clark, D. S., and Blanch, H. W. (2011). A mechanistic model for rational design of optimal cellulase mixtures. *Biotechnol. Bioeng.* 108 (11), 2561–2570. doi:10.1002/bit.23249

Li, B., Yang, T., Li, R., and Kai, X. (2020). Co-generation of liquid biofuels from lignocellulose by integrated biochemical and hydrothermal liquefaction process. *Energy* 200, 117524. doi:10.1016/j.energy.2020.117524

López-Linares, J. C., Ballesteros, I., Tourán, J., Cara, C., Castro, E., Ballesteros, M., et al. (2015). Optimization of uncatalyzed steam explosion pretreatment of rapeseed straw for biofuel production. *Bioresour. Technol.* 190, 97–105. doi:10.1016/j.biortech.2015.04.066

Lyu, H., Zhang, J., Zhou, J., Shi, X., Lv, C., and Geng, Z. (2019). A subcritical pretreatment improved by self-produced organic acids to increase xylose yield. *Fuel Process. Technol.* 195, 106148. doi:10.1016/j.fuproc.2019.106148

Maki, M., Leung, K. T., and Qin, W. (2009). The prospects of cellulase-producing bacteria for the bioconversion of lignocellulosic biomass. *Int. J. Biol.* 5 (5), 500–516. doi:10.7150/ijbs.5.500

McIntosh, S., and Vancov, T. (2011). Optimisation of dilute alkaline pretreatment for enzymatic saccharification of wheat straw. *Biomass Bioenerg.* 35 (7), 3094–3103. doi:10.1016/j.biombioe.2011.04.018

Meng, X., Bhagia, S., Wang, Y., Zhou, Y., Pu, Y., Dunlap, J. R., et al. (2020). Effects of the advanced organosolv pretreatment strategies on structural properties of woody biomass. *Ind. Crops Prod.* 146, 112144. doi:10.1016/j.indcrop.2020.112144

Moioli, E., Salvati, F., Chiesa, M., Siecha, R. T., Manenti, F., Laio, F., et al. (2018). Analysis of the current world biofuel production under a water–food–energy nexus perspective. *Adv. Water Resour.* 121, 22–31. doi:10.1016/j.advwatres.2018.07.007

Mondal, P., Sadhukhan, A. K., Ganguly, A., and Gupta, P. (2021). Optimization of process parameters for bio-enzymatic and enzymatic saccharification of waste broken rice for ethanol production using response surface methodology and artificial neural network–genetic algorithm. *3 Biotech.* 11 (1), 28–18. doi:10.1007/s13205-020-02553-2

Moodley, P., and Kana, E. G. (2019). Bioethanol production from sugarcane leaf waste: Effect of various optimized pretreatments and fermentation conditions on process kinetics. *Biotechnol. Rep.* 22, 00329. doi:10.1016/j.btre.2019.e00329

Mota, T. R., Oliveira, D. M., Simister, R., Whitehead, C., Lanot, A., Dos Santos, W. D., et al. (2021). Design of experiments driven optimization of alkaline pretreatment and saccharification for sugarcane bagasse. *Bioresour. Technol.* 321, 124499. doi:10.1016/j.biortech.2020.124499

Nanda, S., Rana, R., Sarangi, P. K., Dalai, A. K., and Kozinski, J. A. (2018). "A broad introduction to first-, second-, and third-generation biofuels," in *Recent advancements in biofuels and bioenergy utilization* (Singapore: Springer), 1–25. doi:10.1007/978-981-13-1307-3_1

Nawaz, A., Huang, R., Junaid, F., Feng, Y., Haq, I. U., Mukhtar, H., et al. (2022). Sustainable production of bioethanol using levulinic acid pretreated sawdust. *Front. Bioeng. Biotechnol.* 10, 937838. doi:10.3389/fbioe.2022.937838

Padilla-Rascón, C., Ruiz, E., Romero, I., Castro, E., Oliva, J. M., Ballesteros, I., et al. (2020). Valorisation of olive stone by-product for sugar production using a sequential acid/steam explosion pretreatment. *Ind. Crops Prod.* 148, 112279. doi:10.1016/j.indcrop.2020.112279

Paneque, M. (2018). Saltbush biomass for energy. *Agric. Res. Technol.* 15 (2), 001–002. doi:10.19080/artoaj.2018.14.555949

Pellera, F. M., and Gidarakos, E. (2017). Microwave pretreatment of lignocellulosic agroindustrial waste for methane production. *J. Environ. Chem. Eng.* 5 (1), 352–365. doi:10.1016/j.jece.2016.12.009

Rezania, S., Oryani, B., Cho, J., Talaiekhozani, A., Sabbagh, F., Hashemi, B., et al. (2020). Different pretreatment technologies of lignocellulosic biomass for bioethanol production: An overview. *Energy* 199, 117457. doi:10.1016/j.energy.2020.117457

Ruiz, E., Romero, I., Moya, M., Cara, C., Vidal, J. D., and Castro, E. (2013). Dilute sulfuric acid pretreatment of sunflower stalks for sugar production. *Bioresour. Technol.* 140, 292–298. doi:10.1016/j.biortech.2013.04.104

Saha, B. C., Iten, L. B., Cotta, M. A., and Wu, Y. V. (2005). Dilute acid pretreatment, enzymatic saccharification and fermentation of wheat straw to ethanol. *Process Biochem.* 40 (12), 3693–3700. doi:10.1016/j.procbio.2005.04.006

Sahoo, D., Ummalyma, S. B., Okram, A. K., Pandey, A., Sankar, M., and Sukumaran, R. K. (2018). Effect of dilute acid pretreatment of wild rice grass *(Zizania latifolia)* from Loktak Lake for enzymatic hydrolysis. *Bioresour. Technol.* 253, 252–255. doi:10.1016/j.biortech.2018.01.048

Shahid, S. A., Zaman, M., and Heng, L. (2018). "Soil salinity: Historical perspectives and a world overview of the problem," in *Guideline for salinity assessment, mitigation and adaptation using nuclear and related techniques* (Cham: Springer). doi:10.1007/978-3-319-96190-3_2

Shen, J., Zhang, J., Wang, W., Liu, G., and Chen, C. (2020). Assessment of pretreatment effects on anaerobic digestion of switchgrass: Economics-energy-environment (3E) analysis. *Ind. Crops Prod.* 145, 111957. doi:10.1016/j.indcrop.2019.111957

Shokrkar, H., and Ebrahimi, S. (2018). Synergism of cellulases and amylolytic enzymes in the hydrolysis of microalgal carbohydrates. *Biofuel Bioprod. Biorefin.* 12 (5), 749–755. doi:10.1002/bbb.1886

Solarte-Toro, J. C., Romero-García, J. M., Martínez-Patiño, J. C., Ruiz-Ramos, E., Castro-Galiano, E., and Cardona-Alzate, C. A. (2019). Acid pretreatment of lignocellulosic biomass for energy vectors production: A review focused on operational conditions and techno-economic assessment for bioethanol production. *Renew. Sust. Energy Rev.* 107, 587–601. doi:10.1016/j.rser.2019.02.024

Thapa, S., Mishra, J., Arora, N., Mishra, P., Li, H., Hair, J. O., et al. (2020). Microbial cellulolytic enzymes: Diversity and biotechnology with reference to lignocellulosic biomass degradation. *Rev. Environ. Sci. Biotechnol.* 19, 621–648. doi:10.1007/s11157-020-09536-y

Vallander, L., and Eriksson, K. E. (1987). Enzyme recirculation in saccharification of lignocellulosic materials. *Enzyme Microb. Technol.* 9 (12), 714–720. doi:10.1016/0141-0229(87)90030-5

Vu, H. P., Nguyen, L. N., Vu, M. T., Johir, M. A. H., McLaughlan, R., and Nghiem, L. D. (2020). A comprehensive review on the framework to valorise lignocellulosic biomass as biorefinery feedstocks. *Sci. Total Environ.* 743, 140630. doi:10.1016/j.scitotenv.2020.140630

Yang, B., and Wyman, C. E. (2004). Effect of xylan and lignin removal by batch and flowthrough pretreatment on the enzymatic digestibility of corn stover cellulose. *Biotechnol. Bioeng.* 86 (1), 88–98. doi:10.1002/bit.20043

Yu, H. Y., and Li, X. (2015). Alkali-stable cellulase from a halophilic isolate, *Gracilibacillus sp.* SK1 and its application in lignocellulosic saccharification for ethanol production. *Biomass Bioenerg.* 81, 19–25. doi:10.1016/j.biombioe.2015.05.020

Yuan, D., Rao, K., Relue, P., and Varanasi, S. (2011). Fermentation of biomass sugars to ethanol using native industrial yeast strains. *Bioresour. Technol.* 102 (3), 3246–3253. doi:10.1016/j.biortech.2010.11.034

frontiers | Frontiers in Bioengineering and Biotechnology

TYPE Original Research
PUBLISHED 15 March 2023
DOI 10.3389/fbioe.2023.1160698

OPEN ACCESS

EDITED BY
Clemens Kilian Weiss,
Bingen Technical University of Applied Sciences, Germany

REVIEWED BY
Linwu Zhuang,
Jiangsu Ocean University, China
Muhammad Tayyab Akhtar,
Government College University, Lahore, Pakistan

*CORRESPONDENCE
Jing Luo,
597311661@qq.com
Kankan Jiang,
jiangkankan@126.com

SPECIALTY SECTION
This article was submitted to Bioprocess Engineering, a section of the journal Frontiers in Bioengineering and Biotechnology

RECEIVED 07 February 2023
ACCEPTED 06 March 2023
PUBLISHED 15 March 2023

CITATION
Huang R, Xu Y, Kuznetsov BN, Sun M, Zhou X, Luo J and Jiang K (2023), Enhanced hybrid hydrogel based on wheat husk lignin-rich nanocellulose for effective dye removal.
Front. Bioeng. Biotechnol. 11:1160698.
doi: 10.3389/fbioe.2023.1160698

Enhanced hybrid hydrogel based on wheat husk lignin-rich nanocellulose for effective dye removal

Rong Huang[1], Yong Xu[2], Boris N. Kuznetsov[3], Meitao Sun[1], Xin Zhou[2], Jing Luo[2]* and Kankan Jiang[1]*

[1]School of Basic Medical Sciences and Forensic Medicine, Hangzhou Medical College, Hangzhou, China, [2]Jiangsu Co-Innovation Center of Efficient Processing and Utilization of Forest Resources, College of Chemical Engineering, Nanjing Forestry University, Nanjing, China, [3]Institute of Chemistry and Chemical Technology SB RAS, FRC KSC SB RAS, Siberian Federal University, Krasnoyarsk, Russia

Polyvinyl alcohol (PVA) hydrogels were enhanced mechanically through the addition of lignin-rich nanocellulose (LCN), soluble ash (SA) and montmorillonite (MMT) for dye removal. The hybrid hydrogels reinforced with 33.3 wt% of LCN had a 163.0% increase in storage modulus as compared to the PVA/0LCN-33.3SM hydrogel. LCN can be added to the PVA hydrogel to alter its rheological properties. Additionally, hybrid hydrogels were highly efficient in removing methylene blue from wastewater, which was attributed to the synergistic effects of the PVA matrix supporting embedded LCN, MMT, and SA. The adsorption time (0–90 min) showed that the hydrogels containing MMT and SA had high removal efficiency, and the adsorption of methylene blue (MB) by PVA/20LCN-13.3SM was greater than 95.7% at 30°C. It was found that MB efficiency decreased with a high MMT and SA content. Our study provided a new method for the fabrication of polymers-based eco-friendly, low-cost and robust physical hydrogels for the MB removal.

KEYWORDS

dye, adsorption, hybrid hydrogel, lignin-rich nanocellulose, wheat husk

1 Introduction

The uncontrolled releasing of organic dyes into the environment has caused a variety of hazards to humans (Mohammed et al., 2014; Tang et al., 2020). There are several technologies developed for the treatment of hazardous organic dyes from wastewater in order to address this issue (Ge et al., 2022a). The most commonly used technologies are membrane filtration, chemical precipitation, ion exchange, and electrolysis. However, there are several disadvantages associated with these technologies, including their expensiveness, ineffectiveness, and the emission of secondary wastes. Hence, a better approach (i.e., adsorption) could be a cheaper and more effective way to treat organic dyes (El-Dib et al., 2020; Obey et al., 2022).

Biosorbents produced from lignocellulosic biomass like wood and agricultural wastes have recently drawn considerable attention (Freitas et al., 2019). In general, the lignocellulosic biomass particularly those derived from agricultural wastes, can be used to yield a wide range of versatile products at low costs and with substantial sustainability (Han et al., 2015; Chen et al., 2019). Wheat husk (WH), an agricultural by-product abundant throughout the world that contains high amounts of carbohydrates (25.1% cellulose, 21.4%

hemicellulose, and 20.5% lignin), could serve as a promising resource for producing biosorbents for adsorption. Direct combustion of WH results in significant resource waste due to its inefficiency (Ge et al., 2021; Ge et al., 2022b; Liu et al., 2022). In order to maximize the use of lignocellulosic biomass, the hemicellulose of WH is used to prepare xylose-based products such as oligosaccharides (XOS). XOS is composed of a low degree of polymerization of xylan (DP = 2–7) (Otieno and Ahring, 2012). XOS production involves a variety of methods (chemical, enzymatic and auto-hydrolysis). Auto-hydrolysis has been reported as an effective and practical method to produce XOS because of reduced catalyst costs (Carvalho et al., 2013).

When hemicellulose is removed from the WH residue in the XOS production process, the cellulose content of the residue is high (50%–55%). These residues can be used for the preparation of microcrystalline cellulose and nanocellulose. Nanocellulose is produced from cellulose. Most of the literature reports purity cellulose obtained from agricultural residues by chemical pretreatment. In fact, the aim of these treatments is to remove lignin, however, consuming large amounts of chemicals (e.g., sodium hydroxide and sodium chlorite) (Xiao et al., 2022). Therefore, it is conjectured that the production of lignin-containing nanocellulose (LCN) can mitigate environmental issues and difficulties in alkali recovery. Additionally, a low-cost and environmentally friendly pretreatment can also be used to produce LCN directly from WH residues (Bian et al., 2019; Liu et al., 2021). The lignin found in plant biomass may be useful as a binder for other biopolymers and may serve as a component in the production of hydrogels. In addition, since lignin is rich in the active chemical functional groups thus its presence would enhance the adsorption ability of the material (Liu et al., 2020; Gao et al., 2021).

Hydrogel is one of the important materials that widely studied in adsorption research. Hydrogel represents a hydrophilic, highly cross-linked and three-dimensional structure material that has excellent chemical properties. As a result of the presence of hydroxyl groups in each repeating molecular unit of polyvinyl alcohol (PVA), the polymer can form physically cross-linked hydrogels. Despite its adsorption and mechanical properties, hydrogels themselves have poor adsorption and mechanical properties that limit their application in adsorption (Lu et al., 2017; Luo et al., 2021). Although the combination of LCN and PVA may be a potential solution to improve the mechanical properties of PVA hydrogels (Bian et al., 2018). Unfortunately, the adsorption performance of this hydrogel is not promising. Hence, a filler is commonly required to improve the adsorption performance of the hydrogel.

To improve the mechanical properties and adsorption capacity of a hydrogel, we have constructed a composite hydrogel using montmorillonite (MMT) and the soluble ash (SA) as fillers followed by combination with PVA to explore the possibility of such approach. The SA was obtained by washing WH with water to potentially improve its adsorption capacity for organic dyes in the sewage field (Zhou and Wang, 2010; Wu et al., 2019). MMT is phyllosilicate clay; it has a three-dimensional porous structure and a large specific surface area, thus has high adsorption performance (Mao et al., 2022). Moreover, the mechanical properties of the resulted hydrogels can be enhanced which was attributed to the high mechanical strength of MMT (Luo et al., 2021). To the best of our awareness, there are limited literatures on the effects of various SA and MMT contents on the adsorption performance and physical strength of PVA/LCN/SA/MMT hydrogels (PLSM). Therefore, our results would devote to the sum of knowledge in this field while also revealing a new hydrogel based on wheat husk as a cheaper and eco-friendly material for dye removal (Zhang et al., 2022).

TABLE 1 Preparation parameters for PLSM hybrid hydrogels.

Sample	PVA:LCN:SM wt%	Mass ratio of PVA: LCN:SM
PVA	100	1
PVA/0LCN-33.3SM	66.7/0/33.3	1:0:0.50
PVA/3LCN-30.3SM	66.7/3/30.3	1:0.04:0.45
PVA/10LCN-23.3SM	66.7/10/23.3	1:0.15:0.35
PVA/20LCN-13.3SM	66.7/20/13.3	1:0.30:0.20
PVA/33.3LCN-0SM	66.7/33.3/0	1:0.50:0

2 Materials and methods

2.1 Experimental materials

Montmorillonite (MMT) and 99% hydrolyzed polyvinyl alcohol (PVA) with a molecular weight of 125,000 g/mol were procured from Sigma-Aldrich. Wheat husk (WH) was supplied by Shandong Province, China. To remove the insoluble and soluble ash, the raw material was rigorously cleaned for 30 times using distilled water. The soluble ash was collected by rotary evaporation. The washed WH was treated for 60 min at 180°C to obtain XOS and the WH residue (WHR). The LCN (1 wt%) was produced from the WHR through a UH-20 homogenizer at 200 bar (Union-Biotech, China) (Luo et al., 2020).

2.2 Preparation of PLSM hydrogels

About 1.0 g of SA plus 1.5 g of MMT were poured into deionized water (50 mL) under stirring and yielding the 5.0 wt% mixture (i.e., SM). The composite aerogels were prepared by mixing LCN, PVA, and SM. The PVA loading was always fixed at 66.7%, while the LCN loading was 0, 3.0, 10.0, 20.0 and 33.3 wt% with the remaining amount of SM. The control aerogel was prepared by PVA. The total content of the mixture was kept at 4 wt% for all hydrogels (Table 1).

2.3 Characterizations of PLSM hydrogels

The structural characteristics of LCN were measured with a Dimensiona Edge atomic force microscopy (AFM) manufactured by Bruker in Germany. The AFM images were resulted using a tip with a curvature radius of 8 nm and 300 kHz tapping mode. A Quanta 200 scanning electron microscope (SEM) manufactured by FEI in United States was adopted to examine the surface characteristics of PLSM hydrogel. Before the SEM analysis, the moisture of the samples

was minimized followed by sputter-coated with gold to ensure it conducted electricity during analysis. A PerkinElmer Fourier Transform infrared (FTIR) spectrometer operating at wavenumber of 600–4,000 cm^{-1} was applied on the hydrogel samples to study the chemical functional groups. An X-ray diffractometer was utilized to obtain the diffraction patterns of the hydrogels over the 2θ value up to 35°. Additionally, the CrI, which is commonly known as crystallinity index, was then quantified using Eq. 1, consistent with the standard approach (Segal et al., 1959):

$$CrI = \frac{I_{200} - I_{am}}{I_{200}} \times 100 \quad (1)$$

Where I_{200} was the maximum peak intensity of approximately 22.4° at a 2θ angle and I_{am} was the intensity of 18.4° at a 2θ angle.

The hybrid hydrogel was discarded from the 15 × 11 mm sample holder and moisture content was removed at 105°C for 24 h. The water content (W) of the hybrid hydrogel was measured with a decrease in mass according to Eq. 2:

$$W = \frac{m_0 - m_1}{m_0} \times 100 \quad (2)$$

The initial mass (g) of the hydrogel was m_0, while the mass of the treated hydrogel was m_1.

An RS6000 rheometer (HAAKE, Germany) was used to measure the rheological behavior of the hydrogel with a cone plate P20 TiL and Platte P20 TiL. Then, the samples were processed into cylindrical shape with dimension of 20 mm (diameter) and 1 mm (thickness) (Liu et al., 2016).

2.4 Adsorption study of methylene blue (MB) using prepared hydrogels

Adsorption experiments were performed on MB (0.25 mg/mL) at different temperatures in a water bath at 80 rpm. A 0.5 g of the adsorbent dosage was gently mixed to the prepared MB solution (30 mL). Upon completion of the adsorption period, the treated MB solution was sampled into a 0.5 μm syringe. The concentrations after adsorption were immediately quantified at a wavelength of 663 nm using an UV-1800 UV-spectrometer (Japan). Finally, the amount of MB adsorbed was determined according to Eq. 3. All measurements were triplicated with common statistics calculated.

$$Q_t = \frac{V(C_0 - C_e)}{M} \quad (3)$$

C_0 (before) and C_e (after) denote the concentration of the MB solution (mg/L), M (g) represents the adsorbent amount used in adsorption, and V (mL) represents the solution volume.

3 Results and discussion

3.1 Characterization of the prepared PVA/LCN/MMT/SA

SA represents a mixture of inorganic and organic contents with good sorption properties of organic pollutants (Wu et al., 2020). The yield of SA recovered using distilled water treatment was 5.3%

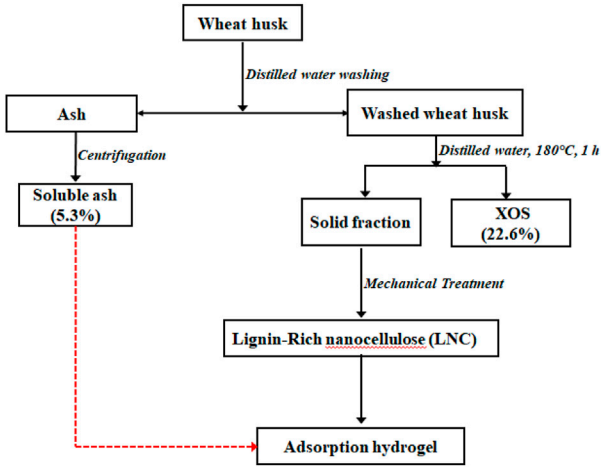

FIGURE 1
Flow diagram of the preparation of soluble ash (SA) and lignin-containing nanocellulose (LCN) of wheat husk.

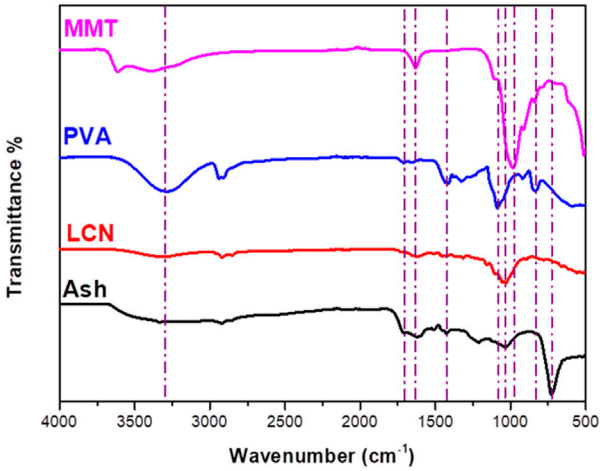

FIGURE 2
FTIR spectra of PVA/LCN/MMT/SA.

(calculated based on the washed ash). 5.0 g of the washed WH was pretreated with 50 mL of distilled water at temperatures (180°C) for 1 h. The XOS yield quantified based on the initial xylan content in the washed WH was 22.6%. The yield of lignin-containing nanocellulose (LCN) obtained from high-pressure homogeneous dispersion of WH residue (WHR) was 99.2% (Figure 1). The FTIR spectra of PVA/LCN/MMT/SA are displayed in Figure 2. The major peaks at 3,614, 1,612, 993 and 910 cm^{-1} of MMT were attributed to the stretching vibrations of OH, Si-O-Si and Al-OH, respectively (Tao et al., 2020). The bands of PVA occurring at 832, 921, 1,085, 1,424 and 3,400 cm^{-1} corresponded to the C–O stretching, $-CH_2$ bending, –CH rocking, –CH and -OH stretching, respectively. The FTIR spectra showed some characteristic peaks that were correlated to the C-OH stretching bonds in the cellulose at 1,033 (secondary alcohol) and 1,052 cm^{-1} (primary alcohol) (Lam et al., 2017). The

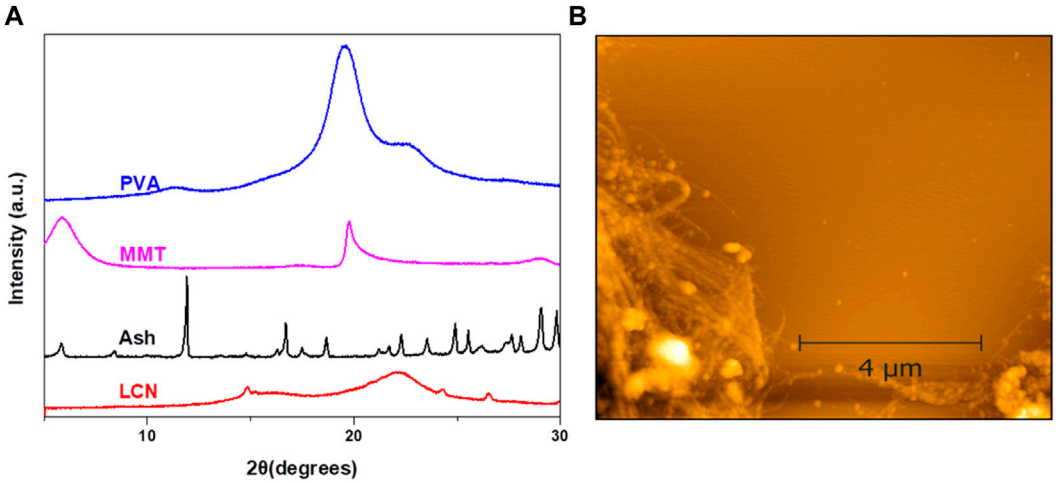

FIGURE 3
(A) XRD patterns of PVA/LCN/MMT/SA; **(B)** AFM image (Scale bar = 1 μm) of LCN.

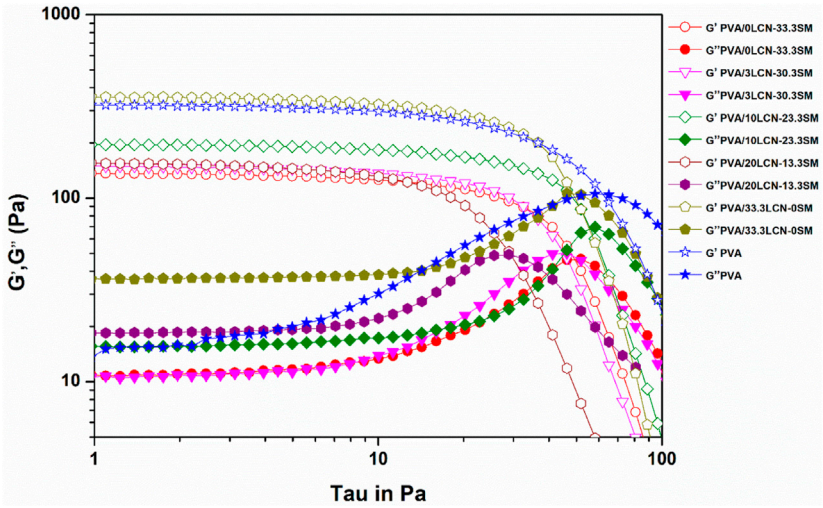

FIGURE 4
Stress scanning of loss modulus (G″) and shear storage modulus (G′) of the hydrogel reinforced by LCN at different loadings.

peak of methoxy group can be assigned at 1,470–1,430 cm^{-1} while the peak of C=C extension of the aromatic hydrocarbon can be found at 1,600–1,460 cm^{-1}. Both peaks in these regions represented the characteristic peaks commonly found in lignin. The carboxyl stretching group was observed around 1732 cm^{-1} in the SA. Then, the Si-O-Si stretching vibration of silicate minerals peak was found at 1,034 cm^{-1}. For the absorption region below 1,000 cm^{-1} is mainly the organic-mineral mixed zone. In this region, the characteristic peaks of different substances interfere with each other and overlap, thus there is no practical reference value (Matamala et al., 2019).

The crystallinity of PVA/LCN/MMT/SA was examined *via* the XRD pattern of each sample displayed in Figure 3A. Based on the results, pure PVA had an orthogonal lattice structure, typical of semi-crystalline PVA, with a diffraction peak at 19.6° (Han et al., 2014). An XRD spectrum of MMT showed the characteristic peak at 6.37°. The XRD spectra of LCN showed two peaks at 16.1° and 22.5°, corresponding to the trigonal structure of cellulose I (Figure 3) with 49.9% crystallinity (Jia et al., 2017). The result indicated that amorphous cellulose was more prone to fracture than crystalline cellulose. The XRD spectra of SA inferred the presence of metal elements (K^+, Na^+, Ca^{2+}, Mg^{2+}) that have a good adsorption effect on MB (Wu et al., 2019). The AFM image showed nanofibers with small widths and narrow size distribution. The result displayed that mechanical treatment was an effective method to prepare LCN with a higher aspect ratio (Figure 3B).

Figure 4 displayed the viscoelasticity tests of PLSM hydrogel at 25°C. Elasticity and viscosity are attributed to storage modulus (G′) and loss modulus (G″), respectively. The loss modulus (G″) of the PLSM hydrogel was lower than the storage modulus (G′), indicating the prepared hydrogels had regular hydrogel

TABLE 2 Physical, rheological and adsorptive properties of the hydrogels at various LCN loadings.

Samples	Moisture content (wt%)	Maximum G′ with LVR, G′ max (Pa)	Maximum G″ with LVR, G″ max (Pa)	Pseudo-first-order kinetic at 40°C (R^2)	Pseudo-second-order kinetic at 40°C (R^2)
PVA	95.4	325.5	14.2	—	—
PVA/0LCN-33.3SM	94.7	136.0	10.4	0.85	0.81
PVA/3LCN-30.3SM	94.8	146.6	10.6	0.98	0.98
PVA/10LCN-23.3SM	94.8	156.5	15.3	0.78	0.98
PVA/20LCN-13.3SM	94.6	194.3	18.4	0.64	0.98
PVA/33.3LCN-0SM	94.8	357.7	36.1	0.88	0.98

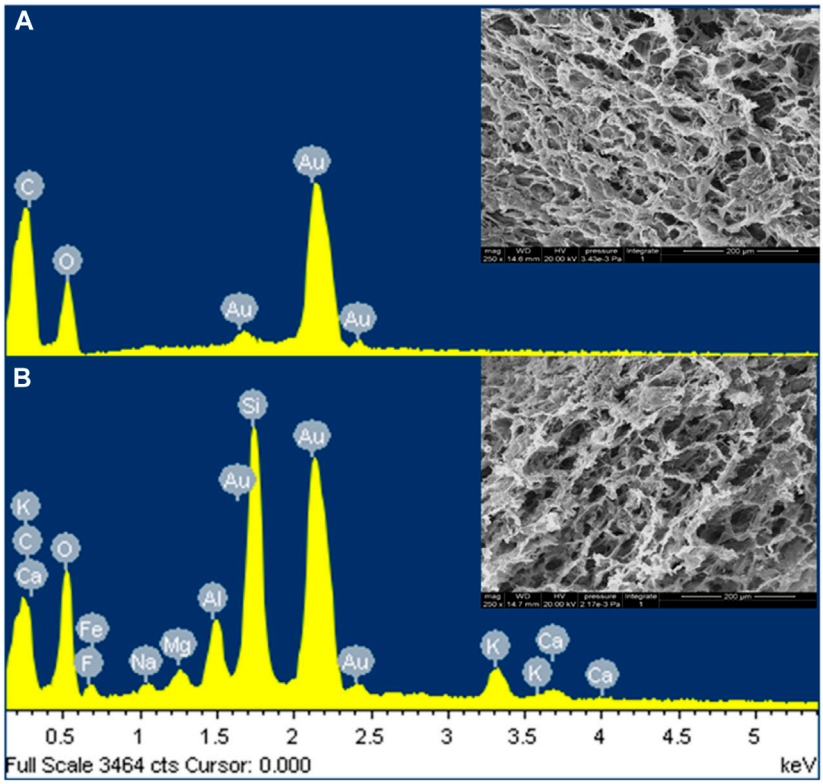

FIGURE 5
The EDX analysis and SEM images of **(A)** PVA and **(B)** PVA/0LCN-33.3SM.

characteristics. The hydrogel flow and stress resistance can be determined by the location and length of the linear viscoelastic regions. The G′ of PLSM hydrogels was 136.0, 146.5, 156.5, 194.3 and 357.7 Pa when LCN was added at 3%, 10%, 20% and 33.3% (Figure 4), respectively. The G′ increased greatly with the increase of LCN dosage. This could be due to the LCN fibrils being long and thin (according to the average height of AFM), which promotes fibril entanglement. Therefore, adding LCN to PVA hydrogels could improve their rheological and mechanical properties (Chang et al., 2008). Comparing pure PVA hydrogels with those containing SM, Table 2 indicated SM decreased rheological and mechanical properties. This may be due to the low molecular weight of SM that reduced the interaction forces between the polymers. PLSM hydrogels with high levels of LCN possess excellent mechanical properties and are therefore suitable for making biomaterials without cross-linking. In addition, the property of having metallic elements on the hydrogels can greatly expand their applications.

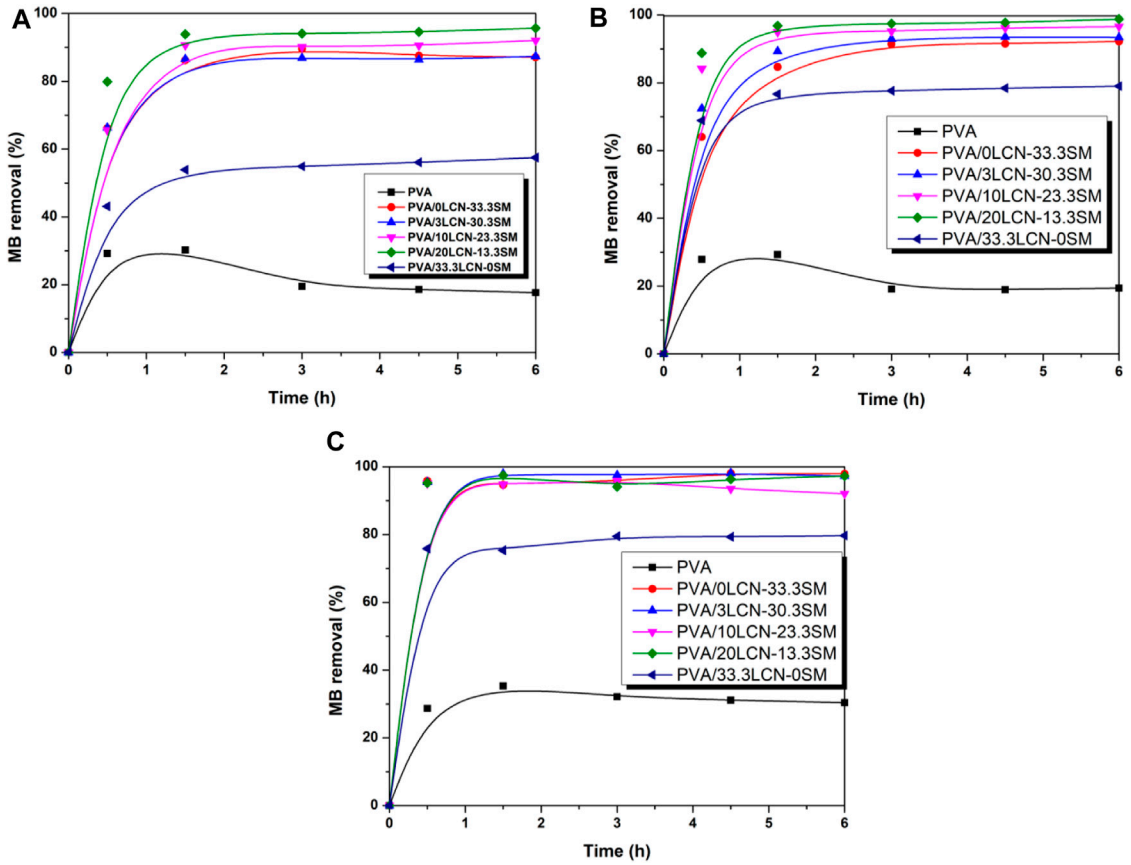

FIGURE 6
Influence of adsorption time on the removal efficiency (R%) of the hydrogels toward 0.25 g/L of MB at **(A)** 30°C, **(B)** 40°C and **(C)** 50°C.

3.2 Characterization of the PLSM hydrogels

The morphological and elemental analyses of the PLSM hydrogels were shown in Figure 5. A microfibrillar structure was observed in PLSM hydrogels. There was homogeneity in the PLSM hydrogel pores, with pore sizes of 40 μm. This porous structure facilitated the swelling of the hydrogels and the diffusion of MB into the interior of the hydrogels. In particular, this structure provided a large specific surface area and abundant active sites, which facilitated the adsorption of MB (Thakur et al., 2017). As can be seen in Figure 5, elemental analysis performed by EDX indicated that the MMT and SA were inserted into the pores of the hydrogel. Moreover, the increased metallic element content was confirmed to be SA embedded in the PLSM hydrogels, suggesting that they were more abundant binding sites in the hydrogels conducive to MB adsorption.

3.3 Absorbing capacity of the PCAM hydrogels

The adsorption efficiency of 0.5 g adsorbent on 0.25 g/L methylene blue (MB) at a contact time of 6 h was investigated. The removal efficiencies of different PCAM hydrogels for MB were shown in Figure 6. The results suggested that the PVA/20LCN-13.3SM sample had the best adsorption capacity and removal efficiency. This could be due to the synergistic effect of the PVA/20LCN-13.3SM sample combined with LCN and SM, thus enhanced adsorption of pollutants by encapsulated LCN and SM was achieved as a result of this synergistic interaction. The MB removal of all hydrogels was quite pronounced at the beginning of 1.5 h and then the slow kinetics persisted until equilibrium. Compared with the adsorption hydrogel prepared by Luo et al., the adsorption efficiency of the hydrogels was higher (Luo et al., 2021). This may be due to the existence of SA which made the crosslinking network of hydrogels loose, which was conducive to the combination of hydrogels and MB.

At different temperatures, hybrid hydrogels removed MB differently as shown in Figures 6A–C. The variation was similar to the kinetic curve reported previously by other literature (Zhu et al., 2023). In spite of the increase in temperature, the removal of MB by hydrogel did not increase significantly. However, the adsorption time was significantly shortened. This could be attributed to an increase in mass transfer driving force (Zhang et al., 2018). The PVA/20LCN-13.3SM sample was adsorbed at 50°C for approximately 1 h, and the removal of MB reached 97.3%. In response to an increase in LCN mass ratio, the adsorption performance decreased. PCAM hydrogel removed only 79.7% of

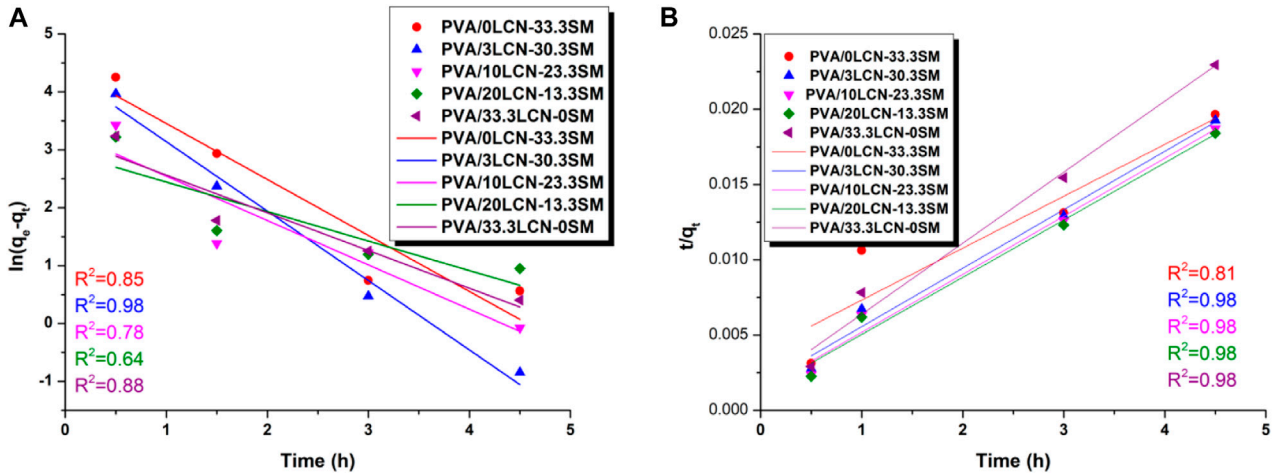

FIGURE 7
Pseudo-first-order **(A)** and second-order kinetics **(B)** of MB by the hydrogels at 40°C.

MB when the LCN content reached 33.3%. The reason could be that MB binds less strongly in LCN than SM; therefore, LCN is not conducive to MB adsorption. It could also be concluded that removing MB with high SM content of hydrogels under high temperatures led to a loosening of the cross-linked hydrogel network, which can rapidly adsorb MB. MMT is the main component of SM that contributed to its high absorbability. The sandwich structure of MMT consists of two tetrahedral layers sandwiched between an edge-bridged octahedral sheet combined with the 3D porous structure that ensures good adsorption performance by providing a large specific surface area. Moreover, the SA fraction contained metal elements (K^+, Na^+, Ca^{2+}, Mg^{2+}), promoting good adsorption effect on MB. Hybrid hydrogels could, however, be mechanically compromised due to the high content of SM. Hence the durability of the product should be investigated further in future work.

3.4 Sorption kinetics of the PCAM hydrogels

An analysis of pseudo first- and second-order kinetic equations of linear form was conducted to study the rate of MB adsorption at 40°C. The kinetic profiles of adsorption were determined during MB adsorption on the hydrogel samples. It was evident that the system was related to the model based on the R^2 of the data with this equation.

Equation of Pseudo-first-order was calculated by Eq. 4

$$\ln\left(q_e - q_t\right) = \ln q_e - \frac{k_1}{t} \tag{4}$$

Equation of Pseudo-second-order was determined by using Eq. 5

$$\frac{t}{q} = \frac{1}{k_2 q_e^2} + \frac{t}{q_e} \tag{5}$$

Where q_t denotes the MB adsorbed capacity (mg/g) at time (t) in hour, k_1 and k_2 denote the pseudo-first- and the pseudo-second-order rate constant of adsorption (g/mg h), respectively, while q_e represents the equilibrium sorption amount (mg/g).

The pseudo first- and second-order kinetic equations of linear form were used to fit this adsorption process as shown in Figure 7. The coefficient of determination of the pseudo-first-order rate constant K_1 was calculated to be greater than that of the pseudo-second-order kinetic constant K_2, and the opposite was true for q_e. This phenomenon was similar to other literature reports (Wang et al., 2022). Moreover, the R^2 values of the pseudo second-order kinetic model were higher than those of the pseudo first-order kinetic model, indicating that the pseudo-second order model was better suited to describe the kinetics of MB dye adsorption on hydrogels (Figures 7A, B). Thus, these findings support that the adsorption rate of MB dye on hydrogels strongly depends on the concentration of MB and hydrogel as well as time (Melo et al., 2018; Sadik et al., 2020). As seen in Figure 7B, the adsorption of MB by PCAM hydrogels at 40°C was consistent with pseudo-second-order kinetics indicating that this adsorption process was a composite multilayer adsorption process. This process was also influenced by the diffusion of the pore network (Bulut et al., 2007; Hubbe et al., 2019).

4 Conclusion

Without the addition of initiators or chemicals, PVA hydrogels with excellent mechanical and adsorption properties were successfully prepared. The mechanical properties of the hybrid hydrogel were altered upon incorporating LCN and SM into the PVA water-based system. Hydrogels containing a high proportion of SM exhibited lower mechanical properties. Due to the low molecular weight of SA in SM, there was less interaction between SM and PVA. Nevertheless, excessive SM content decreased adsorption efficiency. Accordingly, PVA/0LCN-33.3SM can effectively remove 87.1% of MB in 6 h. Lignin did not decrease hydrogel adsorption efficiency, however, and may even increase it. Furthermore, Lagergren's quasi-two-stage

adsorption model was found to explain the removal of MB during the absorption tests, and the results indicated that the adsorption process had taken place on a non-uniform surface. It has therefore been demonstrated in the findings of this study that lignocellulosic materials can be utilized more effectively in wider applications.

Data availability statement

The original contributions presented in the study are included in the article/supplementary material, further inquiries can be directed to the corresponding authors.

Author contributions

KJ and JL: Conceptualization, data curation, formal analysis, experimental design and setup, writing-original draft, funding acquisition. RH: Investigation, experimental design and setup. YX: Conceptualization, management and supervision, writing-review and editing. BK: Data curation, management and supervision. MS: Data curation, methodology and visualization. XZ: Conceptualization and validation.

Funding

This study was supported by the Natural Science Foundation of Jiangsu Province (BK20210623), the Innovation and Entrepreneurship Training Program for College Students of Nanjing Forestry University (2022NFUSPITP0466), and National Innovation and Entrepreneurship Training Program for College Students (202213023009).

Conflict of interest

The authors declare that the research was conducted in the absence of any commercial or financial relationships that could be construed as a potential conflict of interest.

Publisher's note

References

Bian, H., Gao, Y., Dai, H., Jiao, L., Wu, W., Fang, G., et al. (2019). Lignocellulosic nanofibrils produced using wheat straw and their pulping solid residue: From agricultural waste to cellulose nanomaterials. *Waste Manage* 91, 1–8. doi:10.1016/j.wasman.2019.04.052

Bian, H., Wei, L., Lin, C., Ma, Q., Dai, H., and Zhu, J. Y. (2018). Lignin-containing cellulose nanofibril-reinforced polyvinyl alcohol hydrogels. *ACS Sustain. Chem. Eng.* 6, 4821–4828. doi:10.1021/acssuschemeng.7b04172

Bulut, Y., Gözübenli, N., and Aydın, H. (2007). Equilibrium and kinetics studies for adsorption of direct blue 71 from aqueous solution by wheat shells. *J. Hazard Mat.* 144, 300–306. doi:10.1016/j.jhazmat.2006.10.027

Carvalho, A. F. A., Neto, P. O., Silva, D. F., and Pastore, G. M. (2013). Xylooligosaccharides from lignocellulosic materials: Chemical structure, health benefits and production by chemical and enzymatic hydrolysis. *Food Res. Int.* 51, 75–85. doi:10.1016/j.foodres.2012.11.021

Chang, C., Lue, A., and Zhang, L. (2008). Effects of crosslinking methods on structure and properties of cellulose/PVA hydrogels. *Macromol. Chem. Phys.* 209, 1266–1273. doi:10.1002/macp.200800161

Chen, W., Wang, X., Hashisho, Z., Feizbakhshan, M., Shariaty, P., Niknaddaf, S., et al. (2019). Template-free and fast one-step synthesis from enzymatic hydrolysis lignin to hierarchical porous carbon for CO2 capture. *Micropor. Mesopor. Mat.* 280, 57–65. doi:10.1016/j.micromeso.2019.01.042

El-Dib, F. I., Mohamed, D. E., Ei-shamy, O. A. A., and Mishrif, M. R. (2020). Study the adsorption properties of magnetite nanoparticles in the presence of different synthesized surfactants for heavy metal ions removal. *Egypt. J. Pet.* 29, 1–7. doi:10.1016/j.ejpe.2019.08.004

Freitas, G. R., Silva, M. G. C., and Vieira, M. G. A. (2019). Biosorption technology for removal of toxic metals: A review of commercial biosorbents and patents. *Environ. Sci. Pollut. R.* 26, 19097–19118. doi:10.1007/s11356-019-05330-8

Gao, R., Jing, Y., Ni, Y., and Jiang, Q. (2021). Effects of chitin nanocrystals on coverage of coating layers and water retention of coating color. *J. Bioresour. Bioprod.* 7, 201–210. doi:10.1016/j.jobab.2021.11.003

Ge, S., Brindhadevi, K., Xia, C., Khalifa, A. S., Elfasakhany, A., Unpaprom, Y., et al. (2022a). Performance, combustion and emission characteristics of the CI engine fueled with Botryococcus braunii microalgae with addition of TiO2 nanoparticle. *Fuel* 317, 121898. doi:10.1016/j.fuel.2021.121898

Ge, S., Pugazhendhi, A., Sekar, M., Xia, C., Whangchai, K., Brindhadevi, K., et al. (2022b). PM emissions-assessment of combustion energy transfer with Schizochytrium sp. algal biodiesel and blends in IC engine. *Sci. Total Environ.* 802, 149750. doi:10.1016/j.scitotenv.2021.149750

Ge, S., Shi, Y., Xia, C., Huang, Z., Manzo, M., Cai, L., et al. (2021). Progress in pyrolysis conversion of waste into value-added liquid pyro-oil, with focus on heating source and machine learning analysis. *Energy Convers. manage.* 245, 114638. doi:10.1016/j.enconman.2021.114638

Han, J., Lei, T., and Wu, Q. (2014). High-water-content mouldable polyvinyl alcohol-borax hydrogels reinforced by well-dispersed cellulose nanoparticles: Dynamic rheological properties and hydrogel formation mechanism. *Carbohyd. Polym.* 102, 306–316. doi:10.1016/j.carbpol.2013.11.045

Han, Q., Jin, Y., Jameel, H., Chang, H., Phillips, R., and Park, S. (2015). Autohydrolysis pretreatment of waste wheat straw for cellulosic ethanol production in a co-located straw pulp mill. *Appl. Biochem. Biotech.* 175, 1193–1210. doi:10.1007/s12010-014-1349-5

Hubbe, M. A., Azizian, S., and Douven, S. (2019). Implications of apparent pseudo-second-order adsorption kinetics onto cellulosic materials: A review. *Bioresources* 14 (3), 7582–7626. doi:10.15376/biores.14.3.7582-7626

Jia, C., Chen, L., Shao, Z., Agarwal, U. P., Hu, L., and Zhu, J. Y. (2017). Using a fully recyclable dicarboxylic acid for producing dispersible and thermally stable cellulose nanomaterials from different cellulosic sources. *Cellulose* 24, 2483–2498. doi:10.1007/s10570-017-1277-y

Lam, N. T., Chollakup, R., Smitthipong, W., Nimchua, T., and Sukyai, P. (2017). Utilizing cellulose from sugarcane bagasse mixed with poly (vinyl alcohol) for tissue engineering scaffold fabrication. *Ind. Crop. Prod.* 100, 183–197. doi:10.1016/j.indcrop.2017.02.031

Liu, L., Wang, R., Yu, J., Jiang, J., Zheng, K., Hu, L., et al. (2016). Robust self-standing chitin nanofiber/nanowhisker hydrogels with designed surface charges and ultralow mass content via gas phase coagulation. *Biomacromolecules* 17, 3773–3781. doi:10.1021/acs.biomac.6b01278

Liu, T., Wang, P., Tian, J., Guo, J., Zhu, W., Jin, Y., et al. (2022). Polystyrene sulfonate is effective for enhancing biomass enzymatic saccharification under green liquor pretreatment in bioenergy poplar. *Biotechnol. Biofuels.* 15, 10–12. doi:10.1186/s13068-022-02108-y

Liu, T., Zhang, Y., Lu, X., Wang, P., Xiao, H., Tian, J., et al. (2021). Binding affinity of family 4 carbohydrate binding module on cellulose films of nanocrystals and nanofibrils. *Carbohyd. Polym.* 251, 116725. doi:10.1016/j.carbpol.2020.116725

Liu, Y., Huang, Y., Zhang, C., Li, W., Zhang, Y., Zhang, Z., et al. (2020). Nano-FeS incorporated into stable lignin hydrogel: A novel strategy for cadmium removal from soil. *Environ. Pollut.* 264, 114739. doi:10.1016/j.envpol.2020.114739

Lu, C., Blackwell, C., Ren, Q., and Ford, E. (2017). Effect of the coagulation bath on the structure and mechanical properties of gel-spun lignin/poly (vinyl alcohol) fibers. *ACS Sustain. Chem. Eng.* 5, 2949–2959. doi:10.1021/acssuschemeng.6b02423

Luo, J., Huang, K., Zhou, X., and Xu, Y. (2020). Preparation of highly flexible and sustainable lignin-rich nanocellulose film containing xylonic acid (XA), and its application as an antibacterial agent. *Int. J. Biol. Macromol.* 163, 1565–1571. doi:10.1016/j.ijbiomac.2020.07.281

Luo, J., Ma, X., Zhou, X., and Xu, Y. (2021). Construction of physically crosslinked cellulose nanofibrils/alkali lignin/montmorillonoite/polyvinyl alcohol network hydrogel and its application in methylene blue removal. *Cellulose* 28, 5531–5543. doi:10.1007/s10570-021-03847-1

Mao, X., Liu, H. B., Chu, Z. Y., Chen, T. H., Zou, X. H., Chen, D., et al. (2022). Adsorption of lead by kaolinite, montmorillonite, goethite and ferrihydrite: Performance and mechanisms based on quantitative analysis. *Clay Min.*, 1–11. doi:10.1180/clm.2022.41

Matamala, R., Jastrow, J. D., Calderón, F. J., Liang, C., Fan, Z., Michaelson, G. J., et al. (2019). Predicting the decomposability of arctic tundra soil organic matter with mid infrared spectroscopy. *Soil Biol. biochem.* 129, 1–12. doi:10.1016/j.soilbio.2018.10.014

Melo, B. C., Paulino, F. A. A., Cardoso, V. A., Pereira, A. G. B., Fajardo, A. R., and Rodrigues, F. H. A. (2018). Cellulose nanowhiskers improve the methylene blue adsorption capacity of chitosan-g-poly(acrylic acid) hydrogel. *Carbohydr. Polym.* 181, 358–367. doi:10.1016/j.carbpol.2017.10.079

Mohammed, M., Shitu, A., and Ibrahim, A. (2014). Removal of methylene blue using low cost adsorbent: A review. *Res. J. Chem.* 4, 91–102.

Obey, G., Adelaide, M., and Ramaraj, R. (2022). Biochar derived from non-customized matamba fruit shell as an adsorbent for wastewater treatment. *J. Bioresour. Bioprod.* 7, 109–115. doi:10.1016/j.jobab.2021.12.001

Otieno, D. O., and Ahring, B. K. (2012). The potential for oligosaccharide production from the hemicellulose fraction of biomasses through pretreatment processes: Xylooligosaccharides (XOS), arabinooligosaccharides (AOS), and mannooligosaccharides (MOS). *Carbohyd. Res.* 360, 84–92. doi:10.1016/j.carres.2012.07.017

Sadik, A. A., El-Demerdash, A. G. M., Abbas, R., and Gabre, H. A. (2020). Fast synthesis of an eco-friendly starch-grafted poly(n,n-dimethyl acrylamide) hydrogel for the removal of acid red 8 dye from aqueous solutions. *Polym. Bull.* 77, 4445–4468. doi:10.1007/s00289-019-02958-x

Segal, L., Cerrly, J. J., Martin, A. E. J., and Conrad, C. M. (1959). An empirical method for estimating the degree of crystallinity of native cellulose using the X-ray diffractometer. *Text. Res. J.* 29, 786–794. doi:10.1177/004051755902901003

Tang, S., Yang, J., Lin, L., Peng, K., Yao, W., Jin, S., et al. (2020). Construction of physically crosslinked chitosan/sodium alginate/calcium ion double-network hydrogel and its application to heavy metal ions removal. *Chem. Eng. J.* 393, 124728. doi:10.1016/j.cej.2020.124728

Tao, E., Ma, D., Yang, S., and Hao, X. (2020). Graphene oxide-montmorillonite/sodium alginate aerogel beads for selective adsorption of methylene blue in wastewater. *J. Alloy. Compd.* 832, 154833. doi:10.1016/j.jallcom.2020.154833

Thakur, S., Govender, P. P., Mamo, M. A., Tamulevicius, S., and Thakur, V. K. (2017). Recent progress in gelatin hydrogel nanocomposites for water purification and beyond. *Vacuum* 146, 396–408. doi:10.1016/j.vacuum.2017.05.032

Wang, Q., Liu, S., Chen, H., Liu, J., and Zhu, Q. (2022). TEMPO-oxidized cellulose beads for cationic dye adsorption. *Bioresources* 17 (4), 6056–6066. doi:10.15376/biores.17.4.6056-6066

Wu, X., Tang, W., Huang, C., Huang, C., Lai, C., and Yong, Q. (2019). The effects of exogenous ash on the autohydrolysis and enzymatic hydrolysis of wheat straw. *Bioresour. Technol.* 286, 121411. doi:10.1016/j.biortech.2019.121411

Wu, X., Tang, W., Huang, C., Huang, C., Lai, C., and Yong, Q. (2020). Unrevealing model compounds of soil conditioners impacts on the wheat straw autohydrolysis efficiency and enzymatic hydrolysis. *Biotechnol. Biofuels.* 13, 122–129. doi:10.1186/s13068-020-01763-3

Xiao, J., Li, H., Zhang, H., He, S., Zhang, Q., Liu, K., et al. (2022). Nanocellulose and its derived composite electrodes toward supercapacitors: Fabrication, properties, and challenges. *J. Bioresour. Bioprod.* 7, 245–269. doi:10.1016/j.jobab.2022.05.003

Zhang, L., Lu, H., Yu, J., Fan, Y., Yang, Y., Ma, J., et al. (2018). Synthesis of lignocellulose-based composite hydrogel as a novel biosorbent for Cu^{2+} removal. *Cellulose* 25, 7315–7328. doi:10.1007/s10570-018-2077-8

Zhang, X., Tian, J., Wang, P., Liu, T., Ahmad, M., Zhang, T., et al. (2022). Highly-efficient nitrogen self-doped biochar for versatile dyes' removal prepared from soybean cake via a simple dual-templating approach and associated thermodynamics. *J. Clean. Prod.* 332, 130069. doi:10.1016/j.jclepro.2021.130069

Zhou, Q., and Wang, M. (2010). Adsorption–desorption characteristics and pollution behavior of reactive X-3B red dye in four Chinese typical soils. *J. Soil. Sediment.* 10, 1324–1334. doi:10.1007/s11368-010-0247-x

Zhu, H., Chen, S., Duan, H., He, J., and Luo, Y. (2023). Removal of anionic and cationic dyes using porous chitosan/carboxymethyl cellulose-PEG hydrogels: Optimization, adsorption kinetics, isotherm and thermodynamics studies. *Int. J. Biol. Macromol.* 231, 123213. doi:10.1016/j.ijbiomac.2023.123213

Frontiers in
Bioengineering and Biotechnology

Accelerates the development of therapies, devices, and technologies to improve our lives

A multidisciplinary journal that accelerates the development of biological therapies, devices, processes and technologies to improve our lives by bridging the gap between discoveries and their application.

Discover the latest Research Topics

See more →

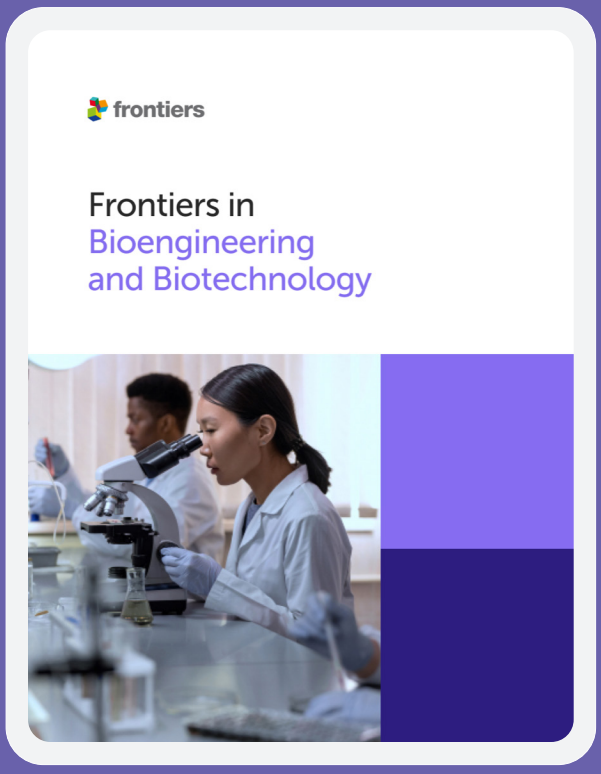

Frontiers

Avenue du Tribunal-Fédéral 34
1005 Lausanne, Switzerland
frontiersin.org

Contact us

+41 (0)21 510 17 00
frontiersin.org/about/contact